UNIVERSITY OF CAPE TOWN
IYUNIVESITHI YASEKAPA • UNIVERSITEIT VAN KAAPSTAD

Department of Chemical Engineering

Centre for Minerals Research

# THE DEVELOPMENT AND APPLICATION OF A SIMULTANEOUS TWO-WAY COUPLED, DISCRETE ELEMENT METHOD AND SMOOTHED PARTICLE HYDRODYNAMIC MODEL FOR SPATIAL SCALE-UP DYNAMICS OF LABORATORY VERTICAL STIRRED MEDIA DETRITORS

**Prepared by:**

DIVINE SSEBUNNYA
BSc (Eng.) Chemical Engineering, 2018

A thesis presented to the Faculty of Engineering and the Built Environment at the University of Cape Town, in fulfilment of the requirements for the degree of Doctor of Philosophy in Engineering

December 2024

**DIVINE SSEBUNNYA**

*The development and application of a simultaneous two-way coupled,*
*discrete element method and smoothed particle hydrodynamic model for spatial scale-up*
*dynamics of laboratory vertical stirred media detritors*

**Supervised by:**

Prof. Aubrey Mainza
*Department of Chemical Engineering, University of Cape Town*

Prof. Stephen Neethling
*Department of Earth Science and Engineering, Imperial College London*

*“you remember their names, you remember your village. so, when the darkness visits,*
*when home seems so far away, start calling all their names and i promise*
*they will come to keep you company.”*

*-Ijeoma Umebinyuo, Questions for Ada*

# ABSTRACT

Stirred grinding processes are becoming more common in industries spanning from ceramics and pigment production to mineral processing. Within the minerals processing industry, stirred milling to produce fine grinds is required to liberate minerals within the more complex ore types. Processing of complex low-grade ore is on the rise due to the depletion of easy to process, high-grade ore bodies. Stirred mills are becoming the dominant mill type for achieving ultrafine grinds within the minerals industry due to their energy efficiency. These mills agitate grinding media, in a chamber with a concentric impeller to facilitate particle size reduction.

The use of laboratory scale systems in the preliminary assessment of the grinding capabilities of larger industrial scale mills is common practice within the industry. For other mill types such as ball mills, methods such as the Bond test are used on laboratory scale mill systems to assess the scale-up effects of the system from laboratory to pilot and industrial scales. However, apart from the signature plot approach, there is no established methodology that incorporates the use of laboratory scale stirred mills in the size reduction scale-up process to larger systems available in the literature. This is because the spatial flow dynamics within stirred mill systems are complex, due to dependencies on multiple parameters spanning from the mill dimensions and design to the grinding media and fluid characteristics. Therefore, the scale-up dynamics, based on media and fluid dynamics within stirred mill systems are not well understood, within the literature.

This study serves to address this through an assessment of spatial scale-up effects on a system of laboratory scale stirred media detritors (SMD). The SMD is a common vertical stirred mill type used to achieve size reduction for fine and ultrafine wet grinding applications. Three scales of laboratory mill systems are assessed as three separate cylindrical vessels using the same concentric impeller shaft and configuration of pins, which vary in length proportionate to the vessel diameter. The flow and energy responses of the mill system are simulated, analysed, and compared across scales.

In the advent of the discrete element method (DEM) and smoothed particle hydrodynamics (SPH), the computational simulation of free surface, particulate, and fluid flow in wet fine grinding mill systems has been executed, with DEM accounting for the grinding media, impeller and mill shell, and SPH accounting for the slurry, modelled as a quasi-compressible fluid. This study presents a two-way coupled DEM-SPH model that computes the DEM and SPH portions of the mill system simultaneously and resolves their interaction forces through a two-way coupling interface. The simultaneous nature of the model provides a significant reduction in the simulation runtime and the feasible SPH resolution. Additionally, a methodology to model media shapes as super quadric surfaces is developed and implemented.

The DEM-SPH model is assessed through analysis of the effects of key variables to gauge its performance prediction capabilities on the largest mill size before its application in the scale-up study. The key variables assessed are media size and density, slurry density and viscosity and media fill. The effects of mill speed and media shape are considered in the scale-up study, with simulations conducted at each of the three mill sizes. The scale-up study considered the spatial distributions within the flow and energy environments and assesses the use of single value quantities, such as dimensionless numbers and intensive variables, as metrics for mill performance. These quantities showed sensitivity to different attributes of mill performance.

# DECLARATION

I, Divine Christine Nalukenge Ssebunnya, hereby declare that the work on which this thesis is based is my original work, except where proper acknowledgements indicate otherwise. Neither the whole work nor any part of it has been, is being, or is to be submitted for another degree in this or any other university.

Signed by candidate

Divine Christine Nalukenge Ssebunnya

# ACKNOWLEDGEMENTS

First and foremost, all glory to God for blessing me with the strength and guidance to see this project through.

I would like to extend my sincerest gratitude to my supervisor Prof. Aubrey Mainza for his guidance and mentorship throughout this journey. I extend the same gratitude to my supervisor Prof. Stephen Neethling for his unwavering support and technical expertise on CSPH_MPI that has added immeasurable value to this project.

I am grateful for the financial support of the Department of Tertiary Education Financing within the Ministry of Tertiary Education, Research, Science and Technology of the Republic of Botswana, through High Commission of Botswana in Pretoria. And in particular, the Office of the Education Attaché, Mr Roy Paledi, for their commitment to supporting me through this program within the uncertain conditions of Covid-19 pandemic.

Special thanks to the Comminution Group within the Centre for Minerals Research for always providing a safe space to dissect and discuss all aspects of this project. I also want to extend gratitude to Tawseef Latona for introducing me to the practicalities of computational simulations. The simulations were performed using facilities provided by the University of Cape Town's ICTS High-Performance Computing team (http://hpc.uct.ac.za).

This endeavour would not have been possible without the support of all my village. I want to express my deepest gratitude to my friends Christopher Mullins and Helda Mandlate whose belief in me has never faltered. And Kalpana Maraj, for being my sounding board and confidante through all stages of this project. Lastly, I would like to thank my parents and siblings for supporting me through this journey.

# TABLE OF CONTENTS

# LIST OF FIGURES

PART ONE: INTRODUCTION, THEORY AND LITERATURE REVIEW

PART TWO: PROBLEM DEFINITION AND SIMULATION METHODOLOGY

PART THREE: RESULTS AND DISCUSSION

APPENDICES

# LIST OF TABLES

# LIST OF ABBREVIATIONS

| | |
|---|---|
| **2D** | Two Dimensional |
| **3D** | Three Dimensional |
| **CAD** | Computational Aided Design |
| **CFD** | Computational Fluid Dynamics |
| **CFL** | Courant-Fredrichs-Lewy |
| **CMR** | Centre for Minerals Research |
| **DEM** | Discrete Element Method |
| **$F_{80}$** | 80% passing size for the feed |
| **LBM** | Lattice Boltzmann Methods |
| **MPI** | Message Passing Interface |
| **MS** | Multi-Sphere |
| **$P_{80}$** | 80% passing size for the product |
| **PEPT** | Positron Emitting Particle Tracking |
| **PBM** | Population Balance Model |
| **PSD** | Particle Size Distribution |
| **SMD** | Stirred Media Detritor |
| **SPH** | Smoothed Particle Hydrodynamics |
| **VTK** | Visualisation Toolkit |

# NOTATION

The following is a guide to the equation notation implemented throughout this thesis.

**Scalar, Vector and Matrix Notation**

- Scalar quantities are indicated in upper- or lower-case italics: $d, \rho, \pi, A \ldots$
- 3D Vector quantities are indicated in upper- or lower-case bold italics: $\boldsymbol{x}, \boldsymbol{v}, \boldsymbol{F} \ldots$
  - The modulus symbol is used to denote vector magnitude: $|\boldsymbol{x}|, |\boldsymbol{v}|, |\boldsymbol{F}| \ldots$
- Second order tensors and matrices are indicated in uppercase bold: $\mathbf{I}, \mathbf{T} \ldots$
- Multiplication between quantities follows the dot product.

**Direction Notation**

- The letters x, y and z are used as direction subscript for the three cartesian dimensions.
- The letters N and n are used as direction subscript for the normal direction.
- The letters T and t are used as direction subscript for the tangential direction.
- The letter r is used as direction subscript for the radial direction.

**Sequence Notation**

- The letter i, j, k and l are used as sequence notation, not to signify direction.
- The letters P and B in summation upper limits are used to signify the SPH particles and DEM bodies, respectively.

**Symbols**

- ′and ″are used to indicate the first and second derivative of a quantity, respectively.
- $^{T}$ is used to represent the transpose of a matrix.
- $^{-1}$ is used to represent the inverse of a matrix.
- The single bar accent ¯ is used to refer to a mean quantity.
- Round brackets () are used to signify multiplication and as function notation.
- Square brackets [] surround quantities inputted into a special function.

**Equation Numbering**

- Equations and expressions are numbered throughout the text in round brackets e.g., equation (13).
- The letters a, b or c after an equation number indicate that the presented equation is descendent from the numbered equation.
- The symbol ′ after an equation indicates that the presented equation is equivalent to the numbered equation but uses different sequence notation.

# PART ONE

# INTRODUCTION, THEORY, AND LITERATURE REVIEW

# CHAPTER 1

# Introduction

## 1.1 Background

Stirred grinding processes are becoming more common in industries spanning from ceramics and pigment production to mineral processing. Within the minerals processing industry, stirred milling to liberate minerals within the more complex ore types is required (Jankovic, 2003). Processing of complex low-grade ore is on the rise due to the decline in easy to process high grade ore bodies.

Stirred mills are the predominant mill type used to achieve ultrafine grinds within the minerals industry due to their apparent energy efficiency compared to other mill types (Wang & Forssberg, 2007). These mills agitate grinding media, which can be balls, beads, smelter slags or sands, in a chamber with a concentric impeller to facilitate particle size reduction. The ball and beads are made of steel or ceramics. Breakage is primarily achieved through the attrition and abrasion of particles between grinding media, induced by large shear forces within these mills. There is also impact breakage, but it is not as dominant as in tumbling mills.

The use of laboratory scale systems in the preliminary assessment of the grinding capabilities of larger industrial scale mills is common practice within the industry. For other mill types such as ball mills, methods such as the Bond test are used on laboratory scale mill systems to assess the scale up effects of the system from laboratory to pilot and industrial scales. For stirred mill systems, apart from the signature plot approach, there is no established methodology that incorporates the use of laboratory scale stirred mills in the scale up process to larger systems, available in the literature. The complex flow dynamics within stirred mill systems, due to dependencies on multiple parameters spanning across the mill dimensions and design, the different impeller types, and the grinding media and feed characteristics, are challenging to decouple and incorporate within scale-up processes. Therefore, the spatial scale-up dynamics within stirred mill systems are not well understood, within the literature.

This study will assess scale-up effects on a system of laboratory scale stirred media detritors (SMD) using computational models involving the discrete element method (DEM) and smoothed particle hydrodynamics (SPH). The DEM-SPH coupled system will be used to simulate the interactions within the mill system to predict both the flow and energy environment. The flow and energy responses of the mill system for different operating conditions are then analysed and compared across the three laboratory SMDs.

The SMD is a common vertical stirred mill type used to achieve size reduction for fine and ultrafine wet grinding applications. The SMD uses an impeller type, consisting of pins attached perpendicular to an axial shaft. The design of the laboratory scale system has been simplified and consists of three sizes of vertical cylindrical vessels with a concentric impeller shaft, with cylindrical pins attached. Consequently, three scales of mill systems were assessed using the same impeller shaft and configuration of pins, with different lengths for each mill size, at a constant pin length to mill radius ratio.

Computational modelling using a two-way coupled DEM and SPH model allows one to track the motion of the grinding media and impeller through DEM, and the mineral slurry as a fluid through SPH, within the confines of the mill vessel. The methods use a lagrangian framework to determine motion characteristics such as position and velocity of the media and the fluid through timesteps. The computational model used in this study uses a two-way simultaneous coupling framework to allow each method to determine and incorporate the relevant interaction forces between the phases back to itself. The coupling interface facilitates the simultaneous solving of DEM and SPH through a unique algorithm. This differs from asynchronous coupling interfaces reported in literature, which alternate between solving one of the two methods.

The computational methodology provides information on the system that cannot be determined through standard physical laboratory experimentation. This allows for analysis of each mill system as a three-dimensional spatial environment. The changes of which can be assessed through condensing and coarse graining the system into two-dimensional figures and one-dimensional variables.

## 1.2 Objectives

The aims of this study are to:

- Develop a DEM-SPH model capable of effectively modelling the flow and energy environment of a stirred mill. The model sets out to simultaneously solve grinding media motion through DEM and slurry motion through SPH, with the phase interactions resolved through a two-way coupling.
- Assess the predictive performance of the model by analysing the effect of critical variables on the mill environment.
- Establish a computational methodology to model different media shapes using super quadric surfaces and use it within the DEM-SPH model to examine the effect of media shape on the three laboratory scale systems.
- Analyse the effects of scale across the three laboratory scale systems through spatial analysis and the use of single value parameters to quantify the relative mill state.

## 1.3 Scope and limitations

The study facilitates the development of coupled computational simulations of three sizes of laboratory scale stirred media detritors. The three mills replicate the three laboratory-scale stirred media detritors used in the Centre for Minerals Research (CMR) minerals laboratory at the University of Cape Town and are to scale in the cylindrical and impeller dimensions.

The simulations are conducted using two-way coupling of Discrete Element Methods (DEM) and Smoothed Particle Hydrodynamics (SPH). The grinding media and mill environment is modelled through DEM while the fluid flow is modelled using SPH. The DEM model uses a Hertz-Mindlin no-slip contact model with viscous damping to define the interactions between components. The mill systems are simulated using proprietary SPH framework developed at Imperial College London. The data outputted by the model is analysed at an effective steady state, with five revolutions of data considered per simulation. The five revolutions are quantified as simulation output in centisecond intervals, providing a minimum of 100 samples of the spatial mill environment assessed for each simulation. Furthermore, each impeller revolution can be considered as a repeatable event with five occurrences within the data sample.

The first portion of the study is focused on the predictive performance of the computational method on the stirred mill system. This analyses the effect of five variables on the model output using the smallest and largest scales of the mill system. The variables investigated are media size and density, slurry density and viscosity and the media fill. This analysis compares the model output against expected trends found in the literature.

The second portion of the study analyses the effect of scale on the mill system by considering the effect of increasing the impeller tip speed simultaneously across the three mill scales. The effects on the flow and energy environment are compared through spatial analysis and the use of scalar variables to quantify the relative mill state.

The final portion of the study investigates the effect of media shape to assess how using non spherical shapes affects the flow behaviour in the mill system. This investigation uses super quadrics to vary the sphericity of the media bodies into three distinct groups of decreasing roundness. The effects of these groups on the three mill scales are compared against the middle speed run of spherical particles using spatial analyses techniques.

## 1.4 Plan of development

This thesis is divided into parts and chapters to ensure that the plan of development is captured in a manner that is easy to follow. Parts are used to group related chapters within the thesis. The overall document structure is as follows:

**PART ONE**: This part contains the introduction, theory, and literature chapters.

CHAPTER 1: This chapter introduces this study by providing a background to this study as well as its objectives and scope.

CHAPTER 2: Relevant theory and literature on stirred milling comminution is provided in this chapter.

CHAPTER 3: Relevant theory and literature on the computational methods used in this study is presented in this chapter.

CHAPTER 4: Relevant literature on the application of computational methods on stirred mills is examined in this chapter.

**PART TWO**: The thesis problem is defined, and the experimental plan is outlined in this part.

CHAPTER 5: The problem statement, hypotheses and key questions of this study, based on the literature, are provided.

CHAPTER 6: The methodology of the computational model and the experimental plan of the study are established in this chapter.

**PART THREE**: All the results and discussion chapters are contained in this part.

CHAPTER 7: This chapter presents and discusses the results of the performance prediction simulations.

CHAPTER 8: This chapter presents and discusses the results of the tip speed scale-up comparison simulations.

CHAPTER 9: This chapter presents and discusses the results of the media shape scale-up comparison simulations.

**PART FOUR**: Conclusions and recommendations on the study are provided in this part.

CHAPTER 10: The main conclusions from the study are given prominence in this chapter, and recommendations relevant to the work carried out in this thesis are given.

# CHAPTER 2

# Theory and Literature on Stirred Milling

## 2.1 Introduction

This chapter is focused on reviewing the literature on stirred media milling in general to use as a basis for this study that is concerned with the effects of scale up in stirred media mills using computational modelling. It begins by discussing and defining relevant comminution mechanisms and establishing the role of stirred mills within the minerals industry. It then distinguishes the various types of stirred mills and defines their critical variables. Literature that provides the tools required to quantify the scale up effects on stirred mills systems is also considered. The chapter then closes with a summary on stirred media milling.

The chapter serves to provide an empirical perspective on the study, before introducing computational methods and evaluating their theoretical agreement to experimental output in the following chapters.

## 2.2 Comminution

Comminution refers to process of reducing the particle size of solid particles, in this case mineral ores. Comminution devices are designed to achieve size reduction by optimising the frequency and the stress intensity of breakage events (Blecher, Kwade & Schwedes, 1996). In the mining industry, these units form the first stage of ore processing, when run in circuit with internal and external classification systems. These circuits ensure that the particle size distribution of the ore is reduced to enable effective separation in the downstream processes such as flotation and leaching.

The comminution grinding circuit forms the most energy intensive stage of most mining operations, hence requiring high capital investment and budget to defray operating costs. Therefore, there is a keen financial incentive to improve the energy efficiency of comminution devices. Furthermore, the declining ore grade of many minerals has led to the processing of ore types with smaller more complex ore deposits (Jankovic, 2003). These requires further grinding to liberate these minerals, which adds additional fine-ultrafine grinding stages onto the already energy intensive comminution circuit.

### 2.2.1 Breakage mechanisms

The particle breakage observed in comminution devices can be characterized through three breakage mechanisms, as the result of different types of stress on a particle. These are impact, compression and abrasion/attrition breakage (Gao & Forssberg, 1995). An interpretation of the isolated effects of each breakage type is visualised in Figure 2.1, along with their respective particle size distributions.

Impact breakage can occurs as the result of swiftly administered high energy stresses, normal to the particle, which cause massive fractures within the particle structure, resulting in a wide particle size distribution (Kelly & Spottiswood, 1982; Gao & Forssberg, 1995; Hogg, 1999). Compression can occurs as a result of relatively intense stresses being applied slowly on a particle. This facilitates breakage along existing grain boundaries, producing a narrow distribution of similarly sized particles.

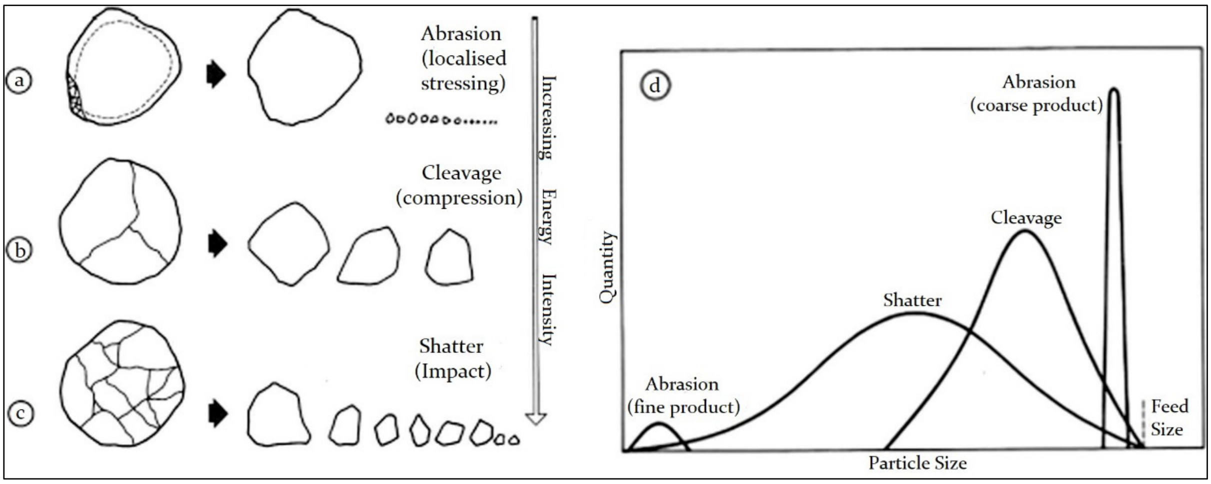

*Figure 2.1: The breakage mechanisms a) attrition/abrasion, b) compression, c) impact and d) their associated particle size distributions. Adapted from Hasan et al. (2017).*

The abrasion and attrition mechanisms are often used interchangeably and interpreted as one breakage mechanism, as they often occur simultaneously as a result of low intensity stresses on the particle surface (Kelly & Spottiswood, 1982; Gao & Forssberg, 1995; Hasan et al., 2017). Studies on agglomerate breakage (Beekman et al., 2002; van Laarhoven et al., 2008) defined the two breakage mechanisms, as the normal and tangential components of the same force, which typically acts at an oblique angle. This is the definition of these mechanisms used in this study. Attrition is defined as the normal component which results in the breakage of the edges on the particle, while abrasion is attributed as the tangential component, which generates a fine dust, through rolling and sliding of the particle. The combined effect results in a bimodal distribution, of distinctly fine and coarse products, with an overall smoothing effect on the parent particle (Kelly & Spottiswood, 1982; Hogg, 1999; Hasan et al., 2017). The two modes of the distribution are representative of the two mechanisms, which are visualised separately in Figure 2.2.

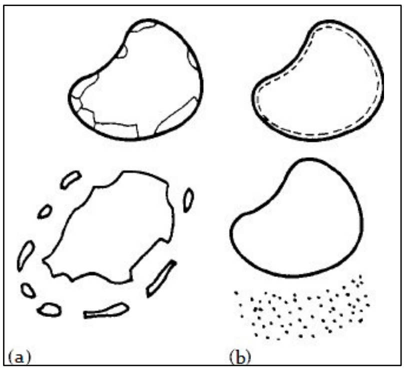

*Figure 2.2: a) Attrition and b) abrasion breakage adapted from Daouadji & Hicher (2010)*

Though the primary breakage mechanism is typically easily identifiable from the particle size distribution and collision analysis, the breakage mechanisms rarely act independent of each other. The ability of a breakage mechanism to produce desired results is dependent on the particle's physical properties, with impact and compression facilitating internal particle breakage by targeting flaws and creating fractures withing the particle body, while abrasion/attrition breakage focuses on surface level deformation and chipping.

### 2.2.2 Grinding mills

The stages of comminuting mineral ore are typically blasting, crushing and grinding, in order of decreasing particle size. This study is focused on stirred media mills, which form part of the grinding stages in a comminution circuit. Within grinding, the comminution devices are employed based on their energy efficiency, which is compared using the ratio of energy input to mass of product as the specific energy input, and their ability to achieve a specific product size, which is influenced by the grinding techniques, operating conditions and geometry of the particular mill type. Wang & Forssberg (2007) reported specific energy requirements for various grinding mill types against their feed and product ranges from their 1981 data shown in Figure 2.3. The size ranges of the mill products are subdivided in this context as coarse (>100 μm), intermediate (100-10 μm), fine (10-1 μm) and ultrafine (<1 μm) (De Bakker, 2014).

Though the advances in mill technology over time may have altered the specific energy requirements, the operation of each mill type to achieve a particular product size remains fairly consistent. From the Figure 2.3, only the pin mill, fluid energy mill and stirred bead mill type are used to achieve a fine-ultrafine grind. The pin mill and the stirred bead mill are both types of stirred media mills. The different varieties of ball mills can comfortably serve the intermediate-fine grind range, with the other mill types producing coarse-intermediate grinds.

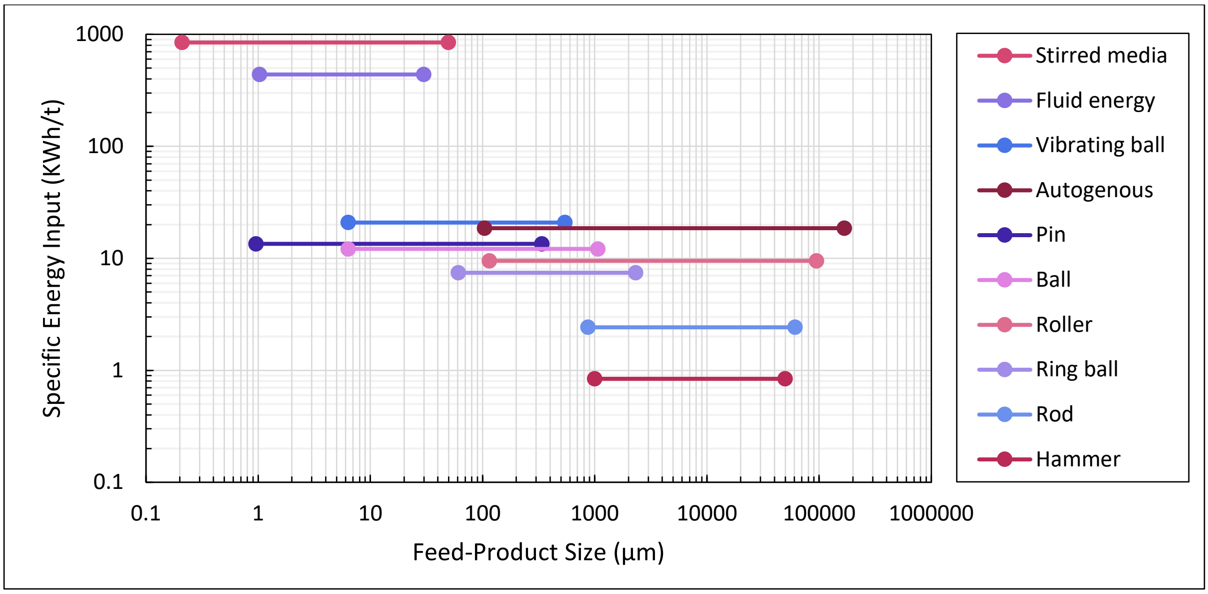

*Figure 2.3: Summary of historical data showing feed and product size results of various mill types and the resultant specific energy input. Adapted from Wang & Forssberg (2007)*

A study into the energy efficiency of stirred media mills by Gao & Holmes (2007) compared the grinding performance a stirred media mill, the IsaMill, against the ball mill, as the next mill type closest in product output, using both to achieve a product with the same $P_{80}$ from the same feed.The PSDs of the feed and the IsaMill and ball mill products are presented in Figure 2.4, along with data from the power draw and throughput that resulted in the product PSDs. This data showed that the stirred media mill maintains a lower specific input energy and requires a shorter time period to produce a product with the same P80 as the ball mill. This indicates a significant difference in the mill dynamics of the two systems that favours stirred media milling for fine grinding. Hence, stirred media mills are used primarily in the additional fine-ultrafine grinding circuits implemented in processing operations to adapt to complex ore deposits (Rule, 2010; Keikkala, Lehto & Roitto, 2015; FLSmidth (Pty) Ltd, 2019).

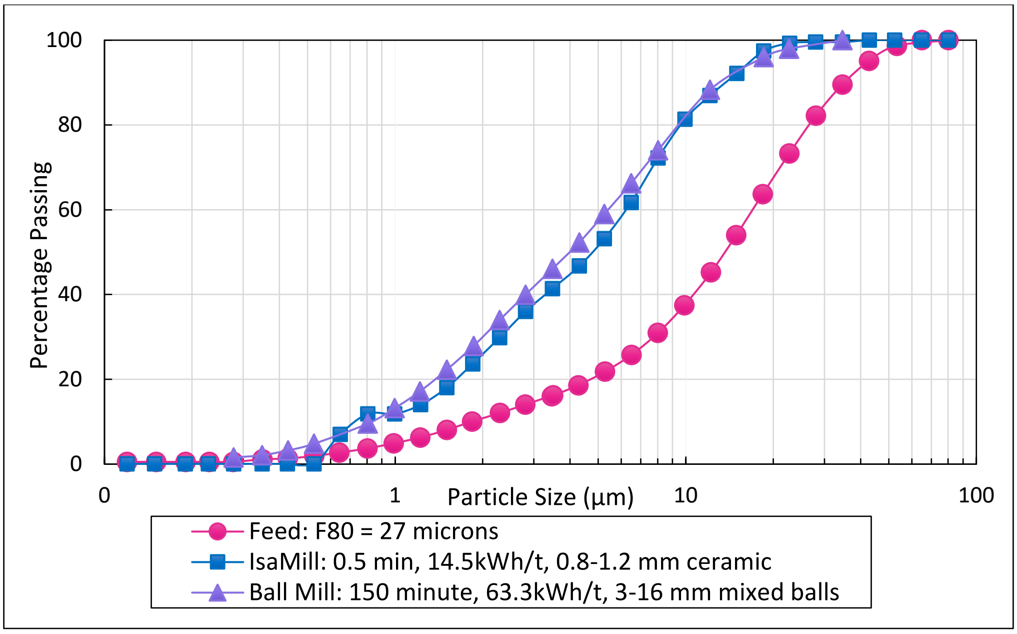

*Figure 2.4: Fine grinding performance comparison between a ball mill and stirred media IsaMill. Adapted from Gao & Holmes (2007).*

## 2.3 Stirred media milling

With origins in surface cleaning by attrition, stirred media milling principles can be dated back past the 1940s (Stehr & Schwedes, 1983; Napier-Munn et al., 2005). The early applications evolved to fine grinding mills used in multiple industries primarily for fine grinding purposes. Stirred media mills in this context are restricted to horizontal or vertical mills with a single concentric impeller, used in the minerals processing industry. The mills are operated industrially in continuous circuit in conjunction with internal (Rule et al., 2008) or external (Swann, Martin & Gurnett, 2023) classification units. These mills use grinding media, typically steel balls, or glass and ceramic beads, to achieve fine to ultrafine grinds. This can either be through wet or dry milling (Zheng, Harris & Somasundaran, 1996). Key distinctions between wet and dry milling noted in the works of Zheng, Harris & Somasundaran (1996), and Kwade & Schwedes (2007) have been that wet milling results in higher fine product, lower agglomerate formation and product loss and lower energy consumption and higher energy efficiency.

This study focuses on the computational modelling of wet stirred media mills, as the fluid motion in wet milling is more adeptly modelled computationally in comparison to the current means of incorporating powder flowability into dry milling models. The computational modelling of either system does not consider the particle size reduction aspect of the grinding in the spatial mill models, instead focuses on the distribution of energy and the flow of grinding media within the mill.

This section discusses the grinding techniques used in stirred media mills as well as the prevalent mill types used industrially, and key variables. This is to set a basis of understanding for how the stirred mill achieves fine-ultrafine grinds from a black box perspective, before correlating the mill output to the internal spatial flow and energy distributions in the following section.

### 2.3.1 Grinding techniques

The primary breakage mechanism in stirred mills is attrition/abrasion breakage, characterised by dominant shearing forces during collisions. This has been well established through the early works of Mankosa, Adel & Yoon (1986), Rydin, Maurice & Courtney (1993), and Kwade (1999) and further supported by stirred mill computational models (Sinnott, Cleary & Morrison, 2006; Kim & Choi, 2008). To achieve this breakage mechanism, stirred mills are designed to use one of two grinding techniques: gravity-induced grinding or fluidized grinding (Ntsele & Allen, 2012). The mills are designed such that they ensure effective contact between the two phases, through either technique. The grinding technique influences the shape and operating speed of the mill stirrer, and for gravity induced grinding, the orientation.

Gravity-induced grinding relies on dense media and gravitational forces to induce grinding through gravity settling (Ntsele & Allen, 2012), hence a vertical orientation is used. This technique uses helical screw impellers. The motion of the screw impeller forces downward flow of media at its edges, which contacts slurry on its descent. Media is pulled upward by the screw at the centre to fall over the edge again, aided by the velocity gradient along the screw radius.

In fluidised grinding, the stirred mill impeller is run at a high speed to fluidise the media and slurry within the bed. This technique is reliant on low density media and high tip speeds, for easy fluidisation. Defining or quantifying the fluidised state in these systems is complex due to the motion of the grinding media and slurry being confined to flow fields brought about by the rotation of the impeller (Conway-Baker et al., 2002). The purpose of fluidising the bed is to ensure that the slurry dilates into the media, allowing for slurry to be present in between each media collision (Ntsele & Allen, 2012). Therefore, the porosity and solids fraction are pseudo-indicators of the fluidised state. The mills that utilize this technique commonly have disk or pin type impellers in either horizontal or vertical orientation.

### 2.3.2 Mill types

There are two main characteristics that differentiate stirred media mill types: orientation and grinding technique. Orientation in industrial stirred mills is limited to horizontal or vertical, therefore the key distinction between mill types is in the grinding technique of the mill. These characteristics are directly reflected in the six primary stirred media mill types considered commercially in the mining industry (Radziszewski & Allen, 2014). These are the IsaMill (Glencore Technology, 2015), VXPmill (FLSmidth A/S, 2011), HIGMill (High Intensity Grinding Mill) (Astholm, 2015), the "Tower Mill" variants (Eirich Technology, 2018; FLSmidth, 2024; Magotteaux, 2024), VertiMill and the Stirred Media Detritor (SMD) (Metso, 2019). Each mill type is available at various sizes within the laboratory to industrial scale. The characteristics of these mill types are summarised in Table 2.1, with each mill type subsequently expanded on. It is key to note the media type and sizes used by the mill type as well as the upper limits for the 80% size passing for the mill feed ($F_{80}$) and product ($P_{80}$). The power intensity of the mill is indicative of the power transferred to the media and slurry/powder through the impeller.

*Table 2.1: Summary of stirred media mill technologies, adapted from Plochberger & Avila (2014)*

| | Producer | Orientation | Impeller type | Power intensity (KW/m$^2$) | Installed power (MW) | Media (mm) | $F_{80}$ (mm) | $P_{80}$ (µm) |
|---|---|---|---|---|---|---|---|---|
| IsaMill | Glencore | Horizontal | Discs | <300 | Up to 7.5 | 1.5-6<br>ceramic | <0.5 | <7 |
| VXPmill | FLSmidth | Vertical | Discs | — | Up to 3 | 1.5-12<br>ceramic | <0.07 | <20 |
| HIGMill | Outotec | Vertical | Discs | 100-200 | Up to 5 | 0.5-6<br>steel,<br>ceramic | <0.3 | <20 |
| Tower Mill | Eirich<br>FLSmidth<br>Magotteaux | Vertical | Screw | — | Up to 1.1 | chromium,<br>steel | <3 | <20 |
| VertiMill | Metso | Vertical | Screw | 30-50 | Up to 2.2 | 5-38<br>steel,<br>ceramic | <6 | <15 |
| SMD | Metso | Vertical | Pins | 100-200 | Up to 1.1 | 1-8<br>sand,<br>ceramic | <0.25 | <5 |

The IsaMill is a horizontal stirred mill developed by Netzsch Gmbt and Mount Isa Mines, now distributed through Glencore. It uses the fluidised grinding technique with a perforated disk impeller and cylindrical mill shell as seen in Figure 2.5. The mill is fed centrally through one end and run in a continuous operation, with internal classification at the discharge end (Gao & Holmes, 2007; Jankovic, 2008).

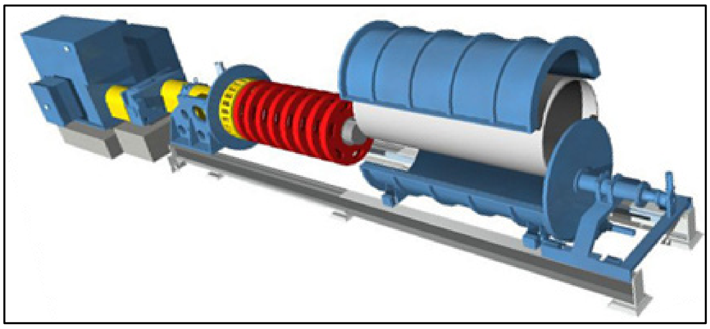

*Figure 2.5: IsaMill (GlencoreTech, 2020)*

The VXPmill and the HIGMill are both vertical disk mills with cylindrical shells and perforated disk impellers. Both mills feed slurry continuously through the bottom and discharge at the top, employing fluidised grinding as the slurry travels up through the disks. The VXP was developed by FLSmidth, and has been used in the ultrafine grinding circuit in the Kibali gold mine in the Democratic Republic of Congo (FLSmidth (Pty) Ltd, 2019). The mill power intensity is reported to be between the low-speed, gravity induced mills, and the more high-speed mills, allowing for a customisable application. The HIGMill developed by Outotec, now Metso Outotec, is also known as the VRMmill when distributed under Swiss Tower Mills AG (Swiss Tower Mills AG, 2025). It is designed with stationary baffles along the mill shell in between the zimpeller disks, to direct the slurry to key grinding zones. The HIGMill is commonly employed in circuits with prior classification by hydrocyclone to avoid over grinding (Keikkala, Lehto & Roitto, 2015).

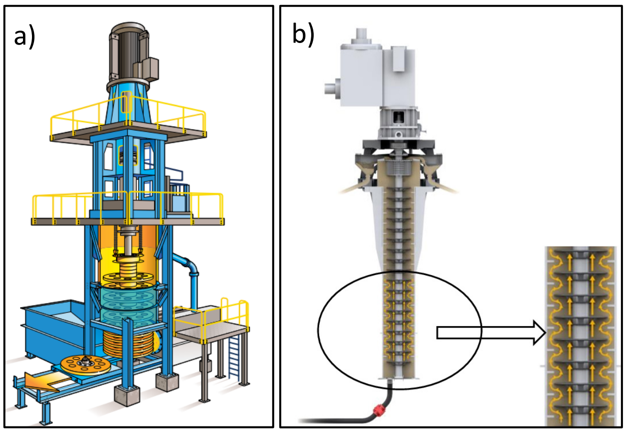

*Figure 2.6: a) VXPmill* (FLSmidth A/S, 2011) *and b) HIGMill (Astholm, 2015)*

In 1953, the Nichitsu Mining Industry Co., Ltd developed a mill under the name “Tower Mill” which consisted of a cylindrical mill shell with a double helical screw impeller. Currently, there are three variants of mills that can be referred to as “Tower Mills” and follow from its original design. These mills are the TowerMill supplied by Nippon-Eirich (Eirich Technology, 2018), the FLS Tower Mill by FLSmidth (FLSmidth, 2024) and the Vertical Tower Mill by Maggoteaux (Magotteaux, 2024). The Nippon-Eirich Tower Mill is pictured in Figure 2.7 a) alongside the VertiMill Figure 2.7 b). The VertiMill is a derivative of the original Tower Mill acquired by Metso (Jankovic, 2008). All these mills consist of a cylindrical mill shell with a helical screw impeller. Of the mill types considered, the “Tower Mill” variants and VertiMill are the only mills that use primarily gravity induced grinding techniques. Because of its grinding technique it can use the largest media sizes of up to 38 mm. Slurry is fed continuously from the bottom of the mill and exits out the top. The VertiMill product grind is comparable to that of a ball mill (Ntsele & Allen, 2012).

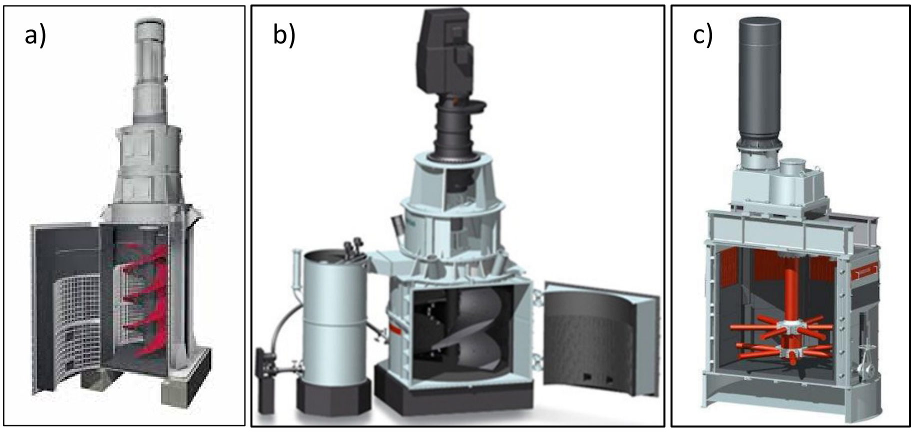

*Figure 2.7: a) Tower Mill* (Eirich Technology, 2018) *b) VertiMill and c) SMD (Metso, 2019)*

The SMD was developed by Metso from sand mills used in the pigment industry for deagglomeration (Jankovic, 2008). Similar to the VXPmill, HIGMill and IsaMill, the SMD uses the fluidised grinding technique. It is vertically orientated, with an octagonal prismatic mill shell and a pin type impeller. The impeller is suspended at a characteristic height from the base of the mill. The pins are arranged in two staggered layers of 6 evenly distributed pins. The mill is fed from the top and operates continuously, using screens at the discharge end on the side to retain the grinding media (Allen, 2013). The laboratory scale of this mill type is used in this study. The specific and full description of the mills used in this study are given in section 6.3.1.

### 2.3.3 Critical variables in stirred milling

There are many variables to consider in the design and operation of stirred mills. These can be subdivided into design variables: these are variables associated with the physical mill design, operating variables: these relate to the mill operation, material variables which relate to properties of the grinding media and the slurry, and interaction variables that govern the relations between the mill elements (Jankovic, 2003; Kwade & Schwedes, 2007; Radziszewski & Allen, 2014). The critical variables discussed in this section are the operating variables of mill speed and fill level, and the material variables of media size, shape and density, and slurry density and viscosity. These variables are chosen as their influence is comparable across mill types. The influences of the variables are considered in fluidised grinding systems, as the mills in this study utilize this grinding technique. Other key variables not investigated include the use of additives to reduce agglomeration and flocculation within the mill, and the mill operation mode, grinding time and throughput. These are excluded from the review because they are not part of the scope of the investigation in this thesis.

This section considers the effects of these variables through a black box directly to the mill outputs of the product particle size distribution and power draw, hence considering only experimental studies. The implications of variables on the spatial mill environment of the laboratory SMDs are considered through experimentation in section 2.4.2 and through predictive computational modelling in section 4.3. This layered approach serves to link the output to mechanisms within the mill internal environment through demonstrated experimentation, to further understand and verify the predictions of computational models.

#### *2.3.3.1 Media size, shape and density*

The grinding media used in stirred mills is either steel, ceramic or sands. For fluidised grinding, the chosen material should balance a high hardness to ensure powerful collisions and a low density to fluidise at easily at low speeds (Gao & Holmes, 2007). He & Forssberg (2007) showed that high-density media is more effective than low-density at low speeds, but as the speed increases the stress intensity of the high-density beads is greater than the slurry requires for breakage, resulting in low energy efficiency. Which supports the use of the different media types for the different grinding techniques. This is the primary reason low-density ceramic media is favoured over steel, which can contaminate the mill product for downstream processes as it wears into the slurry, unlike inert ceramics. The material wear time is an important factor when choosing media, as the rate of replacement adds to the expenditure.

The shape of the media has been challenging to vary experimentally, but studies have claimed that the grinding performance is altered as the material wears (Cho, Waters & Hogg, 1996; Becker & Schwedes, 1999). The wearing down of the media has been shown to increase the coarseness of the PSD in stirred mills (Cho, Waters & Hogg, 1996). Though grinding media is rarely perfectly spherical, lower wear rates were found with rounder media (Becker & Schwedes, 1999). The media material hardness and the feed hardness are very influential in the wear rate as harder media materials wear down slower overall, but the softer feed wears media slower (Kwade & Schwedes, 2007). This is an additional influential parameter to consider when choosing media. The direct influence of media shape has been isolated computationally by Sinnott, Cleary & Morrison (2011b).

Media size is said to be the most important parameter in stirred milling, due to its influence of the product breakage as well as the mill energy consumption (Gao & Holmes, 2007; He & Forssberg, 2007). The relationship between the media size and the particle top size is a highly influential factor in the breakage product. The media size should be large enough to effectively capture and break the largest feed particles and grind the product to the required fineness (De Bakker, 2014). Heuristically, in order to achieve this, the media size should range between 20-30 times the $F_{80}$ (Mankosa, Adel & Yoon, 1986; Gao & Holmes, 2007). Though, this is dependent on the feed and media material properties (Zheng, Harris & Somasundaran, 1996). Increasing media size has been shown to result in a tighter PSD (Gao & Holmes, 2007). De Bakker (2014) studied the effect of changing the media size used in laboratory scale SMDs from 1 mm to 3 mm at Century Mine. This resulted in a 50 % energy reduction as well as a decrease in the fines produced and more effective top size breakage, resulting in a tighter particle size distribution (PSD). Depending on the mode of operation, the size distribution of the grinding media should adapt to the changes in the particle size within the mill. Patel, Chakraborty & Murthy (2014) manipulated the proportion of fine to coarse media to study how the distribution effects the energy consumption and the product PSD. Overall, the choice of media size requires consideration of feed and product PSDs and mill energy consumption.

#### *2.3.3.2 Slurry density and viscosity*

Slurry rheology has an influence on the breakage performance of stirred mills. The rheology is characterised by the relationship between the shear rate and apparent viscosity. This relationship is influenced by the size, shape and distribution of the solid particles, the solids concentration, surface properties, fluid viscosity and other parameters. Decoupling the effects of rheologically influential variables listed in this section in an experimental framework is complex due to interdependencies when manipulating parameters (Jankovic, 2003).

Rheological characterisation of different mineral slurries used in stirred mills has been conducted in literature (Bernhardt, Reinsch & Husemann, 1999; He, Wang & Forssberg, 2004, 2006; He & Forssberg, 2007). Within these studies, solids concentration emerged as a key variable, due to its interdependencies with the density and apparent viscosity of the slurry. Multiple studies report that there is an optimum solids concentration that balances the benefits of increasing the density of the slurry, before the negative viscosity effects take over (Jankovic, 2003; Gao & Holmes, 2007; Kwade & Schwedes, 2007). The optimum solids concentration is dependent on the mineral ore characteristics and has been shown to decrease with increased product fineness (Gao & Holmes, 2007; Kwade & Schwedes, 2007).

Kwade & Schwedes (2007) defined the effect of increasing the solids concentration as increasing the number of particles per given volume. They correlated this to increasing the number of possible stress events, which increase the overall grinding efficiency. The disadvantage of this is that as the particles break, the slurry fineness increases resulting in increased apparent viscosity. When the viscosity gets too high, the energy required to displace the fluid through media collisions to allow particle breakage increases beyond what the media can provide, thus causing a decrease in the grinding efficiency. The negative viscosity effect makes it challenging to operate at high solids concentrations to produce a very fine product without the use of additives.

#### *2.3.3.3 Mill fill level and media-slurry ratio*

The quantities of media and slurry that a mill processes at a time are typically defined through the number of media, as regardless of operation mode, the media should not exit the mill space. The number of media is typically specified as a percentage of the available grinding volume. The available grinding volume is defined as the volume of the internal mill shell, less the volume of the impeller. The porosity of the media packing is incorporated into the media volume when determining the mill fill percentage.

The mill fill level is optimised by balancing the increase in media contacts for grinding that comes with an increased fill level, with the corresponding decrease in distance between media, which limits the freedom of motion, which can decrease the energy of the collisions (Kwade & Schwedes, 2007). The space for bed expansion due to fluidisation and media wear and compression effects are considered in the operation heuristic of keeping the media fill percentage below 85 % (Gao & Holmes, 2007; Kwade & Schwedes, 2007).

In the SMD and detritor type pin mills, the impeller pins are not distributed all along the shaft, like the disks within the IsaMill, HIGMill and VXPmill, but located in the bottom half of the mill. This design requires the reduction of the mill fill level percentage such that the charge structure promotes the formation of the central cavity that recirculates fluid above the top pin layer. For an industrial scale SMD, this corresponds to a fill level of approximately 23 % (Ndimande et al., 2019).

The influence of the corresponding volume of dry or wet particles to the mill media was investigated in a dry vertical pin mill system by Zheng, Harris & Somasundaran (1996). The authors found that the best grinding occurred when the media voids were just filled with particles, characterised by peaks in specific surface area and energy efficiency. However, this media to material ratio has not been explicitly considered in wet systems.

#### *2.3.3.4 Mill speed*

The impeller is the source of energy in the mill. The impeller speed is a dominant factor in the mill power draw, as the power draw is a function of the torque on the impeller. Therefore, increasing the speed results in increased power draw. Increasing the speed also increases the external energy losses through sound and heat, and the wear rate on the media and the mill geometry (Gao & Forssberg, 1995).

What is of greatest importance is the influence of the speed on the product grind. The high impeller speeds are needed for fluidised grinding mills to fluidise the bed and induce breakage through high energy collisions. Increasing the tip speed was found to result in finer ground product with a narrower PSD on various fluidised mill types (Zheng, Harris & Somasundaran, 1996; Jankovic & Sinclair, 2006; Wang & Forssberg, 2007). The intensity of this effect was observed to plateau above a specific speed. This has been attributed to the mill speed being so high that the media and slurry, begin to centrifuge.

## 2.4 Scale up in the SMD

In this section, the laboratory scale SMD systems are defined and introduced. The first step taken towards understanding the internal effects of scale up on the laboratory SMD systems was a dimensionless analysis. To understand the internal mill environment, the flow and energy distributions of different variations of these mills, determined from experimental studies, are discussed, and stirred mill models and scale up techniques are presented.

### 2.4.1 Laboratory scale SMDs

The laboratory scale SMDs are simplified variations of the industrial SMD configuration. They constitute of a cylindrical mill shell and concentric impeller shaft with two layers of two cylindrical straight pins in layers. Three size variations of the laboratory mills are considered in this investigation. The different mill shells, Mill A, Mill B and Mill C, are shown in order of increased milling capacity in Figure 2.8 a). The impeller set up ensures that the pins in the next layer are inserted perpendicular to the one below or above it as shown in front of Mill B in Figure 2.8 a). This complements the industrial SMD configuration of an octagonal prismatic shell and impeller with two staggered layers of six pins each shown in Figure 2.7 b).

The complete milling apparatus with the Mill B connected to the stirring apparatus is shown in Figure 2.8 b). The design of the laboratory SMDs allows the impeller shaft to be shared amongst the different chamber sizes, with each mill experiencing the same characteristic gap between the base of the shaft and the base of the mill shell, and the same pin layer heights. The length of the pins is altered for each chamber size such that the ratio of the length of the pin layer to the mill diameter is consistent for all sizes. This allows for the profiles of the mills, normalised by the mill radius, to be consistent and comparable. The three mills' design specifications are given in section 6.3.1.

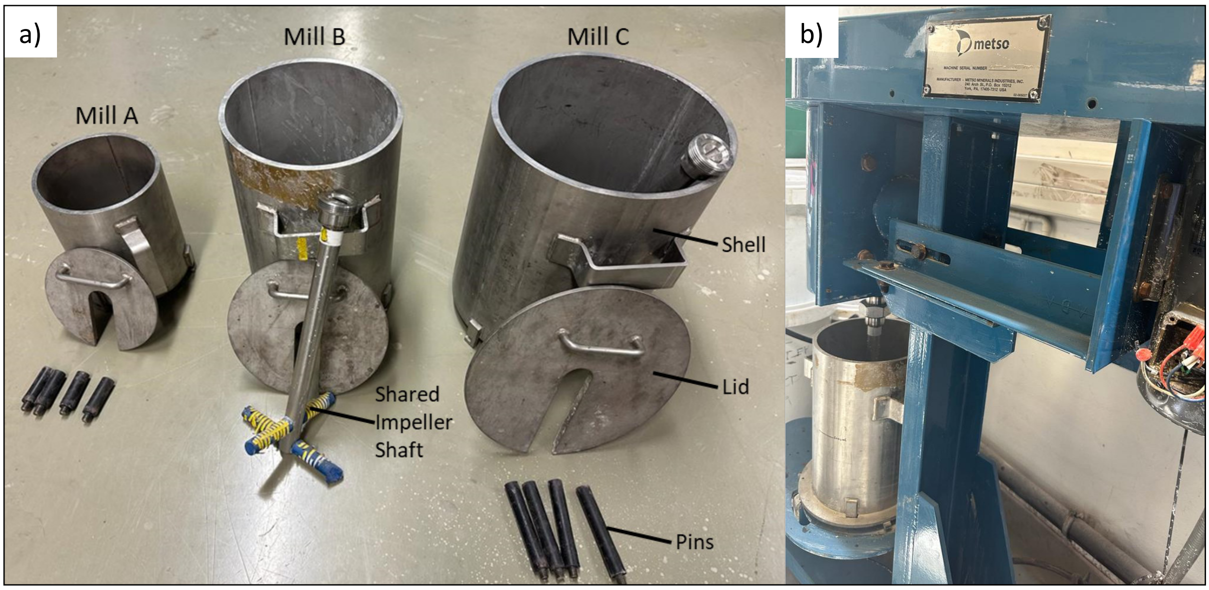

*Figure 2.8: Photographs of a) the three laboratory SMDs: Mill A, Mill B, Mill C, and b) Mill B mounted on the stirring apparatus.*

### 2.4.2 Dimensionless analysis

A dimensionless analysis was conducted on the mill system to identify key dimensionless relationships that may play a part in the scale up dynamics of the mill system. This was structured according to Buckingham's Pi Theorem (Buckingham, 1914). The theorem presents a methodology through which the dimensionless groups in a system are identified by relating $n$ variables relevant to the system to $m$ dimensionally independent scaling variables to form $n - m$ independent product ($\Pi$) groups. Though there are numerous dimensionless groups applicable to each system, groups identified through this approach are dimensionally independent of each other, allowing each group to represent a separate property of the system. The $\Pi$ groups result from considering the product of each n variable with all the m variables as shown in Equation (1). The exponents of the m variables are adjusted to ensure the $\Pi$ group is dimensionless.

$$\Pi = (n\ variable)(m)^a(m)^b(m)^c \cdots \tag{1}$$

The $n$ variables considered in the analysis follow from the definition of the scale up system investigated. The scale up system comprises of the three mill sizes, which exhibit geometric similarity between the impeller pins and mill radius, share the impeller shaft as the central axis, and have the same characteristic height between the shaft and mill base. The mills are filled to the same fill height, at the same media to slurry ratio. The media and slurry characteristics are constant across each mill type. The motion of the media in the slurry is induced by the rotation of the impeller to promote a contact-dominant fluidised flow regime. This is considered a closed system, with no other component besides the media, slurry, and mill geometry. Thermodynamic considerations are ignored for simplicity.

The interactions between all the scale up system components are considered, with particular focus on the bulk flow characteristics of the media and slurry, as these are well determined through the computational modelling tools used in the study. The forces that affect each interaction are explicitly considered, namely drag, gravity, pressure, and the internal flow forces. These are used to determine the relevant $n$ variables. The three dimensionally independent scaling ($m$) variables used for this analysis are the fundamental dimensions of fluid mechanics: mass (M), length (L) and time (T).

The main three $\Pi$ groups identified for this study; the Froude number (Fr), Reynolds number (Re), drag coefficient ($C_D$), shown in equations (2)-(4). The dimensionless groups are to be evaluated in the system bulk flow; therefore, the influence of the system porosity and the media and slurry densities are considered in the variations of the dimensionless groups used. This requires that the particle Re and the particle Fr be the variations presented.

$$Fr_p = \frac{|\boldsymbol{v_{rel}}|}{\sqrt{g \cdot d \cdot \left(\frac{\rho_b}{\rho_f} - 1\right)}} \tag{2}$$

$$Re_p = \frac{\rho_f |\boldsymbol{v_{rel}}| d \cdot \varepsilon}{\mu} \tag{3}$$

$$C_D = \frac{2|\boldsymbol{F}_d|}{\rho |\boldsymbol{v}|^2 A} \tag{4}$$

where, $g$ is gravitational acceleration, $\boldsymbol{v_{rel}}$ is the relative velocity between the solid and fluid phases, $d$ is the diameter/characteristic length of the media, $\rho$ is density, with the subscripts $b$

and $f$ signifying the body and the fluid, respectively. The fluid viscosity is $\mu$ and the porosity is $\varepsilon$. The drag force is indicated as $\boldsymbol{F}_d$ and $A$ denotes the projected area.

The Froude number is used in fluid mechanics to inform on the gravitational effects on a body analysed using the ratio of the body's inertia to its gravitational forces. The Reynolds number is indicative of the viscous flow state as it is a ratio of the inertia on a body to its viscous forces. The relationship between the Reynolds number and the drag coefficient has been well established in literature through the development of numerous correlations for their relationship that are used to determine the drag force (Schiller & Naumann, 1935; Turton & Levenspiel, 1986; Ganser, 1993; Hölzer & Sommerfeld, 2008). This is the method used to determine the drag force within the computational model used in this study, as shown in section 3.4.2. Therefore, within the bulk flow fields the influence of the drag coefficient can be inferred through the Reynolds number.

The drag coefficient is important when considering the influence of the impeller on the bulk flow fields in the system and when determining the power draw. The impeller configuration of the laboratory scale SMD has no predetermined relationship or curve between power draw and the Reynolds number, through the dimensionless Power number. Therefore, defining any of these dimensionless quantities for the impeller configuration would aid in decoupling the forces on the impeller arms which would improve the understanding of the transfer of energy from the impeller to particle breakage.

### 2.4.3 Spatial flow and energy distributions within laboratory scale SMDs

Numerous experimental studies have been conducted on multiple pin mill configurations. Majority of the experimental work on pin mills in literature is focused on the external response of the mill to various stimuli. This looks at the grinding rate influence on the $d_{80}$ and general particle size distribution, often including an energy component through analysis of the effect on the mill power draw. For the context of this study, being based on theoretical computational model prediction, the focus is geared towards the internal response of the mill. This looks at the motion within the mill space and the resulting flow and energy distributions.

The internal response of laboratory scale pin mills has been considered experimentally in the work of Theuerkauf & Schwedes (1999), through the use of light sheet techniques to outline flow fields, and by researchers at the University of Birmingham, through their pioneering of Positron Emission Particle Tracking (PEPT) for use on particulate systems (Conway-Baker et al., 2002; Barley et al., 2004; Riley et al., 2016; Daraio et al., 2019). PEPT is a non-invasive visualisation technique, that tracks positrons emitted from the annihilation of a radioactive particle, that is placed within the mill space (Van Der Westhuizen et al., 2011). The outputs from PEPT experiments provide data on the behaviours of a particle in the internal mill space, and if tracked long enough can provide data which complements the outputs from computational models of the system. This allows PEPT to be used as a validation technique for the computational models (Jayasundara, Yang, Guo, et al., 2011). Another empirical method used to determine the spatial flow and energy environment is the magnetic particle tracking (Böttcher, Schilde & Kwade, 2021). This method was applied to an M4 IsaMill™.

#### *2.4.3.1 PEPT studies on pin mills*

The PEPT studies provide a valuable link between the mill flow structure and its output. The flow structure of the grinding media within a wet pin mill was investigated in response to rotational speed by Conway-Baker et al. (2002). The work established that the motion of media in this mill type can be divided into 3 subsections, namely the lower circuits, impeller band, and upper circuits, as demarcated in Figure 2.9, which shows the generalised flow fields in the pin mill. The pin mill used is similar to the laboratory scale SMDs in the configuration of the mill shell and impeller, though the characteristic height of the impeller shaft from the mill base is significantly larger than what is encountered in the laboratory scale SMDs.

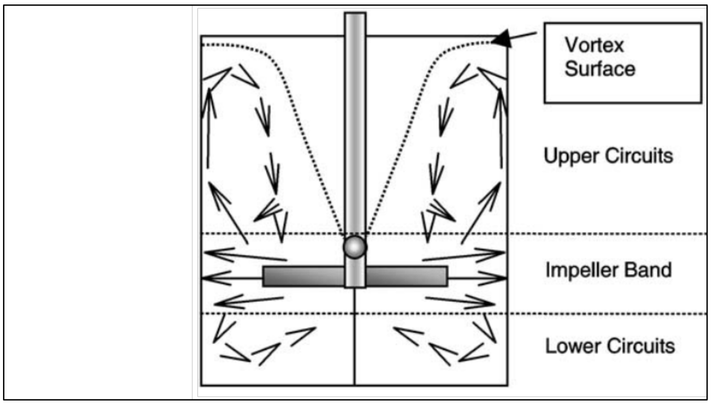

*Figure 2.9: General grinding media motion from PEPT, taken from Conway-Baker et al. (2002)*

The study defined the mill as having a pre-fluidisation period at low speeds, characterised by gentle stirring of the media in the slurry, before the bed dilates, and the circulation flow fields are established. The boundary between the upper circuits and impeller band was consistently located around the top of the top impeller, with the upper circuit height increasing upwards with rotational speed. The solids fraction was observed to show a low fraction of media at the top of the vortex free surface compared to slurry, due to the difference in gravitational forces, as the media was denser. The impeller band showed a low solids fraction due to the displacement of the media at high velocities by the impeller leading to a cavity in the wake of the impeller that easily fills with slurry, due to a lower inertia than the media. The development of these flow fields was correlated to the rotational speed to identify the changes in the product size distribution that correlate to the dominance of different breakage mechanisms. This showed that the dilation and development of the impeller band that occurs at increased speeds, produces a product of lower fineness than the denser packed bed at lower speeds. The authors correlated this development to fracture or more attritive breakage mechanism compared to the high abrasion breakage noted in the product size distribution at low speeds.

The PEPT work was then performed to provide insight on the effects of the media loading, slurry density and media size in Barley et al. (2004). Media loading was defined as the percentage of the total volume of a still mill filled by media, inclusive of the porosity. This was considered at three levels 40 %, 60 % and 70 %. Spatially, the key differences in the mill space were that the upper circuits were underdeveloped at 40 % compared to 60 % and 70 %. However, at 70% the impeller band circuits were less developed than at 60 %. The sizes of the impeller band and lower circuits were constrained, but the upper circuit height peaked at 60 % fill.

The slurry density and viscosity effects were studied by varying the solids concentration of the slurry at three levels namely, 40 %, 60 %, and 70 %. The upper circuits were observed to get higher with solids concentration to make way for an increase in the thickness of the impeller band. The increased impeller band leads to increases in radial velocity and media recirculation. At 40 % the flow fields are clear and separate. They got more chaotic with increasing solids concentration, particularly at 70 % where they become hard to distinguish. Analysis of the product PSDs with increasing solids concentration revealed an increase in fineness which is attributed to increased attrition breakage resulting from to a greater particle-particle contact. The rest is attributed to the changes in the structures of the three flow fields sections, which are consistent with observed PSD changes. An increase in the mill power draw was observed, consistent with the increased viscosity, fines proportion and shear thinning nature of the material.

The effect of media size was considered using polydisperse media in two distinct size classes. The same distribution of media was used in two sets of experiments, where the tracked irradiated medium fell in either size class. Stratification of the media was observed as the occupancy of the larger medium was dominant in the outer lower circuits of the mill space, with a lower peak height of its upper circuit, compared to the smaller medium. The smaller medium had a more evenly distributed occupancy plot with a higher upper circuit peak height. This was the first time such a pattern of flow was reported in a stirred media mill.

The kinetic energy distribution response to tip speed was considered in Riley et al. (2016). This showed how the kinetic energy spatially distribution of the media responded to increases in the rotational speed of the impeller, which inputs energy into the system. The tip speed was increased from 1.77 m/s to 8.48 m/s in 4 increments. Key observations were a decrease in the occupancy of the impeller band with the increase in tip speed, with a corresponding increase in the peak of the upper circuits. The kinetic energy within the impeller band was observed to increase, with little effect on the kinetic energy in the other zones. Less energy transfer between the zones was observed. This can be attributed to the mill approaching a centrifugal state, dominated by high tangential velocities with limited axial and radial mixing as foretold by the experimental studies. The importance of understanding the tip speed was emphasised as an optimisation parameter for the stirred media mills.

### 2.4.4 Stirred mill models and scale-up

The dynamics within stirred mills present a complex problem when it comes to the development of empirical models. The most common stirred mill model is based on the Stress Energy formulations developed by Blecher, Kwade & Schwedes (1996). The model considers the breakage result as a function of the stress energy and stress frequency within the mill during the grinding period. The stress energy, the energy transferred to particles at stress events, is defined as a distribution with dependencies on the particle position and time. The mean of the stress energy distribution ($\overline{\mathrm{SE}}$) is proportional to the stress energy of the grinding media ($\mathrm{SE}_{\mathrm{GM}}$), as shown in equation (5).

$$\overline{SE} \propto SE_{GM} = d_{GM}^{3} v_{tip}^{2} \rho_{GM} \tag{5}$$

where $d_{GM}$ and $\rho_{GM}$ are the grinding media diameter and density respectively, and $v_{tip}$ is the impeller tip speed. This is based on the assumption that the mean energy occurs when tangentially fast-moving grinding media collide with slower moving media, typically around the edges of the impeller. It follows that the fast-moving grinding media are estimated to move at the impeller tip speed.

The model goes on to define an estimated stress number (SN) for each particle size ($x$) as a function of the grinding time (t) and the number of revolutions (n) and the size of the grinding media, as shown in equation (6).

$$SN = n \cdot t \left(\frac{x}{d_{GM}}\right)^{2} \tag{6}$$

The model uses these two parameters to characterise the breakage result. This shows that the breakage result is primarily dependent on the mill tip speed and the media size. There are other expansions to these relationships based on the characteristics such as viscosity, solids concentration and hardness of material being ground in the mill system (Kwade & Schwedes, 2007). The model has been compared to computational models which are able to provide the full energy and frequency distributions within the mill space (Beinert et al., 2015, 2018). These allow for more precise approximations of the stress energy within the mill system.

For systems such as the laboratory scale stirred mills, that are not completely geometrically similar, operating the systems with the same media size and mill tip speed and material characteristics could lead to varying breakage performance as the stress energy distribution evolves as the mill space radially expands. Therefore, the authors of the model propose a stress-energy based scale up, whereby through matching the stress energy distributions of two mill configurations, one can match their breakage results.

Other models exist such as power-based models that define the breakage result by the power draw and population balance models (PBM) that predict breakage based on selectivity and breakage function. Heath et al. (2017) developed a power model for the castellated disc impeller of the HIGMill that considered the effects of the impeller diameter and speed, number of discs media fill, fluidisation effects, and slurry density and viscosity. Though the model does not have direct grinding result considerations, it was developed to inform on the mill size and configuration parameters required for a set power draw investigated across 30, 75 and 700 kW HIGMill sizes.

Guo et al. (2021) applied a PBM to batch fluidised grinding laboratory mill. The PBM uses a selectivity function to define the rate of breakage for a particle size class, and a breakage function to describe how particles in a set size class distribute into lower size classes upon breakage. The functions are calibrated with the ore characteristics. This approach bypasses the internal stirred mill scale up dynamics. The study defined 3 size classes, a coarse class (+45 µm), a desired product class (-45 +10 µm) and an overgrind class (-10 µm) to develop a PBM with a constant selectivity function and first order breakage kinetics to examine the effects of grinding media density and diameter, and stirrer tip speed on the breakage rate.

The gravity-induced stirred mills have been studied using PBM (Mazzinghy et al., 2017). Mazzinghy et al. (2017) used batch ball mill tests to generate data for the scale up of VertiMills. A mechanistic model presented in Oliveira et al. (2020) integrated the collision environment predictions from discrete element method (DEM) media collisions in a batch operated tower mill to a PBM through a particle fracture convolution. The PBM is used to regulate the mass balance of sub-DEM feed material particles in each size and composition class. The particle fracture convolution is based on the model of continuum damage of particle breakage by Tavares & King (2002) and the distribution of particle fracture energies that incorporates the collision spectra of the DEM simulations. The model considers the effects of multiple breakage mechanisms on the feed material and their accumulated implications on the material breakability over time. The mechanistic model was used to predict the effects of operating and design parameters on the product grind of a batch tower mill (Oliveira, Carvalho & Tavares, 2021) and extended to include fluid considerations through CFD (Carvalho et al., 2023; Petit, de Oliveira & Tavares, 2025). This model has not yet been tested on fluidised grinding mills, which have a finer grind and faster tip speed.

## 2.5 Summary on stirred mill comminution and scale-up

- Stirred media mills are the most energy efficient mill type for achieving fine-ultrafine grinds.
- Attrition and abrasion breakage is the dominant breakage mechanism in stirred mills, indicated by high shear forces.
- Fluidised grinding mills are used to achieve finer grinds than gravity induced mills, due to their higher tip speeds and smaller media sizes.
- The two most critical parameters for achieving a specific grind in a stirred mill are the mill speed and media size.
    - The impeller speed is the main source of energy used for breaking particles in the stirred media mills.
    - The media size uses the energy transmitted from the impeller to produce collisions that result in particle breakage. The media size is directly correlated to the feed top size to ensure that breakage of the feed material is effective.
- Laboratory scale SMD's and scale-up dynamics:
    - The laboratory scale SMD consists of a cylindrical shell and concentric impeller with two pin layers.
    - The bulk flow fields in these mills are divided into three sections: the lower circuits, the impeller band, and the upper circuits. PEPT experiments have shown that each circuit responds differently to changes in critical parameters.
    - The dimensionless numbers: Reynolds number and Froude number, can be used to quantify the bulk flow characteristics and their response to changes in scale.

# CHAPTER 3

# Theory and Literature on Computational Models

## 3.1 Introduction

The internal energy and flow environment of stirred mills in this study is predicted through computational modelling. The simulation model used relies on coupling independent computational methods for the solid and fluid components of the mill space. The discrete element method (DEM) is used to detail the solid component, while smooth particle hydrodynamics (SPH) details the fluid component. This chapter is focused on defining the facets of the computational methods and outlining the coupling mechanisms used to connect them. It then closes with a summary on the computational models.

## 3.2 The Discrete Element Method

### 3.2.1 Fundamentals

The discrete element method (DEM) is a lagrangian computational method developed by Cundall & Strack (1979) to simulate the motion of large numbers of independent bodies. The discrete element method has since been used unaccompanied and in coupled variations to simulate multiple comminution process and devices, through cohesive and cohesionless applications such as ore crushing, roller grinding (Weerasekara et al., 2013) and stirred media mills (Jayasundara et al., 2006; Sinnott, Cleary & Morrison, 2006). Its first application to cohesionless comminution systems is attributed to Mishra & Rajamani (1992), who simulated the motion of grinding media in a 2-dimensional ball mill. These models have been used to inform on the flow and energy environment of stirred media mills by detecting and resolving contacts forces generated by collisions amongst the media and between the media and the mill.

The DEM model defines the mobile bodies in the system as interpenetrating, which allows for a controlled degree of overlap during collisions with each other and the environment. The overlap is used to determine the normal and tangential (shear) collision forces based on a specified contact model. The different contact models used to describe the collision forces in stirred mills are discussed in the following subsection. These and other forces on the bodies are used to determine their translational and rotational motion based on Newtons second law of motion. The motion equations for a body i in contact with bodies j are as shown in equations (7) and (8).

$$m_i \frac{d\boldsymbol{v}_i}{dt} = \sum_{j \in B} (\boldsymbol{F}_{N_{ij}} + \boldsymbol{F}_{T_{ij}}) + m_i \boldsymbol{g} + \boldsymbol{F}_{sf_i} \tag{7}$$

$$\mathbf{I}_i \frac{d\boldsymbol{\omega}_i}{dt} = \boldsymbol{T_i} \tag{8}$$

where m is the body mass, v is the linear velocity, ω is the angular velocity, I is the moment of inertia tensor, T is the torque on the body, $F_{sf}$ is the solid-fluid interaction force, and $F_{Nij}$ and $F_{Tij}$ are the normal and tangential components of the contact force, respectively.

These equations are then solved to update the translation vector, x, and angle of rotation through integrating the time dependency according to equations (9) and (10). Note that quaternions along with Euler angles and Rodrigues vectors are data structures used to store the angle of rotation of a body (Jing & Stephansson, 2007; Matuttis & Chen, 2014). Quaternions, Q, are used to store the object rotation as a quantity with both a scalar and vector component.

$$\frac{d\boldsymbol{X}_i}{dt} = \boldsymbol{v}_i \tag{9}$$

$$\frac{d\boldsymbol{Q}_i}{dt} = \frac{1}{2}\boldsymbol{\omega}_i\boldsymbol{Q}_i \tag{10}$$

Because of the lagrangian nature of DEM, the integration timestep is used as a solution stability criterion. The timestep controls the degree of overlap between colliding bodies and is chosen such that within a timestep the disturbances caused by collisions only propagate from a body to its contacts (Thornton, 2015). This is to ensure that mass, momentum and energy are conserved. The theory behind the methods used to determine the timestep and its computational implications are discussed in section 3.2.5.

### 3.2.2 Contact models

The contact models used to determine normal and shear forces resulting from a collision define the collision as having a repulsive force and a dissipative force, approximated using a spring and dashpot, commonly with a tangential slider (Weerasekara et al., 2013). The slider illustrates that the tangential force approximation is subject to Coulomb's law of friction, which sets a maximum to the modulus of force, determined by the product of the normal force and the coefficient of friction of the materials (Di Renzo & Di Maio, 2004). These spring-dashpot-slider systems are illustrated in Figure 3.1 for collisions between spherical media (Mishra & Rajamani, 1992; Tsuji, Tanaka & Ishida, 1992).

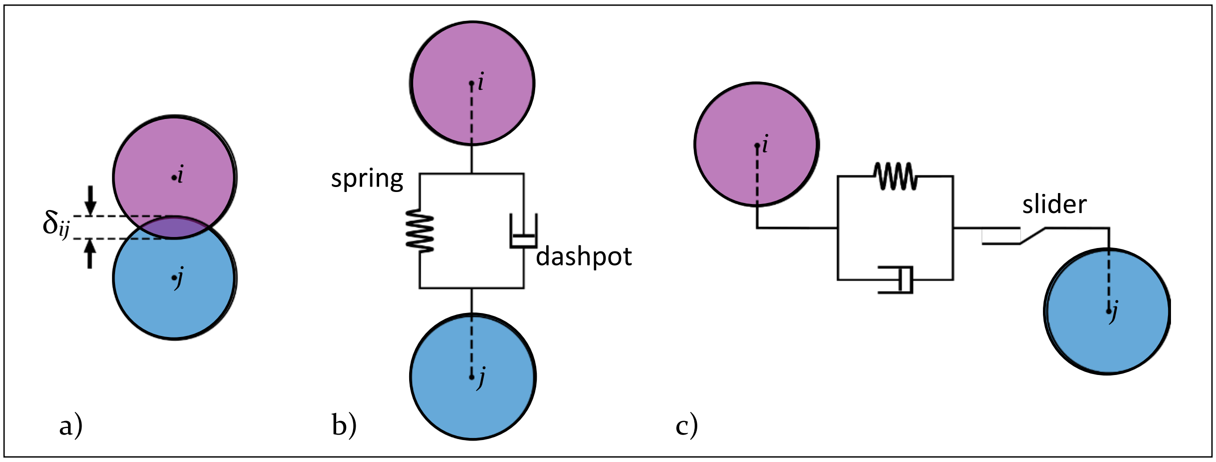

*Figure 3.1: Contact between spherical media a) soft contact overlap b) normal contact force and c) tangential contact force approximation*

The contact models used in stirred mill simulations are categorized into two groups, based on whether the model uses a linear or non-linear spring approximation. The linear model uses spring constants calibrated by Hooke's law of constant proportionality between the spring force and the overlap (Sinnott, Cleary & Morrison, 2006; Gudin, Kano & Saito, 2007a; Kim & Choi, 2008; Yamamoto et al., 2012). The non-linear models are based on variations within Hertzian and Mindlin-Deresiewicz contact theory (Hertz, 1881; Mindlin, 1949; Mindlin & Deresiewicz, 1953). These models integrate the physical properties of colliding materials into non-linear spring constants (Jayasundara et al., 2006; Santhanam & Dreizin, 2012; Beinert et al., 2014). Though one model type is not favoured over the other, because non-linear models link directly to the physical properties, this type is preferred for multi-scale analysis on individual contact motion (Weerasekara et al., 2013; Beinert et al., 2018), and is the model type used in this study.

The normal and tangential force equations for the collision of bodies i and j, using the linear spring dashpot model with a tangential slider, are as follows.

$$\boldsymbol{F}_{N_{ij}} = -k_N \delta_{ij} \boldsymbol{n}_{ij} - (\eta \boldsymbol{v}_{ij} \cdot \boldsymbol{n}_{ij}) \boldsymbol{n}_{ij} \tag{11}$$

$$\boldsymbol{F}_{T_{ij}} = min\left[-k_T \boldsymbol{\delta}_{T_{ij}} - \eta \boldsymbol{v}_{s_{ij}}, \ -\mu \left|\boldsymbol{F}_{N_{ij}}\right| \boldsymbol{t}_{ij}\right] \tag{12}$$

where $k_N$ and $k_T$ are the respective normal and tangential spring constants. The relative velocity of the collision is given by $v_{rel}$, with vs being the slip velocity of the contact point in the tangential direction. The unit vectors in the tangential and normal direction of the collision are given by n and t. The overlap in the normal direction is indicated by δ, with $\delta_T$ being the overlap in the tangential direction. For spherical media, the contact overlap is defined as the difference between the distance between the two bodies, and the sum of their radii. The displacement between the two centres is used as the normal direction. The contact forces are applied to the mid-point between the two body centres. The damping coefficient η is defined by a separate damping model.

The non-linear model presented in this study follows from relationships described in Tsuji, Tanaka & Ishida (1992). Following from Hertzian contact theory, the non-linear normal force is proportional to the normal displacement to the power of three over two, as shown in equation (13). The non-linear tangential force dependency on the tangential displacement remains linear, thus equation 10 still holds. The non-linear spring constants are now defined by physical and interaction properties of the colliding materials. They are shown in equations (14) and (15) for collisions between two spherical bodies i and j. The non-linear tangential spring constant follows from the Mindlin-Deresiewicz approximations, with a no-slip simplification.

$$\boldsymbol{F}_{N_{ij}} = -K_N \delta_{ij}^{\frac{3}{2}} \boldsymbol{n}_{ij} - (\eta \boldsymbol{v}_{ij} \cdot \boldsymbol{n}_{ij}) \boldsymbol{n}_{ij} \tag{13}$$

$$K_N = \frac{\frac{4}{3}\sqrt{R_{eff}}}{\frac{1-\sigma_i^2}{E_i} + \frac{1-\sigma_j^2}{E_j}} \quad ; \quad \frac{1}{R_{eff}} = \frac{1}{r_i} + \frac{1}{r_j} \tag{14}$$

$$k_T = 8G_s\sqrt{R_{eff}\delta_{ij}} \quad ; \quad \frac{1}{G_s} = \frac{2(2-\sigma_i)(1+\sigma_i)}{E_i} + \frac{2(2-\sigma_j)(1+\sigma_j)}{E_j} \tag{15}$$

where E is the Youngs modulus, σ is the Poisson ratio, $G_s$ shear modulus, $R_{eff}$ is the effective radius and r is the radius.

The dissipative models for the dashpot follow from either elastic, plastic or viscous damping models, or combinations of two or more damping models. These models have been integrated into either contact model framework (Thornton, Cummins & Cleary, 2011, 2013, 2017). Following from Tsuji, Tanaka & Ishida (1992), the dissipative model of the dashpot in both the linear and non-linear contact models follows a linear dissipation trend, with constant dissipation in all directions. The dissipative model shown in equations (16) is a viscous damping model, used because it relates the damping coefficient to the coefficient of restitution, which is a property of the collision between two bodies, obtained through experimentation.

$$\eta = \alpha\left(m_{eff} K_N\right)^{\frac{1}{2}} \delta_{ij}^{\frac{1}{4}} \quad ; \quad \frac{1}{m_{eff}} = \frac{1}{m_i} + \frac{1}{m_j} \quad ; \quad \alpha = \frac{\sqrt{5}\ln(e)}{\sqrt{\ln(e)^2 + \pi^2}} \tag{16}$$

where α is an empirical relationship that relates the coefficient of restitution, e, to the damping coefficient and $m_{eff}$ is the effective mass.

### 3.2.3 Non-spherical media

The shapes of the media bodies used in physical stirred mill systems are rarely perfectly spherical. The bodies are often irregular with multiple angularities that worsen with repeated use. Figure 3.2 provides 2D optical microscope images of two kind of grinding media and their cumulative size distributions. Though this media is an order of magnitude smaller than what is used for industrial scale minerals processing mill systems, the ceramic materials, particularly the yttrium-stabilized zirconia, have been used at larger sizes. The images show media as near perfect spheres with some flat edges. Therefore, the modelling of media bodies that can capture some of these angularities in computational models is a necessary step towards accurately approximating the physical mill space (Sinnott, Cleary & Morrison, 2011b).

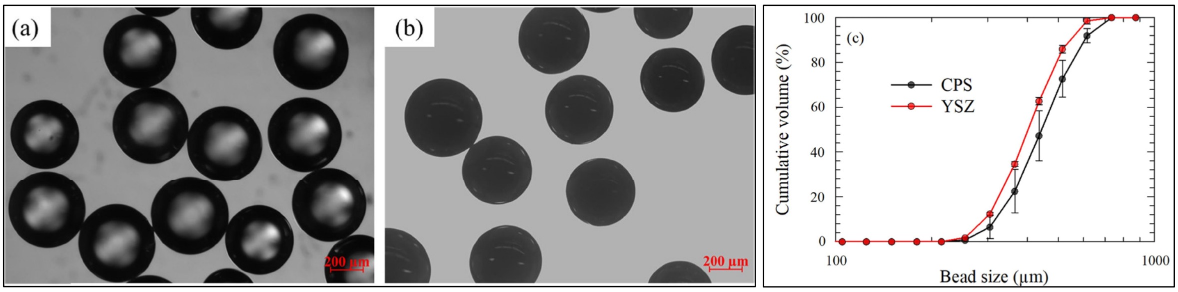

*Figure 3.2: Optical microscope image of 400 µm nominal sized (a) crosslinked polystyrene (CPS) beads (measured median size: 444 µm) and (b) yttrium-stabilized zirconia (YSZ) beads (measured median size: 405 µm), and (c) shows the distribution of characteristic size observed in the media samples. Taken from* Parker, Rahman & Bilgili (2020)

Within this study, super-quadric shapes (Barr, 1981) are used to describe non-spherical media bodies. A super quadric shape (s) is represented mathematically through a singular closed surface equation, shown by equation (17)(Jaklič, Leonardis & Solina, 2000), in a Cartesian coordinate system.

$$s\begin{pmatrix} x \\ y \\ z \end{pmatrix} = \left( \left|\frac{x}{a}\right|^{\frac{2}{n_2}} + \left|\frac{y}{b}\right|^{\frac{2}{n_2}} \right)^{\frac{n_2}{n_1}} + \left|\frac{z}{c}\right|^{\frac{2}{n_1}} - 1 \tag{17}$$

where a, b and c represent the semi-axis lengths of the body in the x, y, z directions of a body centred reference frame. The roundness parameters $n_1$ and $n_2$ are used to control the curvature of the body edges. By adjusting these five parameters, the super quadric equation can describe approximately 80% of real particle shapes (Williams & Pentland, 1992; Zhong et al., 2016).

The motion of particulate systems with super quadric media has been simulated using DEM (Cleary, Stokes & Hurley, 1997; Podlozhnyuk, Pirker & Kloss, 2017; Gao, Yu, Lu, et al., 2021; Wang, Zhang & Ji, 2021; Wang & Shen, 2022). Common super quadric shapes used in particulate systems are ellipsoids and box-like shapes with convex edges. This is because these shapes are two times continuously differentiable, and their definitions reduce the parameters from 5 to 4 by equating $n_1$ and $n_2$. Their roundness is defined such that a value of 1 is circular edge between semi-axis and 0 is a rectangular corner. These constrained super quadrics are defined by equation (18).

$$s\begin{pmatrix} x \\ y \\ z \end{pmatrix} = \left|\frac{x}{a}\right|^{\frac{2}{n}} + \left|\frac{y}{b}\right|^{\frac{2}{n}} + \left|\frac{z}{c}\right|^{\frac{2}{n}} - 1\,, \qquad \begin{matrix} n_1 = n_2 = n \\ n \in (0,1] \end{matrix} \tag{18}$$

The two times differentiability of the super quadric is necessary for accurate contact detection. The first derivative of the shape function (∇s) provides the surface normal, while the second derivative hessian matrix (H) describes the surface curvature. Following from the constrained quadric equation, the gradient and hessian of the surface function are shown in equations (19) and (20), respectively (Podlozhnyuk, Pirker & Kloss, 2017). Notably, the constraints simplify each equation component and reduce the hessian to a diagonal matrix.

$$\nabla s\begin{pmatrix} x \\ y \\ z \end{pmatrix} = \begin{pmatrix} \frac{2}{an}\left|\frac{x}{a}\right|^{\frac{2}{n}-1} sign[x] \\ \frac{2}{bn}\left|\frac{y}{b}\right|^{\frac{2}{n}-1} sign[y] \\ \frac{2}{cn}\left|\frac{z}{c}\right|^{\frac{2}{n}-1} sign[z] \end{pmatrix} \tag{19}$$

$$\mathbf{H}(s) = \begin{pmatrix} \frac{2}{a^2 n}\left(\frac{2}{n}-1\right)\left|\frac{x}{a}\right|^{\frac{2}{n}-2} & 0 & 0 \\ 0 & \frac{2}{b^2 n}\left(\frac{2}{n}-1\right)\left|\frac{y}{b}\right|^{\frac{2}{n}-2} & 0 \\ 0 & 0 & \frac{2}{c^2 n}\left(\frac{2}{n}-1\right)\left|\frac{z}{c}\right|^{\frac{2}{n}-2} \end{pmatrix} \tag{20}$$

### 3.2.3.1 Coordinate systems

The super quadric body as defined in equations (19) and (20) exists in a body centred coordinate system. Its interactions within the mill environment will exist in the mill coordinate system. Therefore, it is necessary to define the super quadric body within the mill coordinate system. This is done by applying a transformation to the body coordinates. The transformation consists of a rotation then a translation. The rotation is carried out using the body rotation quaternion Q. The quaternion Q stores the rotation information of the body in the form of a scalar $q_0$ and a vector with components $q_1$, $q_2$ and $q_3$, as shown in equation (21). The rotation is applicable through the orthogonal rotation matrix A in equation (22). The coordinates are translated by the coordinates of the body centre, $\boldsymbol{X}_C$ in the mill coordinate system.

$$\mathbf{Q} = (q_0, q_1, q_2, q_3)^T \tag{21}$$

$$\mathbf{A} = \begin{pmatrix} q_0^2 + q_1^2 - q_2^2 - q_3^2 & 2(q_1 q_2 + q_0 q_3) & 2(q_1 q_3 - q_0 q_2) \\ 2(q_1 q_2 - q_0 q_3) & q_0^2 - q_1^2 + q_2^2 - q_3^2 & 2(q_2 q_3 + q_0 q_1) \\ 2(q_1 q_3 + q_0 q_2) & 2(q_2 q_3 - q_0 q_1) & q_0^2 - q_1^2 - q_2^2 + q_3^2 \end{pmatrix} \tag{22}$$

The resulting transformation of the super quadric surface from body centred coordinate $\boldsymbol{x}$ to mill coordinate $\boldsymbol{X}$ is shown in equations (23) and (24). The gradient and hessian of the function in the mill coordinate system are defined in equations (25) and (26), respectively (Podlozhnyuk, Pirker & Kloss, 2017).

$$\boldsymbol{x} = \mathbf{A}^T \cdot (\boldsymbol{X} - \boldsymbol{X}_C) \tag{23}$$

$$S(\boldsymbol{X}) = s(\mathbf{A}^T \cdot (\boldsymbol{X} - \boldsymbol{X}_C)) \tag{24}$$

$$\nabla S = \mathbf{A} \cdot \nabla s \tag{25}$$

$$\mathbf{H}(S) = \mathbf{A} \cdot \mathbf{H}(s) \cdot \mathbf{A}^T \tag{26}$$

### *3.2.3.2 Contact detection*

Unlike spherical media where the contact detection is simplified by the constant body radius, super quadrics contact detection is solved in the form of an optimisation problem (Cleary, Stokes & Hurley, 1997; Podlozhnyuk, Pirker & Kloss, 2017). A contact exists between two super quadrics when there is an overlap between the two surface functions. The following solution methodology presented has been referred to as the 'middle point method' (Gao et al., 2019).

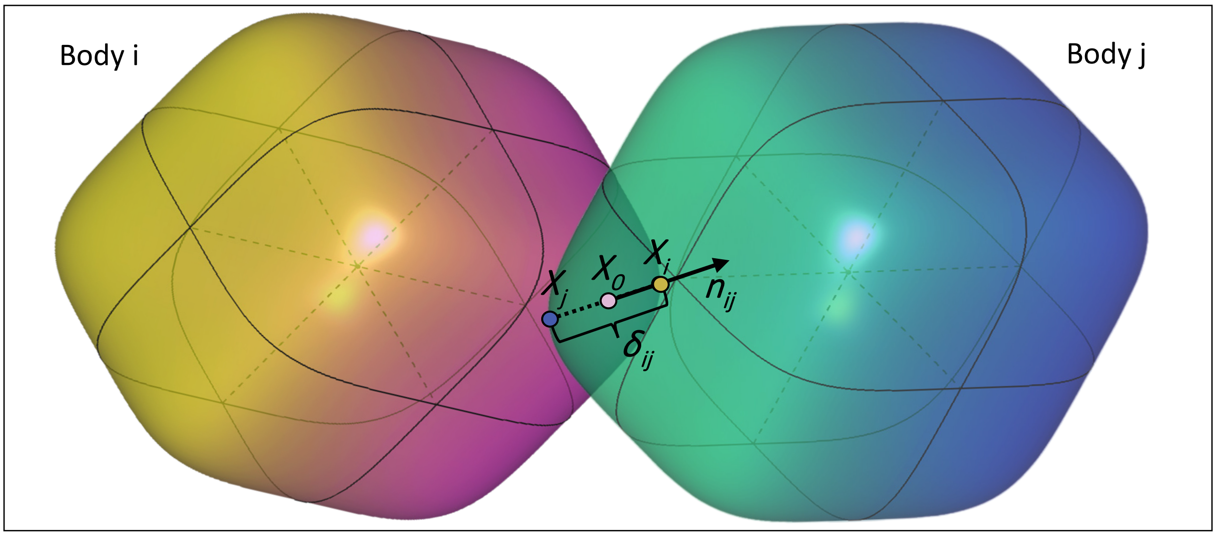

*Figure 3.3: Contact between two super quadric bodies*

The contact point $\boldsymbol{X}_0$ is defined as a point within both surface boundaries, 'the middle point' between their overlap. This results in $\boldsymbol{X}_0$ being the solution to the two equations presented in equation (27), for the contact between two super quadrics i and j, where $\mu$ is a stabilisation parameter.

$$\begin{cases} \boldsymbol{\nabla} S_i(\boldsymbol{X}_0) + \mu^2 \boldsymbol{\nabla} S_j(\boldsymbol{X}_0) = 0 \\ S_i(\boldsymbol{X}_0) - S_j(\boldsymbol{X}_0) = 0 \end{cases} \tag{27}$$

The equations are solved using Newton's method as a system of 4 equations and 4 unknowns. This system is expressed in equation (28), where $\boldsymbol{\Psi}$ is the matrix of equations and $\mathbf{J}$ is its Jacobian (Podlozhnyuk, Pirker & Kloss, 2017). Within $\mathbf{J}$, upper and lower triangular partial derivatives may arise from the rotation of the hessian into the mill reference frame.

$$\boldsymbol{Z}^{n+1} = \boldsymbol{Z}^{n} + \boldsymbol{\delta Z}$$

$$\boldsymbol{Z} = (X \quad Y \quad Z \quad \mu)^{-1}, \qquad \boldsymbol{\delta Z} = -\mathbf{J}^{-1} \cdot \boldsymbol{\Psi}$$

$$\boldsymbol{\Psi} = \begin{pmatrix} S'_{i_X} + \mu^2 S'_{j_X} \\ S'_{i_Y} + \mu^2 S'_{j_Y} \\ S'_{i_Z} + \mu^2 S'_{j_Z} \\ S_i - S_j \end{pmatrix}; \mathbf{J} = \begin{pmatrix} S''_{i_{XX}} + \mu^2 S''_{j_{XX}} & S''_{i_{XY}} + \mu^2 S''_{j_{XY}} & S''_{i_{XZ}} + \mu^2 S''_{j_{XZ}} & 2\mu S'_{j_X} \\ S''_{i_{YX}} + \mu^2 S''_{j_{YX}} & S''_{i_{YY}} + \mu^2 S''_{j_{YY}} & S''_{i_{YZ}} + \mu^2 S''_{j_{YZ}} & 2\mu S'_{j_Y} \\ S''_{i_{ZX}} + \mu^2 S''_{j_{ZX}} & S''_{i_{ZY}} + \mu^2 S''_{j_{ZY}} & S''_{i_{ZZ}} + \mu^2 S''_{j_{ZZ}} & 2\mu S'_{j_Z} \\ S'_{i_X} - S'_{j_X} & S'_{i_Y} - S'_{j_Y} & S'_{i_Z} - S'_{j_Z} & 0 \end{pmatrix} \tag{28}$$

The system is iterated until $|\boldsymbol{\Psi}(\boldsymbol{Z}^{n+1})|$ is less than a termination criterion. Convergence of the method has been reported in 1-5 iterations (Cleary, Stokes & Hurley, 1997; Podlozhnyuk, Pirker & Kloss, 2017). The solution provides $\boldsymbol{X}_0$, which is used to determine the contact normal $\boldsymbol{n}_{ij}$ and the overlap $\delta_{ij}$ in equations (29). $\boldsymbol{X}_i$ and $\boldsymbol{X}_j$ are the points on their respective surfaces in line with $\boldsymbol{X}_0$ and the contact normal (Podlozhnyuk, Pirker & Kloss, 2017).

$$\boldsymbol{X}_0 = \boldsymbol{Z}^{\mathrm{n}+1}[x,y,z]^T\ ;\ \ \boldsymbol{n}_{ij} = \frac{\boldsymbol{\nabla} S_i(\boldsymbol{X}_0)}{|\boldsymbol{\nabla} S_i(\boldsymbol{X}_0)|}\ or\ \boldsymbol{n}_{ij} = -\frac{\boldsymbol{\nabla} S_j(\boldsymbol{X}_0)}{\left|\boldsymbol{\nabla} S_j(\boldsymbol{X}_0)\right|} \tag{29}$$

$$\delta_{ij} = \left|\boldsymbol{X}_i - \boldsymbol{X}_j\right|$$

The contact normal and overlap can then be used to determine the normal and tangential contact forces in a linear contact model. The Hertz-Mindlin-Deresiewicz non-linear contact model has been modified for super quadric bodies by using the radius of curvature at the contact surface points, $\boldsymbol{X}_\mathrm{i}$ and $\boldsymbol{X}_\mathrm{j}$, to approximate the body radius used in the spring constants $K_N$ and $K_T$, described in equations (14) and (15) (Podlozhnyuk, Pirker & Kloss, 2017; Gao, Yu, Lu, et al., 2021; Wang & Shen, 2022). In this approach, the mean curvature, equation (30) (Goldman, 2005), of the bodies at $\boldsymbol{X}_\mathrm{i}$ and $\boldsymbol{X}_\mathrm{j}$ is used to determine the respective radii. A simpler modification is to use the radius of the sphere of equivalent volume to the quadric to approximate its radius within the contact model (Wang, Zhang & Ji, 2021).

$$K_M(\boldsymbol{X}) = \frac{\boldsymbol{\nabla} S^{\mathrm{T}} \cdot \mathbf{H}(S) \cdot \boldsymbol{\nabla}\mathrm{S} - |\boldsymbol{\nabla} S|^2 Trace[\mathbf{H}]}{2|\boldsymbol{\nabla} S|^3} \tag{30}$$

$$r_i = \min\left[\frac{1}{K_M(\boldsymbol{X}_i)}\ , q \cdot R_{Veq_i}\right]\ \ and\ r_j = \min\left[\frac{1}{K_M(\boldsymbol{X}_j)}\ , q \cdot R_{Veq_j}\right] \tag{31}$$

The approach presented in equation (31) is taken from Podlozhnyuk, Pirker & Kloss (2017). This defines the body radius as the minimum of the mean radius of curvature and the product of the radius of the volume equivalent sphere and a limiting coefficient, q. This is done to ensure that radius of curvature does not become infinite as the contact point approaches any semiaxis of the super quadric.

#### *3.2.3.3 Other non-spherical media methods*

Other than super quadric shapes, non-spherical media in densely populated systems have been simulated mainly through multi-sphere (MS) models (Khazeni & Mansourpour, 2018; Soltanbeigi et al., 2018; Berry, Zhang & Haeri, 2023; Giannis et al., 2023) and polyhedrons (Yang et al., 2008; Nassauer, Liedke & Kuna, 2013; Liu & Ji, 2020). The MS models approximate non-spherical media as a cluster of numerous spherical media in fixed contact. The primary limitation of this method is that it requires many spheres to approximate highly angular shapes and the fixed contact or overlap between spheres creates concavity. This can lead to situations where multiple spheres are involved in a single contact event which would require a complex method to resolve the contact forces (Berry, Zhang & Haeri, 2023). Polyhedrons represent non-spherical media as a closed set of connected flat surfaces in 3D. This approach is restricted because the contact force methodology between the polyhedral shapes is still underdeveloped. Convex super quadric media shapes were chosen for this thesis due to their closed surface equation, which ensures one contact point per contact event, and their directly controlled angularity.

### 3.2.4 Media-wall contact

Within the mill space the grinding media is modelled to interact with the mill impeller and shell through wall contact. This is facilitated through the application of linear or non-linear contact theory to walls as an object. A wall is a closed planar region of space defined by a normal vector and the points that form its edges. Walls interact with the media within the soft contact model by allowing the media to overlap with the wall plane. This interaction is illustrated for spherical and super quadric media in Figure 3.4.

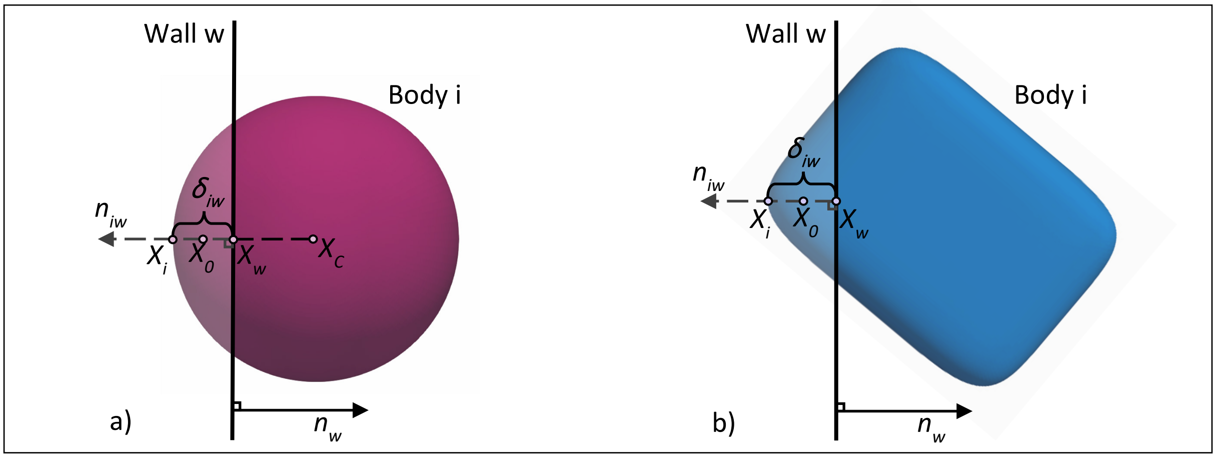

*Figure 3.4: Soft contact overlap with walls for a) spherical and b) super quadric media*

The contact forces are determined similarly to media-media contacts through equations (11)-(16). For non-linear contact forces, the material properties of the wall and the media are used to determine its shear modulus, and the coefficient of restitution for the wall and media interaction is used. The effective radius and mass of the contact default to those of the media body, for most wall types (Tsuji, Kawaguchi & Tanaka, 1993). With spherical media, the contact normal, overlap and contact point are determined using the equations (32).

$$\boldsymbol{n}_{iw} = \frac{\boldsymbol{X}_w - \boldsymbol{X}_C}{|\boldsymbol{X}_w - \boldsymbol{X}_C|}, \qquad \delta_{iw} = r_i - |\boldsymbol{X}_w - \boldsymbol{X}_C| \quad and \quad \boldsymbol{X}_0 = \boldsymbol{X}_C + \frac{(r_i - \delta_{iw}) \cdot \boldsymbol{n}_{iw}}{2} \tag{32}$$

For super quadric media the contact normal, point and overlap are determined through the following equations (33) adapted from (Podlozhnyuk, Pirker & Kloss, 2017) for constrained super quadrics.

$$\boldsymbol{n}_{iw} = -\boldsymbol{n}_w \quad and \quad \begin{aligned} \alpha &= \left(\frac{\left|b \cdot \boldsymbol{n}_{iw_y}\right|}{\left|a \cdot \boldsymbol{n}_{iw_x}\right|}\right)^{\frac{n}{2-n}} \\ \gamma &= \left(1 + \alpha^{\frac{2}{n}}\right)^{\frac{2}{2-n}} \\ \beta &= \left(\frac{\gamma\left|c \cdot \boldsymbol{n}_{iw_z}\right|}{\left|a \cdot \boldsymbol{n}_{iw_x}\right|}\right)^{\frac{n}{2-n}} \end{aligned} \quad s.t.\ \boldsymbol{X_i} = \begin{cases} x = \dfrac{a}{\left(1 + \alpha^{\frac{2}{n}} + \beta^{\frac{2}{n}}\right)^{\frac{n}{2}}} \cdot sign\left[\boldsymbol{n}_{w_x}\right] \\ y = \alpha \cdot \dfrac{b}{a}|x| \cdot sign\left[\boldsymbol{n}_{w_y}\right] \\ z = \beta \cdot \dfrac{c}{a}|x| \cdot sign\left[\boldsymbol{n}_{w_z}\right] \end{cases} \tag{33}$$

$$\delta_{iw} = |\boldsymbol{X}_w - \boldsymbol{X}_i| \ and \ \boldsymbol{X}_0 = \boldsymbol{X}_i + \frac{(\boldsymbol{X}_w - \boldsymbol{X}_i)}{2}$$

The super quadric media-wall contact equations define $\boldsymbol{X}_i$, which is the point on the media surface that is furthest past the wall boundary. This point is projected onto the wall in the direction of the wall normal to define $\boldsymbol{X}_w$. For spherical media, $\boldsymbol{X}_w$ is defined as the point on the wall closest to the mill centre. The point $\boldsymbol{X}_w$ serves as the point of the wall that is on the contact line. Its position relative to the media centre $\boldsymbol{X}_C$ for spherical media, or to the super quadric surface point $\boldsymbol{X}_i$ for super quadric media is used to determine the overlap $\delta_{iw}$ and the contact point $\boldsymbol{X}_O$.

### 3.2.5 Timesteps

The Hertz-Mindlin soft contact DEM model uses a minimum timestep as a stability criterion to ensure that the degree of particle overlap is controlled and that the system conserves energy. This is done through determining a critical timestep and running the simulation at a reasonable fraction of it. The critical timestep is usually determined by considering the mechanics of the undamped contact system, in the direction normal to the contact plane which categorically has the largest critical timestep (Burns & Hanley, 2017). Though the addition of damping decreases the critical timestep, its effect should be contained by using a safety factor. For systems with numerous monodispersed cohesionless DEM bodies the minimum timestep is typically constant throughout the simulation.

The critical timestep is commonly determined through one of three approaches. The first considers a linear spring system and determines the critical timestep through the modal decomposition of the system by determining the Eigenvalues of the spring amplification matrix (Burns & Hanley, 2017). This results in equation (34). This is the critical timestep definition used by Tsuji, Tanaka & Ishida (1992) and older models.

$$\Delta t_{Min} = C\sqrt{\frac{m_{eff}}{K_n}} \tag{34}$$

where, C is a safety factor, and the effective mass is of the collision between the smallest bodies.

The second approach to determine the timestep follows from the assumption that the energy is propagated through Rayleigh waves and the criterion that collision energy cannot propagate beyond its neighbours in a single timestep (Thornton, 2015; Burns & Hanley, 2017; Otsubo, O'Sullivan & Shire, 2017). This method is often implemented in non-linear contact models. This approach is independent on the velocity of the system, which is a concern in highly dynamic systems as the timestep should intuitively reduce when the body velocities are high. This is the approach used by the DEM simulation software EDEM (DEM Solutions, 2014), in equation (35).

$$\begin{gathered}\Delta t_{Min} = C\frac{\pi \cdot \bar{r}}{\lambda}\sqrt{\frac{\rho}{G_s}} \\ \lambda = 0.1631\sigma + 0.8766\end{gathered} \tag{35}$$

where $\bar{r}$ is the mean radius, $\rho$ is the body density and $\lambda$ the equivalent wavelength and Gs is the shear modulus of the collision between the smallest bodies.

The third approach was developed specifically for Hertz-Mindlin non-linear contact models by Burns & Hanley (2017). It follows from the criteria that the velocity sign reversal of the body cannot take place within one timestep, which is why it is dependent on the maximum velocity in the system, to ensure that there is stability within the fastest moving particles. This shown in equation (36).

$$\Delta t_{Min} = C\left(\frac{m_{eff}}{K_n \cdot \sqrt{v_{max}}}\right)^{\frac{2}{5}} \tag{36}$$

where $v_{max}$ is the maximum velocity anticipated in the system.

The safety factor used for the first two approaches is typically overconservative at approximately 0.2 (Tsuji, Tanaka & Ishida, 1992; DEM Solutions, 2014). As the third approach is determined specific to the contact system, less conservative safety factors of up to 0.6 can be used (Burns & Hanley, 2017). The timestep is usually kept constant throughout the simulation even though some of the time dependent variables used to determine it may change. This aspect is considered when choosing the safety factor.

The size of the safety factor and more importantly the timestep is critical as systems with low body timesteps are inherently computationally expensive, as more iterations are required. In an effort to reduce the simulation time, multiple models have modified the spring coefficient, in linear models (Landry et al., 2003), and lowered the Young's modulus in non-linear models (Jayasundara et al., 2006). The effect of this on the overall system output quality has been reported as negligible to an extent that may be system specific. This effect is analysed in the calibration phase of DEM model development.

#### 3.2.5.1 Super quadric critical timesteps

The theory used to determine the minimum timestep to use when simulating super quadric bodies has not been extensively reported in literature. The approach to calculating critical timesteps for super quadric media is expected to differ significantly from spherical media due to the variability of the effective radius, which is considered in all timestep approaches for spherical media, either directly or through the normal coefficient. The effective radius of a super quadric is dependent on the curvature at the surface point on the contact line of the collision. This creates a wide scope of variability within the system that should be accounted for in determining the critical timestep and safety factor used in the simulation.

In Gao, Yu, Lu, et al. (2021), the authors detail their timestep calculation approach that incorporated the variability of a super quadric system in their safety factor. Their minimum timestep formula used reworked and presented in equation (37). The authors used the bounding sphere radius, instead of the effective radius of curvature, and used a safety factor of 0.05, which is an order of magnitude lower than any spherical system safety factor.

$$\Delta t_{Min} = C \cdot \pi \sqrt{\frac{4m_{eff}}{4K_n - \eta^2}} \tag{37}$$

However, dense particulate systems are computationally limited to timesteps above $10^{-8}$ s. Table 3.1 summarizes the timestep and Young's Modulus data from published simulations of dense super quadric systems, by the size of the largest media semi-axis. From this we observed all simulation timesteps above $10^{-7}$ s, and Young's Moduli as low as 0.001 GPa. The exact timestep used with their Young's modulus in Wang & Shen (2022) was not provided, however the authors state their use of the Raleigh timestep (35), with a safety factor between 0.1 to 0.5 and an unqualified body radius, to determine their DEM minimum timestep. Based on the size of the Young's Moduli, it can be assumed that these have been lowered significantly for computationally efficiency. In comparison, spherical systems have been simulated at lowered Young's Modulus of 1 GPa (Jayasundara et al., 2006), to approximate the motion of ceramic media materials with approximate Young's Modulus of 100 GPa (Gudin et al., 2006). The effect of this practice on super quadric systems has yet to be studied extensively.

*Table 3.1: Published super quadric simulation timestep data from non-linear contact systems*

| Longest Semi-axis (m) | Density (kg/m$^3$) | Young's Modulus (GPa) | Timestep (μs) | Referenced Publication |
|---|---|---|---|---|
| 0.0025 | 6370 | 15.50 | 0.4 | Grohn et al. (2023) |
| 0.0026 | 730 | 12.00 | 0.4 | Grohn et al. (2023) |
| 0.0040 | 747 | 0.01 | - | Wang & Shen (2022) |
| 0.0040 | 1164 | 1.15 | 0.5 | Gao, Yu, Portal, et al. (2021) |
| 0.0065 | 1377 | 0.05 | 2.2 | Gao, Yu, Portal, et al. (2021) |
| 0.0068 | 1338 | 0.01 | 2.4 | Gao, Yu, Portal, et al. (2021) |
| 0.0068 | 1338 | 0.001 | 16.8 | Gao, Yu, Portal, et al. (2021) |

### 3.2.6 Energy outputs

Parameters used to analyse energy dissipation within the mill are the collision frequency and energy, as well as the power draw and energy dissipation rates. Collision energy in these systems is defined by the net kinetic energy of the collision, relative to the mass of the grinding media. The collision energy and frequency are of particularly importance, as comminution activity in stirred mills is characterised by the number of stress events and the stress intensity (Kwade, 1999), which these parameters correspond to, respectively. The energy dissipation rate refers to the amount of energy that is dissipated in collisions over its duration, dt. These outputs encapsulate the collision energy spectra of the mill. The energy dissipated in the collisions should result in breakage of particles caught in between the media, either dry or wet.

For systems with monodispersed DEM media the collision energy (CE) is defined relative to the mass of one media body as shown in equation (38) (Jayasundara et al., 2006).

$$CE_{ij} = \frac{1}{2}m\left(\boldsymbol{v}_i^2 - \boldsymbol{v}_j^2\right) \tag{38}$$

The energy dissipation (ED) is calculated based on the dissipative force that results from the dashpot. Following from the dissipative force component of the contact models, the energy dissipation in the normal and tangential directions is determined from equations (39) and (40).

$$ED_{N_{ij}} = \frac{1}{2}\left(\eta \boldsymbol{v}_{rel_{ij}}^2\right) dt_{ij} \tag{39}$$

$$ED_{T_{ij}} = min\left[\frac{1}{2}\left(\eta \boldsymbol{v}_{s_{ij}}^2\right) \; ; \; \mu_s \left|\boldsymbol{F}_{N_{ij}}\right| \boldsymbol{t}_{ij}\boldsymbol{v}_s\right] \cdot dt_{ij} \tag{40}$$

The collision energy spectra are commonly visualised as collision frequency plots and energy dissipation rate plots as shown in Figure 3.5.

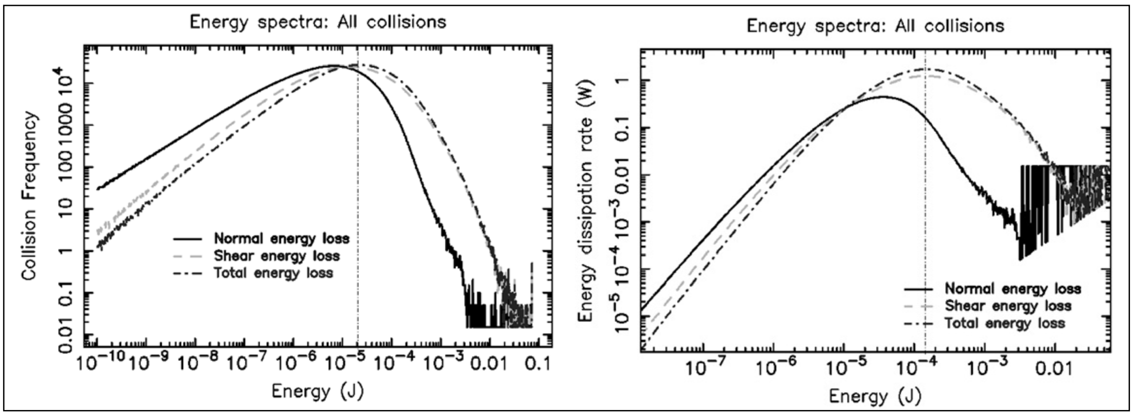

*Figure 3.5: Collision frequency and energy dissipation rate spectra for the same stirred mill, taken from Sinnott, Cleary & Morrison (2006)*

Within these plots the modal peaks of the energy dissipation rate and the corresponding collision energy have been used as performance indicators in comparative studies (Sinnott, Cleary & Morrison, 2006; Cleary & Sinnott, 2015; Cleary, Sinnott & Pereira, 2015; Ndimande et al., 2019).

### 3.2.7 Flow outputs

The outputs of the DEM models focused on illustrating flow patterns and energy distributions in their mill environment. Key output parameters from the DEM analysis that are used to characterise the flow within the mill are the normal, tangential, radial and axial profiles and distributions of velocity, force and energy, and spatial distributions. The spatial occupancy of the mill space is of specific interest, as it shows regions of high or low body density, which when correlated with the spatial velocity and energy profiles is informative on the mechanisms at play within the mill space. Figure 3.6 shows an example representation of the solids fraction and velocity profiles of an attritor mill from Daraio et al. (2020). These are typically illustrated through axial and radial cross sections of the mill. These indicate the direction and speed of flow of media within the mill, as well as the porosity and media distribution. The trajectory of particles has been used to give an indication of the degree of transport and mixing within the mill, an illustration of this for a horizontal disk mill is shown in Figure 3.7 (Jayasundara, Yang & Yu, 2012).

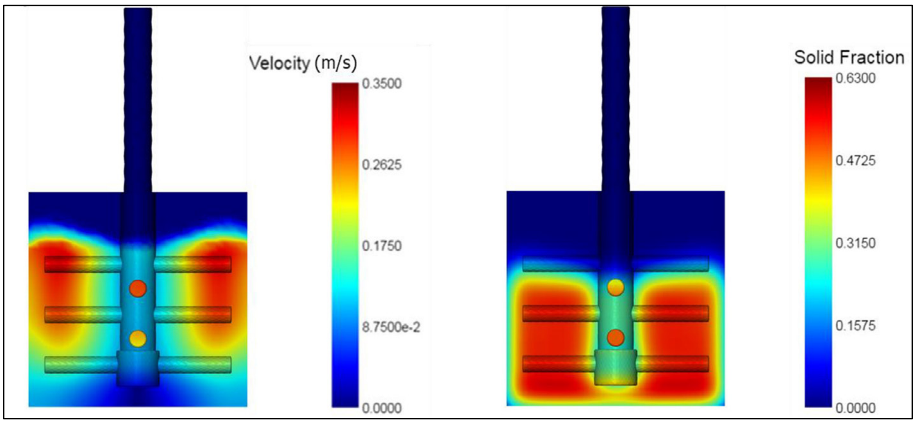

*Figure 3.6: Colour plots of velocity and solids fraction from the DEM simulation of laboratory scale attritor mill, taken from Daraio et al. (2020)*

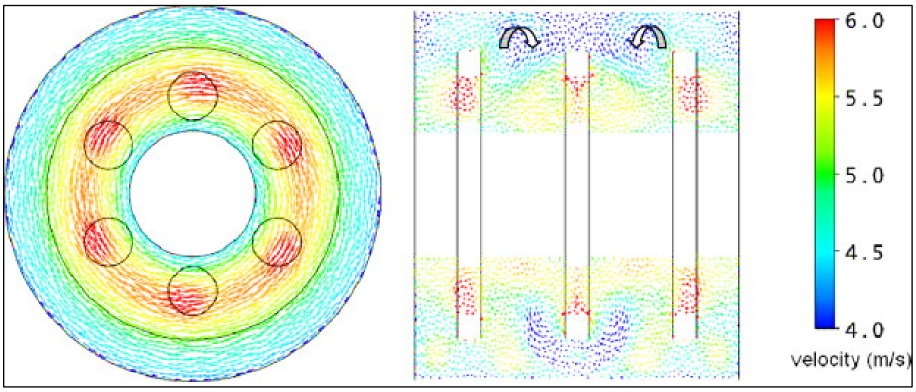

*Figure 3.7: Coloured trajectory quiver plots of velocity from the DEM simulation of laboratory scale horizontal disk mill, taken from Jayasundara, Yang & Yu (2012)*

## 3.3 Smoothed Particle Hydrodynamics

### 3.3.1 Fundamentals

Smoothed particle hydrodynamics is a computational method developed by Lucy (1977) and Gingold & Monaghan (1977) as a tool to simulate non axisymmetric phenomena in astrophysical fluid dynamics. Its uses have evolved to include free surface fluid dynamics, in particular those present in the grinding media and slurry interactions of stirred mill comminution (Sinnott, Cleary & Morrison, 2011a; Cleary & Sinnott, 2015; Ndimande et al., 2019) and other slurry operations within mineral processing (Cleary, Hilton & Sinnott, 2017; He et al., 2018; Tan, Xu & Chen, 2018; Tang, Jiang & Zhou, 2018; Xu, Dong & Ding, 2019).

The basis of SPH is to compute density from an arbitrary distribution of mobile point mass particles (Monaghan, 2005; Price, 2012). SPH makes use of a discretised grid of particles. Their resolution follows mass, instead of volume in grid-based methods used in traditional computational fluid dynamics (CFD). The SPH method achieves discretisation through its approximation of a basic interpolator of a field value (A) using a kernel weighted sum. This is the basis upon which the systems of equations that conserve desired fluid properties are constructed. This discretisation is shown in equation (41), taken from Neethling & Barker (2016).

$$\langle A\rangle(x) = V_0 \sum_{j\in P} A_j W\left(\left|\boldsymbol{x}-\boldsymbol{x}_j\right|, h\right) \tag{41}$$

where $V_0$ is the rest volume associated with a particle, P is the set of integration points, $A_j$ is the value of the field A at point j and A(x) is the weighted average value of the field at the particle's location, x. The smoothing kernel W is a function of the distance between the location being considered ($x_j$) and the particle's location, as well as the smoothing length, h.

The kernel functions used in most SPH simulations are B-Spline functions, which approximate the shape of a gaussian function, but are set to truncate at a multiple greater than the set smoothing length. As a minimum, fluid equations require continuity within the first and second derivatives. Therefore, the lowest order of B-Spline functions possible for SPH is the cubic or $M_4$ spline truncated at 2h (Monaghan, 2005; Price, 2012; Xu, Dong & Ding, 2019). Use of this kernel, along with the higher order quintic $M_6$ spline is widely reported in the literature (Potapov, Hunt & Campbell, 2001; Hu & Adams, 2006). The quintic kernel, truncated at 3h, is represented in equation (42) (Price, 2012).

$$W\left(\left|\boldsymbol{x}-\boldsymbol{x}_j\right|, h\right) = \frac{1}{120h}\cdot\begin{cases}(3-q)^5-6(2-q)^5+15(1-q)^5, & 0\le q\le 1;\\ (3-q)^5-6(2-q)^5, & 1<q\le 2;\\ (3-q)^5, & 2<q\le 3;\\ 0, & q>3.\end{cases} \tag{42}$$

$$q = \frac{\left|\boldsymbol{x}-\boldsymbol{x}_j\right|}{h}$$

In SPH, the kernel uses the magnitude of the distance between the particle and its neighbour relative to the smoothing length, q, which is one dimensional.

The application of the discretisation to the first derivatives of the field values is commonly done through attributing the derivative function to the kernel as it is a differentiable function. This approximation has been used in Cleary & Morrison (2009) and Price (2012) as shown in equation (25).

$$\langle \nabla A \rangle(\boldsymbol{x}) = V_0 \sum_{j \in P} A_j \nabla W\left(\left|\boldsymbol{x} - \boldsymbol{x}_j\right|, h\right) \tag{43}$$

Neethling & Barker (2016) took this further by defining the gradient such that it is symmetric, which allows for explicit conservation of the fluid properties, and the solution achieves zero order complete convergence. This formulation is a modification of the work of Hu & Adams (2006) and is as shown in equation (44).

$$\begin{gathered} \langle \nabla A \rangle_i = \frac{1}{V_0} \sum_{j \in P} \left( \frac{A_i}{\sigma_i^2} + \frac{A_j}{\sigma_j^2} \right) \nabla W_{ij} \\ \nabla W_{ij} = \nabla W\left(\left|\boldsymbol{x} - \boldsymbol{x}_j\right|, h\right) \quad \sigma(x) = \sum_{j \in P} W\left(\left|\boldsymbol{x} - \boldsymbol{x}_j\right|, h\right) \end{gathered} \tag{44}$$

The use of σ(x) is as a correction factor to account for the variation of particle spacing with position and its effect on the total weighting for the particles around a particular point.

The second derivative of field values is often determined through calculations based on a finite difference approximation of the second derivative, using Taylor series (Monaghan, 2005; Cleary & Morrison, 2009), instead of differentiating the kernel twice, for greater solution stability and conservation of fluid properties. For the case with the first derivative as defined by Neethling & Barker (2016), their second derivative follows from a combination of the discretised first derivative with a finite difference approximation for the first derivative, resulting in the following formulation in equation (45)

$$\begin{gathered} \langle \nabla^2 A \rangle_i = \frac{1}{V_0} \sum_{j \in P} \left( \frac{1}{\sigma_i^2} + \frac{1}{\sigma_j^2} \right) \frac{\left(A_i - A_j\right)}{r_{ij}} \frac{\partial W_{ij}}{\partial r_{ij}} \\ r_{ij} = \left|\boldsymbol{x} - \boldsymbol{x}_j\right| \end{gathered} \tag{45}$$

### 3.3.2 Application to minerals processing fluids

Having defined the discretisation equations, SPH in mineral processing fluids goes on to incorporate continuum fluid properties through the construction of conservation equations. The lagrangian nature of SPH allows for the equations to carry the following inherent features: exact time independency in the solutions, exact and simultaneous conservation of mass, linear and angular momentum, and energy and zero intrinsic dissipation. Following from the basis of fluid dynamics, in its application to minerals processing fluids, the SPH particle approximation is governed by the following equations: the momentum equation, the continuity equation and an equation of state. These equations ensure the conservation of mass and momentum within the fluid. In a simplification of the system, the conservation of energy is not explicitly specified, and the system is assumed isothermal, with no temperature dependency in the equation of state.

The conservation of momentum is explicitly stated through the momentum equation, which applies Newtons second law to the SPH point mass particles. This consists of a pressure term, stress term and body forces on the fluid. The SPH models used in the minerals industry can be distinguished by the stress term in the equation, which is a result of their approximation of the rheological behaviour of the fluid. Cleary & Morrison (2009) use empirical stress models to describe their fluids, while Neethling & Barker (2016) uses a Newtonian model which results in the momentum equation presenting as the Navier-Stokes equation. The Navier-Stokes form, as discretised in the previous section is as follows, for a fluid particle i and its neighbours j.

$$\rho a = -\boldsymbol{\nabla} P + \mu \boldsymbol{\nabla}^2 u + f$$

$$\boldsymbol{a}_i = \frac{1}{V_0 \rho_0}\left(-\sum_{j\in P}\left(\frac{P_i}{\sigma_i^2} + \frac{P_j}{\sigma_j^2}\right)\boldsymbol{\nabla} W_{ij} + \mu \sum_{j\in P}\left(\frac{1}{\sigma_i^2} + \frac{1}{\sigma_j^2}\right)\frac{\boldsymbol{v}_i - \boldsymbol{v}_j}{r_{ij}}\frac{\partial W_{ij}}{\partial r_{ij}}\right) + \frac{\boldsymbol{F}_i}{\rho_0} \tag{46}$$

where a is acceleration, $V_0$ is initial volume, $\rho_0$ is the fluid rest density, μ is the fluid dynamic viscosity, P is pressure, v is velocity, and $F_i$ and f represent the body forces on the fluid. The body forces are determined by the simulated system. In stirred mills, this is limited to the interaction forces between the slurry and grinding media. In other operations custom force models have been incorporated (Tan, Xu & Chen, 2018).

The SPH formulations all use quasi-compressible fluids, of which the relationship between pressure and density is defined by the following equation of state (Morrison, Cleary & Sinnott, 2009; Tang, Jiang & Zhou, 2018; Xu, Dong & Ding, 2019).

$$P_i = \frac{\rho_0 c_0^2}{n}\left(\left(\frac{\rho_i}{\rho_0}\right)^n - 1\right) \tag{47}$$

where ρi is the fluid density, $c_0$ is the speed of sound through the fluid and n is a compressibility constant, typically 7. This equation is fundamental in defining the fluid free surface as it defines the pressure at the rest density as zero.

The continuity equation is used to regulate the density used in the fluid equation of state and explicitly conserve mass in the fluid (Neethling & Barker, 2016). The formulation is as follows.

$$\frac{\partial \rho_i}{\partial t} = \rho_0 \boldsymbol{\nabla} \cdot \boldsymbol{v_i} \tag{48}$$

### 3.3.3 Timesteps

A key feature of SPH is that its solutions are time independent. Due to this, there is no clear theory to determine the optimal timestep. Traditionally, the timestep is chosen according to empirical laws based on the fluid properties. Neethling & Barker (2016) based their critical timestep as the minimum of multiple criteria. The first being the Courant–Friedrichs–Lewy (CFL) condition (Courant, Friedrichs & Lewy, 1928). This defines the critical timestep, $\Delta t_{CFL}$ based on the smoothing length and the relative velocity between a particle *i* and its neighbours *j*.

$$\Delta t_{CFL} = min\left[\frac{h}{|\boldsymbol{v}_{ij}|}\right] \tag{49}$$

A critical acoustic CFL timestep, $\Delta t_A$, is introduced. This defines the timestep using the speed of sound and the ratio of the current density to rest density in place of the relative velocity. This condition is rarely violated due to speed of sound being set at an order of magnitude larger than the expected maximum system velocity.

$$\Delta t_A = min\left[\frac{h}{c_0\sqrt{\left(\frac{\rho_i}{\rho_0}\right)^{n-1}}}\right] \tag{50}$$

A critical acceleration timestep, $\Delta t_F$, is included to ensure that the acceleration of a particle is not so high that velocity causes the CFL condition to be violated. Using a predictor-corrector method, this criterion would be applied on predictor step to ensure no violation on corrector step.

$$\Delta t_F = min\left[\sqrt{\frac{h}{|\boldsymbol{a}_i|}}\right] \tag{51}$$

The final timestep criterion is a fluid viscous dissipation timestep, $\Delta t_v$. This is considered in small coupled systems like the one used in the study, because of the significance of the microscale solid-fluid interactions determined by the coupling interface.

$$\Delta t_v = min\left[\frac{h^2\rho_0}{2\mu}\right] \tag{52}$$

The overall SPH timestep, $\Delta t_{SPH}$, must be less than the minimum of the critical time steps. Therefore, a safety factor C is introduced.

$$\Delta t_{SPH} = C \cdot min[\Delta t_{CFL}, \Delta t_A, \Delta t_F, \Delta t_v\ ] \tag{53}$$

### 3.3.4 Model outputs

The SPH simulation of the fluid motion provides outputs such as fluid pressure gradients, vorticity, trajectory and velocity distributions, viscous energy dissipation and relative density distributions. Within the mill space, SPH when coupled to DEM provides insight on the porosity of the mill which informs on the interaction between the two phases and the extent of fluidisation within the bed. Figure 3.8 shows how the SPH fluid is able to interact and flow between spherical particles, while Figure 3.9 show the fluid velocity within an industrial SMD, and its effect on the mill solids fraction.

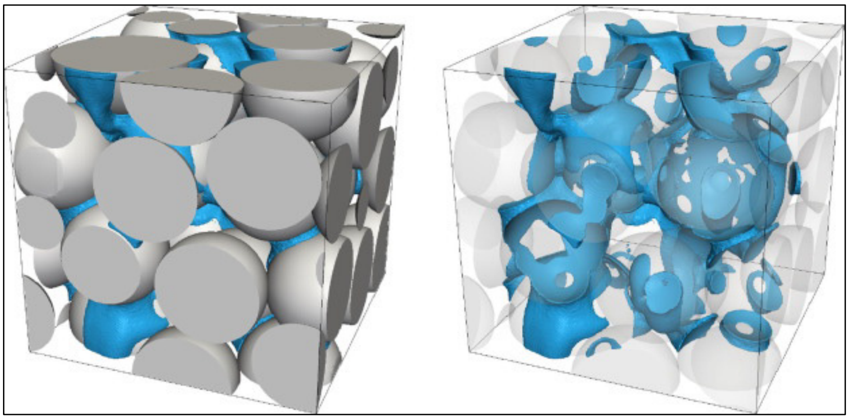

*Figure 3.8: SPH fluid flow through a fully packed bed of spherical particles, taken from Neethling & Barker (2016)*

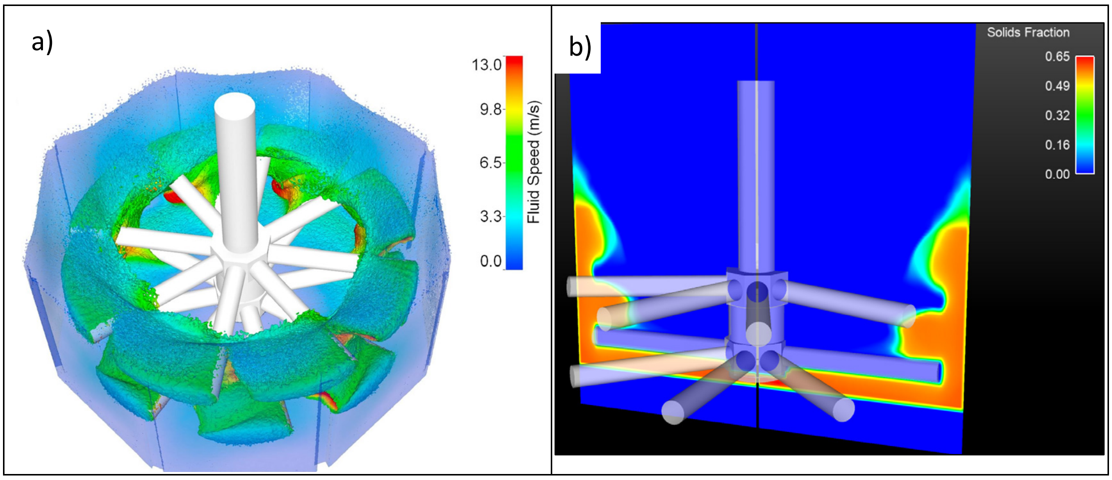

*Figure 3.9: a) Still of the SPH fluid velocity and b) the solids fraction cross section in an industrial SMD modelled through coupling DEM and SPH, taken from Ndimande et al. (2019)*

### 3.3.5 Other fluid models

There are two other computational fluid modelling techniques that could be used to model mineral processing fluids. These are traditional Computational Fluid Dynamics (CFD) and Lattice Boltzmann Methods (LBM). Traditional CFD is a Eulerian method that defines the fluid using a fixed grid. The formation of a central vortex in the laboratory scale SMDs used in this thesis require computation of the fluid free surface. This is more easily defined in the mobile grid of SPH than in a fixed grid system. The LBM use microscopic models and mesoscopic kinetic equations to represent free surface fluids. Therefore, LBM can effectively characterise the fluid, but has yet to be widely developed for these purposes, particularly in coupled systems (Pereira et al., 2012).

## 3.4 Coupling schemes

### 3.4.1 Coupling fundamentals

The application of coupled DEM-SPH and DEM-CFD models has been extensively reported in literature. Inclusion of a fluid force in DEM models of two phase systems was prevalent in the earliest models of Tsuji, Kawaguchi & Tanaka (1993) and Gudin, Kano & Saito (2007). This has since evolved to the coupling frameworks used in modern simulations that inform on the combined motion of the solid and the fluid (Jayasundara et al., 2009; Sinnott, Cleary & Morrison, 2011a). The coupling interface is used to determine the interaction forces between the solid (DEM) and the continuum fluid (SPH/CFD) phases. The interaction forces are detailed in section 3.4.2, but consist predominantly of the drag force and a buoyant or pressure gradient force.

Cleary (2015), presented two main methods of coupling the two phases. The first is a resolved coupling, where the drag force from the fluid onto the bodies is explicitly determined based on the boundary conditions and the shear stress applied to the fluid. This method is heavily dependent on a fluid resolution small enough to ensure calculation accuracy. The resolution has a controlling influence on the simulation timestep as well as the number of grid points or particles, which leads to small resolutions being of great computational expense. This is the primary reason this method is not commonly applied to larger complex systems. The second coupling method is unresolved, which uses grid averaging to determine the solids fraction distribution, that is used by the coupling interface to determine the drag force based on empirical correlations (Kloss et al., 2012). The resolution in these models should be small enough to capture the local features of the solids distribution (He et al., 2018). This is the method used by majority of the coupled models of mineral processing systems (Jayasundara, Yang, Guo, et al., 2011; Kloss et al., 2012; He et al., 2018; Tan, Xu & Chen, 2018; Tang, Jiang & Zhou, 2018; Ndimande et al., 2019; Xu, Dong & Ding, 2019).

The coupled models are further defined by whether the coupling interfaces incorporates the forces back into both DEM bodies and SPH particles in a two-way coupling or just one phase in a one-way coupling. This practice uses the nature of the expected flow to determine whether it is worth the computational expense to incorporate the forces back (Norouzi et al., 2016). In contact dominant flow the solid phase is expected to have the overriding influence on the flow and hence in some models the forces are only incorporated into DEM phase. While the inverse is expected in dilute systems.

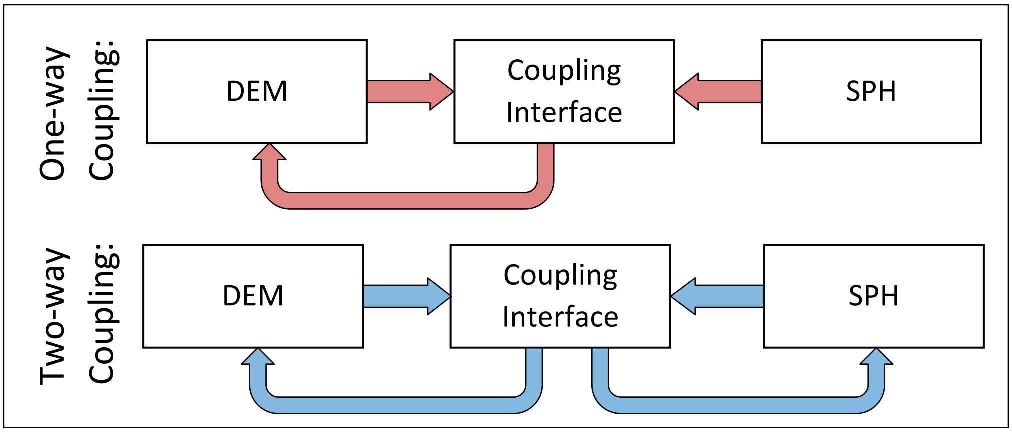

*Figure 3.10: Outline of coupling interface interactions of one-way and two-way coupled models*

Stirred mill systems were thought to experience contact dominant flow due to the large media influence, hence the first models disregarded the fluid completely, while the first coupled models were one-way coupled, where the fluid model information was fed back into the DEM model but the DEM model did not inform the fluid model (Jayasundara et al., 2009; Sinnott, Cleary & Morrison, 2011a). The use of two-way coupled models was adopted by these systems when it became computationally feasible to do so. The difference between a one way and two-way coupled model in this context is illustrated in Figure 3.10 above. Ndimande et al. (2019) used a two-way coupled model to show that the fluid can contribute up to a third of the overall power draw and that neglecting the fluid influence causes an underestimation of the overall power draw.

### 3.4.2 Solid-Fluid interactions

The purpose of coupling is to allow the solid-fluid interaction forces to be accounted for in the calculation of their respective trajectories. These solid-fluid interactions are defined by hydrostatic and hydrodynamic forces. The hydrostatic force is the buoyancy force, which is defined as the force due to the fluid pressure gradient around a body (Zhao, 2017).

$$\boldsymbol{F}_B = -V_b \cdot \nabla \boldsymbol{P}_f \tag{54}$$

where, $V_b$ is the volume of the solid body and $P_f$ is the fluid pressure.

The hydrodynamic forces in solid-fluid interactions are virtual mass, lift and drag. The drag force has been known to dominate the hydrodynamics at low Reynolds numbers (Zhao, 2017). It is for this reason that it is the primary hydrodynamic force considered in mill system simulations (Jayasundara et al., 2009; Sinnott, Cleary & Morrison, 2011a).

#### *3.4.2.1 Drag force on spherical media*

The appropriate drag force formulation is heavily dependent on the system characteristics. One of the stirred mill systems under consideration is a system of monodispersed spherical bodies in a contact dominant flow regime where the bodies do not disperse but remain fluidised. The formation of a vortex concentric to the impeller in the mill is indicative of a radial velocity gradient, which results in variation of the particle Reynold’s numbers within the mill. The drag force approximations used by these systems are based on empirical formulations of dimensionless drag, normalised by the Stokes-Einstein drag force. These follow one of two approaches; the first approach considers the drag on an isolated body over the complete range of Reynold’s numbers using the drag coefficient and accounts for crowding effects through a porosity dependent factor. These are the empirical formulations of Wen & Yu (1966) and Di Felice (1994). The basis drag force equation for these formulations is as shown in equation (55), for a fluid f and spherical body b.

$$\begin{gathered} \boldsymbol{F}_D = 3\pi\mu d\boldsymbol{v}_{rel} \cdot \frac{C_D}{24} Re_b \cdot \varepsilon^{-\chi} \\ Re_b = \frac{\rho_f d|\boldsymbol{v}_{rel}|\varepsilon}{\mu} \quad ; \ \boldsymbol{v}_{rel} = \boldsymbol{v}_f - \boldsymbol{v}_b \end{gathered} \tag{55}$$

where ε is the porosity, χ is the porosity dependent factor, d is the body diameter, μ is the fluid viscosity, ρ is density and $C_D$ is the drag coefficient for a single spherical body.

The two empirical formulations differ in the porosity dependent factor used. The Di Felice drag force accounts for the full range of possible systems, using a porosity dependant factor that varies with the particle Reynolds number, as shown in equation (56). The Wen & Yu formulation was designed specifically for high porosity systems, with its porosity raised to a constant figure that is representative of the upward limit of the Di Felice factor (57). Because the Di Felice approximation is valid over the full range of particle Reynolds numbers, it has been used extensively in DEM-SPH/CFD simulations (Jayasundara et al., 2009; Cleary, 2015; Zhao, 2017; Markauskas & Kruggel-Emden, 2019).

$$\chi_{Di\,Felice} = 3.7 - 0.65 \cdot \mathrm{e}^{\left(-\frac{(1.5-\log_{10}(Re_b))^2}{2}\right)} \tag{56}$$

$$\chi_{Wen\,\&\,Yu} = 3.65\ ;\ \varepsilon > 0.8 \tag{57}$$

The drag coefficient is determined from empirical correlations with Reynolds number, such is the Schiller-Nauman correlation in equation (58) (Schiller & Naumann, 1935). Which is commonly employed with the above drag formulations (Zhao, 2017).

$$C_D = \frac{24}{Re_b}\left(1 + 0.15Re_b^{0.687}\right) \tag{58}$$

The second approach to determining the drag force is considers at the drag force on a number of particles. Such formulations are those of Ergun (1952) in equation (59), and the Darcy approximation in equation (60), based on Darcy's law on hydraulic conductivity (Darcy, 1856). The Ergun approximation has been used in a stepwise configuration with the Wen & Yu approximation to encompass the full spectrum of porosity (Beetstra, van der Hoef & Kuipers, 2007; He et al., 2018), though the disparity in its prediction in the transition region has been shown by Kafui, Thornton & Adams (2002). Because of this, additional correlations have been added for the transition region (Zhao, 2017). The Darcy approximation has been used by Cleary & Morrison (2009) in a two-stage configuration where it determines the drag on the SPH particles, while the Di Felice approximation determines the drag on the DEM bodies, and the two resulting forces are scaled equal to conserve momentum.

$$\boldsymbol{F}_{D_{Ergun}} = \left(\frac{150}{18}\cdot\frac{1-\varepsilon}{\varepsilon^2} + 1.75\frac{Re_b}{18\varepsilon^2}\right)\frac{\boldsymbol{v}_{rel}}{\rho_f}\ \ ;\ \ \varepsilon \leq 0.8 \tag{59}$$

$$\boldsymbol{F}_{D_{Darcy}} = \varepsilon^2\mu\frac{\boldsymbol{v}_{rel}}{\rho_f K}\ ;\ \ K = \frac{\varepsilon^3}{CT(1-\varepsilon)^2}S^2 \tag{60}$$

#### 3.4.2.2 *Drag force on super quadric media*

The drag force on super quadric media has been approximated by considering the drag on an isolated super quadric body and accounting for the crowding effects through the Di Felice porosity dependent factor (Hilton, Mason & Cleary, 2010; Gao, Yu, Lu, et al., 2021; Wang & Shen, 2022). The resulting drag equation is presented in equation (61). Which follows from equation (55), using the diameter of the volume equivalent sphere, $d_{Veq}$, in the body Reynolds number.

$$\begin{aligned} F_D &= 3\pi\mu d_{V_{eq}}\boldsymbol{v}_{rel}\cdot\frac{C_D}{24}Re_b\cdot\varepsilon^{-\chi_{Di\,Felice}} \\ Re_b &= \frac{\rho_f d_{V_{eq}}|\boldsymbol{v}_{rel}|\varepsilon}{\mu} \end{aligned} \tag{61}$$

The most prominent drag coefficient models used to simulate the fluidisation of non-spherical bodies are the Ganser (1993) and the Hölzer & Sommerfeld (2008) models. The models are favoured because they directly incorporate shape effects (Hilton, Mason & Cleary, 2010; Wang

& Shen, 2022). Both models were assessed by Gao et al. (2021) using the De Felice approximation, where the Hölzer & Sommerfeld model provided the better performance across all simulated super quadric shapes. The Hölzer & Sommerfeld drag coefficient model is provided in equation (62).

$$C_D = \frac{8}{Re_b}\frac{1}{\sqrt{\Phi_\perp}} + \frac{16}{Re_b}\frac{1}{\sqrt{\Phi}} + \frac{3}{\sqrt{Re_b}}\frac{1}{\Phi^{3/4}} + 0.42 \cdot 10^{0.4(-\log_{10}\Phi)^{0.2}}\frac{1}{\Phi_\perp}$$

$$\Phi = \frac{4\pi R_{V_{eq}}}{\mathrm{SA}} \quad ; \quad \Phi_\perp = \frac{\pi R_{V_{eq}}^2}{\mathrm{A}_\perp} \tag{62}$$

where $\Phi$ is the conventional sphericity ratio of the surface area of the volume equivalent sphere to the surface area (SA) of the super quadric. And $\Phi_\perp$ is the cross-wise sphericity, which is a ratio of the projected cross-sectional area of the volume equivalent sphere to the projected cross-sectional area ($A_\perp$) of the super quadric in the direction of flow. The projected cross-sectional area of the super quadric is calculated by determining the closed rim of the super quadric in the direction of flow (Jaklič, Leonardis & Solina, 2000; Hilton, Mason & Cleary, 2010; Gao, Yu, Lu, et al., 2021). A discretized equation of the rim is given in the spherical coordinates $\theta$ and $\phi$ in equation (63) (Jaklič, Leonardis & Solina, 2000). Where the direction of flow is represented in the super quadric reference frame through the unit vector u. The spherical coordinates are converted to Cartesian using the parametric form in equation (64) (Jaklič, Leonardis & Solina, 2000) of the super quadric equation (18).

$$\phi_i(\theta) = arctan\left[\left(-\frac{c}{u_z}\left(\frac{u_x}{a}\cos^{2-n}(\theta) + \frac{u_y}{b}sin^{2-n}(\theta)\right)\right)^{\frac{1}{2-n}}\right], \qquad \theta_i = \frac{2\pi i}{N} \tag{63}$$

$$P_i\begin{pmatrix} x \\ y \\ z \end{pmatrix} = \begin{cases} x(\phi_i, \theta_i) = a \cdot cos^n(\phi_i)\cos^n(\theta_i) \\ y(\phi_i, \theta_i) = b \cdot cos^n(\phi_i)\, sin^n(\theta_i) \\ z(\phi_i, \theta_i) = \mathrm{c} \cdot \sin^n(\phi_i) \end{cases} \tag{64}$$

$$Note\!: the\ exponent\ n\ is\ a\ signed\ power\ such\ that\ q^n = |q|^n sign[q]$$

The points on the rim are then projected onto the plane perpendicular to the flow direction. The projected area can then be calculated by triangulating points on the projected rim to the particle centre and summating the area of the individual triangles.

### 3.4.3 DEM-SPH two-way coupling algorithms

Within DEM-SPH two-way coupling frameworks, the coupling algorithm dictates the order of computational operations done to simulate the motion and interactions of the DEM bodies and SPH particles. All models will need to perform the same operations to simulate their systems. However, the order and synchronicity of operations evolves to allow more computationally efficient configurations. Figure 3.11 contrasts a traditional linear coupling algorithm against a contemporary configuration.

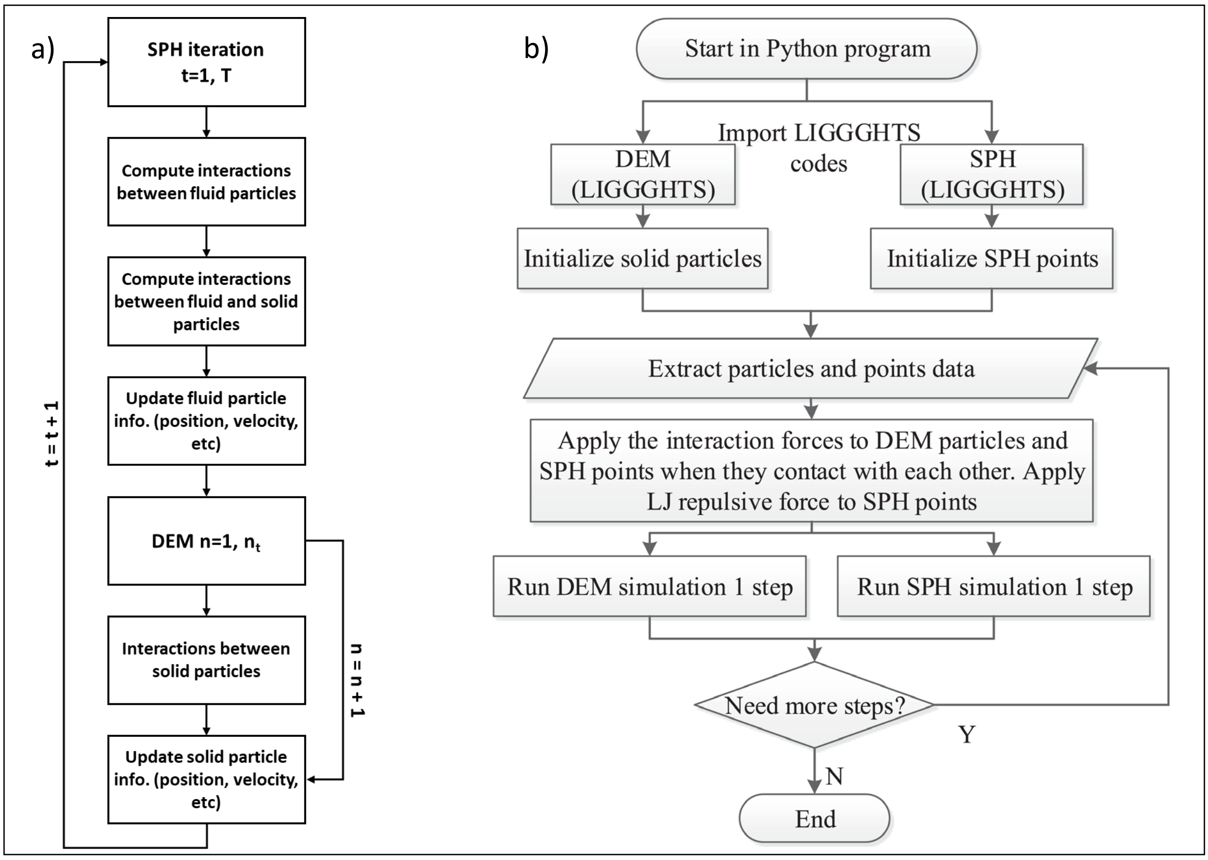

*Figure 3.11: a) Asynchronous two-way coupling algorithm adapted from Tang, Jiang & Zhou (2018), and b) simultaneous two-way coupling algorithm taken from Chen et al. (2020)*

Traditionally the two-way coupling algorithm is similar to Tang, Jiang & Zhou (2018) illustrated in Figure 3.11 a). This is a linear algorithm that starts by calculating the SPH properties to update the coupled properties before determining the DEM properties. The system operates at separate timesteps for DEM and SPH respectively, allowing for the sub-cycling of the DEM calculations. This allows for the optimisation of the DEM and SPH separately, instead of lowering the critical timestep of one to meet the other. Similar algorithm layouts have been presented by Cleary (2015) and He et al., (2018). Chen et al. (2020) in Figure 3.11 b) present a contemporary algorithm that performs the DEM and SPH calculations simultaneously. This is an effective change in that the DEM calculations are not waiting on the SPH calculations to finish, instead running at the same time and meeting at the coupling interface to update interactions forces. However, this configuration runs both systems at the same timestep, which may require the slowing down of one to meet the others critical timestep.

## 3.5 Summary of computational methods

- The discrete element method (DEM) is a lagrangian method used to determine the motion of cohesionless bodies based on the body conservation of momentum.
    - Collision forces are determined using a contact model, which includes a dissipation model. The forces are resolved through either a linear model based on Hooke's Law, or a non-linear model based in Hertzian contact theory.
    - Super quadric shapes allow non-spherical media to be modelled using DEM, through a closed surface equation. This uses the middle point method to detect contact between media. The curvature of the particle at the contact surface is used to determine the effective radius within non-linear contact models.
    - A constant integration timestep is determined as a fraction of a critical timestep determined by empirical correlations to ensure energy does not dissipate beyond immediate contacts within a timestep.
    - The method has been used to determine the energy spectra and internal flow environment of grinding media in stirred mills.
- Smooth particle hydrodynamics (SPH) is a lagrangian method used to define a continuum fluid through discretized point-mass particles.
    - Discretization of properties at particle points is achieved using a kernel-weighted sum. The first and second derivatives of properties are explicitly determined from the kernel.
    - Multiple empirical timestep correlations are used to determine a critical timestep that is evaluated for each time integration.
    - Mineral processing fluids are subject to explicit conservation laws for mass, momentum, and energy. This allows SPH to effectively determine the internal flow and energy environment of fluid within stirred mills.
- The coupling of these two models is done to transfer solids-fluid interaction forces between the media and slurry within stirred mills.
    - A two-way coupling interface allows these forces to be incorporated into both the DEM bodies and SPH particles. The shared lagrangian nature of SPH and DEM ensures compatibility and stability within the coupling.
    - The two-way coupling is either asynchronous or simultaneous in its calculation of the DEM and SPH properties. This influences the speed of the overall simulation.
    - The solid-fluid forces in question are typically restricted to the buoyancy force and the drag force in stirred mill systems.
    - Various methods are employed to ensure that the crowding effects of densely populated systems are considered in the drag model. Super-quadric media further consider shape effects on the drag force by using the projected area and media sphericity in drag coefficient correlations.

# CHAPTER 4

# Review of computational model applications on stirred mills

## 4.1 Introduction

The evolution and development of computational models of stirred mills has been progressing steadily over the years. These models use the discrete element method (DEM) and/or fluid models such as smoothed particle hydrodynamics (SPH) or traditional computational fluid dynamics (CFD) to inform on the spatial flow and energy distributions of the stirred mill space. Computational models have been applied in studies that aid in understanding the spatial response of the mill beyond what can be achieved through empirical studies on operating mills in laboratories, pilot plants or industrial plants.

This chapter discusses the development and application of computational models of stirred mills, current gaps in the body of knowledge, and technical limitations of the current systems.

## 4.2 Model development and evolution

The earliest DEM models of stirred mills in the minerals industry modelled dry systems, at either laboratory or pilot scale. Jayasundara et al. (2006) and Yang et al. (2006) began the dry modelling of a laboratory scale IsaMill. Their dry model has formed the basis of seven studies with various applications on the same mill (Jayasundara et al., 2008, 2009, 2010; Jayasundara, Yang, Guo, et al., 2011; Jayasundara, Yang, Yu, et al., 2011; Jayasundara, Yang & Yu, 2012; McElroy et al., 2012). Cleary, Sinnott & Morrison (2006) and Sinnott, Cleary & Morrison (2006) started modelling dry vertical tower and pin mills. The computational techniques developed from these models have been applied in studies of horizontal disk mills (Cleary & Sinnott, 2015; Cleary, Sinnott & Pereira, 2015) and an SMD (Ndimande et al., 2019). Kim & Choi (2008) and Santhanam & Dreizin (2012) developed dry DEM models for pin detritors.

### 4.2.1 The evolution and significance of fluid modelling

Gudin et al. (2006) and Gudin, Kano & Saito (2007a,b) first studied wet grinding in a bead pin mill by incorporating the Navier Stokes drag force into their DEM contact model of wet gibbsite grinding. This Navier Stokes drag inclusive DEM model approach was incorporated into the DEM model of Yamamoto et al. (2012) to analyse the velocity profiles in a bead disk mill, using an enlarged particle approach, which simulated the media motion in the mill with larger diameter media than an experimental mill system. Yamamoto et al. (2012) extracted velocity profiles from their experimental mill system using highspeed camera imaging and particle tracking analysis. These velocity profiles were compared against the simulated DEM velocity profiles and showed strong correlation.

The modelling of wet grinding in stirred mills has evolved to coupling either traditional CFD or SPH to the DEM model. The inclusion of the fluid model allows the simulation to provide more information on the fluid system that can be verified through experimental means such as PEPT. Sinnott, Cleary & Morrison (2011a) used a one way coupled DEM-SPH model of a tower mill, based on their 2006 dry DEM model, to analyse the flow patterns of the slurry. The model incorporated DEM data into the fluid model, but the fluid data was not incorporated back into the DEM model. This approach assumed that the fluid effect on the motion of the grinding media was limited, however the fluid model showed a reduced solids fraction near the impeller, as well as slurry pooling on top of media at the top of mill, which shows how the presence of the fluid required the mill system to adapt to enable fluid mobility. Jayasundara et al. (2009) used a two-way coupled DEM-CFD model of a horizontal disk mill, to analyse the effects of the slurry on the particle motion. This model transferred fluid data between the DEM and CFD models every 10° of rotation. The two-way coupling of the DEM-CFD resulted in an improved circulation around the disks and increased velocities, due to the additional drag forces, compared to their DEM-only model.

The Sinnott, Cleary & Morrison (2009) model has since evolved to a two-way coupled DEM-SPH model, used in Ndimande et al. (2019) to simulate an industrial SMD and compare it to a dry DEM only model. Their work showed that modelling the presence of the fluid between colliding particles provided a more realistic representation of the dilation of the fluid bed and the velocity profiles of the media. Their dry DEM simulation produced higher collision energies than the DEM-SPH coupled simulations. The DEM-SPH coupled simulations showed that SPH particles can be responsible for 34 % of the total mill power draw. Although the coupled simulation had a larger total power draw, the DEM-only model significantly overestimated the DEM component of the total power draw from the coupled simulation, which is the proportion of power drawn that is available for collisions. This challenged the effectiveness of running DEM-only simulations to approximate the energy environment of wet systems. The influence of the fluid on the industrial SMD dampened the collision energy of the media. This contrasts the effect of the fluid in the horizontal disk mill (Jayasundara et al., 2009), which increased the media velocity. This disagreement can be attributed to their mill orientations and operating speeds. The solid-fluid interaction forces work with gravity in the faster moving horizontal disk mill system to improve circulation. In the vertical SMD, the interaction forces are directed primarily perpendicular to gravity resulting in the dampening of energy as the weight of the fluid strengthens the gravitational forces in the mill, making it harder to fluidise.

Beinert et al. (2014) simulated an annular gap mill using a dry DEM model as well as one-way and two-way coupled DEM-CFD models. The resulting stress energy distributions showed significant differences in shape and mean that emphasise the importance of using the model that best estimates the flow behaviour of the system and its components.

## 4.3 Model applications and findings

The stirred mill computational models have been applied in the literature to evaluate breakage mechanisms, analyse grinding rates, determine the effects of material properties, operating parameters, and mill design parameters, and in numerous alternative applications. This section is catalogued by the application, where all the findings from different models are considered. The output from the models offers unique information that provides a computational perspective on causative or correlative mechanisms within the mill environment that affect performance. Where multiple papers consider the same parameters, the ranges investigated are provided for comparison.

The horizontal disk mill is the most extensively modelled and studied stirred mill type and has the most applications, with duplicate studies with different modelling approaches. This allows for direct comparison of the model types and their relative findings on an application. The inclusion of the fluid effect through wet modelling influences provided an opportunity to assess how the trends that have been established within dry systems change after incorporating fluid.

### 4.3.1 Breakage mechanisms

The energy and force data generated from DEM simulations is typically separated into shear and normal components, which allows for comparisons between attrition breakage, through the normal component, and abrasion breakage, through the tangential component. Sinnott, Cleary & Morrison (2006) concluded that for dry grinding in pin and tower mills, the average shear energy dissipation was three times the normal energy dissipation. The dominance of shear forces and energies is noted in Kim & Choi (2008) and Ndimande et al. (2019). Beinert et al. (2015, 2018) categorised the energy dissipated through collisions into normal, shear and rolling components from the respective translational and rotational relative velocities of the collisions. The categories are indicative of the type of contacts that are present within the mill space. Their work highlighted the significance of the normal energy in inducing breakage, although the shear energy is significantly larger.

### 4.3.2 Grinding output correlations

The grinding rate describes the change in the grind of a material with time. Within the fine-ultrafine particle size region, grinding limit theory proposes that the particle size reduction will approach a grinding limit, based on the properties of the material (Austin, 1971). Gudin, Kano & Saito (2007b), Kim, Chung & Choi (2009) and Jayasundara et al. (2010) showed through experimental studies that the grinding rate in stirred mills follow a first order kinetic profile of exponential decay. The resulting grinding rate equations are as shown in (65) and (66).

$$\frac{dCI}{dt} = K(CI_{\infty} - CI) \tag{65}$$

$$\frac{(CI_{\infty} - CI)}{(CI_{\infty} - CI_0)} = e^{-Kt} \tag{66}$$

where CI refers to the comparison index, K is the grinding rate constant, t is time and $CI_0$ and $CI_\infty$ denote the comparison indexes at t=0 and at the grinding limit, respectively. The comparison index for the material grind is typically the 50% or 80% passing particle size, or the specific surface area of the material.

The rate of energy consumption by the material is directly proportional to the grinding rate, as it is the cause of the size reduction (Kano et al., 2001). Gudin, Kano & Saito (2007b) further evaluated their wet grinding model by correlating the specific impact energy per unit time to the grinding rate constant. Kim, Chung & Choi (2009) performed a similar analysis on their dry pin mill model but correlated the grinding rate constant to the product of the average force per grinding media and coordination number. These analyses showed strong correlations. Jayasundara et al. (2010) observed a non-linear correlation between the grinding rate constant and the total impact energy per unit time on their horizontal disk mill model. Further development of this analytical approach is still necessary to determine the most appropriate unit to correlate to the grinding rate. Through a combination of experiments and DEM-CFD simulation, Jayasundara, Yang & Yu (2012) confirmed that the grinding rate and impact energy correlation is independent of the grinding media size.

The mechanistic model of a tower mill system presented in Oliveira, Carvalho & Tavares (2021) used the collision environment output from DEM simulations and a microscale PBM model to estimate apparent breakage rates and breakage distribution of a copper-gold ore. The system considered a feed of 1.18-1.00 mm for a product with a P80 around 40 μm. The study observed that the breakage rates that varied with particle size, with first order breakage rates observed for finer particles. This work evolved to a PBM-DEM-CFD model of a continuous tower mill by Petit, Oliveira & Tavares (2025), which was able to predict the products sizes within 10% of measured values for a wide range of operating conditions.

### 4.3.3 Grinding media properties

Jayasundara et al. (2008), Jayasundara, Yang & Yu (2012) and Cleary, Sinnott & Pereira (2015) studied the effect of media size on a horizontal disk mill. Cleary and colleagues considering a dry, industrial scale model of the M10000 IsaMill™ with a classifier, while Jayasundara and colleagues looked at a lab scale three-disk mill model, dry (2008) and CFD coupled (2012). The ranges of grinding media simulated in each study are summarised in Figure 4.1. The system in the study on media size by Cleary used media diameters of 9, 15 and 25 mm. The study showed similar velocity spatial distributions along the axial plane for the 9 mm and 15 mm media, experiencing their highest velocities around the upper half of the disk, from the disk holes towards the mill wall. The 25 mm media showed a more balanced distribution of high velocity regions, centred around the disk holes and disk edge. This observation shows the limitations of the approach of simulating mill systems with larger media to represent the performance of smaller media in physical systems, to improve computational efficiency, because velocity spatial distribution can change significantly in response to changing media size. The similarity in flow patterns for smaller charge was noted in Jayasundara et al. (2008) and Jayasundara, Yang & Yu (2012), which considered 2-4 mm and 2-6 mm media, respectively. The main difference observed in the flow patterns was higher velocities for smaller media, at the same rotational speed. High shear zones within the horizontal disk mill surrounded the disk holes. The size of these shear zones is typically in the order of a dozen media diameters, therefore as the media size decrease so do the shear zones (Cleary, Sinnott & Pereira, 2015). This is quantified in the media size effect on collision energy and power draw as both studies noted that they increased with media size. Jayasundara, Yang & Yu (2012) defined the ratio of specific impact energy to power draw as the mill efficiency, which decreased with increasing media size across their 2-6 mm systems. All studies acknowledged that the media size effect is strongly influenced by the particle size distribution of the ground material. It was noted in Cleary & Sinnott (2015) that the energy absorbed by the impeller through collisions decreased with increasing media size.

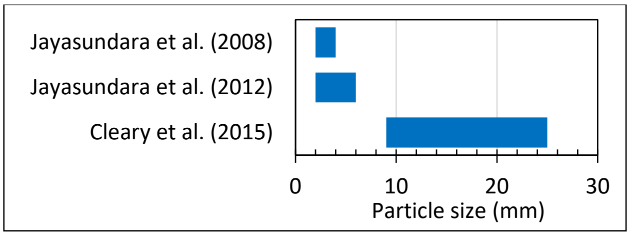

*Figure 4.1: Ranges of particle size examined in literature*

The effect of media shape on the flow and energy environments of a tower mill was investigated in Sinnott, Cleary & Morrison (2011b). They evaluated the performance of grinding media ranging from spheres to near perfect cuboids, grouped by their sphericity through super quadrics. The particles with only slight angularity behaved similar to spherical particles, while the particles of sphericity ranging between 0.93 to 0.58 showed distinct changes in the flow and energy environment of the mill. The axial flow speed and recirculation rate of the mill decreased with the decreased sphericity. This is a result of reduced mobility of the outer layers of the mill, due to their angular shape. This decreased the shear zones located at the mill edge, though increasing the shear rate and power dissipation within the zone. This autogenous slow-moving layer reduced the collision power, resulting in a strong reduction in the power draw. The outer layer reduced the active bed volume creating a shield for the mill wall, which resulted in a decrease in energy dissipation though media-liner collisions. The effect of media shape is significant as spherical media is often modelled due to its easy contact point detection, but physical grinding media is rarely perfectly spherical and as media wears down, it develops angularities which, as shown by Sinnott, Cleary & Morrison (2011b), can have a drastic effect on the mill power draw and energy dissipation. The yield stress of the material is therefore an important factor in its wear and replacement rate.

The density of the grinding media was found to have little effect on the mill flow pattern in a horizontal disk mill (Jayasundara et al., 2008). It should be noted that the horizontal disk mill was operated at a high rotational speed of 1 000 rpm. The densities investigated ranged from 1000 to 7500 kg/m$^3$. Its effect translated directly to the collision frequency and energy. Higher energy collisions were observed for heavier particles, due to their higher kinetic energy on impact for a constant speed. The collision frequency increased with density to a maximum, before decreasing. The power draw increased with density, as heavier particles require more energy to fluidize. This observation was experimentally validated by Jayasundara et al. (2008) using materials of similar interaction parameters but different densities.

### 4.3.4 Interaction properties

The coefficient of restitution is the ratio of the particle velocity before and after the collision. The quantity is calibrated through collision experiments. The calibration process typically accounts for the presence of product between colliding particles (Weerasekara et al., 2013). This property is used by some dissipation models incorporated into DEM contact models to determine the damping coefficients, which account for the portion of energy dissipated into the dry or wet product by the collision. The relationship between the restitution coefficient and damping coefficients is inversely proportional, as shown in equation (16), for the specified dissipation model. Higher restitution coefficients, and hence lower damping coefficients, have been linked proportionally to material hardness (Jayasundara et al., 2008).

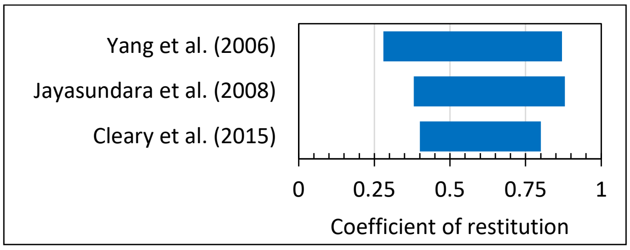

*Figure 4.2: Ranges of restitution coefficient examined in literature*

Their effect was evaluated directly through the damping coefficient in Yang et al. (2006), then as the coefficient of restitution in Jayasundara et al. (2008) and Cleary, Sinnott & Pereira, (2015). Overall, the studies considered the coefficient of restitution from 0.28-0.87 (Yang et al., 2006), 0.38-0.88 (Jayasundara et al., 2008), and 0.4-0.8 (Cleary, Sinnott & Pereira, 2015), as shown in Figure 4.2. All investigations considered dry horizontal disk mill computational models, with Yang and Jayasundara at laboratory scale and Cleary at industrial scale. All the studies indicated that the effect of the coefficient of restitution on the bulk velocity and porosity distributions, and power draw was negligible. Large restitution coefficients result in less energy lost in collisions, increasing collision energy for a constant input power (Jayasundara et al., 2008; Cleary, Sinnott & Pereira, 2015). Collision frequency is improved through more vigorous particle movement as shown by a larger mean and broader distribution (Jayasundara et al., 2008). An exponential decrease in the particle impact forces is noted with increasing damping coefficient (Yang et al., 2006). Cleary, Sinnott & Pereira, (2015) observed slight decreases and increases in the energy absorption of the impeller and shell, respectively, and limited influence on the flow patterns and media distribution leading to their conclusion that the overall mill performance is insensitive to the coefficient of restitution.

The sliding friction coefficient is used to determine the resistance force to sliding in media-media and media-mill interactions and is dependent on the properties of the interacting materials. Yang et al. (2006) found that increasing the sliding friction coefficient decreases the flow velocity and compressive forces to a minimum before they begin to increase. They attributed this effect to the competition between the energy flow and energy dissipation mechanisms influenced by the sliding friction, with energy dissipation dominating before the minimum. Gudin, Kano & Saito (2007a) stressed the importance of using specific sliding coefficients for interactions between different materials. This was enforced in Jayasundara et al. (2008), who analysed the influence of the media-media sliding friction coefficient on the radial flow fields of a horizontal disk mill. They noted that at higher coefficients, the flow patterns stratify and dilate, indicative of more effective energy transfer and increased flow velocity. Higher sliding coefficients increase the power draw, through increasing the collision energy and frequency (Yang et al., 2006; Jayasundara et al., 2008). Cleary, Sinnott & Pereira (2015) considered the impact of varying the friction coefficient of both the media-media and media-wall interactions simultaneously by equating them. The resulting simulations showed that the effect of sliding friction on the power draw and peak collision energy is minimal for small media sizes but shows positive exponential correlations for larger media sizes. They attributed this to the positive effect the media size has on the size of the shear zones within the mill, which have high frictional energy losses. The media size effect is minimal in the percent energy absorption of the impeller, which shows a clear decreasing trend irrespective of media size. The contrary is observed for the percent energy absorption of the mill shell where a positive trend is observed for larger media, while the smaller media experience little to no variation. This is a result of the high-speed layer of media entrained towards the mill shell observed at high friction coefficients.

### 4.3.5 Slurry properties

Introducing the slurry into the system through DEM coupling with SPH or CFD allows for the evaluation of fluid flow properties such as slurry viscosity and density. The effects of the viscosity were evaluated on a horizontal disk mill using two-way DEM-CFD coupling from (Jayasundara et al., 2009), and a vertical tower mill (Sinnott, Cleary & Morrison, 2011a) and a horizontal disk mill (Cleary & Sinnott, 2015), using one-way DEM-SPH coupling. The ranges of slurry viscosity investigated in these studies are summarized in Figure 4.3.

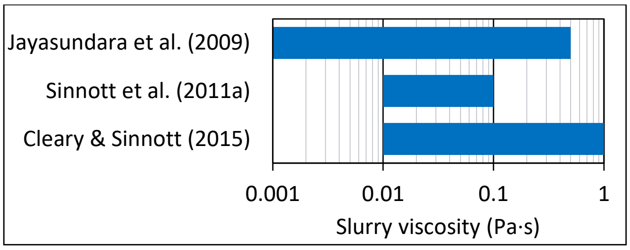

*Figure 4.3: Ranges of slurry viscosity examined in literature*

Jayasundara et al. (2009) noted high circulating velocity flow fields with increasing viscosity. This trend was visualised through a decrease in the size of the central cavity surrounding the shaft. At higher viscosities the particles move towards the disk holes in a more dispersed distribution. This was observed in Cleary & Sinnott (2015), along with increased viscosity suppressing axial flow and regions of high shear across the disks. Sinnott, Cleary & Morrison (2011a) considered the effect of viscosity on the fluid pressure distribution in a tower mill. They showed that at low viscosities the fluid pressure was hydrostatic, with the weight of the slurry translating to the bottom of the mill, while at high viscosities, the fluid pressure was more evenly distributed throughout the mill.

The increase in viscosity corresponds to higher viscous forces in the system, leading to more effective energy transfer, as shown through stronger circulating velocity fields. Increases in the collision energy and the collision frequency, particularly the media- impeller collisions (Jayasundara et al., 2009), were observed, with increasing viscosity. This resulted in an increase in the power draw and impact energy. Increasing the circulating velocity limits the ability of the slurry to move independent of the grinding media, resulting in the general damping of flow in the axial direction noted in all the studies. Cleary & Sinnott (2015) suggested that there exists a critical viscosity above which all axial flow is suppressed and grinding media will begin to centrifuge. This critical viscosity was found to be proportionally dependent on the media size, due to its influence on the pore spacing (Cleary & Sinnott, 2015).

The slurry density was investigated by Jayasundara et al. (2009) through examining its effect on the slurry and particle velocity fields, porosity, as well as the collision energy and frequency, total impact energy and power draw. The densities investigated ranged from 2000 – 3000 kg/m$^3$. With increasing density, higher circulating velocities were observed, with more particles near the disk holes. The increase in circulating velocity is to be expected as the drag force is proportional to the slurry density. The combination of higher velocities and more hole interactions result in a higher collision frequency. The collision energy is observed to peak then decrease with increasing density. Increasing density resulted in non-linear and near linear increases trends for the total impact energy and power draw, respectively.

The interdependence between density and viscosity increases in the mill operation was noted by Sinnott, Cleary & Morrison (2009). This occurs through the accumulation of fine particles in the slurry, which indicates that effective classification in the mill circuit is needed as a control measure.

### 4.3.6 Operating properties

The rotating impeller is the energy input mechanism of stirred mills. The speed of the rotation is an important variable that directly influences the energy dissipation in the mill. Its effect on the flow and energy within the system was studied by Yang et al. (2006), Jayasundara et al. (2010), Jayasundara, Yang & Yu (2012), and Cleary, Sinnott & Pereira (2015). The investigations were on a horizontal disk mill, at both lab and industrial scale. It was investigated as the rotational speed and as the tip speed at the edge of the disk, which considers the scale of the mill through the radius of the disk. The ranges of tip speed investigated by the studies are summarized in Figure 4.4. The average velocity of the media increases with the tip speed, before levelling off (Yang et al., 2006; Jayasundara et al., 2010; Cleary, Sinnott & Pereira, 2015). This was indicative of an optimum speed where the particles reach the maximum collision energy, before the increased energy input does not result in increased energy dissipation. This effect is visualised in the flow patterns. The flow patterns showed minimal difference at higher speeds, while lower rotational speeds experience a large reduction in the highspeed particles, that typically exhibit high velocity motion resulting in the suppression of the characteristic upper void of the disk mill. The dilation of the central cavity with increased speed is a result of the increased compressive forces, which are proportional to the square of the rotational speed (Yang et al., 2006). The horizontal disk mill is particularly dependent on the agitator to fluidize the particles, as the mill rotation opposes gravity. For the dry systems (Yang et al., 2006; Jayasundara et al., 2010; Cleary, Sinnott & Pereira, 2015) a positive linear relationship between the tip speed and power draw was observed and found to be independent of the media size (Cleary, Sinnott & Pereira, 2015). The wet system studied in Jayasundara, Yang & Yu (2012) showed a non-linear trend between tip speed and power draw.

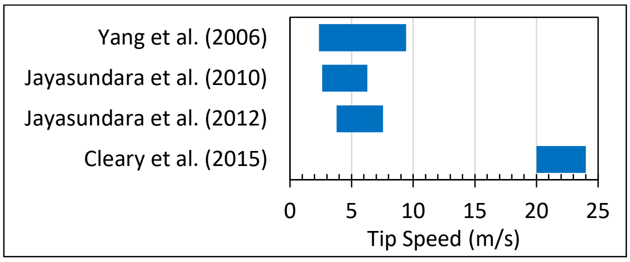

*Figure 4.4: Ranges of tip speeds examined in literature*

The effect of the fill level was investigated in Yang et al. (2006), Jayasundara et al. (2010) and Cleary, Sinnott & Pereira (2015) on horizontal disk mills. The fill level is presented as the volumetric percentage occupied by the media loading. The ranges of fill level varied in these studies is shown in Figure 4.5. The velocity profiles of the media at different fill levels revealed that at low fill levels (40%) a large portion of the media is stagnant at the base of the mill, while the charge in the upper mill is dilated. This distribution changes to become more symmetric as the fill level increases. The closer packing of the mill with the increasing fill level dampens the high-speed media at the disk holes of the mill. The speed of the media close to the disks is observed to increase with the fill level, as the media is being pressed closer to the disks.

Within the energy environment, Jayasundara et al. (2010) observed an increasing trend in the collision frequency and a corresponding decreasing trend in the collision energy with increasing fill level. The trend in the power draw showed an exponential increase with fill level, while the total impact energy had a linear increase with the fill level that peaks at 90% fill, then decreased at the 100% fill level. The operation of the mill at higher fill levels above 80% would be unfeasible due to the increased power draw and decreased collision energy. The mill uses the fluidised grinding technique, which requires an allowance for the expansion of the media bed when inducing breakage through fluidising the media.

Cleary, Sinnott & Pereira (2015) further analysed the mill loading effect on the portion of the total energy that is absorbed by the impeller, which influences the wear. This fraction decreased with the increasing fill level, noting that the media-media collisions increased for similar media to impeller collisions. They further looked at the ratio of impact (attrition) to shear (abrasion) energy absorption, through the normal and shear energy components respectively, on the impeller and shell. The attrition component contribution decreases with increasing fill level, as the charge has less space between collisions, resulting in the decreased impact collision forces. The attrition component is significantly less than the abrasion, which is consistent with the expected breakage mechanism in stirred mills of attrition/abrasion breakage characterised by high shear forces.

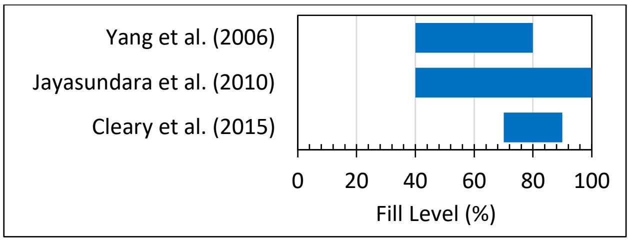

*Figure 4.5: Ranges of fill levels examined in literature*

### 4.3.7 Mill design applications

The application of DEM models in studies that involve varying design parameters of a stirred mill are rare in the literature. Plochberger & Avila (2014) used DEM to simulated media motion around six different agitator disk designs in a vertical chamber. The three-blade propeller and the six-pin agitator designs showed the most promising motion behaviour, characterized by high media speeds and expansive regions of high velocity. This led to the development of a three-tier pin agitator pilot mill, which evolved to an industrial scale machine concept. However, minimal data on the performance of the pilot mill in trial tests was provided.

Daraio et al. (2020), which considered the effect of the length of the impeller arms of a laboratory scale attritor mill. A dry DEM model was used. The study considered the effect of two different impeller lengths on the motion of media within the mill, agitated at rotational speeds ranging from 50-250 rpm. The results showed distinctions between the impeller arm lengths in the solids fraction, and kinetic and hydrostatic pressure distributions within the bulk mill space. This was pronounced at higher rotational speeds, where the mill bulk fluidised. The longer impeller arms provide greater agitation within the bulk, resulting in higher upper circuit peak heights. Figure 4.6 shows the radial profiles of velocity magnitude for both impeller lengths at different axial heights. The longer arms had a higher tip speed than the shorter arms, resulting in a higher velocity magnitudes and power dissipation into the bulk. Higher hydrostatic pressures were noted at the mill base for the longer arms. This was correlated to the powder compaction effect observed in these locations in corresponding experimental mill systems. This effect decreased for the shorter arms.

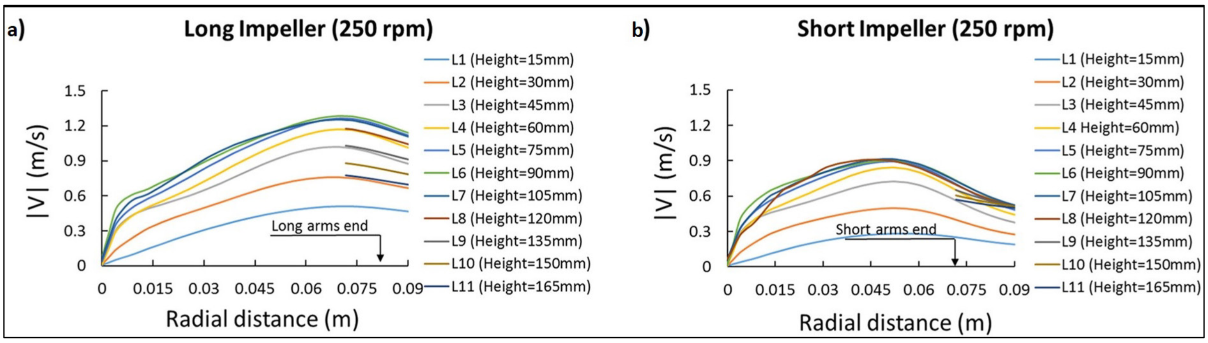

*Figure 4.6: Radial profile of velocity magnitude at various heights in a pin mill for the long (a) and short (b) impeller arm variations at 250 rpm, adapted from Daraio et al. (2020)*

### 4.3.8 Other applications

The alternative applications of stirred mill models are classified into the development and study of wear models, the comparison of different mill types, and different novel applications.

#### *4.3.8.1 Mill wear*

The wear on the lining of the impeller and shell in a mill is described as a function of the energy absorbed by the surface during the media-mill collisions. The wear distributions for dry grinding have been characterised for tower and pin mills (Cleary, Sinnott & Morrison, 2006; Sinnott, Cleary & Morrison, 2011b), and horizontal disk mills, using both laboratory (Jayasundara et al., 2011) and industrial scale models (Cleary, Sinnott & Pereira, 2015). Cleary, Sinnott & Morrison (2006) and Cleary, Sinnott & Pereira (2015) characterised wear by considering the time averaged normal and shear stress distributions, and the impact and abrasion energy absorption from the media-mill collisions. These parameters are considered in Jayasundara et al. (2011), which additionally considers the kinetic energy weighted by the collision angle, and the media and liner material properties to estimate the volume of liner material removed by that abrasion. This is based on the Finnie model for erosion of a material by solid materials (Finnie, 1960).

For all mill types studied, the energy absorption by the mill liner from abrasion was significantly larger than the impact component. This was expected as abrasion is the dominant grinding mechanism in stirred mills. For tower mills, regions of high abrasive wear are found on the outer edge of the top surface of the screw and around the spiral outer surface. Sinnott, Cleary & Morrison (2011) considered the effect of particle sphericity on the abrasive wear. This showed that the pattern of the abrasion damage remained the same, but the magnitude of the damage increased and the wear rates at low radii near the screw shaft decreased with decreasing sphericity. The abrasive damage in pin mills was focused on the edges of the pin and the shaft, which would lead to the pins flattening over time (Cleary, Sinnott & Morrison, 2006).

For horizontal disk mills, the normal stress was significantly greater than the shear stress, with both of them generally increasing towards the discharge end of the mill, in the presence of an axial pressure gradient (Cleary, Sinnott & Pereira, 2015). The influence of the axial pressure gradient on the flow structure of the mill was very significant, as it pushed the particles towards the rear end of mill, in a structure that replicates the dynamics of operating the horizontal mill as a continuous system. Impact damage was concentrated at the disk holes, which is a region of high particle density as the media is pressed against the holes and ejected radially from them. Abrasion damage dominated the edges of the disk as ejected particles slid over the disk towards the edges. This was consistent in both disk mill models.

#### *4.3.8.2 Mill type comparison*

The advent of DEM simulation has allowed for the comparison between different mill types based on their flow and energy characteristics. The desire to compare systems to optimise grinding has been present since the first dry DEM models, when Cleary, Sinnott & Morrison (2006) and Sinnott, Cleary & Morrison (2006) compared the tower mill to the pin mill. The tower mill creates a gravity-induced grinding system, dependent on shear created by the upwards axial transport provide by the screw against the downwards axial transport beyond the screw edge, due to gravity. The pin mill creates a fluidized mill environment, with limited axial mixing. Their study focused on determining which of two pilot scale systems, operated at their respective industry optimised conditions, created a superior grinding environment.

Morrison, Cleary & Sinnott (2009) compared the energy efficiency of the tumbling ball mill against the tower mill. This showed the difference in the proportions of energy dissipated through impact and shear in the two mill types. The tower mill system had a significantly larger energy dissipation rate through shear than impact, compared to the ball mill, which had similar distributions for shear and impact dissipation. Beinert et al. (2015) considered the reproducibility of the predictions of their DEM-CFD model for ball mill and annular gap mill systems. Santhanam & Dreizin (2012) compared shakers and planetary ball mills to a pin detritor, as these mill types are often used for laboratory scale ultrafine grinding. The comparisons focus on differences in the energy dissipation mechanisms and rates of the mills at similar scales.

#### 4.3.8.3 Novel applications

Some novel uses of the DEM models in stirred mills are found in McElroy et al., (2012) and Santhanam & Dreizin (2012). McElroy et al. (2012) showed the possibility of using a dry DEM model to predict internal impact energy intensity. The study matched surface vibrations from an external accelerometer on the shell of the mill to simulated external impact energies to monitor the internal state of the mill online. Santhanam & Dreizin (2012) introduced the concept of using a milling dose parameter to predict the mill time required to achieve the same grind in any mill type. This milling dose parameter was based on the energy dissipation rate, mill time and mass of milled powder.

## 4.4 Validation

Validation of DEM models is an important process as it ensures that the model is able to accurately depict the mill environment and produce reliable data that can provide understanding of the comminution mechanisms in the system. Simply calibrating the model properties is not sufficient enough to validate the model as the values are not evaluated in mill environment and non-physical properties can be calibrated (Weerasekara et al., 2013). Validation of stirred mill models has been conducted by comparing experimental and simulation outputs through two methods: high speed film and photography, and x-ray or PEPT imaging. Magnetic tracking of media particle motion within stirred mills is a promising technology that could be effective for model validation (Buist et al., 2017; Böttcher, Schilde & Kwade, 2021).

Validation methods based on high-speed film and photography rely of the comparison of key features in the flow patterns such as cavity development and particle dilation. This provides a qualitative analysis which can be subjective and is not informative on the collision environment within the mill. It is therefore often coupled with a comparison of actual and simulated power draw to provide a form of quantitative validation. However, the simulated power draw does not account for energy dissipation through sound or heat and is characteristically larger than its experimental counterpart (Jayasundara, Yang & Yu, 2012). This method was used to validate the earliest DEM models (Jayasundara et al., 2006; Sinnott, Cleary & Morrison, 2006; Gudin, Kano & Saito, 2007a; Kim & Choi, 2008), as well as Yamamoto et al. (2014). Beinert et al. (2015) used this method to validate their one way coupled DEM-CFD model. The model was further compared against the Stress Energy model (Kwade & Schwedes, 2007), which is an analytical model used to predict the maximum possible stress energy of a contact as well as the contact frequency. These values, as well as their product, were compared against the DEM-CFD simulation results and showed trends of good and acceptable agreement for the contact frequency and stress energy respectively.

PEPT imaging methods have been developed to validate DEM models of stirred mills by capturing the internal flow environment at sub-millimetre spatial and sub-millisecond temporal precisions (Weerasekara et al., 2013; Sykes et al., 2024). This validation method provides a quantitative analysis of the flow and energy environment within the mills through comparing position and velocity data from the PEPT experiments against DEM model predictions. Jayasundara et al. (2011) provides an account of PEPT being used to validate a horizontal disk mill model on his DEM-CFD model of a horizontal disk mill. Its results showed strong correlations between the non-linear model and the PEPT data. Daraio et al. (2019) used PEPT to validate the attritor mill model used in Daraio et al. (2020) to investigate the effect of the impeller arm lengths, with strong correlation.

## 4.5 Challenges and gaps identified

Weerasekara et al. (2013) summarised the challenges facing DEM application in comminution processes. The challenges most pertinent to its application in stirred mills are the lack of accurate representation of the milled fine particles in dry models, the use of simplified contact models to analyse breakage events, the simulation of batch models for continuous processes and the challenges surrounding model validation.

Additional gaps have been identified in the current computational work on stirred mills. The first is the lack of diversity in the mill configurations modelled. Although different mills use the same grinding techniques, their orientation or impeller configuration can alter their parameter relationships. Majority of the studies considered in this chapter simulated a horizontal fluidised grinding mill, and of the vertical mills simulated only three systems considered a vertical mill with a suspended impeller, which is the mill type studied in this thesis. Therefore, there has not been extensive simulation of the behaviour of an SMD mill type and its response to key parameters. Secondly, there is a lack of information on the stirred mill scale up dynamics, to use when applying the results of laboratory or pilot scale models to industrial systems. And finally, there is need for more work that challenges the design configuration of stirred mill systems. There is little evidence in literature of how altering mill design parameters affects the mill performance, most work in this area focuses on comparison between two different mill types.

# PART TWO

## PROBLEM DEFINITION AND SIMULATION OVERVIEW

# CHAPTER 5

# Problem Statement and Research Novelty

## 5.1 Introduction

This chapter provides the problem statement of the study as well as the hypotheses and key research questions, informed by the reviewed literature, and an overview of the novel contributions the study makes to the current body of knowledge.

## 5.2 Problem statement

The flow and energy environments of laboratory scale stirred media mills can be effectively captured using a two-way coupled DEM-SPH model that resolves both particle and fluid dynamics simultaneously. This is determined through an assessment of the model performance in response to changes in critical variables and investigating how the expansion in radial scale between mills of increasing scale affects the mill performance. This is assessed through analysis of the spatial response of three sizes of laboratory scale SMDs to the changes in tip speed and media body angularity.

## 5.3 Hypotheses

From literature that assisted in developing the problem statement and the body of work conceptualised for this study, the following three hypotheses are proposed to guide the work plan for the performance assessment of the two-way coupled DEM-SPH model and the investigation of scale-up phenomena.

A. A two-way coupled DEM-SPH model that resolves both particle and fluid dynamics simultaneously can be used to predict the flow and energy environments of laboratory scale stirred media detritors, because the energy is dissipated through the resistance of motion of the particles and fluid in the system.

B. The variations in the spatial mill environment of laboratory stirred media detritors with scale, for a constant tip speed and media body sphericity, can be captured through dimensionless and intensive properties, because these properties are independent of the scale of the system.

C. At the same tip speed of the impeller, there is a decreasing trend in the velocity and energy profiles as the diameter of the stirred mill increases because of the dampening of energy as it propagates through the expanded radius, and the reduced rotational speed required to maintain the same tip speed.

## 5.4 Key questions

The following four key questions are proposed to guide the experimental approach of the study:

1. Can the DEM-SPH model, that solves particle and fluid dynamics simultaneously, capture the effects of critical variables, namely, tip speed, media shape, size and density, slurry density and viscosity and the media fill, correctly?
2. Are the trends observed between mill sizes consistent between the flow and energy environments?
3. How do the trends observed between mill sizes vary with tip speed and media shape?

4. How does the media shape influence the flow and energy environment of a stirred media detritor?

## 5.5 Novelty statement

Most DEM-SPH or DEM-CFD coupled simulation systems use an asynchronous solving method that passes information from the media to the fluid solver and vice versa. In this study the DEM-SPH solver computes the DEM and SPH simultaneously for a system containing fast moving particles and fluid encountered in a stirred media detritor. This simultaneous solver provides an improved computational efficiency due to its unique configuration that optimized memory allocation, as the simulations are run under a single framework, and uses load balancing parallelization. This allows for extensive computational work to be completed feasibly.

The approach developed for modelling particle shape computationally that allows contact detection by modelling the media as two-times differentiable, continuous closed super quadric surfaces has not been implemented in a simultaneous solver. Its development and application within this thesis expand the capabilities of the simulation solver.

Dimensionless quantities such as the Froude and Reynolds numbers have yet to be applied to evaluate the scale up effects within the bulk environment of stirred media mills. Their application in this thesis will aid in quantifying the fluidisation state of the mill and its response to increase in mill size.

# CHAPTER 6

# Methodology

## 6.1 Introduction

This chapter describes the approach that was taken in the development of the DEM-SPH models for the mill simulations. It outlines the simulation software and parameters, processing algorithms, and analytical methods used in the DEM-SPH modelling and expands on the overall simulation plan for performance prediction assessment and the scale-up study.

## 6.2 DEM-SPH software

All the DEM-SPH simulations for this project are done using CSPH_MPI, a proprietary framework developed by Prof. Stephen Neethling and collaborators at Imperial College London. It follows from the SPH framework outlined in Neethling & Barker (2016), expanded to incorporate discrete element modelling. The contact detection method for super quadric media is presented in section 6.4.2. The overall DEM-SPH coupling algorithm used is described in section 6.4.3.

The framework is written in C++ and supports parallelisation with load balancing, through the Message Passing Interface (MPI). The framework uses domain decomposition to divide the 3D mill environment into parallelepiped shaped regions that simulate as parallel processes. Additionally, the DEM bodies and SPH particles on the edges of these regions are disclosed to their neighbouring processes. The parallel processes are consolidated at each SPH timestep. The regions are subject to dynamic load balancing, which iteratively varies their size to minimise idle time across processes. Use was made of the University of Cape Town ICTS-HPC cluster to perform all simulations. Each simulation is performed on a single node Dell PowerEdge C6420 with two 20-core Intel Xeon 6138 processors, running 40 processes in parallel.

The framework makes use of ancillary C++ programs SurfConverter and Mill_Fill to prepare model inputs, and CreateVTPfromData for post processing the data into Visualization ToolKit (VTK) formats. Paraview is used as the three-dimensional visualisation software, while MATLAB scripts are used for further post processing and analysis.

## 6.3 Simulation parameters

### 6.3.1 Mill geometries

The mill geometries used in the model were designed using computer aided design (CAD) software. Each mill is designed in a 3D cartesian coordinate system, where the mill base is on the x-y plane, and the impeller shaft is on the central z axis. The impeller consists of two layers of two cylindrical pins each. The two pins in each layer are at straight angles to each other and centred on the shaft, while the two pin layers are perpendicular. The mill shell consists of the mill base and cylindrical walls, and a lid. The impellers and shells are exported as separate stereolithography (.STL) surface files, with a fine mesh size generated using AutoDesk Inventor. This is essential to configure of the correct input files.

Representations of all three mill systems are shown in Figure 6.1 to Figure 6.3. Figure 6.1 provides a 3D rendering of each mill space, from the same viewpoint, indicated by the axis. Figure 6.2 and Figure 6.3 are dimensioned schematics of each mill space at the same scale. Figure 6.2 provides a front view schematic, while Figure 6.3 provides a top view schematic. Note that the dimensions are in metres.

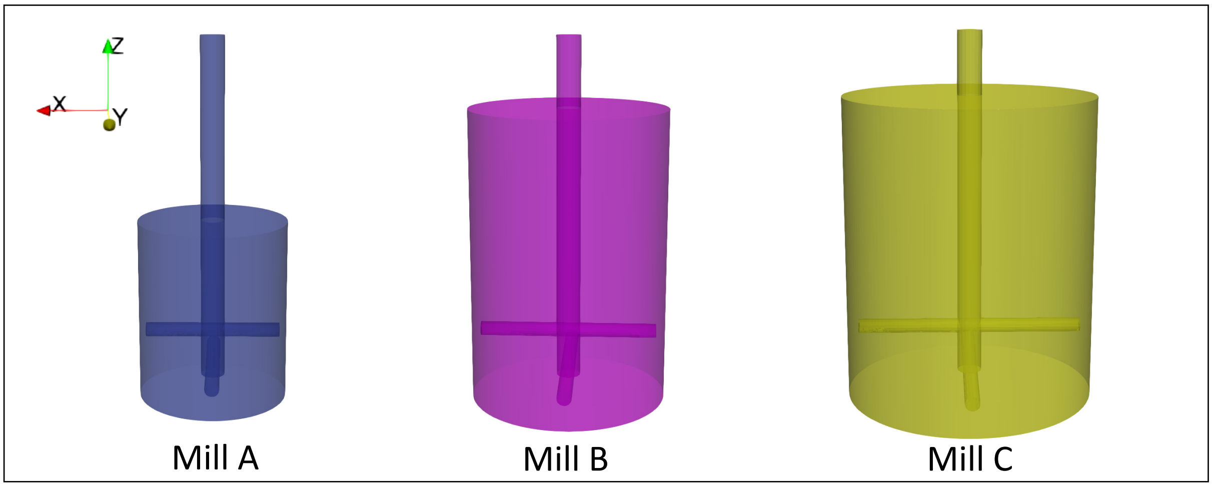

*Figure 6.1: 3D rendering of the three mill sizes from the same viewpoint.*

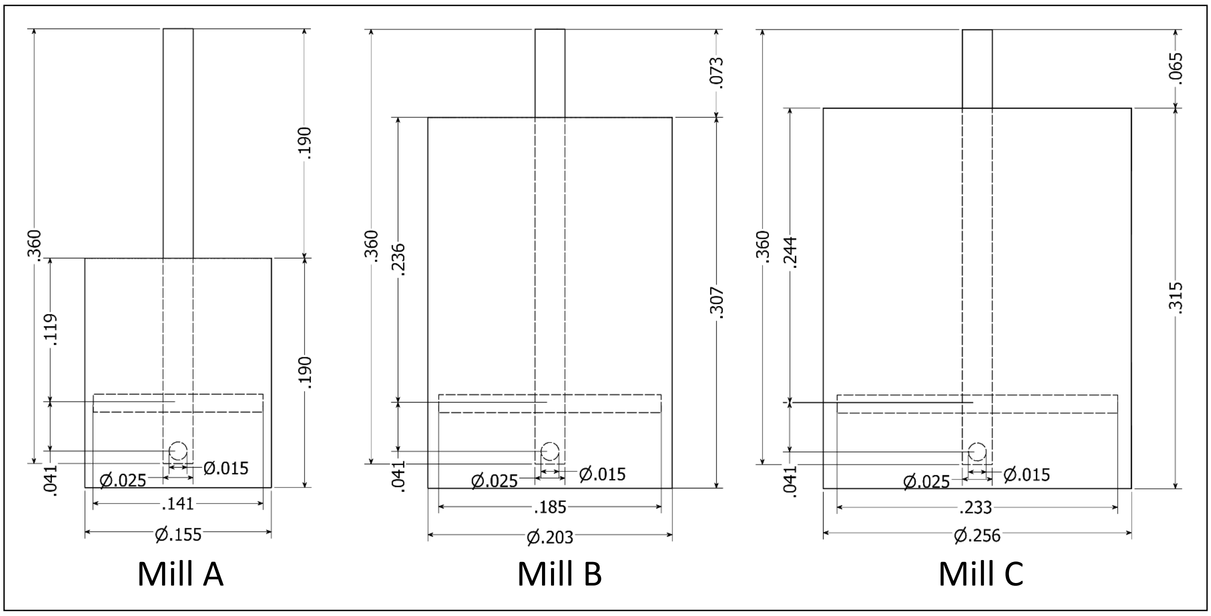

*Figure 6.2: Front view schematic of all three mill types*

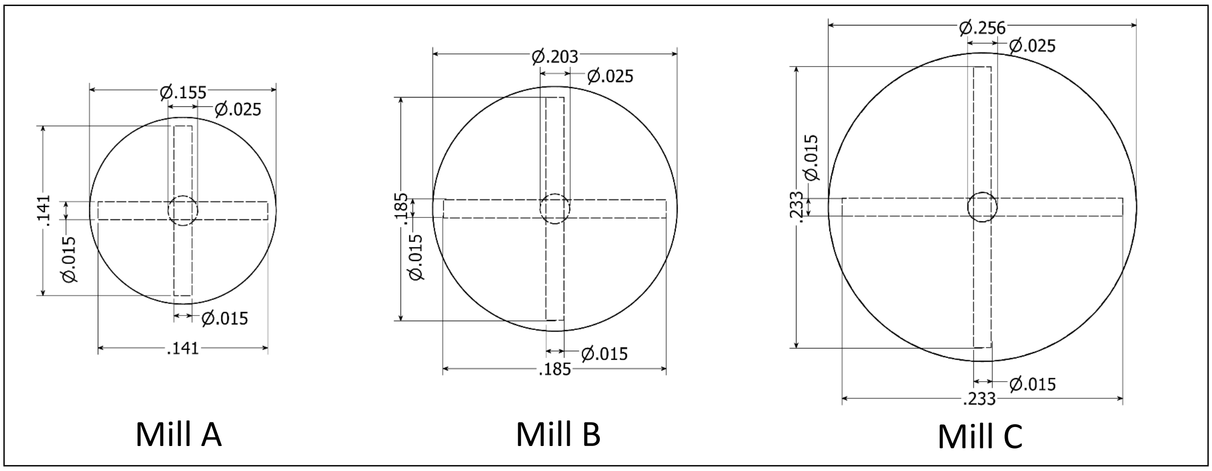

*Figure 6.3: Top view schematic of all three mill types*

### 6.3.2 Physical properties and interaction parameters

The physical properties of the mill geometry, grinding media and fluid properties are needed to ensure that the simulation of the model is close to the reality of the mill system. The mill geometry was modelled as 304 steel, which is the material of construction used for the shaft and the mill shell. The grinding media is modelled as 5 mm ceramic casting and the fluid is modelled as a mineral slurry with a 40% solids content. The majority of the physical and interaction properties were taken from Ndimande et al. (2019), which looked at DEM-SPH modelling of an industrial scale SMD. Table 6.1 lists the physical properties that form the basis of the models.

*Table 6.1: Physical properties of the mill geometry, grinding media and fluid.*

| Mill Geometry | | Units |
|---|---:|---|
| Young's modulus | $10^9$ | Pa |
| Poisson ratio | 0.3 | |
| Grinding Media | | |
| Diameter | 5 | mm |
| Density | 2700 | Kg/m$^3$ |
| Young's modulus | $10^9$ | Pa |
| Poisson ratio | 0.3 | |
| Fluid | | |
| Resolution | 4 | mm |
| Speed of sound | 20 | m/s |
| Rheology | Newtonian | |
| Density | 1379 | Kg/m$^3$ |
| Dynamic viscosity | 0.0022 | Pa·s |

The study adapts the parameters from Ndimande et al. (2019) by choosing to operate at lower Young's moduli for the mill geometry and the grinding media and calibrating the fluid resolution and the speed of sound. The Young's moduli were decreased from moduli of commonly used ceramics, such as yttria stabilized zirconia at ~$10^{11}$ Pa to $10^9$ Pa (Gudin et al., 2006). This was done to improve the speed of the simulations and minimise computational expenses as the decreased Young's modulus increases the minimum time step for the DEM simulations. This practice is often reported to be effective in reducing computational time with minimal effect on mill performance in literature (Landry et al., 2003; Jayasundara et al., 2006). For super quadric media simulations, the Young's moduli for the mill geometry and media are further reduced to $10^7$ to ensure solution stability. The fluid speed of sound was set at 20 m/s to ensure system stability by being greater than the expected system speeds (estimated to maximise at the lab SMD mill tip speed) by a factor of 5. The fluid resolution selected was calibrated to ensure stability and minimise computational expense.

The interaction parameters used in the DEM simulations are the coefficients of restitution and sliding friction. These are defined separately for the media-media interactions and media-mill interactions. The values were taken from Ndimande et al. (2019) and are shown in Table 6.2.

*Table 6.2: Media-media and media-mill interaction parameters*

| | Media-Media interactions | Media-Mill interactions |
|---|:---:|:---:|
| Coefficient of restitution | 0.6 | 0.5 |
| Coefficient of sliding friction | 0.4 | 0.3 |

### 6.3.3 Media geometries

Spheres and super quadric (SQ) bodies are used as grinding media in the simulations. The super-quadric bodies used in this study range from ellipsoidal to box-like shapes with rounded edges, following the definition in section 3.2.3, equation (18). These super-quadrics are defined by their scale parameter, which is a vector of the three semi-axes (a, b, c) of the body, and their edge roundness (n). The super-quadrics have been divided into three groups of increasing angularity and decreasing aspect ratio taken from the media shape study by Sinnott, Cleary & Morrison (2011b). The parameter ranges are shown in Table 6.3.

*Table 6.3: Grouping for super-quadrics, adapted from Sinnott, Cleary & Morrison (2011b)*

| | n | b÷a | c÷a |
|---|---|---|---|
| Group 1 | [0.80, 1.00) | [0.9, 1.0] | [0.9, 1.0] |
| Group 2 | [0.57, 0.80) | [0.8, 1.0] | [0.8, 0.9] |
| Group 3 | [0.33, 0.50] | [0.7, 0.8] | [0.6, 0.8] |

For each body to be able to participate in the collision environment, its volume (V), moment of inertia tensor (I) and surface area (SA) need to be calculated. For super quadric bodies these values are determined by equations (67) and (68) from Jaklič, Leonardis & Solina (2000) and equation (69), respectively, in the body centred coordinate system. Where, $B$ refers to Euler's integral of the first kind, and the surface area is determined through the divergence theorem.

$$V_{SQ} = 2abcn^2 \cdot B\left[\frac{n}{2} + 1, n\right] \cdot B\left[\frac{n}{2}, \frac{n}{2}\right] \tag{67}$$

$$\mathbf{I}_{SQ} = \begin{cases} \mathrm{I}_{xx} = \frac{\rho_{SQ}}{2} abcn^2(b^2 + c^2) \cdot B\left[\frac{3n}{2}, \frac{n}{2}\right] \cdot B\left[\frac{n}{2}, 2n + 1\right] \\ \mathrm{I}_{yy} = \frac{\rho_{SQ}}{2} abcn^2(b^2 + c^2) \cdot B\left[\frac{3n}{2}, \frac{n}{2}\right] \cdot B\left[\frac{n}{2}, 2n + 1\right] \\ \mathrm{I}_{zz} = \frac{\rho_{SQ}}{2} abcn^2(b^2 + c^2) \cdot B\left[\frac{3n}{2}, \frac{n}{2}\right] \cdot B\left[\frac{n}{2}, 2n + 1\right] \end{cases} \tag{68}$$

$$SA_{SQ} = \iiint \boldsymbol{\nabla} \cdot \begin{pmatrix} \dfrac{a^{-\frac{2}{n}} x^{\frac{2}{n}-1}}{\sqrt{\left(a^{-\frac{2}{n}} x^{\frac{2}{n}-1}\right)^2 + \left(b^{-\frac{2}{n}} y^{\frac{2}{n}-1}\right)^2 + \left(c^{-\frac{2}{n}} z^{\frac{2}{n}-1}\right)^2}} \\ \dfrac{b^{-\frac{2}{n}} y^{\frac{2}{n}-1}}{\sqrt{\left(a^{-\frac{2}{n}} x^{\frac{2}{n}-1}\right)^2 + \left(b^{-\frac{2}{n}} y^{\frac{2}{n}-1}\right)^2 + \left(c^{-\frac{2}{n}} z^{\frac{2}{n}-1}\right)^2}} \\ \dfrac{c^{-\frac{2}{n}} z^{\frac{2}{n}-1}}{\sqrt{\left(a^{-\frac{2}{n}} x^{\frac{2}{n}-1}\right)^2 + \left(b^{-\frac{2}{n}} y^{\frac{2}{n}-1}\right)^2 + \left(c^{-\frac{2}{n}} z^{\frac{2}{n}-1}\right)^2}} \end{pmatrix} dxdydz \tag{69}$$

The super quadric bodies simulated are constrained such that their volume is equivalent to that of the 5 mm diameter sphere used in the spherical media simulations, correct to 6 significant figures. This allows for equivalent mass and number of bodies to be used in super-quadric media simulations. Within each group of super quadrics specified, a few shapes of increasing roundness were simulated. The different shapes are equally distributed within the media. The parameters of these bodies are specified in Table 6.4 and their shapes illustrated in Figure 6.4.

*Table 6.4: Specification for super-quadric bodies used in simulations.*

| | | Scale (mm) | | | Roundness | Surface Area | | Moment of Inertia ($10^{-10}$kg·m$^2$) | | |
|---|---|---|---|---|---|---|---|---|---|---|
| | | *a* | *b* | *c* | *n* | *SA* (mm$^2$) | *Φ* | $I_{xx}$ | $I_{yy}$ | $I_{zz}$ |
| Sphere | | 2.50000 | 2.50000 | 2.50000 | 1.000000 | 78.5398 | 1.000 | 4.41786 | 4.41786 | 4.41786 |
| Group 1 | i | 2.57101 | 2.41675 | 2.49388 | 0.991672 | 78.5807 | 0.999 | 4.28610 | 4.55955 | 4.42494 |
| | ii | 2.57103 | 2.36533 | 2.36533 | 0.915794 | 78.7275 | 0.998 | 4.18164 | 4.56109 | 4.56109 |
| | iii | 2.51628 | 2.26466 | 2.26466 | 0.800000 | 79.2241 | 0.991 | 4.13343 | 4.61821 | 4.61821 |
| Group 2 | i | 2.55251 | 2.27199 | 2.16959 | 0.771858 | 79.5154 | 0.988 | 4.04939 | 4.60468 | 4.79131 |
| | ii | 2.55265 | 2.27215 | 2.04212 | 0.702743 | 80.2257 | 0.979 | 4.00074 | 4.58089 | 5.00630 |
| | iii | 2.55236 | 2.09295 | 2.09295 | 0.633496 | 80.8880 | 0.971 | 3.92034 | 4.87531 | 4.87531 |
| | iv | 2.55269 | 2.04215 | 2.04215 | 0.571429 | 81.7285 | 0.961 | 3.87523 | 4.96514 | 4.96514 |
| Group 3 | i | 2.79573 | 1.95701 | 1.84550 | 0.500000 | 83.8692 | 0.936 | 3.50567 | 5.43697 | 5.64241 |
| | ii | 2.69998 | 2.07897 | 1.75496 | 0.464596 | 84.3643 | 0.931 | 3.65919 | 5.12631 | 5.74040 |
| | iii | 2.69955 | 1.91636 | 1.83533 | 0.408560 | 85.2442 | 0.921 | 3.58977 | 5.43292 | 5.58791 |
| | iv | 2.50021 | 1.87528 | 1.97526 | 0.367778 | 85.3863 | 0.920 | 3.86457 | 5.28904 | 5.08848 |
| | v | 2.70274 | 2.00172 | 1.67844 | 0.333333 | 87.3143 | 0.900 | 3.61773 | 5.36611 | 5.99682 |

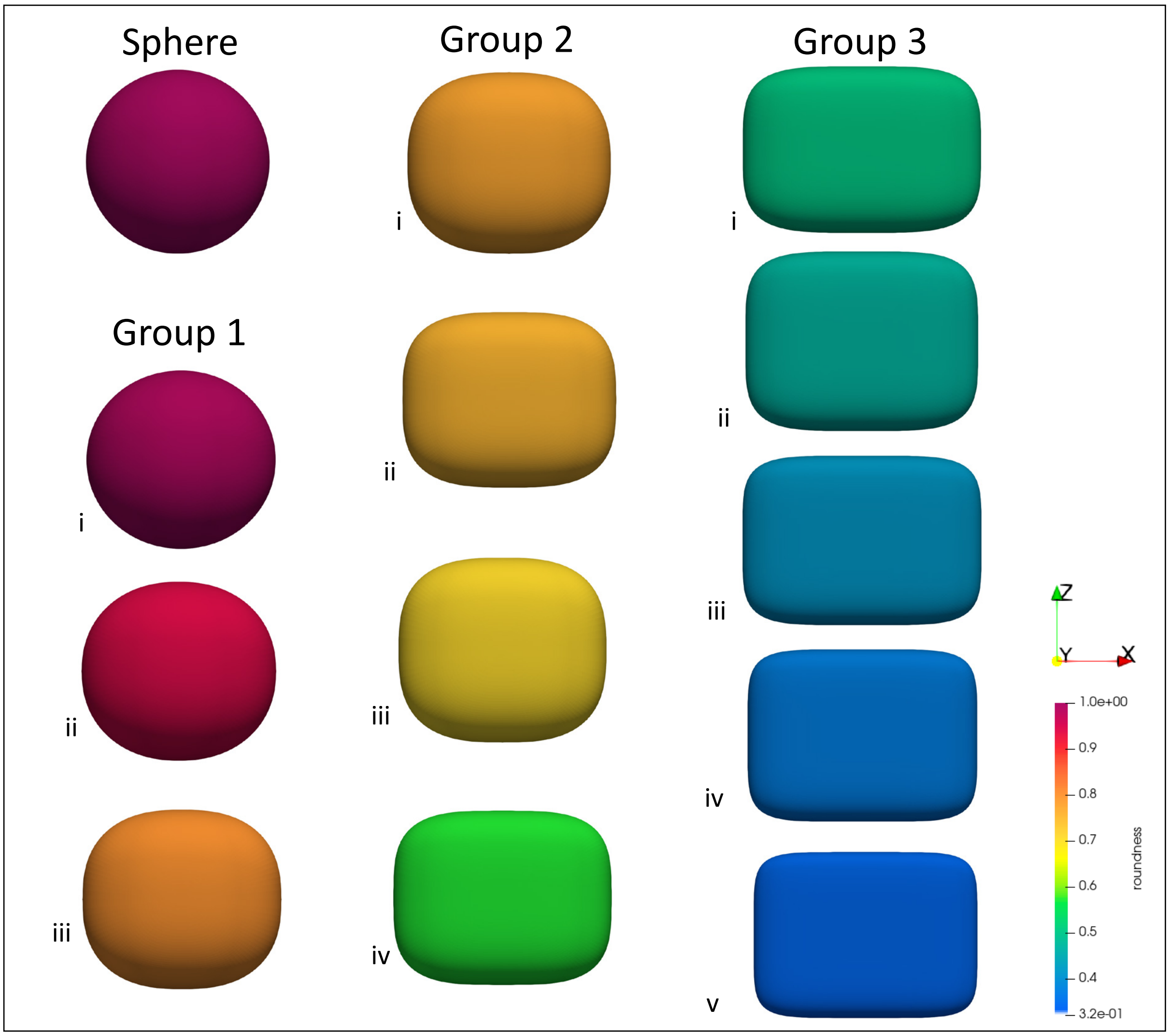

*Figure 6.4: VTK rendering of super-quadrics in groups, coloured according to their roundness.*

For super quadric media, the mean radius of curvature at the surface is used to determine the effective radius, which informs the spring constants in non-linear collisions. Figure 6.5 provides colormaps of the mean radius of curvature on the surface of Group 1.ii (n = 0.92), 2.iv (n = 0.57) and 3.v (n = 0.33) super quadrics, with black lines of intersection between the surfaces and the cartesian axial planes. The mean radius of curvature colourmaps for the all the media shapes are provided in Figure A.1 in Appendix A.1. The radius of curvature is lowest at the furthest point from the centre, which becomes the corner point in the more box-like super quadrics and increases towards each of the cartesian semi-axes. An octant of the mean radius of curvature points that inform these colormaps was extracted for each super quadric in all the groups and their volume equivalent sphere, with a sampling density of $10^6$ points of the same polar and azimuthal spherical coordinates. For each shape, these points were arranged in ascending order, from the point of lowest radius of curvature to the highest radius of curvature. These radius of curvature ranges are presented in Figure 6.6.

From Figure 6.6, it is observed that the minimum radius of curvature decreases with the media roundness. The radius increases towards the semi-axes, as the radius function approaches infinity at these points, but is truncated at a maximum of 0.025 m in Figure 6.6. This follows from equation (31) using a q of 10. This is applied to most super quadrics but, for solution stability super quadrics 1.i (n = 0.99) and 1.ii (n = 0.92) use q values of 2.5 and 5, respectively. The range of the radius of curvature increases with decreasing roundness. This expands the probability spectrum for the effective radius for a collision, based on where on each super quadric the contact surface point is located.

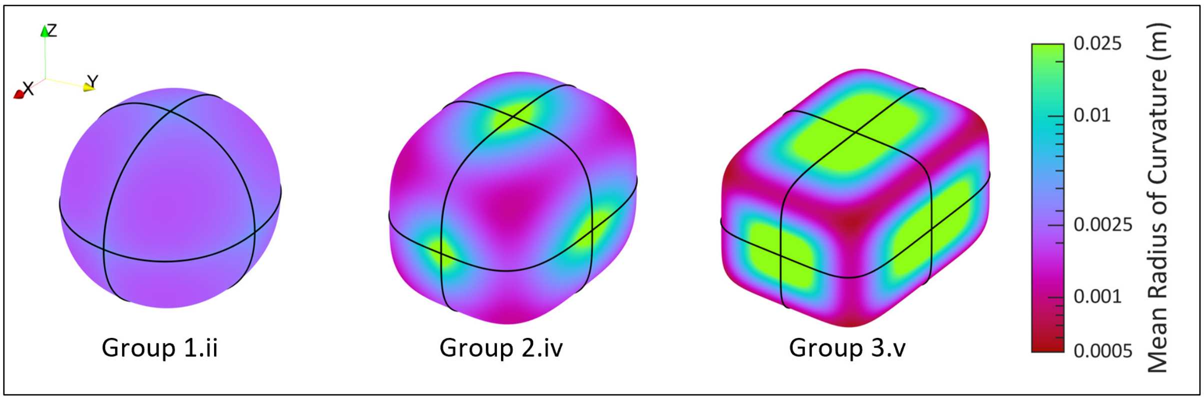

*Figure 6.5: Super quadric surface plots showing the mean radius of curvature of the super quadrics Group 1.ii, Group 2.iv and Group 3.v*

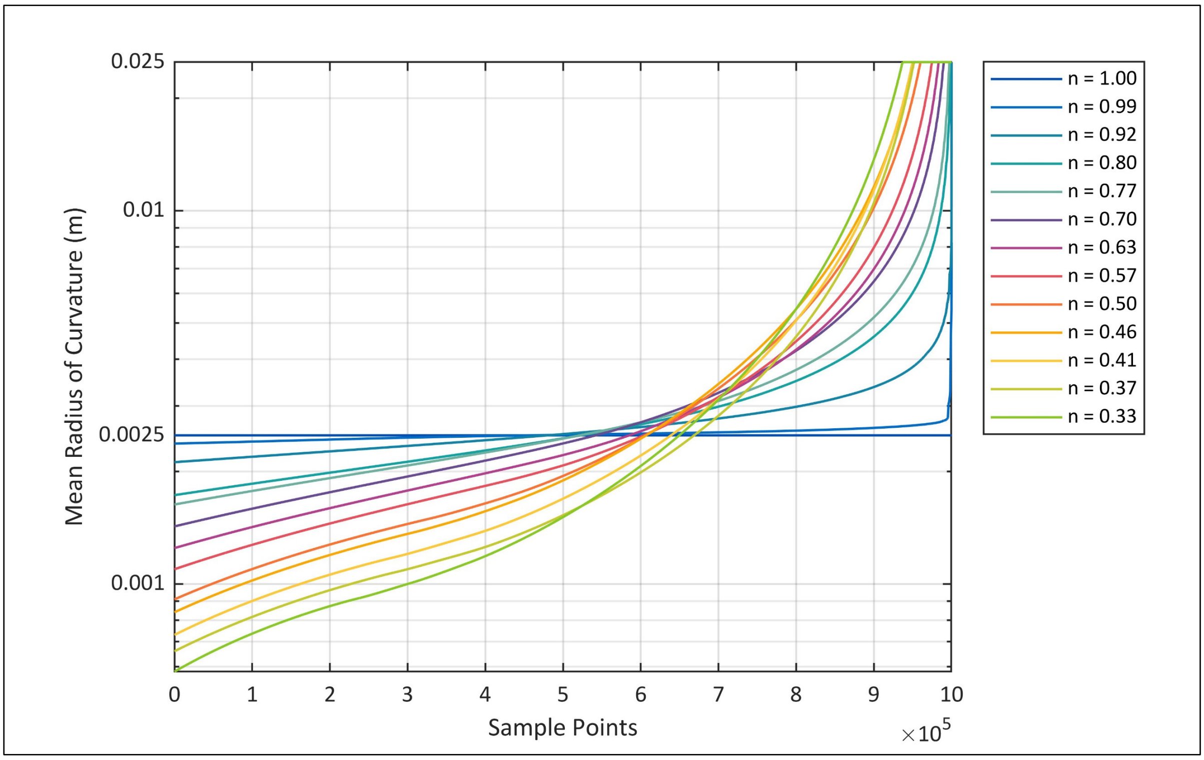

*Figure 6.6: Plot showing the range of mean radius of curvature across points sampled on the surface of each super quadric geometry in the three groups, and their volume equivalent sphere.*

### 6.3.4 Timesteps

The DEM timestep in all mill systems is determined using the approach by Burns & Hanley (2017) for non-linear contact model systems, described in section 3.2.5, equation (36). The velocity used in the equation is the SPH speed of sound as neither the DEM nor the SPH particles should exceed that speed within the simulation. The DEM safety factor used is 0.5. This timestep is kept constant throughout the runtime.

For super quadric media, the timestep is determined using the bounding sphere radius of the media, similar to the approach adopted by Gao, Yu, Lu, et al. (2021). For stability within the super quadric solutions, an additional safety factor of 0.05 is applied to the timestep. This further reduction is to account for the variations in the radius of curvature at the surface of the quadrics as shown in Figure 6.6. This generates timesteps in the range of the super quadric simulations of Grohn et al. (2023), who simulated similar sized super quadrics within a CFD-DEM framework. However, given the mean radius curvature ranges and their relationship to the media roundness shown in Figure 6.6, a more accurate approach to determining the critical timestep should directly consider the particle roundness.

The SPH timestep is determined as the minimum of the SPH time stepping criteria given in section 3.3.3. This timestep is recalculated as the simulation progresses. The SPH safety factor is 0.2. The file write time for all the simulations is set to 0.01 s.

### 6.3.5 Operating conditions

The operating conditions for this mill type in a batch configuration are the fill level and the rotational speed. The rotational speed is a manipulated variable within the experiments. The range of rotational speeds and their significance is explained in the experimental plan in section 6.7. The fill level of media and slurry for each mill type is consistently set to the height of the topmost layer of the impeller pins. The basis volume ratio of grinding media to fluid is 1:1, based on the feed of the industrial SMD modelled by Ndimande et al. (2019). The observations made by Ndimande et al. (2019) for the operations of the industrial SMD formed the basis for the quantities of media and fluid in each mill shown in Table 6.5. The methods used to calculate these quantities are shown in Appendices A.2 and A.3, for media and slurry, respectively.

*Table 6.5: Mill fill levels*

| Mill A | 2-layer impeller |
|---|---|
| Number of media | 10 639 |
| Volume of fluid (cm$^3$) | 696 |
| Mill B | |
| Number of media | 18 512 |
| Volume of fluid (cm$^3$) | 1 212 |
| Mill C | |
| Number of media | 29 694 |
| Volume of fluid (cm$^3$) | 1 944 |

### 6.3.6 Model configuration

The model is fed a .sphml configuration file that consists of all the input parameters, as well as the directories for the three input files. The input parameters can be divided into 3 sections, general settings, SPH settings and DEM settings. The general settings require you to specify the geometric dimensions and the directories for the input files, to turn on gravity in the downward direction and the hydrostatic pressure gradient for the fluid, and specify the maximum simulation run time and the file write time.

The SPH settings consist of the fluid physical properties and the fluid material region. The fluid material region specifies how the fluid will fill the mill. This is through a flood fill mechanism in cuboid form, where the bottom left and top right corner of a cuboid are specified within the mill, where the fluid will flow from during the model initialization stage. This requires the fill height of the fluid to be calculated and used as input. The method used to determine this is shown in Appendix A. The DEM settings require the specification of the contact-force model and drag relation and the physical and interaction parameters of the DEM bodies.

### 6.3.7 Model input files

The model requires 3 input files to run the DEM-SPH mill simulation. The first is a .VEF file that consists of the combined impeller and shell configuration. This is obtained by converting the geometry from its .STL configuration, obtained from CAD software, using an ancillary program SurfConverter. The .VEF file is used to define the mill triangular surface mesh of the initial configuration. It provides the coordinates for the vertices, defines the edges in terms of two vertices and the walls as three edges, and assigns a boundary name for the configuration. The impeller geometry is designed separately to the mill shell geometry then combined to ensure that the edges of the impeller are listed before the mill, as these are required to be consistent with in the second file type.

The second file type is the .BOD file. This file is used to account for the motion of large bodies, in this case the impeller. The file lists the VEF edges of the impeller and assigns a body number and the centre of mass, the rotational velocity, and the moment of inertia. It is generated using SurfConverter. The final file type is the .SBOD file, which contains the placement of the specific number of spheres that are used as grinding media. This file is generated using another ancillary program Mill_Fill that randomly assigns the positions of the spheres in the top section of the mill, considering their size and the offset of the shaft on the mill radius. The file assigns each body its number and characteristics, position, density and size. The numbering of these small bodies follows from that of the .BOD file. The contents of the three input files are visualised in the mill space and summarised in Figure 6.7

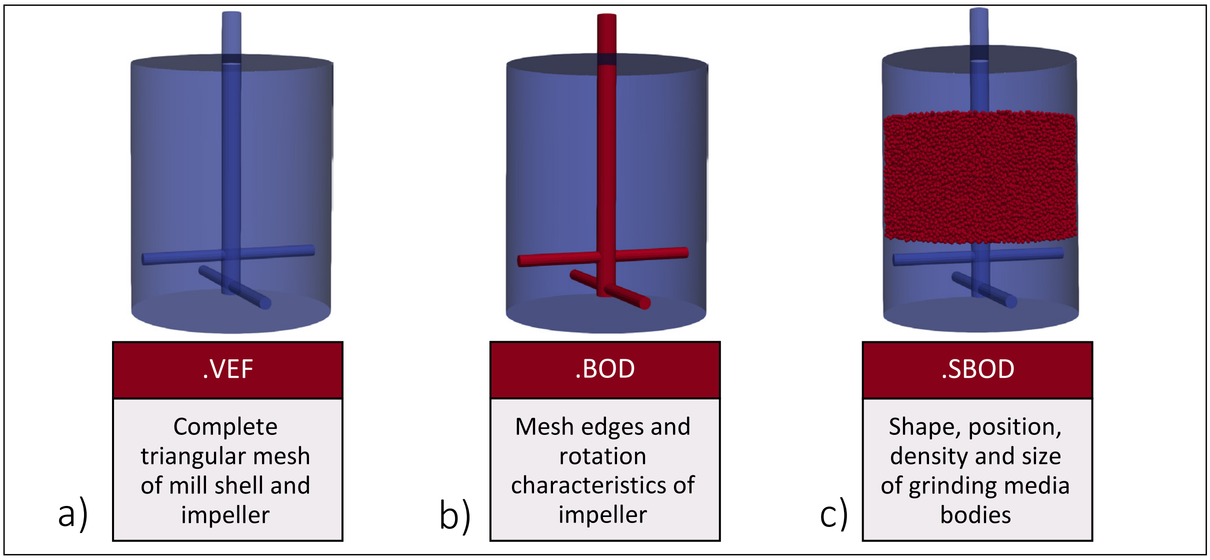

*Figure 6.7: Visual and summary of the components of the a) .VEF, b) .BOD and c) .SBOD files.*

## 6.4 Simulation numerical methods

The model processing is divided into the initialization phase, which loads and configures the model system, and the simulation phase, which relies heavily on the DEM contact detection algorithm and the DEM-SPH coupling algorithm.

### 6.4.1 Initialization

The initialization phase is where the mill is virtually configured from the input files, according to the specifications of the configuration file. The mill shell and impeller are constituted prior to the loading of the grinding media, which are placed above the fluid level. The impeller is configured to run at the set tip speed. The fluid is then flood filled at the mill base. Therefore, the simulation will begin with the gravity assisted descent of the grinding media to the base of the mill, where the fluid will be stirred by the impeller.

### 6.4.2 Contact detection algorithm

For spherical media-media collisions, contact is detected when the distance between the centres of the bodies is less than the sum of their radii. That signifies that there is a positive overlap between the bodies. The contact point is assigned as the midpoint of the overlap, and the normal vector is the direction between the centres of the bodies. With super quadric media, accurate contact detection between media is a computationally expensive process. A contact detection algorithm is used to determine whether two super quadric media bodies are in contact. This uses bounding volume methods to minimize the expense by rejecting contact pairs with bounding volumes that do not intersect (Podlozhnyuk, Pirker & Kloss, 2017; Gao et al., 2019). Two bounding volume methods are employed by CSPH_MPI for contact detection, namely the bounding sphere and the oriented bounding box (OBB). The methods are employed before the super quadric contact is detected using the middle point method, detailed in section 3.2.3.2. These methods are visualised in Figure 6.8.

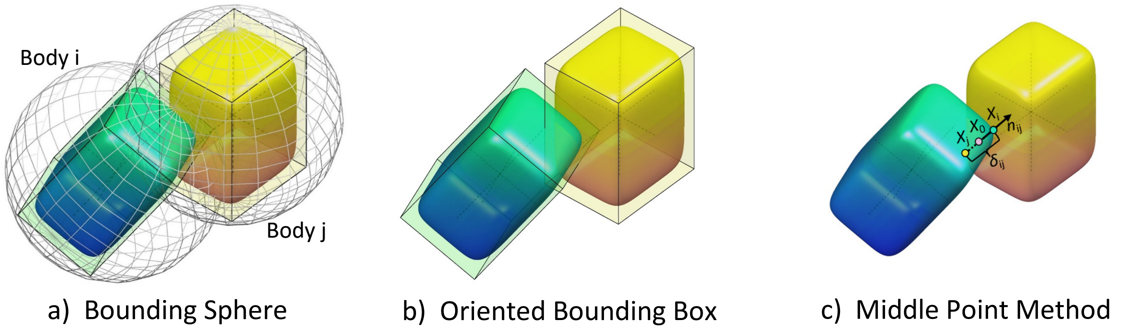

a) Bounding Sphere b) Oriented Bounding Box c) Middle Point Method

*Figure 6.8: Illustrations of bounding volumes and the contact detection used in CSPH_MPI*

The super quadric contact detection algorithm is presented in Figure 6.9, for a possible contact between super quadric bodies i and j. The CSPH_MPI code employed is provided in Appendix B.3. The algorithm begins with a bounding sphere contact detection method, which defines the minimum bounding radius of the super quadric through equation (71) (Podlozhnyuk, Pirker & Kloss, 2017). This is calculated for both bodies and used to determine the overlap in equation (72). If the overlap is negative, the algorithm registers no contact between the bodies.

A positive overlap proceeds to test the intersection between the OBBs of the bodies. The OBB of a super quadric is defined as a cuboid with its centre, semi-axes, and orientation consistent with the super quadric's, as shown in Figure 6.8b. The intersection test between two OBBs is based on the computational geometry theorem that states that "*two non-intersecting convex polyhedral can be separated by a plane that is parallel to a face of one of the polyhedral or that contains an edge from each of the polyhedral*" (Eberly, 2008). Therefore, the position and orientation of the OBBs is examined for a separating axis perpendicular to the planes in the theorem. There are 15 possible separating axes: 3 for the independent faces of i, 3 for the independent faces of j and 9 for the edges of the two OBBs, that are calculated as the cross products of the axes of i and j. For super quadric bodies, it is simpler to define the axes of both OBB's in the reference frame of i, using the rotation matrices of each body as shown in equation (73). The separating axis test asks if the distance between the two object centres projected onto the possible separating axis (L) is greater than the sum of the projection of each semi-axis length of both super quadrics onto the possible separating axis as shown in expression (70).

$$\begin{gathered} R_{\boldsymbol{IJ}} > R_{\boldsymbol{I}} + R_{\boldsymbol{J}} \\ |\boldsymbol{IJ} \cdot \boldsymbol{L}| > |\boldsymbol{I}_x \cdot a_i \cdot \boldsymbol{L}| + |\boldsymbol{I}_y \cdot b_i \cdot \boldsymbol{L}| + |\boldsymbol{I}_z \cdot c_i \cdot \boldsymbol{L}| + |\boldsymbol{J}_x \cdot a_j \cdot \boldsymbol{L}| + |\boldsymbol{J}_y \cdot b_j \cdot \boldsymbol{L}| + |\boldsymbol{J}_z \cdot c_j \cdot \boldsymbol{L}| \end{gathered} \tag{70}$$

This test is run on each of the 15 potential separating axes such that if a separating axis is found, the remaining tests are not computed, and no contact is registered between the two bodies. The test parameters for each axis in the body-centred reference frame of i are tabulated in Table A.1 in Appendix 0, adapted from Portal, Dias & Sousa (2010).

If no separating axis is found, the contact proceeds to the super quadric overlap test, using the 'middle point' method outlined in section 3.2.3.2. This uses an iterative method to solve for the contact point $\mathbf{X}_0$ that should be inside both surfaces and closest to both bodies. The method used in CSPH_MPI follows from Podlozhnyuk, Pirker & Kloss (2017), where the first guess in the iteration is the contact point from the bounding sphere test, and the system of equations is iterated in a step-wise linear transition from spherical shape parameters to those of the two super quadrics. The resulting contact point is then evaluated to ensure that it is inside both surfaces by having equal negative values for both surface functions. If not, the algorithm registers no contact between the two bodies. When there is contact, the collision information for the contact pair is updated by calculating the contact normal, overlap and effective radius.

Determining the overlap requires the calculation of the points on each surface along the contact line defined by the contact point and contact normal. The surface points are solved iteratively through equation (75) taken from Podlozhnyuk, Pirker & Kloss (2017). These are used to determine the effective radius using the mean curvature from equation (30) in equation (76), with a q value determined by the super quadric shape curvature per section 6.3.3. Once the contact point, normal, overlap and effective radius are determined, the collision forces are evaluated, and the motion of the bodies determined within the DEM-SPH coupling algorithm.

Wall contact detection for both media types is carried out using the equations in section 3.2.4 to directly determine if a body is in contact with the wall for each media shape. The wall contact code for super quadric media in CSPH_MPI is shown in Appendix B.2.

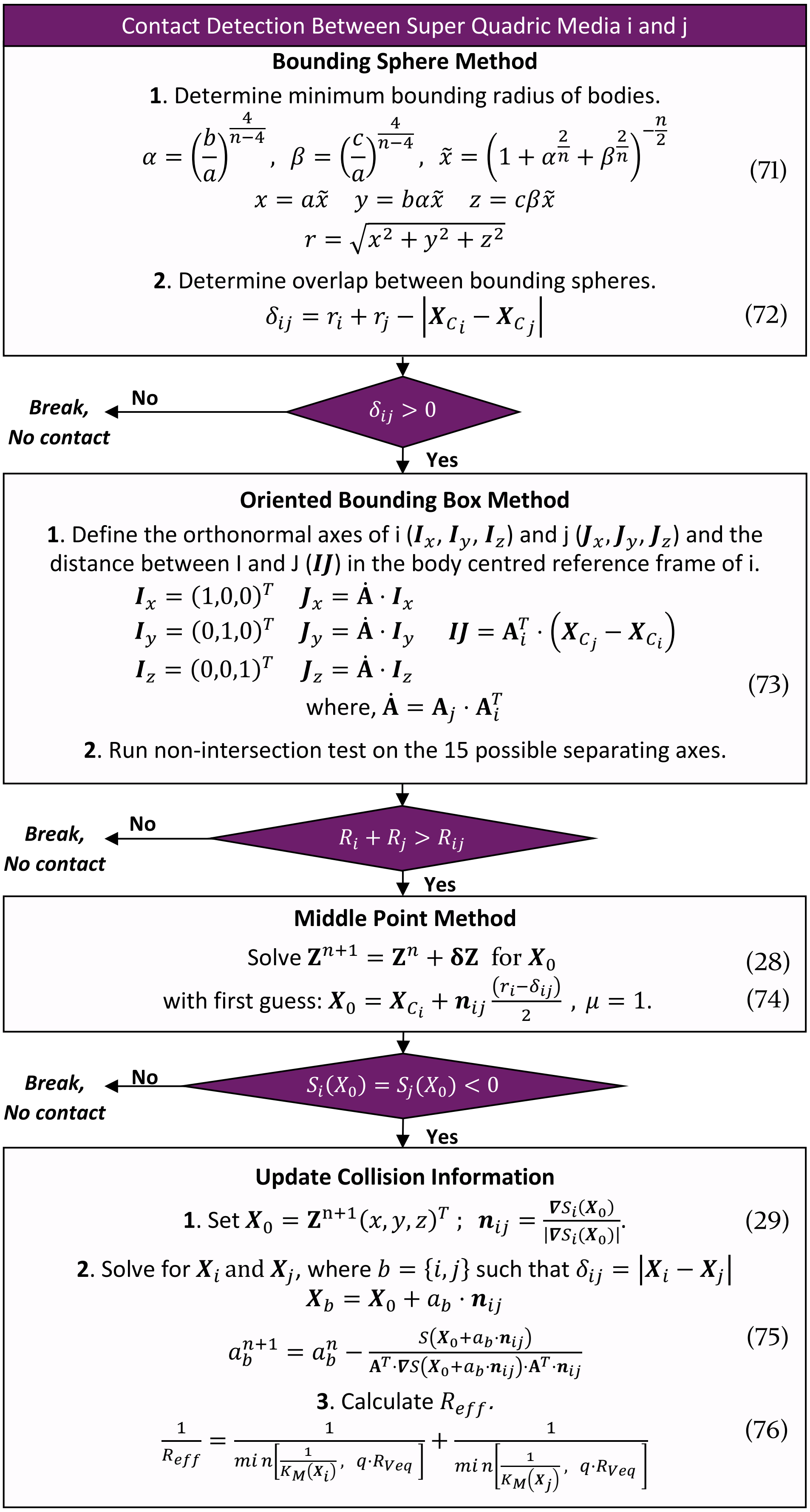

Contact Detection Between Super Quadric Media i and j

**Bounding Sphere Method**

**1**. Determine minimum bounding radius of bodies.

$$\alpha = \left(\frac{b}{a}\right)^{\frac{4}{n-4}}, \ \beta = \left(\frac{c}{a}\right)^{\frac{4}{n-4}}, \ \tilde{x} = \left(1 + \alpha^{\frac{2}{n}} + \beta^{\frac{2}{n}}\right)^{-\frac{n}{2}} \tag{71}$$

$$x = a\tilde{x} \quad y = b\alpha\tilde{x} \quad z = c\beta\tilde{x}$$

$$r = \sqrt{x^2 + y^2 + z^2}$$

**2**. Determine overlap between bounding spheres.

$$\delta_{ij} = r_i + r_j - \left|\boldsymbol{X}_{C\,i} - \boldsymbol{X}_{C\,j}\right| \tag{72}$$

**Oriented Bounding Box Method**

**1**. Define the orthonormal axes of i ($\boldsymbol{I}_x, \boldsymbol{I}_y, \boldsymbol{I}_z$) and j ($\boldsymbol{J}_x, \boldsymbol{J}_y, \boldsymbol{J}_z$) and the distance between I and J ($\boldsymbol{IJ}$) in the body centred reference frame of i.

$$\begin{aligned} \boldsymbol{I}_x &= (1,0,0)^T & \boldsymbol{J}_x &= \dot{\mathbf{A}} \cdot \boldsymbol{I}_x \\ \boldsymbol{I}_y &= (0,1,0)^T & \boldsymbol{J}_y &= \dot{\mathbf{A}} \cdot \boldsymbol{I}_y \qquad \boldsymbol{IJ} = \mathbf{A}_i^T \cdot \left(\boldsymbol{X}_{C_j} - \boldsymbol{X}_{C_i}\right) \\ \boldsymbol{I}_z &= (0,0,1)^T & \boldsymbol{J}_z &= \dot{\mathbf{A}} \cdot \boldsymbol{I}_z \end{aligned} \tag{73}$$

where, $\dot{\mathbf{A}} = \mathbf{A}_j \cdot \mathbf{A}_i^T$

**2**. Run non-intersection test on the 15 possible separating axes.

**Middle Point Method**

$$\text{Solve } \mathbf{Z}^{n+1} = \mathbf{Z}^n + \boldsymbol{\delta}\mathbf{Z} \ \text{ for } \boldsymbol{X}_0 \tag{28}$$

$$\text{with first guess: } \boldsymbol{X}_0 = \boldsymbol{X}_{C_i} + \boldsymbol{n}_{ij}\frac{(r_i - \delta_{ij})}{2}, \ \mu = 1. \tag{74}$$

**Update Collision Information**

$$\textbf{1}.\ \text{Set } \boldsymbol{X}_0 = \mathbf{Z}^{\mathrm{n}+1}(x,y,z)^T \ ; \ \ \boldsymbol{n}_{ij} = \frac{\boldsymbol{\nabla} S_i(\boldsymbol{X}_0)}{|\boldsymbol{\nabla} S_i(\boldsymbol{X}_0)|}. \tag{29}$$

**2**. Solve for $\boldsymbol{X}_i$ and $\boldsymbol{X}_j$, where $b = \{i, j\}$ such that $\delta_{ij} = \left|\boldsymbol{X}_i - \boldsymbol{X}_j\right|$

$$\boldsymbol{X}_b = \boldsymbol{X}_0 + a_b \cdot \boldsymbol{n}_{ij}$$

$$a_b^{n+1} = a_b^n - \frac{S(\boldsymbol{X}_0 + a_b \cdot \boldsymbol{n}_{ij})}{\mathbf{A}^T \cdot \boldsymbol{\nabla} S(\boldsymbol{X}_0 + a_b \cdot \boldsymbol{n}_{ij}) \cdot \mathbf{A}^T \cdot \boldsymbol{n}_{ij}} \tag{75}$$

**3**. Calculate $R_{eff}$.

$$\frac{1}{R_{eff}} = \frac{1}{min\left[\frac{1}{K_M(X_i)}, \ q \cdot R_{Veq}\right]} + \frac{1}{min\left[\frac{1}{K_M(X_j)}, \ q \cdot R_{Veq}\right]} \tag{76}$$

*Figure 6.9: Contact detection algorithm for super-quadric media*

### 6.4.3 DEM-SPH coupling algorithm

The algorithm for the DEM-SPH coupling framework used by CSPH_MPI and all the relevant equations are shown in Figure 6.10. The algorithm begins with the initialisation phase, where starting properties of the DEM bodies and SPH particles are set. The SPH particles follow from the discretisation formulation of Neethling & Barker (2016) outlined in section 3.3.1. The particles are governed by the discretised Navier-Stokes formation in equations (46)a-c in combination with the continuity equation (45) and the equation of state (47). These equations determine the properties of a fluid particle, i, surrounded by its neighbours, j. The DEM formulation follows from governing equations (7)' and (8)' discussed in section 3.2, reproduced for a body, k, in contact with other bodies, l. The contact model used is the non-linear contact model described in section 3.2.2 and represented by equations (12)' and (13)' to determine the contact forces from the body-body and body-mill interactions.

The DEM bodies and the SPH particles interact through the coupling interface, which determines the solid-fluid interaction forces. The interaction forces considered in the simulation are the sum of the drag and buoyancy forces as shown in equation (79). The coupling interface of the models is structured around the interaction between one DEM body and one SPH particle, considering that the DEM body may be influenced by multiple SPH particle and the SPH particle by multiple DEM bodies. The resulting interaction forces follow from Newton's third law, with forces positive on the particle being negative on the body and vice versa. Equations (79)a and (79)b are the resultant solid-fluid force on the particle and the body, respectively. The resultant is the summation of all the particle-body interactions that the particle or body takes part in.

The coupling interface defines the porosity as a particle specific interaction variable in equation (78), which considers the influence of the volume of the neighbouring bodies surrounding a fluid particle. This contrasts with the model of Xu, Dong & Ding (2019), which defines porosity as a local variable, which all the bodies and particles of a region contribute to. The porosity is used in conjunction with properties of the particle, its neighbouring particles, and the body to determine the De Felice drag force, equation (55), resulting from this specific interaction. Spherical media use the Schiller & Naumann (1935) drag coefficient in the drag force calculation (equation (58)), while super quadric media use the Holzer Sommerfeld (Hölzer & Sommerfeld, 2008) approximation (equation (62)). The code used to calculate the drag force is shown in Appendix B.4 for super quadric media. The buoyancy force is as given in equation (54), this is interpreted by the model through the first term of equations (79)a and (79)b. The second addend is the model drag force interpretation. This procedure is followed for each interaction, with the resulting interaction forces being added to the resultant force for the relevant bodies.

Once all the interaction forces are determined, the body governing equations are integrated for the next timestep. Because the timestep of the DEM bodies is significantly lower than the SPH timestep, the DEM calculation is sub-cycled using the same fluid particle characteristics. This is done until the DEM time is equal to or exceeds the next SPH timestep, represented by the while loop in equation (80). Once the loop is invalid, the characteristics of both the bodies and particles are integrated and updated simultaneously, according to their respective timesteps, shown in equations (81) and (77), and the cycle begins again.

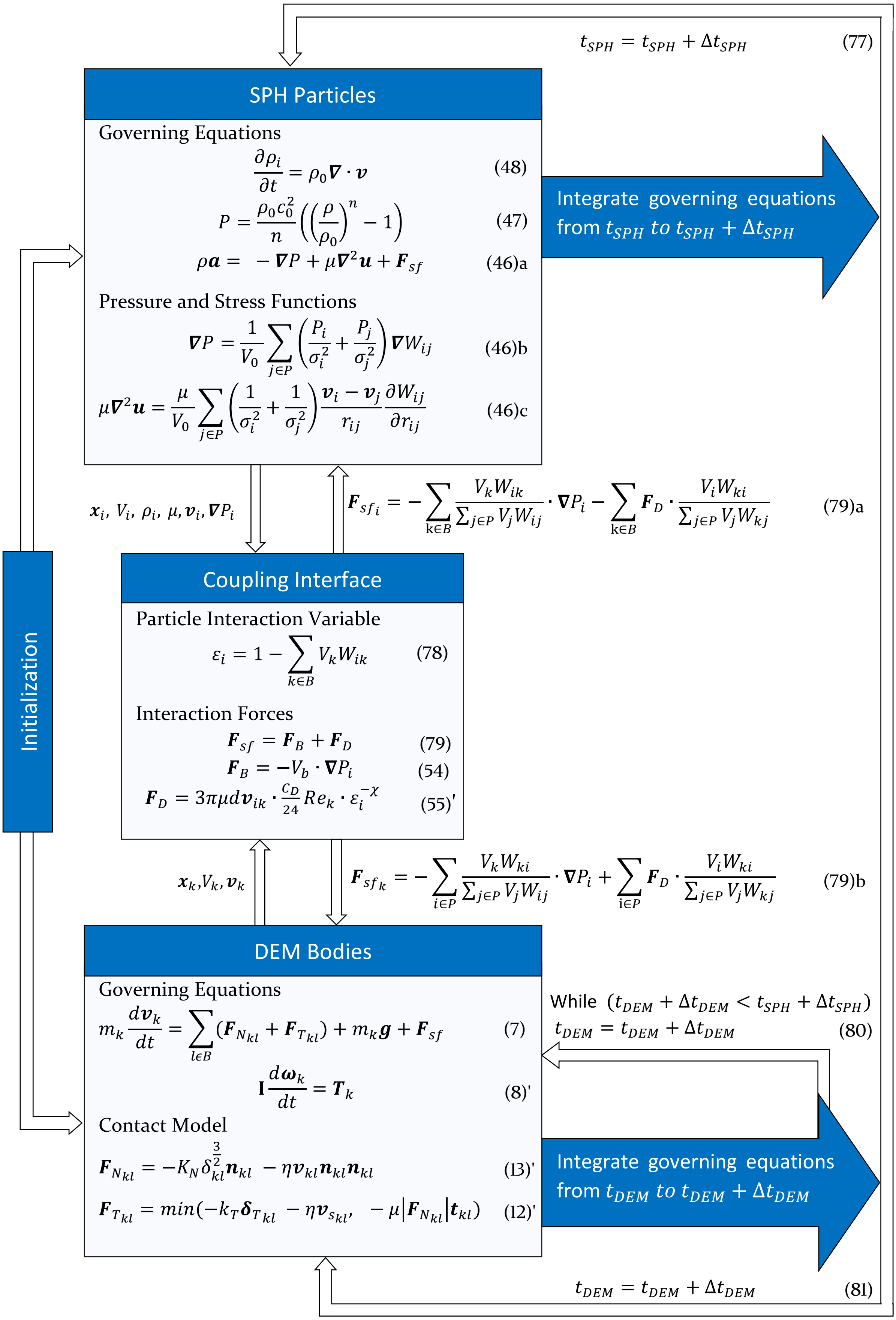

*Figure 6.10: DEM-SPH coupling algorithm for CSPH_MPI*

## 6.5 Model Output

The model produces three types of output. The first is overall output on the mill performance for each recorded timestep. This is recorded in an output file, which is ancillary to the other outputs. The output file records the model initialisation and summarises the model output for each recorded time step by providing a fluid and body count, the SPH minimum time step, the maximum velocity and the range of fluid pressures, the volume ratio of the fluid to the grinding media, and the average time per iteration.

The two main outputs are system data and contact data. The system data is outputted separately from each of the parallel cores running the simulation. Its output informs on the geometry, grinding media and fluid motion. This is read and collated by an ancillary program, CreateVTPfromData. The program generates VTK data files for the geometry data (grinding media and mill geometry) and the particle data (SPH fluid). VTK interprets the geometry data according to a specified resolution to generate points on the surface of the body that are connected in the VTK images. Therefore, the outputted data is in point form and holds for each point generated on the body. The VTK files are then processed using Paraview to generate images of the geometry and fluid motion at a given timestep. The geometry files collate data for each body in the system, with body number -1 being the mill shell, number 0 being the impeller and the rest of the numbers denoting the small grinding media bodies. CreateVTPfromData is used to generate the iso-normal free surface of the fluid as well as a volume mesh of the data properties used in the 3D imaging. The full dataset is read and viewed in Paraview. The contact data output records every collision that took place between recorded timesteps.

The large volumes of data generated by the simulation are managed through a process of selective extraction, in which three phases of initial data analysis are conducted using MATLAB. The system data from Paraview is used to conduct the steady state and velocity flow analyses. Subsequently, the contact data has a separate MATLAB analytical procedure. The flow of data from the simulation output to the analytical procedures is summarised in Figure 6.11. All the file types of the datasets are shown above each block or block set.

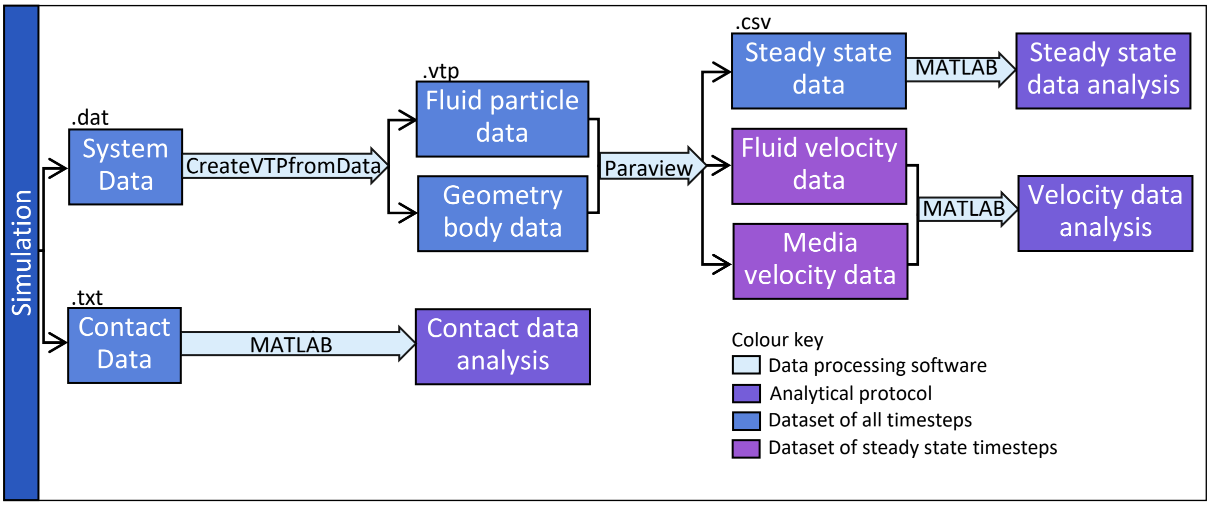

*Figure 6.11: Flowsheet of data from the simulation output to the analytical procedure*

### 6.5.1 Steady state analysis

This stability analysis phase is used to determine whether the system reached an effective equilibrium within the simulated time. It then determines the time intervals that are valid for the other analytical phases. The analysis is conducted by extracting the full dataset of kinetic and potential energies of the grinding media and the fluid as well as the power draw from the system data in Paraview, across all timesteps. The data is imported into MATLAB, where the geometry point data is converted to body data. The MATLAB code for the complete analysis is shown in Appendix C.5.

The effective steady state is defined by timesteps where the total kinetic and potential energies (KE and PE) of the fluid and media, and the power draw of the impeller stabilise. The formulae used to determine the kinetic and potential energies of the media and fluids are shown in equations (82)-(83) and equation (84), respectively.

$$KE_{media} = \frac{1}{2}m|\boldsymbol{v}|^2 + \frac{1}{2}\left(\mathbf{I}_{xx}\boldsymbol{\omega}_x^2 + \mathbf{I}_{yy}\boldsymbol{\omega}_y^2 + \mathbf{I}_{zz}\boldsymbol{\omega}_z^2\right) \tag{82}$$

$$KE_{fluid} = \frac{1}{2}m|\boldsymbol{v}|^2 \tag{83}$$

$$PE_{media\,\&\,fluid} = m\boldsymbol{g}_z\boldsymbol{X}_z \tag{84}$$

Total kinetic and potential energy stabilisation has been used by Beinert et al. (2014) and Ndimande et al. (2019) to determine the effective steady state. Figure 6.12 shows the energy stabilisation of an industrial scale SMD reported in Ndimande et al. (2019). The energies stabilise in less than 2 seconds, with a gradual increase in the media kinetic energy and longform, low-amplitude periodicity noted in the fluid kinetic energy. Figure 6.13 shows a similar graph generated from CSPH_MPI data, tracked across each recorded timestep, illustrating the energy stabilisation of Mills A, B and C at a 2.2 m/s tip speed. In Figure 6.13, the kinetic and potential energies of the fluid and media have minimal fluctuations from approximately 1 s, with no periodicity or increase noted. The four energies tracked exhibit consistent behaviour across the three mill sizes studied. The energy stabilisation is checked for each of the simulations to ensure that the data analysed in further stages of the simulation is representative of the overall behaviour within the mill space.

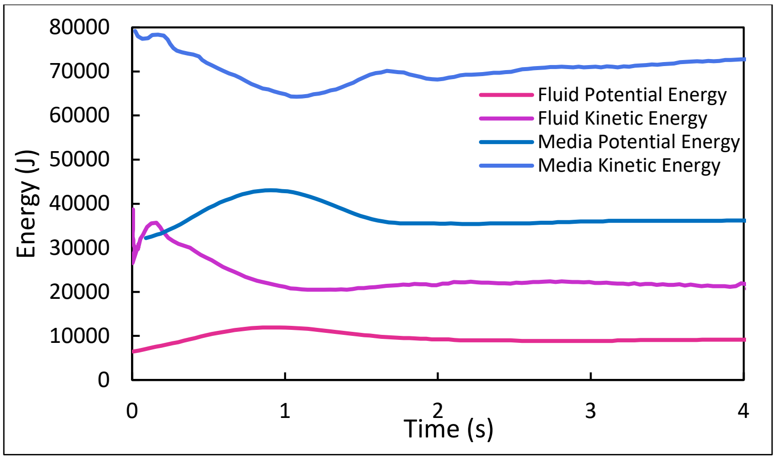

*Figure 6.12: Time plot of the total kinetic and potential energies for the DEM and SPH components of an industrial scale SMD model, adapted from Ndimande et al. (2019)*

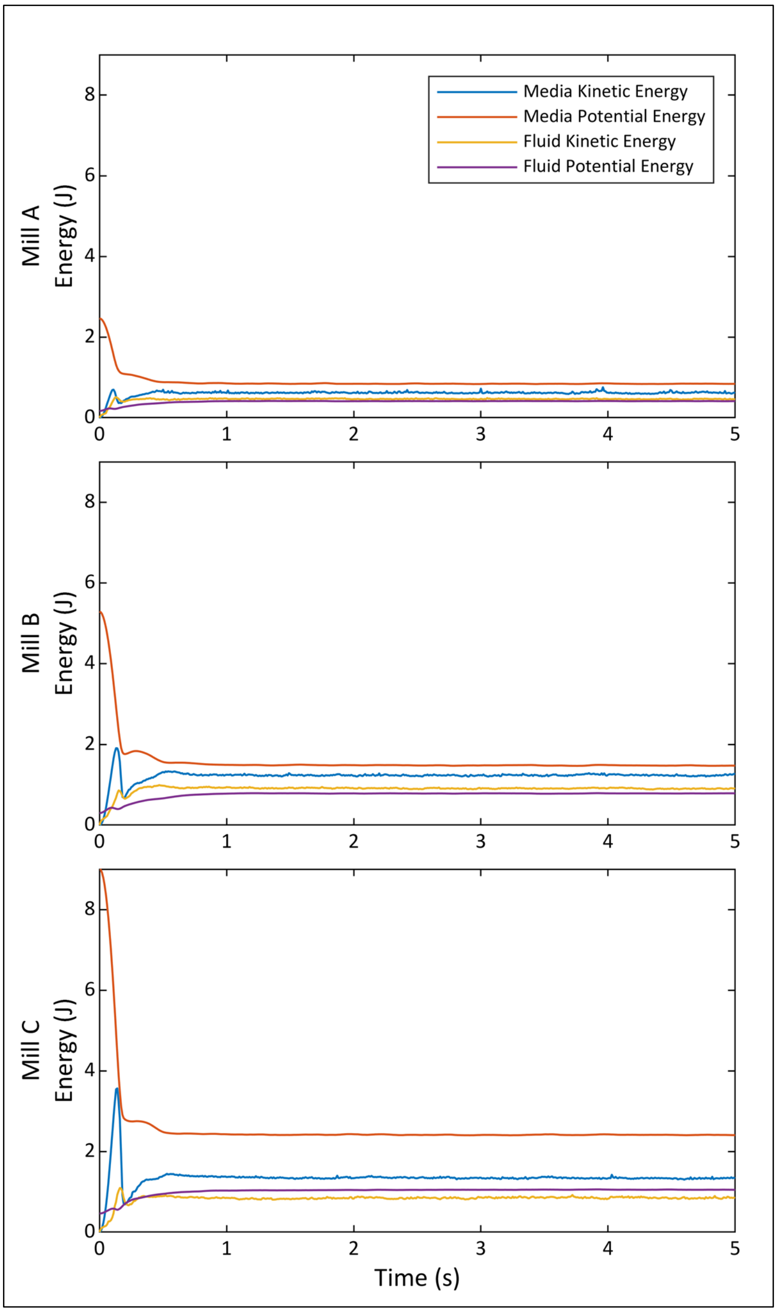

*Figure 6.13: Total kinetic and potential energies of the media and fluid against time for Mills A, B and C at a 2.2 m/s tip speed*

The power draw (PD) is determined from the torque on the impeller due to resistance from the media and the fluid. Equation (85) is used to determine the power draw from the simulation.

$$PD = 2\pi\left|\boldsymbol{\tau_f} + \boldsymbol{\tau_c}\right|\boldsymbol{\omega}_{z_{RPM}} \tag{85}$$

where $\tau_f$ and $\tau_c$ represent the fluid and media contact torque, respectively, and $\omega_{zRPM}$ is the angular velocity of the impeller in rpm. This power draw is tracked at each recorded timestep. CSPH_MPI generated data is used in Figure 6.14 to show the power draw stabilisation of Mill A at 300 rpm. The blue line shows the raw data, and the orange line shows the smoothed trend, using a 10 % moving average. This supports the energy stabilisation data and is used to generate the average power draw at steady state, which is used as a comparative variable. The steady state variables used in the analysis are summarized in Table 6.6.

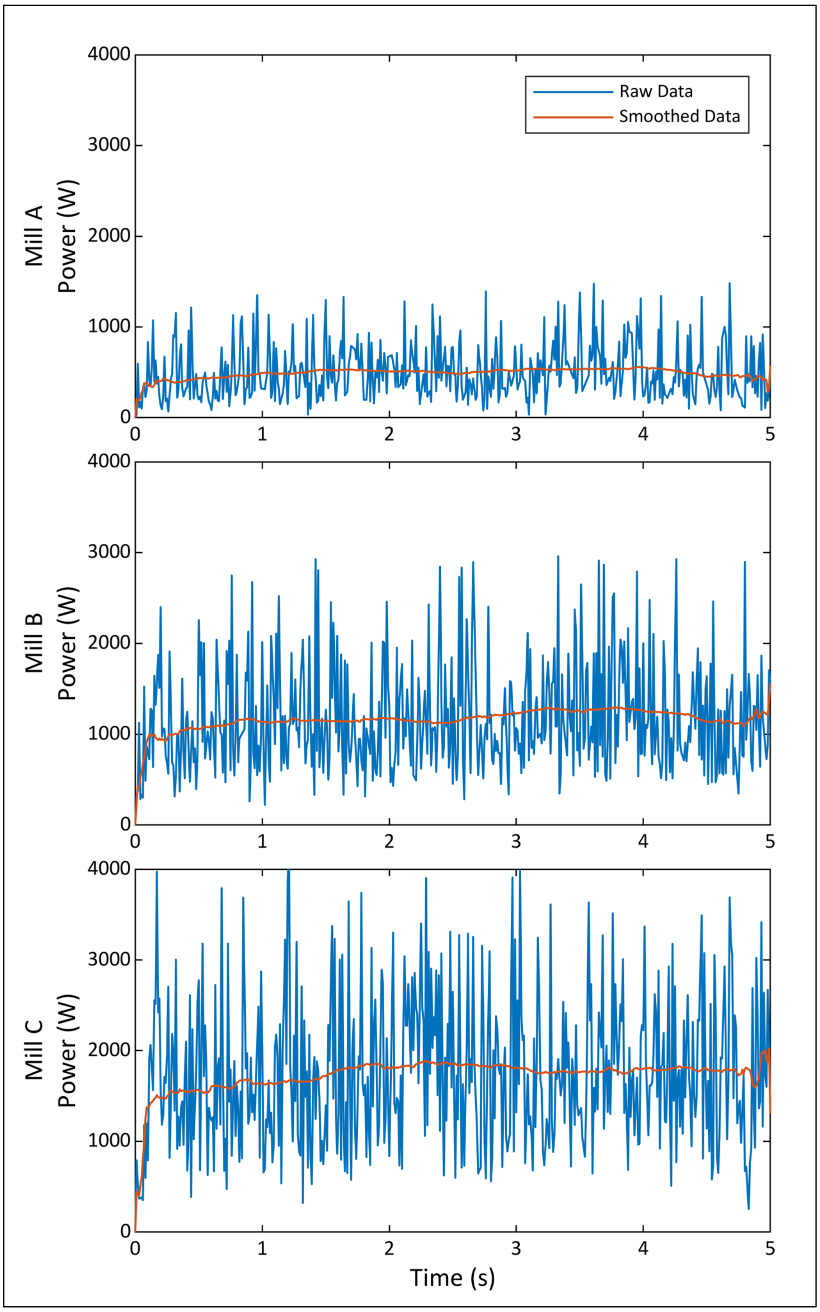

*Figure 6.14: Power drawn by impeller against time for Mills A, B and C at a 2.2 m/s tip speed*

*Table 6.6: Summary of steady state variables*

| Steady state variables | Units |
|---|---|
| Impeller torque (fluid and media)<br>Power draw | Nm<br>W |
| Total kinetic energy (fluid and media)<br>Total potential energy (fluid and media) | J<br>J |

### 6.5.2 Contact data analysis

The contact data from each core is collated using MATLAB. This is done for data at effective steady state timesteps. The data required is a record of each contact, the body numbers of the two bodies involved, the start and end collision times, the collision energy, coordinates, and the normal, shear and total energy dissipation as summarised in Table 6.7. This is used to create collision frequency and energy distributions. Collision energy and energy dissipation are defined as described in section 3.2.6 .

*Table 6.7: Summary of contact variables*

| Contact Variables | Units |
|---|---|
| Body number 1<br>Body number 2 | |
| Contact position (cartesian) | m |
| Start time<br>End time | s<br>s |
| Collision energy<br>Normal dissipation<br>Shear dissipation | J<br>J<br>J |

Examples of the collision frequency and energy dissipation rate distributions at steady state, are shown in Figure 6.15 and Figure 6.16, respectively. The data is assessed through logarithmic binning on the raw contact data. The complete analytical code used is given in Appendix D. The analyses are done either for revolution intervals or per second. Outlier collisions, where the start and end time are equal, are excluded from the distributions as these collisions are located at the base of the vortex and do not contribute significantly to the energy distribution. The spatial distribution of the collisions within the mill space is considered using the two-dimensional projection methods outlined in section 6.5.4. The collision frequency plot shown in Figure 6.15, presents the total collision distribution as well as that of the different collision types (media-media, media -shell and media-impeller).

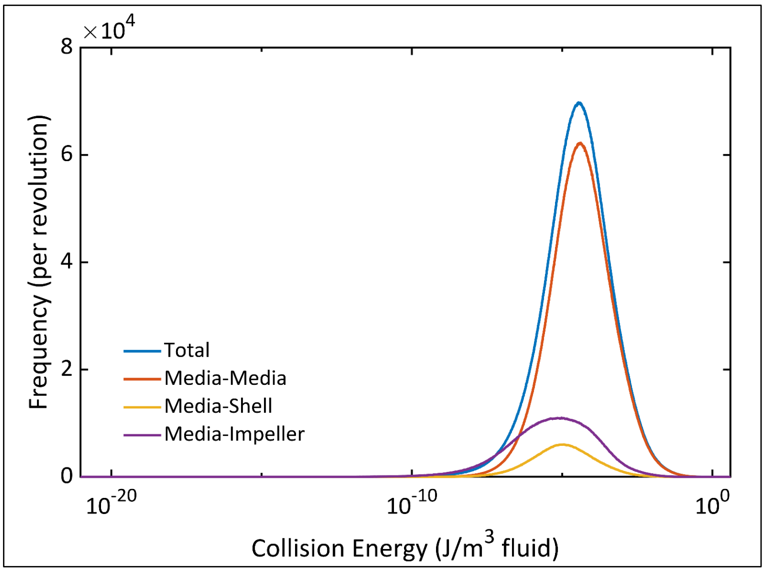

*Figure 6.15: Collision frequency plot for Mill C at a tip speed of 1.5 m/s*

The energy distribution plot in Figure 6.16 shows the dissipation of energy in the normal and shear directions as well as the total dissipation for all collision. The total dissipation is determined as the resultant energy vector of the normal and shear components. Trends in the modal peak of the collision energy and its corresponding dissipation rate are monitored across simulations.

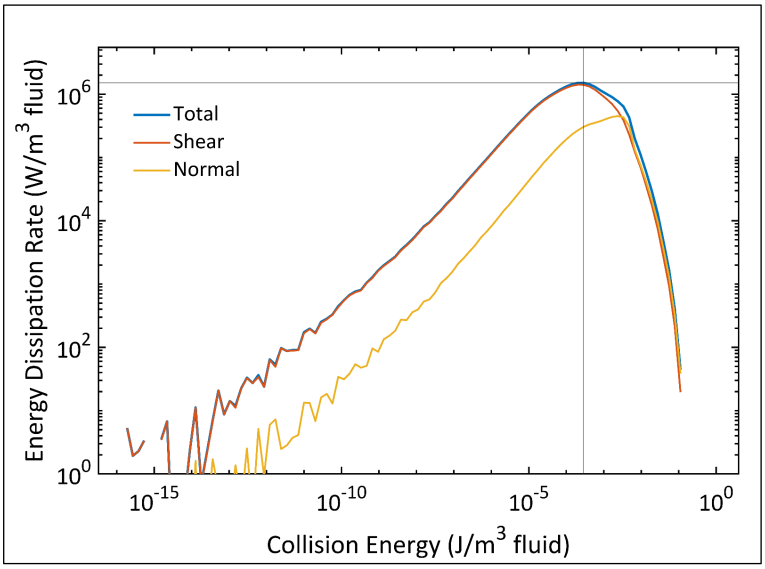

*Figure 6.16: Energy dissipation against collision energy for Mill A at a tip speed of 1.8 m/s*

### 6.5.3 Velocity data analysis

The velocity parameters for body geometry and fluid particle data at effective steady state are extracted from Paraview and the geometry data is converted from point to body data. This is used to develop 2D and 3D profiles of the mill. The velocity data is analysed spatially using the two-dimensional projection techniques outlined in section 6.5.4. The velocity of the particles and bodies are outputted in their vector forms and converted to the radial and tangential components relative to the central axis of the mill. Equations (86) and (87) are used for the radial and tangential velocities, respectively. The output parameters from the geometry and particle files are listed in Table 6.8.

$$v_r = \boldsymbol{v}_x \cos\theta + \boldsymbol{v}_y \sin\theta \tag{86}$$

$$v_t = -\boldsymbol{v}_x \sin\theta + \boldsymbol{v}_y \cos\theta \tag{87}$$

*Table 6.8: Summary of body and particle variables*

| Body and Particle Variables | Units |
|---|---|
| Identity number | |
| Position (polar and cartesian) | m |
| Velocity (cartesian, radial and tangential) | m/s |
| Particle Variables | |
| Solids fraction | |
| Relative density | |
| Pressure | Pa |

### 6.5.4 Spatial analyses

The data used for contacts and velocity analyses is outputted as a three-dimensional representation of the mill space. The mill space for these laboratory scale SMD vertical stirred mill systems is best described in a cylindrical coordinate system with the impeller as the central longitudinal axis and the origin at the base of the mill shell. The contact data provides the location for each collision within the space, while the velocity data delivers the positions of the bodies and fluid particles.

Three-dimensional images provide a qualitative representation of the mill space, however, to quantify and compare the visualised trends, two-dimensional projections are used to visualise spatial trends, as an intermediary step to the development of two-dimensional line graphs and to produce single values representative of the bulk mill space. The three variations of two-dimensional projection of the cylindrical mill space are shown in Figure 6.17.

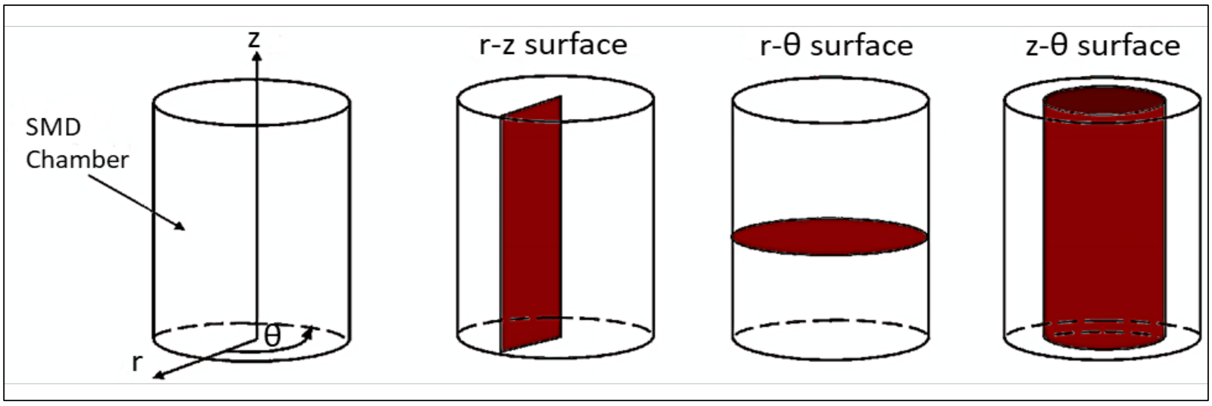

*Figure 6.17: Types of 2 dimensional projections of the 3D mill space in a cylindrical coordinate system, adapted from Daraio et al. (2020)*

Three reference surface projections used to describe motion in the mill space are the r-z surface, which defines motion in a vertical plane from the mill centre to the wall; the r- θ surface, which defines motion from a birds-eye perspective, compacting the mill into a horizontal circular plane; and a z- θ surface which defines the relative rotational motion radially from the mill centre (Rydin, Maurice & Courtney, 1993; Daraio et al., 2020). A combination of cartesian and cylindrical binning is used to coarse grain the spatial data into these projections. All of the code used for the binning and projections can be found in Appendix C.5. The two-dimensional projections used for this analysis are the r-z and the r-θ surfaces. These projections have been used by Daraio et al., 2020 in similar techniques to analyse three dimensional data as shown in Figure 6.18 a).

The r-z surface projections show bulk flow trends, as the mill space is symmetrical on the z axis. Therefore, azimuthally averaging the data in this plane provides a fair representation of the mill space. This surface projection is applied in this study primarily through averaging the spatial data into two halves of the azimuth, which are represented as surface plots of the two halves of the mill on the r-z plane, commonly with a normalised radius, as shown in Figure 6.18 b). The normalised radius is used to compare the mill sizes along their radial axis, which is similar across the laboratory mill sizes.

The r-z surface projection is further used to illustrate trends in the different flow regions as defined in section 2.4.3.1 as the upper circuits, impeller band and lower circuits regions. Figure 6.19 a) shows the mill segmentation regions: the lower circuits are defined as the region below the bottom pin (pin 1), the impeller band is the region from the bottom of pin 1 to the top pin

(pin 2), and the upper circuits are the regions are above pin 2. These segments are used to create two-dimensional line plots of spatial variables against the mill radius, as shown in Figure 6.20 a) for tangential velocity. This is achieved by azimuthally averaging of all data in the r-z plane, then segmenting it according to the bounds shown in Figure 6.19 a). These radial profiles use a normalised radius, with the impeller pin length demarcated, to show how the variable response changes along the radius at each of the three flow region segments.

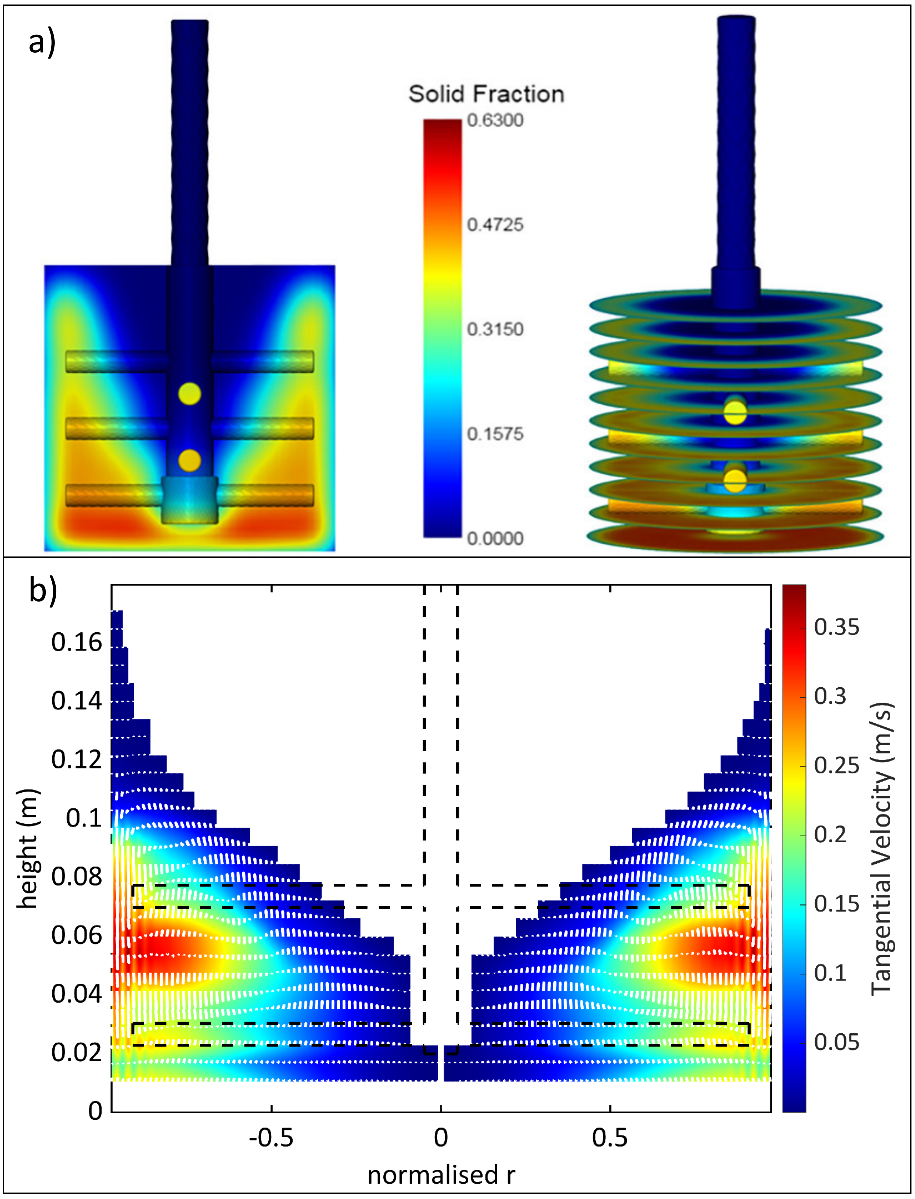

*Figure 6.18: R-Z surface projections a) solids fractions of attritor mill, extracted from Daraio et al. (2020) and b) tangential velocity plot with radial and axial quiver for Mill C, at 1.8 m/s*

Stills of the mill space from perspective of r-θ surfaces have been used by Kim & Choi (2008) at each impeller pin height of a pin mill to evaluate the velocity patterns and central cavity structure. Their mill used a suspended impeller shaft with four rows of pin, compared to the laboratory SMDs two pin rows. The impeller pins rotate in a counterclockwise direction and are numbered from the bottom to the top row. The resulting DEM flow fields, generated for each width of the four pins, are shown as r-θ surfaces in Figure 6.21, for mill speeds of 300 rpm (A) and 700 rpm (B). These velocity fields show the displacement of media in the direct wake of the impeller, as well as how the shape of the central cavity changes at each pin width. In this thesis, r-θ surfaces are used similarly to show the distribution of the spatial variables around the pin arms. This is achieved by overlapping timestep data at the same impeller rotation angle to observe trends in the areas preceding the impeller and in its wake. This technique evaluates the volume regions centred on each impeller pins that range axially from a pin diameter above to a pin diameter below the pin centre, as shown in Figure 6.19 b), to examine the influence of the top and bottom pin layers separately. An example of the resulting r-θ surface is shown in Figure 6.20 b) for the bottom pin layer.

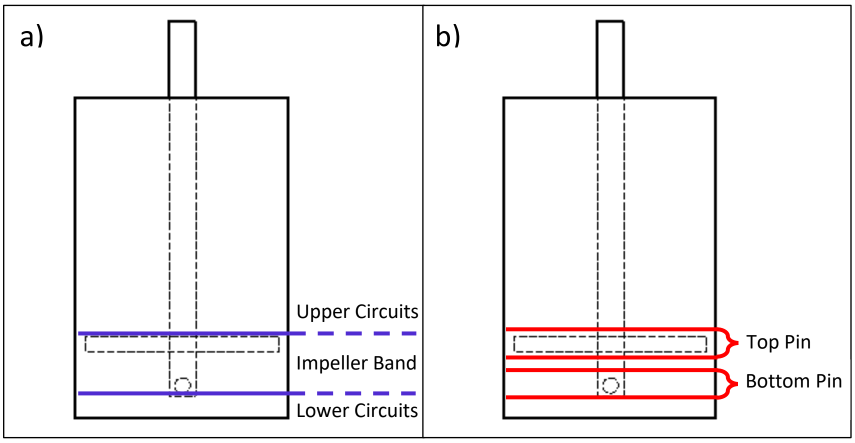

*Figure 6.19: Mill segmentation a) into upper circuits, impeller band and lower circuits, based on expected flow patterns and b) into the top pin and bottom pin regions of high influence*

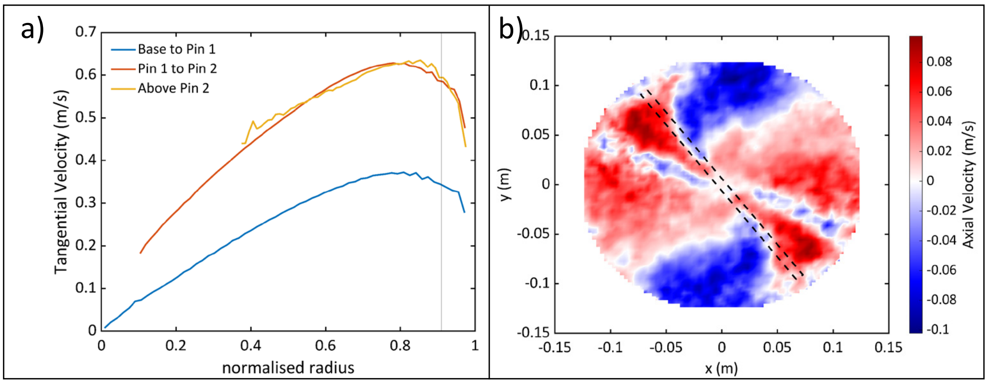

*Figure 6.20: a) Three-part segmentation plot for the tangential velocity and b) bottom impeller segment of axial velocity of Mill C at a tip speed of 1.8 m/s*

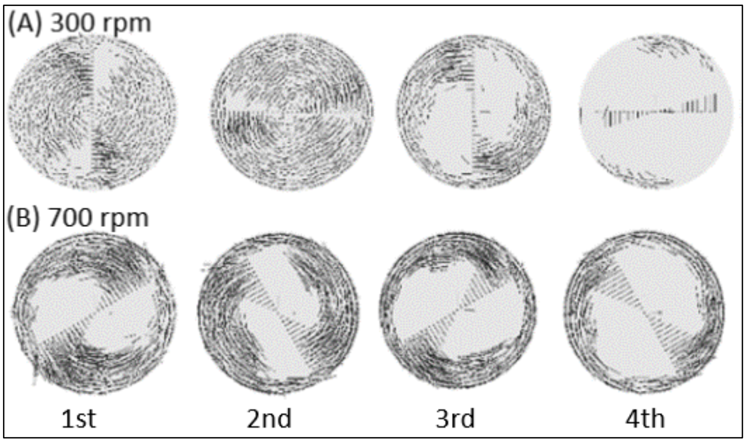

*Figure 6.21: Stills of r-θ surfaces of velocity fields at the height of each impeller pin from the bottom (1st) to the top (4th) of a pin mill modelled using DEM. Taken from Kim & Choi (2008).*

## 6.6 Summary of CSPH_MPI

The CSPH_MPI model for mill simulations is summarized through the following diagram into three phases. The first is the configuration phase, where the mill input files, and configuration file are processed. The images accompanying the input files provide a physical interpretation of the file components. The mill then enters the simulation phase, which begins with initialisation. This puts together the mill components and flood fills the liquid. The simulation then begins according to the algorithm illustrated in Figure 6.10. The final phase is output, which details the processing of the system and contact data through the different analytical methods.

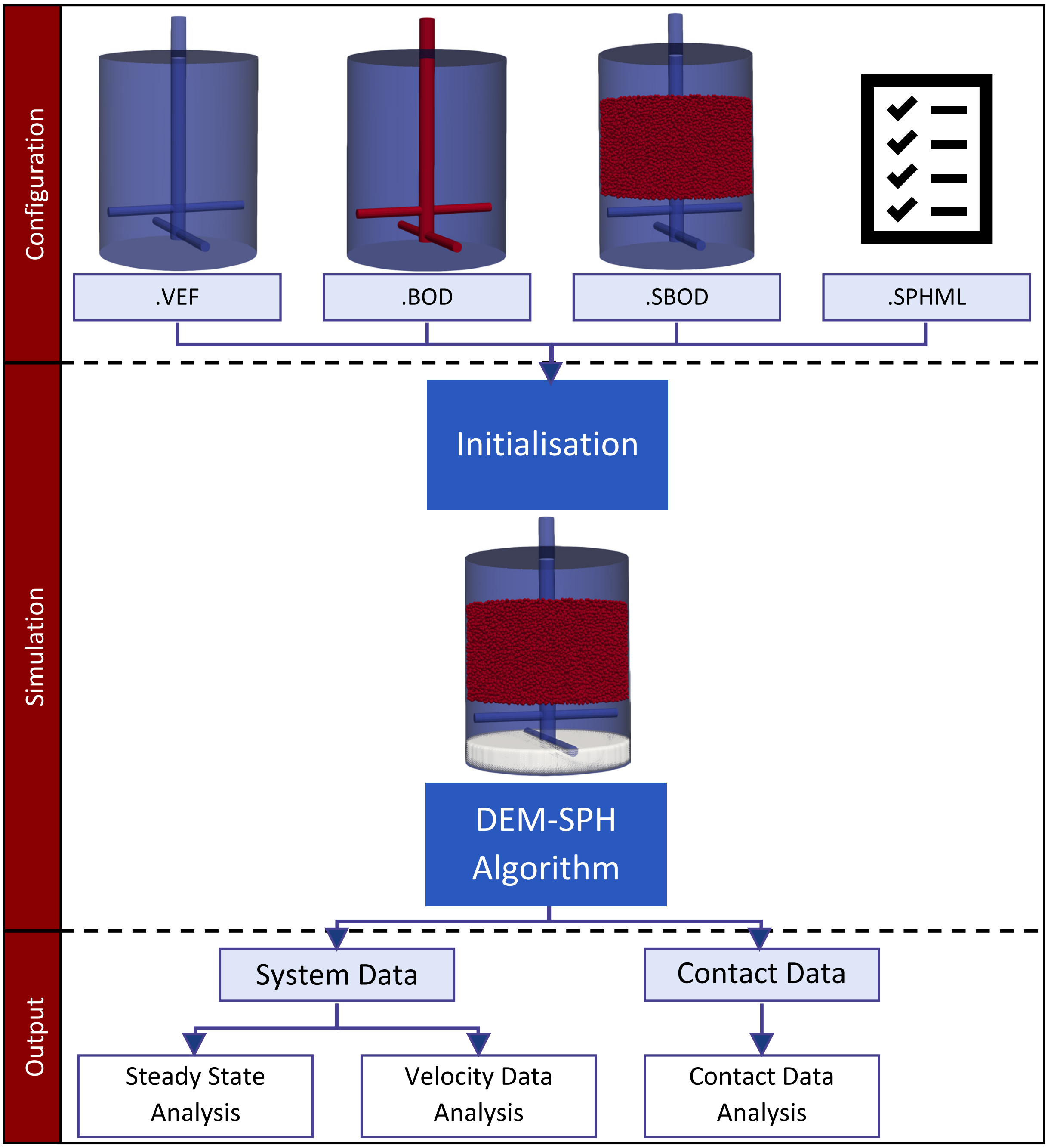

*Figure 6.22: The flow of components in the CSPH_MPI mill simulations*

## 6.7 Simulation plan

The simulations conducted in this thesis are divided into two parts, performance assessment simulations and scale-up comparison simulations. For the performance assessment simulations, the critical variables in the mill are manipulated to evaluate the DEM-SPH model's ability to reproduce trends and effects that have been well established in the literature, to investigate the first hypothesis of the study. The scale-up comparison simulations serve to evaluate the effect of the radial increase between the mill sizes on the flow and energy environments in the mill space, to examine the second and third hypotheses.

Each simulation is run to provide 5 impeller revolutions at steady state, with a write time of 0.01 s. The simulation speed is influenced by numerous factors such as media shape, mill size, number and timesteps of DEM bodies and SPH particles, impeller speed, and other influences on the performance of the node. The most time efficient simulations are run with spherical media, these compute 5 seconds of data within 12 hours, while lengths of super quadric media simulations are in the order of weeks, due to their lower DEM timestep and more vigorous contact detection. Detailed run time data for the simulations is provided in Appendix E.1.

### 6.7.1 Performance assessment simulations

The performance assessment simulations were chosen to test the response of the DEM-SPH model to changes in critical parameters. The parameters chosen are media size and density, slurry density and viscosity, and the media fill. All the other parameters used in these experiments are the basis parameters specified in section 6.3. These tests were performed using spherical media on Mill C. The speed of the mill was not evaluated as a performance assessment parameter, as its evaluation was absorbed into the scale up comparison tests, as it is the variable which influences the energy of the system the most. Therefore, all the performance prediction experiments were run at 300 rpm, with 5 steady state revolutions (1.00 s) of data analysed.

*Table 6.9: Low, medium, and high critical variables tested in prediction experiments*

| | low | medium | high |
|---|---|---|---|
| Media size (mm)<br>• Number of media: | 2.5<br>237 551 | 5<br>29 694 | 7.5<br>8 798 |
| Media density (kg/m$^3$) | 2 700 | 5 000 | 7 500 |
| Slurry density (kg/m$^3$) | 1 379 | 2 000 | 3 000 |
| Slurry viscosity (Pa·s) | 0.001 | 0.01 | 0.1 |
| Media fill<br>• Number of media:<br>• Number of fluid particles:<br>• Volume of fluid (cm$^3$): | 40%<br>23 755<br>66 647<br>2 332 | 50%<br>29 694<br>51 442<br>1 943 | 60%<br>35 623<br>36 852<br>1 555 |

The testing ranges of the various parameters are shown in Table 6.9. Three level testing is used to evaluate the parameters at low, medium, and high values. The media size range was chosen in line with the SMD operating conditions specified by Metso-Outotec. The density range was chosen to represent ceramic media at the low priority and steel media at the high priority, with an intermediary medium. The slurry density and viscosity ranges were tested within the ranges of the reviewed literature, to enable comparison of the effects, though the combined effect of the parameters was not evaluated. The media fill was evaluated with the medium level at equal quantities of media and slurry at 50% media fill, with the low level being more slurry than media at 40 % media fill and vice versa for the high level at 60% media fill.

### 6.7.2 Scale-up comparison simulations

The scale-up comparison simulations are conducted using the two-way coupled DEM-SPH model, CSPH_MPI. These simulations serve to evaluate the effect of the radial increase between the three mill sizes on the flow and energy environments in the mill space. These simulations are designed to target the effects of tip speed and media shape on the radial expansion between mill sizes. It follows that each property has a separate set of simulations to examine its effects.

The tip speed simulations consisted of running each of the mill sizes at 3 tip speeds, using spherical media. Tip speed is used as the independent variable because the impeller tip speed has been used in stress energy models in the approximation for the mean particle stress energy and using the same tip speed across all mill sizes would result in the same prediction using those models. The media shape simulations use 3 groups of super quadric media to simulate increasing angularities observed in real media shapes. The super quadrics range from near spherical to box-like shapes with rounded edges. These simulations are run at a constant tip speed.

#### *6.7.2.1 Scale-up tip speed simulations*

The tip speeds correspond to the smallest system, Mill A, being run at 200, 250 and 300 rpm. The resulting tip speeds are 1.5, 1.8 and 2.2 m/s. Table 6.10, Table 6.11 and Table 6.12 report the rotational speed and time taken for 5 revolutions (revs) at steady state for each mill, at the chosen tip speed. Note that CSPH_MPI uses SI units therefore, rotational speed is set in rad/s.

Tip speed is used instead of rotational speed to keep consistent tip speed at a normalised radius when analysing each system. This is done to analyse not only the resultant flow and energy profiles, but to examine the response of the dimensionless parameters within the bulk flow.

*Table 6.10: Properties of 1.5 m/s tip speed experiments at three scales*

| Mill | tip speed (m/s) | rotational speed (rad/s) | (RPM) | 5 revs (s) |
|---|---|---|---|---|
| A | 1.477 | 20.9440 | 200 | 1.50 |
| B | 1.477 | 15.9627 | 152 | 1.97 |
| C | 1.477 | 12.6742 | 121 | 2.48 |

*Table 6.11: Properties of 1.8 m/s tip speed experiments at three scales*

| Mill | tip speed (m/s) | rotational speed (rad/s) | (RPM) | 5 revs (s) |
|---|---|---|---|---|
| A | 1.846 | 26.1799 | 250 | 1.20 |
| B | 1.846 | 19.9534 | 190 | 1.57 |
| C | 1.846 | 15.8428 | 151 | 1.98 |

*Table 6.12: Properties of 2.2 m/s tip speed experiments at three scales*

| Mill | tip speed (m/s) | rotational speed (rad/s) | (RPM) | 5 revs (s) |
|---|---|---|---|---|
| A | 2.215 | 31.4159 | 300 | 1.00 |
| B | 2.215 | 23.9440 | 229 | 1.31 |
| C | 2.215 | 19.0114 | 182 | 1.65 |

A final set of tip speed experiments are run using the same parameters as the 2.2 m/s tip speed but, run using DEM only. This is done to analyse and compare the energy environments of both a wet and a dry system with regards to scale.

### *6.7.2.2 Scale-up media shape simulations*

The media shape simulations are conducted using the three groups of super quadric shapes shown in section 6.3.3. The properties of each group of media shape simulations are summarised in Table 6.13. Each of the three groups of super quadric media is simulated in each of the three mill sizes.

*Table 6.13: Properties of media shape experiments at three scales*

| media shape group | types of super quadrics | average sphericity | roundness | aspect ratios | | tip speed | mill sizes | 5 revs |
|---|---|---|---|---|---|---|---|---|
| | | $\Phi$ | n | b/a | c/a | (m/s) | | (s) |
| Group 1 | 3 | 0.996 | [0.80; 1.00) | 0.9-1.0 | 0.9-1.0 | 1.846 | A | 1.20 |
| | | | | | | | B | 1.57 |
| | | | | | | | C | 1.98 |
| Group 2 | 4 | 0.975 | [0.57; 0.80) | 0.8-0.1 | 0.8-0.9 | 1.846 | A | 1.20 |
| | | | | | | | B | 1.57 |
| | | | | | | | C | 1.98 |
| Group 3 | 5 | 0.922 | [0.33; 0.50] | 0.7-0.8 | 0.6-0.8 | 1.846 | A | 1.20 |
| | | | | | | | B | 1.57 |
| | | | | | | | C | 1.98 |

Within the groups of super quadrics, The ranges of the aspect ratios and roundness are consistent with the super quadric media groups simulated by Sinnott, Cleary & Morrison (2011b), for ease of comparison. Each group of media consists of an equal distribution of a specified number of super quadric shapes. All the media shapes have a volume equivalent to the 5 mm spherical media. Therefore, the number of media used in each mill is consistent with the fill levels of Table 6.5. The media groups are used in simulations of each mill scale at a constant tip speed of 1.8 m/s. All the Group 3 simulations and the Group 1 and 2 simulations of Mill A are repeated using DEM only with no fluid model coupled to it. This is done to better characterize the behaviour of super quadric shapes within the mill space.

To ensure that energy does not propagate beyond bodies in contact within in a timestep, the Young's Modulus of the super quadrics has been lowered to $10^7$ Pa. Significantly lower Young's Moduli have been used in super quadric simulations as shown in Table 3.1. The Young's Modulus was changed for these simulations because reducing the timestep beyond $10^{-7}$s in order of magnitude is not currently computationally feasible for these scales of systems. All the remaining properties are as given in Table 6.1.

# PART THREE

## RESULTS AND DISCUSSION

# CHAPTER 7

# Results and discussion: Performance assessment simulations

## 7.1 Introduction

The purpose of this Chapter is to present the results showing that the DEM-SPH model developed is able to capture the mechanisms and effects of varying some key operating and design parameters. The outputs from the simultaneous two-way coupled models are assessed in a similar way as results from other computational modelling studies approached in the literature are presented. This will show that the mechanisms within the CSPH_MPI models can be used to simulate the flow and energy environment within a stirred mill.

The five parameters evaluated are the media size, media density, slurry density, slurry viscosity and media fill. The structure of the simulation test work is outlined in section 6.7.1. The parameters effects are evaluated on the largest of the three mill sizes being studied in this thesis, Mill C. The results showing the flow and energy environments of the experiments for each parameter studied are discussed, and the chapter concludes with an overall summary. The results are abridged to show the key mechanisms within the parameter effect, in conjunction with the reviewed literature.

## 7.2 Media size

The media diameter range used within industrial SMD applications is 1-8 mm (Metso, 2019). This allows the mill to effectively grind a range of particle sizes within the slurry. The simulations to evaluate the effect of the media size were performed on Mill C at three spherical media diameters: 2.5 mm, 5.0 mm, and 7.5 mm. The simulations were conducted at the physical parameters and operating conditions specified in sections 6.3.2 and 6.3.3. A key parameter to note is the 300 rpm impeller speed, which corresponds to a 3.66 m/s tip speed in Mill C. For the 7.5 mm media size test, to ensure stability within the coupling, the SPH resolution was increased to 8 mm. Snapshots of the simulated mill space are shown for each media size in Figure 7.1, with the media coloured by its average velocity magnitude and the fluid free surface shown at 60 % opacity.

The computational studies on media size reviewed in literature were all conducted on horizontal disk mills by Jayasundara et al. (2008), Jayasundara, Yang & Yu (2012) and Cleary, Sinnott & Pereira (2015), as discussed in section 4.3.3. Cleary, Sinnott & Pereira (2015) observed that the flow patterns were similar for media below 15 mm. This is supported by Jayasundara et al. (2008) and Jayasundara, Yang & Yu (2012) for 2-6 mm media, which observed that the media velocity range was larger for smaller media. Within the energy environment, Cleary, Sinnott & Pereira (2015) observed the modal peak collision energy and power draw increasing with media size, while Jayasundara, Yang & Yu (2012) observed a decrease in the ratio of specific impact energy to power draw with increasing media size.

Looking at the flow environment captured within the snapshots, there is a visible trend in the proportion of fluid and media that make up the overall free surface of the mill space. The fluid free surface is shown as a translucent white film over the media bodies. At the media size of 2.5 mm, the fluid dominates the free surface of the upper circuits while at 5.0 mm, there is a combination of fluid and media, and at 7.5 mm, the media dominates. This is attributed to the increase in the size of the pores within the packing structure of the media bed, with increasing media size. The bulk solids fraction distributions from the simulations are shown in Figure 7.2.

The distribution for each simulation is shown as a r-z surface colour plot of the mill space. Note that the solids fraction presented in Figure 7.2 is an SPH property, and its free surface is a function of the bulk occupancy of the fluid and the solids fractions of fluid particles across the timesteps. The trend shows the bulk solids fractions decreasing and the appearance of fluid dominant regions as the media size increases, due to the larger particles leaving larger voids as they dilate with fluid.

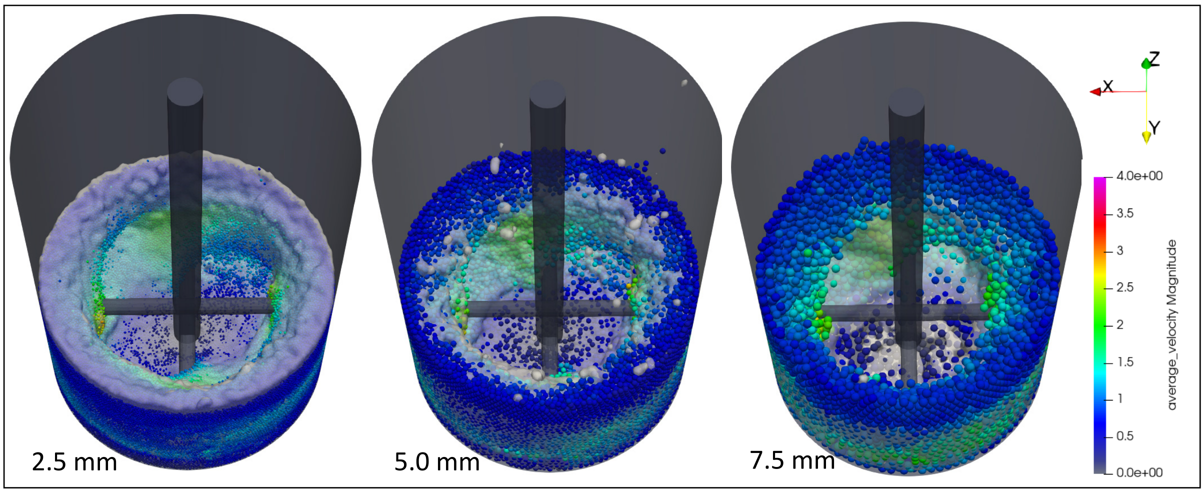

*Figure 7.1: Velocity stills of the mill space for small, medium, and large media size experiments*

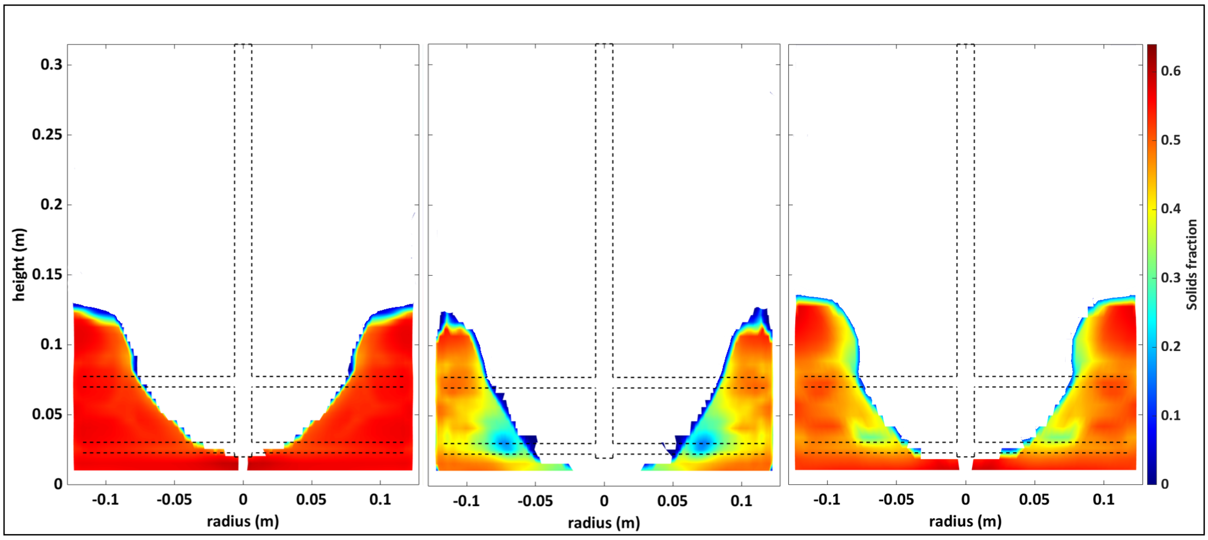

*Figure 7.2: Bulk solid fraction of small, medium and large media size simulations, respectively*

The collision frequency spectra for the small, medium and large media size simulations are shown in Figure 7.3. The collisions subsections of media-media, media-impeller and media-shell collisions are presented. The number of collisions is proportional to the number of media in each system. Consequently, the number of collisions decreases exponentially with increasing media size, as the total volume in the mill occupied by media is kept constant.

The modal peak dissipation rate and its corresponding collision energy are plotted for each media size simulation in Figure 7.4. The total energy dissipation rate spectra from which the plotted values are extracted is presented in Figure E.1, in Appendix E.2. An increasing trend is observed for both the modal peak dissipation rate and the collision energy, with the corresponding collision energy spanning across 4 orders of magnitude. This can be attributed to the increase in mass that corresponds to the increase in media size leading to higher collision energies at the same impeller speed.

The total average power draw of the mill and the average DEM power draw for all the media sizes simulated are shown in Figure 7.5. The average DEM power draw is determined through the average percentage that the DEM bodies contribute to the total torque on the impeller, which includes contribution from the SPH particles (Ndimande et al., 2019). The total power draw is observed to increase steadily with media size, while the DEM power draw increases from 2.5 to 5 mm, but no significant difference is observed between the 5 mm and 7.5 mm media sizes. The percentage of the total power draw attributed to DEM is also plotted for each media size in Figure 7.5. The mill system maintains a contact dominant flow, as the DEM component consistently constitutes the majority of the power draw. However, the DEM percentage of the power draw shows an increasing trend that peaks at 5 mm, before decreasing.

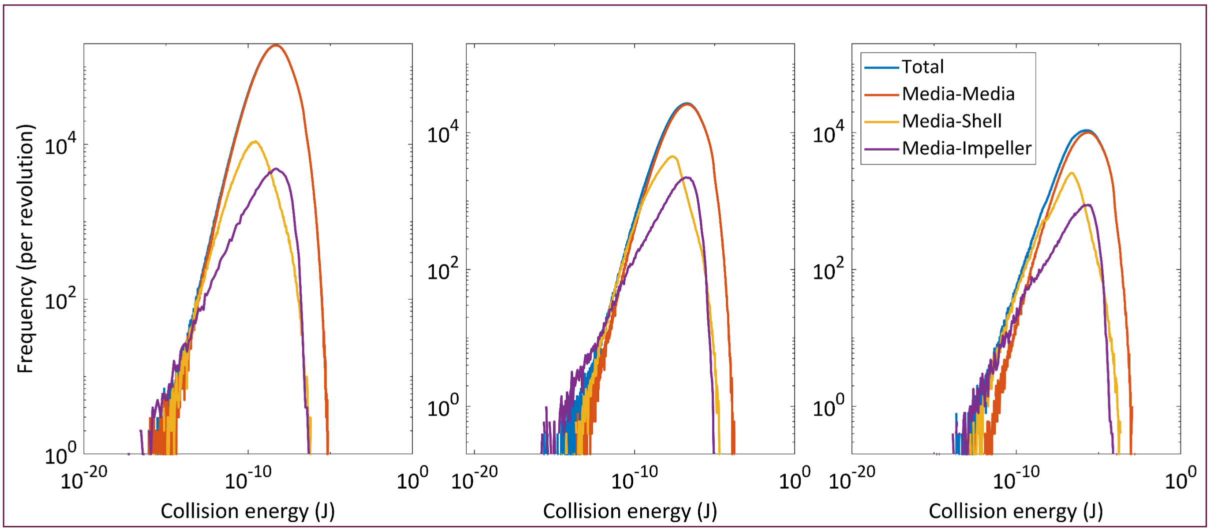

*Figure 7.3: Collision frequency spectra over collision energy for small, medium and large media size simulations, respectively*

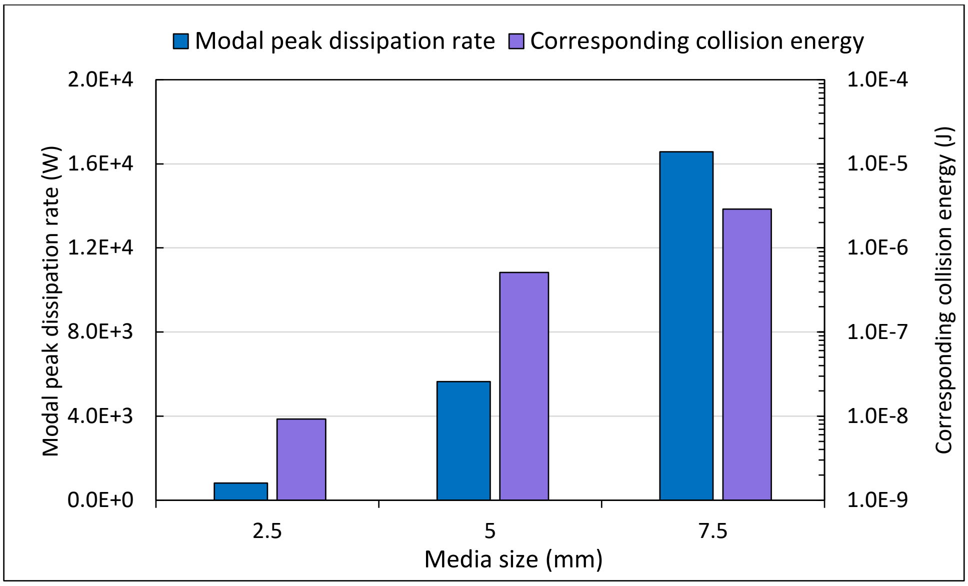

*Figure 7.4: Modal peak dissipation rate and corresponding collision energy of the media sizes*

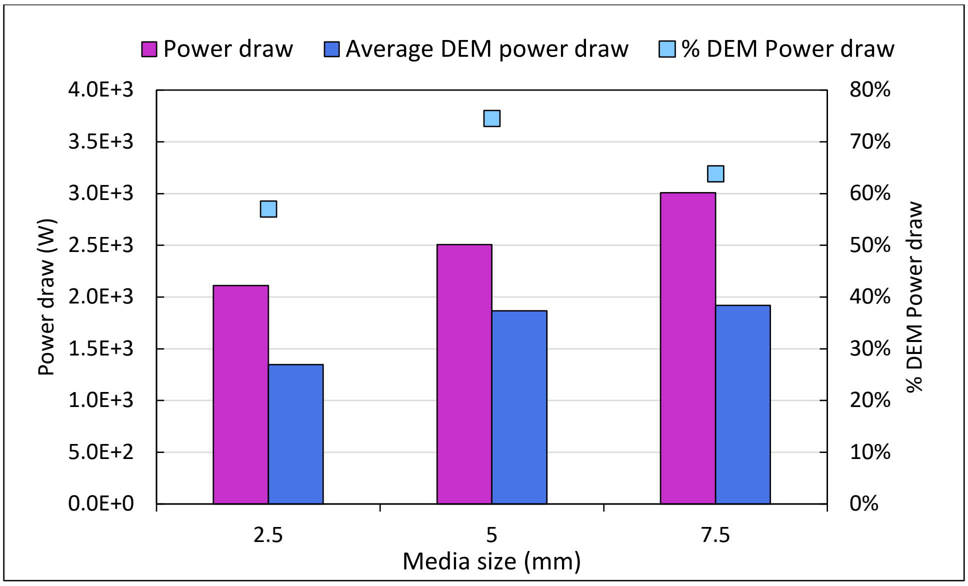

*Figure 7.5: Total power draw and average DEM power draw of the media size simulations*

## 7.3 Media density

The media density corresponds to different material types, ranging from low density ceramic beads to high density steel balls. The media density and mill speed both have an influence on the collision spectra of the mill. The media density was simulated in Mill C at three values: 2 700, 5 000 and 7 500 kg/m$^3$. The simulations were conducted using the physical and interaction parameters, and operating conditions specified in sections 6.3.2 and 6.3.3. The key parameters to note are the media size of 5 mm and the slurry density of 1 379 kg/m$^3$.

The media density study of Jayasundara et al. (2008) observed that density of the grinding media had no significant effect on the mill flow pattern in the horizontal disk mill studied. The densities investigated ranged from 1 000 to 7 500 kg/m$^3$. The effect translated directly to the collision frequency and energy. Higher energy collisions were observed for heavier particles, due to their higher kinetic energy on impact for a constant speed. The collision frequency increased with density to a maximum, before decreasing. The power draw increased with density, as the heavier particles required more energy to fluidize. This observation was experimentally validated by Jayasundara et al. (2008) using materials similar to what was used to set up the interaction parameters, but different densities. However, it should be noted that the horizontal disk mills operate at significantly higher speeds than laboratory SMDs, with different flow patterns.

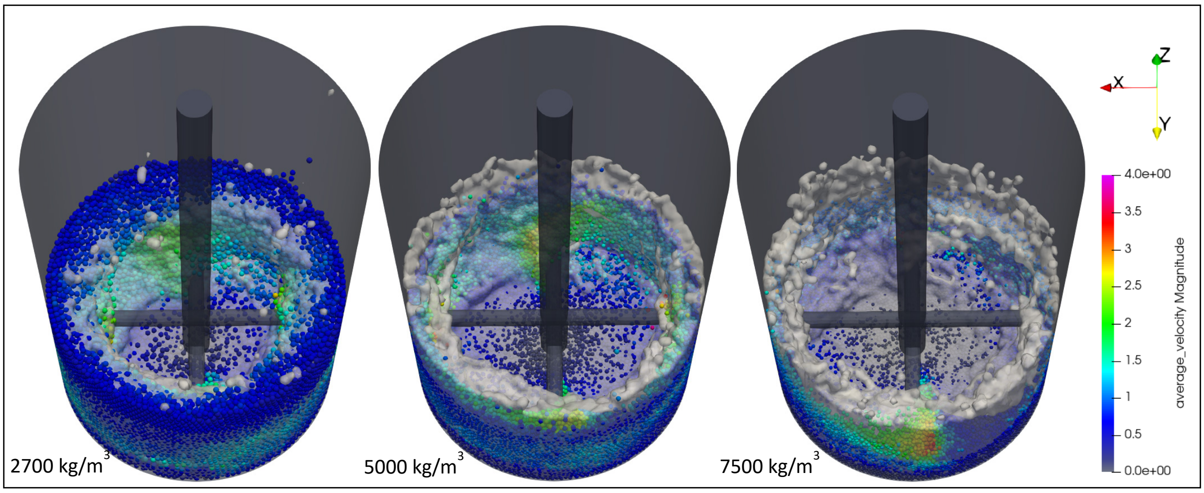

*Figure 7.6: Media density stills for low, medium and high media density simulations at 300 rpm*

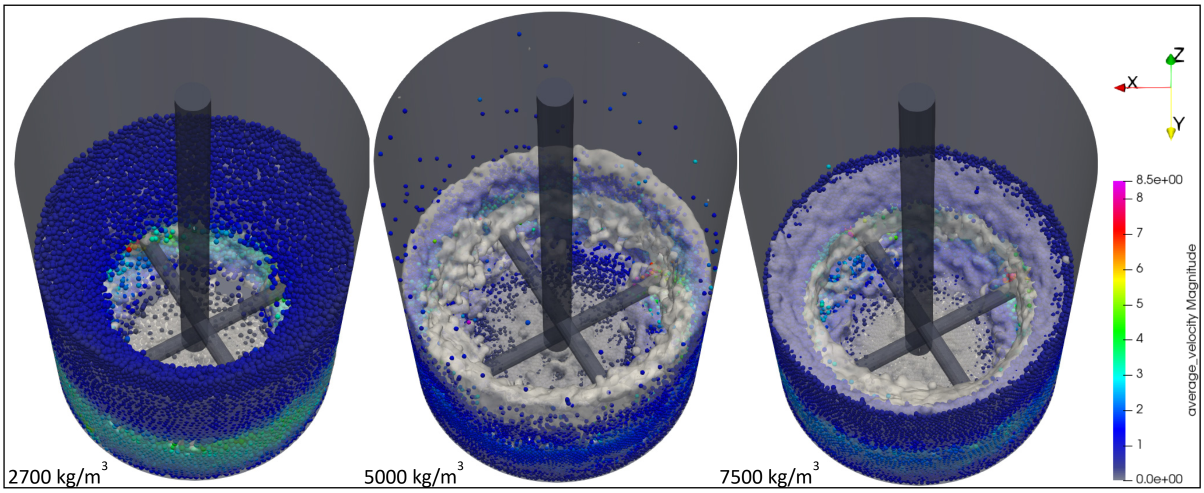

*Figure 7.7: Media density stills for low, medium and high media density simulations at 700 rpm*

The still images of the mill space for the media density simulations at 300 rpm and 700 rpm are shown in Figure 7.6 and Figure 7.7, respectively. The media are coloured by their average velocity magnitude and the fluid free surface is shown at 60 % opacity. The fluidisation state of the mill is important to consider when studying the effect of media density in fluidisation induced grinding mills. Therefore, to ensure that the media fluidised, the simulations were performed at 300 rpm and at a higher rotational speed of 700 rpm, which translates to a tip speed of 8.52 m/s. The results at 300 rpm show a trend of compression of the media bed with increasing media density. This is visualised in the decreasing height of the bulk media bed, with the fluid dominating the upper circuits of the mill space with increasing media density. This is because the impeller is unable to effectively fluidise the 5 000 and 7 500 kg/m$^3$ media at its current speed. When the speed is increased to 700 rpm, the media bed height is increased for all densities. At 2 700 kg/m$^3$, the increased rotational speed caused the media to expand significantly into the upper circuits, with the media bed height above the fluid free surface.

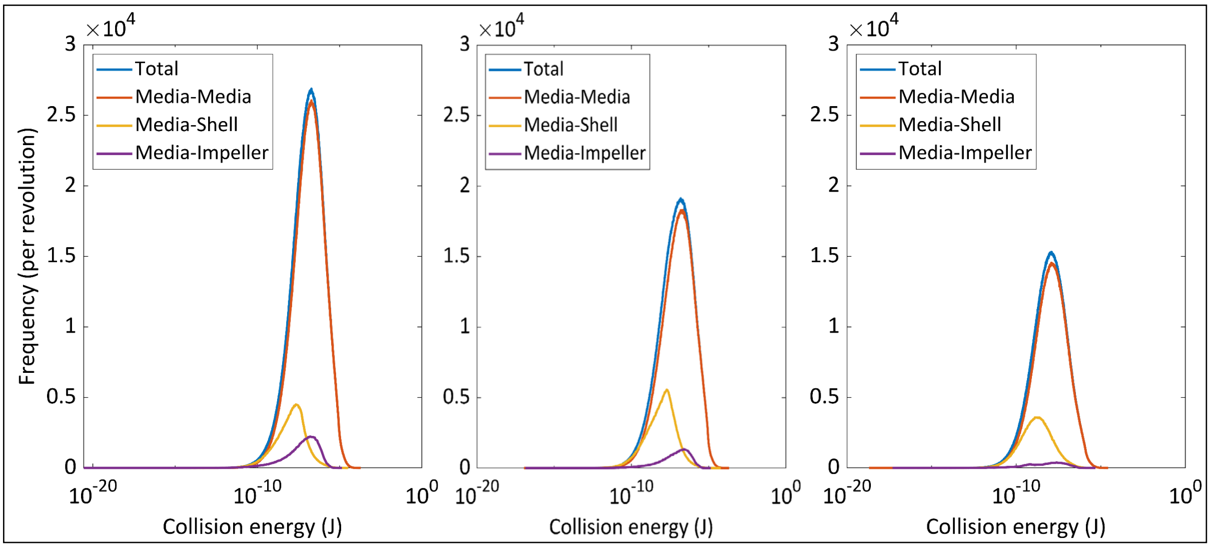

*Figure 7.8: Collision frequency spectra over collision energy for low, medium and high media density simulations, respectively at 300 rpm*

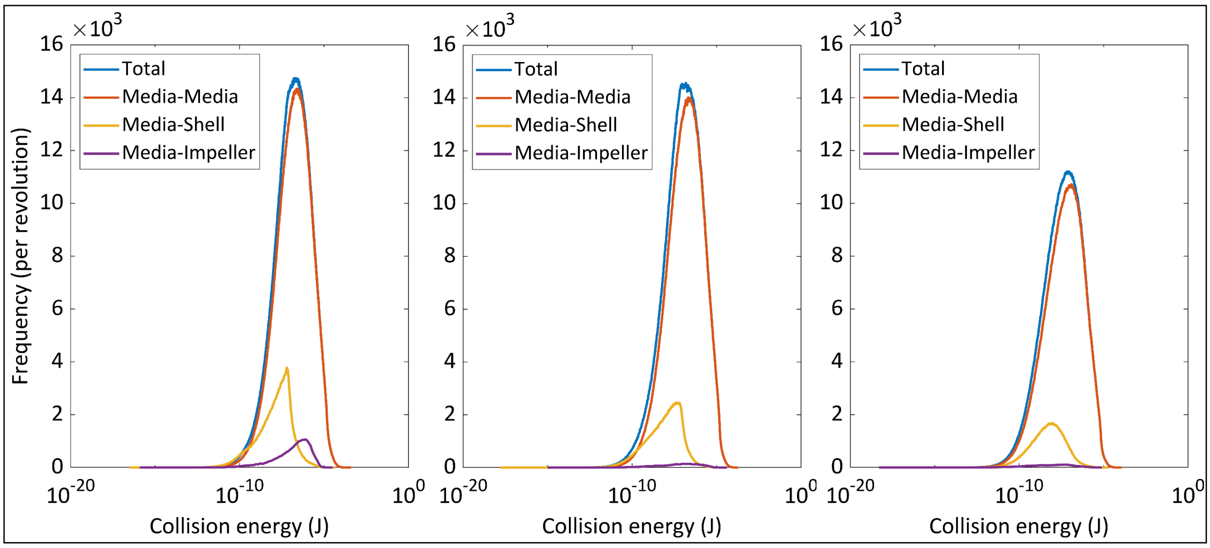

*Figure 7.9: Collision frequency spectra over collision energy for low, medium and high media density simulations, respectively at 700 rpm*

The energy environment for the simulations involving variation of the media density was assessed. The collision frequency spectra for the two rotational speeds of media density simulations are shown in Figure 7.8 and Figure 7.9, respectively. At 300 rpm, the total collision frequency decreases with increasing media density. The media-media collisions were the dominant collisions in this mill. A similar trend was observed for the media-shell collisions. The contribution of the media-impeller collisions was minimal. At 700 rpm, the media-media collisions were the dominant collisions. No significant difference was observed in the media-media collisions for the 2 700 to 5 000 kg/m$^3$, but a lower value was observed for the 7 500 kg/m$^3$. For the media-shell collisions, a steady decrease in collision energy was observed with increasing media density.

The modal peak dissipation rate and corresponding collision energy for the 300 and 700 rpm simulations are plotted in Figure 7.10. The purpose behind increasing the velocity was to observe if the trends across media density change at higher energy levels. The modal peak dissipation rate at 300 rpm shows a decreasing trend with increased media density. The corresponding collision energies at 300 rpm show no significant difference between the 2 700 to 5 000 kg/m$^3$ media densities, but a much lower collision energy was observed for 7 500 kg/m$^3$. At 700 rpm the 2 700 kg/m$^3$ media showed a significantly higher collision energy compared to that of the 5 000 kg/m$^3$ media. A decreasing trend in both the modal peak dissipation rate and collision energy was observed with increase in media density from 2 700 to 7 500 kg/m$^3$. To attain high impact collisions from the 7 500 kg/m$^3$ density media would require rotational speed beyond what was considered in these studies. Vertical stirred mills are not operated at higher rotational speeds than what was considered and in general vertical stirred mills are designed to operate with relatively low tip speeds compared to horizontal stirred mills.

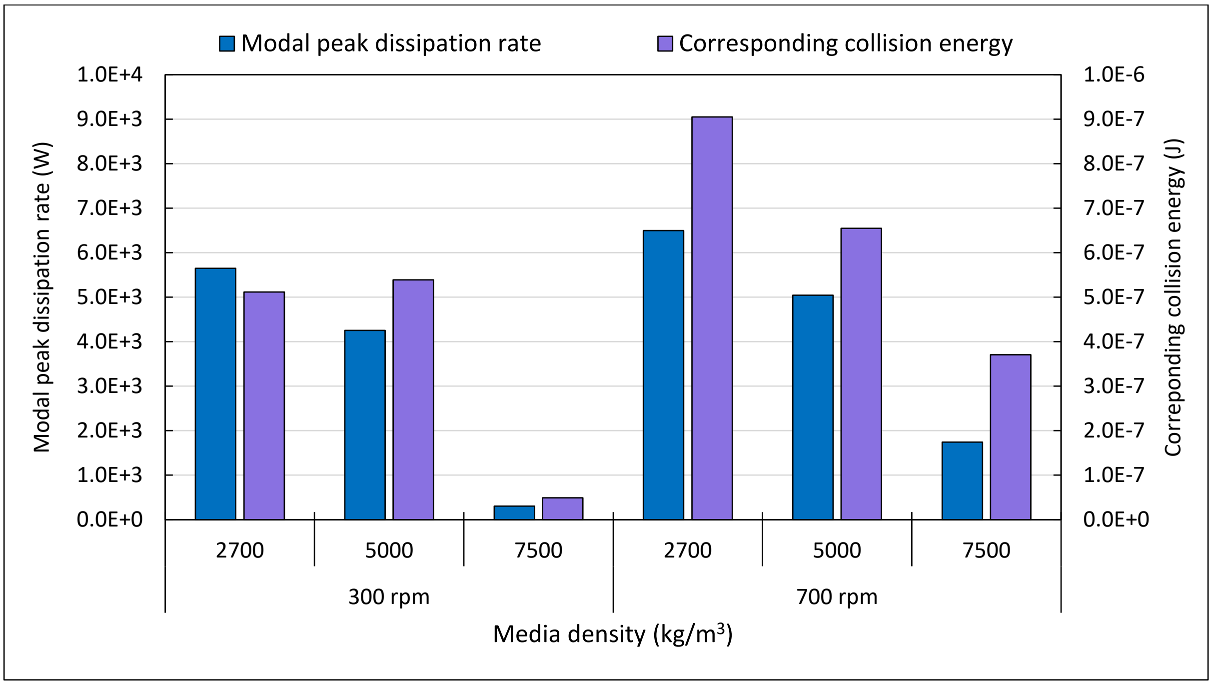

*Figure 7.10: Modal peak dissipation rate and corresponding collision energy for all the media density simulations*

The power draw results for the media density simulations at 300 and 700 rpm are shown in Figure 7.11 and Figure 7.12, respectively. Both set of simulations show a decrease in total power draw and DEM power draw with increasing density. The average proportion of the DEM contribution of the power draw decreases with increasing density. This indicates that the SPH percentage contribution increases with increasing density. The velocity stills in Figure 7.6 and

Figure 7.7 show an increased amount of fluid at the mill free surface and media bed compression due to poor fluidisation of the beds as the media density increases. This is indicative of regions of fluid dominant flow which contribute to the SPH component of the total power draw. The overall decrease in the total power draw and the decreased collision frequency and energy with increasing media density show that, at the rotational speeds simulated, increasing the media density reduces the breakage efficiency of the mill. It is necessary to consider the relationship between the mill speed and the media density when selecting a media type to ensure effective fluidisation in the mill to induce breakage within the slurry.

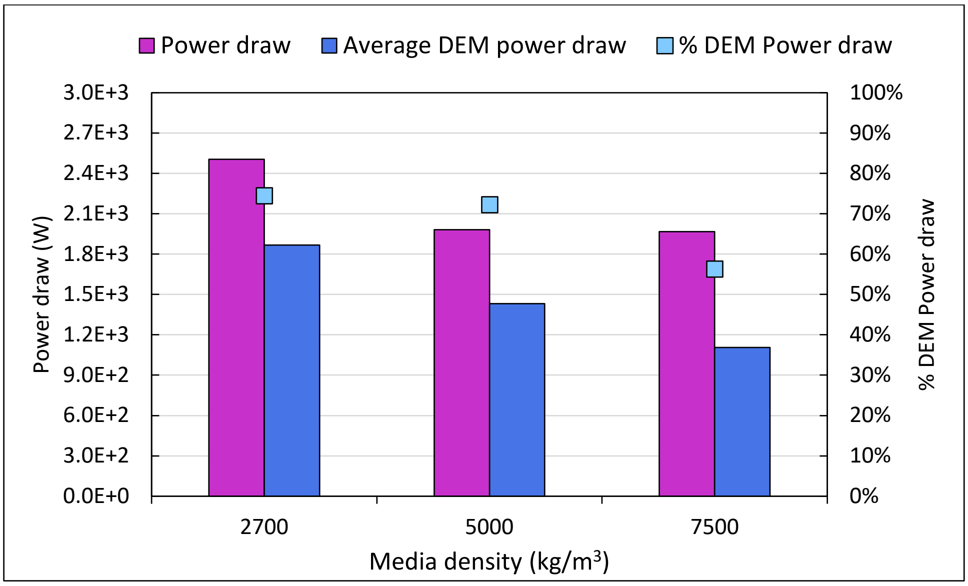

*Figure 7.11: Total power draw and average DEM power draw for the 300 rpm simulations*

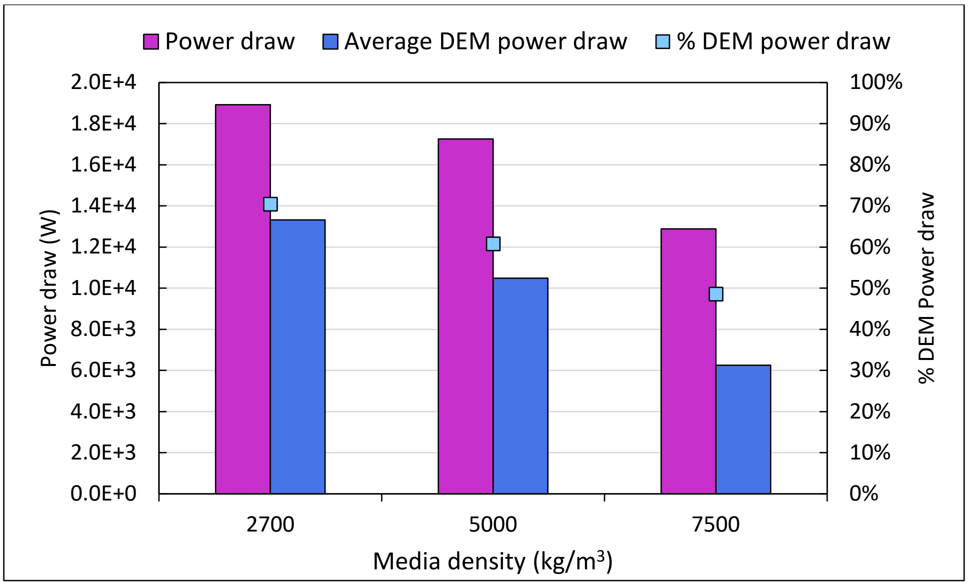

*Figure 7.12: Total power draw and average DEM power draw for the 700 rpm simulations*

## 7.4 Slurry density

The SPH fluid modelled is representative of a mineral slurry of small ore particles suspended in water. In modelling the slurry as a continuous fluid, the slurry density and viscosity are the primary parameters that influence its rheological behaviour. Within the formulation of SPH used in CSPH_MPI, the slurry is modelled as a slightly compressible Newtonian fluid. Its density is calculated according to the equation of state (47) that is dependent on the fluid rest density and speed of sound. Within the context of these simulations, it is the rest density of the fluid that is varied, while the speed of sound is constant. Mill C was simulated at three different slurry rest densities: 1 379 kg/m$^3$, 2 000 kg/m$^3$ and 3 000 kg/m$^3$. The simulations were conducted using the physical and interaction parameters, and operating conditions specified in sections 6.3.2 and 6.3.3. The key parameters were the 300 rpm rotational speed, the media fill of 50% and the slurry viscosity of 0.0022 Pa·s. Still images of the simulated mill space are shown for each slurry density in Figure 7.13.

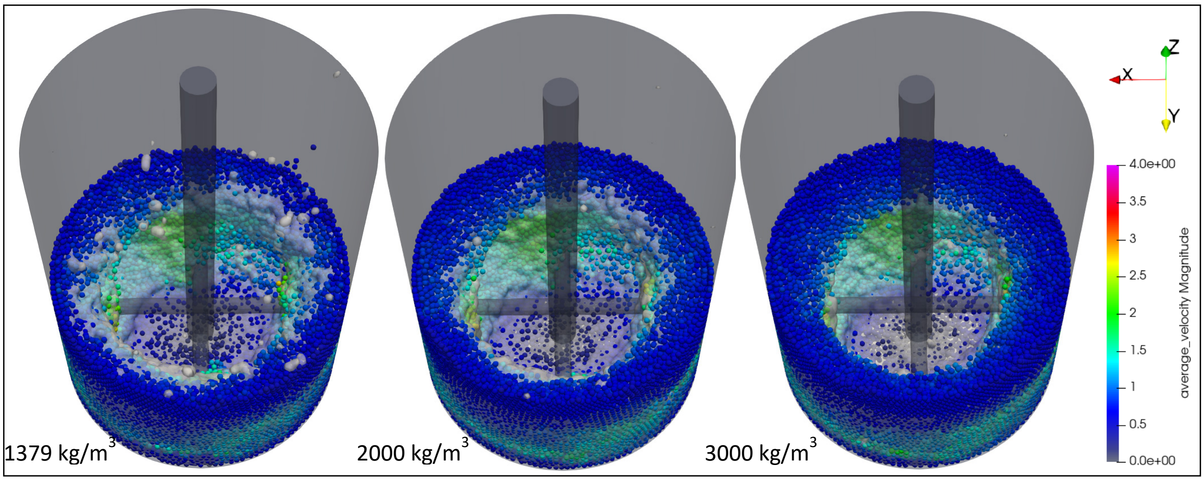

*Figure 7.13: Media velocity snapshots with the media coloured by its velocity magnitude and the fluid free surface shown at 60 % opacity*

The key observation from the computational study on slurry density performed on horizontal disk mill (Jayasundara et al., 2009) was an increase in the circulating velocities in the r-z plane, due to the direct proportionality of the slurry density to the drag force. The study showed that the collision energy increased to a peak with increasing density. Increases were noted in the total impact energy and power draw, with increasing density. The PEPT study of a vertical detritor mill by Barley et al. (2004), which considered the effect of slurry density, observed increased axial velocities and greater media recirculation in the r-z plane when the solids concentration of the slurry was increased from 40% to 70%.

The still images show that as the slurry density increases, the slurry bed shrinks beneath the outer boundary of the media bodies. To examine the circulatory velocities, 2D velocity profiles using r-z surface colour plots of the bulk mill space bisected and averaged azimuthally are presented. Figure 7.14 show the 2D velocity profiles for the 1 379, 2 000 and 3 000 kg/m$^3$ densities. The media tangential velocity colour plots in Figure 7.14 are overlayed with black quiver plot of the axial and radial velocities. For all the slurry densities, the peak tangential velocity intensity is between the two pin layers towards the free surface. Circular flow is observed in the quivers for all densities around the two pin layers of the impeller band, with downward flow towards the walls and upward flow towards the vortex. However, for the slurry density of 2 000 kg/m$^3$ another circulatory field is observed to form above the top impeller, in the upper circuit region of the mill space. This is characterised by dominant downward flow right above the top impeller, near the vortex. This circulatory flow field is more developed at 3 000 kg/m$^3$. The increase in circulatory flow fields due to slurry density is captured by the CSPH_MPI DEM-SPH model and corresponds to the PEPT observations of Barley et al. (2004).

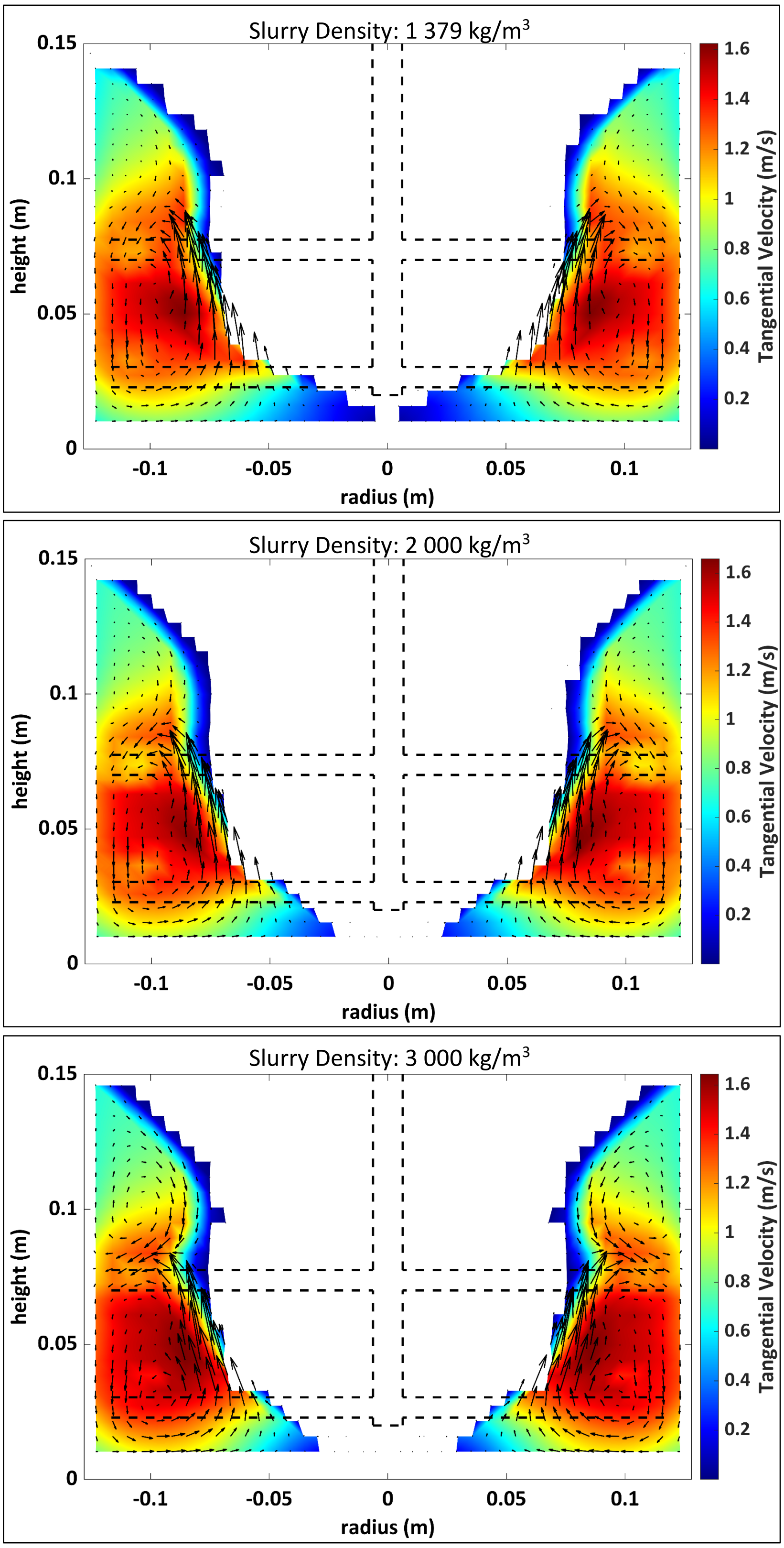

*Figure 7.14: Tangential velocity colour plots with axial and radial velocity quivers for 1 379, 2000 and 3 000 kg/m$^3$slurry densities*

Within the energy environment, the collision frequency spectra over collision energy are given in Figure 7.15. A decrease in the number of collisions at the peak collision energy with increase in slurry density was observed. The total number of collisions, represented by the area under the curve, decreases with increased slurry density. Notably, the decrease is observed in the media shell and media-media collisions. The modal peak energy dissipation rate and the corresponding collision energy are summarised in Figure 7.16. A decrease in both properties with increased slurry density was observed.

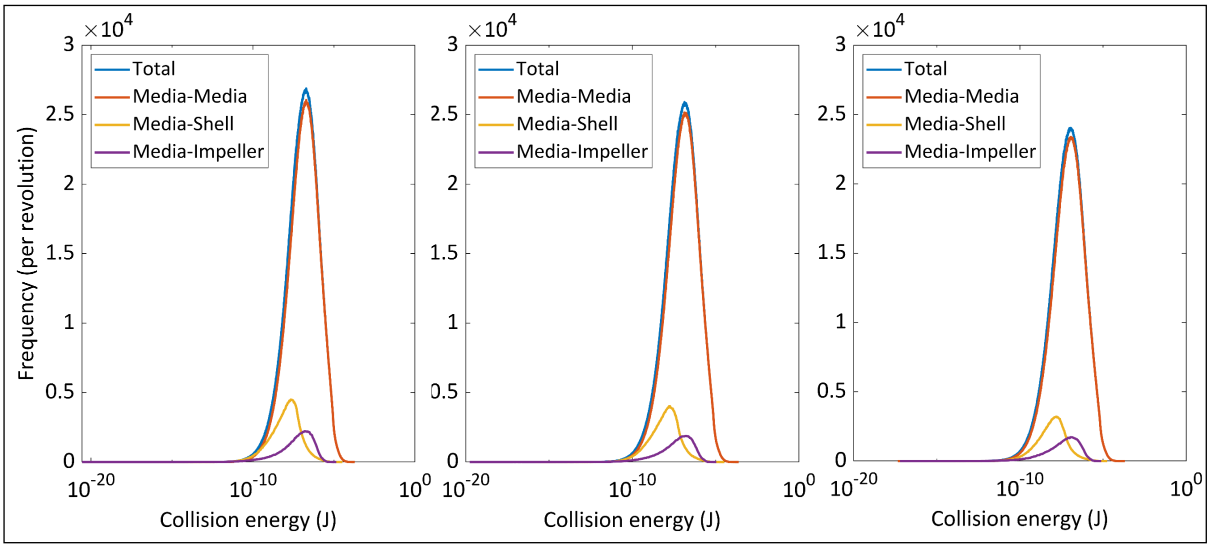

*Figure 7.15: Collision frequency spectra over collision energy for low, medium and high slurry density experiments, respectively*

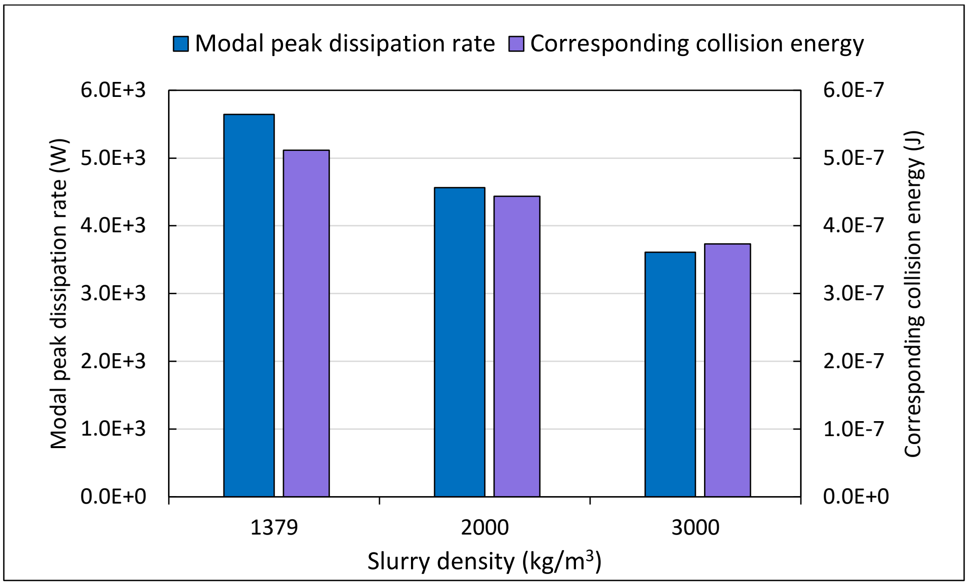

*Figure 7.16: Modal peak dissipation rate and corresponding collision energy for slurry density*

The power draw of the simulations was assessed through the average combined torque from the DEM media and the SPH fluid on the impeller. The total power draw and the average DEM contribution are shown in Figure 7.17. Average DEM power draw is also represented as a percentage of the total power draw within the figure. No significant change in the total power draw was observed between the slurry density of 1 379 kg/m$^3$ and 2 000 kg/m$^3$. However, the total power draw increased from 2.5×10$^3$ W to 3.0×10$^3$ W when the slurry density increased from 2 000 kg/m$^3$ to 3 000 kg/m$^3$. The DEM power draw component showed a decrease from 1.9×10$^3$

W to 1.5×10$^3$ W for the slurry density increase from 1 379 kg/m$^3$ to 2 000 kg/m$^3$. However, further increase in slurry density showed no significant change in DEM power draw. The percentage of the total power draw that is attributed to DEM decreases steadily with increasing slurry density. As the total power draw comprises of DEM and SPH contributions, this infers that the power draw from the SPH slurry increases with increasing slurry density. This is attributed to the increased slurry mass resulting in a greater resistance to the constant impeller motion as the slurry density increases.

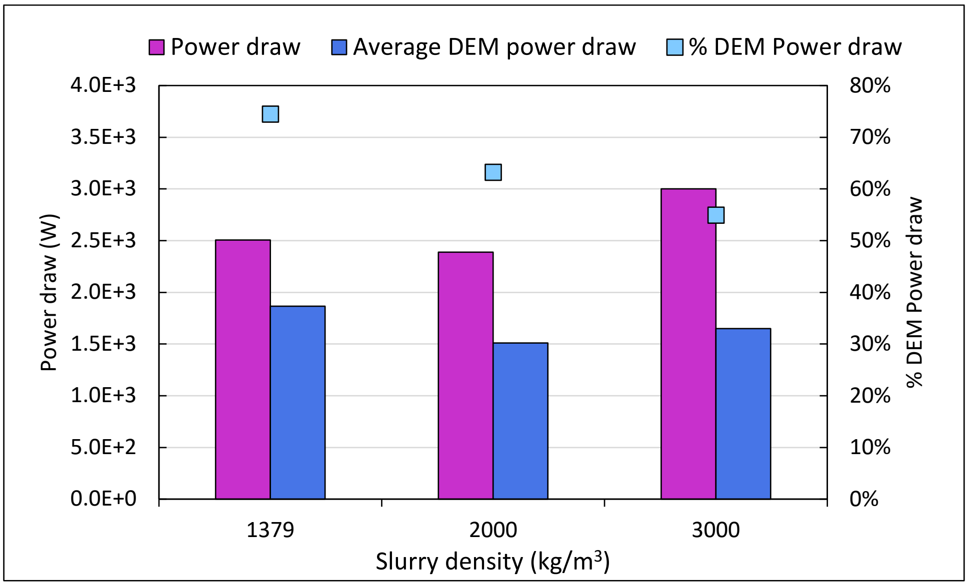

*Figure 7.17: Total power draw and average DEM power draw for the slurry density experiments*

## 7.5 Slurry viscosity

In the SPH slurry formulation, the apparent dynamic viscosity of the slurry is constant within the Newtonian model. The dynamic viscosity is a measurement of the internal resistance to flow of the slurry. The dynamic viscosity in literature on mineral slurry simulations ranged from 0.001 to 1 Pa·s. The slurry dynamic viscosity in Mill C was studied by performing simulations at three different values: 0.001, 0.01 and 0.1 Pa·s. The simulations were conducted using the physical and interaction parameters, and operating conditions specified in sections 6.3.2 and 6.3.3. Like previous parametric studies the mill was run at the speed of 300 rpm, the media fill 50% was used, and the slurry density was 1 379 kg/m$^3$. Still images of the simulated mill space are shown for each slurry viscosity in Figure 7.18.

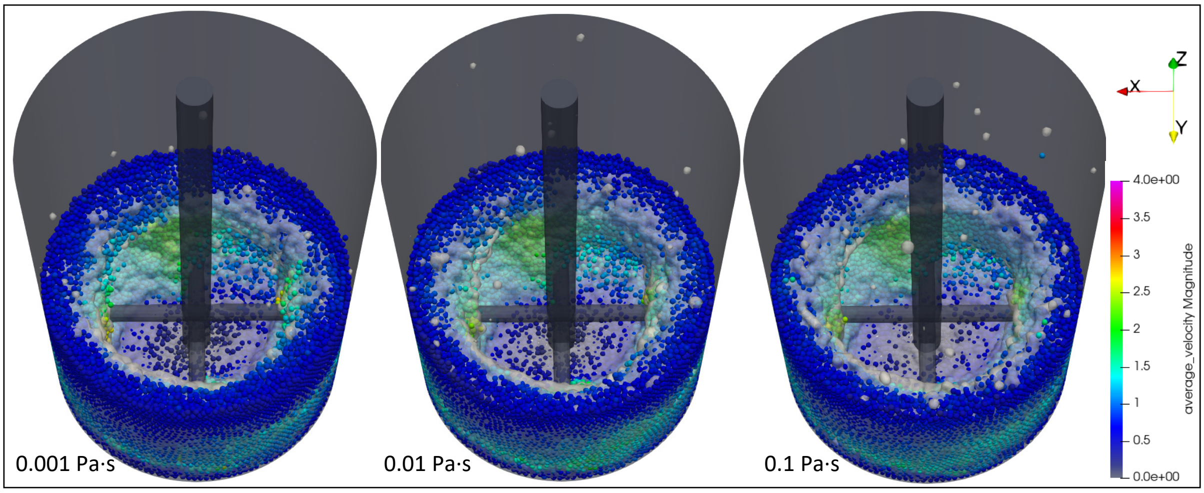

*Figure 7.18: Media velocity stills for the low, medium and high slurry viscosity experiments*

Studies on slurry viscosity on horizontal disk mills, using computational methods were conducted by Jayasundara et al. (2009), Sinnott, Cleary & Morrison (2009) and Cleary & Sinnott (2015). From the flow environment, they observed increased circulating media velocity flow fields in the r-θ plane with increasing viscosity. The increasing circulating velocities resulted in the general damping of flow in the axial direction noted in all the studies. This resulted in a decrease in the size of the central cavity surrounding the shaft. The effect of viscosity on the fluid pressure distribution showed that at low viscosities the fluid pressure was hydrostatic at equilibrium, with the weight of the slurry translating to the bottom of the mill, while at high viscosities, the fluid pressure was more evenly distributed throughout the mill. Within the energy environment, increases in the collision energy and the collision frequency, particularly the media-impeller collisions, were observed, with increasing viscosity (Jayasundara et al., 2009). This resulted in an increase in the power draw and impact energy.

From the stills in Figure 7.18, the increasing viscosity results in larger proportions of fluid pooling upwards, towards the central cavity. To determine the viscosity effect on the media flow patterns, the velocity was analysed in its three components of tangential, axial and radial velocity. This is relative to the coordinate system of the mill space, with the impeller shaft being the central axis and the coordinate plane as the mill base. The distributions of the three variables at each of the experimental conditions are summarised in box and whisker plots in Figure 7.19. The box consists of the median between the lower and upper quartiles, while the whiskers represent the minimum and maximum values, excluding outliers which are computed based on the interquartile range. The three viscosities studies exhibit similar distribution ranges for the tangential, axial, and radial velocity, respectively. Therefore, the slurry viscosity had no significant effect on the velocity descriptors assessed over the range studied.

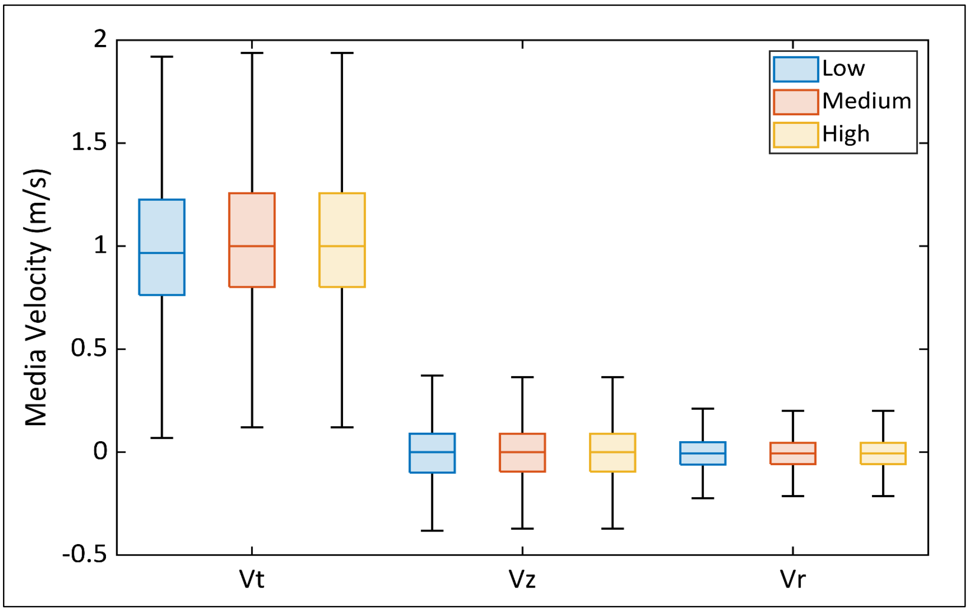

*Figure 7.19: Box and whisker plots of the tangential, axial and radial velocities the low, medium and high slurry viscosity simulations*

The fluid pressure distribution within the mill space was analysed. These results are shown in 2D r-z surfaces of the bulk mill space in Figure 7.20. The pressure is expected to be more evenly distributed throughout the bulk mill space with increasing viscosity. At 0.001 Pa·s, a more hydrostatic distribution is observed, with the highest pressures located at the bottom of the mill near the mill wall and decrease upwards and towards the central axis. At 0.01 Pa·s, the fluid pressure distribution is similar to 0.001 Pa·s, but with lower pressures observed at the central cavity and increased pressure in the upper circuits, stemming from the mill wall. At 0.1 Pa·s, the fluid pressure continues to increase along the tip of the impeller and reduce along the central cavity. The overall effect can be described as a slight evening of the fluid pressure distribution, within the mill space, with increasing slurry viscosity.

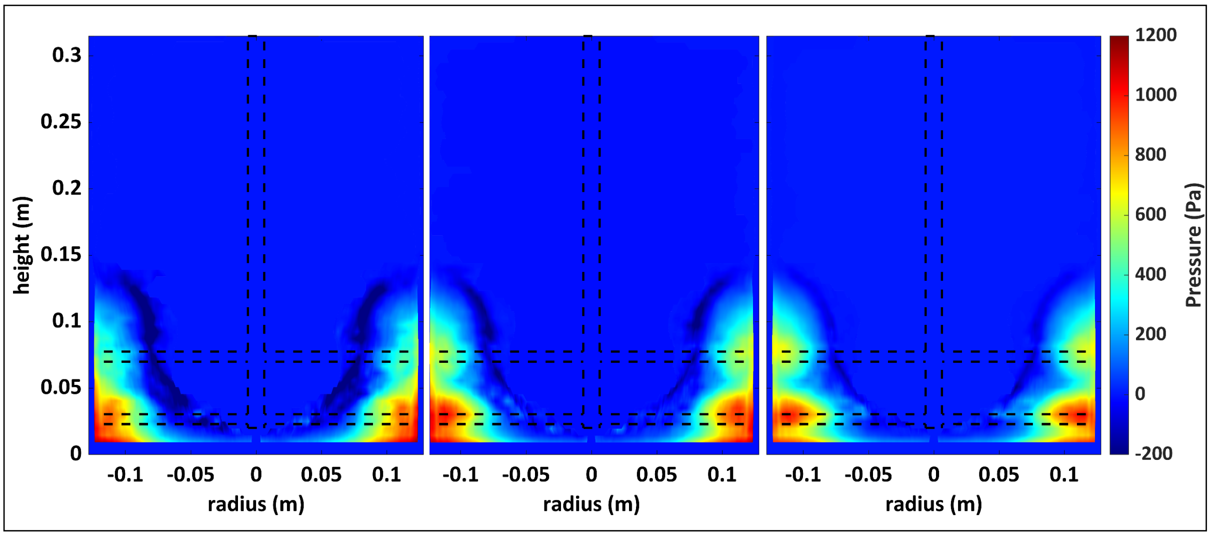

*Figure 7.20: Fluid pressure (Pa) for low, medium and high slurry viscosity experiments, respectively*

The analysis of collision frequency of each mill space is shown in Figure 7.21. The peak frequency of the collisions, and hence the total number of collisions per revolution, is observed to decrease with increased viscosity. The decrease is not significant from 0.001 to 0.01 Pa·s, but observed from 0.01 to 0.1 Pa·s. This trend is visible in the media-media and media-shell collisions, though no significant difference is observed within the media-impeller collisions.

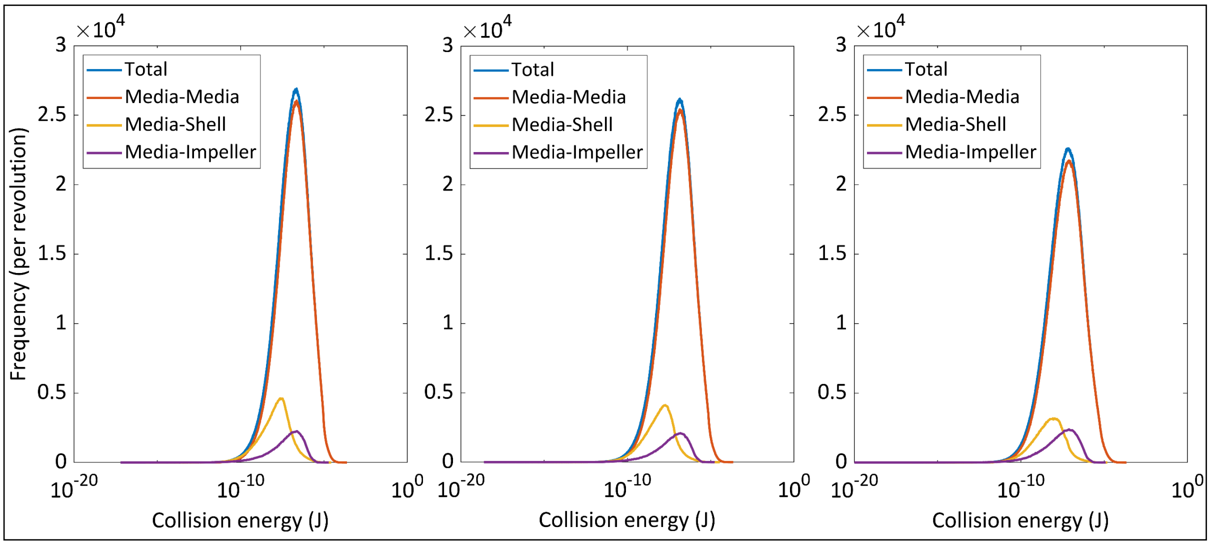

*Figure 7.21: Collision frequency spectra over collision energy for low, medium and high slurry viscosity experiments, respectively*

The analysis on the energy dissipation rate spectra over collision energy are summarised in Figure 7.22. The modal peak energy dissipation rate and the corresponding collision energy show a decreasing trend with increasing viscosity. The difference in collision energy from 0.001 to 0.01 Pa·s was 0.25×10$^{-7}$ W, which was smaller than the observed change from 0.01 to 0.1 Pa·s of 2.05×10$^{-7}$ W. The modal peak dissipation rate decreases steadily from 6.1×10$^{3}$ W at 0.001 Pa·s to 4.7×10$^{3}$ W at 0.01 Pa·s and 2.9×10$^{3}$ W at 0.1 Pa·s. The higher slurry viscosities dampen the media collision energies and their dissipation rate.

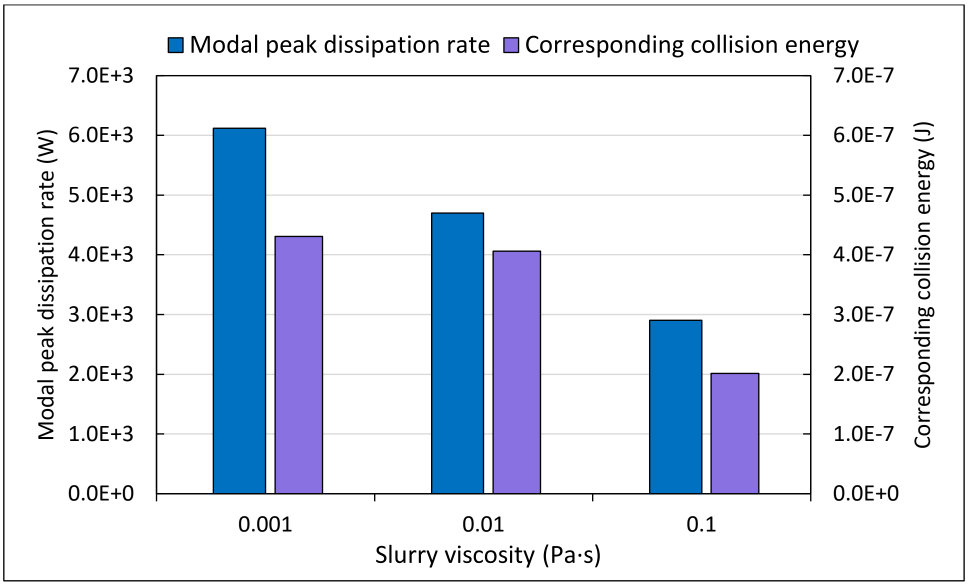

*Figure 7.22: Modal peak dissipation rate and corresponding collision energy for the slurry viscosity experiments*

The power draw was studied by segmenting it into the total power draw and its average DEM component in Figure 7.23. The percentage of the DEM component is presented in Figure 7.23 in the form of a data point. The overall power draw and its DEM component show minimal variation with changes in viscosity.

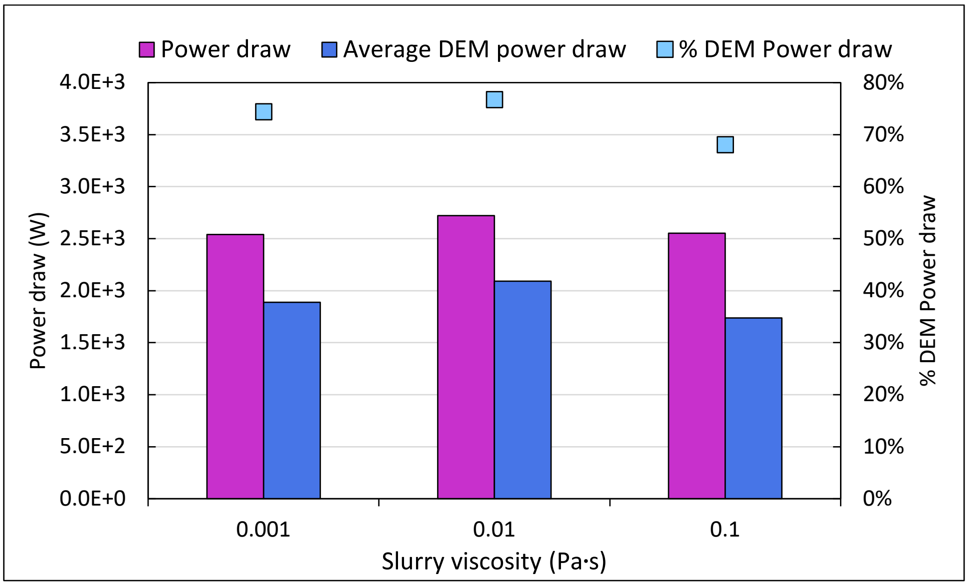

*Figure 7.23: Total power draw and average DEM power draw for the slurry viscosity experiments*

## 7.6 Media fill

The media fill in this study refers to the percentage of the total fill volume occupied by media, with the slurry accounting for the remaining fill volume. The total fill volume in the laboratory SMDs is set at a fill height to the top of the top impeller pin. This is kept constant throughout the simulations. The media fill was simulated at three different levels: 40%, 50% and 60%. Note that the remaining fill volume of fluid is defined at initial conditions, before the influence of the hydrostatic pressure gradient and the fluid equation of state. The simulations were conducted using the physical and interaction parameters, and operating conditions specified in sections 6.3.2 and 6.3.3. A rotational speed of 300 rpm, media density of 2 700 kg/m$^3$ and the slurry density of 1 379 kg/m$^3$ were used for these simulations. Still images of the simulated mill space are shown for each media size in Figure 7.24.

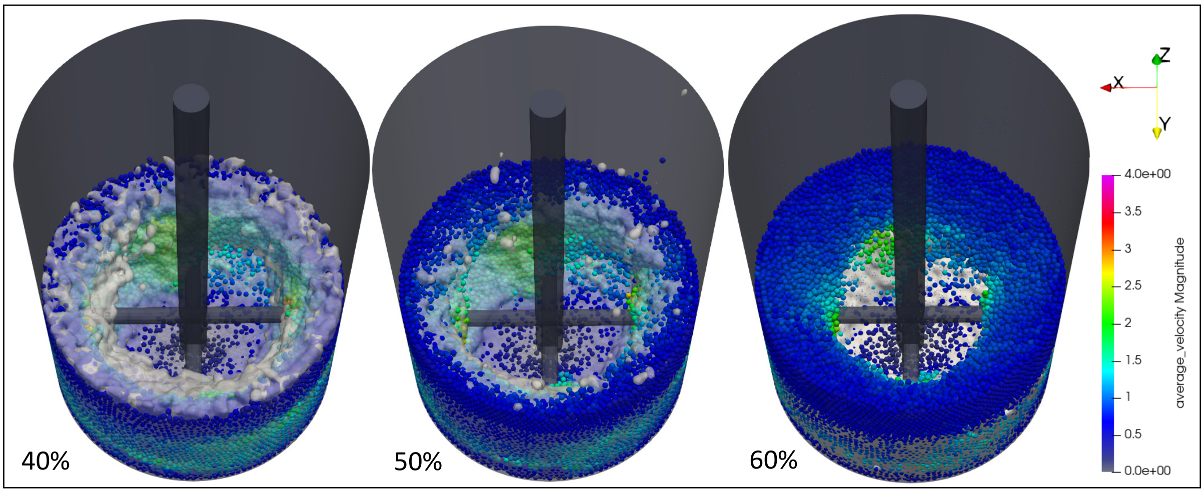

*Figure 7.24: Stills of the mill space for low, medium and high media fill experiments*

The effect of the media fill in wet SMD type mills has not been reported directly in computational literature. However, it can be inferred from computational studies on the mill fill level in dry systems and experimental work on the media fill level. The effect of solids fill level was investigated in Yang et al. (2006), Jayasundara et al. (2010) and Cleary, Sinnott & Pereira (2015) on dry horizontal disk mills. Higher speeds of media bodies near the impeller tips were observed and attributed to the increased packing. Within the energy environment, the power draw was observed to increase exponentially, while the total impact energy increased to a plateau with increasing fill level. These observations were indicative of a decrease in the proportion of the power drawn that contributes to grinding at higher fill levels. Zheng, Harris & Somasundaran (1996) determined that the most energy effective grinding in wet stirred mill systems occurred when the media voids were just filled with slurry, but did not show any parametric study results.

The simulation results show how the phase distribution within the mill space responds to an excess volume of either media or slurry and how this influences the frequency and energy of collisions and the system power draw. The bulk solids fraction at each of the media fill levels is shown through r-z surface projections in Figure 7.25. The distribution between the phases appears to become more even radially towards the edge of the vortex as the proportion of media increases. This results in a decrease in the bulk height of the media bed observed in the bulk solids fraction spatial distributions of Figure 7.25.

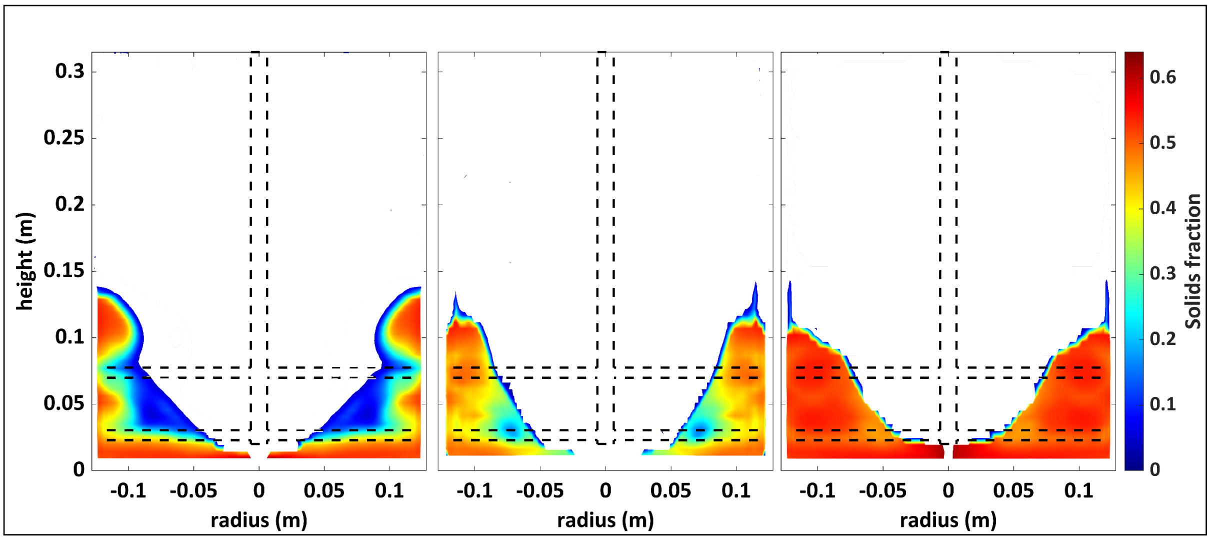

*Figure 7.25: Bulk solid fraction of 40%, 50% and 60% media fill simulations, respectively*

The collision frequency spectra over collision energy for the different ratios are shown in Figure 7.26. The spectra show an increase in the total number of collisions, particularly the media-media collisions with increase in the media fraction in the charge.

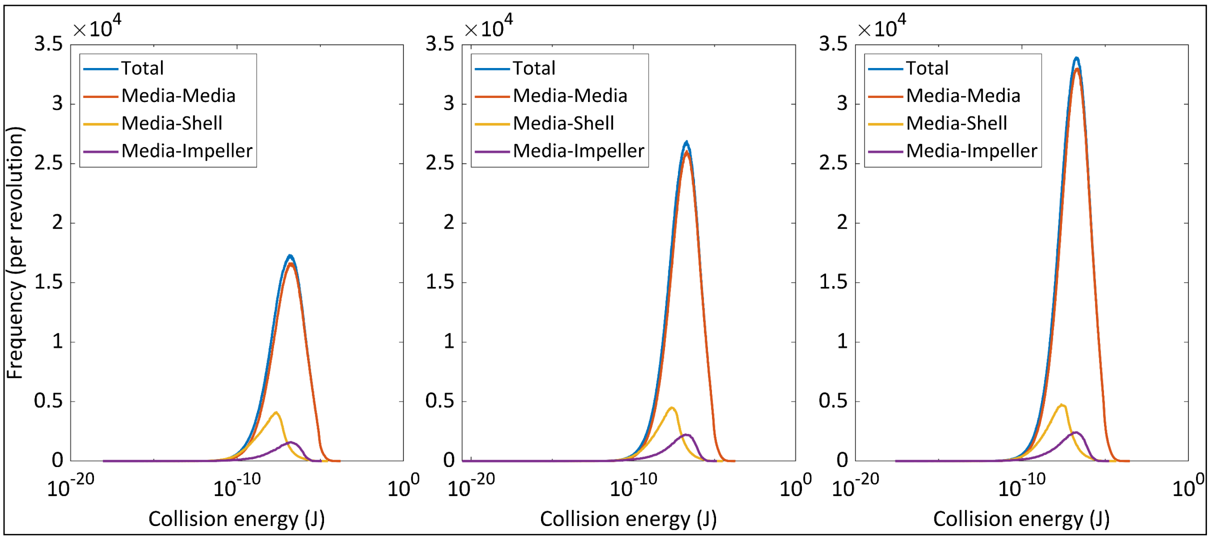

*Figure 7.26: Collision frequency spectra over collision energy 40%, 50% and 60% media fill simulations, respectively*

The energy dissipation rate spectra over collision energy for the simulations are characterised through the modal peak energy dissipation rate and its corresponding collision energy. These values are compared in Figure 7.27 in their intensive form, divided by the volume of slurry. This was done to evaluate the mill performance per unit fluid volume across the media fill simulations. The raw energy figure is provided in Figure E.6 in Appendix E.2. Both properties increase with increasing ratio of media to slurry encountered as the media fill is increased, though the rate of the increase in the collision energy dampens with increasing solids fraction in charge while the peak dissipation rate appears more linear.

The total power draw and its average DEM proportion are presented in Figure 7.28 per unit volume of fluid. The trend of the total power draw increases from 40% to 50% media fill but shows no significant changes from 50% to 60% media fill. This is echoed in the trend of the DEM power draw. The average proportion of the power draw that results from the DEM bodies increases, at a decreasing rate, with increasing ratio and media proportion. The raw power draw is shown in Figure E.7 in Appendix E.2.

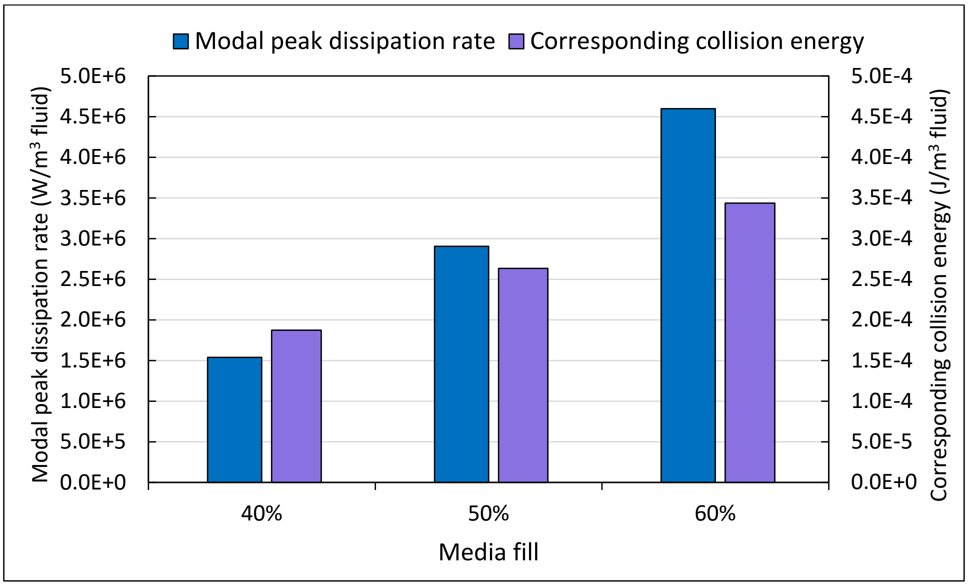

*Figure 7.27: Modal peak dissipation rate and collision energy for the media fill simulations*

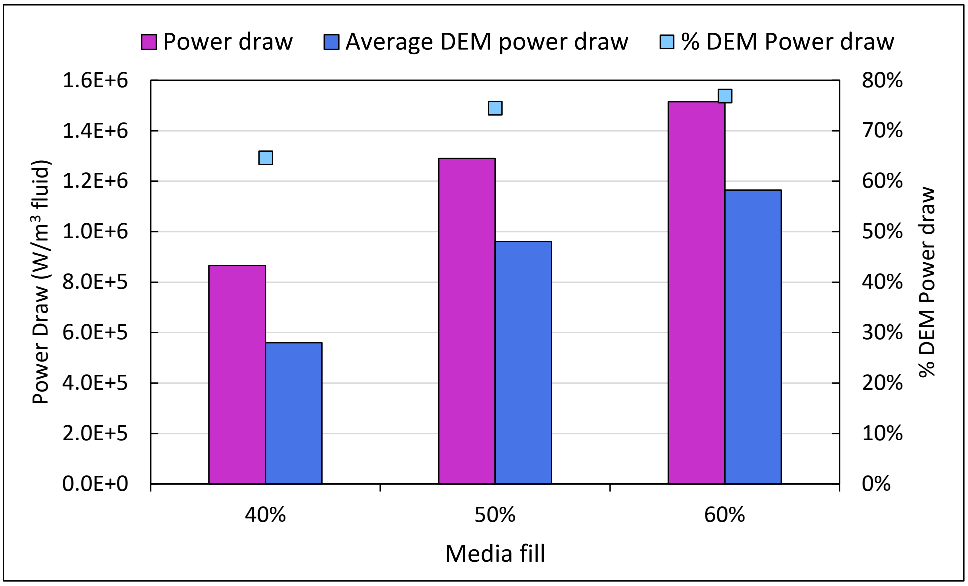

*Figure 7.28: Total power draw and average DEM power draw for the media fill simulations*

## 7.7 Summary of performance assessment results

Five parametric studies were conducted on the media size, media density, slurry density, slurry viscosity and media fill, separately. These studies varied the parameter at three levels in DEM-SPH simulations of the largest laboratory scale SMD, Mill C. The results obtained were compared to what has been reported in literature to evaluate the performance of the two-way coupled model used in this study. The findings of each study are summarised as follows:

- The media size simulations showed increases in the collision energy and power draw with increasing media size. This showed agreement with the observations in Jayasundara, Yang & Yu (2012) and Cleary, Sinnott & Pereira (2015), which noted similar increases in collision energy and power draw for media below 15 mm.
- The media density was simulated at two impeller speeds (300 rpm and 700 rpm) in attempt to ensure that the media was fluidised in the system. Both sets of results showed overall decreases in the power draw, and collision frequency and energy, with increases in media density. This contradicts the observations of Jayasundara et al. (2008), who tested densities ranging from 1 000 to 6 000 kg/m$^3$ in a dry horizontal disk mill at 1 000 rpm.
- With increasing slurry density, the simulations showed increased circulatory velocities in the r-z plane, decreasing collision energy and an overall increase in the power draw. These effects are in agreement with the observations of increased r-z circulatory velocities in Jayasundara et al. (2009). The SPH proportion of the power draw increased steadily with increased slurry density.
- The slurry viscosity results showed no significant changes in the velocity distributions and hence no visible changes in the r-θ circulatory flow fields. However, the results did show evening out of the fluid pressure distribution with increasing viscosity, in agreement with the findings of Cleary & Sinnott (2015). An overall decrease in the collision frequency and energy was observed, which disagrees with the findings of Jayasundara et al. (2009). This study operated at a higher tip speed (1 000 rpm) and tested viscosities ranging from 0.001 - 0.5 Pa·s in a horizontal disk mill.
- The media fill study showed overall increases in the collision energy and power draw, particularly the DEM proportion of the power draw, with increasing media proportion. These trends are in agreement with dry simulation results varying the mill fill level in Yang et al. (2006), Jayasundara et al. (2010) and Cleary, Sinnott & Pereira (2015), which all observed increased power draw with increased media fill.

Across the parameters investigated, the media size, slurry density and media fill showed good agreement with literature studies. The media density and slurry viscosity results had discrepancies in the energy environment comparisons against computational studies performed on horizontal disk mills at a higher speed. This disagreement can be attributed to multiple factors such as the mill speed and impeller configuration, but more studies on vertical stirred media mills is required.

# CHAPTER 8

# Results and discussion: Scale-up tip speed simulations

## 8.1 Introduction

This chapter contains the discussion focusing on comparison of simulation outputs from the three mill sizes at the same tip speeds of 1.5, 1.8 and 2.2 m/s. The simulation parameters for this set of test work are described in section 6.7.2.1. Nine (9) simulations were performed using the simultaneous two-way coupled DEM-SPH framework, CSPH_MPI, to generate sets of data to use in comparing three laboratory scale SMDs. An additional three simulations of the three scales at 2.2 m/s were performed in a dry DEM system.

The aim of performing these simulations is to provide an understanding of how the flow and energy distributions within the mill space change with radial expansion and to evaluate the use of single-value parameters to comparatively represent the bulk mill state. This is done through analysing relevant bulk dimensionless quantities, for the flow environment, and assessing the intensive energy spectra of the energy environment.

The results are presented in three sections. The first section focuses on the flow environment in the mill. This deals with information extracted through the velocity data analysis protocol. The second section is considered the energy environment of the mill, and uses information extracted through the contact data analysis protocol. Dimensionless numbers and intensive quantities are examined from the findings of these sections to assess scale up effects in the final section.

## 8.2 Flow environment

The flow environment focuses on the motion of media and slurry within the mill space. Stills providing a 3D rendering of the mill space for the nine simulations are shown in Figure 8.1. The stills show the media coloured by its velocity and the fluid at 60 % opacity. The results for the flow environment are analysed in three parts. The first part discusses the distribution of the two phases, media and slurry, within the mill space. This is done to establish where each phase is located relative to the other, and to visualise the degree of fluidisation experienced in each mill scale at each tip speed.

The second part discusses the velocity distributions of the media and slurry. A combination of velocity colour maps and profiles segmented in the tangential, radial and axial components within the mill coordinate system are presented. These are used to establish regions of high velocity within the mill space, as well as the degree of circulation through velocity component distributions within the mill space.

The final part combines the information on the phase and velocity distributions to determine the dimensionless groups of Reynolds number and Froude number within the bulk flow. The variations within these dimensionless quantities, examined through spatial distributions and measures of central tendency, are indicative of the balance of forces within the mill space.

### 8.2.1 Phase distributions

The distribution of the media and slurry in all 9 DEM-SPH simulations was examined and 2D spatial profiles of the solids fraction are given in Figure 8.2 and the relative density of the fluid in Figure 8.3. The profiles show variable colour plots of the mill space azimuthally averaged into two (r-z) surfaces, using methods explained in section 6.5.4. The warmer red colours represent high solid fraction and relative density regions while the cooler blue colours represent low regions for each variable, respectively. The colour maps presented comprise of averaged data from 5 revolutions. The bulk free surface shown is a function of the mill occupancy and the lower limit of the variable, given in Appendix D.8. The mill space is radially normalized for ease of comparison, due to the constant mill radius to impeller radius ratio across all mill sizes. The results displayed are for the 3 mill sizes at the 3 tip speeds, to allow visual comparison across the rows and columns. The same colour axis is used across each of the variables, for all nine plots.

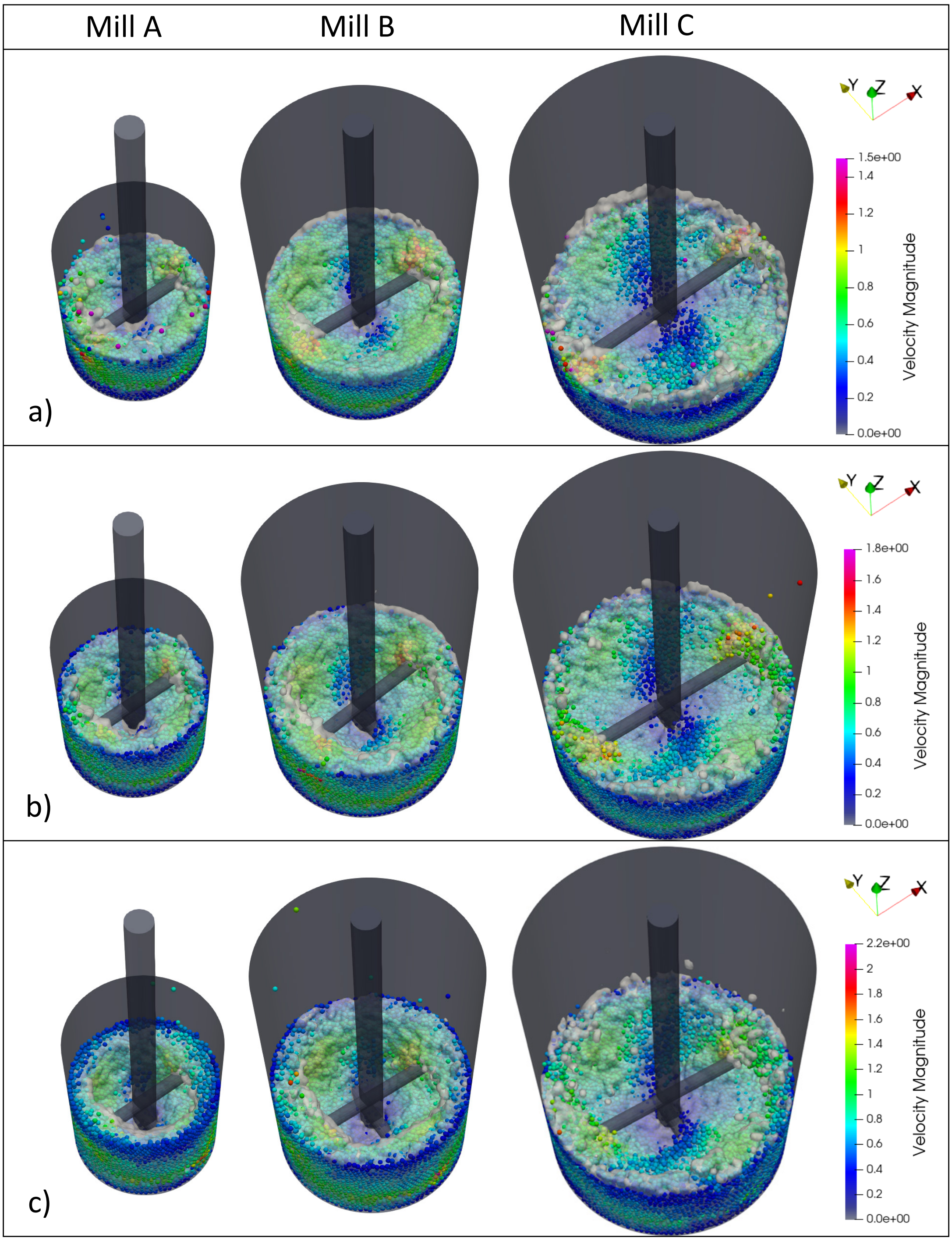

*Figure 8.1: Snapshots of the 3D mill space, with a velocity colour plot for the media and fluid for all three mill sizes at a) 1.5 m/s, b) 1.8 m/s and c) 2.2 m/s tip speeds*

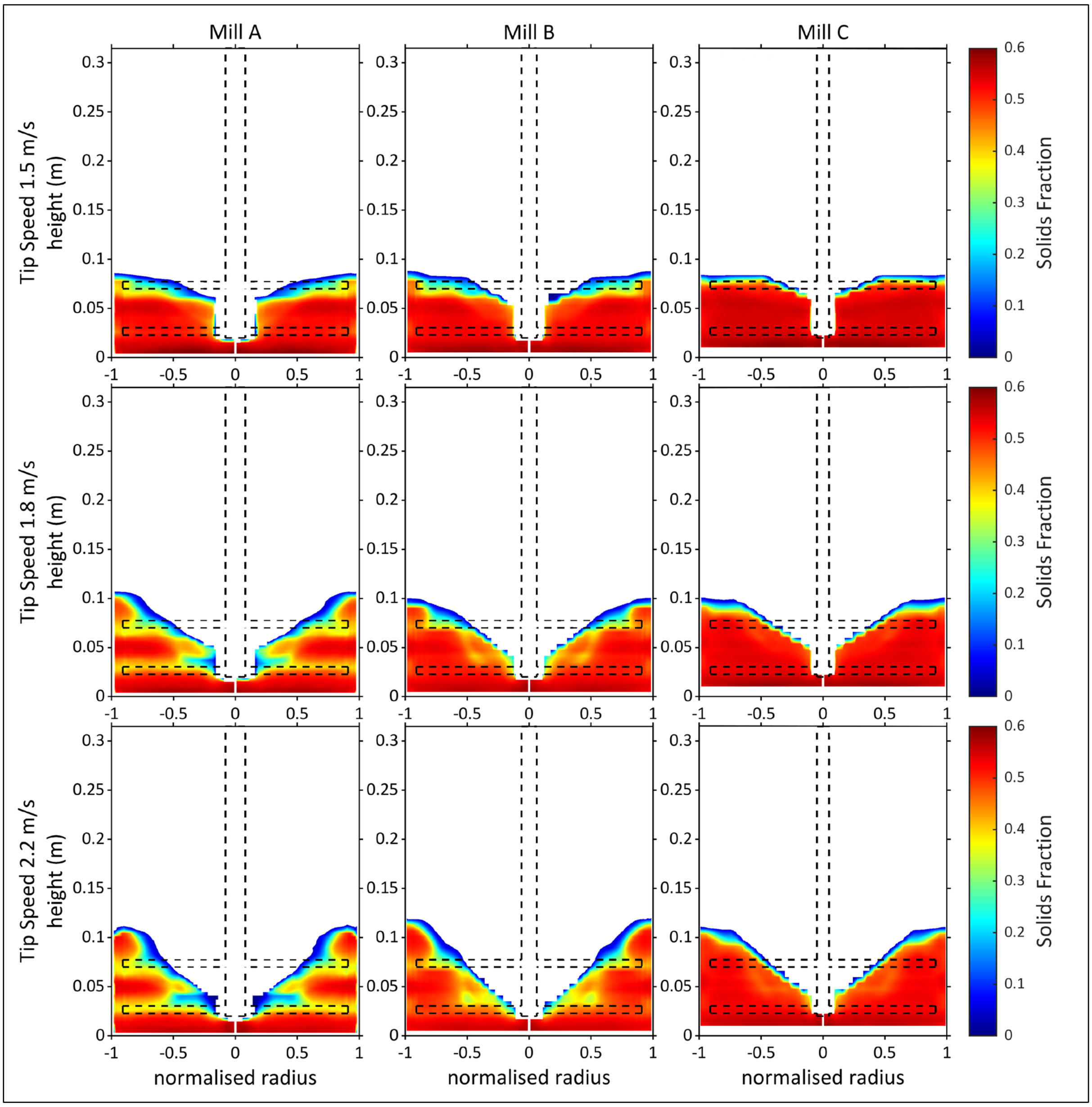

*Figure 8.2: Colourmaps of the bulk solids fraction at each scale of simulated mill system at tip speeds of 1.5, 1.8 and 2.2 m/s, normalised along the radial axis*

The solids fraction and relative density are both SPH properties, extracted from the fluid velocity data. The solids fraction is determined from the fluid particle specific interaction variable of porosity and ranges between 0 to 1. The typical solids fraction observed in a packed bed of mono-size spherical particles is 0.6, with the maximum solids fraction for a random close packing of mono-size spherical particles being 0.64 (Wu, Fan & Lu, 2003). The relative density is the kernel weighted density of the fluid particle relative to the rest density, therefore because the fluid itself is slightly compressible this value can exceed 1, due to variability in the fluid pressure. Figure 8.2 and Figure 8.3 show the average spatial distribution of the solids fraction and relative density, respectively, within the mill space.

The solids fraction spatial distributions (Figure 8.2) across mill sizes at 1.5 m/s have a shape consistent with the 2D projections from the DEM-only simulation on a pin mill at a low speed by Daraio et al. (2020), shown in Figure 3.6. However, as the tip speed increases, the shape of bed, particularly Mill A at 2.2 m/s, bears more similarity with the 2D slice of the industrial SMD, simulated using DEM-SPH by Ndimande et al. (2019) shown in Figure 3.9, than the pin mill at a higher speed in Figure 6.18. The change in shape of the bulk mill environment occurs as a result of increased tip speed. Increased rotation around the impeller shaft results in the formation of a vortex at the free surface of the mill, centred around the impeller shaft. Starting from a stationary mill, where the material is filled to the height of the top impeller pin, as the rotational speed of the impeller increases, material vacates from the centre, where the rotation is fastest to pool in the wake of the tips of the impeller pins. This effect creates a vortex at the free surface. The vortex deepens in response to increased rotational speed and dilation of the mill bed. Dilation within the mill bed is characterized by regions of decreased solids concentration.

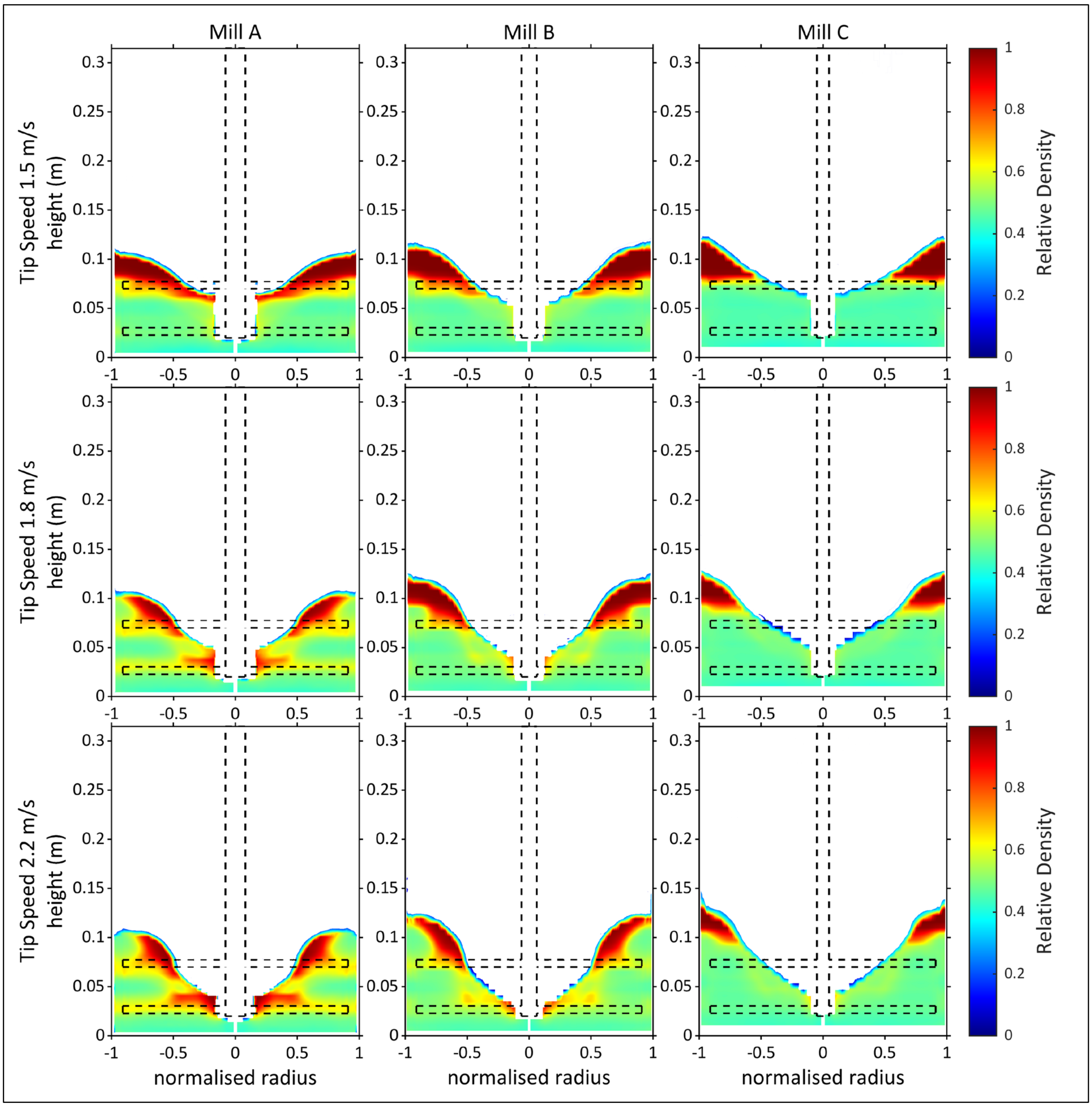

*Figure 8.3: Colourmaps of the bulk relative density at each scale of simulated mill system at tip speeds of 1.5, 1.8 and 2.2 m/s, normalised along the radial axis*

Figure 8.2 shows visible axial dilation along the lower impeller pin in at 1.5 m/s for the Mill A and Mill B colourmaps, indicated by the decrease in the intensity of the red colouring of the bulk regions to the area along the pin. At 1.8 m/s, Mill A is observed to dilate significantly along the lower impeller pin, with the colour intensity of the region decreasing to yellow, ahead of Mills B which is still only slightly dilated. At 2.2 m/s, Mill B begins to dilate more around the lower impeller pin, while the degree of dilation of Mill A extends further as the intensity of the yellow colouring increases. As the tip speed increases from 1.5 m/s to 2.2 m/s, only slight dilation occurs for Mill C, visible as a decrease in the intensity of red colouring, primarily along the bottom impeller and then within the bulk mill space.

The relative density plots in Figure 8.3 provide a more definitive indication of the overall bed height and the shape of the central cavity compared to the solids fraction plots. This is due to the relative density variable having a closer association to the bulk free surface, as its value maximizes at the free surface unlike the solids fraction, which minimises. The observed trend with the bed height from Figure 8.3 is that it increases with the mill size and tip speed, this corresponds with the deepening of the central cavity. The central cavity increases in size across all three mill sizes with increased tip speed. This was observed in the horizontal disk mill simulated in Yang et al. (2006) and attributed to the increased compressive forces in the mill space with increased tip speed. At 1.5 m/s, the central cavity of each mill is only as deep as to expose the bottom of the top impeller pin. The mills all have a predominant layer of fluid towards the free surface due to its lower density than the media. This is the region with a deep red intensity in Figure 8.3. The bed height is observed to increase with the mill size. At 1.8 m/s the central cavity of each mill has deepened to expose the shaft in between the impeller layers and the height of the media bed has increased, while a decrease in the size of the fluid layer towards the free surface is noted. The fluid layer is observed to drain inward towards the mill centre as the height of media increases at the mill wall. At 2.2 m/s, further increases in the depth of the central cavity and the height of the media bed are observed, with the cavity of Mill A and Mill B deepening to expose the top of the bottom impeller pin. Further decrease in the size of the dominant fluid area towards the free surface is noted at 2.2 m/s for all mill sizes.

The flow environment within a fluidized grinding stirred mill exists in 1 of 3 states: pre-fluidisation, fluidisation or post-fluidisation (Conway-Baker et al., 2002; Jayasundara et al., 2010). Figure 8.2 and Figure 8.3 can be used to assess the fluidisation state within the mills. The transition from pre-fluidisation into fluidisation can be assessed for these systems using the observations of the dilation axially along of lower impeller pin, increases in the height of the media bed, and deepening of the central vortex. Considering all the observations on the dilation of around the lower impeller pin, the depth of the central cavity and the height of the media bed, the following evaluations on the overall fluidisation state of the mills can be made. At 1.5 m/s, all the mills are observed in a pre-fluidisation state, with only slight dilation observed at the lower pin and a shallow central cavity. At 1.8 m/s, Mill A is observed to enter into fluidisation, characterised by the combined increases in the lower pin dilation and depth of the cavity and the decrease in the fluid layer at the free surface. Mills B and C are still pre-fluidisation, with no significant dilation. At 2.2 m/s, Mill B is in the early stages of fluidisation, as more significant dilation along the lower pin is observed, but it is still less than Mill A at 1.8 m/s. Mill C is still pre-fluidisation, with no significant dilation observed. The transition into a post fluidisation state is challenging to define as Mill A at 2.2 m/s meets the fluidisation criteria, but is observed to be ‘more’ fluidised than at 1.8 m/s. Post-fluidisation is determined through evaluating the energy efficiency of the system and its ability to convert the energy input from the impeller tip speed into effective collisions (Jayasundara et al., 2010). The ability of the dimensionless quantities to evaluate the fluidisation state of a mill from its flow characteristics, relative to its tip speed and comparative to other scales is assessed in section 7.2.3. Using the spatial distributions of the solids fraction and relative density as indicators of the fluidisation state, it can be observed that the degree of fluidisation of the bed is proportional to the tip speed. It is noted that as the mills radially expand in size, the effect of the tip speed on the fluidisation state is dampened.

Figure 8.4 shows box and whisker plots of the distribution of the solids fraction data taken from all the fluid particles, recorded at 0.01 s intervals for 5 revolutions. This is used to evaluate the effectiveness of defining the porosity, and hence solid fraction, as a fluid particle specific variable. The box consists of the median between the lower and upper quartiles, while the whiskers represent the minimum and maximum values, excluding outliers which are displayed as points outside the whiskers, and computed based on the interquartile range. All of the distributions maintain a negative skew, with median values ranging from 0.48-0.53. The boxes of Mill A and B show the lower quartiles increase as the tip speed increases. This shows that larger proportions of fluid particles are interacting with media. The distributions of Mill C however show the lower quartile decreasing, with a large proportion of outliers at the low solids fraction end of the distribution. The range of outlier decreases as the tip speed increases. This effect occurs because Mill C has a large proportion of fluid pooling at the free surface, not interacting with media, creating a secondary peak in the distribution that outlies the larger peak of the distribution at high solids fractions. Therefore, the decrease in the outlier range with increase tip speed indicates that the fluid pool is being incorporated into the bulk mill space. The solids fraction of any fluid particle is capped at 0.62, this does not exceed the random packing fraction of 0.64. This individual particle solids fraction data of Figure 8.4 is spatially averaged into the profiles of Figure 8.2, which shows the average solids fraction in the bulk of each mill system.

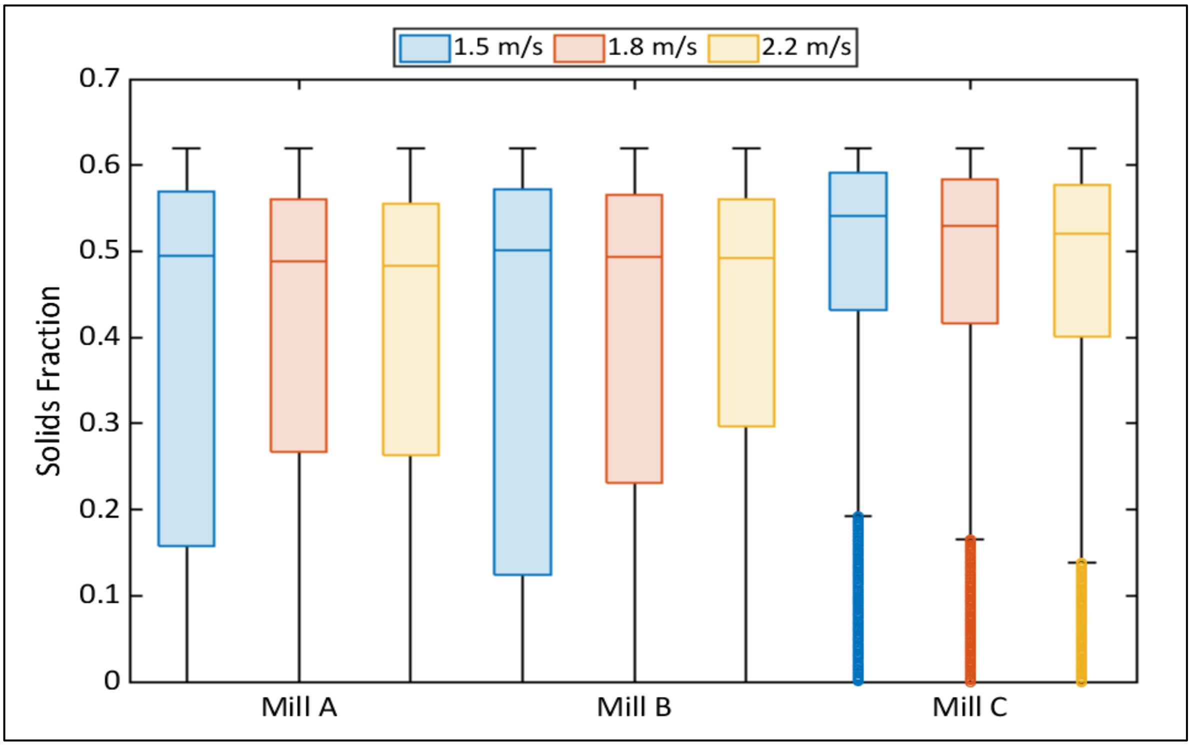

*Figure 8.4: Box and whisker plots of solids fraction within each scale of simulated mill system at tip speeds of 1.5, 1.8 and 2.2 m/s*

### 8.2.2 Velocity distributions

The media velocity is analysed in terms of magnitude through colour plots followed by tangential component profile plots and axial and radial component segmented colour plots. The four methods provide an analysis of the motion of media in the mill. The motion of the fluid is assessed through its magnitude in colour plots. The motion of the media has been given more attention than the fluid because collisions of these bodies are responsible for the energy dissipation that results in the breakage of ore.

The media and fluid velocity magnitudes are shown in Figure 8.5 and Figure 8.6, respectively. The figures provide radially normalised 2D r-z colour plots of the bulk mill space. The hot colours represent high velocities, and the cold colours represent low velocity regions. The bulk media and fluid velocities are extracted from the media and fluid velocity datasets, respectively.

Considering the media velocity plots in Figure 8.5, high velocity events occur in the region between the lower and upper impeller pins towards the mill wall. Lower speed events are observed mainly in the regions near the free surface, and the area directly below the central shaft at the bottom of the mill. Looking at Mill C, the high velocity events are most intense around the top impeller pin and spread lowers towards the bottom pin with increasing with tip speed, but does not fully reach the intensity around the bottom pin visualized in Mills A and B. The observation of the high velocity zones not encompassing all the impeller pins is visible in the media velocity 2D projection from the DEM-only simulation on a pin mill at a low speed by Daraio et al. (2020) in Figure 3.6.

The bulk fluid velocity maps in Figure 8.6 differ from the media velocity plots, in that the areas covered by high velocity events extend significantly above the top pin into the top fluid layer observed in the phase distributions (Figure 8.3). The regions of high velocity events within Mill A and B have a similar shape of two high intensity regions centred along each pin length. The region around the top pin is more intense than the lower region and the separation between the two regions becomes less visible as the tip speed increases. The concentration of high velocity events for Mill C is unique in that it is limited to the region above the top pin that extends downwards with increasing tip speed, but never reaches the bottom pin. This correlates with the bulk media velocity and solids fraction data, which show that Mill C is in a pre-fluidized state at each tip speed, characterized by high solids fraction around the bottom impeller.

Comparatively across mill sizes, the high velocity regions of the media and fluid are coloured at similar intensities for Mill A and Mill B and least intense for Mill C, with the fluid achieving higher bulk velocities than the media. The similarity of Mill A and Mill B velocity distributions was unexpected as high velocities were expected to more easily propagate in bulk of Mill A due to the shorter arc lengths media bodies and fluid particles must travel between the impeller arms, allowing the impeller wake to reach higher velocities in the bulk. This similarity could be attributed to the effect of the gap between the mill wall and impeller tip. When scaling the impeller pin lengths of the mill sizes, it was ensured that the gap was large enough to fit at least one media particle, but because the media size is consistent throughout the mills the effect of the gap on the particle flow pattern around the impeller could influence the high velocity intensity of Mill B, as proportionately more particles are able to pass through the gap and influence the flow in the region between the two impellers. Though the influence of impeller pin lengths on the flow pattern was studied by Daraio et al. (2020), the study did not consider the limitations around increasing the length and closing the gap between the pin tip and the impeller wall.

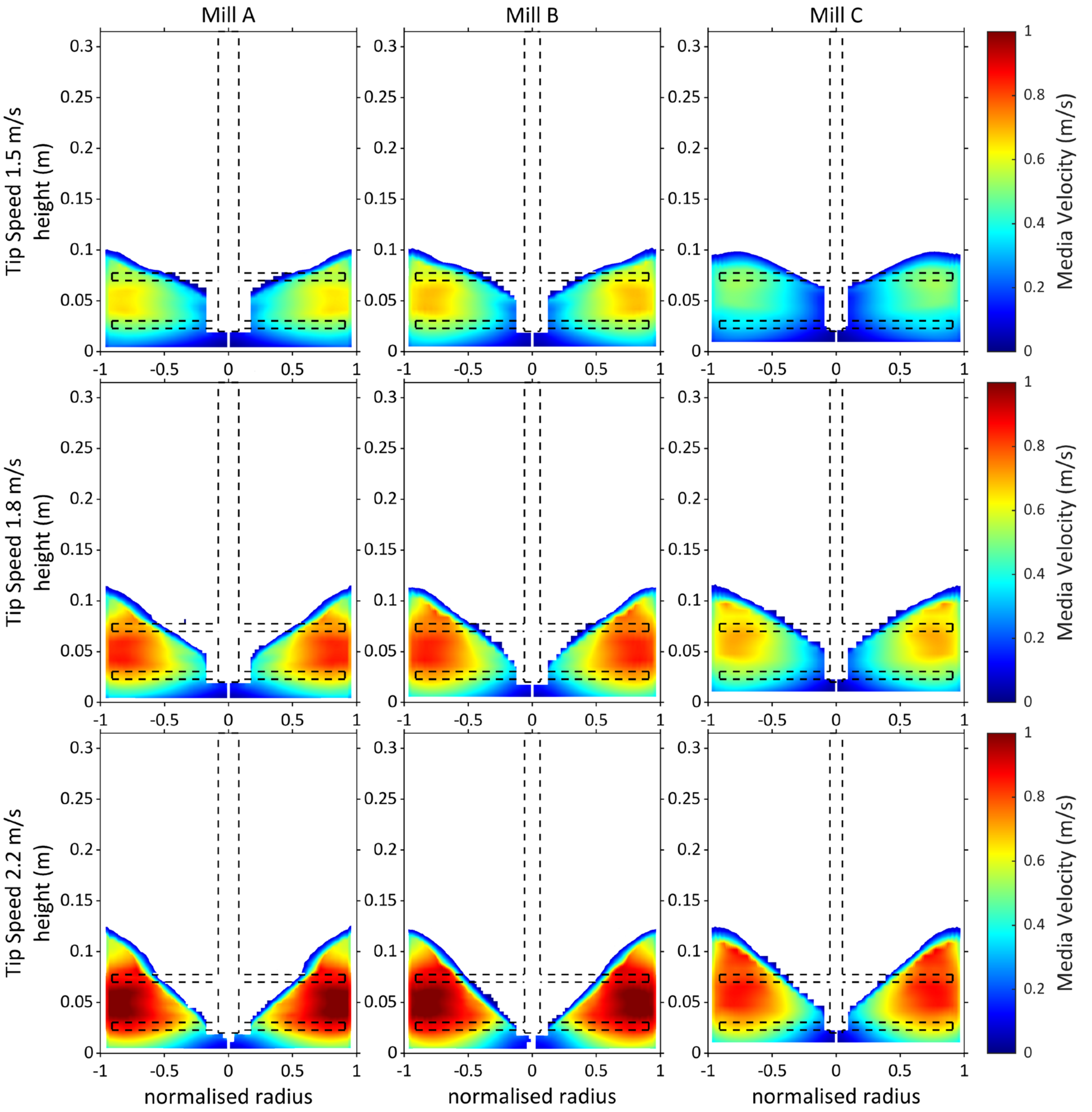

*Figure 8.5: Colourmaps of the bulk media velocity (m/s) at each scale of simulated mill system at tip speeds of 1.5, 1.8 and 2.2 m/s, normalised along the radial axis*

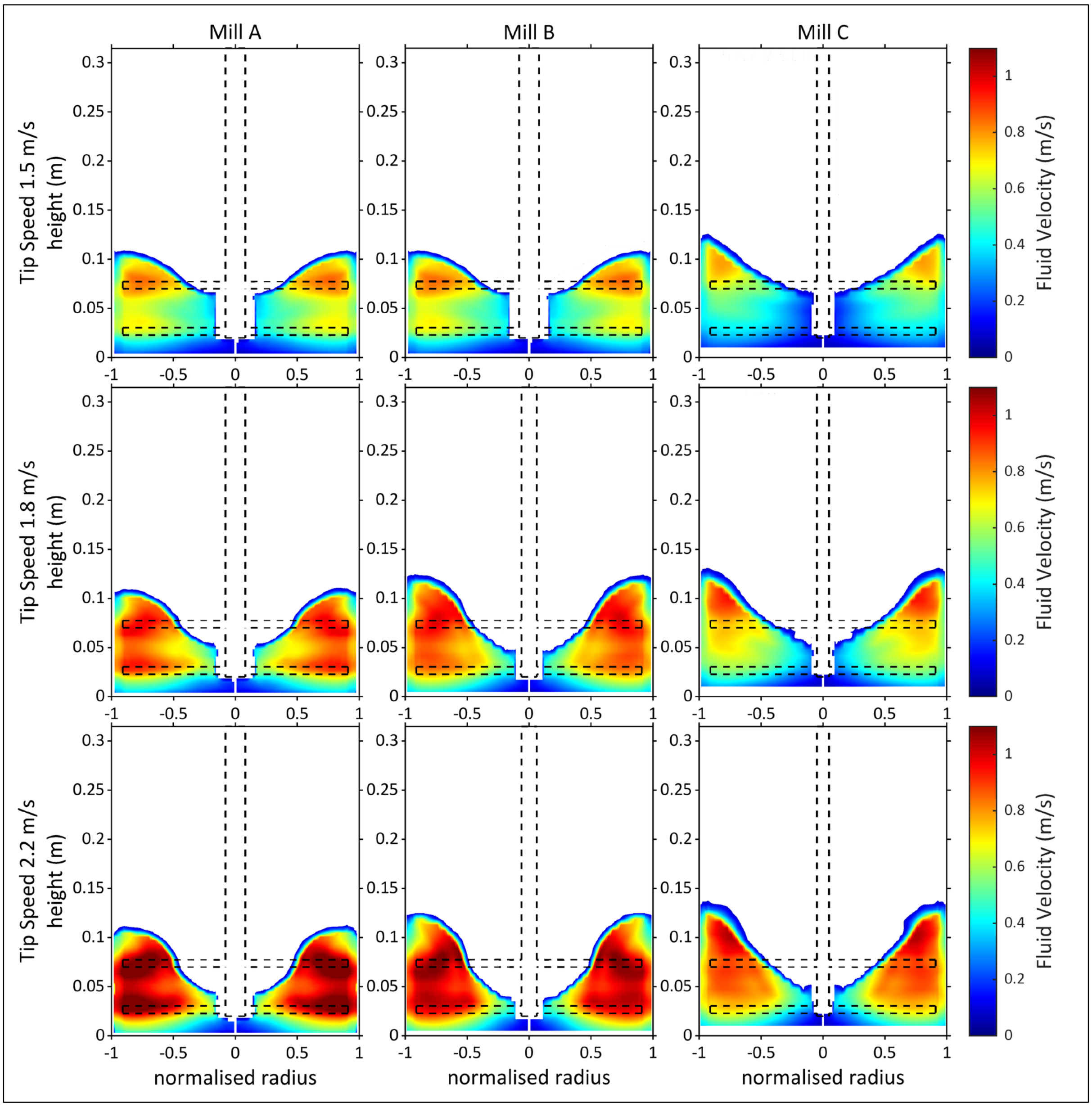

*Figure 8.6: Colourmaps of the bulk fluid velocity (m/s) at each scale of simulated mill system at tip speeds of 1.5, 1.8 and 2.2 m/s, normalised along the radial axis*

#### *8.2.2.1 Tangential velocity profiles*

Figure 8.7 shows the tangential velocity profiles along the normalised radius for all three mill scales at 1.5 m/s, 1.8 m/s and 2.2 m/s tip speeds. Within each plot, the length of the impeller is delineated on the normalised radius at 0.91. The tangential velocity profiles are divided axially into three segments represented as coloured lines: the mill base to the bottom of the lower pin 1 (blue line), the base of pin 1 to the top of the upper impeller pin 2 (red line), and above pin 2 (yellow line). The mill is segmented this way to give an indication of how the tangential velocity changes within the three segments of attritor mills as defined in sections 2.4.3.1 and 6.5.4.

A distinct peak was observed at a normalised radius just above 0.8 for of the two bottom segments, the blue and red lines, in each of the tangential velocity profiles presented in Figure 8.7. These two segments have similar profiles along the normalised radii. They reach their peak around the same point between the radius of 0.75 and 0.85, then decrease sharply after the tip of the impeller pin to the mill wall. The specific location for the peak of the tangential velocity profiles for the upper segment of the mill, the yellow line, shifts from a radius of 0.8 at the 1.5 m/s tip speed to a radius 0.6 at 1.8 and 2.2 m/s, for Mills A and B. The peak of this segment for Mill C at 1.5 m/s is consistently around a radius of 0.8, like the other two sections. The shape of the profile, with the peak occurring before the impeller tip position is observed in the axially segmented radial profiles for velocity magnitude for short and long impeller arms in Daraio et al. (2020) shown in Figure 4.6.

The assessment of the velocities showed that Mills A and B peak at similar velocity values, while Mill C has a comparably lower peak velocity. This is attributed to the ability of the velocity to propagate throughout the wake of the impeller within the rotation period. Because Mill C has the largest radius, its media have extended tangential arc lengths to travel over a longer rotation period. The velocities of the bottom segment, the blue line, are consistently less than the segments shown in the red and yellow lines, for each mill at each tip speed. This segment is a region of high solids fraction, as indicated in Figure 8.2. The media in this region is unable to attain higher velocities like the other segments that are either in the impeller path or of lower bulk solids fraction.

The starting point of the profile indicates the average radius of the central cavity in that segment of the mill. This is particularly visible in the upper segment, the yellow line, as the bottom two segments are influenced by presence of the impeller shaft. For Mills B and C, the shift of the starting point towards the mill wall is visible from the 1.5 to the 1.8 m/s tip speed. This is indicative of the widening of the cavity with increased tip speed. In Mill A, the velocities in this segment display erratic behaviour from their starting point to radius of 0.5, for all the tip speeds. This is characterised as erratic flow behaviour, due to the high rotational speeds experienced in that mill, given its small diameter.

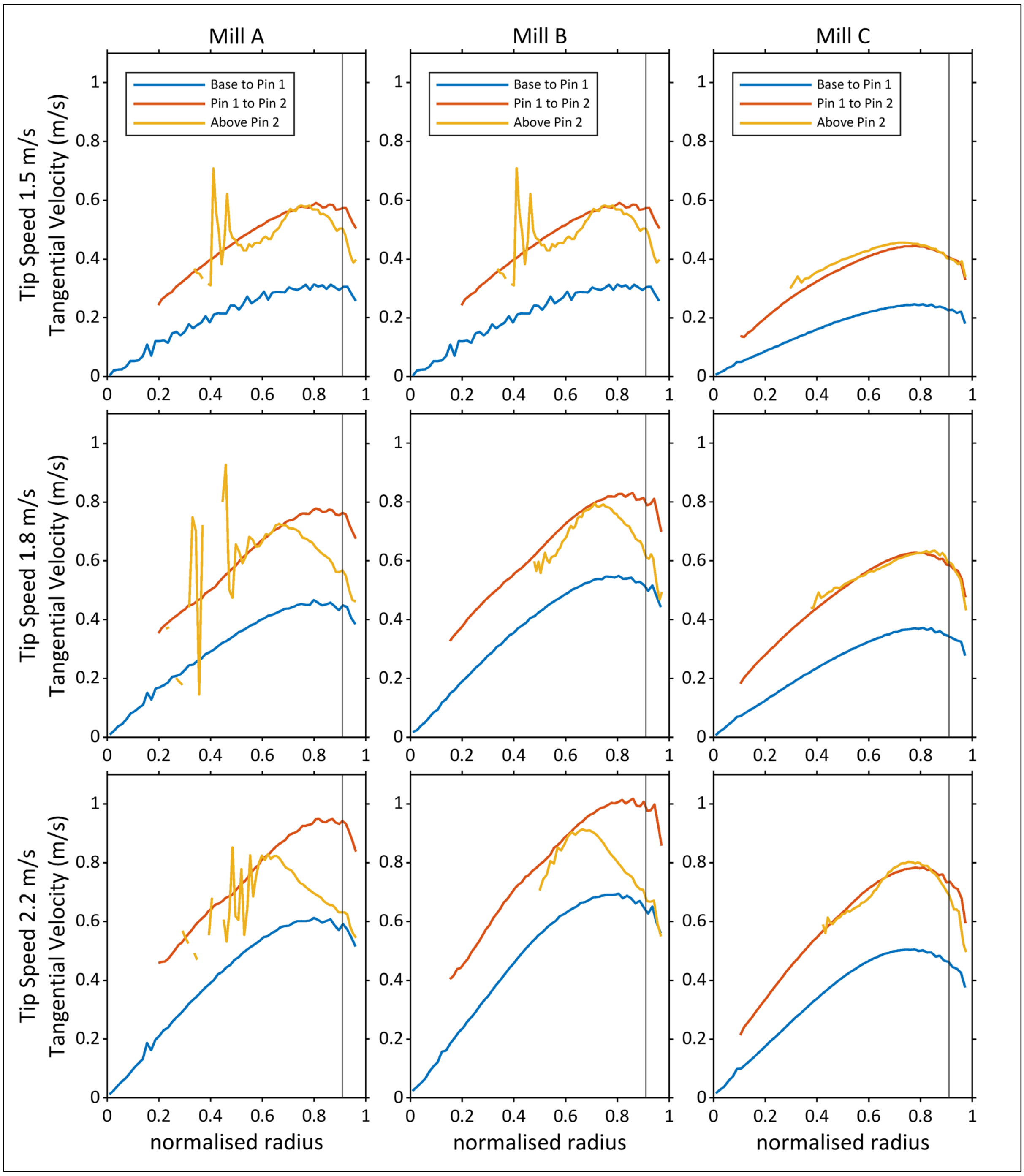

*Figure 8.7: Segmented radial profiles for tangential velocity (m/s), over the normalised radius for each mill size at the simulated tip speeds of 1.5, 1.8 and 2.2 m/s*

#### *8.2.2.2 Axial velocity*

The axial velocities are presented in the form of r-θ colour maps at the region ranging axially from a pin radius above to a pin radius below the impeller pin, for both the top and bottom pin, as illustrated in Figure 6.19. The two regions were chosen because they give an indication of how the impeller action influences the motion of the media amidst slurry in the stirred media detritor.

The r-θ colour maps presented are the result of the segmentation and averaging of five timesteps of the mill at the same impeller positions, approximated to the nearest centi-second. The colour maps provide a snapshot of how the system responds to the rotation of the pins through the segmented region. All the colour maps display 2-fold rotational symmetry around the mill centre, due to the configuration of the impeller pins. Though the images represent specific timesteps, because the mill rotates consistently, these colour maps would effectively rotate with the impeller. The maps use a colour scale centred on a velocity of 0 m/s being white, with red being positive axial velocities and blue being negative axial velocities. In terms of flow, the red regions indicate motion upward, above the surface plane and the blue regions represent downward flow, below the surface plane. The impeller rotates in an anticlockwise direction.

These results are presented in two matrix figures. The first matrix, Figure 8.8, shows the top and bottom impeller colour maps for the three mill sizes at a tip speed of 2.2 m/s, with focus on the radial expansion scale-up effects. In the second matrix, Figure 8.9, both colourmaps for Mill C at the three tip speeds are provided to inform on the effect of increasing the tip speed. Therefore, the colourmaps for Mill C at 2.2 m/s are shown in both Figure 8.8 and Figure 8.9. Figure 8.8 compares the top and bottom impeller slices for the three mill sizes at 2.2 m/s. The white area near the impeller shaft of the top impeller represents the vortex. The size of the vortex relative to the normalised circular r-θ surface of the mill is seen to decrease with the radial expansion across the mill sizes. The approximated shape of the vortex shows a longer side parallel to the impeller pin and a shorter one perpendicular to the pin. Considering one semi-circle divided by the top impeller pin, the shape shows that media is displaced by the impeller pin and carried in the wake to form the longer edge. Similar vortex shapes were observed in the stills of the r-θ surfaces at each impeller pin of the pin mill modelled by Kim & Choi (2008) in Figure 6.21.

Considering the top impeller plot for Mills B and C, a distinct region of upward velocity is found in the wake of each impeller pin, visualised by the red colouring. As the impeller rotates, it displaces particles in its path, causing them to travel upward or downward around the impeller pin. The average axial velocity of the regions in the wake of the impeller is positive, indicating that majority of the displaced particles in the region move upward. The regions ahead of the impeller pins are characterised by blue negative axial velocities, indicative of downward motion in the region. This is attributed to downward return of the particles that were previously moving upwards in the wake of earlier timesteps. The top impeller of Mill A has four regions of upward motion, with the two larger regions in the wake of the impeller perpendicular to two smaller regions. Each region is followed by a blue region of downward motion. This is indicative of influence of the bottom impeller on the flow field surrounding the top impeller, as the smaller area of upward velocity occurs in the wake of the bottom impeller.

The axial velocity field surrounding the top impeller achieves higher intensity regions of upward velocity, than the bottom impeller, particularly for Mills B and C. This can be attributed to the loose packing in the region surrounding the top impeller allowing for more movement between the media and how the packing around the bottom impeller was observed tighter with increased mill size.

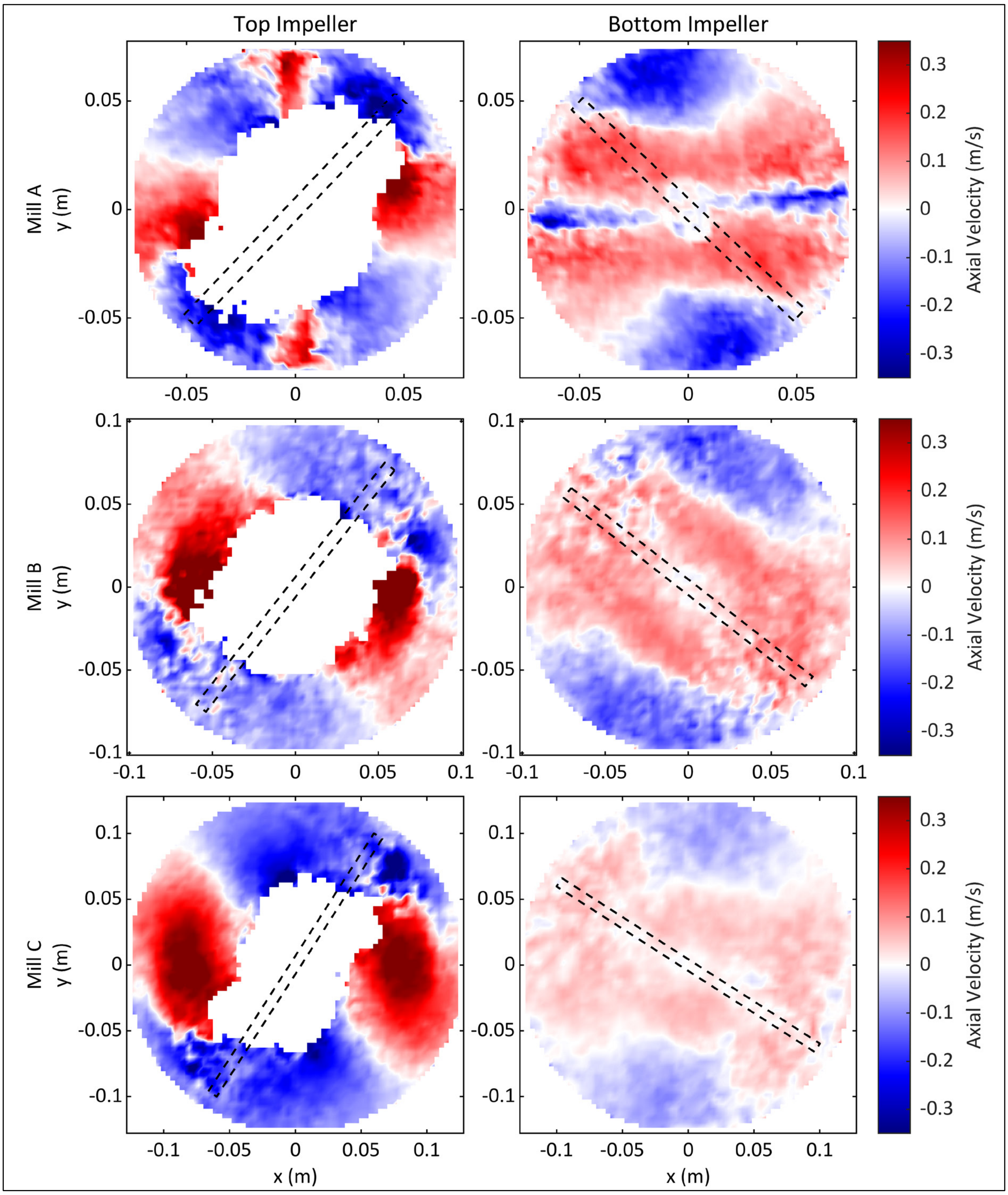

*Figure 8.8: Axial velocity (m/s) colourmaps of the region around the top and bottom impeller pin, for all three mill scales at a tip speed of 2.2 m/s, with an anticlockwise rotation*

The bottom impeller plots can be divided into 4 main regions. Two regions of upward velocity that run across the centre of the mill system, separated by a line of zero velocity that runs through the centre. For Mill A this separation is by a line of downward velocity. The impeller shaft is visible at the centre of each mill system as a zero-velocity region. The other two regions are of downward velocity. These run from the mill wall inward to the edge of the red regions. The large regions of upward velocity of the top impeller segment overlap with the red regions of the bottom impeller. The wake of the bottom pin is a region of downward velocity, unlike the top pin, indicating that majority of the bodies displace downward.

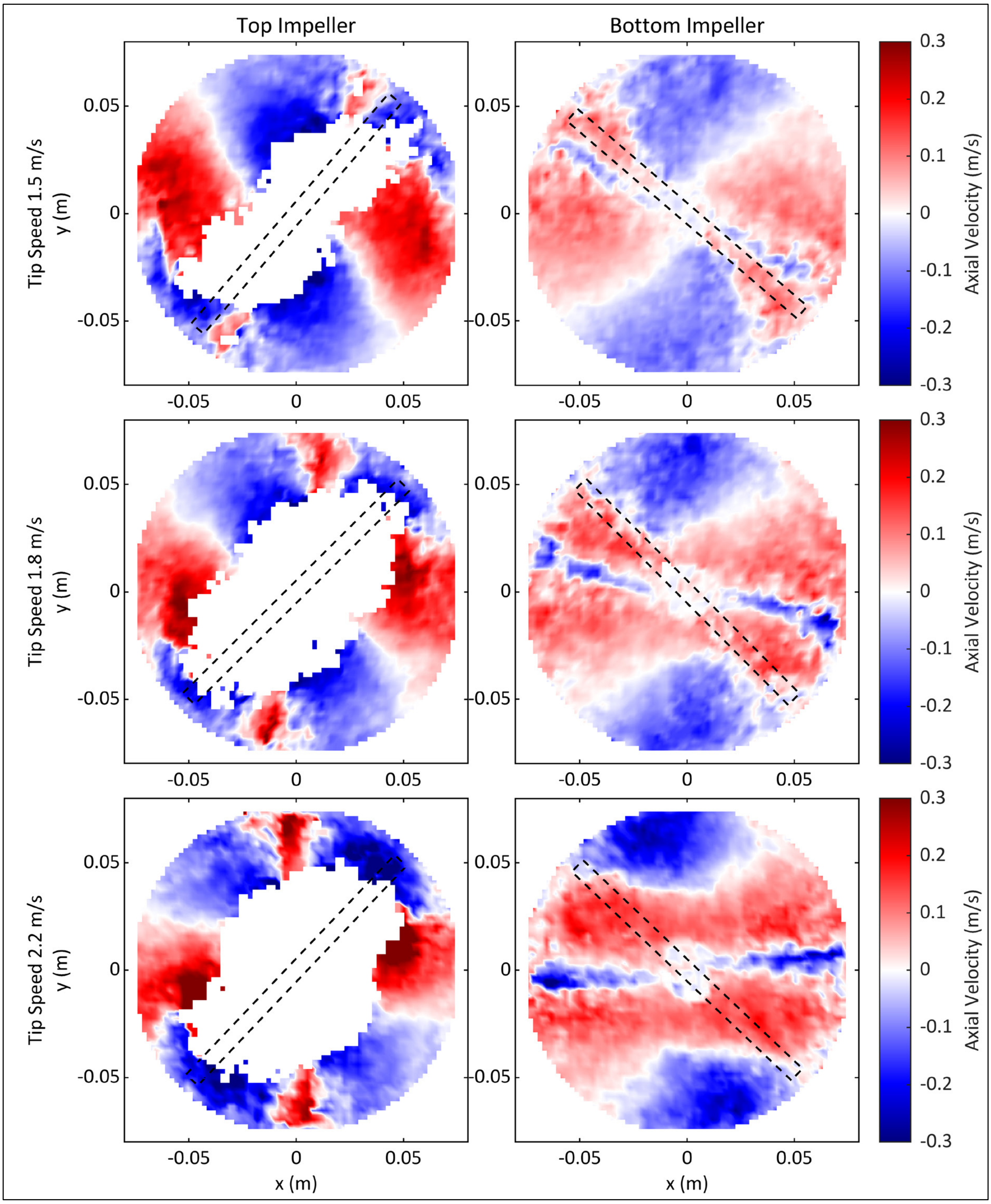

*Figure 8.9: Axial velocity (m/s) colourmaps of the region around the top and bottom impeller pin, for Mill A at each of the three tip speeds, with an anticlockwise rotation*

Figure 8.9 show the segmented axial velocity response of Mill A at tip speeds of 1.5, 1.8 and 2.2 m/s. The shape of the vortex expands along the shorter edge with increasing tip speed, with the long edge staying consistent. This is due to the higher tip speeds increasing the tangential velocity of the system and the apparent centrifugal force experienced by the media bodies, which pushes them towards the wall. The intensity of the upward and downward velocities increases with tip speed. The influence of the bottom impeller on the flow of the top impeller region becomes more visible as the tip speed increases. This is visualised as smaller red regions of positive axial velocity that appear in the Mill A top impeller colourmap of Figure 8.8, but not in Mills B and C. These smaller regions occur perpendicular to the larger regions of positive axial velocity and are visible across all tip speeds in Mill A in Figure 8.9. The larger regions of positive axial velocity occur in the wake of the impeller, due to its motion displacing media above the impeller pin. It follows that the smaller regions occur in the wake of the bottom impeller, with their intensity increasing with tip speed, concurrent with the dilation of the media bed around the bottom impeller observed in Figure 8.2.

#### *8.2.2.3 Radial velocity*

The radial velocity is interpreted as inward and outward motion from the centre of the surface plane. The radial velocity of the mills is displayed in colour maps of axial segments of the mill space surrounding the top and bottom pins of the impeller. These colour maps correspond to those of the axial velocity. Within the colourmaps, the red colour denotes flow areas that are radially outward, and blue colour is inward flow. The impeller rotates in the anticlockwise direction.

Figure 8.10 shows the radial velocity response of the three mills at a tip speed of 2.2 m/s. Considering the top impeller segments, the radial flow fields show large regions of outward flow in the wake of the impeller, along the long edges of the vortex. Inward flow is noted along the shorter edges of the cavity particularly in the larger systems of Mills B and C. In the bottom impeller segment, red regions of outward flow are found in the wake of the impeller, with majority of the segment showing blue inward flow. The top impeller colourmap is dominated by outward flow and the bottom impeller colourmap with inward flow. The combination of the radial flow patterns with the axial flow patterns is indicative of regions of circulatory flow where the top impeller displaces media in its wake upwards and outwards causing the media below it to flow downwards and inwards. The proportion of the regions of outward flow appears to decrease with mill size. The radial velocities observed in the bottom impeller segment decrease with increasing mill size. This shows that the circulatory flow patterns are stronger in the smaller mills, where there is less media to circulate and a looser packing at the bottom impeller. Figure 8.11 shows the radial velocity response of Mill A at the three tip speeds simulated. Looking at the top impeller segments, there are red areas of outward flow around the edges of the central cavity. These areas intensify as they extend along the longer edges of the central cavity with increasing tip speed. The bottom impeller colourmaps show red regions of outward flow in the wake of the bottom impeller. These regions expand with increasing tip speed and disperse slightly in intensity.

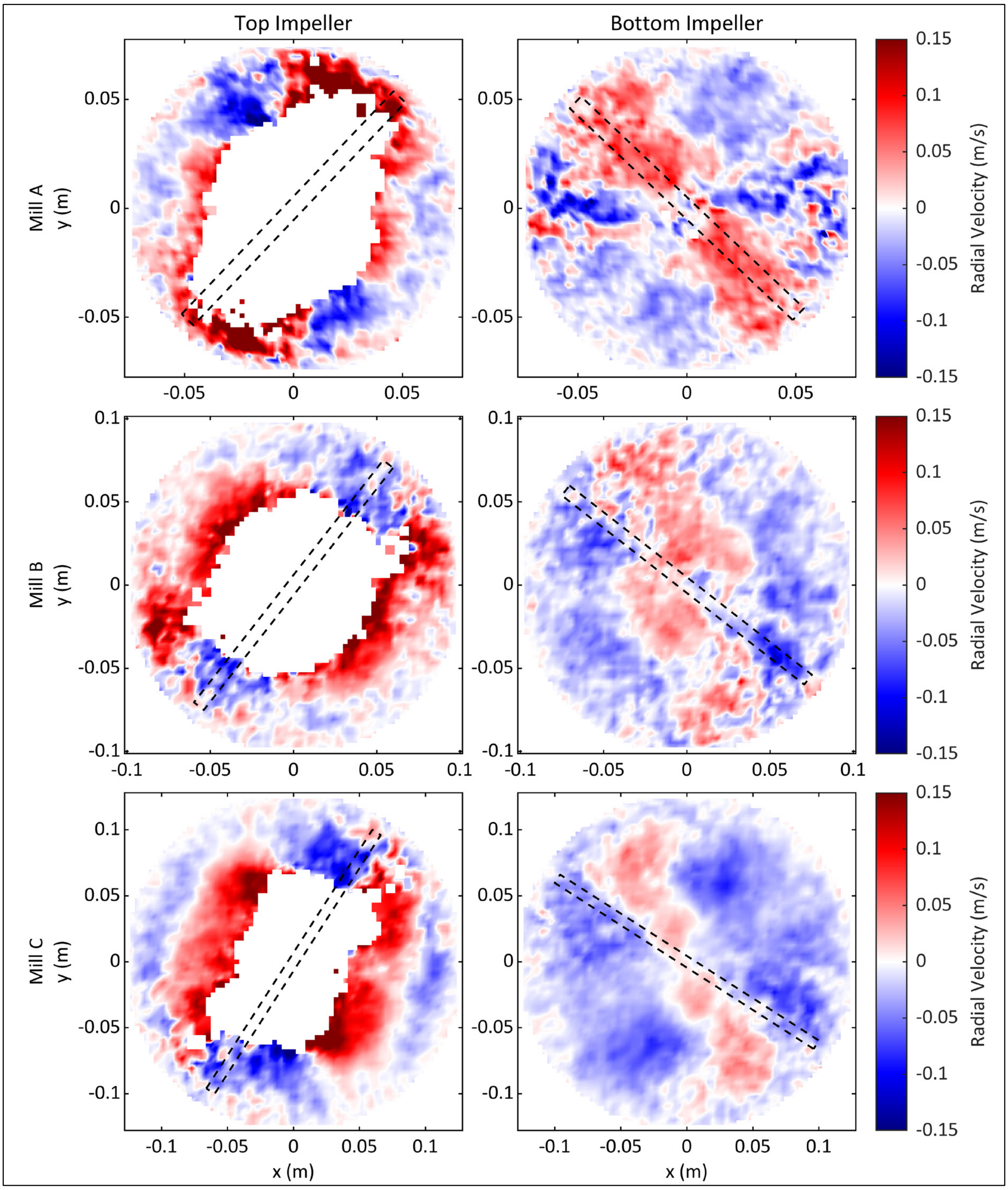

*Figure 8.10: Radial velocity (m/s) colourmaps of the region around the top and bottom impeller pin, for all three mill scales at a tip speed of 2.2 m/s*

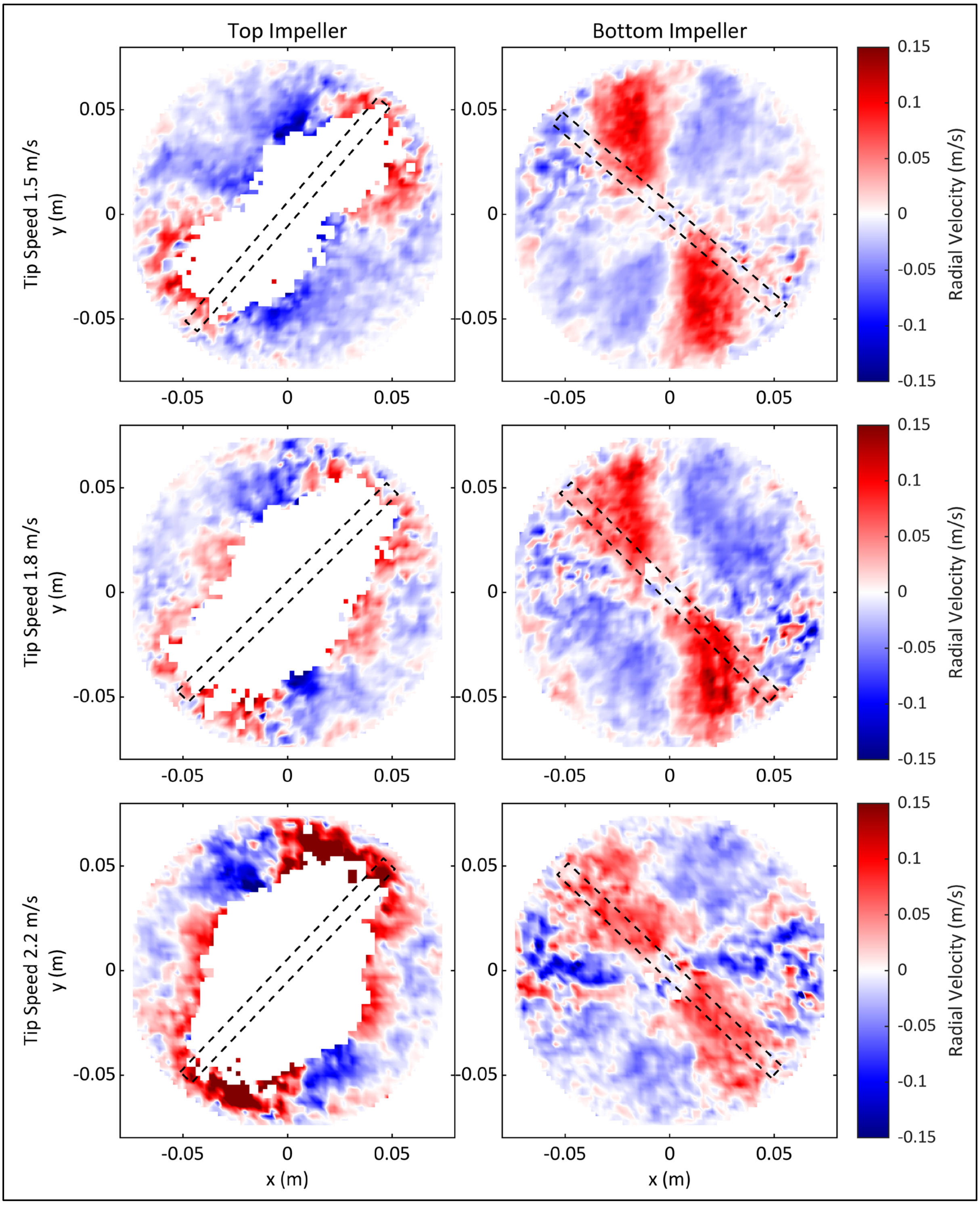

*Figure 8.11: Radial velocity (m/s) colourmaps of the region around the top and bottom impeller pin, for Mill A at each of the three tip speeds.*

### *8.2.2.4 Box and whisker distributions*

The distributions of the media and fluid velocity magnitudes of the SPH particles and DEM bodies are summarised in the box and whisker plots as shown in Figure 8.12. Data from five impeller revolutions, at an output rate of one centisecond is used for each condition. As indicated in section 8.2.1, the box represents the lower and upper quartiles, with the median in the middle. The whiskers represent the maximum and minimum values, excluding outliers.

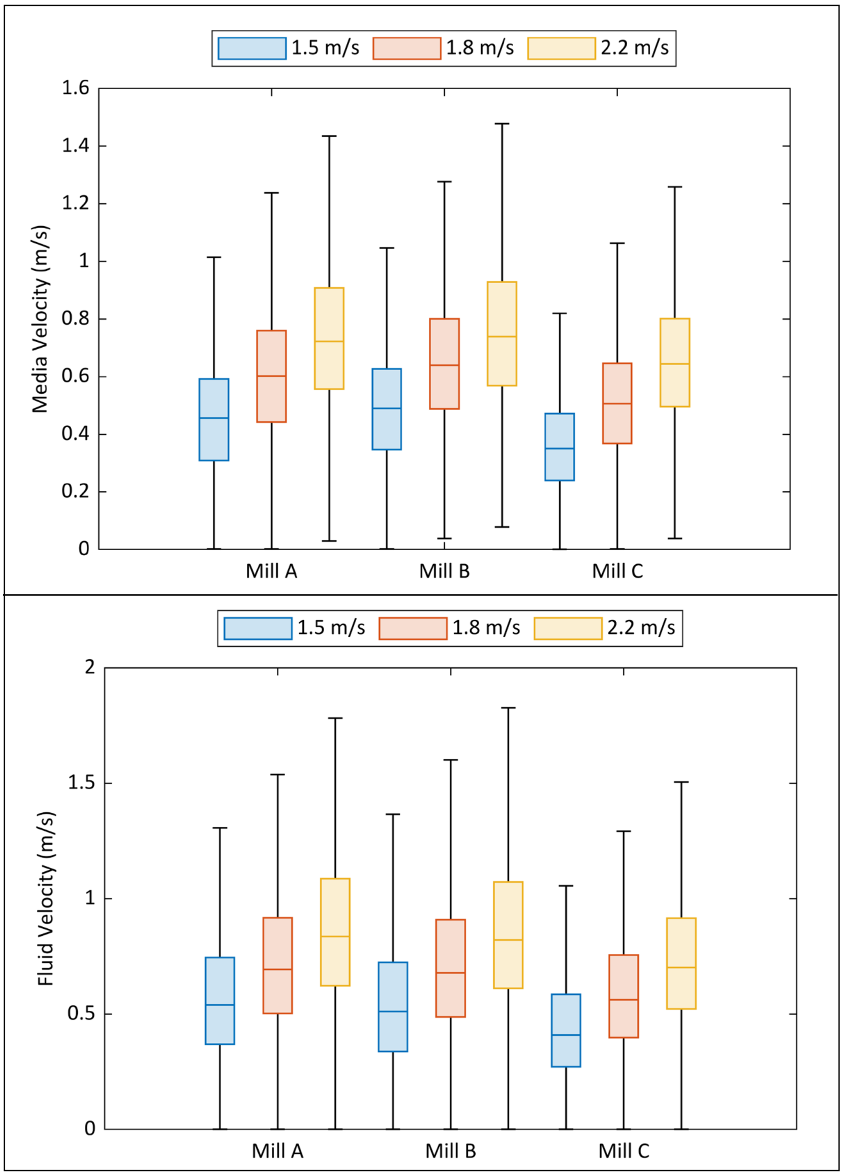

*Figure 8.12: Box plots for the media velocity and fluid velocity over the experimental conditions.*

The median velocity is shown to increase with the impeller speed for both the media and fluid across the three mill sizes simulated. This behaviour is as anticipated and noted for the average media velocity in the rotational speed studies of Yang et al. (2006), Jayasundara et al. (2010) & Cleary, Sinnott & Pereira (2015). The studies observed that the increase with impeller speed reaches a plateau, which is not observed for any mill size within this tip speed range. The fluid velocity exhibits similar behaviour to the media velocity largely because majority of the fluid is located in the interstices of the media charge, with the exception of the fluid in the vicinity of the free surface or vortex. The fluid around the free surface is influenced by the direct motion of the impeller, the media and the air core, which makes it behave differently than the fluid in the interstices. This results in the median fluid velocity being characteristically higher than the media velocity, with its distribution having a slight negatively skew. The media and fluid distributions of mills A and B, across tip speeds simulated, show similar values within the box with Mill B having a slightly extended range. Mill C has a distinctly smaller distribution range for the media and fluid velocities.

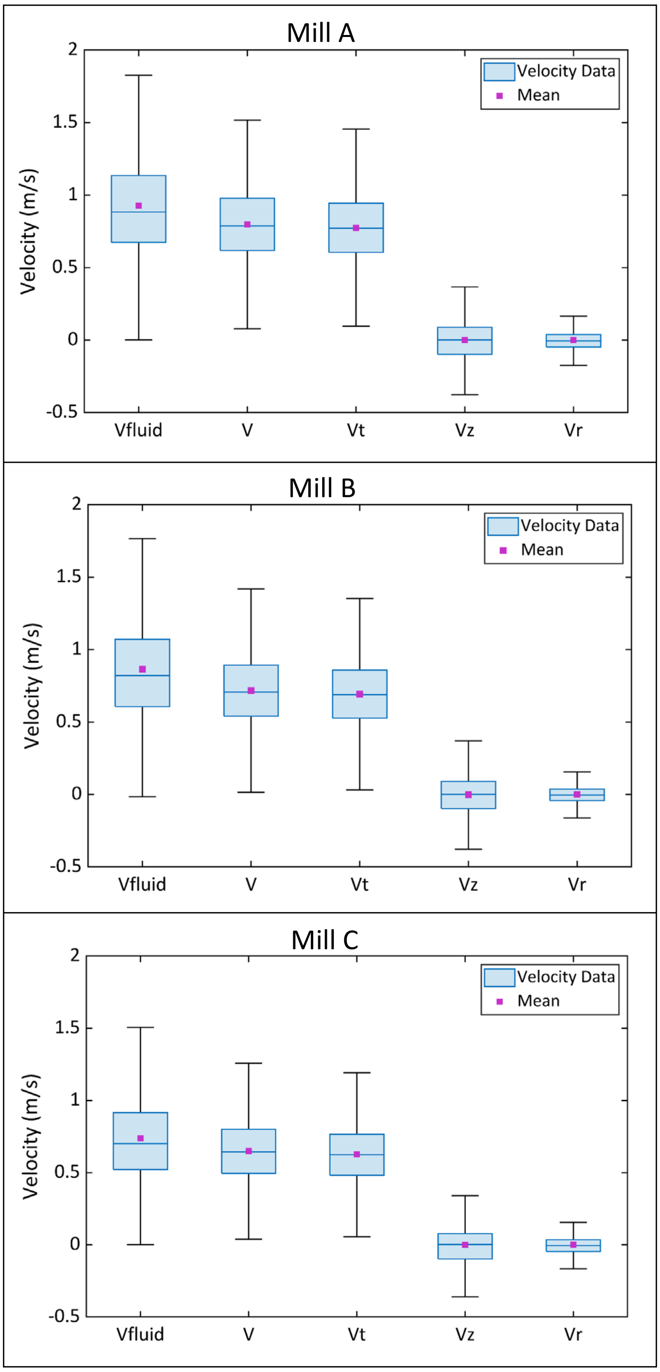

*Figure 8.13: Box plots of fluid velocity (Vfluid), media velocity (V) and media velocity components (Vt, Vz and Vr) for each of the Mills A, B and C at 2.2 m/s*

The box plots in Figure 8.13 show the fluid and media velocity distributions alongside distributions of the media velocity components for the simulation performance with the impeller speed rotating at 2.2 m/s. These box plot have the mean overlayed to show the normal distribution of the fluid velocity and the media velocity and its tangential, radial and axial components. Within each mill size, the velocity magnitude and the tangential velocity have similarly distributed boxes, with the tangential velocity range contained within the velocity magnitude distribution. This is expected as motion within the mill space is dominant in the positive tangential direction as it is the direction of the impeller rotation. The axial and radial velocities are evenly distributed between positive and negative values, showing stability within the circulation pathways of each mill size. The mills all achieve greater velocity in the axial direction compared to the radial, due to gravitational forces.

### 8.2.3 Dimensionless numbers

Dimensionless numbers are important in determining the flow behaviour of the system. Following from the dimensionless analysis of the SMD system in section 2.4.2, the two dimensionless numbers that were used to study the flow behaviour in the simulated systems were the Reynolds number and the Froude number. Information from the coupled DEM-SPH simulation was used to determine the localised Reynolds and Froude numbers for the systems, according to the formulations in equations (2) and (3), respectively. The analytical code used to calculate the localised dimensionless quantities is shown in Appendix D.7. The intent is that assessing the distributions of these numbers will provide comparable values that are indicative of the flow state of the mill. The Reynolds number is indicative of the ratio between the inertial and viscous forces, while the Froude number indicates the ratio between the inertial and gravitational forces.

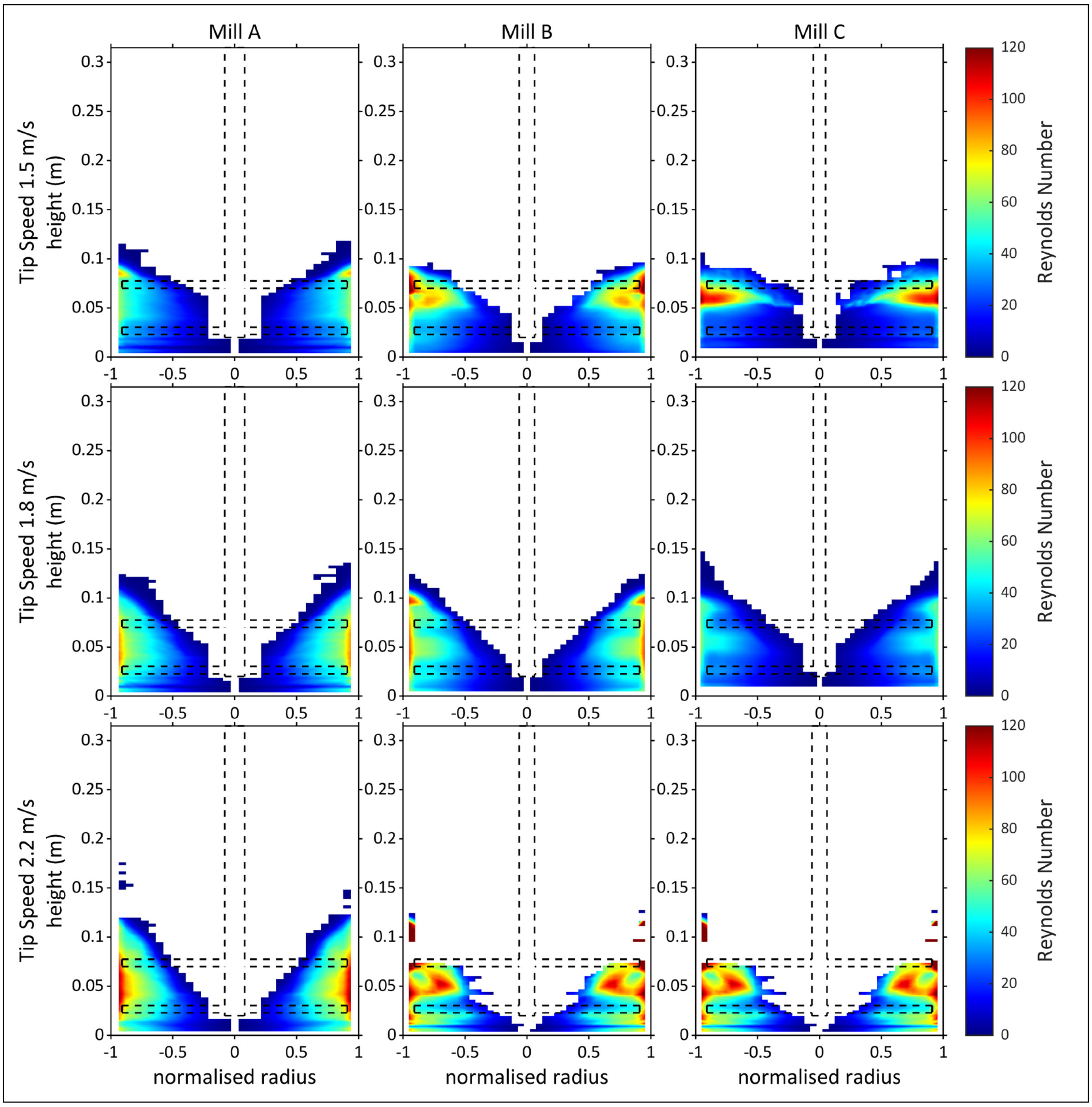

*Figure 8.14: Colourmaps of the localised Reynolds number at each scale of simulated mill system at tip speeds of 1.5, 1.8 and 2.2 m/s, normalised along the radial axis.*

The localised Reynolds and Froude numbers were analysed using 2D colour plots of r-z surfaces of the mill space. This indicates spatial hotspots of increased intensity. The Reynolds number colour maps are shown in Figure 8.14. At the 1.5 m/s tip speed, the regions of increased intensity are observed around the top impeller, particularly in Mill C and Mill B. In Mill C, these regions of high intensity were located at the base of the top impeller, towards the wall. For Mill B the regions are centred between the mill wall and the pin tip of the top impeller, spreading downwards. The Reynolds number colour map shows some changes as the tip speed increases. The regions with high Reynolds numbers become larger with increased tip speed. The peak intensity of the Reynolds number for Mill C, particularly at higher tip speeds is lower than what was observed in Mills A and B. This is because Mill C has lower media and fluid velocity distributions and a tighter packing, resulting in lower relative velocities and porosities, which are both directly proportional to Reynolds number.

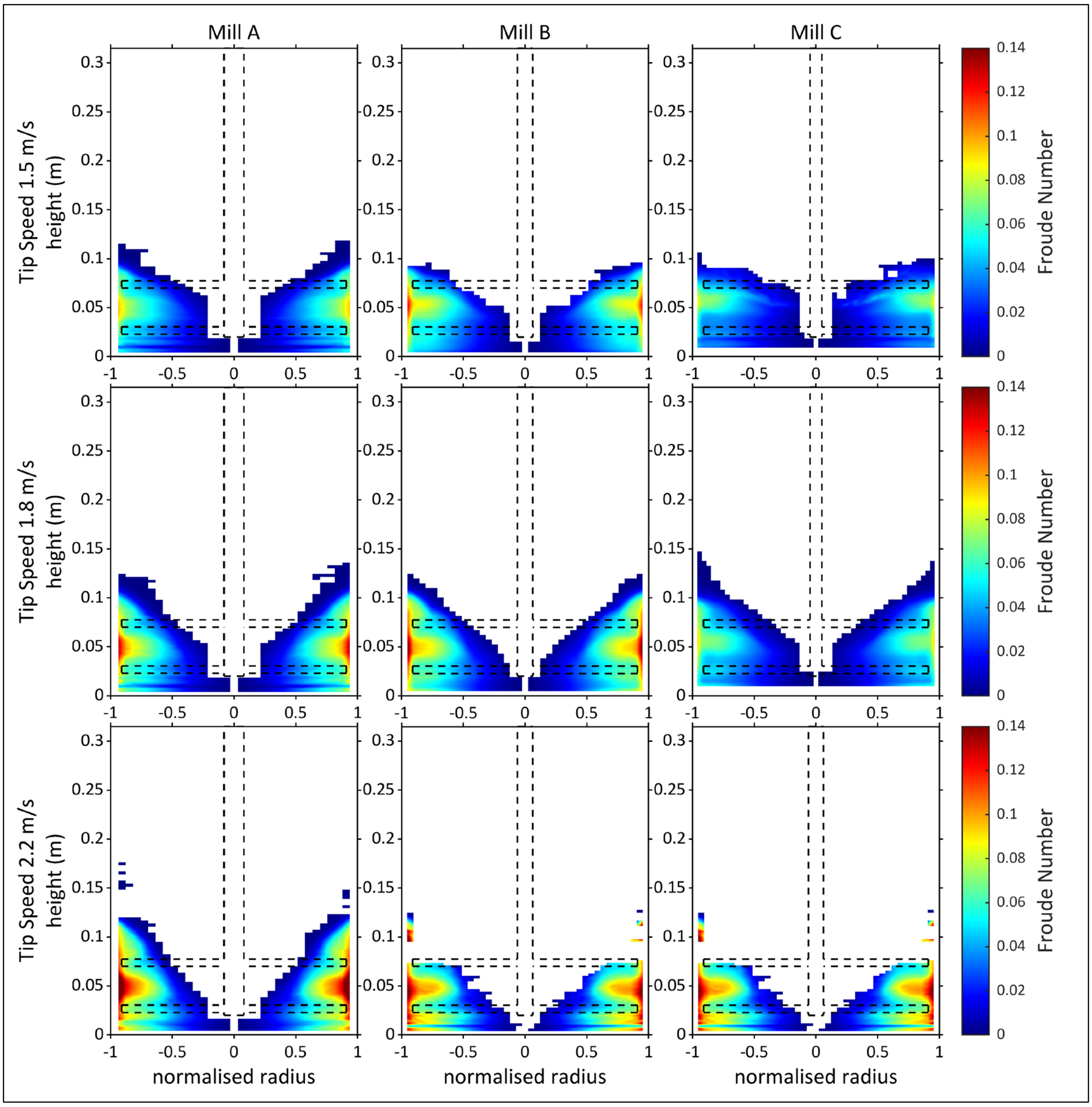

*Figure 8.15: Colourmaps of the localised Froude number at each scale of simulated mill system at tip speeds of 1.5, 1.8 and 2.2 m/s, normalised along the radial axis.*

The colour maps for the localised Froude number are presented in Figure 8.15. The region of high intensity was between the pins near the wall. The region with the peak Froude number increased with tip speeds for each mill simulated. Among mill sizes, Mill B exhibited a consistently larger region of high Froude numbers compared to Mill A and C. This could be due to the mill having a higher spatial relative velocity.

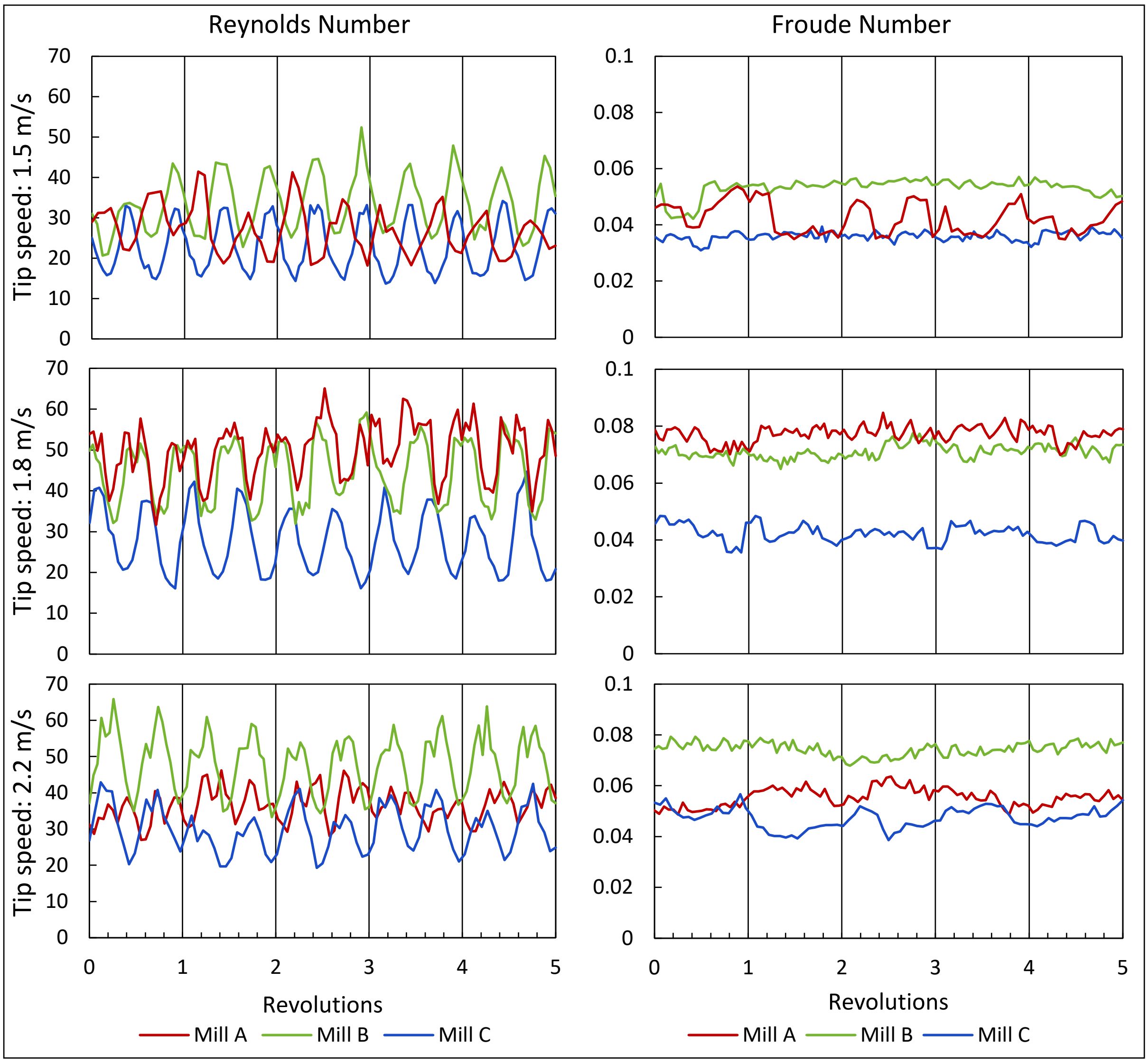

*Figure 8.16: Plots of the median Reynolds and Froude numbers at each recorded timestep as a function of the impeller revolutions for each scale of simulated mill system at tip speeds of 1.5, 1.8 and 2.2 m/s*

The medians of the distributions of the dimensionless numbers were plotted as a function of time for each recorded timestep in Figure 8.16. This was done to assess the variability of these values. The median was monitored as the indicator of the distribution, due to the positive skew consistently observed in the distributions of both dimensionless quantities at a given time as shown in Appendix E.3. The resulting trends are shown in Figure 8.16. The Reynolds number shows evidence of periodicity with the revolutions of the impeller for all the mills sizes at the three tip speeds evaluated. This behaviour is peculiar because none of the parameters that make up Reynolds number show this periodic trend. The trend for the fluid density plot, Figure E.11, is the only one with a behaviour similar to this. Example profiles of the parameters that define the Reynolds number are shown for Mill A in Appendix E.4. The Froude number does not show any periodicity over 5 revolutions. Therefore, this eliminates the dependence of the periodicity on the relative velocity. The profiles for the Froude number show minor variations, except for Mill A at 1.5 m/s and Mill C at 1.8 and 2.2 m/s.

The periodicity seen in Reynolds number could be due to the influence of the fluid density. The fluid density influence on the Froude number may be dampened by the dominant media density. The fluid pressure is proportional to the fluid density to the power of the compressibility constant, through the equation of state (47) used in the SPH formulation. A key influence on the fluid pressure is the central vortex within the mill space. As the impeller rotates, the shape of the vortex changes with the sections of the mill having an expansion of the air core and others a contraction. It is this motion that results in the periodicity of the Reynolds number. The shape of the wave changes with rotational speed and mill size.

Figure 8.17 shows the average median of the Reynolds and Froude number for each simulation, with error bars indicating a standard deviation above and below the average. The behaviour exhibited by both dimensionless quantities is similar for all mill size at the tip speeds simulated. The main disparity is in the standard deviation, due to the periodicity of the Reynolds number.

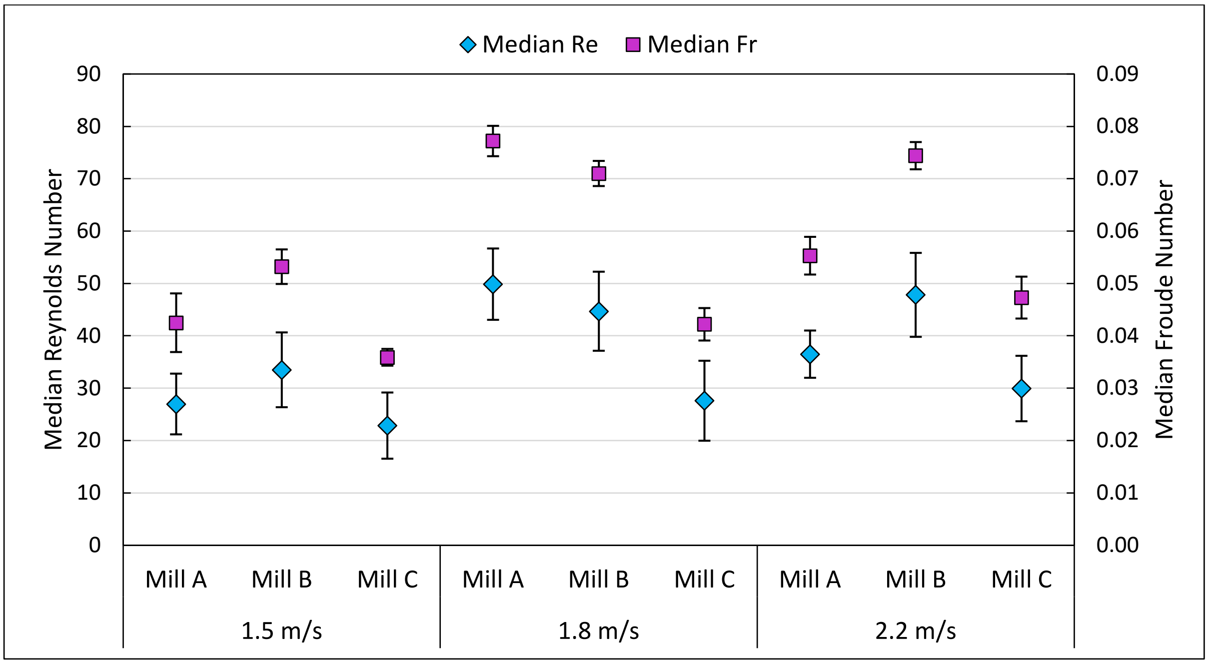

*Figure 8.17: Average median Reynolds and Froude numbers for each mill at all the tip speeds simulated, with error bars indicating the standard deviation of the distribution of medians over 5 revolutions.*

The behaviour exhibited across dimensionless numbers for Mills B and C show positive increases with increasing tip speed, with the increase from 1.5 to 1.8 m/s being larger than that from 1.8 to 2.2 m/s. Mill A, however, exhibits a peculiar trend. Its Reynolds number increased from 27 to 50 with the increase in impeller speed from 1.5 to 18 m/s and decreases from 50 to 36 with the increase in tip speed to 2.2 m/s. The Froude number exhibited a similar trend. This behaviour at 1.8 m/s is inconsistent with the spatial trends observed across mill sizes. Mill B also exhibited greater dimensionless numbers than Mill A at 1.5 and 2.2 m/s. this can attributed to the erratic behaviour of the tangential velocity in the upper circuits of Mill A, due to its higher rotational velocity resulting in erratic relative velocities that skew the bulk dimensionless variables. The raw data of this figure is provided in Table E.2 in Appendix E.5.

## 8.3 Energy environment

The energy environment was analysed from the frequency and intensity of the media collisions that are assumed to induce breakage, and the power drawn from the impeller. To make the simulated systems comparable across the different mill sizes, all energy and power variables were normalised through dividing by the initial volume of fluid in the system. The fluid volume is used because it is the fluid material in the simulation that absorbed the energy dissipated.

There are three aspects considered in relation to the energy environment:

1. The first aspect considers the spatial distribution of key contact variables. This is done to establish key physical hots spots within the mill space for collisions and energy dissipation.
2. The collision energy spectra. This is done to establish comparative value on an energy basis for the systems of experiments. The analysis of the spectra and key variables used in it is adopted from the works of Cleary and colleagues (Cleary, Sinnott & Pereira, 2015; Ndimande et al., 2019), as discussed in section 6.5.2.
3. Analysis of the power draw. The power is the only energy environment variable not determined from the Contact Data Analysis but within the Steady State Analysis. This is done to provide a comparative representation of how the systems distributes power through the impeller to the DEM bodies and SPH particles to maintain a constant tip speed. The power draw analysis includes a comparison against the dry DEM-only runs of the set of simulations at 2.2 m/s.

### 8.3.1 Spatial distributions

The energy spatial distributions assessed are the frequency, total energy dissipation and total energy dissipation rates of the collisions. These are shown in Figure 8.18, Figure 8.19 and Figure 8.20, respectively, for simulations of the three mill sizes at each of the tip speeds simulated. The rows in the figure represent mill sizes, and the tip speeds are columns. The collisions for 5 revolutions in each mill size at each tip speed were used in the analysis. The distributions are shown as 2D colour plots of the mill space r-z surface bisected in θ.

Within Figure 8.18, the hot colours are indicative of regions of high collision frequency in the mill space, while the cold colours are regions of low frequency. The collision hotspots at 1.5 m/s across the mill sizes are along the impeller pin width of the bottom impeller, the between impeller pins towards the mill wall and at the base of the mill shell. These regions of high collision frequency decrease in intensity with increasing impeller tip speed. As the tip speed increases, the media attains higher tangential velocities in the same direction as the rotation and thus decreasing the collisions in a revolution. The number of collisions increases with mill size, as expected due to the increased number of particles within the mill.

Figure 8.19 shows the total energy dissipation of the collisions for the three mills at the three defined tip speeds. The hot colours represent high energy dissipation, and the cold colours show low energy dissipation. At 1.5 m/s, the collisions that dissipate the most energy are the collisions at the base of the mill shell. Across mill sizes, these regions increase in intensity with increasing tip speed. As this occurs, the energy dissipated around the bottom impeller increases in intensity, specifically for Mills A and B. The range of dissipated energy per $m^3$ of fluid, decreases with the increasing mill size, as indicated by the colour bars. Note that energy dissipation for Mill C is visualised within a range that is an order of magnitude lower than Mills A and B.

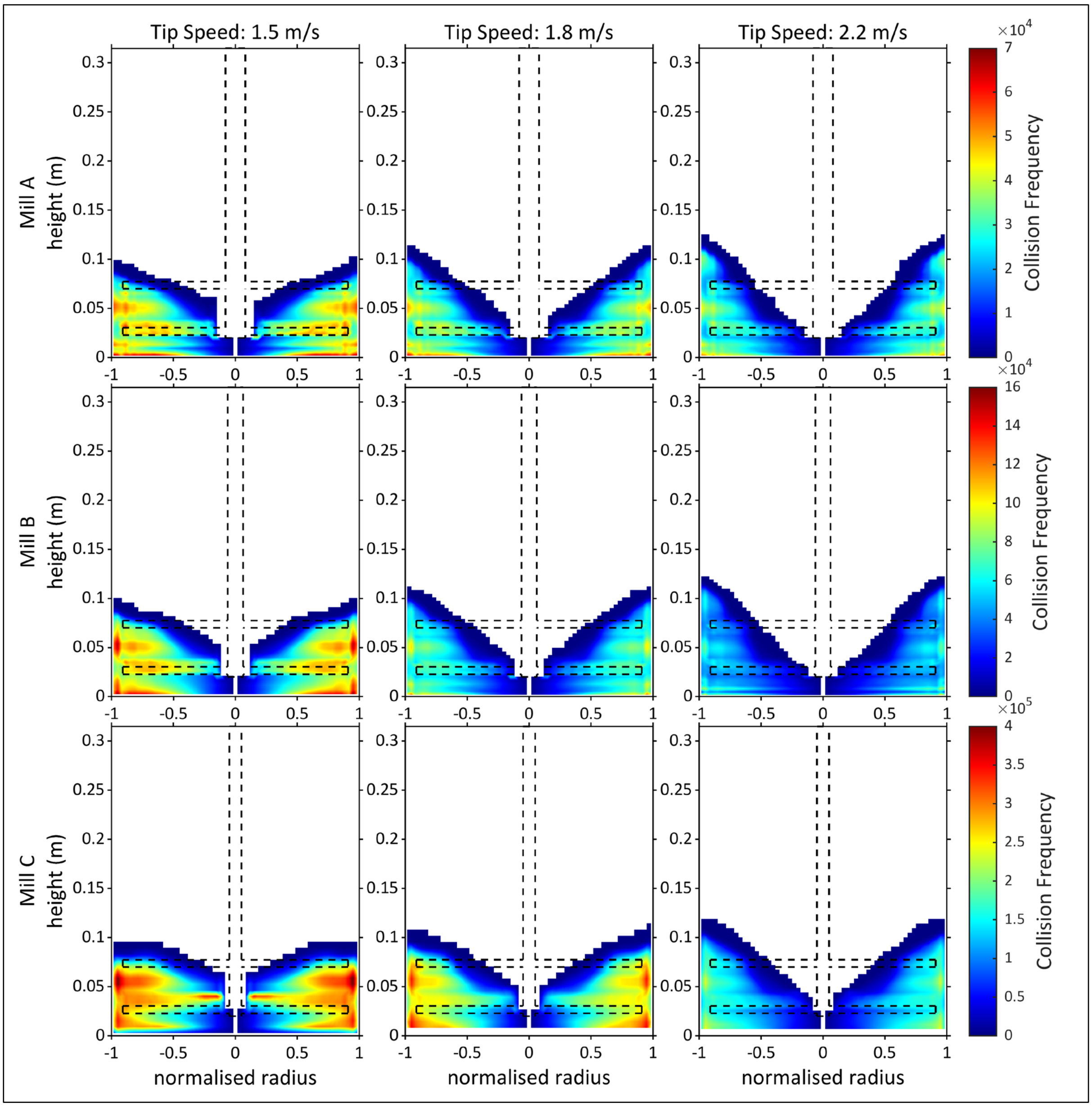

*Figure 8.18: Colourmaps of the spatial collision frequency at each scale of simulated mill system at tip speeds of 1.5, 1.8 and 2.2 m/s, normalised along the radial axis*

Figure 8.20 shows the spatial distribution of the total energy dissipated in a collision divided by the collision duration. At 1.5 m/s, the highest intensity region for energy dissipation rate is observed along the length of the bottom impeller pin, across mill types. With increasing tip speed this region increases in intensity. This is because the source of energy into the system are the impeller pins, and the media packing is tighter around the bottom impeller, so for it to rotate it requires energy to overcome the resistance. For Mills A and B, another local region of high energy dissipation rate forms along the length of the top impeller with increasing tip speed, visible at 2.2 m/s. At 2.2 m/s, Mill C has an additional region of high intensity along the mill base.

Comparing this to the energy dissipation in Figure 8.19, the energy dissipation rate colour bar ranges also decrease with increasing mill size. However, the regions of intense energy dissipation are not consistent with the regions of high energy dissipation rate. Particularly for Mills A and B at 2.2 m/s, which show the base of the mill as a region of high energy dissipation, but low energy dissipation rate. This is attributed to the duration of the individual collisions, indicating that the collision at the mill base have a long duration. The long duration occurs as a result of the lower media velocities and tighter spacing along the mill base, as observed in sections 8.2.1 and 8.2.2.

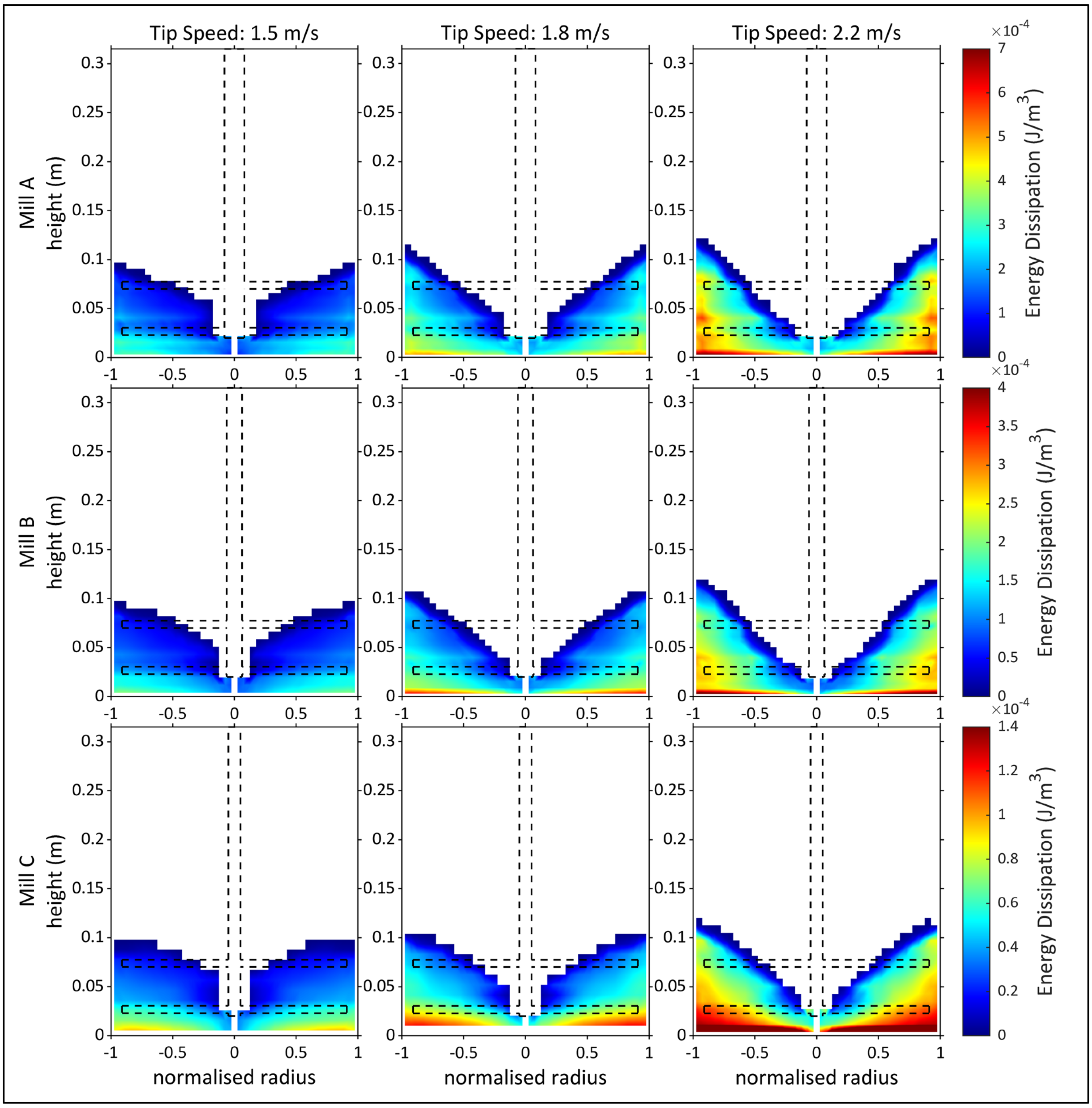

*Figure 8.19: Colourmaps of the spatial total energy dissipation of the collisions (J/m$^3$ fluid) at each scale of simulated mill system at tip speeds of 1.5, 1.8 and 2.2 m/s, normalised along the radial axis*

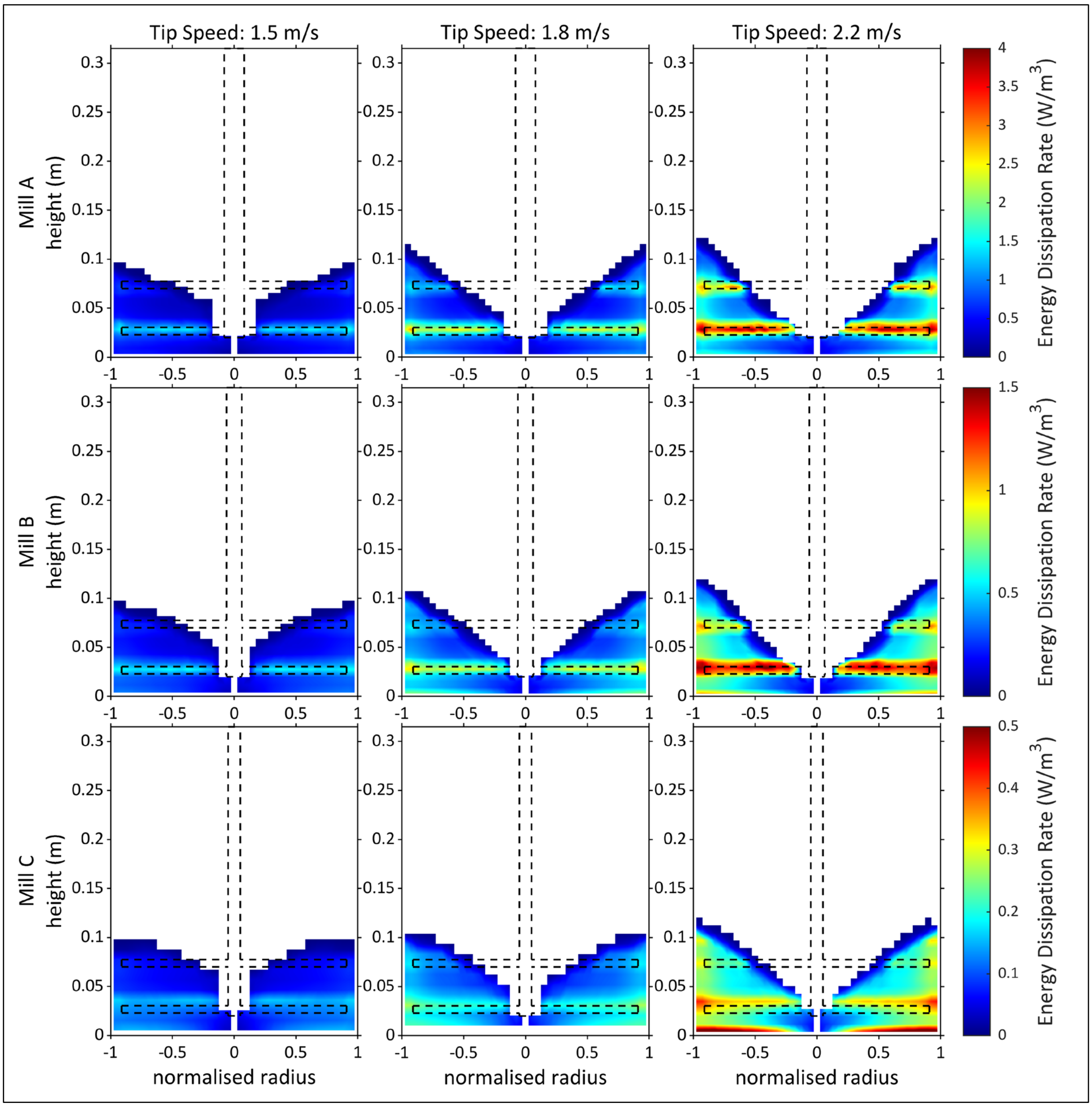

*Figure 8.20: Colourmaps of the spatial total energy dissipation rate of the collisions (W/m3 fluid) at each scale of simulated mill system at tip speeds of 1.5, 1.8 and 2.2 m/s, normalised along the radial axis*

### 8.3.2 Energy spectra

This section analyses the collision frequency and energy dissipation rate spectra as defined in section 6.5.2. Figure 8.21 and Figure 8.22 show a comparison across simulations with tip speed presented as rows and mill sizes as columns. The energy dissipation rate data is presented per volume of fluid.

The collision frequency spectra for the three mill sizes at the three tip speeds are shown in Figure 8.21. The spectra consist of the collision energy against the frequency per revolution, which is averaged over 5 revolutions of the data analysed. The frequency distributions are plotted on a logarithmic x-axis and linear y-axis so that the differences in collision energy can be observed. In addition to the total collisions, the frequencies of the different collision categories (media-media, media-impeller and media-shell) are shown. The media-media collisions have the largest contribution. Similar to what was observed in the collision frequency spatial distribution, Figure 8.18, the number of collisions decreases with increasing tip speed, across mill sizes.

The energy dissipation rate spectra of each mill size at the three tip speeds simulated are shown in Figure 8.22. These spectra consist of the collision energy against the intensive energy dissipation rate, for collisions from 5 revolutions. The total energy dissipation rate of the collisions is further represented through curves of its normal and shear (tangential) motion components. The energy dissipation rate spectra were analysed for each of the collision categories. An example is given for Mill A at 2.2 m/s in Figure 8.23. The distributions are presented on logarithmic axes. The curves show an increasing trend till a peak, followed by a sharp decline. The total dissipation rate curve closely follows the shear component curve, while the normal curve is significantly lower than the shear and total curves on its increasing section, with its modal peak shifted to the right. This indicates a lower modal peak normal energy dissipation rate at a higher normal collision energy than observed in the tangential component.

The modal peak energy dissipation rate and corresponding collision energy for the total energy dissipation rate spectra are indicated with horizontal and vertical lines in Figure 8.22, respectively. The collision energy that corresponds to the modal peak total energy dissipation rate has been used as a measure of central tendency within the spectra for comparison of collision energy across simulations (Cleary, Sinnott & Pereira, 2015). These values are plotted for all nine simulations as shown in Figure 8.24 for ease of comparison. The collision energy presented include error bars of its standard deviation for the 5 revolutions of the impeller. The full dataset is provided in Table E.3 in Appendix E.5.

At tips speeds of 1.5 and 1.8 m/s, no significant difference was observed in the modal peak dissipation rate for Mills A and B, but Mill C was lower. Additionally, Mill C has the lowest modal dissipation rate of mill sizes at 2.2 m/s. These observations for Mill C are consistent with the spatial energy dissipation rate, which showed that the intensive energy dissipation rate for this mill size is at a lower spectrum than the smaller mill sizes.

At 2.2 m/s, the modal peak dissipation rate for Mill A is significantly higher than what was observed at 1.5 and 1.8 m/s. Mill B has a lower modal peak dissipation rat than Mill A at 2.2 m/s. The increase in dissipation for Mill A is attributed to the significant increase in energy dissipation around the impeller arms observed in the energy dissipation rate spatial distribution (Figure 8.20). This can be correlated to the decrease in solids fraction in those regions observed in the spatial distributions in Figure 8.2.

At each tip speed simulated, the intensive corresponding collision energy is observed to decrease with increasing mill size. Each mill size shows increases in collision energy with increasing tip speed. It can be inferred that within the tip speed range simulated, the mills do not achieve high enough media velocities to show evidence of a maximum collision energy, theorised to occur at high tip speed post-fluidisation states (Yang et al., 2006; Jayasundara et al., 2010; Cleary, Sinnott & Pereira, 2015). The standard deviation of the collision energy data is observed to increase with tip speed and decrease with increasing mill size.

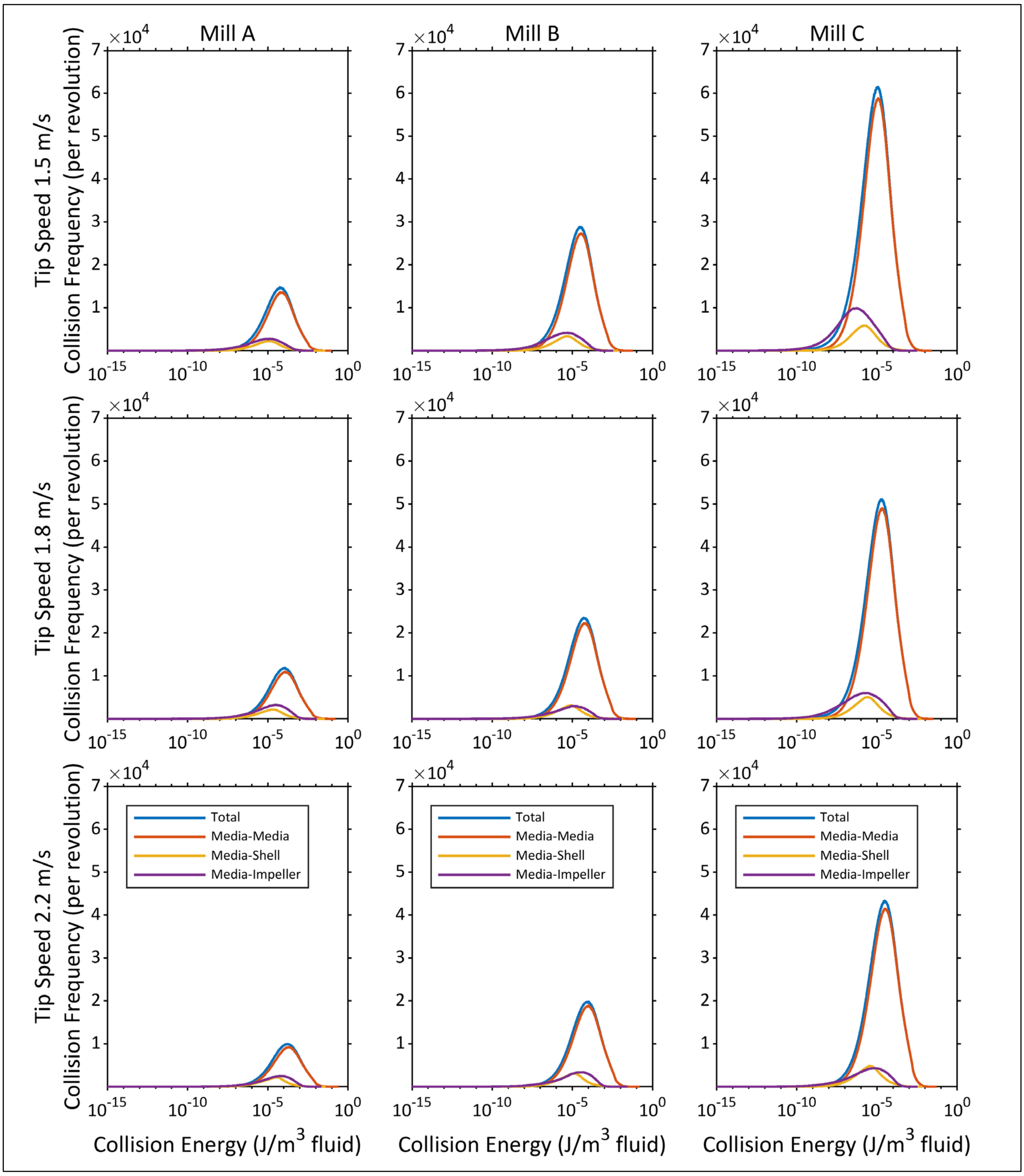

*Figure 8.21: Collision frequency per revolution against collision energy (J/m$^3$ fluid) plots for each scale of simulated mill system at tip speeds of 1.5, 1.8 and 2.2 m/s*

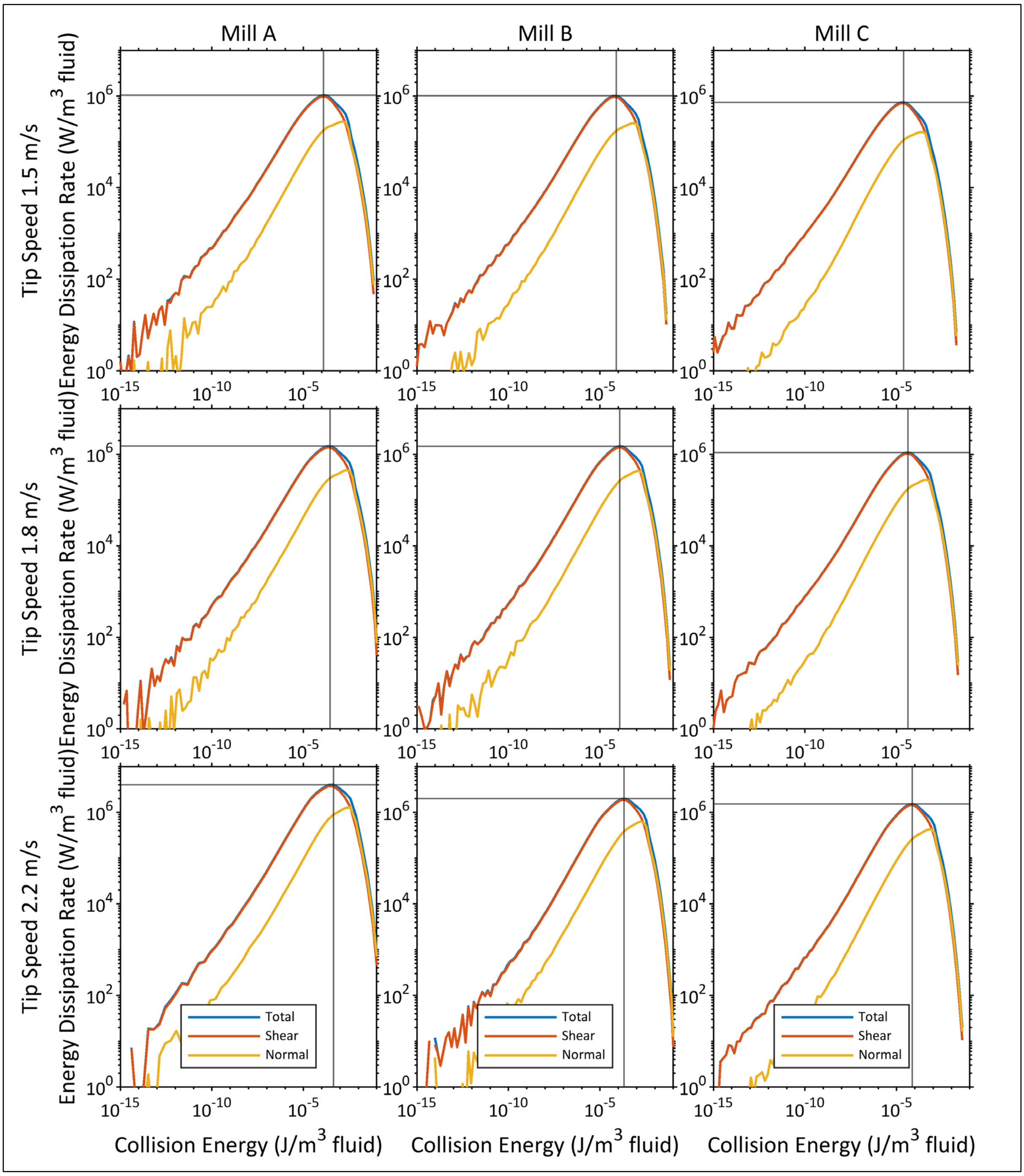

*Figure 8.22: Energy dissipation rate (W/m$^3$ fluid) against collision energy (J/m$^3$ fluid) plots for each scale of simulated mill system at tip speeds of 1.5, 1.8 and 2.2 m/s*

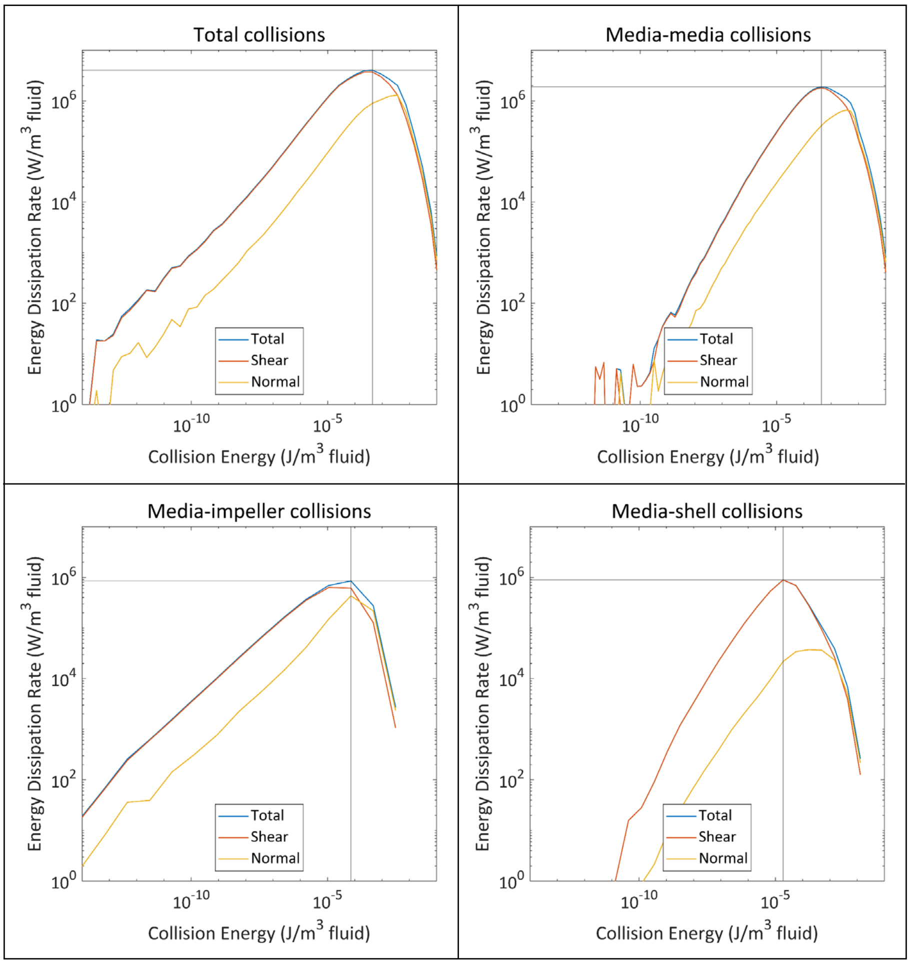

*Figure 8.23: Energy dissipation rate (W/m$^3$ fluid) against collision energy (J/m$^3$ fluid) by collision type for Mill A at 2.2 m/s tip speed*

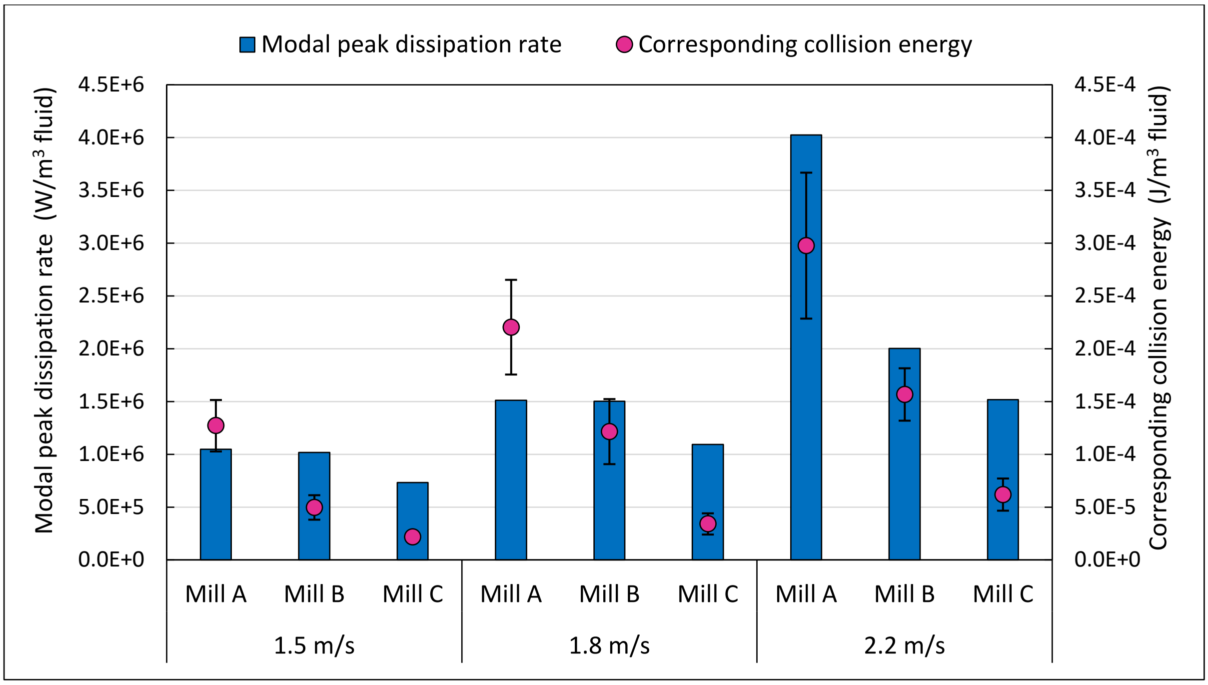

*Figure 8.24: Modal peak dissipation rate and the corresponding collision energy per m$^3$ of fluid for the three mill sizes at the three tip speeds*

### 8.3.3 Power draw

As defined in section 6.5.1 by equation (85), the total power draw is determined from the combined torque of DEM bodies and SPH particles on the impeller. The total power draw is presented in Figure 8.25. The proportion of the power draw attributed to either DEM or SPH was determined by averaging their percent contribution. The plotted data is tabulated in Table E.4 in Appendix E.5.

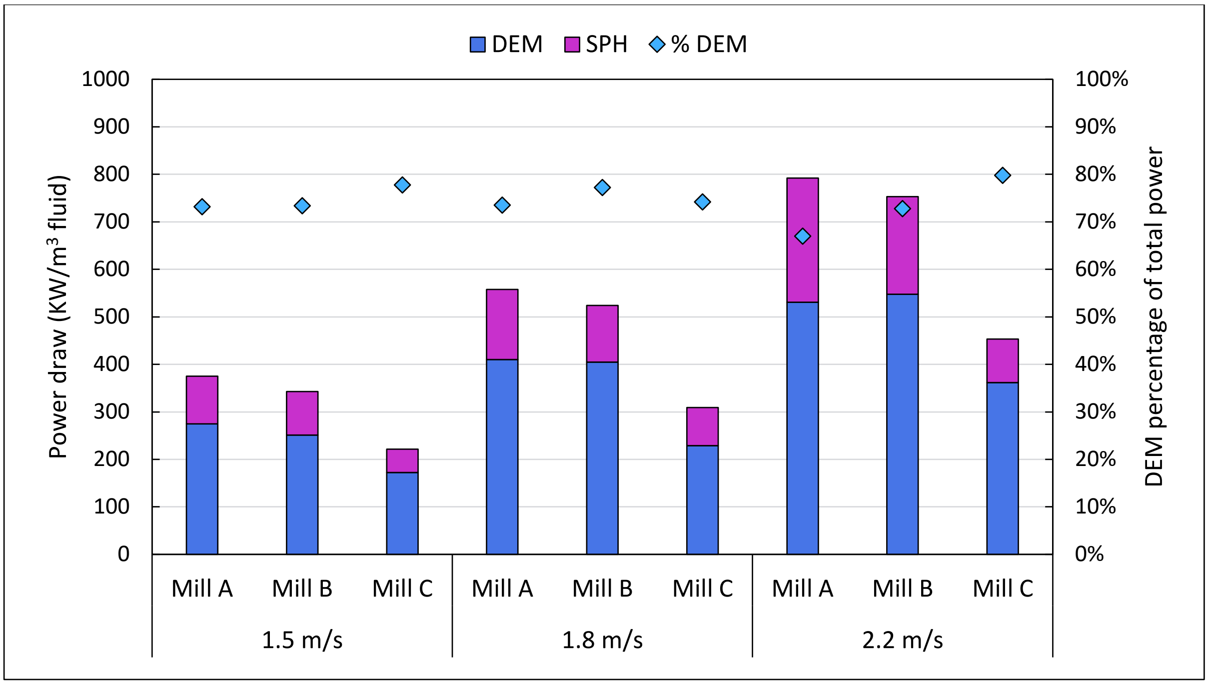

*Figure 8.25: Distribution of the total power draw to DEM bodies and SPH particles for the three mill sizes at the three simulated tip speeds*

Each mill size shows a positive non-linear increase in the total power draw with increasing tip speed. This trend has also been observed in a wet stirred mill by Jayasundara, Yang & Yu (2012). The DEM power draw for Mills A and B shows no significant difference at each tip speed simulated, while Mill C is consistently lower. This trend correlates to the observations made within the tangential velocity profiles for the area between the two impeller arms, where Mills A and B achieved similar velocities while Mill C had lower velocities. In all cases, the contribution from DEM is dominant and accounts for between 66 to 80 % of the total power draw, with SPH accounting for the remainder. This is similar to the observation made by Ndimande et al. (2019).

#### *8.3.3.1 Dry DEM comparison*

Simulations were performed on the three mill sizes using DEM only at a tip speed of 2.2 m/s. The power draw was extracted and compared against what was obtained in the DEM-SPH simulation as shown in Figure 8.26 . The dry power draw is divided by the fluid volume for ease of comparison. The complete dataset is tabulated in Table E.5 in Appendix E.5. The comparison of the power draw from the dry simulation and the total power draw from the DEM-SPH simulation and the DEM component of the DEM-SPH simulation shows that the addition of the fluid model results in increased power draw. The comparison between the dry DEM only and wet DEM contribution is significant in that it is only through the collisions of the DEM bodies that breakage is induced.

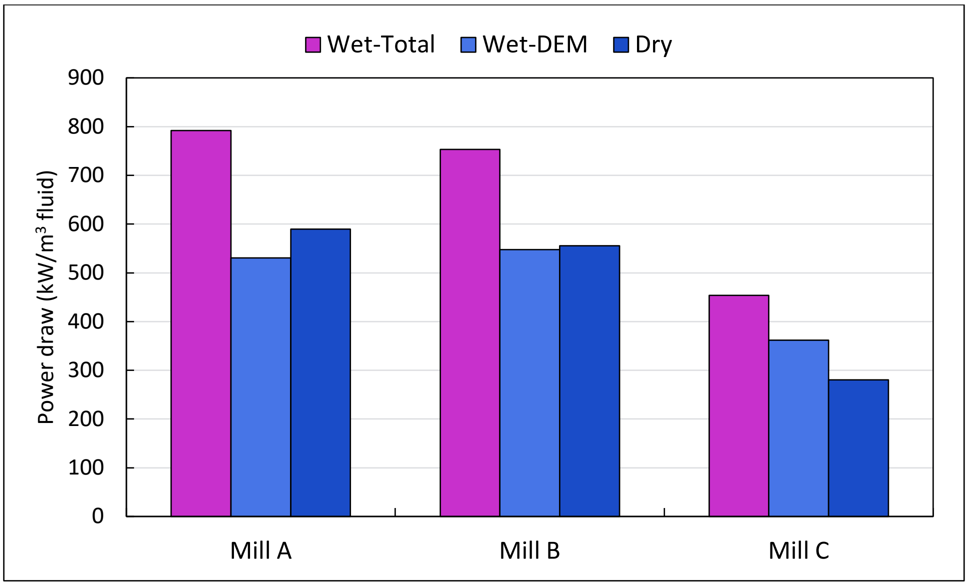

*Figure 8.26: Power draw comparison between wet and dry simulations*

## 8.4 Scale-up assessment

Scale up effects on the laboratory stirred mill system were evaluated at three tip speeds. The resulting flow and energy environments have been assessed separately. The mill performance was evaluated spatially and then reduced to key single value parameters. The key parameters from both the flow and energy environments are summarised in Table 8.1.

Within the flow environment, the mean of the media velocity distribution and the medians of the spatial distributions of the Froude and Reynolds numbers were the key parameters used. The mean velocity consistently showed a decreasing trend with increasing mill size for each tip speed evaluated. Noticeably, Mills A and B have a smaller difference than Mills B and C. The median Froude and Reynolds numbers divert from this as they observe Mill B peaking at 1.5 and 2.2 m/s. Within the spatial distributions, it was observed that the mean of the relative velocity of Mill A experienced inconsistencies over time, beyond those observed in Mills B and C as shown in Figure E.9. This observation combined with the comparable media velocity distributions of Mills A and B results in the median dimensionless quantities of Mill B peaking over Mill A, as both dimensionless numbers are dependent on the relative velocity. Determining the dimensionless quantities at a media body level, instead of as a bulk mesh could improve the accuracy of this calculation.

*Table 8.1: Average media velocity, median Froude number, median Reynolds number, intensive modal peak dissipation rate and intensive collision energy of the tip speed DEM-SPH simulations*

| | | Mean Velocity (m/s) | Median Froude Number | Mean Reynolds Number | Modal Peak Dissipation Rate ($\times 10^6$ W/ m$^3$) | Collision Energy ($\times 10^{-4}$ J/m$^3$) |
|---|---|---|---|---|---|---|
| 1.5 m/s | Mill A | 0.46 | 0.043 | 27 | 1.05 | 1.27 |
| | Mill B | 0.44 | 0.053 | 34 | 1.02 | 0.50 |
| | Mill C | 0.35 | 0.036 | 23 | 0.73 | 0.22 |
| 1.8 m/s | Mill A | 0.60 | 0.077 | 50 | 1.51 | 2.20 |
| | Mill B | 0.59 | 0.071 | 45 | 1.50 | 1.22 |
| | Mill C | 0.51 | 0.042 | 28 | 1.09 | 0.34 |
| 2.2 m/s | Mill A | 0.73 | 0.055 | 36 | 4.03 | 2.98 |
| | Mill B | 0.68 | 0.074 | 48 | 2.00 | 1.57 |
| | Mill C | 0.65 | 0.047 | 30 | 1.52 | 0.62 |

The intensive modal peak energy dissipation rate and collision energy were used to characterise the scale up response of the energy environment. These values were provided per the initial volume of slurry in each mill size. The modal peak dissipation rate and collision energy decreased consistently with increasing mill size. The collision energy decreased consistently, however at 1.5 and 1.8 m/s, only slight decreases in the modal peak dissipation rate were observed from Mill A to Mill B, similar to the mean velocity. Within this tip speed study, the mean velocity and the modal peak dissipation rate both provide insight on the mill's ability to convert its energy input. The mean velocity, compared against the tip speed, is a measure of the mill's ability to propagate energy from the impeller that results in media velocity, while the modal peak dissipation rate informs on the bulk dissipation of that energy through collisions.

The overview of how the scale up trends in the three different mill sizes are captured by the single value parameters shows the complex nature of the flow and energy environments in the mill space. The overall mill space would best be described by a combination of three single value parameters that describe critical influences on the mill performance. The trends in the median Froude number, collision energy, and the mean velocity or modal peak dissipation rate could provide a complete overview of the mill performance. The Froude number, as a stable dimensionless quantity, describes the bulk fluidisation state of the mill. The collision energy provides insight on the breakage capability of the mill. The mean velocity or modal peak dissipation rate inform on the energy conversion within the mill.

# CHAPTER 9

# Results and discussion: Scale-up media shape simulations

## 9.1 Introduction

This chapter contains the results and discussions of the scale-up simulations designed to investigate the effect of media shape on the stirred mill space and scale-up characteristics of the three laboratory scale SMD's, using super quadric media. The simulations investigated follow from the simulation plan given in section 6.7.2.2. Three groups of super quadric media of decreasing roundness (increasing angularity) are simulated in each of the three mill sizes at a 1.8 m/s tip speed. The super quadric media groups are as described in section 6.3.3 and referred to as Group 1, Group 2 and Group 3, in order of increasing angularity. Additionally, 5 dry DEM simulations of each mill size with Group 3 super quadrics, and of Group 1 and 2 super quadrics in the smallest mill size, Mill A, were performed to compare against the wet simulations. Direct comparison to the spherical media simulations is limited to the flow environment because the reduction in the Young's Moduli required for stability and computational efficiency in the super quadric simulations alters the reference point of the collision/energy environments from the spherical simulations. All simulations considered in this chapter operate at a 1.8 m/s impeller tip speed. All DEM-SPH simulations are filled to the height of the top impeller at a 50:50 media to slurry volume ratio as per the quantities stated in Table 6.5. All dry DEM simulations use the same quantity of media as their wet counterparts. The relevant physical and interaction parameters for the simulations are as presented in section 6.3.2.

The chapter continues with the analytical approach used in CHAPTER 8 in assessing the media shape parameter effect on the three mill sizes. This was done through the evaluation of single-value parameters as a comparative representation of the bulk mill space. Similarly, the results are presented and discussed in three sections. It begins with an assessment of phase, velocity, and dimensionless number distributions within the flow environment. This is followed by analysis of the energy environment focused on spatial distributions, energy spectra and power draw. The chapter concludes with an overall assessment of the scale up effects observed.

## 9.2 Flow environment

The nine DEM-SPH simulations are used to discuss the effect of changing the media shape on the mill space across mill sizes. The three groups of super quadric media were simulated in each of the three mill sizes. The difference in the media shapes of each super quadric group is visible in the snapshots of each simulation shown in Figure 9.1, with the media bodies coloured by its velocity and the fluid free surface shown at 60% opacity. The snapshots show high velocity media bodies surrounding the impeller tips of each mill. There is a visible increase in the number of low velocity, blue coloured media bodies with the increasing angularity across the super quadric groups. These bodies increase in prominence around the mill base and at the edge of the impeller wake.

The flow environment of these simulations is discussed in three sections. Firstly, phase distributions are used to establish the bulk media and fluid locations within the mill space. The response of the velocity distributions to the super quadric groups is then assessed. Lastly, the dimensionless number distributions are considered and reduced to single-value parameters.

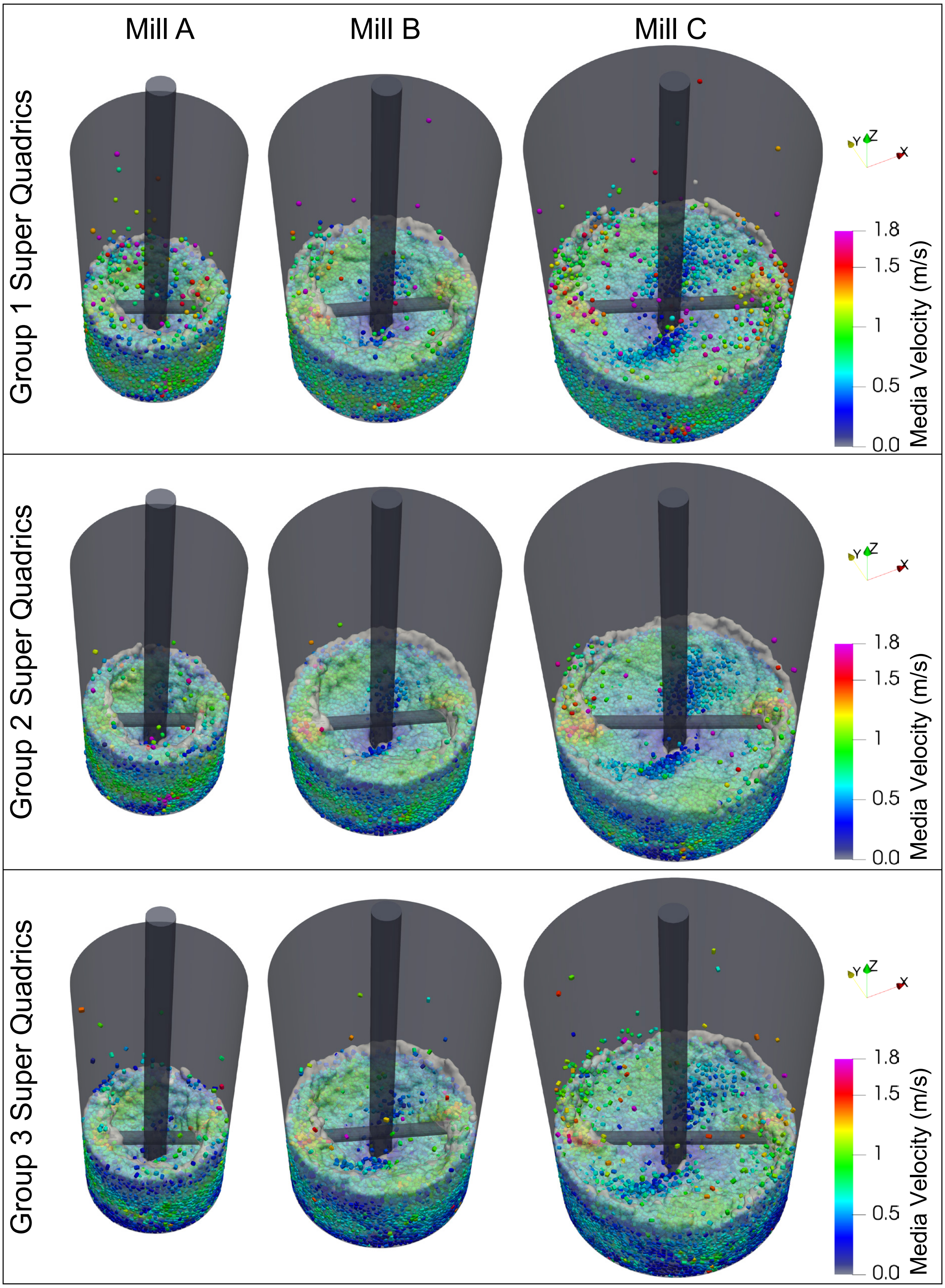

*Figure 9.1: Snapshot of the DEM-SPH stirred mills simulated with each of the super quadric media groups*

### 9.2.1 Phase distributions

The bulk distributions of solids fraction and relative density of the nine DEM-SPH simulations and the three spherical media DEM-SPH simulations at 1.8 m/s are visualised in 2D colormaps of the azimuthally averaged mill space, shown in Figure 9.2 and Figure 9.3, respectively. Considering the solids fraction colour maps in Figure 9.2, the distribution of the bulk solids fraction of Group 1 super quadrics is similar that of the spherical media simulations at 1.8 m/s, but with greater compaction observed around the bottom impeller arm for mills A and B, indicated by an increased solids fraction across the length of impeller arm. As the super quadrics increase in angularity, increased compaction is observed towards the base of the mill visible as a deep red coloured band for the Group 2 and 3 super quadrics. The compaction is further observed through the decrease in the size of the media dominant areas above the impeller, specifically observed for Mill A, as the media angularity increases across the super quadric groups. Across mill sizes, the packing is consistently tighter as the mill increases at the constant tip speed, as observed in the spherical simulations, and a deepening and spreading of the red colour high solids fraction regions, visible along the central cavity.

The spatial distribution of the bulk relative density of the DEM-SPH simulations in Figure 9.3 shows a fluid dense layer above the top impeller for each simulation, visualized through a deep red colouring. The fluid dense layer becomes more pronounced moving from Group 1 towards Group 3 super quadrics across mill sizes. This fluid layer stretches downwards, below the top impeller and towards the base of the central cavity. This corresponds with the compaction of the media, reducing the size of voids at the walls and base of the mill, forcing the fluid upwards towards the central cavity. However, the volume occupied by the dense fluid decreases with increase in the mill diameter. This change is more visible for Group 1 and 2 super quadrics in Mill A and Mill C.

Within the computational framework, the solids fraction is a SPH particle specific variable, and therefore its accuracy is limited by the resolution of the fluid. As the media packing capability gets tighter, the voids in the system get smaller, therefore requiring smaller fluid particles to properly characterize the solids fraction in those tight packed regions. However, the resolution was kept constant across these DEM-SPH simulations. Looking at the solids fraction distribution in Figure 9.4, this could be a limiting factor for the simulations of Group 2 and Group 3 super quadrics in Mill C, as this mill experienced a generally tighter packing. To provide more insight into the media shape effects, comparison against the dry simulations is used here and in further sections to evaluate the media shape effects in systems without the fluid which should result in an overall tighter packing. This should allow conclusions to be drawn on the dominant media shape effects in the mill space.

The dry systems are expected to have higher solids concentrations at the base of the mill, because of the absence of the fluid phase. A comparison of the wet DEM-SPH to the 5 dry DEM simulations is made throughout this chapter to observe their flow and energy environment to assess if the observations made for the wet system are consistent with dry systems. If the overall observed trends are consistent between the tighter packed dry simulations and the wet systems that may have a higher solids fraction at a lower fluid resolution, the trends can be substantiated. The dry simulations are assessed in two sets of three. The first set considers dry simulations of each of the three mill sizes with Group 3 super quadrics, to investigate the systems with the highest compaction capabilities, visualised in Figure 9.5. The second set consists of three dry simulations of Mill A with each of the three super quadric groups, visualised in Figure 9.7. It follows that the dry simulation of Mill A with group 3 super quadrics is assessed in each set of dry simulations.

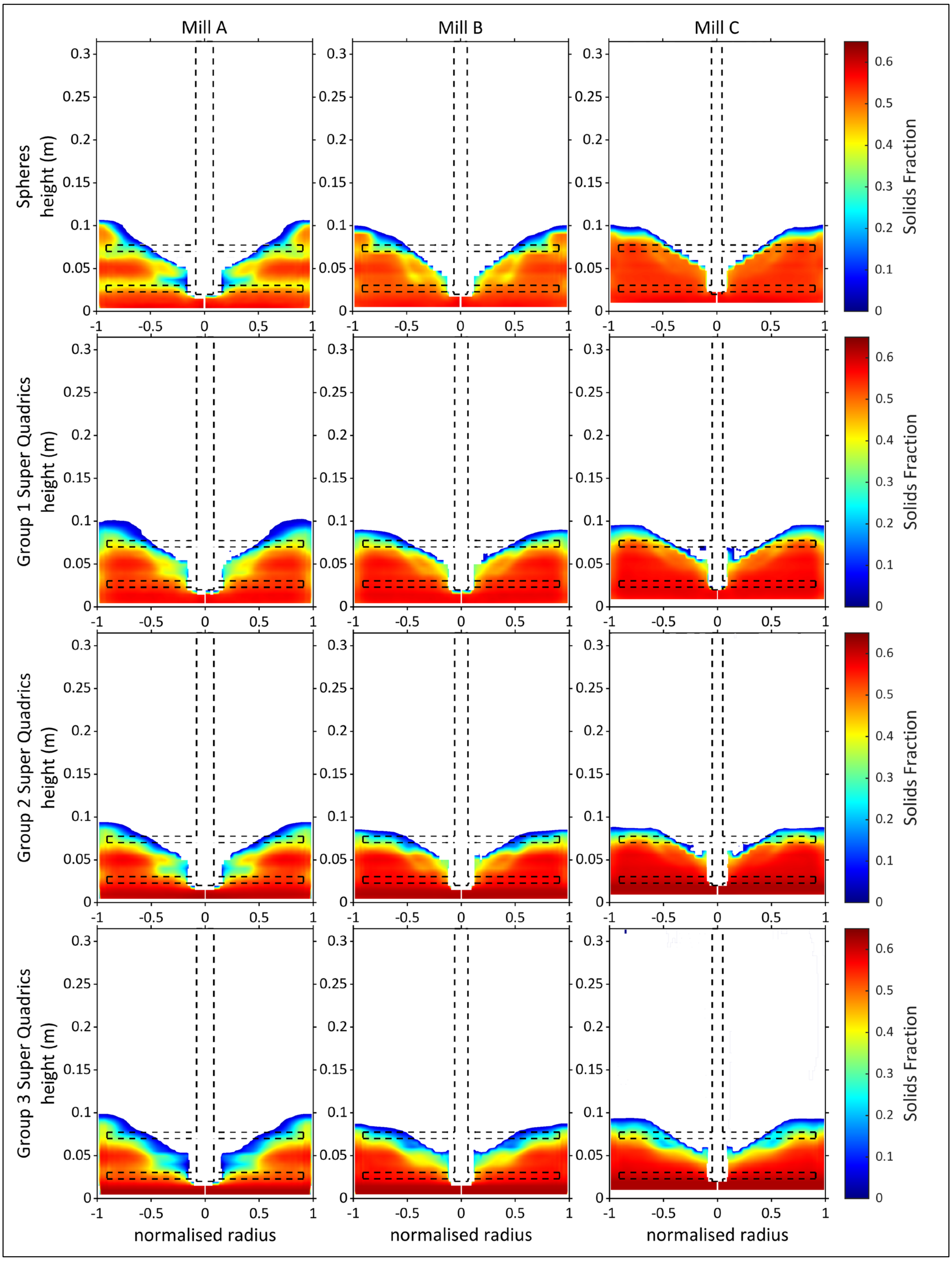

*Figure 9.2: Colourmaps of the bulk solids fraction for the DEM-SPH media shape simulations, arrayed such that the rows show the media groups and the columns show the three mill sizes*

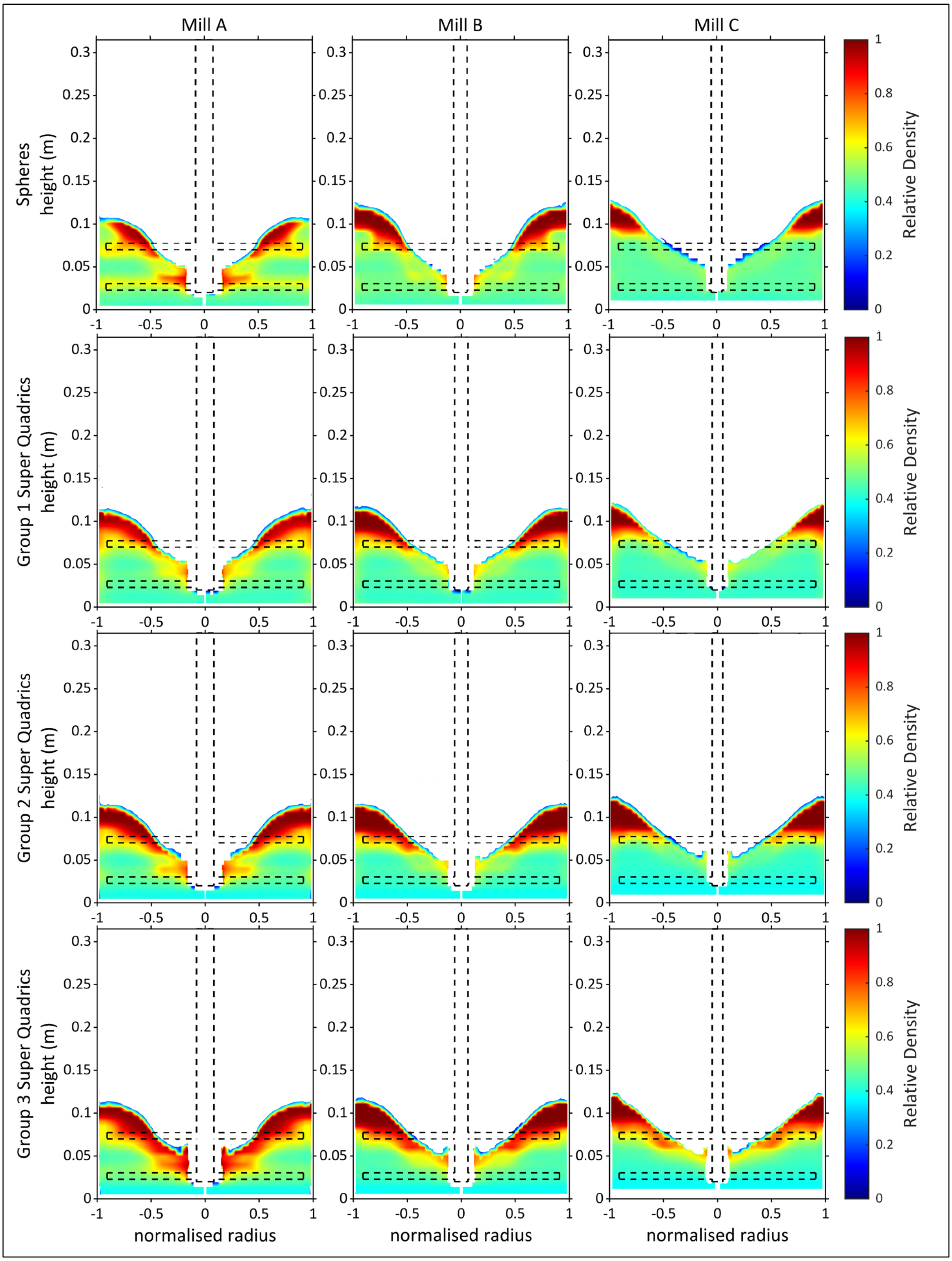

*Figure 9.3: Colourmaps of the bulk relative density for the DEM-SPH media shape simulations, arrayed such that the rows show the media groups and the columns show the three mill sizes*

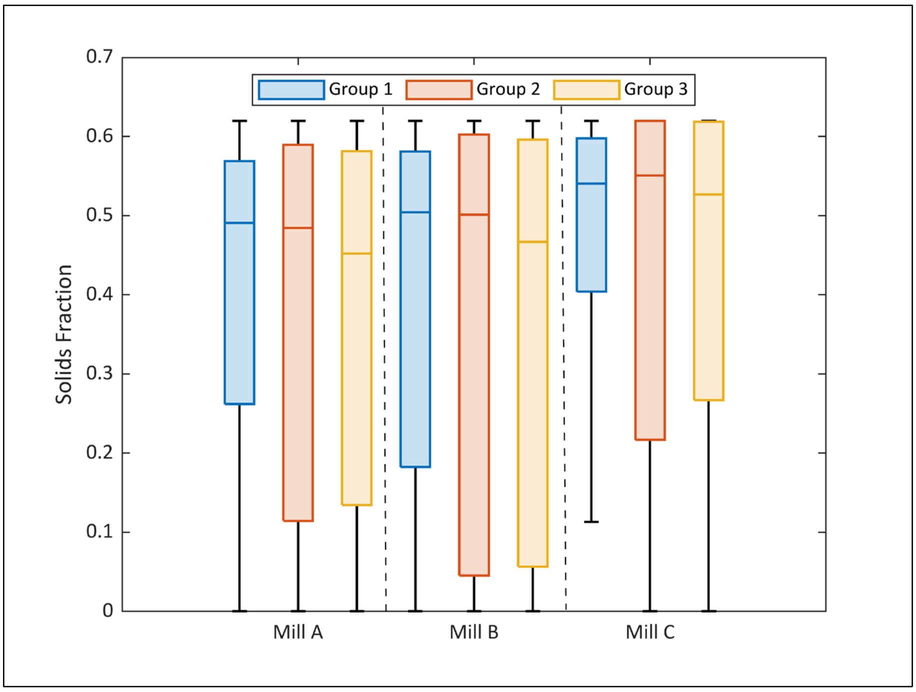

*Figure 9.4: Solids fraction box and whisker plots for all three mill sizes with all three groups of super quadrics.*

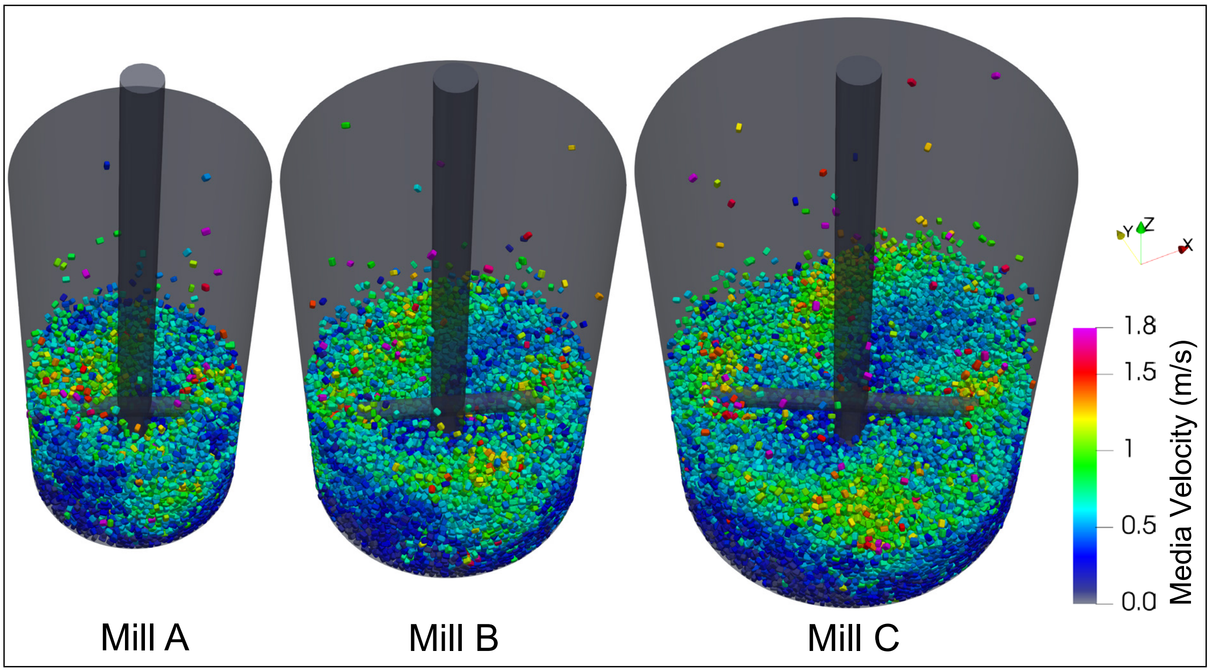

*Figure 9.5: Snapshots of all sizes of dry mill simulations with Group 3 super quadrics*

The solids fraction for the dry simulations was approximated as the ratio of the media occupancy over the five revolutions examined, and the volume of the half cylindrical or half-annular volumetric cells occupied multiplied by the number of timesteps examined. The resulting bulk spatial solids fractions are shown in Figure 9.6, for all the mill sizes with Group 3 super quadrics, and in Figure 9.8, for Mill A simulations with all super quadric groups. The Group 3 simulations of the mill space (Figure 9.6) show a distinctly compact region at the base of the mill, under the bottom impeller. This region experiences solids fractions of approximately 0.6-0.8, which is significantly higher than what was observed in their wet counterparts. The bulk regions above the bottom impeller experience a lower solids fraction ranging from 0.3 – 0.6 which is similar to the solids fraction in the wet simulations.

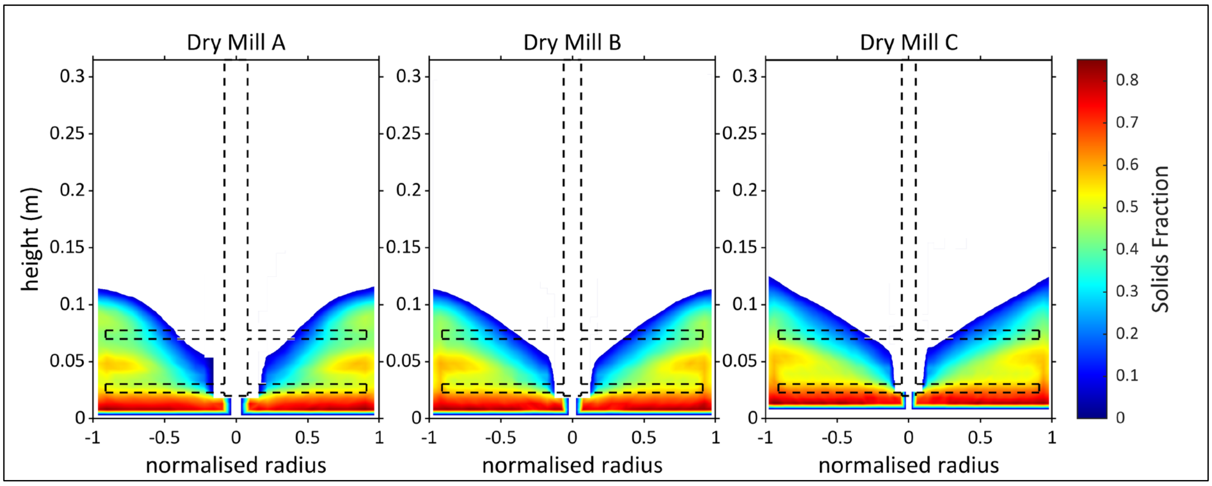

*Figure 9.6: Occupancy based bulk solids fraction spatial distribution colormaps for all mill sizes with Group 3 super quadrics*

Considering all media shape groups in dry simulations of Mill A (Figure 9.8), the compacting of the region below the bottom impeller is visible as the region darkens with increased angularity. The bulk distribution of the solids fraction in the mill with Group 1 super quadrics shows an even distribution above and below the bottom impeller, similar to its dry counterpart. The Group 2 system shows an increase in the solids fraction above 0.6 in the region below the bottom impeller, which increases above 0.7 in the Group 3 simulations. Concurrently, the solids fraction of the region above the bottom impeller decreases with increased angularity.

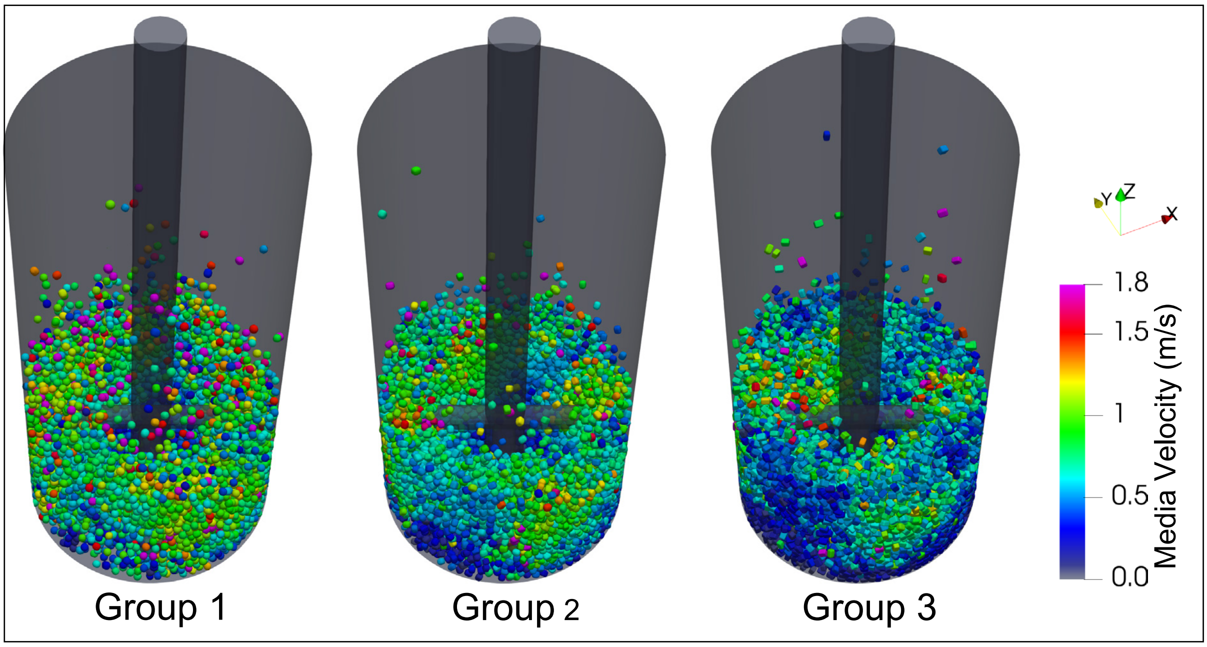

*Figure 9.7: Snapshots of the dry Mill A simulations at each super quadric media group*

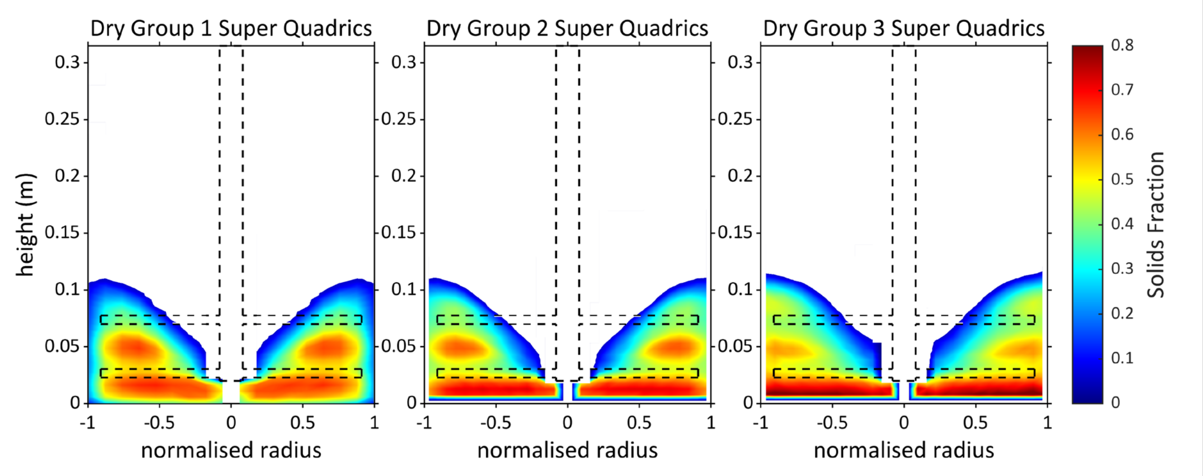

*Figure 9.8: Occupancy based bulk solids fraction spatial distribution colourmaps for dry Mill C at all super quadric groups*

### 9.2.2 Velocity distributions

The bulk spatial velocity distributions of the DEM-SPH super quadric media simulations are shown in Figure 9.9, along with the distributions of the spherical media simulations at 1.8 m/s. The bulk regions of high velocity are generally found in the regions between the impeller pins, towards the wall for all mill sizes and media shapes. The largest region of high intensity and the highest bulk velocities are seen in Mill A with Group 1 super quadrics. This region decreases in intensity and size as the mill size increases. The decrease in intensity is visible by the colour changing from very hot red colours to cooler yellow-blue colours, while the size decrease is observed as the region of high intensity retreats upwards, away from the bottom impeller. This reduction in size and intensity is also observed as the super quadric groups become more angular for each mill size. This is consistent with the decreased media velocity with increasing angularity observed in the super quadric Tower Mill simulations of Sinnott, Cleary & Morrison (2011b).

Figure 9.10 shows the spatial distribution of the bulk fluid velocity in the DEM-SPH super quadric simulations and the spherical media simulations at 1.8 m/s. Similar to the spherical simulations, the fluid in the super quadric simulations had higher bulk velocities than the media. The bulk velocities for Mills A and B can be characterised into two high intensity regions, one around each impeller tip. These regions are not pronounced for Mill C, which has its highest intensity region around the fluid free surface, above the top impeller and around the tip of the top impeller. Its bottom impeller region experiences a distinctly lower intensity compared to the top impeller. The fluid velocity intensity is low at the mill base in all mill sizes. The observations made are consistent across all media shapes with the intensity diminishing as the media become more angular.

To further evaluate the media and fluid velocity distributions, box and whisker plots of the media and fluid velocity are shown in Figure 9.11 and Figure 9.12, respectively. The box plots show the distributions of the velocity of the individual media bodies across the five revolutions assessed. With increasing mill size, the range of the media distributions decreases. The median of these distributions decreases with increasing media angularity for each mill size (Figure 9.11). Considering the fluid distributions (Figure 9.12), which are representative of the velocity distribution of the individual fluid particles across the five revolutions, the decrease in the distribution median with increasing angularity is less pronounced compared to what was observed for the media. The insignificant shift in the median for the distributions shows that the bulk fluid velocity distributions do not change much for the different media angularities, particularly in Mill A.

The spatial distributions of media velocity for the 5 dry DEM simulations were investigated to assess the media velocity at tighter packings. The media velocity spatial distributions of all the mill sizes with Group 3 super quadrics are shown in Figure 9.13. The media velocity distribution is similarly to what was observed for the DEM-SPH Group 3 simulations (Figure 9.9, row three). The main distinction is that there is a greater reduction in velocity from the bottom impeller arm to the mill base. This can be attributed to the tighter packing in this area making it harder for the bodies to maintain high velocities. Figure 9.14 shows the bulk media velocity for the dry Mill A simulations of each media shape group. Similar to their DEM-SPH counterparts (Figure 9.9, column one), the media velocity intensity decreases as the angularity of the media increases. However, higher velocities are observed in their high intensity regions than in the DEM-SPH simulations.

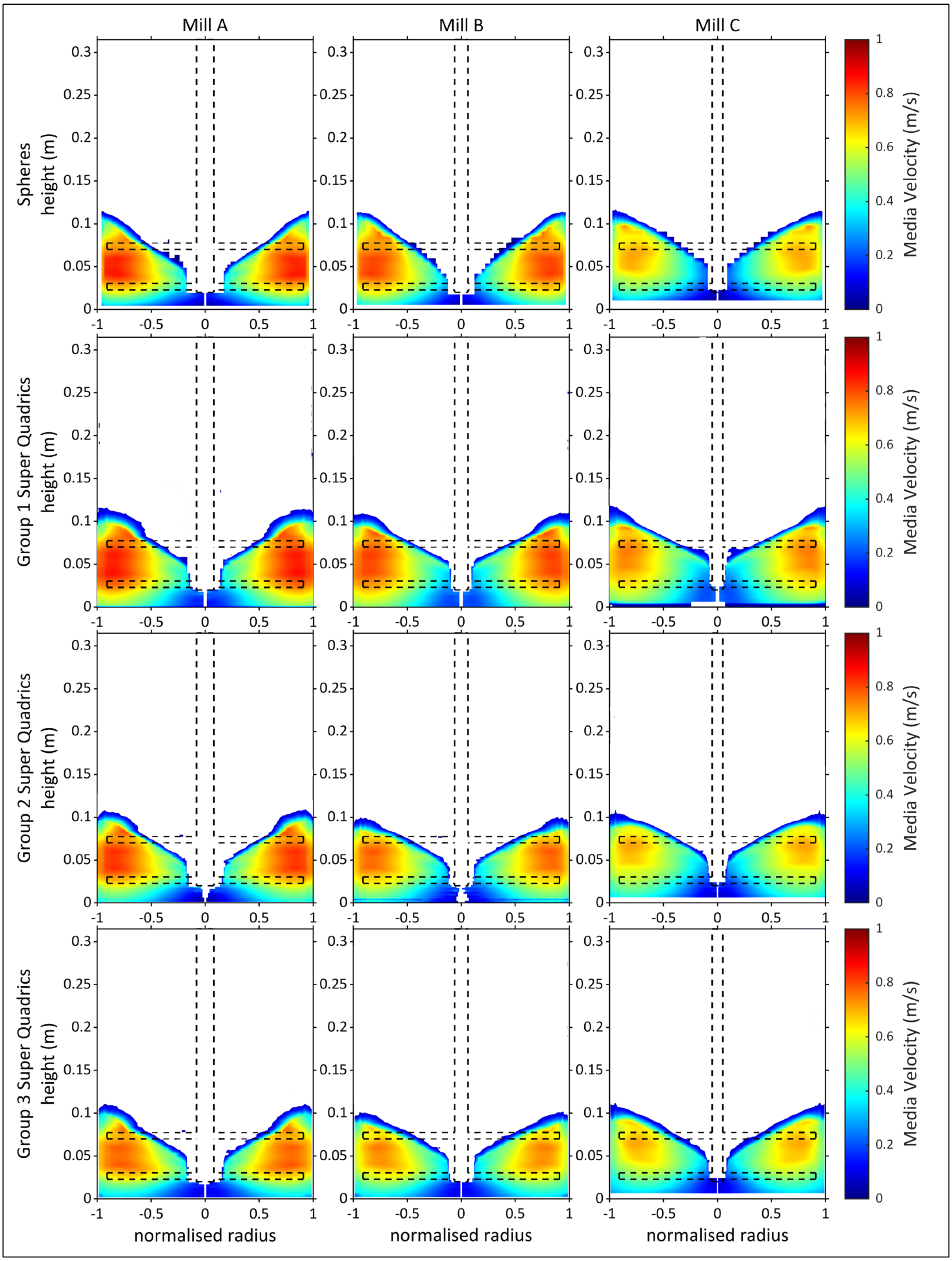

*Figure 9.9: Colourmaps of the bulk media velocity for the DEM-SPH simulations, arrayed such that the rows show the spherical simulations and three super quadric media groups and the columns show the three mill sizes, all simulated at 1.8 m/s tip speed*

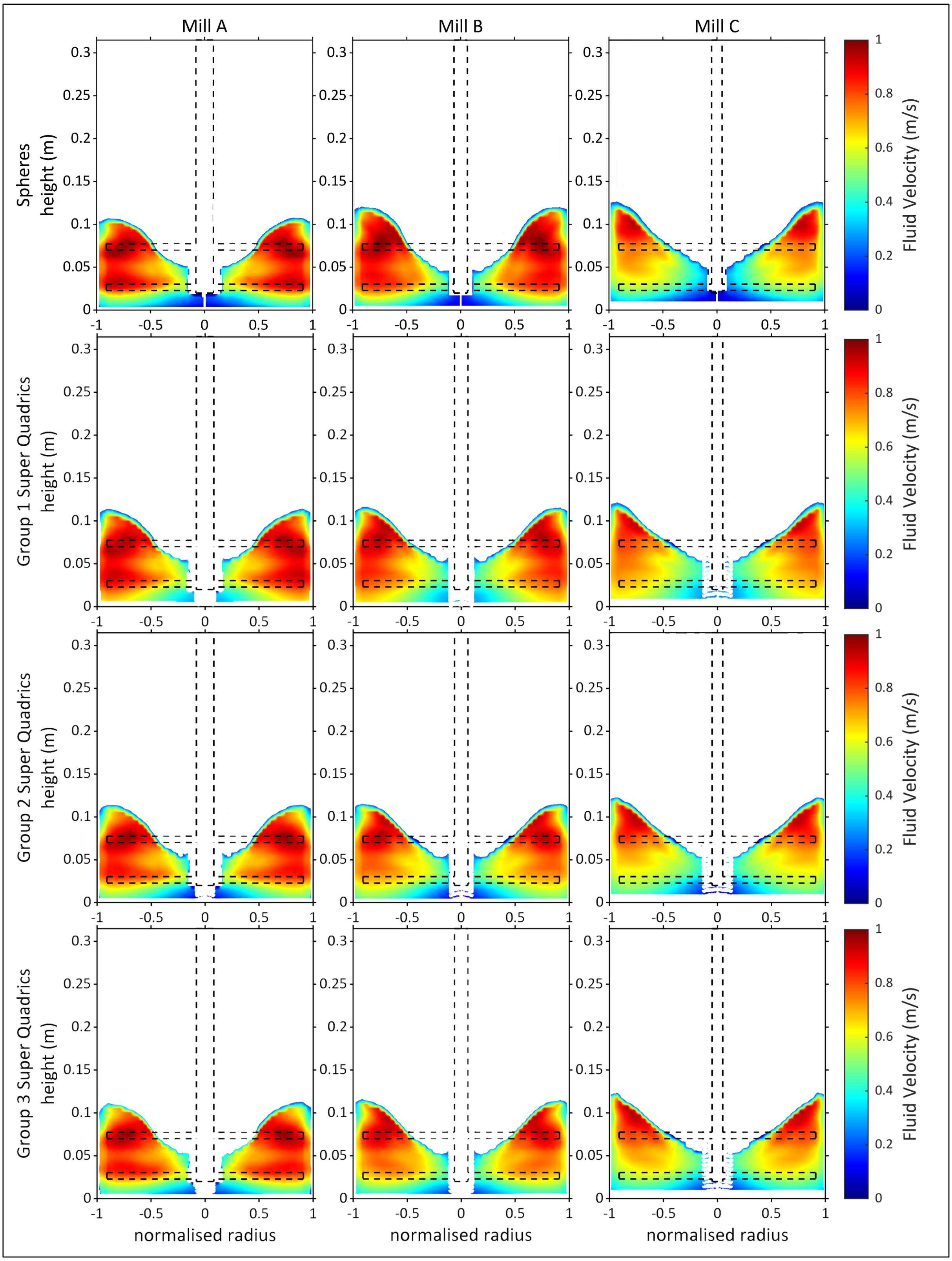

*Figure 9.10: Colourmaps of the bulk fluid velocity for the DEM-SPH media shape simulations, arrayed such that the rows show the three super quadric media groups and the columns show the three mill sizes*

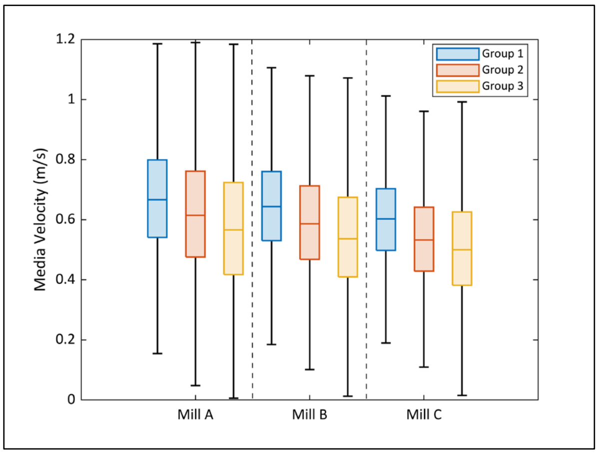

*Figure 9.11: Media velocity box and whisker plots*

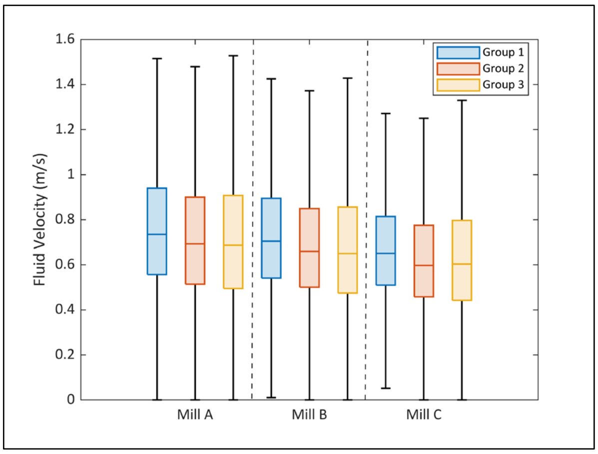

*Figure 9.12: Fluid velocity box and whisker plots*

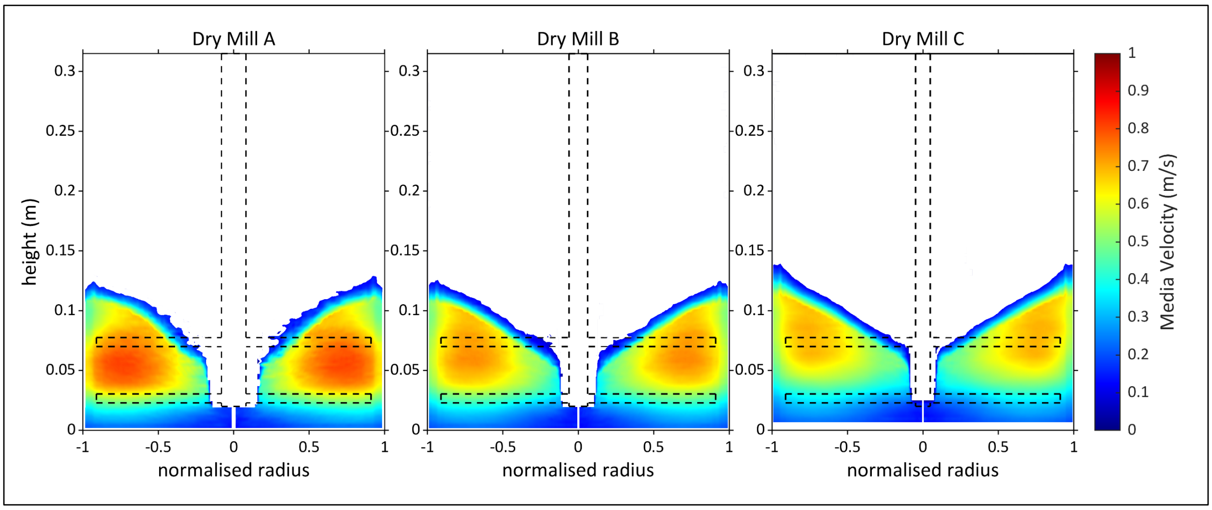

*Figure 9.13: Media velocity colourmaps for dry DEM simulations of each mill size with group 3 super quadrics*

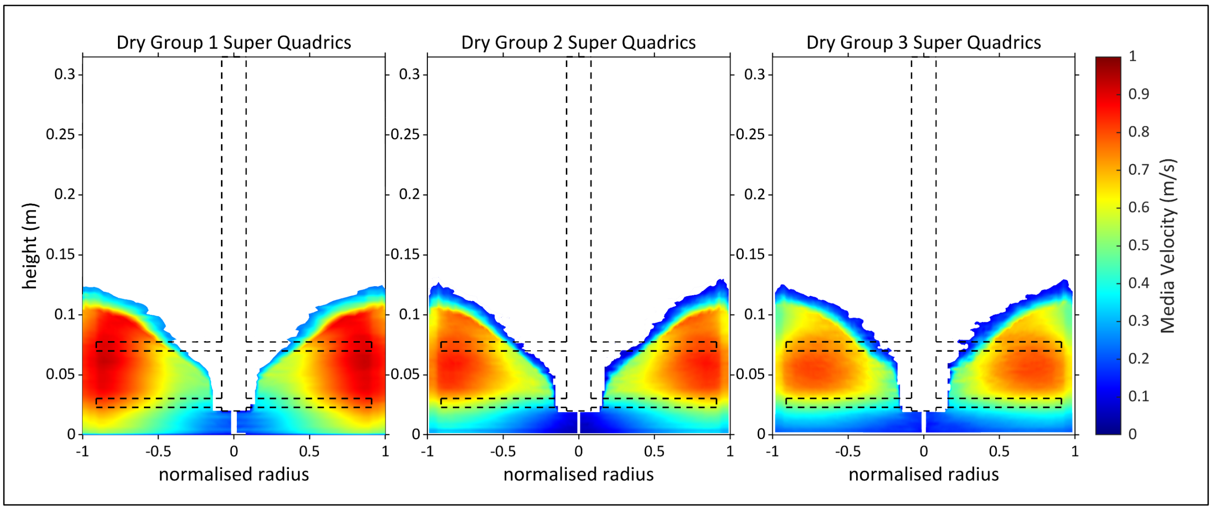

*Figure 9.14: Media velocity colourmaps for dry Mill A simulations of group 1, 2 and 3 super quadrics*

The box plots of the media velocity distribution for the dry simulations are shown in Figure 9.15 and Figure 9.16. The media velocity range across the dry simulations is significantly larger than the DEM-SPH simulations. This corresponds to the higher bulk intensities observed in their spatial distributions.

To further characterize the distributions, the mean media velocity of each of the 9 DEM-SPH simulations and the 5 dry DEM simulations is plotted in Figure 9.17. Similar to their medians, the mean velocities decrease with increasing mill size for both wet and dry systems, across the super quadric groups simulated. The dry Group 3 simulations have a consistently lower mean velocity than the wet Group 3 simulations, even though they experience higher bulk intensities, due to the low velocities experienced at the mill base. From its flow environment, the dry system with Group 3 super quadrics can be characterized as having two distinct regions, dividing the mill into a top and bottom section at a variable height. The top region is characterized by higher intensity speeds and less dense packing. The bottom region is characterized by a significantly tighter packing, causing lower velocities. Compared against the wet systems, the distinction between the regions is sharper in the dry systems. This is evident in their solids fraction distributions and the media velocity box plots, that show that the dry systems have a larger velocity range than the wet systems, but a lower mean value.

This differs for dry Mill A simulations, where the mean velocity is significantly higher than the wet simulations for Group 1 super quadrics, then slightly below for Group 2, and significantly lower for Group 3. Considering the spatial distributions of Mill A in the dry Group 1 simulations (Figure 9.14), the bulk velocities around the mill base and the bottom impeller are greater than observed in the wet simulations, resulting in this increased mean velocity. The dry and wet Group 2 spatial velocity distributions of Mill A have similar intensities throughout the bulk mill space. Considering Mill A's dry and wet Group 3 systems, the fluid in the wet system dampens the velocities in the better fluidised top region of the mill compared to the dry system. However, the tighter packing capabilities of the more angular Group 3 media, without fluid to dilate the media bed decrease velocities in the poorer fluidised bottom region of the mill, resulting in the dry system having lower mean velocities than the wet system.

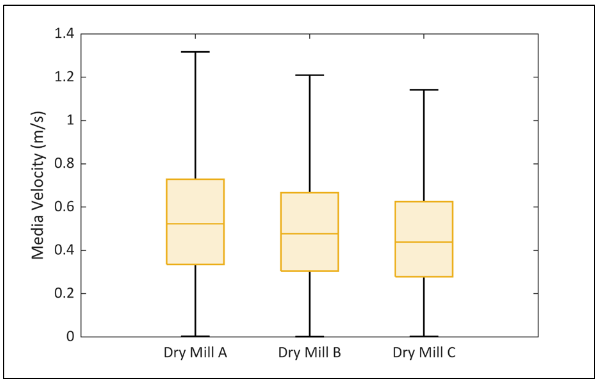

*Figure 9.15: Dry DEM media velocity box plots for group 3 super quadrics*

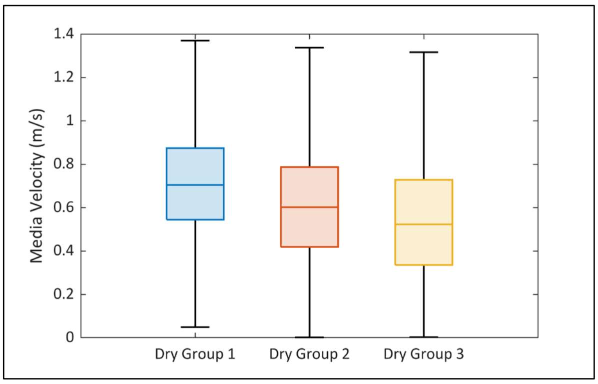

*Figure 9.16: Dry Mill A media velocity box and whisker plots for all groups of super quadrics*

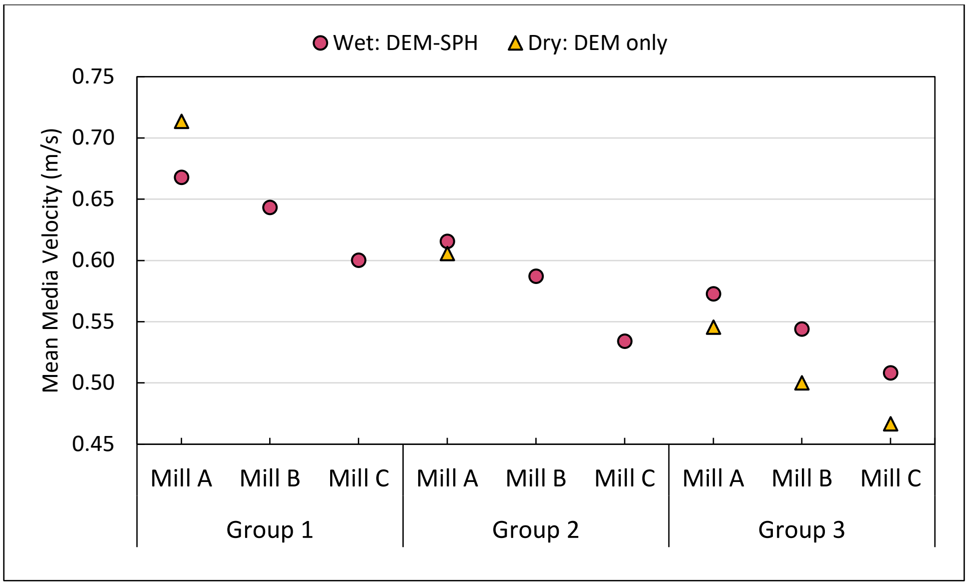

*Figure 9.17: Mean media velocity for DEM-SPH and DEM only mill simulations at each super quadric group*

### 9.2.3 Dimensionless numbers

The Reynolds and Froude number distributions were examined for the nine DEM-SPH simulations to gain some insight on the ratio of inertial forces to the viscous forces and the gravitational forces, respectively, within the bulk mill space. These quantities are determined based on equation (2) for the Froude number and equation (3) for the Reynolds number. For these systems of super quadric bodies, the same characteristic length is used in both calculations, the diameter of their volume equivalent sphere, 5 mm.

The spatial distribution of the Reynolds and Froude numbers in the bulk mill space were approximated from the spatial distributions of the flow environment variables. Figure 9.18 and Figure 9.19 show the bulk spatial distributions of the Reynolds and Froude numbers, respectively.

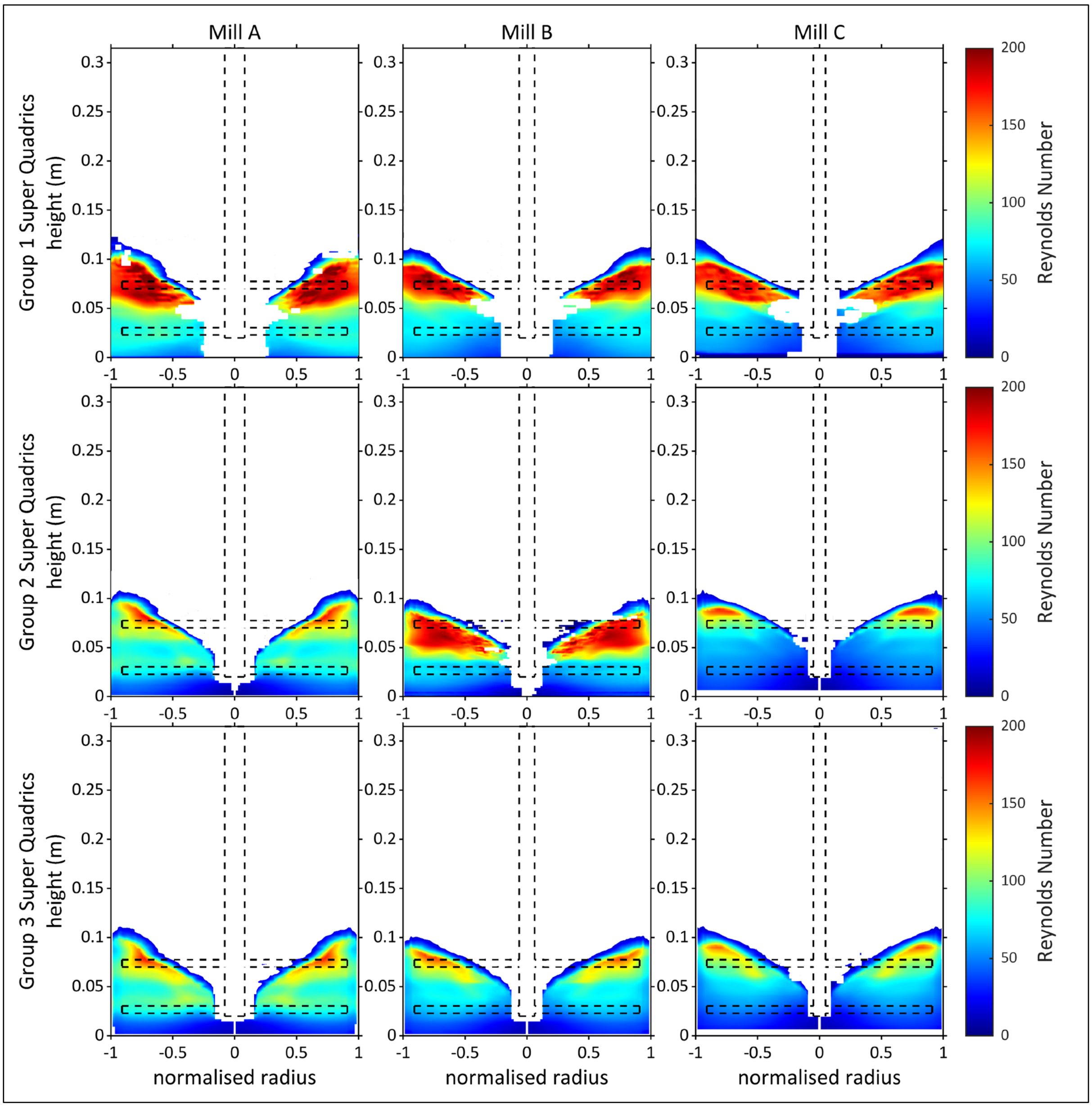

*Figure 9.18: Colourmaps of the bulk Reynolds number for the DEM-SPH media shape simulations, arrayed such that the rows show the three super quadric media groups and the columns show the three mill sizes*

From its spatial distributions, the Reynolds number achieves its highest intensity in the fluid dense regions of the mill space, where the porosity of the system is highest. The fluid dense regions are located above the top impeller and creep down the central cavity as the angularity increases, as shown in the relative density spatial distributions (Figure 9.3). Noticeably, the more media dense regions at the base of the mills, particularly in Group 3 simulations, experience low Reynolds numbers.

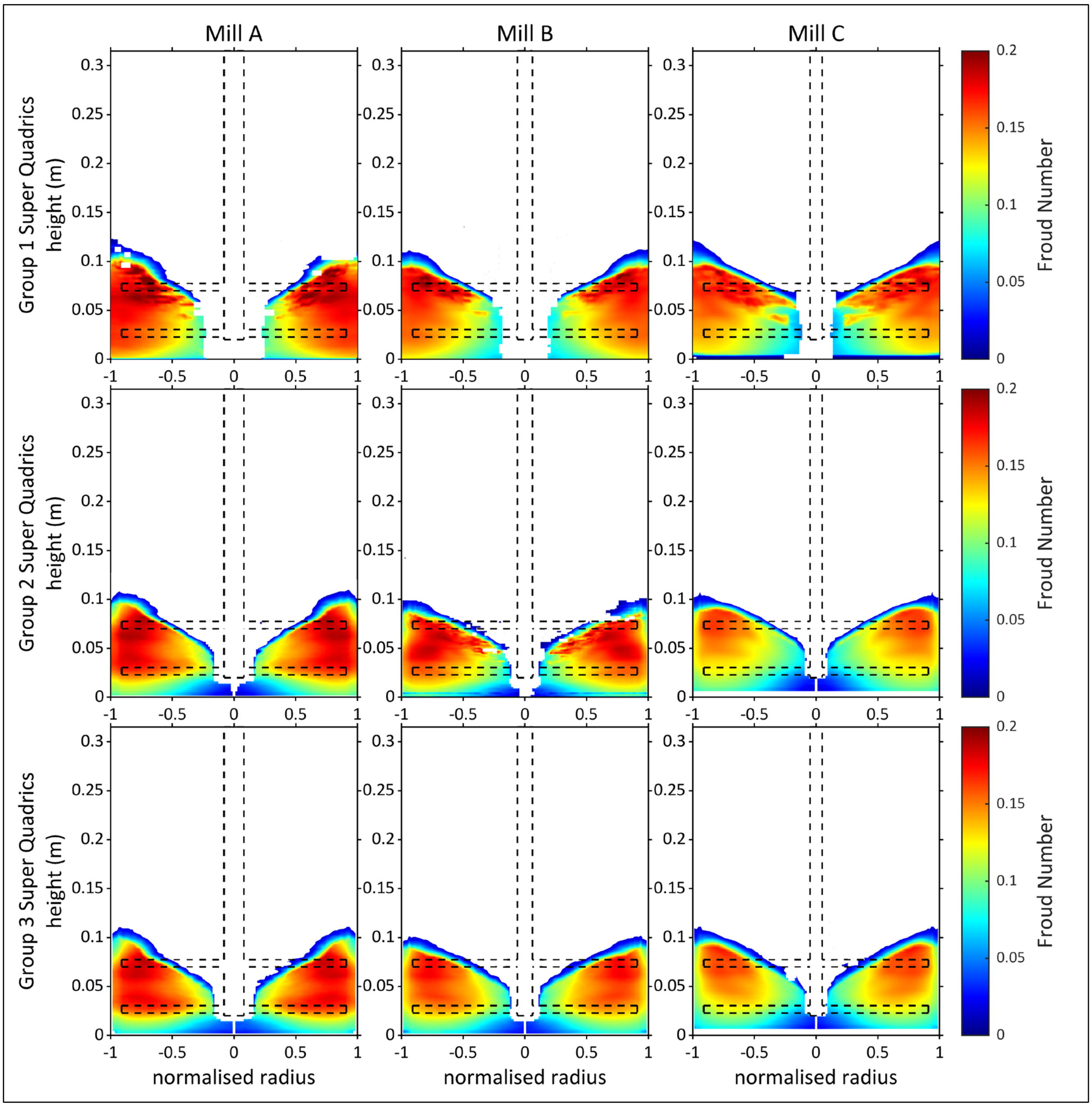

*Figure 9.19: Colourmaps of the bulk Froude number for the DEM-SPH media shape simulations, arrayed such that the rows show the three super quadric media groups and the columns show the three mill sizes*

The bulk spatial Froude number distributions show a peak intensity around the top impeller towards the free surface. In this bulk visualisation, the Froude number is a function of the relative velocity. Following from the media and fluid spatial distributions and box plots, the fluid maintains higher velocities than the media throughout simulations. The fluid velocity also experiences a dampened response to the media angularity as its distributions for each mill size only decrease slightly with increased mill size. Therefore, the Froude number spatial distribution begins to resemble the fluid velocity spatial distribution at lower angularities, specifically for Group 3 systems, where the media component has decreased more than its fluid counterparts.

Both dimensionless number distributions were further spatially analysed in cartesian 3D volumetric cells of the mill space, at each of the time steps considered. The spatial data at each time step, of the five revolutions of data assessed, was distributed similarly to the spherical data, with a positively skewed distribution. Therefore, the median was used to characterize the distribution at each time step. The means of the distributions of median values for each time step are shown in Figure 9.20 for the Reynolds and Froude numbers for all mills at each group of super quadrics. The error bars on the data points show the standard deviation of the average median across the timesteps assessed. The dimensionless number distribution data from the spherical 1.8 m/s simulations (Figure 8.17) is also included in Figure 9.20.

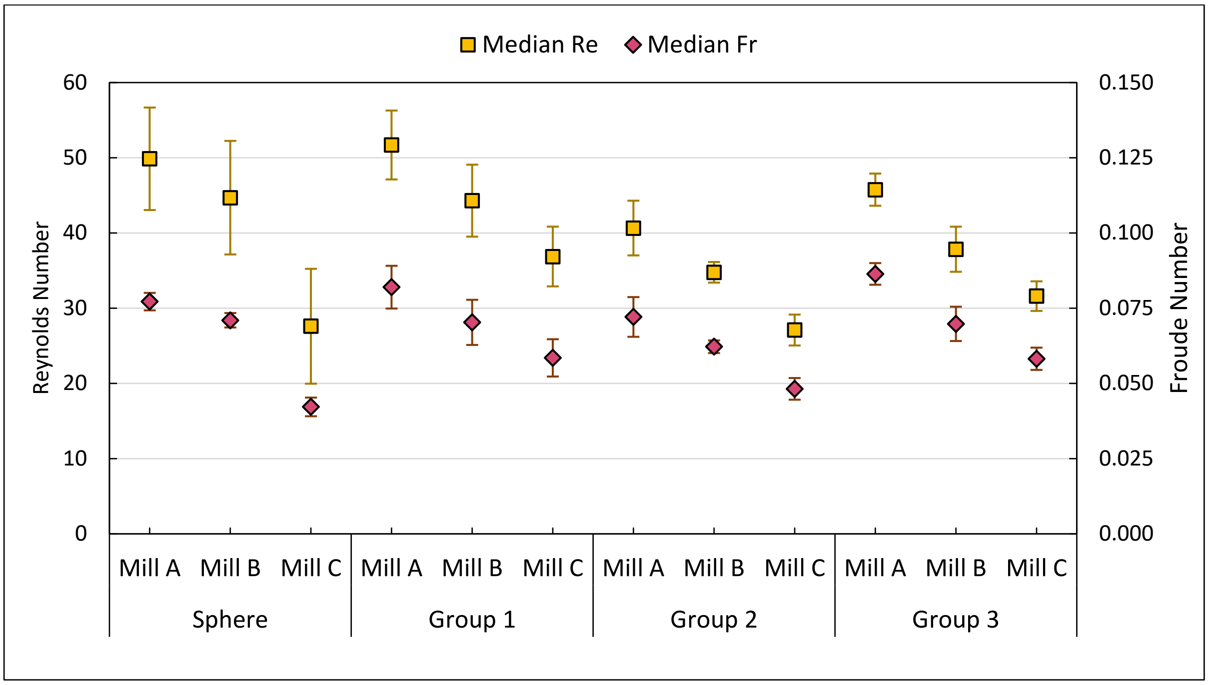

*Figure 9.20: Average median Reynolds and Froude numbers for DEM-SPH media shape simulations*

As previously observed in the tip speed simulations, the trends are consistent between the Reynolds number and the Froude number. The Reynolds and Froude numbers decrease consistently with increasing mill size. The average Reynolds and Froude numbers of the spherical simulations and the Group 1 super quadrics are in good agreement for Mills A and B, however, the Mill C values for the spherical simulations are significantly lower than the Group 1 super quadrics. Transitioning from Group 1 to Group 2 media, the Reynolds and Froude numbers for each mill size decrease. This is consistent with their spatial observations where the increased media packing density and its lower velocity result in lower spatial intensities of the Reynolds and Froude number. The Group 3 systems show an increase from the Group 2 values. This can be attributed to the Group 3 mill systems having similar packing densities and fluid velocities, but lower media velocities than the Group 2 systems. Because of the possibility that the model underestimated the packing density of the Group 3 systems, it could be argued that the dimensionless quantities should be lower due to the tighter packing and its reduction effect on the fluid velocities.

## 9.3 Energy environment

The response of the energy environment of the nine DEM-SPH stirred mills to the angularity of the super quadric groups is assessed in this section. The assessment is divided into three sections. The first section investigates the bulk spatial distributions of the collision frequency, energy dissipation and energy dissipation rate, to characterize the types of collisions experienced in each system. The bulk energy spectra over collision energy are then assessed and reduced to the single-value parameters of the modal peak energy dissipation rate and its corresponding collision energy. Finally, the power draw distributions of the simulations are examined. The response of the five dry DEM simulations is considered to assess if the trends observed in the wet system are replicated in the media angularity response of the dry environments. The energy variables used in this section are normalised by dividing by the volume of the fluid. Their non-normalised form is only used when comparing between dry and wet simulations of the same mill size.

### 9.3.1 Spatial distributions

The bulk spatial distributions of the collision frequency, energy dissipation and energy dissipation rate of the nine DEM-SPH simulations are shown in Figure 9.21, Figure 9.22 and Figure 9.23, respectively. The collision frequency distributions (Figure 9.21) show that the number of collisions increase with increased media angularity for each mill size. The highest intensities of collisions are observed the the regions between the impeller pins and between the bottom pin and mill base. This is consisent across mill sizes and angularities. This differs from the spherical media, which experienced an additional high collsion intensity region around the bottom impeller pin (Figure 8.18, row two).

Spherical media can better maintain contact while rotating and translating, due to their constant radius. However, the more angular the super quadric, its changes in radius can cause breaks in contact due to the media rotation. In tightly packed spaces, where spherical media can a maintain extended contact as they rotate, the rotation of super quadric media could cause breaks in contact that can be reestablished due to the tight packing. This results in an increase in the number of contact events. The increase in the number of collisions for the same number of media in the same mills at the same speed, with the increase media angularity can be attributed in part to this effect. Another factor is the increased solids fraction of media at the base and walls with increased media angularity, observed in Figure 9.2, indicative of a denser media packing which increase the collision probability of the region. The number of collisions increased with increased mill size, due to the increased number of media required to fill the larger mill sizes.

The energy dissipation bulk spatial distributions for the DEM-SPH superquadric simulations are shown in Figure 9.22. The highest intensities of energy dissipation are observed with Group 1 super quadrics for each mill size. Group 1 observed regions of high intensity energy dissipation that radiated from the base of the mill to the bottom impeller and up the mill wall. Group 2 and Group 3 observed lower intensity energy dissipation that also radiated from the base of the mill but did not reach the bottom impeller. Notably, the distribution of energy dissipation is more even for Group 3 super quadrics than Group 2. The Group 2 super quadrics have a sharper distinction between the high intensity energy dissipation regions at the base and walls of the mill and the rest of the bulk mill space, while Group 3 observes its highest dissipation at the base of the mill and significant energy dissipation throughout the bulk mill space. Different color scales are used on the colourmaps for each set of mill simulations to best visualize its internal energy response. These colour scales decrease in range with increasing mill size. This is done to ensure a good resolution for comparison of the media angularity effects on each mill size.

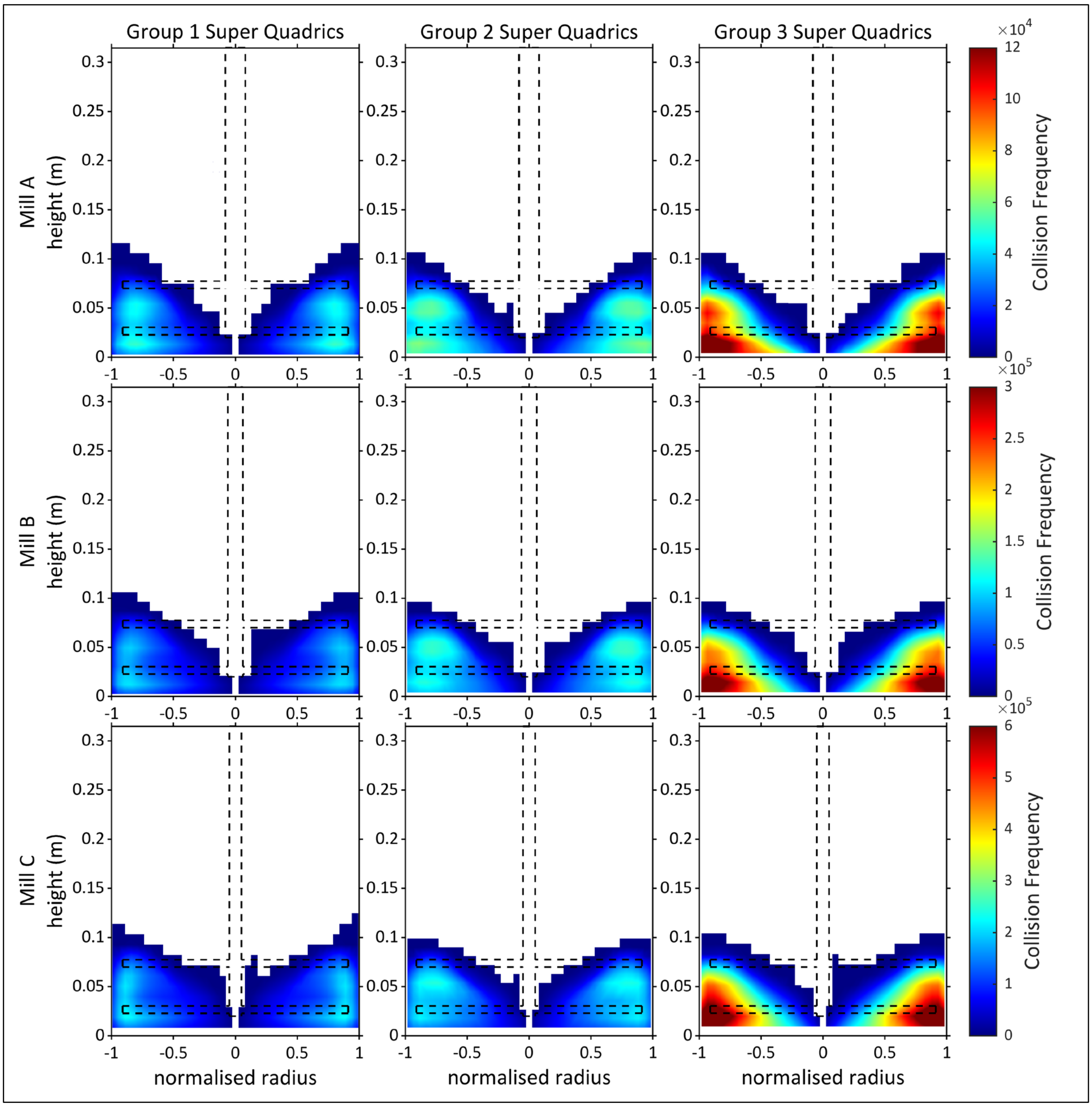

*Figure 9.21: Colourmaps of the bulk collision frequency for the DEM-SPH media shape simulations, arrayed such that the rows show the three mill sizes and the columns show the three super quadric media groups*

Figure 9.23 shows the spatial distributions of the energy dissipation rate in the nine DEM-SPH mills. These colourmaps use different colour scales for each mill size. The highest intesity energy dissipation rates are found at the base of the mill, similar to the energy dissipation. This is consistent across all nine simulations. This however is not the preferred location for high energy dissipation as the dense packing and low velocities of the area produce low energy collisions. High energy dissipation rate is preferred in fast moving spacious regions that produce high energy collisions to induce effective breakage. Mill A has an additional region of high intensity at the tip of the top impeller pin for Group 1 super quadrics. Unlike energy dissipation, the largest regions of high intensity energy dissipation rate are observed in Group 3 superquadric simulations, across mill sizes. These regions are significantly smaller in Group 1 and least visible at this colourscale in Group 2.

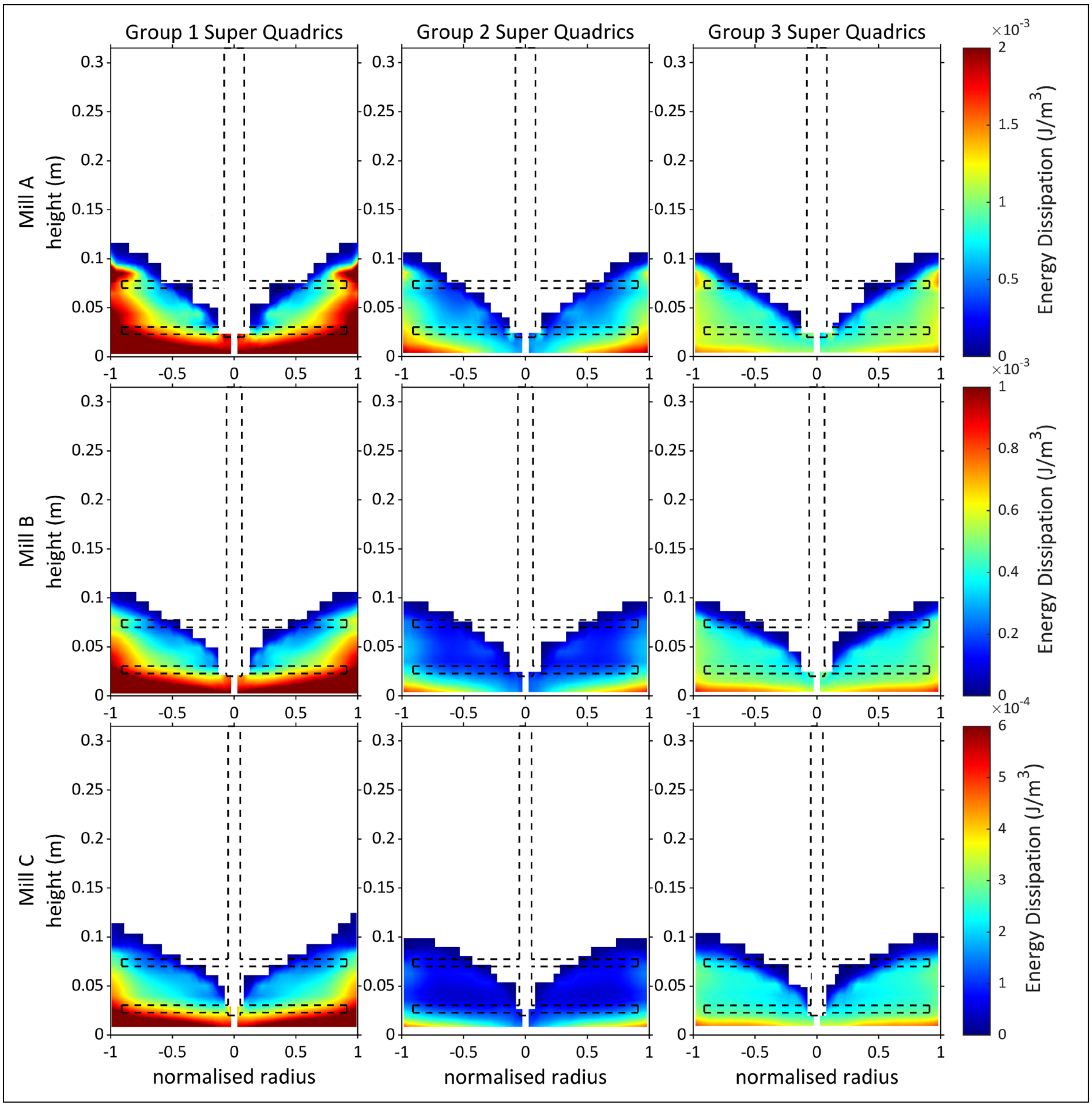

*Figure 9.22: Colourmaps of the bulk intensive energy dissipation for the DEM-SPH media shape simulations, arrayed such that the rows show the three mill sizes and the columns show the three super quadric media groups*

Considering both relationships of energy dissipation and energy dissipation rate with increasing angularity, the location of the high intensity regions correspond, and the overall intensity trend is the same as it decreases from Group 1 to Group 2, then increases to Group 3. The difference is that the systems with the highest energy dissipation do not have the highest energy dissipation rate. Group 1 has the highest energy dissipation. This can be attributed to the high media velocities (Figure 9.9) allowing for high energy collisions. Increasing the angularity to Group 2 reduces the media velocity which reduces the energy dissipation. The bulk energy dissipation increases in Group 3 even with lower velocities due to the increase in the collision frequency. The energy in these systems is being dissipated by short duration collisions of tightly packed angular media. Figure 9.24 shows box and whisker plots of the contact duration of each collision in each mill system over five revolutions. The median contact duration decreases slightly from Group 1 to Group 2 and more significantly from Group 2 to Group 3. These short collision durations in Group 3 systems are also responsible for the increased energy dissipation rate of the Group 3 mill space.

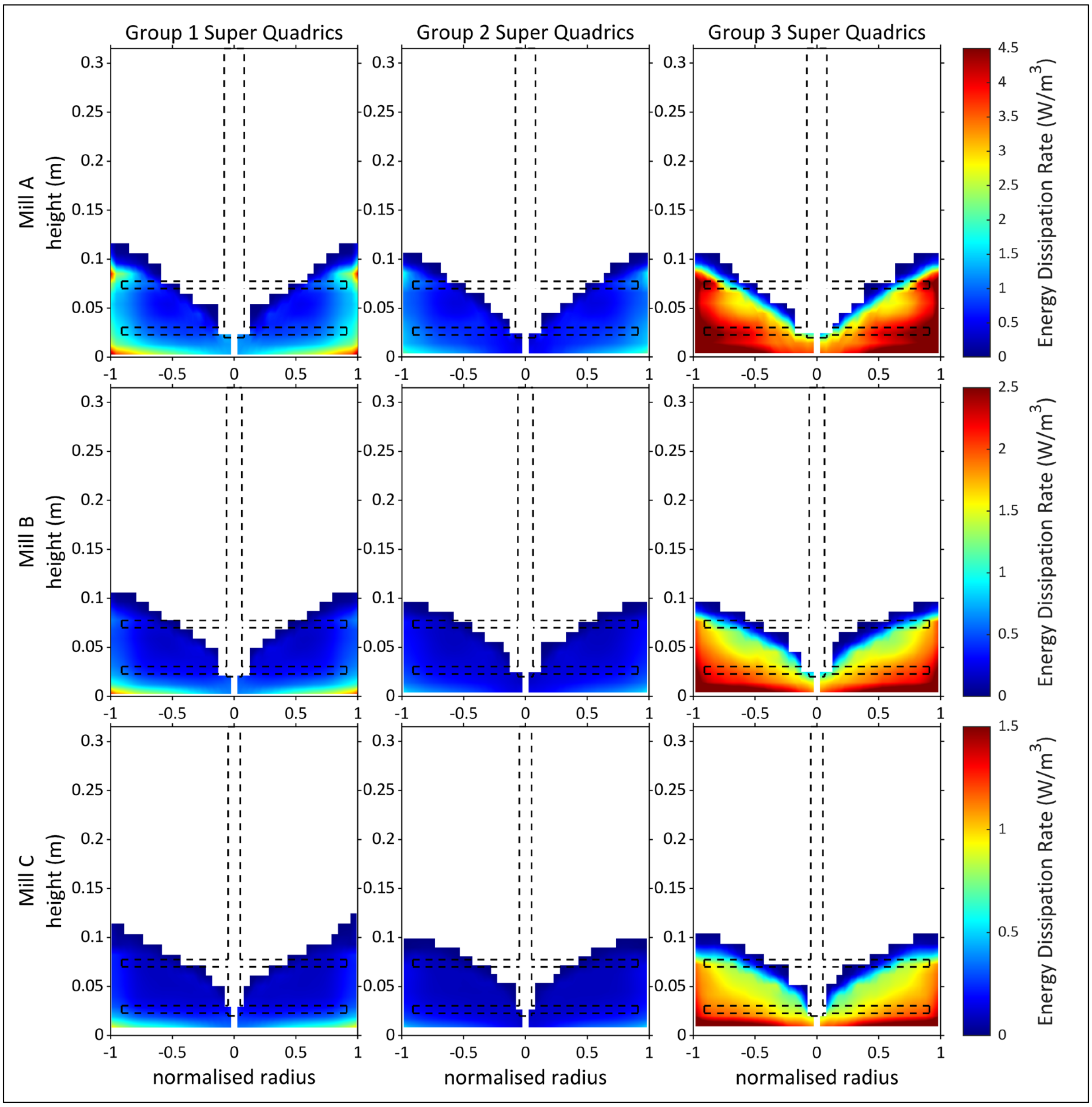

*Figure 9.23: Colourmaps of the bulk intensive energy dissipation rate for the DEM-SPH media shape simulations, arrayed such that the rows show the three mill sizes and the columns show the three super quadric media groups*

The spatial energy distributions of the dry DEM simulations can be found in the Appendix E.6. The collision frequency, energy dissipation and energy dissipation rate spatial distributions are shown in Figure E.12 for the dry Group 3 simulations of all the mill sizes, and in Figure E.13 for the dry Mill A simulations at each super quadric group. Considering the dry Group 3 simulations, the collision frequency increases with mill size and has its highest intensity between the mill base and the walls. There is an even distribution of energy dissipation and energy dissipation rate throughout the bulk mill space that has its highest intensity between the impeller arms towards the mill wall but not at the mill base as observed in the wet simulations. The dry Mill A simulations showed an increase in collision frequency with increased angularity. Similar to the wet simulations, their energy dissipation and energy dissipation rate have their peak intensity at the mill base and walls with Group 1, then intensity decreased into Group 2, and in Group 3 the bulk distribution evened out.

The distributions of contact duration for the dry Group 3 simulations and the dry Mill A simulations were also examined. These are represented as box and whisker plots in Figure 9.25 and Figure 9.26, respectively. Similar to the DEM-SPH simulation contact duration box plots (Figure 9.24), the figures show that the Group 3 super quadric simulations experience a distinct reduction in the contact duration, which has been correlated to the increase in bulk energy dissipation rate.

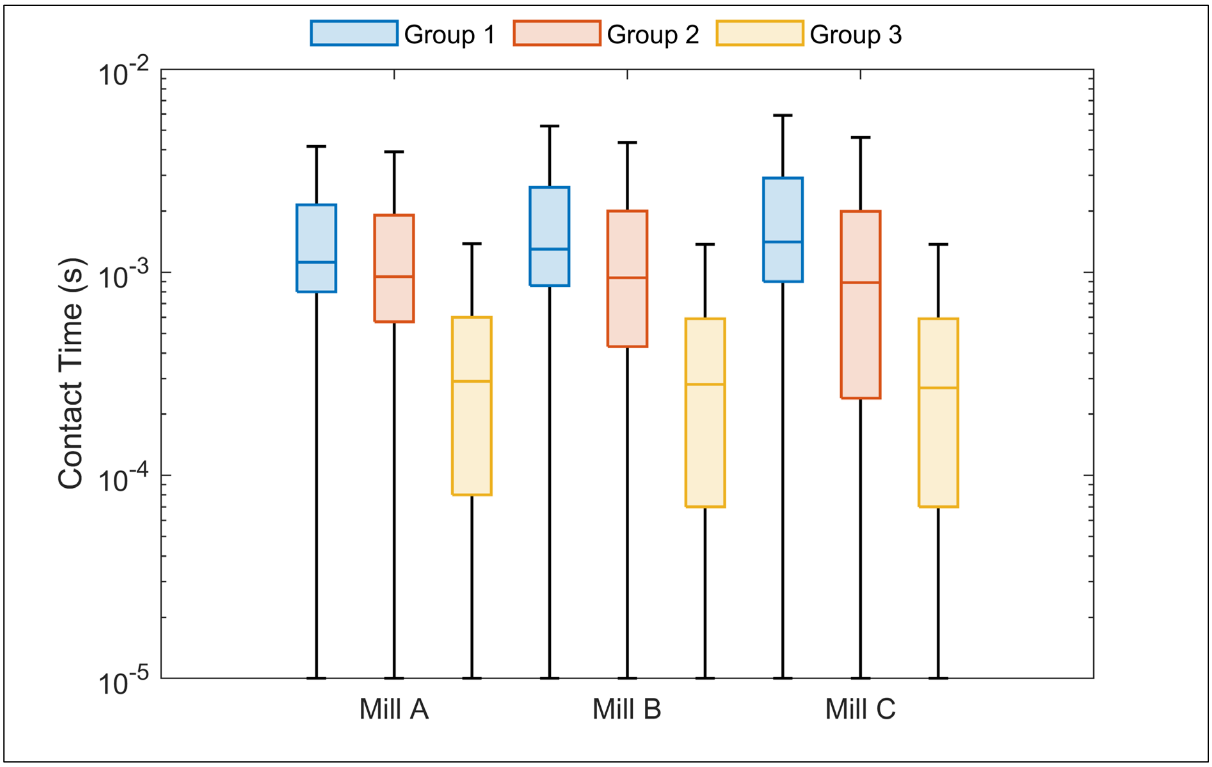

*Figure 9.24: Box plot of the contact duration distribution for the 9 DEM-SPH simulations*

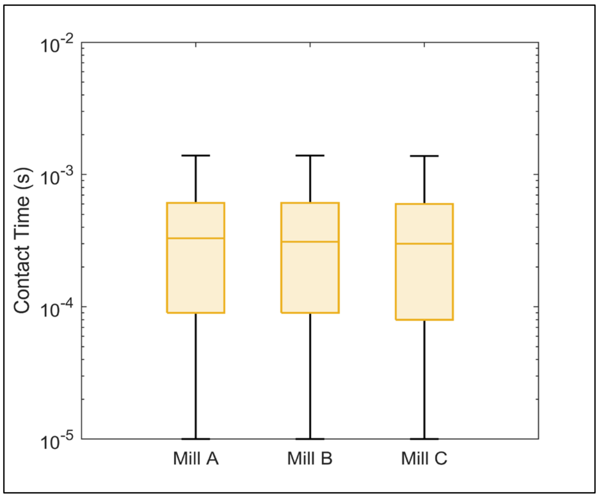

*Figure 9.25: Dry DEM contact duration box plots for group 3 super quadrics*

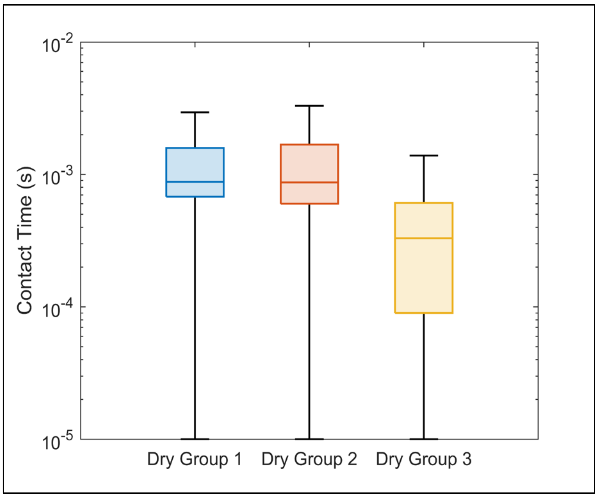

*Figure 9.26: Dry Mill A contact duration box plots for all groups of super quadric*

### 9.3.2 Energy spectra

The collision frequency spectra over collision energy for the nine DEM-SPH simulations is shown in Figure 9.27. These collision spectra for the total collision frequency, media-media collisions, media-shell collisions and media-impeller collisions are represented separately. The media-media collisions are the most significant collisions in all the systems studied. They account for the bulk of the collision makeup of the total collisions. Increasing angularity across the super quadric groups shows an increase in the number of collisions across mill sizes, specifically the number of media-media collisions. Going from Group 2 to Group 3, a significant increase in the media-shell collisions is observed as they become more dominant than the media-impeller collisions. This corresponds to the increased packing density at the mill base and walls observed in Figure 9.2.

Figure 9.28 shows the energy dissipation rate spectra over collision energy for the DEM-SPH simulations. These spectra consider all collisions over the complete five revolution period. Their modal peak energy dissipation rate and the corresponding collision energy are delineated on their respective axes. The trends in the modal peak energy dissipation rate and collision energy for each revolution were examined. Their mean values, for each revolution, are plotted in Figure 9.29, with error bars showing the standard deviation of the five means sampled. The trend observed with each mill size was consistent as the collision energy decreased with increased angularity. However, the dissipation rate decreased from Group 1 to Group 2, then increase to Group 3. The collision energy trend is consistent with the velocity decrease with increased angularity observed in its spatial distributions (Figure 9.9) and box plots (Figure 9.11). The collision energy is directly dependent on the velocity of the colliding media. It follows that the faster moving simulations will have higher collision energies. The energy dissipation rate trend is consistent with energy spatial distributions, which shows how the nature of collisions experienced in the system changed significantly from Group 1 and 2 with the angularity of Group 3, as the bulk mill space began experiencing an increase in energy dissipation through short duration collisions. However, both the spatial distributions and the energy spectra, which considered the full 5 revolutions of data, suggested that the highest energy dissipation rate of all mill sizes is observed in Group 3 instead of Group 1. Though this may be the case for Mill C, the revolution averaged data shows that Mills A and B experience their highest energy dissipation rate in Group 1.

Considering each media group, Group 1 shows the dissipation rate and collision energy decreasing with increased mill size. The collision energy and dissipation rate continue to decrease into Group 2, though the error bars show a similar value range for the collision energies of Mill B and Mill C. The collision energies decrease significantly in order of magnitude from Group 2 to Group 3, while the dissipation rates for Group 3 have significantly increased from Group 2. Mill A has the highest dissipation rate in Group 3 while Mills B and C experience similar values.

The complete collision frequency and energy dissipation rate spectra for the three dry mill simulations with Group 3 super quadrics over five revolutions is shown in Figure E.14 in Appendix E.6. The wet and dry modal peak dissipation rate and collision energy are compared against each other in Figure 9.30. The values for the dry system are characteristically higher than the wet system. This is supported by the findings of Ndimande et al. (2019), which reported higher collision energies for their dry industrial SMD simulation, compared against their DEM-SPH coupled simulation. The higher collision energies can be attributed to the dry system having higher intensities in their peak media velocity regions. Therefore, the collisions in these regions are higher energy as shown in their spatial distributions (Figure E.12) and energy spectra (Figure E.14). Figure 9.30 shows that the modal dissipation rate and collision energy for both the wet and dry systems follow the same trend. The collision energy decreases with increasing mill size, while the peak energy dissipation rate decreases from Mill A to Mill B then picks up slightly for Mill C.

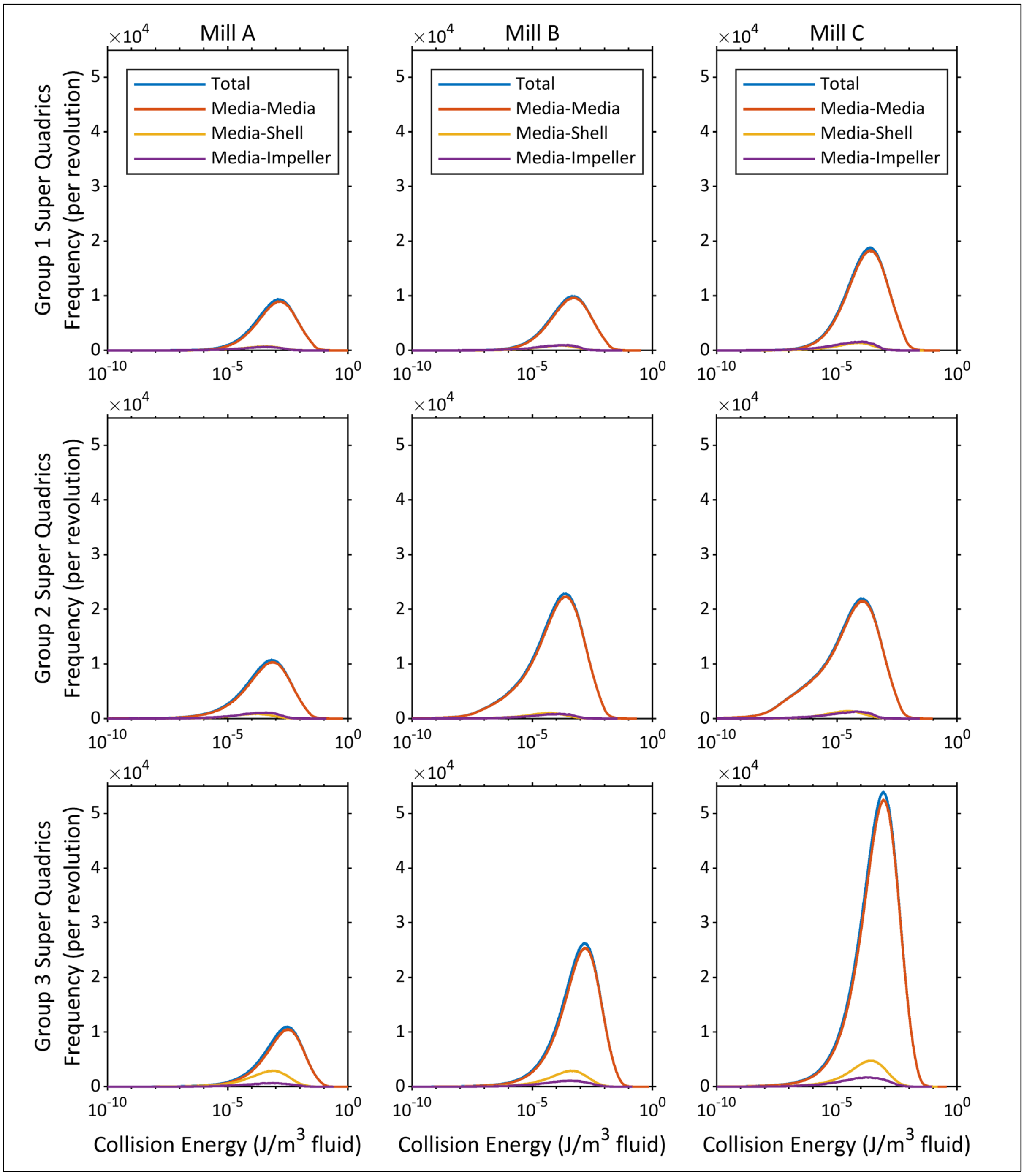

*Figure 9.27: Collision frequency spectra over collision energy for the DEM-SPH media shape simulations, arrayed such that the rows show the three super quadric media groups and the columns show the three mill sizes*

The modal peak energy dissipation rate and collision energy for the set of dry simulations of Mill A at each super quadric group is compared against their wet counterparts in Figure 9.31. The complete spectra for this set of simulations are shown in Figure E.15 in Appendix E.6.

Similar to the first set of dry-wet comparisons in Figure 9.30, the dry values are higher than the wet values. This is consistent with their spatial distributions and energy spectra. The overall trend of these variables with increasing angularity is consistent between the two simulation groups. The collision energy decreases with increased angularity. The modal peak dissipation rate decreases from Group 1 to Group 2, then picks up significantly for Group 3. This is consistent with the observations of the spatial dissipation rate which picks up at Group 3 due to the reduced collision duration due to the media angularity creating an even distribution for energy dissipation rate.

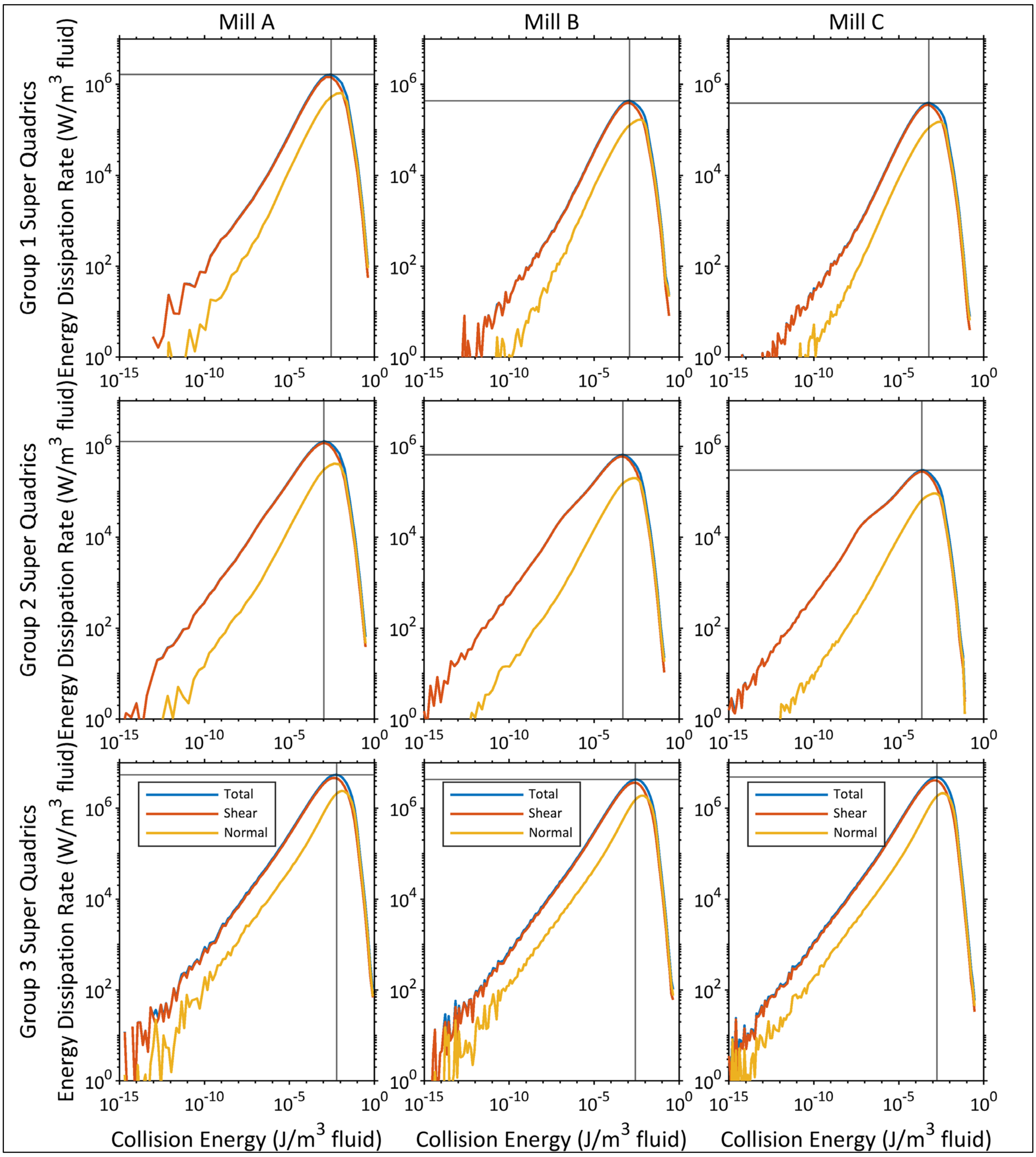

*Figure 9.28: Energy dissipation rate spectra over collision energy for the DEM-SPH media shape simulations, arrayed such that the rows show the three super quadric media groups and the columns show the three mill sizes*

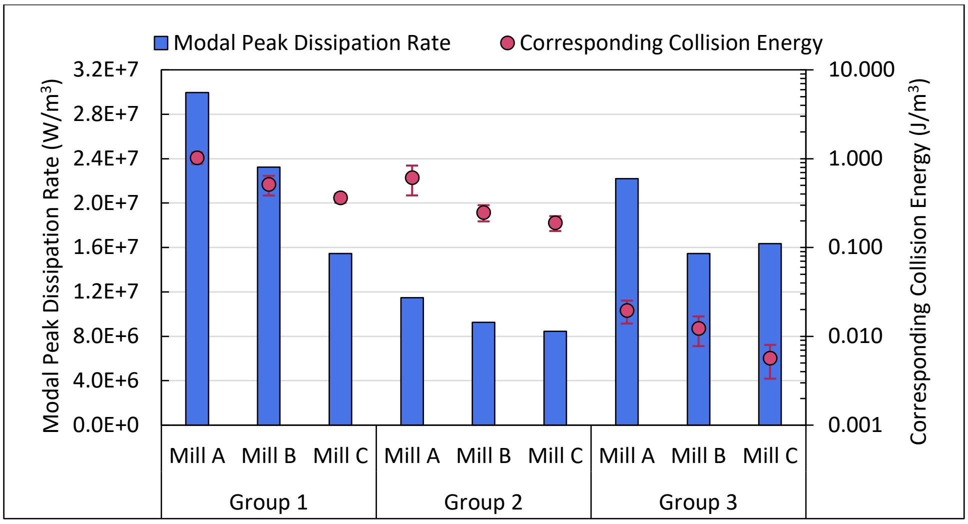

*Figure 9.29: Modal peak dissipation rate and the corresponding collision energy for each of the three mill sizes, simulated using each of the super quadric media groups.*

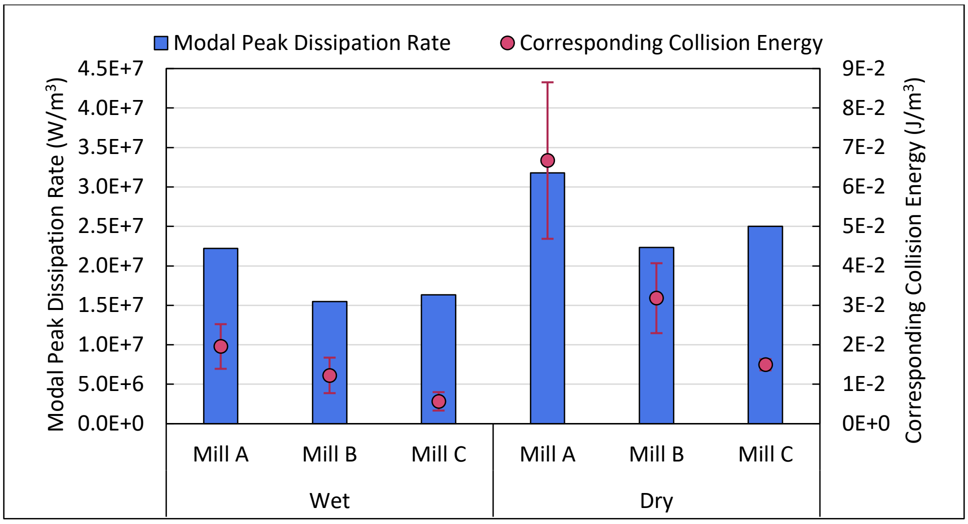

*Figure 9.30: Modal peak dissipation rate and corresponding collision energy for the three mill scales simulated using group 3 super quadrics in wet and dry systems*

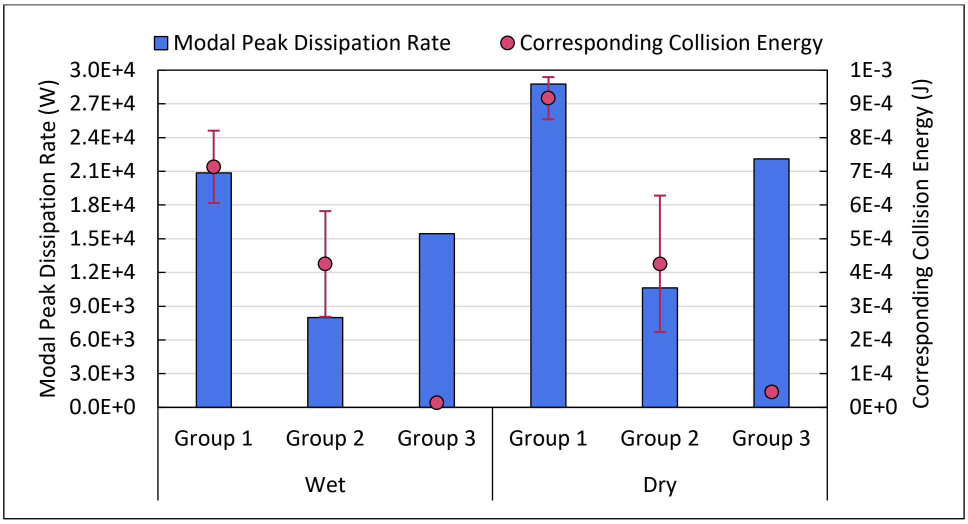

*Figure 9.31: Modal peak dissipation rate and corresponding collision energy for Mill A, simulated wet and dry, using each of the three super quadric groups*

### 9.3.3 Power draw

The average intensive power draw for the DEM-SPH simulations at each media angularity group was assessed in its totality and as separate DEM and SPH components. Figure 9.32 shows the total power draw in its DEM and SPH components, along with the DEM percentage of the total power draw. Consistently across media shape groups, the power draw decreases as the mill size increases. This was also observed in the spherical simulations. The smaller mill sizes having the larger intensive power draw corresponds to them having larger regions of high velocities in the normalised mill space. As the bulk velocity decreases with expanding mill size, a lower power draw is observed.

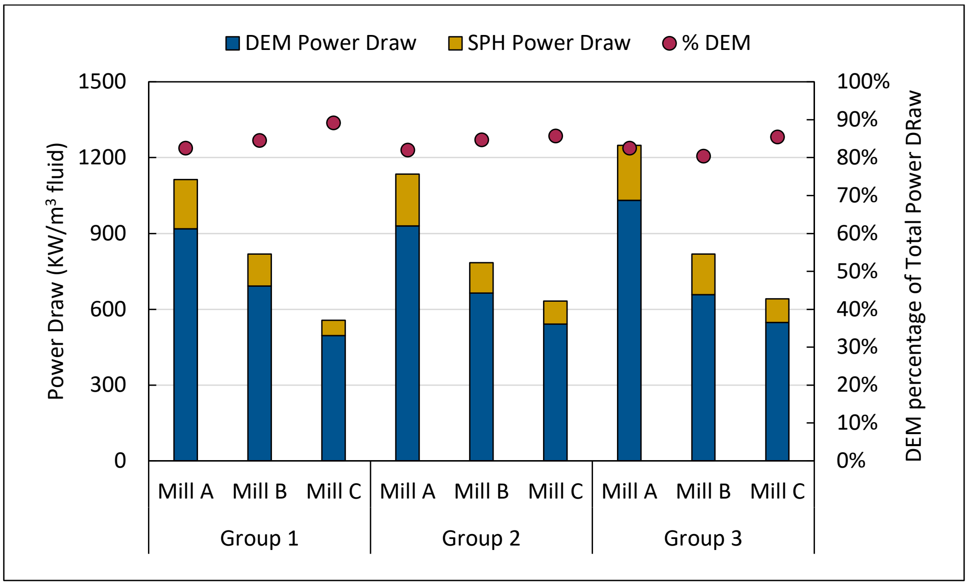

*Figure 9.32: Total power draw and the DEM power draw component for the three mill sizes simulated using the three super quadric groups*

Slight increases in the power draw for each mill size as the media angularity increase are also noted for Mill A and C. The power draw split between the DEM and SPH components of the power draw ranges between 80 and 90 % toward the DEM component. This is higher than the spherical media split which ranged between 70 and 80 %. The Group 1 simulations show an increase in the DEM power draw percentage with increased mill size, while Group 2 increases from Mill A to Mill B then plateaus at Mill C. Group 3 shows a decreased DEM percentage from Mill A to Mill B then increases again to Mill C. Throughout the different media shape groups, Mill C consistently has the highest DEM percentage in its power draw. From observing the spherical simulations, the power draw split has been seen as an indicator of the dominant flow type in the mill system. Therefore, Mill C, which experiences the greatest proportion of contact dominant flow, in each media shape group, due to its denser packing and low velocities has a higher DEM power draw percentage than the other mill sizes that experience a greater degree of fluidisation within their mill spaces.

Figure 9.33 compares the power draw of the wet and dry Group 3 simulations of each mill size. The figure shows the total wet power draw, its DEM component, and the total power draw of the dry DEM only simulations. Similar to the spherical simulations, the dry power draw is lower than that of the wet systems for Mills A and B. However, as the mill size increases the difference between the wet and dry power draw decreases, till it is not significant for Mill C.

The wet power draw for Mill A was compared against the dry Mill A simulations across all the media shape groups. Figure 9.34 shows the total wet power draw, the wet DEM power draw component, and the dry power draw experienced in Mill A across all super quadric groups. Both the wet and dry power draw increase with increased angularity, with their most significant increases being from Group 2 to Group 3. The dry power draw is consistently lower than the wet power draw, however, the difference between the two decreases as the angularity of the media increases.

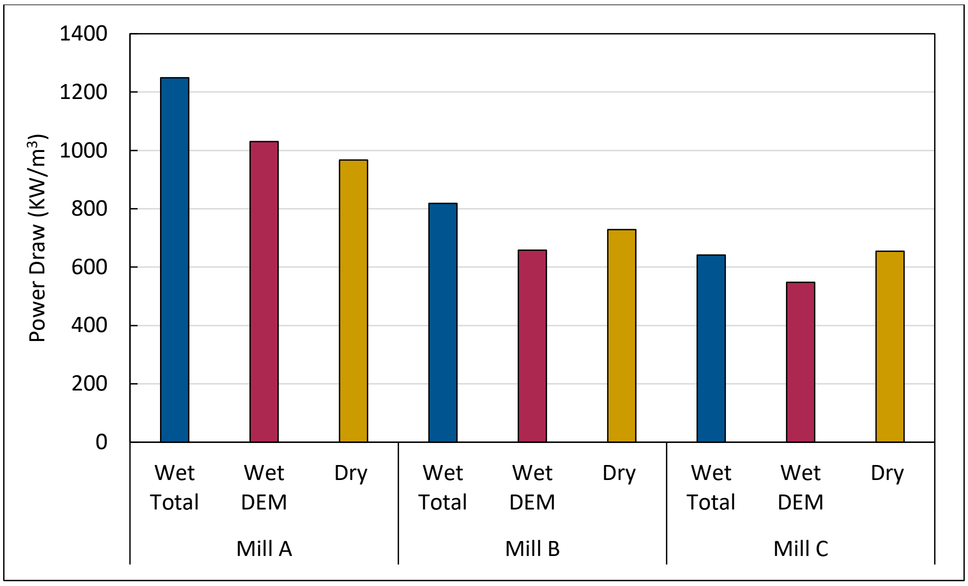

*Figure 9.33: Power draw of Group 3 super quadrics, simulated wet and dry in the three mill sizes*

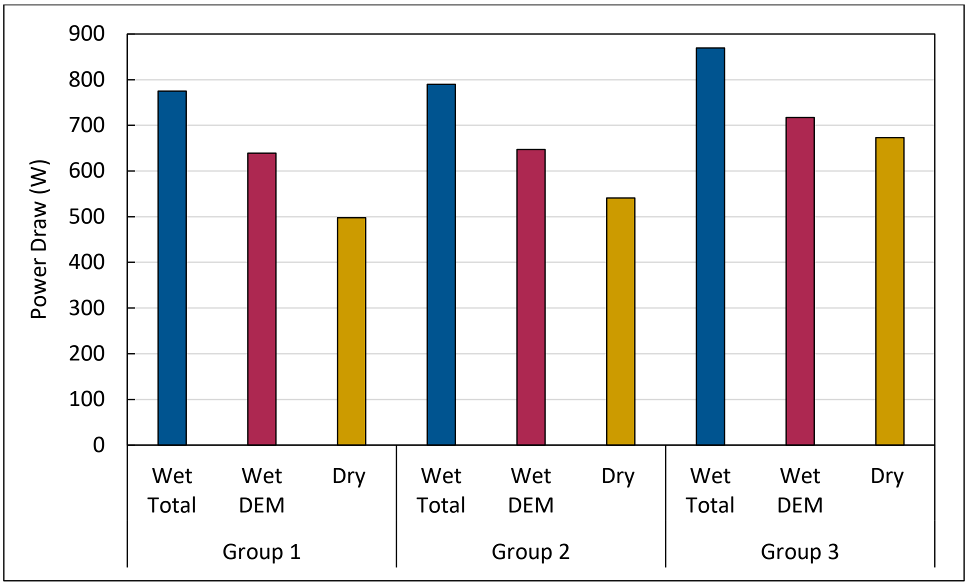

*Figure 9.34: Power draw for Mill A, simulated wet and dry, using each of the three super quadric groups*

## 9.4 Scale-up assessment

The relationship established between the mill size and the tip speed in Chapter 8 showed a reduction in the fluidisation state and breakage potential of the mill as it radially expands at a constant tip speed. It followed that entering the media shape simulations, Mill A should experience better fluidisation and breakage potential, followed by Mill B and lastly Mill C. Good fluidisation was characterised by high bulk velocities and an even media distribution in the flow environment, and high intensive modal peak dissipation rate and corresponding collision energy in the energy environment. The media shape effect on the three sizes of stirred mills has been assessed spatially, through parameter distributions and lastly through single value parameters. The results of four key single value parameters have been tabulated in Table 9.1 for the three mill sizes evaluated at each super quadric media group.

Table 9.1 shows the median Froude number, median Reynolds number, average media velocity, and the modal peak energy dissipation rate and its collision energy. Each parameter provides its estimation of the mill performance. The average media velocity and collision energy observe similar decreasing trends with both media angularity and mill size. The median Froude number and modal peak dissipation rate both experience decreases in performance from Group 1 to Group 2, then increases to Group 3. However, Group 1 still retains a higher modal energy dissipation rate compared to Group 3. The Froude number maintains a decreasing trend with mill size throughout the media shape groups, while the modal peak dissipation rate attains this in Groups 1 and 2, but Group 3 sees Mill C overtake or equate Mill B in performance. While the trend in the dimensionless numbers might shift when the solids fraction is more accurately captured, the trend in modal peak dissipation rate in substantiated by the same observations occurring in the dry simulation sets.

*Table 9.1: Average media velocity, median Froude number, median Reynolds number, intensive modal peak dissipation rate, and intensive collision energy of the nine DEM-SPH simulations*

| | | Media Velocity (m/s) | Median Froude Number | Median Reynolds Number | Modal Peak Dissipation Rate ($\times 10^7$ W/ $m^3$) | Collision Energy (J/$m^3$) |
|---|---|---|---|---|---|---|
| Group 1 | Mill A | 0.67 | 0.082 | 52 | 3.00 | 1.025 |
| | Mill B | 0.64 | 0.070 | 44 | 2.32 | 0.513 |
| | Mill C | 0.60 | 0.059 | 37 | 1.55 | 0.361 |
| Group 2 | Mill A | 0.62 | 0.072 | 41 | 1.15 | 0.611 |
| | Mill B | 0.59 | 0.062 | 35 | 0.93 | 0.248 |
| | Mill C | 0.53 | 0.048 | 27 | 0.84 | 0.189 |
| Group 3 | Mill A | 0.57 | 0.086 | 46 | 2.22 | 0.020 |
| | Mill B | 0.54 | 0.070 | 38 | 1.55 | 0.012 |
| | Mill C | 0.51 | 0.058 | 32 | 1.63 | 0.006 |

The media shape study in the stirred mills showed that the interactions in these systems are complex, as increasing the media angularity between the different super quadric groups had a unique influence on the nature of the media collision environment. This was observed in the relationship between the modal peak energy dissipation rate and its corresponding collision energy as the media angularity and mill size increased. The mill system responded to the increased angularity of Group 3 super quadrics by reducing the collision duration. This resulted from the combination of low media velocities and tight packing creating an energy environment more similar to gravity induced grinding, around the bottom impeller towards the mill base, than the fluidised grinding the mill is designed to induce. This was visualised in an increase in the bulk spatial energy dissipation and dissipation rate in these low velocity regions. The shift in grinding technique within the media bed is responsible for the high modal peak dissipation rates corresponding to low collision energies.

From the tip speed scale up study, the single value parameters were described based on what spatial characteristics in the mill performance their trends are sensitive to. The Froude and Reynolds numbers were sensitive to the mill fluidisation state, the collision energy informed on the overall breakage potential, while the media velocity and modal peak energy dissipation rate showed the energy transfer dynamics, from the impeller to the media via the mean velocity and from the media to the slurry material via the modal peak dissipation rate. Using these descriptions in the media shape scale up study, the relationship between the mean velocity and modal peak energy dissipation rate and their trends can be used to summarize the mill behaviour. The consistent decreasing trend in the mean velocity with increased angularity at each mill size shows inefficient transfer from the impeller to the media with increased angularity. This is supported by the increased impeller power draw at constant tip speeds. The modal peak energy dissipation rate trend decreases at each mill size initially from Group 1 to Group 2 super quadrics but increases from Group 2 to Group 3 super quadrics. The trend is attributed to the reduced collision duration and increased collision frequency due to increasingly angular media changing the nature of the collision environment.

In response to changes in media angularity, the collision energy trends similar to the mean velocity, more sensitive to the impeller-media dynamics, while the Froude and Reynolds numbers trend similar to the modal peak energy dissipation rate, more sensitive to the bulk media-slurry dynamics. As single value parameters, the collision energy and media velocity give a better overall assessment of the mill's breakage potential, but the modal peak dissipation rate and dimensionless quantities are able to provide a better understanding of how the system dynamics are changing in response to the media angularity.

# PART FOUR

## CONCLUSIONS AND RECOMMENDATIONS

# CHAPTER 10

# Conclusions and recommendations

## 10.1 Introduction

This thesis was concerned with developing a two-way coupled, simultaneous DEM-SPH model of laboratory scale stirred media detritors and used it to investigate the effects of scale on their flow and energy environment. Within this work, the effects of critical variables were assessed to determine the performance prediction capabilities of the model and integrated into the scale-up assessment methodology. This chapter begins with a summary of key observations from the simulation work, before presenting conclusions drawn in response to the hypotheses of the thesis. It closes with recommendations for future work to improve all aspects of the study.

## 10.2 Observations

The simulation work assessed in this thesis considered the effects of media parameters, fluid parameters, operating conditions, and scale up relationships, across thirty-three (33) individual DEM-SPH simulations and eight (8) individual dry DEM only simulations of a laboratory SMD mill. Within this body of work, key observations have been made about the capabilities of the simultaneous DEM-SPH model, the parameter effects on the laboratory scale stirred mill system, and the scale-up effects and use of single value parameters to evaluate mill performance.

On the DEM-SPH model and its prediction capabilities, the following was observed:

- The simultaneous two-way coupled DEM-SPH model developed was able captured the mechanisms of multiple variable effects. The expansion of the model into super quadric media shapes exposed the current limits of viable simulation criteria through its stability requirements of a further reduced Young's Modulus to simulate at a computationally affordable rate. The use of super quadric media also showed that the coupling algorithm is limited in extremely densely packed media situations as the accuracy of the solids fraction is dependent on the fluid resolution, due to its fluid-particle specific nature. Overall, when properly parameterized, the model is capable of effectively resolving both phases and their interactions within a stirred mill system.
- The performance prediction capabilities of the model were explicitly investigated through the media size, media density, slurry density, slurry viscosity and media fill. Across the parameters investigated, the media size, slurry density and media fill showed good agreement with literature studies. The media density and slurry viscosity results had discrepancies in the energy environment comparisons against computational horizontal disk mill studies at a higher speed. The performance predictions were sensible for the mill orientation and impeller configuration but lack foundation in computational literature. More studies on different stirred mill types are necessary to build the literature on how factors such as orientation and impeller configuration affects the mill performance.

On the effects of critical parameters of the media, slurry and operating conditions, the following was observed:

- The media size simulations showed an increase in the collision energy with increasing media size. The collision frequency decreased as the number of media decreased with increased media size. Within the simulated size range, the modal peak energy dissipation rate and total power draw increased consistently with media size. It follows that within the simulated size range, the tip speed is not low enough or the media size not large enough to result in a decrease the energy dissipation rate. However, the percentage contribution of DEM component of the power draw peaked within the size range due to the DEM power draw plateauing with increasing size. This is indicative of the tip speed of the mill imposing a limit to the fluidisation capabilities of larger media sizes.

- The media density was simulated at two impeller speeds (300 rpm and 700 rpm) in an attempt to ensure that the impeller fluidised the media. Both sets of results showed overall decreases in the power draw, and collision frequency and energy dissipation rate, with increases in media density.
- Increasing the media angularity resulted in a reduced media velocity and a tighter packing at the mill base and walls. The average media velocity and collision energy observe decreasing trends with both media angularity and mill size. The Reynolds and Froude numbers, and the modal peak dissipation rate both experience decreases in performance from Group 1 to Group 2, then increases to Group 3. While the trend in the dimensionless numbers might shift when the solids fraction is more accurately captured, the trend in modal peak dissipation rate is substantiated by the same observations occurring in the dry simulation sets. The increased media angularity creating an energy environment more similar to gravity induced grinding around the bottom impeller towards the mill base, than the fluidised grinding the mill is designed to induce. This was visualised in an increase in the bulk spatial energy dissipation and dissipation rate in these low velocity regions. This shift in grinding technique within the media bed is responsible for the high modal peak dissipation rates corresponding to low collision energies. The power draw increased very slightly with increased media angularity for the simulations at the same mill size and tip speed.
- Increasing the slurry density resulted in increased r-z media circulatory velocities. This resulted in an increase in the total power draw, with its SPH component proportion increasing significantly. Within the conditions simulated, increases in the collision frequency and energy due to the increased velocities were not observed. Instead, the collision energy and frequency decreased, as the power required by the SPH slurry dampened the energy available for the DEM collisions.
- The slurry viscosity results showed no changes in the r-θ circulatory flow fields. However, the results did show homogenisation of the fluid pressure distribution with increasing viscosity. An overall decrease in the collision frequency and energy was observed.
- The bulk solids fraction distribution evened out with increased media fill. This resulted in overall increases in the intensive collision energy and power draw, particularly the DEM proportion of the power draw, with increasing media proportion.
- Within the ranges of impeller tip speed studied, increasing the tip speed resulted in an increased energy dissipation rate, collision energy and power draw.

On the scale up effects on the laboratory mill space and the use of single value parameters, the following was observed:

- The scale up effects across the three laboratory scale systems were assessed by varying tip speed and media shape. Single value parameters derived from the flow or energy environments were examined as metrics to comparatively represent a mill system's fluidisation state and breakage potential across mill scales. Individually, intensive collision energy and average media velocity gave an overall assessment of the breakage potential, while the dimensionless quantities and the intensive modal peak energy dissipation rate informed on the state of system dynamics such as the fluidisation state and collision environment, respectively, informing on how breakage is attained within the system.

## 10.3 Conclusions

Three hypotheses were proposed in the investigation of the flow and energy environments of laboratory scale vertical stirred media detritors, for this thesis involving the development of a two-way coupled, simultaneous DEM-SPH model. The three hypotheses were proposed to guide the work plan for the performance assessment of the two-way coupled DEM-SPH model and the investigation of scale-up phenomena. The following conclusions were drawn in response to the hypotheses proposed:

A. *A two-way coupled DEM-SPH model that resolves both particle and fluid dynamics simultaneously can be used to predict the flow and energy environments of laboratory scale stirred media detritors, because the energy is dissipated through the resistance of motion of the particles and fluid in the system.*

   The two-way coupled simultaneous DEM-SPH model was able to effectively simulate the solid and fluid components and solid-fluid interactions within the stirred mill environment. The inherent responses of the predicted flow and energy environments to changes in critical variables were similar to observations made for the criteria in stirred mill systems from several computational and physical experimental literature studies.

B. *The variations in the spatial mill environment of laboratory stirred media detritors with scale, for a constant tip speed and media body sphericity, can be captured through dimensionless and intensive properties, because these properties are independent of the scale of the system.*

   Dimensionless properties, specifically the Reynolds and Froude numbers were used to characterize the flow environment of the three scales of laboratory SMD simulated. The numbers provided a metric for comparison of flow performance across mills at different tip speeds and media shapes. Similar trends were captured by each dimensionless number. Of the two dimensionless properties, the Froude number showed little periodicity in the system and hence minimal deviation in the system at steady state. The modal peak energy dissipation rate and its corresponding collision energy, and impeller power draw were made intensive by dividing by the volume of fluid with each mill size. Trends in all these properties captured variations in the mill environment due to scale in response to tip speed and media shape but showed sensitivity to different aspects of the mill dynamics. Therefore, at least two properties are recommended to accurately describe the mill space.

C. *At the same tip speed of the impeller, there is a decreasing trend in the velocity and energy profiles as the diameter of the stirred mill increases because of the dampening of energy as it propagates through the expanded radius, and the reduced rotational speed required to maintain the same tip speed.*

   The three simulated stirred mill sizes consistently showed a decrease in the intensity of velocity and energy spatial profiles with expansion in the radial direction with increasing mill size, across all the tip speeds and media shapes simulated. Though the decreasing trend is consistent, the response of each mill at each tip speed, quantified through dimensionless and intensive properties, showed that the gradient of change between the mill sizes is not consistent and is directly related to the fluidisation state of the mill.

## 10.4 Recommendations

Following from the results and conclusions drawn from this thesis, the following recommendations for future work are proposed:

- Expand the tested critical variable ranges beyond what was considered in this thesis to examine their full spectrum of influence on the mill space.
- Validate the internal mill environment through comparison of simulated spatial data against single or multiple particle tracking experimental results from experiments such as PEPT or magnetic tracking.
- Simulate a stirred mill as a continuous system with an SPH slurry inlet and outlet to model the continuous flow dynamics that occur when stirred mill systems are operated in circuit.
- Extend the SPH fluid model to allow for variability in the viscosity of the slurry fluid, possibly through modelling non-Newtonian fluids or varying the viscosity with time in a continuous stirred mill system to better understand the influence of the viscosity distribution that occurs due to particle breakage in a continuous mill system.
- Couple a PBM model to the simultaneous DEM-SPH framework to model the breakage result of feed suspended in slurry as microscale system, influenced by the media collisions with effects on fluid density and viscosity in a fluidized mill system.
- Develop an AI program to generate an approximation equation for the projected area of super quadric shapes based on their characteristics and the direction of flow to reduce computation expenses.
- Perform tests to define an empirical law for the critical timestep of super quadric collisions that explicitly considers the variability of the mean radius of curvature.

# REFERENCES

Allen, J. 2013. Stirred Milling machine development and application extension. *Metso*.

Astholm, M. 2015. *[Presentation] Outotec technology for fine and ultra-fine grinding in minerals processing*.

Austin, L.G. 1971. Introduction to the mathematical description of grinding as a rate process. *Powder Technology*. 5(1):1–17. DOI: 10.1016/0032-5910(71)80064-5.

De Bakker, J. 2014. Energy Use of Fine Grinding in Mineral Processing. *Metallurgical and Materials Transactions E*. 1(1):8–19. DOI: 10.1007/s40553-013-0001-6.

Barley, R.W., Conway-Baker, J., Pascoe, R.D., Kostuch, J., McLoughlin, B. & Parker, D.J. 2004. Measurement of the motion of grinding media in a vertically stirred mill using positron emission particle tracking (PEPT) Part II. *Minerals Engineering*. 17(11–12):1179–1187. DOI: 10.1016/j.mineng.2004.06.034.

Barr, A.H. 1981. Superquadrics and Angle-Preserving Transformations. *IEEE Computer Graphics and Applications*. 1(1):11–23. DOI: 10.1109/MCG.1981.1673799.

Becker, M. & Schwedes, J. 1999. Comminution of ceramics in stirred media mills and wear of grinding beads. *Powder Technology*. 105(1–3):374–381. DOI: 10.1016/S0032-5910(99)00161-8.

Beekman, W.J., Meesters, G.M.H., Scarlett, B. & Becker, T. 2002. Measurement of granule attrition and fatigue in a vibrating box. *Particle and Particle Systems Characterization*. 19(1):5–11. DOI: 10.1002/1521-4117(200204)19:1<5::AID-PPSC5>3.0.CO;2-I.

Beetstra, R., van der Hoef, M.A. & Kuipers, J.A.M. 2007. Numerical study of segregation using a new drag force correlation for polydisperse systems derived from lattice-Boltzmann simulations. *Chemical Engineering Science*. 62(1–2):246–255. DOI: 10.1016/j.ces.2006.08.054.

Beinert, S., Schilde, C., Gronau, G. & Kwade, A. 2014. CFD-discrete element method simulations combined with compression experiments to characterize stirred-media mills. *Chemical Engineering and Technology*. 37(5):770–778. DOI: 10.1002/ceat.201300716.

Beinert, S., Fragnière, G., Schilde, C. & Kwade, A. 2015. Analysis and modelling of bead contacts in wet-operating stirred media and planetary ball mills with CFD-DEM simulations. *Chemical Engineering Science*. 134:648–662. DOI: 10.1016/j.ces.2015.05.063.

Beinert, S., Fragnière, G., Schilde, C. & Kwade, A. 2018. Multiscale simulation of fine grinding and dispersing processes: Stressing probability, stressing energy and resultant breakage rate. *Advanced Powder Technology*. 29(3):573–583. DOI: 10.1016/j.apt.2017.11.034.

Bernhardt, C., Reinsch, E. & Husemann, K. 1999. The influence of suspension properties on ultra-fine grinding in stirred ball mills. *Powder Technology*. 105(1–3):357–361. DOI: 10.1016/S0032-5910(99)00159-X.

Berry, N., Zhang, Y. & Haeri, S. 2023. Contact models for the multi-sphere discrete element method. *Powder Technology*. 416:118209. DOI: 10.1016/j.powtec.2022.118209.

Blecher, L., Kwade, A. & Schwedes, J. 1996. Motion and stress intensity of grinding beads in a stirred media mill. Part 1 : Energy density distribution and motion of single grinding beads. *Powder Technology*. 86(1):59–68. DOI: 10.1016/0032-5910(95)03038-7.

Böttcher, A.C., Schilde, C. & Kwade, A. 2021. Experimental assessment of grinding bead velocity distributions and stressing conditions in stirred media mills. *Advanced Powder Technology*. 32(2):413–423. DOI: 10.1016/j.apt.2020.12.022.

Buckingham, E. 1914. On Physically Similar Systems; Illustrations of the Use of Dimensional Equations. *Physical Review*. 4(4):345–376. DOI: 10.1103/PhysRev.4.345.

Buist, K.A., Jayaprakash, P., Kuipers, J.A.M., Deen, N.G. & Padding, J.T. 2017. Magnetic particle tracking for nonspherical particles in a cylindrical fluidized bed. *AIChE Journal*. 63(12):5335–5342. DOI: 10.1002/aic.15854.

Burns, S.J. & Hanley, K.J. 2017. Establishing stable time-steps for DEM simulations of non-collinear planar collisions with linear contact laws. *International Journal for Numerical Methods in Engineering*. 110(2):186–200. DOI: 10.1002/nme.5361.

Carvalho, R.M. De, Oliveira, A.L.R., Petit, H.A. & Marcelo, L. 2023. Comparing modeling approaches in simulating a continuous pilot-scale wet vertical stirred mill using PBM-DEM-CFD. *Advanced Powder Technology*. 34(9):104135. DOI: 10.1016/j.apt.2023.104135.

Chen, J., Orozovic, O., Williams, K., Meng, J. & Li, C. 2020. A coupled DEM-SPH model for moisture migration in unsaturated granular material under oscillation. *International Journal of Mechanical Sciences*. 169(November 2019):105313. DOI: 10.1016/j.ijmecsci.2019.105313.

Cho, H., Waters, M.A. & Hogg, R. 1996. Investigation of the grind limit in stirred-media milling. *International Journal of Mineral Processing*. 44–45(SPEC. ISS.):607–615. DOI: 10.1016/0301-7516(95)00069-0.

Cleary, P.W. 2015. Prediction of coupled particle and fluid flows using DEM and SPH. *Minerals Engineering*. 73:85–99. DOI: 10.1016/j.mineng.2014.09.005.

Cleary, P.W. & Morrison, R.D. 2009. Particle methods for modelling in mineral processing. *International Journal of Computational Fluid Dynamics*. 23(2):137–146. DOI: 10.1080/10618560802680229.

Cleary, P.W. & Sinnott, M.D. 2015. Computational prediction of performance for a full scale Isamill: Part 2 - Wet models of charge and slurry transport. *Minerals Engineering*. 79:239–260. DOI: 10.1016/j.mineng.2015.04.013.

Cleary, P.W., Stokes, N. & Hurley, J. 1997. Efficient Collision Detection for Three Dimensional Super-ellipsoidal Particles Paul W. Cleary and Nick Stokes Jarrod Hurley. *Computational Techniques and Applications*. 1–7.

Cleary, P.W., Sinnott, M. & Morrison, R. 2006. Analysis of stirred mill performance using DEM simulation: Part 2 - Coherent flow structures, liner stress and wear, mixing and transport. *Minerals Engineering*. 19(15):1551–1572. DOI: 10.1016/j.mineng.2006.08.013.

Cleary, P.W., Sinnott, M.D. & Pereira, G.G. 2015. Computational prediction of performance for a full scale Isamill: Part 1 - Media motion and energy utilisation in a dry mill. *Minerals Engineering*. 79:220–238. DOI: 10.1016/j.mineng.2015.04.005.

Cleary, P.W., Hilton, J.E. & Sinnott, M.D. 2017. Modelling of industrial particle and multiphase flows. *Powder Technology*. 314:232–252. DOI: 10.1016/j.powtec.2016.10.072.

Conway-Baker, J., Barley, R.W., Williams, R.A., Jia, X., Kostuch, J., McLoughlin, B. & Parker, D.J. 2002. Measurement of the motion of grinding media in a vertically stirred mill using positron emission particle tracking (PEPT). *Minerals Engineering*. 15(1–2):53–59. DOI: 10.1016/S0892-6875(01)00199-6.

Courant, R., Friedrichs, K. & Lewy, H. 1928. Über die partiellen Differenzengleichungen der mathematischen Physik. *Mathematische Annalen*. 100(1):32–74. DOI: 10.1007/BF01448839.

Cundall, P.A. & Strack, O.D.L. 1979. A discrete numerical model for granular assemblies. *Géotechnique*. 29(1):47–65. DOI: 10.1680/geot.1979.29.1.47.

Daouadji, A. & Hicher, P.Y. 2010. An enhanced constitutive model for crushable granular materials. *International Journal for Numerical and Analytical Methods in Geomechanics*. 34(6):555–580. DOI: 10.1002/nag.815.

Daraio, D., Villoria, J., Ingram, A., Alexiadis, A., Stitt, E.H. & Marigo, M. 2019. Validation of a discrete element method (DEM) model of the grinding media dynamics within an attritor mill using positron emission particle tracking (PEPT) measurements. *Applied Sciences (Switzerland)*. 9(22):1–23. DOI: 10.3390/app9224816.

Daraio, D., Villoria, J., Ingram, A., Alexiadis, A., Stitt, E.H. & Marigo, M. 2020. Investigating grinding media dynamics inside a vertical stirred mill using the discrete element method: Effect of impeller arm length. *Powder Technology*. 364:1049–1061. DOI: 10.1016/j.powtec.2019.09.038.

Darcy, H. 1856. *Les fontaines publiques de la ville de Dijon: exposition et application ...* Victor Dalmont. Available: https://books.google.co.za/books?id=DOwbgyt_MzQC.

DEM Solutions. 2014. EDEM 2 . 4 Theory Reference Guide. 19. Available: https://www.edemsimulation.com/.

Eberly, D. 2008. Dynamic collision detection using oriented bounding boxes. *Geometric Tools, Inc*. 48. Available: http://www.geometrictools.com/Documentation/DynamicCollisionDetection.pdf.

Eirich Technology. 2018. *EIRICH TowerMill Vertical agitated media mill.*

Ergun, S. 1952. Fluid flow through packed columns. *Chem. Eng. Prog.* 48:89–94.

Di Felice, R. 1994. The voidage function for fluid-particle interaction systems. *International Journal of Multiphase Flow*. 20(1):153–159. DOI: 10.1016/0301-9322(94)90011-6.

Finnie, I. 1960. Erosion of surfaces by solid particles. *Wear*. 3(2):87–103. DOI: https://doi.org/10.1016/0043-1648(60)90055-7.

FLSmidth. 2024. *FLS Tower Mill A vertical leap in fine grinding Introducing our newest agitated steel media mill for fine grinding*.

FLSmidth (Pty) Ltd. 2019. [Media Release] All Go For VXP mills at Kibali. 1–4.

FLSmidth A/S. 2011. FLSmidth ® VXPmill. 1–12.

Ganser, G.H. 1993. A rational approach to drag prediction of spherical and nonspherical particles. *Powder Technology*. 77(2):143–152. DOI: 10.1016/0032-5910(93)80051-B.

Gao, M. & Forssberg, E. 1995. Prediction of product size distriutions for a stirred ball mill. *Power Technology*. 84:101–106.

Gao, M. & Holmes, R.J. 2007. DEVELOPMENTS IN FINE AND ULTRAFINE GRINDING TECHNOLOGIES FOR THE MINERALS INDUSTRY. 1–11.

Gao, X., Yu, J., Portal, R.J.F. & Rogers, W.A. 2019. Superquadric particle method for non-spherical DEM simulation in open source MFiX : development , implementation and verification. In *2019 AIChE Annual Meeting*. Orlando, Florida.

Gao, X., Yu, J., Lu, L., Li, C. & Rogers, W.A. 2021. Development and validation of SuperDEM-CFD coupled model for simulating non-spherical particles hydrodynamics in fluidized beds. *Chemical Engineering Journal*. 420(P2):127654. DOI: 10.1016/j.cej.2020.127654.

Gao, X., Yu, J., Portal, R.J.F., Dietiker, J.F., Shahnam, M. & Rogers, W.A. 2021. Development and validation of SuperDEM for non-spherical particulate systems using a superquadric particle method. *Particuology*. 61:74–90. DOI: 10.1016/j.partic.2020.11.007.

Giannis, K., Kwade, A., Finke, J.H. & Schilde, C. 2023. The Effect of Particle Shape on the

Compaction of Realistic Non-Spherical Particles—A Multi-Contact DEM Study. *Pharmaceutics*. 15(3):1–17. DOI: 10.3390/pharmaceutics15030909.

Gingold, R.A. & Monaghan, J.J. 1977. Smoothed particle hydrodynamics: theory and application to non-spherical stars. *Monthly Notices of the Royal Astronomical Society*. 181(3):375–389. DOI: 10.1093/mnras/181.3.375.

Glencore Technology. 2015. *IsaMill Breaking the boundaries*.

GlencoreTech. 2020. *[Twitter] You can buy an IsaMill™ from Glencore Technology as mill only or as a complete package with auxiliary equiment. The IsaMill™ therefore fits your flowsheet context no matter what that context is.#IsaMill #mining #mineralprocessing #comminution #e.* Available: https://twitter.com/glencoretech/status/1213994858106494976 [2020, February 13].

Goldman, R. 2005. Curvature formulas for implicit curves and surfaces. *Computer Aided Geometric Design*. 22(7 SPEC. ISS.):632–658. DOI: 10.1016/j.cagd.2005.06.005.

Grohn, P., Schaedler, L., Atxutegi, A., Heinrich, S. & Antonyuk, S. 2023. CFD-DEM Simulation of Superquadric Cylindrical Particles in a Spouted Bed and a Rotor Granulator. *Chemie-Ingenieur-Technik*. 95(1–2):244–255. DOI: 10.1002/cite.202200121.

Gudin, D., Turczyn, R., Mio, H., Kano, J. & Saito, F. 2006. Simulation of the movement of beads by the DEM with respect to the wet grinding process. *AIChE Journal*. 52(10):3421–3426. DOI: 10.1002/aic.10956.

Gudin, D., Kano, J. & Saito, F. 2007a. Effect of the friction coefficient in the discrete element method simulation on media motion in a wet bead mill. *Advanced Powder Technology*. 18(5):555–565. DOI: 10.1163/156855207782146625.

Gudin, D., Kano, J. & Saito, F. 2007b. Correlation between the Grinding Rate Constant and the Impact. *Journal of Chemical Engineering of Japan*. 40(11):980–985.

Guo, W., Gao, P., Tang, Z., Han, Y. & Meng, X. 2021. Effect of grinding media properties and stirrer tip speed on the grinding efficiency of a stirred mill. *Powder Technology*. 382:556–565. DOI: 10.1016/j.powtec.2021.01.022.

Hasan, M., Palaniandy, S., Hilden, M. & Powell, M. 2017. Calculating breakage parameters of a batch vertical stirred mill. *Minerals Engineering*. 111(May):229–237. DOI: 10.1016/j.mineng.2017.06.024.

He, M. & Forssberg, E. 2007. Influence of slurry rheology on stirred media milling of quartzite. *International Journal of Mineral Processing*. 84(1–4):240–251. DOI: 10.1016/j.minpro.2006.08.001.

He, M., Wang, Y. & Forssberg, E. 2004. Slurry rheology in wet ultrafine grinding of industrial minerals: A review. *Powder Technology*. 147(1–3):94–112. DOI: 10.1016/j.powtec.2004.09.032.

He, M., Wang, Y. & Forssberg, E. 2006. Parameter effects on wet ultrafine grinding of limestone through slurry rheology in a stirred media mill. *Powder Technology*. 161(1):10–21. DOI: 10.1016/j.powtec.2005.08.026.

He, Y., Bayly, A.E., Hassanpour, A., Muller, F., Wu, K. & Yang, D. 2018. A GPU-based coupled SPH-DEM method for particle-fluid flow with free surfaces. *Powder Technology*. 338:548–562. DOI: 10.1016/j.powtec.2018.07.043.

Heath, A., Keikkala, V., Paz, A. & Lehto, H. 2017. A power model for fine grinding HIGmills with castellated rotors. *Minerals Engineering*. 103–104:25–32. DOI: 10.1016/j.mineng.2016.07.017.

Hertz, H. 1881. J. reine angew. Math. 92, 156. Reprinted in an English translation in Hertz's 'Miscellaneous Papers'".

Hilton, J.E., Mason, L.R. & Cleary, P.W. 2010. Dynamics of gas-solid fluidised beds with non-spherical particle geometry. *Chemical Engineering Science*. 65(5):1584–1596. DOI: 10.1016/j.ces.2009.10.028.

Hogg, R. 1999. Breakage mechanisms and mill performance in ultrafine grinding. *Powder Technology*. 105(1–3):135–140. DOI: 10.1016/S0032-5910(99)00128-X.

Hölzer, A. & Sommerfeld, M. 2008. New simple correlation formula for the drag coefficient of non-spherical particles. *Powder Technology*. 184(3):361–365. DOI: 10.1016/j.powtec.2007.08.021.

Hu, X.Y. & Adams, N.A. 2006. A multi-phase SPH method for macroscopic and mesoscopic flows. *Journal of Computational Physics*. 213(2):844–861. DOI: 10.1016/j.jcp.2005.09.001.

Jaklič, A., Leonardis, A. & Solina, F. 2000. Superquadrics and Their Geometric Properties. 13–39. DOI: 10.1007/978-94-015-9456-1_2.

Jankovic, A. 2003. Variables affecting the fine grinding of minerals using stirred mills. *Minerals Engineering*. 16(4):337–345. DOI: 10.1016/S0892-6875(03)00007-4.

Jankovic, A. 2008. A review of regrinding and fine grinding technology - the facts and myths. In *Metso Minerals Process Technology Australia and Asia*.

Jankovic, A. & Sinclair, S. 2006. The shape of product size distributions in stirred mills. *Minerals Engineering*. 19(15):1528–1536. DOI: 10.1016/j.mineng.2006.07.006.

Jayasundara, C.T., Yang, R.Y., Yu, A.B. & Curry, D. 2006. Discrete particle simulation of particle flow in the IsaMill process. *Industrial and Engineering Chemistry Research*. 45(18):6349–6359. DOI: 10.1021/ie060474s.

Jayasundara, C.T., Yang, R.Y., Yu, A.B. & Curry, D. 2008. Discrete particle simulation of particle flow in IsaMill-Effect of grinding medium properties. *Chemical Engineering Journal*. 135(1–2):103–112. DOI: 10.1016/j.cej.2007.04.001.

Jayasundara, C.T., Yang, R.Y., Guo, B.Y., Yu, A.B. & Rubenstein, J. 2009. Effect of slurry properties on particle motion in IsaMills. *Minerals Engineering*. 22(11):886–892. DOI: 10.1016/j.mineng.2009.04.009.

Jayasundara, C.T., Yang, R.Y., Yu, A.B. & Rubenstein, J. 2010. Effects of disc rotation speed and media loading on particle flow and grinding performance in a horizontal stirred mill. *International Journal of Mineral Processing*. 96(1–4):27–35. DOI: 10.1016/j.minpro.2010.07.006.

Jayasundara, C.T., Yang, R.Y., Guo, B.Y., Yu, A.B., Govender, I., Mainza, A., Westhuizen, A. Van Der & Rubenstein, J. 2011. CFD-DEM modelling of particle flow in IsaMills - Comparison between simulations and PEPT measurements. *Minerals Engineering*. 24(3–4):181–187. DOI: 10.1016/j.mineng.2010.07.011.

Jayasundara, C.T., Yang, R.Y., Yu, A.B. & Curry, D. 2011. Prediction of the disc wear in a model IsaMill and its effect on the flow of grinding media. *Minerals Engineering*. 24(14):1586–1594. DOI: 10.1016/j.mineng.2011.08.011.

Jayasundara, C.T., Yang, R.Y. & Yu, A.B. 2012. Effect of the size of media on grinding performance in stirred mills. *Minerals Engineering*. 33:66–71. DOI: 10.1016/j.mineng.2011.10.012.

Jing, L. & Stephansson, O. 2007. Fundamentals of Discrete Element Methods for Rock Engineering: Theory and Applications. *Developments in Geotechnical Engineering*. 85:1–545.

Kafui, K.D., Thornton, C. & Adams, M.J. 2002. Discrete particle-continuum fluid modelling of gas-solid fluidised beds. *Chemical Engineering Science*. 57(13):2395–2410. DOI: 10.1016/S0009-2509(02)00140-9.

Kano, J., Mio, H., Saito, F. & Miyazaki, M. 2001. Correlation of grinding rate of gibbsite with impact energy in tumbling mill with mono-size balls. *Minerals Engineering*. 14(10):1213–1223. DOI: 10.1016/S0892-6875(01)00138-8.

Keikkala, V., Lehto, H. & Roitto, I. 2015. Recent progress of regrinding circuits with Outotec HIGmills. *CUPRUM – Czasopismo Naukowo-Techniczne Górnictwa Rud*. 2(75):37–46.

Kelly, E.G. & Spottiswood, D.J. 1982. Introduction to mineral processing.

Khazeni, A. & Mansourpour, Z. 2018. Influence of non-spherical shape approximation on DEM simulation accuracy by multi-sphere method. *Powder Technology*. 332:265–278. DOI: 10.1016/j.powtec.2018.03.030.

Kim, S. & Choi, W.S. 2008. Analysis of ball movement for research of grinding mechanism of a stirred ball mill with 3D discrete element method. *Korean Journal of Chemical Engineering*. 25(3):585–592. DOI: 10.1007/s11814-008-0099-x.

Kim, S., Chung, H. & Choi, H. 2009. Analysis of grinding rate constant on a stirred ball mill using discrete element method simulation. *Journal of the American Ceramic Society*. 92(2):531–534. DOI: 10.1111/j.1551-2916.2008.02897.x.

Kloss, C., Goniva, C., Hager, A., Amberger, S. & Pirker, S. 2012. Models, algorithms and validation for opensource DEM and CFD-DEM. *Progress in Computational Fluid Dynamics*. 12(2–3):140–152. DOI: 10.1504/PCFD.2012.047457.

Kwade, A. 1999. Determination of the most important grinding mechanism in stirred media mills by calculating stress intensity and stress number. *Powder Technology*. 105(1–3):382–388. DOI: 10.1016/S0032-5910(99)00162-X.

Kwade, A. & Schwedes, J. 2007. Chapter 6 Wet Grinding in Stirred Media Mills. In *Handbook of Powder Technology*. 251–382. DOI: 10.1016/S0167-3785(07)12009-1.

van Laarhoven, B., Wiers, S.C.A., Schaafsma, S.H. & Meesters, G.M.H. 2008. Attrition strength of different coated agglomerates. *Chemical Engineering Science*. 63(5):1361–1369. DOI: 10.1016/j.ces.2007.07.006.

Landry, J.W., Grest, G.S., Silbert, L.E. & Plimpton, S.J. 2003. Confined granular packings: Structure, stress, and forces. *Physical Review E - Statistical Physics, Plasmas, Fluids, and Related Interdisciplinary Topics*. 67(4):9. DOI: 10.1103/PhysRevE.67.041303.

Liu, L. & Ji, S. 2020. A new contact detection method for arbitrary dilated polyhedra with potential function in discrete element method. *International Journal for Numerical Methods in Engineering*. 121(24):5742–5765. DOI: 10.1002/nme.6522.

Lucy, L.B. 1977. A numerical approach to the testing of the fission hypothesis. *The Astronomical Journal*. 82(12):1013. DOI: 10.1086/112164.

Magotteaux. 2024. *Addressing key challenges in the mining industry Vertical Tower Mill Castings & grinding media Our offering*.

Mankosa, M.J., Adel, G.T. & Yoon, R.H. 1986. Effect of media size in stirred ball mill grinding of coal. *Powder Technology*. 49(1):75–82. DOI: 10.1016/0032-5910(86)85008-2.

Markauskas, D. & Kruggel-Emden, H. 2019. Coupled DEM-SPH simulations of wet continuous screening. *Advanced Powder Technology*. 30(12):2997–3009. DOI: 10.1016/j.apt.2019.09.007.

Matuttis, H.-G. & Chen, J. 2014. *Understanding the Discrete Element Method*. DOI: 10.1002/9781118567210.

Mazzinghy, D.B., Lichter, J., Schneider, C.L., Galéry, R. & Russo, J.F.C. 2017. Vertical stirred mill scale-up and simulation: Model validation by industrial samplings results. *Minerals Engineering*.

103–104:127–133. DOI: 10.1016/j.mineng.2016.11.018.

McElroy, L., Bao, J., Jayasundara, C.T., Yang, R.Y. & Yu, A.B. 2012. A soft-sensor approach to impact intensity prediction in stirred mills guided by DEM models. *Powder Technology*. 219:151–157. DOI: 10.1016/j.powtec.2011.12.031.

Metso. 2019. Stirred Milling Vertimill Grinding Mills & Stirred Media Detritor. 1–8.

Mindlin, R.D. 1949. Compliance of elastic bodies in contact. *J. Appl. Mech., ASME*. 16:259–268.

Mindlin, R.D. & Deresiewicz, H. 1953. Elastic spheres in contact under varying oblique forces. *J. Applied Mech.* 20:327–344.

Mishra, B.K. & Rajamani, R.K. 1992. The discrete element method for the simulation of ball mills. *Applied Mathematical Modelling*. 16(11):598–604. DOI: 10.1016/0307-904X(92)90035-2.

Monaghan, J.J. 2005. Smoothed particle hydrodynamics. *Reports on Progress in Physics*. 68(8):1703–1759. DOI: 10.1088/0034-4885/68/8/R01.

Morrison, R.D., Cleary, P.W. & Sinnott, M.D. 2009. Using DEM to compare the energy efficiency of pilot scale ball and tower mills. *Minerals Engineering*. 22(7–8):665–672. DOI: 10.1016/j.mineng.2009.01.016.

Napier-Munn, T.J., Morrell, S., Morrison, R.D. & Kojovic, T. 2005. *Mineral Comminution Circuits: Their Operation and Optimisation*. Julius Kruttschnitt Mineral Research Centre.

Nassauer, B., Liedke, T. & Kuna, M. 2013. Polyhedral particles for the discrete element method: Geometry representation, contact detection and particle generation. *Granular Matter*. 15(1):85–93. DOI: 10.1007/s10035-012-0381-9.

Ndimande, C.B., Cleary, P.W., Mainza, A.N. & Sinnott, M.D. 2019. Using two-way coupled DEM-SPH to model an industrial scale Stirred Media Detritor. *Minerals Engineering*. 137(February):259–276. DOI: 10.1016/j.mineng.2019.03.001.

Neethling, S.J. & Barker, D.J. 2016. Using Smooth Particle Hydrodynamics (SPH) to model multiphase mineral processing systems. *Minerals Engineering*. 90:17–28. DOI: 10.1016/j.mineng.2015.09.022.

Norouzi, H.R., Zarghami, R., Sotudeh-Gharebagh, R. & Mostoufi, N. 2016. CFD-DEM Formulation and Coupling. *Coupled CFD-DEM Modeling*. 257–340. DOI: 10.1002/9781119005315.ch6.

Ntsele, C. & Allen, J. 2012. Technology selection of stirred mills for energy efficiency in primary and regrinding applications for the platinum industry. *South African Institute of Mining and Metallurgy*. 781–808.

Oliveira, A.L.R., Rodriguez, V.A., Carvalho, R.M. De, Powell, M.S. & Tavares, L.M. 2020. Mechanistic modeling and simulation of a batch vertical stirred mill. *Minerals Engineering*. 156(January):106487. DOI: 10.1016/j.mineng.2020.106487.

de Oliveira, A.L.R., de Carvalho, R.M. & Tavares, L.M. 2021. Predicting the effect of operating and design variables in grinding in a vertical stirred mill using a mechanistic mill model. *Powder Technology*. 387:560–574. DOI: 10.1016/j.powtec.2021.04.057.

Otsubo, M., O'Sullivan, C. & Shire, T. 2017. Empirical assessment of the critical time increment in explicit particulate discrete element method simulations. *Computers and Geotechnics*. 86:67–79. DOI: 10.1016/j.compgeo.2016.12.022.

Parker, N., Rahman, M. & Bilgili, E. 2020. Impact of media material and process parameters on breakage kinetics–energy consumption during wet media milling of drugs. *European Journal of Pharmaceutics and Biopharmaceutics*. 153(December 2019):52–67. DOI:

10.1016/j.ejpb.2020.05.024.

Patel, C.M., Chakraborty, M. & Murthy, Z.V.P. 2014. Enhancement of stirred media mill performance by a new mixed media grinding strategy. *Journal of Industrial and Engineering Chemistry*. 20(4):2111–2118. DOI: 10.1016/j.jiec.2013.09.040.

Pereira, G.G., Dupuy, P.M., Cleary, P.W. & Delaney, G.W. 2012. Comparison of permeability of model porous media between SPH and LB. *Progress in Computational Fluid Dynamics*. 12(2–3):176–186. DOI: 10.1504/PCFD.2012.047460.

Petit, H.A., de Oliveira, A.L.R. & Tavares, L.M. 2025. Validation of a rheology-dependent PBM-DEM-CFD simulation model of a continuous vertical stirred mill operating under different conditions. *Chemical Engineering Science*. 306(November 2024). DOI: 10.1016/j.ces.2025.121260.

Plochberger, T. & Avila, M.B. 2014. Development of an Energy Optimized Stirred Media Grinding Mill. *BHM Berg- und Hüttenmännische Monatshefte*. 159(6):253–258. DOI: 10.1007/s00501-014-0276-7.

Podlozhnyuk, A., Pirker, S. & Kloss, C. 2017. Efficient implementation of superquadric particles in Discrete Element Method within an open-source framework. *Computational Particle Mechanics*. 4(1):101–118. DOI: 10.1007/s40571-016-0131-6.

Portal, R.J.F., Dias, J.M.P. & Sousa, L.A.G. 2010. Contact Detection Between Convex Superquadric Surfaces. *Archive of Mechanical Engineering*. 57(2):165–186. DOI: 10.2478/v10180-010-0009-8.

Potapov, A. V., Hunt, M.L. & Campbell, C.S. 2001. Liquid-solid flows using smoothed particle hydrodynamics and the discrete element method. *Powder Technology*. 116(2–3):204–213. DOI: 10.1016/S0032-5910(00)00395-8.

Price, D.J. 2012. Smoothed particle hydrodynamics and magnetohydrodynamics. *Journal of Computational Physics*. 231(3):759–794. DOI: 10.1016/j.jcp.2010.12.011.

Radziszewski, P. & Allen, J. 2014. Towards a better understanding of stirred milling technologies - Estimating power consumption and energy usage. In *46th Annual Canadian Mineral Processors Operators Conference*. 1–27.

Di Renzo, A. & Di Maio, F.P. 2004. Comparison of contact-force models for the simulation of collisions in DEM-based granular flow codes. *Chemical Engineering Science*. 59(3):525–541. DOI: 10.1016/j.ces.2003.09.037.

Riley, M., Pinkney, S., Blackburn, S. & Rowson, N.A. 2016. Spatial distributions of media kinetic energy as measured by positron emission particle tracking in a vertically stirred media mill. *Minerals Engineering*. 98:177–186. DOI: 10.1016/j.mineng.2016.08.004.

Rule, C. 2010. Stirred milling — new comminution technology in the PGM industry. In *The 4th International Platinum Conference, Platinum in transition 'Boom or Bust'*. The Southern African Institute of Mining and Metallurgy. 71–78.

Rule, C.M., Knopjes, L., Clermont, B. & Philippe, C. 2008. Fine grinding — Developments in ceramic media technology and resulting improved plant performance at Anglo Platinum. *Technology*. 53–62.

Rydin, R.W., Maurice, D. & Courtney, T.H. 1993. Milling dynamics: Part I. Attritor dynamics: Results of a cinematographic study. *Metallurgical Transactions A*. 24(1):175–185. DOI: 10.1007/BF02669614.

Santhanam, P.R. & Dreizin, E.L. 2012. Predicting conditions for scaled-up manufacturing of materials prepared by ball milling. *Powder Technology*. 221:403–411. DOI:

10.1016/j.powtec.2012.01.037.

Schiller, L. & Naumann, A. 1935. A drag coefficient correlation. *Zeit. Ver. Deutsch. Ing.* 77:318–320.

Sinnott, M., Cleary, P.W. & Morrison, R. 2006. Analysis of stirred mill performance using DEM simulation: Part 1- Media motion, energy consumption and collisional environment. *Minerals Engineering*. 19(15):1537–1550. DOI: 10.1016/j.mineng.2006.08.012.

Sinnott, M., Cleary, P.W. & Morrison, R.D. 2011a. Slurry flow in a tower mill. *Minerals Engineering*. 24(2):152–159. DOI: 10.1016/j.mineng.2010.11.002.

Sinnott, M.D., Cleary, P.W. & Morrison, R.D. 2011b. Is media shape important for grinding performance in stirred mills? *Minerals Engineering*. 24(2):138–151. DOI: 10.1016/j.mineng.2010.10.016.

Soltanbeigi, B., Podlozhnyuk, A., Papanicolopulos, S.A., Kloss, C., Pirker, S. & Ooi, J.Y. 2018. DEM study of mechanical characteristics of multi-spherical and superquadric particles at micro and macro scales. *Powder Technology*. 329:288–303. DOI: 10.1016/j.powtec.2018.01.082.

Stehr, N. & Schwedes, J. 1983. Investigation of the grinding behaviour of a stirred ball mill. *German Chemical Engineering*. 6(6):337–343.

Swann, A., Martin, S. & Gurnett, I. 2023. *Stirred Mill Optimisation-Am I Getting the Most Out of My Mill?*

Swiss Tower Mills AG. 2025. *Products: Product Range*. Available: https://www.stmminerals.com/en/products/product-range/ [2025, May 05].

Sykes, J.A., Weston, D., Adio, N., Che, H., Hart-Villamil, R., Nicușan, A.L., Peace, W., Rhymer, D., et al. 2024. Validation of simulations of particulate, fluid and multiphase systems using positron emission particle tracking: A review. *Particuology*. (xxxx). DOI: 10.1016/j.partic.2024.06.015.

Tan, H., Xu, Q. & Chen, S. 2018. Subaerial rigid landslide-tsunamis: Insights from a block DEM-SPH model. *Engineering Analysis with Boundary Elements*. 95(February):297–314. DOI: 10.1016/j.enganabound.2018.07.013.

Tang, Y., Jiang, Q. & Zhou, C. 2018. A Lagrangian-based SPH-DEM model for fluid–solid interaction with free surface flow in two dimensions. *Applied Mathematical Modelling*. 62:436–460. DOI: 10.1016/j.apm.2018.06.013.

Tavares, L.M. & King, R.P. 2002. Modeling of particle fracture by repeated impacts using continuum damage mechanics. *Powder Technology*. 123(2–3):138–146. DOI: 10.1016/S0032-5910(01)00438-7.

Theuerkauf, J. & Schwedes, J. 1999. Theoretical and experimental investigation on particle and fluid motion in stirred media mills. *Powder Technology*. 105(1–3):406–412. DOI: 10.1016/S0032-5910(99)00165-5.

Thornton, C. 2015. *Granular Dynamics, Contact Mechanics and Particle System Simulations: A DEM study*. V. 24. DOI: 10.1007/978-3-319-18711-2.

Thornton, C., Cummins, S.J. & Cleary, P.W. 2011. An investigation of the comparative behaviour of alternative contact force models during elastic collisions. *Powder Technology*. 210(3):189–197. DOI: 10.1016/j.powtec.2011.01.013.

Thornton, C., Cummins, S.J. & Cleary, P.W. 2013. An investigation of the comparative behaviour of alternative contact force models during inelastic collisions. *Powder Technology*. 233:30–46. DOI: 10.1016/j.powtec.2012.08.012.

Thornton, C., Cummins, S.J. & Cleary, P.W. 2017. On elastic-plastic normal contact force models, with and without adhesion. *Powder Technology*. 315:339–346. DOI: 10.1016/j.powtec.2017.04.008.

Tsuji, Y., Tanaka, T. & Ishida, T. 1992. Lagrangian numerical simulation of plug flow of cohesionless particles in a horizontal pipe. *Powder Technology*. 71(3):239–250. DOI: 10.1016/0032-5910(92)88030-L.

Tsuji, Y., Kawaguchi, T. & Tanaka, T. 1993. Discrete particle simulation of two-dimensional fluidized bed. *Powder Technology*. 77(1):79–87. DOI: 10.1016/0032-5910(93)85010-7.

Turton, R. & Levenspiel, O. 1986. A short note on the drag correlation for spheres. *Powder Technology*. 47(1):83–86. DOI: 10.1016/0032-5910(86)80012-2.

Wang, S. & Shen, Y. 2022. Super-quadric CFD-DEM simulation of chip-like particles flow in a fluidized bed. *Chemical Engineering Science*. 251. DOI: 10.1016/j.ces.2022.117431.

Wang, Y. & Forssberg, E. 2007. Enhancement of energy efficiency for mechanical production of fine and ultra-fine particles in comminution. *China Particuology*. 5(3):193–201. DOI: 10.1016/j.cpart.2007.04.003.

Wang, S., Zhang, Q. & Ji, S. 2021. GPU-based Parallel Algorithm for Super-Quadric Discrete Element Method and Its Applications for Non-Spherical Granular Flows. *Advances in Engineering Software*. 151(August 2020):102931. DOI: 10.1016/j.advengsoft.2020.102931.

Weerasekara, N.S., Powell, M.S., Cleary, P.W., Tavares, L.M., Evertsson, M., Morrison, R.D., Quist, J. & Carvalho, R.M. 2013. The contribution of DEM to the science of comminution. *Powder Technology*. 248:3–24. DOI: 10.1016/j.powtec.2013.05.032.

Wen, C.Y. & Yu, Y.H. 1966. A generalized method for predicting the minimum fluidization velocity. *Aiche Journal*. 12(3):610–612. DOI: 10.1002/aic.690120343.

Van Der Westhuizen, A.P., Govender, I., Mainza, A.N. & Rubenstein, J. 2011. Tracking the motion of media particles inside an IsaMill$^{TM}$ using PEPT. *Minerals Engineering*. 24(3–4):195–204. DOI: 10.1016/j.mineng.2010.07.018.

Williams, J.R. & Pentland, A.P. 1992. Superquadrics and modal dynamics for discrete elements in interactive design. *Engineering Computations*. 9(2):115–127. DOI: 10.1108/eb023852.

Wu, Y., Fan, Z. & Lu, Y. 2003. Bulk and interior packing densities of random close packing of hard spheres. *Journal of Materials Science*. 38(9):2019–2025. DOI: 10.1023/A:1023597707363.

Xu, W.J., Dong, X.Y. & Ding, W.T. 2019. Analysis of fluid-particle interaction in granular materials using coupled SPH-DEM method. *Powder Technology*. 353:459–472. DOI: 10.1016/j.powtec.2019.05.052.

Yamamoto, Y., Soda, R., Kano, J. & Saito, F. 2012. DEM simulation of bead motion during wet bead milling using an enlarged particle model. *International Journal of Mineral Processing*. 114–117:93–99. DOI: 10.1016/j.minpro.2012.10.001.

Yamamoto, Y., Soda, R., Kano, J. & Saito, F. 2014. Application of DEM modified with enlarged particle model to simulation of bead motion in a bead mill. *Particuology*. 14:103–108. DOI: 10.1016/j.partic.2013.06.002.

Yang, R.Y., Jayasundara, C.T., Yu, A.B. & Curry, D. 2006. DEM simulation of the flow of grinding media in IsaMill. *Minerals Engineering*. 19(10):984–994. DOI: 10.1016/j.mineng.2006.05.002.

Yang, Z., Fan, X., Bakalis, S., Parker, D.J. & Fryer, P.J. 2008. A method for characterising solids translational and rotational motions using Multiple-Positron Emission Particle Tracking (Multiple-PEPT). *International Journal of Multiphase Flow*. 34(12):1152–1160. DOI:

10.1016/j.ijmultiphaseflow.2008.06.002.

Zhao, T. 2017. *Coupled DEM-CFD analyses of landslide-induced debris flows*. DOI: 10.1007/978-981-10-4627-8.

Zheng, J., Harris, C.C. & Somasundaran, P. 1996. A study on grinding and energy input in stirred media mills. *Powder Technology*. 86(2):171–178. DOI: 10.1016/0032-5910(95)03051-4.

Zhong, W., Yu, A., Liu, X., Tong, Z. & Zhang, H. 2016. DEM/CFD-DEM Modelling of Non-spherical Particulate Systems: Theoretical Developments and Applications. *Powder Technology*. 302:108–152. DOI: 10.1016/j.powtec.2016.07.010.

# LIST OF COMMUNICATIONS

## Publication

- D. Ssebunnya, A. Mainza, and S. Neethling. 2024. Modelling of particulate and fluid flow in laboratory scale SMDs using coupled DEM-SPH simulations. *Miner. Eng.*, vol. 213. DOI: 10.1016/j.mineng.2024.108736.

## Oral Presentations

- D. Ssebunnya, A. Mainza, P. Cleary, C. Ndimande, M. Sinnott and S. Neethling. 2019. Review of DEM/SPH/CFD applications in stirred mills and a demonstration of particle and fluid flow from the SMD. *6th European Symposium on Comminution and Classification (ESCC)*, 2-4 September 2019, Leeds, United Kingdom.
- D. Ssebunnya, A. Mainza, and S. Neethling. 2022. Two-way coupled DEM/SPH modelling of particulate and fluid flow in laboratory scale vertical stirred media detritors. *5th African Conference on Computational Mechanics (AfriComp5),* 2-4 November 2022, Cape Town, South Africa.
- D. Ssebunnya, A. Mainza, and S. Neethling. 2023. Modelling particulate and fluid flow in laboratory scale stirred media detritors. *Comminution '23,* 17-20 April 2023, Cape Town, South Africa.

# APPENDICES

# Appendix A: Pre-Simulation Supplementary Materials

The calculation of the number of media and fill height of slurry sampled below for Mill A.

## A.1 Super Quadric Media Curvature

The surface plots for the mean radius of curvature of all simulated media shapes, ranging from spherical media to Group 1, 2 and 3 super quadrics are presented in Figure A.1.

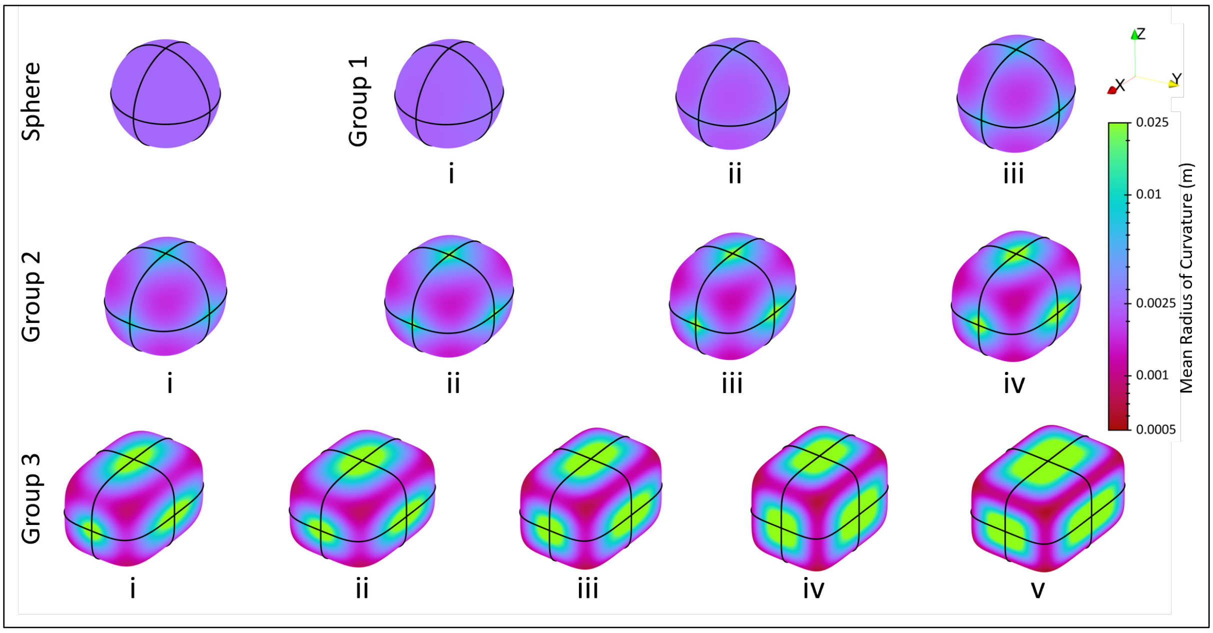

*Figure A.1: Surface plots of the mean radius of curvature for all media shapes simulated*

## A.2 Number of Media

- The mill is filled to the height of the top impeller arm with media and slurry, which for a two-layer impeller is at 7.75 cm above the mill base.
- The volume of Mill A at this height is:

$$V_{MillA,s} = \pi r^2 h$$

$$= \pi\,(7.75)^2 \cdot 7.75$$

$$= 1462\ cm^3$$

- The volume of the impeller to be submerged as determined as follows:

$$V_{pin} = \pi r^2 h$$

$$= \ \pi \cdot 0.75^2 \cdot 14.1$$

$$= 24.9\ cm^3$$

$$V_{shaft_{base\ to\ pin\ 2}} = \pi r^2 h$$

$$= \pi \cdot 1.25^2 \cdot 5.75$$

$$= 28.2\ cm^3$$

$$
\begin{aligned}
V_{Steinmetz} &= \frac{8}{3} r_{shaft} \left[ \left( r_{shaft}^2 + r_{pin}^2 \right) \cdot E\left( \frac{r_{shaft}}{r_{pin}} \right) - \left( r_{shaft}^2 - r_{pin}^2 \right) \cdot K\left( \frac{r_{shaft}}{r_{pin}} \right) \right] \\
&= \frac{8}{3} \cdot 1.25 \cdot [(1.25^2 + 0.75^2) \cdot 1.42 \; - (1.25^2 - 0.75^2) \cdot 1.75 \\
&= 4.21 \; cm^3
\end{aligned}
$$

  - Note: K(x) and E(x) refer to the complete elliptic integral of the first and second kind, respectively

$$
\begin{aligned}
V_{ImpellerA,s} &= 2 \cdot V_{pin} + V_{shaft_{base\ to\ pin\ 2}} - 2 \cdot V_{SteinmetzSolid} \\
&= 2 \cdot 24.9 + 28.2 - 2 \cdot 4.21 \\
&= 69.94 \; cm^3
\end{aligned}
$$

- The Media-Slurry combined volume:

$$
\begin{aligned}
V_{Media+Slurry} &= V_{Mill} - V_{Impeller} \\
&= 1462 - 69.64 \\
&= 1393 \; cm^3
\end{aligned}
$$

- The media volume is 696 $cm^3$ at the media-slurry volume ratio of 1:1.
- The number of media was determined as follows:

$$
\begin{aligned}
N_{Media} &= \frac{V_{Media}}{V_{medium}} = \frac{696}{0.06545} \\
&= 10639
\end{aligned}
$$

## A.3 Fill Height of Slurry

- The volume of slurry was determined following from the number of media calculation to be 696 $cm^3$ at a media to slurry volume ratio of 1:1.
- This volume fills the base of the mill and submerges the bottom impeller and part of the shaft between the two impellers. This height is determined as follows.

$$
\begin{aligned}
H_{fill} &= \frac{V_{slurry} - \left( V_{Mill_{base-shaft\ base}} + V_{Mill_{shaft\ base-pin1\ base}} + V_{Mill_{pin1}} \right)}{A_{Mill-Shaft\ Annulus}} + H_{pin1} \\
&= \frac{696 - (377 + 54 + 259)}{184} + 3.79 \\
&= 3.82 \text{ cm}
\end{aligned}
$$

  - ▪ Note this is the fill height before the hydraulic pressure gradient is applied to the fluid.

## A.4 Expanded table of non-intersection test results

*Table A.1: Non-intersection test parameters of the OBB method, in the reference frame of body i*

| Axis($\boldsymbol{L}$) | R$_i$ | R$_j$ | R$_{ij}$ |
|---|---|---|---|
| $\boldsymbol{I}_x$ | $a_i$ | $a_j\lvert\dot{\mathbf{A}}_{xx}\rvert + b_j\lvert\dot{\mathbf{A}}_{yx}\rvert + c_j\lvert\dot{\mathbf{A}}_{zx}\rvert$ | $\lvert\boldsymbol{IJ}_x\rvert$ |
| $\boldsymbol{I}_y$ | $b_i$ | $a_j\lvert\dot{\mathbf{A}}_{xy}\rvert + b_j\lvert\dot{\mathbf{A}}_{yy}\rvert + c_j\lvert\dot{\mathbf{A}}_{zy}\rvert$ | $\lvert\boldsymbol{IJ}_y\rvert$ |
| $\boldsymbol{I}_z$ | $c_i$ | $a_j\lvert\dot{\mathbf{A}}_{xz}\rvert + b_j\lvert\dot{\mathbf{A}}_{yz}\rvert + c_i\lvert\dot{\mathbf{A}}_{zz}\rvert$ | $\lvert\boldsymbol{IJ}_z\rvert$ |
| $\boldsymbol{J}_x$ | $a_i\lvert\dot{\mathbf{A}}_{xx}\rvert + b_i\lvert\dot{\mathbf{A}}_{yx}\rvert + c_i\lvert\dot{\mathbf{A}}_{zx}\rvert$ | $a_j$ | $\lvert\boldsymbol{IJ}_x\dot{\mathbf{A}}_{xx} + \boldsymbol{IJ}_y\dot{\mathbf{A}}_{yx} + \boldsymbol{IJ}_z\dot{\mathbf{A}}_{zx}\rvert$ |
| $\boldsymbol{J}_y$ | $a_i\lvert\dot{\mathbf{A}}_{xy}\rvert + b_i\lvert\dot{\mathbf{A}}_{yy}\rvert + c_i\lvert\dot{\mathbf{A}}_{zy}\rvert$ | $b_j$ | $\lvert\boldsymbol{IJ}_x\dot{\mathbf{A}}_{xy} + \boldsymbol{IJ}_y\dot{\mathbf{A}}_{yy} + \boldsymbol{IJ}_z\dot{\mathbf{A}}_{zy}\rvert$ |
| $\boldsymbol{J}_z$ | $a_i\lvert\dot{\mathbf{A}}_{xz}\rvert + b_i\lvert\dot{\mathbf{A}}_{yz}\rvert + c_i\lvert\dot{\mathbf{A}}_{zz}\rvert$ | $c_j$ | $\lvert\boldsymbol{IJ}_{\boldsymbol{x}}\dot{\mathbf{A}}_{\boldsymbol{xz}} + \boldsymbol{IJ}_{\boldsymbol{y}}\dot{\mathbf{A}}_{\boldsymbol{yz}} + \boldsymbol{IJ}_{\boldsymbol{z}}\dot{\mathbf{A}}_{\boldsymbol{zz}}\rvert$ |
| $\boldsymbol{I}_x \times \boldsymbol{J}_x$ | $b_i\lvert\dot{\mathbf{A}}_{zx}\rvert + c_i\lvert\dot{\mathbf{A}}_{yx}\rvert$ | $b_j\lvert\dot{\mathbf{A}}_{xz}\rvert + c_j\lvert\dot{\mathbf{A}}_{xy}\rvert$ | $\lvert\boldsymbol{IJ}_z\dot{\mathbf{A}}_{yx} - \boldsymbol{IJ}_y\dot{\mathbf{A}}_{zx}\rvert$ |
| $\boldsymbol{I}_x \times \boldsymbol{J}_y$ | $b_i\lvert\dot{\mathbf{A}}_{zy}\rvert + c_i\lvert\dot{\mathbf{A}}_{yy}\rvert$ | $a_j\lvert\dot{\mathbf{A}}_{xz}\rvert + c_j\lvert\dot{\mathbf{A}}_{xx}\rvert$ | $\lvert\boldsymbol{IJ}_z\dot{\mathbf{A}}_{yy} - \boldsymbol{IJ}_y\dot{\mathbf{A}}_{zy}\rvert$ |
| $\boldsymbol{I}_x \times \boldsymbol{J}_z$ | $b_i\lvert\dot{\mathbf{A}}_{zz}\rvert + c_i\lvert\dot{\mathbf{A}}_{yz}\rvert$ | $a_j\lvert\dot{\mathbf{A}}_{xy}\rvert + b_j\lvert\dot{\mathbf{A}}_{xx}\rvert$ | $\lvert\boldsymbol{IJ}_z\dot{\mathbf{A}}_{yz} - \boldsymbol{IJ}_y\dot{\mathbf{A}}_{zz}\rvert$ |
| $\boldsymbol{I}_y \times \boldsymbol{J}_x$ | $a_i\lvert\dot{\mathbf{A}}_{zx}\rvert + c_i\lvert\dot{\mathbf{A}}_{xx}\rvert$ | $b_j\lvert\dot{\mathbf{A}}_{yz}\rvert + c_j\lvert\dot{\mathbf{A}}_{yy}\rvert$ | $\lvert\boldsymbol{IJ}_x\dot{\mathbf{A}}_{zx} - \boldsymbol{IJ}_z\dot{\mathbf{A}}_{xx}\rvert$ |
| $\boldsymbol{I}_y \times \boldsymbol{J}_y$ | $a_i\lvert\dot{\mathbf{A}}_{zy}\rvert + c_i\lvert\dot{\mathbf{A}}_{xy}\rvert$ | $a_j\lvert\dot{\mathbf{A}}_{yz}\rvert + c_j\lvert\dot{\mathbf{A}}_{yx}\rvert$ | $\lvert\boldsymbol{IJ}_x\dot{\mathbf{A}}_{zy} - \boldsymbol{IJ}_z\dot{\mathbf{A}}_{xy}\rvert$ |
| $\boldsymbol{I}_y \times \boldsymbol{J}_z$ | $a_i\lvert\dot{\mathbf{A}}_{zz}\rvert + c_i\lvert\dot{\mathbf{A}}_{xz}\rvert$ | $a_j\lvert\dot{\mathbf{A}}_{yy}\rvert + b_j\lvert\mathbf{A}_{yx}\rvert$ | $\lvert\boldsymbol{IJ}_x\dot{\mathbf{A}}_{zz} - \boldsymbol{IJ}_z\dot{\mathbf{A}}_{xz}\rvert$ |
| $\boldsymbol{I}_z \times \boldsymbol{J}_x$ | $a_i\lvert\dot{\mathbf{A}}_{yx}\rvert + b_i\lvert\dot{\mathbf{A}}_{xx}\rvert$ | $b_j\lvert\dot{\mathbf{A}}_{zz}\rvert + c_j\lvert\dot{\mathbf{A}}_{zy}\rvert$ | $\lvert\boldsymbol{IJ}_y\dot{\mathbf{A}}_{xx} - \boldsymbol{IJ}_x\dot{\mathbf{A}}_{yx}\rvert$ |
| $\boldsymbol{I}_z \times \boldsymbol{J}_y$ | $a_i\lvert\dot{\mathbf{A}}_{yy}\rvert + b_i\lvert\dot{\mathbf{A}}_{xy}\rvert$ | $a_j\lvert\dot{\mathbf{A}}_{zz}\rvert + c_j\lvert\dot{\mathbf{A}}_{zx}\rvert$ | $\lvert\boldsymbol{IJ}_y\dot{\mathbf{A}}_{xy} - \boldsymbol{IJ}_{\boldsymbol{x}}\dot{\mathbf{A}}_{yy}\rvert$ |
| $\boldsymbol{I}_z \times \boldsymbol{J}_z$ | $a_i\lvert\dot{\mathbf{A}}_{yz}\rvert + b_i\lvert\dot{\mathbf{A}}_{xz}\rvert$ | $a_j\lvert\dot{\mathbf{A}}_{zy}\rvert + b_j\lvert\dot{\mathbf{A}}_{zx}\rvert$ | $\lvert\boldsymbol{IJ}_y\dot{\mathbf{A}}_{xz} - \boldsymbol{IJ}_x\dot{\mathbf{A}}_{yz}\rvert$ |

# Appendix B: Super-Quadric Contact and Interaction Code

## B.1 Super-Quadric Code Overview

The interactions of super-quadric media within the mill space are modelled in CSPH_MPI exclusively in three categories, contact with the mill shell and impeller walls, contact with other super quadrics and interactions with fluid. Key segments of the C++ code used to model these interactions are presented in this Appendix. The contact check methodology for wall collisions and body-body collisions is presented along with the drag force calculation methodology. This code was written by the author into the CSPH_MPI framework and makes use of some of its internal functionality.

## B.2 Wall Contact Check

The wall contact check methodology was adapted from Podlozhnyuk, Pirker & Kloss (2017).

```
double CQuadric::Contact_Check_Wall(CWall* Object, real3 &n, real3 &xc, double
&r_eff, bool &on_convex_edge)
{
      double offset, a, b, y,mag, surf;
      real3 xn, xp, xw, x0, u;

      n = -Object->norm.unit();
      u = q_rot[0].Rotation_Matrix().transpose() * n;
      u = u.unit();

      if (u[0] != 0) {
            a = pow(fabs(scale[1] * u[1]) / fabs(scale[0] * u[0]), roundness /
(2 - roundness));
            y = pow(1 + pow(a, 2 / roundness), 2 / (2 - roundness));
            b = pow(y * fabs(scale[2] * u[2]) / fabs(scale[0] * u[0]),
roundness / (2 - roundness));

            xn[0] = scale[0] / pow(1 + pow(a, 2 / roundness) + pow(b, 2 /
roundness), roundness / 2) * signof(u[0]);
            xn[1] = a * scale[1] * fabs(xn[0]) / scale[0] * signof(u[1]);
            xn[2] = b * scale[2] * fabs(xn[0]) / scale[0] * signof(u[2]);
      }
      else if (u[1] != 0) {
            a = pow(fabs(scale[0] * u[0]) / fabs(scale[1] * u[1]), roundness /
(2 - roundness));
            y = pow(1 + pow(a, 2 / roundness), 2 / (2 - roundness));
            b = pow(y * fabs(scale[2] * u[2]) / fabs(scale[1] * u[1]),
roundness / (2 - roundness));

            xn[1] = (scale[1] / pow(1 + pow(a, 2 / roundness) + pow(b, 2 /
roundness), roundness / 2)) * signof(u[1]);
            xn[0] = (a * scale[0] * fabs(xn[1]) / scale[1]) * signof(u[0]);
            xn[2] = (b * scale[2] * fabs(xn[1]) / scale[1]) * signof(u[2]);
      }
      else if (u[2] != 0) {
            a = pow(fabs(scale[1] * u[1]) / fabs(scale[2] * u[2]), roundness /
(2 - roundness));
            y = pow(1 + pow(a, 2 / roundness), 2 / (2 - roundness));
            b = pow(y * fabs(scale[0] * u[0]) / fabs(scale[2] * u[2]),
roundness / (2 - roundness));

            xn[2] = scale[2] / pow(1 + pow(a, 2 / roundness) + pow(b, 2 /
roundness), roundness / 2) * signof(u[2]);
            xn[1] = a * scale[1] * fabs(xn[2]) / scale[2] * signof(u[1]);
            xn[0] = b * scale[0] * fabs(xn[2]) / scale[2] * signof(u[0]);
```

```
	}

	xw = Object->closestPoint(xn, false, on_convex_edge);
	xw = q_rot.Rotation_Matrix().transpose() * (xw - centre);

	x0 = xn + (((xw - xn).dot(u)) * u);
	x0 = q_rot.Rotation_Matrix() * x0 + centre;

	xn = q_rot.Rotation_Matrix() * xn + centre;
	r_ef = reff(xn);

	xc = x0 + (xn - x0) / 2.0;

	mag = (x0 - xn).magnitude()*0.5;
	surf = surface(x0);

	offset = -mag * signof(surf) + SPH_CONTACT_FAC * CMetric::dx;
	return offset;
}
```

## B.3 Body-Body Contact Check

The body-body collision check methodology is adapted from Podlozhnyuk, Pirker & Kloss (2017) .

```
double CQuadric::Contact_Check_Quadric(CQuadric* Object, real3 &n, real3 &xc,
double &r_ef)
{
	//Bounding sphere test
	double r1 = getBoundingSphere();
	double r2 = Object->getBoundingSphere();

	double offset, magnitude;
	bool cross;

	cross = Object->cross_period || cross_period;
	real3 m = CMetric::dxp(Object->centre, centre, cross);
	magnitude = m.magnitude();

	offset = (r1 + r2 + SPH_CONTACT_FAC * CMetric::dx) - magnitude;

	if (offset <= 0.0)
		return offset;

	//Oriented bounding box test
	//Adapted from https://stackoverflow.com/a/52010428
	matrix3x3 J = (Object->q_rot.Rotation_Matrix() *
q_rot.Rotation_Matrix().transpose()).transpose();
	matrix3x3 I = matrix3x3(real3(1.0, 0.0, 0.0), real3(0.0, 1.0, 0.0),
real3(0.0, 0.0, 1.0));

	real3 IJ = q_rot.Rotation_Matrix().transpose() * m;
	real3 ai = scale;
	real3 aj = Object->scale;

	if (getSeparatingPlane(IJ, I[0], I, ai, J, aj) ||
		getSeparatingPlane(IJ, I[1], I, ai, J, aj) ||
		getSeparatingPlane(IJ, I[2], I, ai, J, aj) ||
		getSeparatingPlane(IJ, J[0], I, ai, J, aj) ||
		getSeparatingPlane(IJ, J[1], I, ai, J, aj) ||
		getSeparatingPlane(IJ, J[2], I, ai, J, aj) ||
		getSeparatingPlane(IJ, I[0].cross(J[0]), I, ai, J, aj) ||
```

```
                getSeparatingPlane(IJ, I[0].cross(J[1]), I, ai, J, aj) ||
                getSeparatingPlane(IJ, I[0].cross(J[2]), I, ai, J, aj) ||
                getSeparatingPlane(IJ, I[1].cross(J[0]), I, ai, J, aj) ||
                getSeparatingPlane(IJ, I[1].cross(J[1]), I, ai, J, aj) ||
                getSeparatingPlane(IJ, I[1].cross(J[2]), I, ai, J, aj) ||
                getSeparatingPlane(IJ, I[2].cross(J[0]), I, ai, J, aj) ||
                getSeparatingPlane(IJ, I[2].cross(J[1]), I, ai, J, aj) ||
                getSeparatingPlane(IJ, I[2].cross(J[2]), I, ai, J, aj))
                return -offset;


        // Middle point test
        int N = 5;
        double mu = 1.0;
        double surf1, surf2, det, a1, b1, c1, n1, a2, b2, c2, n2, psi;
        double jacob[4][4]{}, adj[4][4]{}, phi[4]{};

        real3 X = (r1 * centre + r2 * Object->centre) / (r1 + r2);
        real3 grad1, grad2;
        matrix3x3 hess1, hess2;

        for (int k = 1; k < N + 1; k++) {

                a1 = r1 + k * (scale[0] - r1) / N;
                b1 = r1 + k * (scale[1] - r1) / N;
                c1 = r1 + k * (scale[2] - r1) / N;
                n1 = 1 - k * (1 - roundness) / N;

                a2 = r2 + k * (Object->scale[0] - r2) / N;
                b2 = r2 + k * (Object->scale[1] - r2) / N;
                c2 = r2 + k * (Object->scale[2] - r2) / N;
                n2 = 1 - k * (1 - Object->roundness) / N;

                surf1 = surface(X, a1, b1, c1, n1);
                grad1 = gradient(X, a1, b1, c1, n1);
                hess1 = hessian(X, a1, b1, c1, n1);
                surf2 = Object->surface(X, a2, b2, c2, n2);
                grad2 = Object->gradient(X, a2, b2, c2, n2);
                hess2 = Object->hessian(X, a2, b2, c2, n2);

                phi[0] = grad1[0] + pow(mu, 2) * grad2[0];
                phi[1] = grad1[1] + pow(mu, 2) * grad2[1];
                phi[2] = grad1[2] + pow(mu, 2) * grad2[2];
                phi[3] = surf1 - surf2;

                jacob[0][0] = hess1[0][0] + pow(mu, 2) * hess2[0][0];  jacob[0][1]
= hess1[0][1] + pow(mu, 2) * hess2[0][1];  jacob[0][2] = hess1[0][2] + pow(mu,
2) * hess2[0][2]; jacob[0][3] = 2 * mu * grad2[0];
                jacob[1][0] = hess1[1][0] + pow(mu, 2) * hess2[1][0];  jacob[1][1]
= hess1[1][1] + pow(mu, 2) * hess2[1][1];  jacob[1][2] = hess1[1][2] + pow(mu,
2) * hess2[1][2]; jacob[1][3] = 2 * mu * grad2[1];
                jacob[2][0] = hess1[2][0] + pow(mu, 2) * hess2[2][0];  jacob[2][1]
= hess1[2][1] + pow(mu, 2) * hess2[2][1];  jacob[2][2] = hess1[2][2] + pow(mu,
2) * hess2[2][2]; jacob[2][3] = 2 * mu * grad2[2];
                jacob[3][0] = grad1[0] - grad2[0]; jacob[3][1] = grad1[1] -
grad2[1]; jacob[3][2] = grad1[2] - grad2[2]; jacob[3][3] = 0;

                det = jacob[0][0] * (jacob[1][2] * jacob[2][3] * jacob[3][1] +
jacob[1][3] * jacob[2][1] * jacob[3][2] - jacob[1][1] * jacob[2][3] *
jacob[3][2] - jacob[1][3] * jacob[2][2] * jacob[3][1])
                        + jacob[0][1] * (jacob[1][0] * jacob[2][3] * jacob[3][2] +
jacob[1][3] * jacob[2][2] * jacob[3][0] - jacob[1][2] * jacob[2][3] *
jacob[3][0] - jacob[1][3] * jacob[2][0] * jacob[3][2])
```

```
                   + jacob[0][2] * (jacob[1][1] * jacob[2][3] * jacob[3][0] +
jacob[1][3] * jacob[2][0] * jacob[3][1] - jacob[1][0] * jacob[2][3] *
jacob[3][1] - jacob[1][3] * jacob[2][1] * jacob[3][0])
                   + jacob[0][3] * (jacob[1][0] * jacob[2][2] * jacob[3][1] +
jacob[1][1] * jacob[2][0] * jacob[3][2] + jacob[1][2] * jacob[2][1] *
jacob[3][0] - jacob[1][0] * jacob[2][1] * jacob[3][2] - jacob[1][1] *
jacob[2][2] * jacob[3][0] - jacob[1][2] * jacob[2][0] * jacob[3][1]);

             adj[0][0] = jacob[3][1] * (jacob[1][2] * jacob[2][3] - jacob[1][3]
* jacob[2][2]) + jacob[3][2] * (jacob[1][3] * jacob[2][1] - jacob[1][1] *
jacob[2][3]);
             adj[1][0] = jacob[3][0] * (jacob[1][3] * jacob[2][2] - jacob[1][2]
* jacob[2][3]) + jacob[3][2] * (jacob[1][0] * jacob[2][3] - jacob[2][0] *
jacob[1][3]);
             adj[2][0] = jacob[3][0] * (jacob[1][1] * jacob[2][3] - jacob[1][3]
* jacob[2][1]) + jacob[3][1] * (jacob[2][0] * jacob[1][3] - jacob[1][0] *
jacob[2][3]);
             adj[3][0] = jacob[3][0] * (jacob[1][2] * jacob[2][1] - jacob[1][1]
* jacob[1][1]) + jacob[3][1] * (jacob[1][0] * jacob[1][3] - jacob[2][0] *
jacob[1][2]) + jacob[3][2] * (jacob[2][0] * jacob[1][1] - jacob[1][0] *
jacob[2][1]);

             adj[0][1] = jacob[3][1] * (jacob[0][3] * jacob[2][2] - jacob[0][2]
* jacob[2][3]) + jacob[3][2] * (jacob[0][1] * jacob[2][3] - jacob[0][3] *
jacob[2][1]);
             adj[1][1] = jacob[3][0] * (jacob[0][2] * jacob[2][3] - jacob[0][3]
* jacob[2][2]) + jacob[3][2] * (jacob[2][0] * jacob[0][3] - jacob[0][0] *
jacob[2][3]);
             adj[2][1] = jacob[3][0] * (jacob[0][3] * jacob[2][1] - jacob[0][1]
* jacob[2][3]) + jacob[3][1] * (jacob[0][0] * jacob[2][3] - jacob[2][0] *
jacob[0][3]);
             adj[3][1] = jacob[3][0] * (jacob[0][1] * jacob[2][2] - jacob[0][2]
* jacob[2][1]) + jacob[3][1] * (jacob[2][0] * jacob[0][2] - jacob[0][0] *
jacob[2][2]) + jacob[3][2] * (jacob[0][0] * jacob[2][1] - jacob[2][0] *
jacob[0][1]);

             adj[0][2] = jacob[3][1] * (jacob[0][2] * jacob[1][3] - jacob[0][3]
* jacob[1][2]) + jacob[3][2] * (jacob[0][3] * jacob[1][1] - jacob[0][1] *
jacob[1][3]);
             adj[1][2] = jacob[3][0] * (jacob[0][3] * jacob[1][2] - jacob[0][2]
* jacob[1][3]) + jacob[3][2] * (jacob[0][0] * jacob[1][3] - jacob[0][3] *
jacob[1][0]);
             adj[2][2] = jacob[3][0] * (jacob[0][1] * jacob[1][3] - jacob[0][3]
* jacob[1][1]) + jacob[3][1] * (jacob[0][3] * jacob[1][0] - jacob[0][0] *
jacob[1][3]);
             adj[3][2] = jacob[3][0] * (jacob[0][2] * jacob[1][1] - jacob[0][1]
* jacob[1][2]) + jacob[3][1] * (jacob[0][0] * jacob[1][2] - jacob[0][2] *
jacob[1][0]) + jacob[3][2] * (jacob[0][1] * jacob[1][0] - jacob[0][0] *
jacob[1][1]);

             adj[0][3] = jacob[2][1] * (jacob[0][3] * jacob[1][2] - jacob[0][2]
* jacob[1][3]) + jacob[2][2] * (jacob[0][1] * jacob[1][3] - jacob[0][3] *
jacob[1][1]) + jacob[2][3] * (jacob[0][2] * jacob[1][1] - jacob[0][1] *
jacob[1][2]);
             adj[1][3] = jacob[2][0] * (jacob[0][2] * jacob[1][3] - jacob[0][3]
* jacob[1][2]) + jacob[2][2] * (jacob[0][3] * jacob[1][0] - jacob[0][0] *
jacob[1][3]) + jacob[2][3] * (jacob[0][0] * jacob[1][2] - jacob[0][2] *
jacob[1][0]);
             adj[2][3] = jacob[2][0] * (jacob[0][3] * jacob[1][1] - jacob[0][1]
* jacob[1][3]) + jacob[2][1] * (jacob[0][0] * jacob[1][3] - jacob[0][3] *
jacob[1][0]) + jacob[2][3] * (jacob[0][1] * jacob[1][0] - jacob[0][0] *
jacob[1][1]);
             adj[3][3] = jacob[2][0] * (jacob[0][1] * jacob[1][2] - jacob[0][2]
* jacob[1][1]) + jacob[2][1] * (jacob[0][2] * jacob[1][0] - jacob[0][0] *
```

```
jacob[1][2]) + jacob[2][2] * (jacob[0][0] * jacob[2][2] - jacob[0][1] *
jacob[1][0]);

                X[0] = X[0] - (adj[0][0] * phi[0] + adj[0][1] * phi[1] + adj[0][2]
* phi[2] + adj[0][3] * phi[3])/det;
                X[1] = X[1] - (adj[1][0] * phi[0] + adj[1][1] * phi[1] + adj[1][2]
* phi[2] + adj[1][3] * phi[3])/det;
                X[2] = X[2] - (adj[2][0] * phi[0] + adj[2][1] * phi[1] + adj[2][2]
* phi[2] + adj[2][3] * phi[3])/det;
                mu = mu - (adj[3][0] * phi[0] + adj[3][1] * phi[1] + adj[3][2] *
phi[2] + adj[3][3] * phi[3])/det;
        }

        surf1 = surface(X);
        surf2 = Object->surface(X);

        if (surf1 >= 0.0 || surf2 >= 0.0)
                return -offset;

        grad1 = gradient(X);
        grad2 = Object->gradient(X);

        phi[0] = grad1[0] + pow(mu, 2) * grad2[0];
        phi[1] = grad1[1] + pow(mu, 2) * grad2[1];
        phi[2] = grad1[2] + pow(mu, 2) * grad2[2];
        phi[3] = surf1 - surf2;

        psi = phi[0] * phi[0] + phi[1] * phi[1] + phi[2] * phi[2] + phi[3] *
phi[3];

        double chk[4]{};
        double alpha = 1;
        double pi{}, mu0{};
        real3 X0;
        while (psi > crit)
        {
                surf1 = surface(X);
                grad1 = gradient(X);
                hess1 = hessian(X);
                surf2 = Object->surface(X);
                grad2 = Object->gradient(X);
                hess2 = Object->hessian(X);



                jacob[0][0] = hess1[0][0] + pow(mu, 2) * hess2[0][0];  jacob[0][1]
= hess1[0][1] + pow(mu, 2) * hess2[0][1];  jacob[0][2] = hess1[0][2] + pow(mu,
2) * hess2[0][2]; jacob[0][3] = 2 * mu * grad2[0];
                jacob[1][0] = hess1[1][0] + pow(mu, 2) * hess2[1][0];  jacob[1][1]
= hess1[1][1] + pow(mu, 2) * hess2[1][1];  jacob[1][2] = hess1[1][2] + pow(mu,
2) * hess2[1][2]; jacob[1][3] = 2 * mu * grad2[1];
                jacob[2][0] = hess1[2][0] + pow(mu, 2) * hess2[2][0];  jacob[2][1]
= hess1[2][1] + pow(mu, 2) * hess2[2][1];  jacob[2][2] = hess1[2][2] + pow(mu,
2) * hess2[2][2]; jacob[2][3] = 2 * mu * grad2[2];
                jacob[3][0] = grad1[0] - grad2[0]; jacob[3][1] = grad1[1] -
grad2[1]; jacob[3][2] = grad1[2] - grad2[2]; jacob[3][3] = 0;

                det = jacob[0][0] * (jacob[1][2] * jacob[2][3] * jacob[3][1] +
jacob[1][3] * jacob[2][1] * jacob[3][2] - jacob[1][1] * jacob[2][3] *
jacob[3][2] - jacob[1][3] * jacob[2][2] * jacob[3][1])
                        + jacob[0][1] * (jacob[1][0] * jacob[2][3] * jacob[3][2] +
jacob[1][3] * jacob[2][2] * jacob[3][0] - jacob[1][2] * jacob[2][3] *
jacob[3][0] - jacob[1][3] * jacob[2][0] * jacob[3][2])
```

```
                   + jacob[0][2] * (jacob[1][1] * jacob[2][3] * jacob[3][0] +
jacob[1][3] * jacob[2][0] * jacob[3][1] - jacob[1][0] * jacob[2][3] *
jacob[3][1] - jacob[1][3] * jacob[2][1] * jacob[3][0])
                   + jacob[0][3] * (jacob[1][0] * jacob[2][2] * jacob[3][1] +
jacob[1][1] * jacob[2][0] * jacob[3][2] + jacob[1][2] * jacob[2][1] *
jacob[3][0] - jacob[1][0] * jacob[2][1] * jacob[3][2] - jacob[1][1] *
jacob[2][2] * jacob[3][0] - jacob[1][2] * jacob[2][0] * jacob[3][1]);

             adj[0][0] = jacob[3][1] * (jacob[1][2] * jacob[2][3] - jacob[1][3]
* jacob[2][2]) + jacob[3][2] * (jacob[1][3] * jacob[2][1] - jacob[1][1] *
jacob[2][3]);
             adj[1][0] = jacob[3][0] * (jacob[1][3] * jacob[2][2] - jacob[1][2]
* jacob[2][3]) + jacob[3][2] * (jacob[1][0] * jacob[2][3] - jacob[2][0] *
jacob[1][3]);
             adj[2][0] = jacob[3][0] * (jacob[1][1] * jacob[2][3] - jacob[1][3]
* jacob[2][1]) + jacob[3][1] * (jacob[2][0] * jacob[1][3] - jacob[1][0] *
jacob[2][3]);
             adj[3][0] = jacob[3][0] * (jacob[1][2] * jacob[2][1] - jacob[1][1]
* jacob[1][1]) + jacob[3][1] * (jacob[1][0] * jacob[1][3] - jacob[2][0] *
jacob[1][2]) + jacob[3][2] * (jacob[2][0] * jacob[1][1] - jacob[1][0] *
jacob[2][1]);

             adj[0][1] = jacob[3][1] * (jacob[0][3] * jacob[2][2] - jacob[0][2]
* jacob[2][3]) + jacob[3][2] * (jacob[0][1] * jacob[2][3] - jacob[0][3] *
jacob[2][1]);
             adj[1][1] = jacob[3][0] * (jacob[0][2] * jacob[2][3] - jacob[0][3]
* jacob[2][2]) + jacob[3][2] * (jacob[2][0] * jacob[0][3] - jacob[0][0] *
jacob[2][3]);
             adj[2][1] = jacob[3][0] * (jacob[0][3] * jacob[2][1] - jacob[0][1]
* jacob[2][3]) + jacob[3][1] * (jacob[0][0] * jacob[2][3] - jacob[2][0] *
jacob[0][3]);
             adj[3][1] = jacob[3][0] * (jacob[0][1] * jacob[2][2] - jacob[0][2]
* jacob[2][1]) + jacob[3][1] * (jacob[2][0] * jacob[0][2] - jacob[0][0] *
jacob[2][2]) + jacob[3][2] * (jacob[0][0] * jacob[2][1] - jacob[2][0] *
jacob[0][1]);

             adj[0][2] = jacob[3][1] * (jacob[0][2] * jacob[1][3] - jacob[0][3]
* jacob[1][2]) + jacob[3][2] * (jacob[0][3] * jacob[1][1] - jacob[0][1] *
jacob[1][3]);
             adj[1][2] = jacob[3][0] * (jacob[0][3] * jacob[1][2] - jacob[0][2]
* jacob[1][3]) + jacob[3][2] * (jacob[0][0] * jacob[1][3] - jacob[0][3] *
jacob[1][0]);
             adj[2][2] = jacob[3][0] * (jacob[0][1] * jacob[1][3] - jacob[0][3]
* jacob[1][1]) + jacob[3][1] * (jacob[0][3] * jacob[1][0] - jacob[0][0] *
jacob[1][3]);
             adj[3][2] = jacob[3][0] * (jacob[0][2] * jacob[1][1] - jacob[0][1]
* jacob[1][2]) + jacob[3][1] * (jacob[0][0] * jacob[1][2] - jacob[0][2] *
jacob[1][0]) + jacob[3][2] * (jacob[0][1] * jacob[1][0] - jacob[0][0] *
jacob[1][1]);

             adj[0][3] = jacob[2][1] * (jacob[0][3] * jacob[1][2] - jacob[0][2]
* jacob[1][3]) + jacob[2][2] * (jacob[0][1] * jacob[1][3] - jacob[0][3] *
jacob[1][1]) + jacob[2][3] * (jacob[0][2] * jacob[1][1] - jacob[0][1] *
jacob[1][2]);
             adj[1][3] = jacob[2][0] * (jacob[0][2] * jacob[1][3] - jacob[0][3]
* jacob[1][2]) + jacob[2][2] * (jacob[0][3] * jacob[1][0] - jacob[0][0] *
jacob[1][3]) + jacob[2][3] * (jacob[0][0] * jacob[1][2] - jacob[0][2] *
jacob[1][0]);
             adj[2][3] = jacob[2][0] * (jacob[0][3] * jacob[1][1] - jacob[0][1]
* jacob[1][3]) + jacob[2][1] * (jacob[0][0] * jacob[1][3] - jacob[0][3] *
jacob[1][0]) + jacob[2][3] * (jacob[0][1] * jacob[1][0] - jacob[0][0] *
jacob[1][1]);
             adj[3][3] = jacob[2][0] * (jacob[0][1] * jacob[1][2] - jacob[0][2]
* jacob[1][1]) + jacob[2][1] * (jacob[0][2] * jacob[1][0] - jacob[0][0] *
```

```
jacob[1][2]) + jacob[2][2] * (jacob[0][0] * jacob[2][2] - jacob[0][1] *
jacob[1][0]);

             chk[0] = (adj[0][0] * phi[0] + adj[0][1] * phi[1] + adj[0][2] *
phi[2] + adj[0][3] * phi[3]);
             chk[1] = (adj[1][0] * phi[0] + adj[1][1] * phi[1] + adj[1][2] *
phi[2] + adj[1][3] * phi[3]);
             chk[2] = (adj[2][0] * phi[0] + adj[2][1] * phi[1] + adj[2][2] *
phi[2] + adj[2][3] * phi[3]);
             chk[3] = (adj[3][0] * phi[0] + adj[3][1] * phi[1] + adj[3][2] *
phi[2] + adj[3][3] * phi[3]);

             X0 = X;
             mu0 = mu;

             X[0] = X0[0] - alpha * chk[0] / det;
             X[1] = X0[1] - alpha * chk[1] / det;
             X[2] = X0[2] - alpha * chk[2]/det;
             mu = mu0 - alpha * chk[3] / det;

             surf1 = surface(X);
             surf2 = Object->surface(X);
             grad1 = gradient(X);
             grad2 = Object->gradient(X);

             phi[0] = grad1[0] + pow(mu, 2) * grad2[0];
             phi[1] = grad1[1] + pow(mu, 2) * grad2[1];
             phi[2] = grad1[2] + pow(mu, 2) * grad2[2];
             phi[3] = surf1 - surf2;

             pi = phi[0] * phi[0] + phi[1] * phi[1] + phi[2] * phi[2] + phi[3]
* phi[3];

             while (pi > psi) {

                    alpha /=  2;

                    X[0] = X0[0] - alpha * chk[0] / det;
                    X[1] = X0[1] - alpha * chk[1] / det;
                    X[2] = X0[2] - alpha * chk[2] / det;
                    mu = mu0 - alpha * chk[3] / det;

                    surf1 = surface(X);
                    surf2 = Object->surface(X);
                    grad1 = gradient(X);
                    grad2 = Object->gradient(X);

                    phi[0] = grad1[0] + pow(mu, 2) * grad2[0];
                    phi[1] = grad1[1] + pow(mu, 2) * grad2[1];
                    phi[2] = grad1[2] + pow(mu, 2) * grad2[2];
                    phi[3] = surf1 - surf2;

                    pi = phi[0] * phi[0] + phi[1] * phi[1] + phi[2] * phi[2] +
phi[3] * phi[3];
             }
             psi = pi;
             alpha = 1;

             N++;
             if (N==10) break;
      }

      if (surf1 >= 0.0 || surf2 >= 0.0)
                    return -offset;
```

```
        xc = X;
        n = gradient(xc).unit();

        a1 = 1.0;
        a2 = -1.0;

        double Sa1 = surface(X + a1 * n);
        double Sa2 = Object->surface(X + a2 * n);

        while (fabs(Sa1) >= crit)
        {
                a1 = a1 - surface(X + a1 * n) / ((gradientbcf(X + a1 * n) *
q_rot.Rotation_Matrix().transpose()).dot(n));
                Sa1 = surface(X + a1 * n);
        }

        while (fabs(Sa2) >= crit)
        {
                a2 = a2 - Object->surface(X + a2 * n) / ((Object->gradientbcf(X +
a2 * n) * Object->q_rot.Rotation_Matrix().transpose()).dot(n));
                Sa2 = Object->surface(X + a2 * n);
        }

        r1 = reff(X + a1 * n);
        r2 = Object->reff(X + a2 * n);
        r_ef = (r1* r2) / (r1 + r2);

        offset = ((a1 - a2) * n).magnitude() + SPH_CONTACT_FAC * CMetric::dx;
        return offset;


}
```

## B.4 Drag Force Calculation

The drag force methodology was adapted from Jaklič, Leonardis & Solina (2000) & Hilton, Mason & Cleary (2010).

```
case De_Felice_Quadric:
{
        double Solid_frac = fast_min(current->body_fraction, 
SPH_BODY_DRAG_FORCE_CUTOFF);
        double d = 2.0 * body->r_eff;

        real3 vrel = (body->v[0] - current->v[ndelta]);

        double phi1 = 1;
        double phi2 = 1;

        if (vrel.magnitude() > 0) {
                real3 u = (body->Rotation.transpose() * vrel).unit();
                double a = body->scale[0], b = body->scale[1], c = body->scale[2], 
n = body->roundness;
                int N = 505;
                double theta, s, phi, area{};
                real3  p, p0, p1;

                if (u[2] != 0) { // rim calculation with projection onto u and 
embedded area calculation
                        for (int k = 0; k < N + 1; k++) {
                                theta = -M_PI + 2 * M_PI * k / N;

                                s = (-c / u[2]) * ((u[0] / a) * signof(cos(theta)) * 
pow(fabs(cos(theta)), 2 - n) + (u[1] / b) * signof(sin(theta)) * 
pow(fabs(sin(theta)), 2 - n));
                                phi = atan(pow(fabs(s), 1 / (2 - n)) * signof(s));

                                p[0] = a * pow(fabs((cos(phi))), n) * 
pow(fabs((cos(theta))), n) * signof(cos(phi)) * signof(cos(theta));
                                p[1] = b * pow(fabs((cos(phi))), n) * 
pow(fabs((sin(theta))), n) * signof(cos(phi)) * signof(sin(theta));
                                p[2] = c * pow(fabs((sin(phi))), n) * 
signof(sin(phi));

                                p = p - u.dot(p) * u;

                                if (k == 0) {
                                        p0 = p;
                                        p1 = p;
                                }
                                else {
                                        area += 0.5 * (p1.cross(p)).magnitude();
                                        p1 = p;
                                }
                                if (k == N) {
                                        area += 0.5 * (p1.cross(p0)).magnitude();
                                }
                        }
                }
                else if (u[1] != 0) {
                        for (int k = 0; k < N + 1; k++) {
                                theta = -M_PI + 2 * M_PI * k / N;
```

```
                s = (-b / u[1]) * ((u[0] / a) * signof(cos(theta)) *
pow(fabs(cos(theta)), 2 - n) + (u[2] / c) * signof(sin(theta)) *
pow(fabs(sin(theta)), 2 - n));
                phi = atan(pow(fabs(s), 1 / (2 - n)) * signof(s));

                p[0] = a * pow(fabs((cos(phi))), n) *
pow(fabs((cos(theta))), n) * signof(cos(phi)) * signof(cos(theta));
                p[2] = c * pow(fabs((cos(phi))), n) *
pow(fabs((sin(theta))), n) * signof(cos(phi)) * signof(sin(theta));
                p[1] = b * pow(fabs((sin(phi))), n) *
signof(sin(phi));

                p = p - u.dot(p) * u;

                if (k == 0) {
                    p0 = p;
                    p1 = p;
                }
                else {
                    area += 0.5 * (p1.cross(p)).magnitude();
                    p1 = p;
                }
                if (k == N) {
                    area += 0.5 * (p1.cross(p0)).magnitude();
                }
            }
        }
        else if (u[0] != 0) {
            for (int k = 0; k < N + 1; k++) {
                theta = -M_PI + 2 * M_PI * k / N;

                s = (-a / u[0]) * ((u[2] / c) * signof(cos(theta)) *
pow(fabs(cos(theta)), 2 - n) + (u[1] / b) * signof(sin(theta)) *
pow(fabs(sin(theta)), 2 - n));
                phi = atan(pow(fabs(s), 1 / (2 - n)) * signof(s));

                p[2] = c * pow(fabs((cos(phi))), n) *
pow(fabs((cos(theta))), n) * signof(cos(phi)) * signof(cos(theta));
                p[1] = b * pow(fabs((cos(phi))), n) *
pow(fabs((sin(theta))), n) * signof(cos(phi)) * signof(sin(theta));
                p[0] = a * pow(fabs((sin(phi))), n) *
signof(sin(phi));

                p = p - u.dot(p) * u;

                if (k == 0) {
                    p0 = p;
                    p1 = p;
                }
                else {
                    area += 0.5 * (p1.cross(p)).magnitude();
                    p1 = p;
                }
                if (k == N) {
                    area += 0.5 * (p1.cross(p0)).magnitude();
                }
            }
        }

        phi1 = 4 * M_PI * pow(0.0025, 2) / body->surface_area;
        phi2 = M_PI * pow(0.0025, 2) / area;
    }
```

```
        double vmag = vrel.magnitude(), Re = rho * d * vmag * (1.0 - Solid_frac)
/ mu;
        double chi = 3.7 - 0.65 * exp(-0.5 * pow(1.5 - log10(Re), 2));
        double Beta = (Re / 24) * ((8 / Re) * pow(phi2, -0.5) + (16 / Re) *
pow(phi1, -0.5) + (3 / pow(Re, 0.5)) * pow(phi1, -0.75) + 0.42 * pow(10, 0.4 *
pow(-log10(phi1), 0.2)) / phi2) * pow(1.0 - Solid_frac, -chi);


        F_tot = ((3.0 * M_PI * mu * Beta) * (current->V * Wv *
inv_sigmaV_apparent)) * vrel;

}
break;
```

# Appendix C: Raw Data Excerpts

## C.1 Raw Data Overview

The raw data from the contact data output and the data extracted from Paraview is stored in text files with a 6-digit precision. The following figures show snapshots of the data files.

## C.2 Contact Data

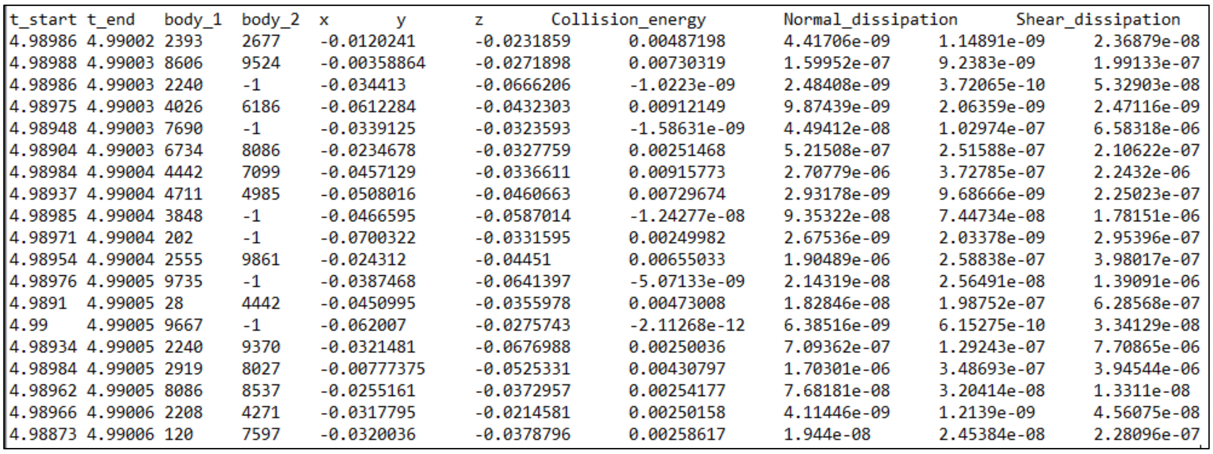

```
t_start t_end   body_1  body_2  x         y         z         Collision_energy        Normal_dissipation       Shear_dissipation
4.98986 4.99002 2393    2677    -0.0120241          -0.0231859     0.00487198     4.41706e-09     1.14891e-09     2.36879e-08
4.98988 4.99003 8606    9524    -0.00358864         -0.0271898     0.00730319     1.59952e-07     9.2383e-09      1.99133e-07
4.98986 4.99003 2240    -1      -0.034413           -0.0666206     -1.0223e-09    2.48408e-09     3.72065e-10     5.32903e-08
4.98975 4.99003 4026    6186    -0.0612284          -0.0432303     0.00912149     9.87439e-09     2.06359e-09     2.47116e-09
4.98948 4.99003 7690    -1      -0.0339125          -0.0323593     -1.58631e-09   4.49412e-08     1.02974e-07     6.58318e-06
4.98904 4.99003 6734    8086    -0.0234678          -0.0327759     0.00251468     5.21508e-07     2.51588e-07     2.10622e-07
4.98984 4.99004 4442    7099    -0.0457129          -0.0336611     0.00915773     2.70779e-06     3.72785e-07     2.2432e-06
4.98937 4.99004 4711    4985    -0.0508016          -0.0460663     0.00729674     2.93178e-09     9.68666e-09     2.25023e-07
4.98985 4.99004 3848    -1      -0.0466595          -0.0587014     -1.24277e-08   9.35322e-08     7.44734e-08     1.78151e-06
4.98971 4.99004 202     -1      -0.0700322          -0.0331595     0.00249982     2.67536e-09     2.03378e-09     2.95396e-07
4.98954 4.99004 2555    9861    -0.024312           -0.04451       0.00655033     1.90489e-06     2.58838e-07     3.98017e-07
4.98976 4.99005 9735    -1      -0.0387468          -0.0641397     -5.07133e-09   2.14319e-08     2.56491e-08     1.39091e-06
4.9891  4.99005 28      4442    -0.0450995          -0.0355978     0.00473008     1.82846e-08     1.98752e-07     6.28568e-07
4.99    4.99005 9667    -1      -0.062007           -0.0275743     -2.11268e-12   6.38516e-09     6.15275e-10     3.34129e-08
4.98934 4.99005 2240    9370    -0.0321481          -0.0676988     0.00250036     7.09362e-07     1.29243e-07     7.70865e-06
4.98984 4.99005 2919    8027    -0.00777375         -0.0525331     0.00430797     1.70301e-06     3.48693e-07     3.94544e-06
4.98962 4.99005 8086    8537    -0.0255161          -0.0372957     0.00254177     7.68181e-08     3.20414e-08     1.3311e-08
4.98966 4.99006 2208    4271    -0.0317795          -0.0214581     0.00250158     4.11446e-09     1.2139e-09      4.56075e-08
4.98873 4.99006 120     7597    -0.0320036          -0.0378796     0.00258617     1.944e-08       2.45384e-08     2.28096e-07
```

*Figure C.1: Excerpt of contact data from CSPH_MPI*

## C.3 SPH Data

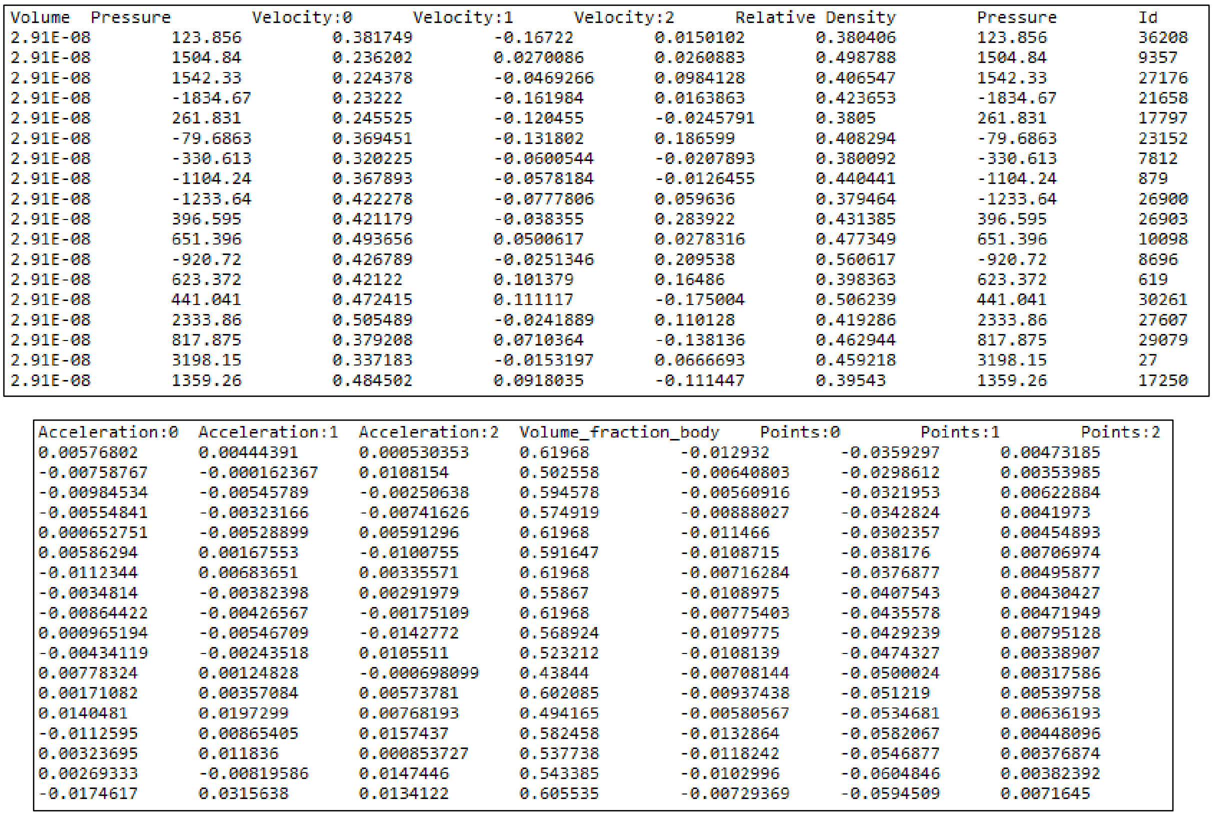

```
Volume   Pressure        Velocity:0       Velocity:1       Velocity:2       Relative Density       Pressure         Id
2.91E-08        123.856         0.381749        -0.16722        0.0150102       0.380406        123.856         36208
2.91E-08        1504.84         0.236202        0.0270086       0.0260883       0.498788        1504.84         9357
2.91E-08        1542.33         0.224378        -0.0469266      0.0984128       0.406547        1542.33         27176
2.91E-08        -1834.67        0.23222         -0.161984       0.0163863       0.423653        -1834.67        21658
2.91E-08        261.831         0.245525        -0.120455       -0.0245791      0.3805          261.831         17797
2.91E-08        -79.6863        0.369451        -0.131802       0.186599        0.408294        -79.6863        23152
2.91E-08        -330.613        0.320225        -0.0600544      -0.0207893      0.380092        -330.613        7812
2.91E-08        -1104.24        0.367893        -0.0578184      -0.0126455      0.440441        -1104.24        879
2.91E-08        -1233.64        0.422278        -0.0777806      0.059636        0.379464        -1233.64        26900
2.91E-08        396.595         0.421179        -0.038355       0.283922        0.431385        396.595         26903
2.91E-08        651.396         0.493656        0.0500617       0.0278316       0.477349        651.396         10098
2.91E-08        -920.72         0.426789        -0.0251346      0.209538        0.560617        -920.72         8696
2.91E-08        623.372         0.42122         0.101379        0.16486         0.398363        623.372         619
2.91E-08        441.041         0.472415        0.111117        -0.175004       0.506239        441.041         30261
2.91E-08        2333.86         0.505489        -0.0241889      0.110128        0.419286        2333.86         27607
2.91E-08        817.875         0.379208        0.0710364       -0.138136       0.462944        817.875         29079
2.91E-08        3198.15         0.337183        -0.0153197      0.0666693       0.459218        3198.15         27
2.91E-08        1359.26         0.484502        0.0918035       -0.111447       0.39543         1359.26         17250
```

```
Acceleration:0  Acceleration:1  Acceleration:2  Volume_fraction_body    Points:0        Points:1        Points:2
0.00576802      0.00444391      0.000530353     0.61968         -0.012932       -0.0359297      0.00473185
-0.00758767     -0.000162367    0.0108154       0.502558        -0.00640803     -0.0298612      0.00353985
-0.00984534     -0.00545789     -0.00250638     0.594578        -0.00560916     -0.0321953      0.00622884
-0.00554841     -0.00323166     -0.00741626     0.574919        -0.00888027     -0.0342824      0.0041973
0.000652751     -0.00528899     0.00591296      0.61968         -0.011466       -0.0302357      0.00454893
0.00586294      0.00167553      -0.0100755      0.591647        -0.0108715      -0.038176       0.00706974
-0.0112344      0.00683651      0.00335571      0.61968         -0.00716284     -0.0376877      0.00495877
-0.0034814      -0.00382398     0.00291979      0.55867         -0.0108975      -0.0407543      0.00430427
-0.00864422     -0.00426567     -0.00175109     0.61968         -0.00775403     -0.0435578      0.00471949
0.000965194     -0.00546709     -0.0142772      0.568924        -0.0109775      -0.0429239      0.00795128
-0.00434119     -0.00243518     0.0105511       0.523212        -0.0108139      -0.0474327      0.00338907
0.00778324      0.00124828      -0.000698099    0.43844         -0.00708144     -0.0500024      0.00317586
0.00171082      0.00357084      0.00573781      0.602085        -0.00937438     -0.051219       0.00539758
0.0140481       0.0197299       0.00768193      0.494165        -0.00580567     -0.0534681      0.00636193
-0.0112595      0.00865405      0.0157437       0.582458        -0.0132864      -0.0582067      0.00448096
0.00323695      0.011836        0.000853727     0.537738        -0.0118242      -0.0546877      0.00376874
0.00269333      -0.00819586     0.0147446       0.543385        -0.0102996      -0.0604846      0.00382392
-0.0174617      0.0315638       0.0134122       0.605535        -0.00729369     -0.0594509      0.0071645
```

*Figure C.2: Excerpt of fluid data from Paraview*

## C.4 DEM Steady-State Data

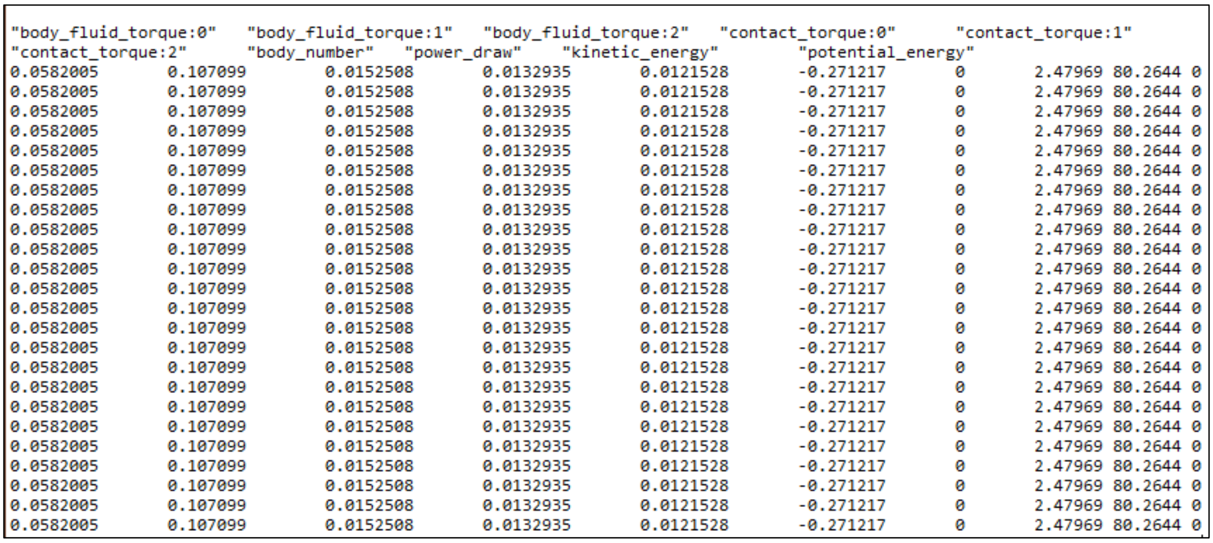

```
"body_fluid_torque:0"    "body_fluid_torque:1"    "body_fluid_torque:2"    "contact_torque:0"      "contact_torque:1"
"contact_torque:2"       "body_number"    "power_draw"    "kinetic_energy"        "potential_energy"
0.0582005       0.107099        0.0152508       0.0132935       0.0121528       -0.271217       0       2.47969 80.2644 0
0.0582005       0.107099        0.0152508       0.0132935       0.0121528       -0.271217       0       2.47969 80.2644 0
0.0582005       0.107099        0.0152508       0.0132935       0.0121528       -0.271217       0       2.47969 80.2644 0
0.0582005       0.107099        0.0152508       0.0132935       0.0121528       -0.271217       0       2.47969 80.2644 0
0.0582005       0.107099        0.0152508       0.0132935       0.0121528       -0.271217       0       2.47969 80.2644 0
0.0582005       0.107099        0.0152508       0.0132935       0.0121528       -0.271217       0       2.47969 80.2644 0
0.0582005       0.107099        0.0152508       0.0132935       0.0121528       -0.271217       0       2.47969 80.2644 0
0.0582005       0.107099        0.0152508       0.0132935       0.0121528       -0.271217       0       2.47969 80.2644 0
0.0582005       0.107099        0.0152508       0.0132935       0.0121528       -0.271217       0       2.47969 80.2644 0
0.0582005       0.107099        0.0152508       0.0132935       0.0121528       -0.271217       0       2.47969 80.2644 0
0.0582005       0.107099        0.0152508       0.0132935       0.0121528       -0.271217       0       2.47969 80.2644 0
0.0582005       0.107099        0.0152508       0.0132935       0.0121528       -0.271217       0       2.47969 80.2644 0
0.0582005       0.107099        0.0152508       0.0132935       0.0121528       -0.271217       0       2.47969 80.2644 0
0.0582005       0.107099        0.0152508       0.0132935       0.0121528       -0.271217       0       2.47969 80.2644 0
0.0582005       0.107099        0.0152508       0.0132935       0.0121528       -0.271217       0       2.47969 80.2644 0
0.0582005       0.107099        0.0152508       0.0132935       0.0121528       -0.271217       0       2.47969 80.2644 0
0.0582005       0.107099        0.0152508       0.0132935       0.0121528       -0.271217       0       2.47969 80.2644 0
0.0582005       0.107099        0.0152508       0.0132935       0.0121528       -0.271217       0       2.47969 80.2644 0
0.0582005       0.107099        0.0152508       0.0132935       0.0121528       -0.271217       0       2.47969 80.2644 0
0.0582005       0.107099        0.0152508       0.0132935       0.0121528       -0.271217       0       2.47969 80.2644 0
0.0582005       0.107099        0.0152508       0.0132935       0.0121528       -0.271217       0       2.47969 80.2644 0
0.0582005       0.107099        0.0152508       0.0132935       0.0121528       -0.271217       0       2.47969 80.2644 0
0.0582005       0.107099        0.0152508       0.0132935       0.0121528       -0.271217       0       2.47969 80.2644 0
0.0582005       0.107099        0.0152508       0.0132935       0.0121528       -0.271217       0       2.47969 80.2644 0
```

*Figure C.3: Excerpt of DEM steady state data from Paraview*

## C.5 DEM Velocity Data

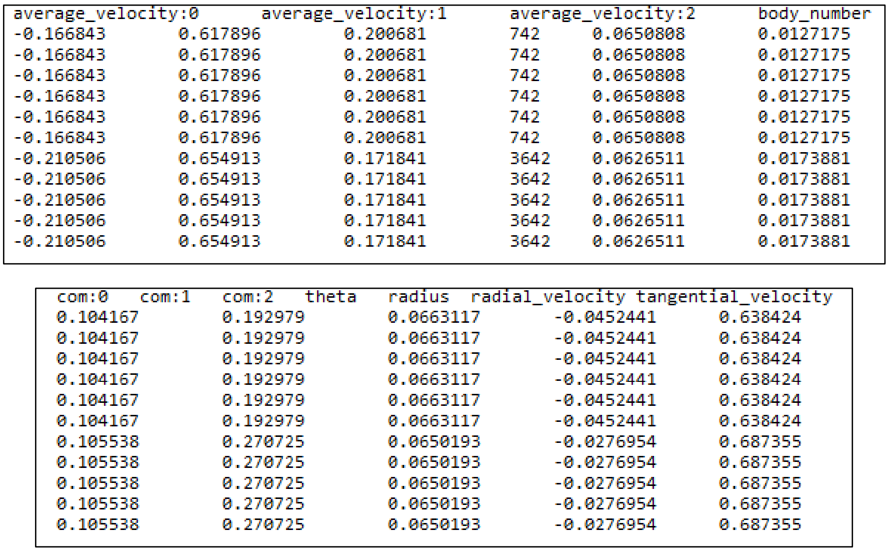

```
average_velocity:0      average_velocity:1      average_velocity:2      body_number
-0.166843       0.617896        0.200681        742     0.0650808       0.0127175
-0.166843       0.617896        0.200681        742     0.0650808       0.0127175
-0.166843       0.617896        0.200681        742     0.0650808       0.0127175
-0.166843       0.617896        0.200681        742     0.0650808       0.0127175
-0.166843       0.617896        0.200681        742     0.0650808       0.0127175
-0.166843       0.617896        0.200681        742     0.0650808       0.0127175
-0.210506       0.654913        0.171841        3642    0.0626511       0.0173881
-0.210506       0.654913        0.171841        3642    0.0626511       0.0173881
-0.210506       0.654913        0.171841        3642    0.0626511       0.0173881
-0.210506       0.654913        0.171841        3642    0.0626511       0.0173881
-0.210506       0.654913        0.171841        3642    0.0626511       0.0173881
```

```
com:0   com:1   com:2   theta   radius  radial_velocity tangential_velocity
0.104167        0.192979        0.0663117       -0.0452441      0.638424
0.104167        0.192979        0.0663117       -0.0452441      0.638424
0.104167        0.192979        0.0663117       -0.0452441      0.638424
0.104167        0.192979        0.0663117       -0.0452441      0.638424
0.104167        0.192979        0.0663117       -0.0452441      0.638424
0.104167        0.192979        0.0663117       -0.0452441      0.638424
0.105538        0.270725        0.0650193       -0.0276954      0.687355
0.105538        0.270725        0.0650193       -0.0276954      0.687355
0.105538        0.270725        0.0650193       -0.0276954      0.687355
0.105538        0.270725        0.0650193       -0.0276954      0.687355
0.105538        0.270725        0.0650193       -0.0276954      0.687355
```

*Figure C.4: Excerpt of DEM velocity data from Paraview*

# Appendix D: Analytical Code

## D.1 Analysis Overview

The data analysis was conducted in MATLAB through a mill script that uses functions to extract steady state, contact and velocity data from the model outputs, prior to the execution of the spatial analyses graphing functions and distribution analytical methods. The mill script is updated with the specifications of the mill being processed. It executes a complete analysis of that system from the raw output data, storing relevant figures and the final workplace variables.

The mill script is shared in D.2, followed by the steady state analysis function, the contact and velocity data extraction functions, the dimensionless number distribution data extraction function and key spatial analysis graphing functions. The code makes reference to auxiliary functions used for data binning and sorting that are not the authors own and therefore excluded.

## D.2 Mill Script

```
% Author: Divine Ssebunnya
% Mill Analysis Protocol

%% Mill Specs

Mill = 'A';
tip= 1.477;

if Mill=='C'
    rimp= 0.0705;
    radius= 0.0775;
    rshaft=(0.00625/0.0775);
elseif Mill =='B'
    rimp= 0.0815;
    radius= 0.1015;
    rshaft=(0.00625/0.1015);
elseif Mill == 'A'
    rimp= 0.1165;
    radius = 0.128;
    rshaft=(0.00625/0.128);
end

rpm = tip*60/(pi*2*rimp)

%% Physical Properties

SStStop = 500;
tStop = 100-1;
tStart = SStStop - tStop;

Sect = [0.0229,0.0775];% Heights of impeller pins for axial segmentation

bdensity = 2700;%kg/m3 density of media bodies
diameter = 0.005;%m

density0 = 1379;%kg/m3 fluid density
viscosity = 0.022;%Pa.s
c0 = 20;%m/s
```

```
n = 7;
gravity = 9.81;%m/s2

%% Steady State Analysis

[SSE, State, SSPD] =readSteadyState(density0, rpm, SStStop);

savefig(SSE,strcat(sprintf('%.1f',round(tip,1)),'_',Mill,'_','SSE','.fig'))
;
savefig(SSPD,strcat(sprintf('%.1f',round(tip,1)),'_',Mill,'_','SSPD','.fig'
));

clear SSE SSPD

%% Power Draw Analysis

States.PD = cell2mat(State.PD);
States.FT = cell2mat(State.FT);
States.CT = cell2mat(State.CT);
States.TT = cell2mat(State.TT);
States.t = cell2mat(State.t);
States.FC = States.CT./(States.TT);

ptmp = applyIndex_gen(States, ~isoutlier(States.PD) & all(States.t >=
tStart & States.t <= SStStop);

meanPD = mean(ptmp.PD);
meanFT = mean(ptmp.FT);
meanCT = mean(ptmp.CT);
meanTT = mean(ptmp.TT);
meanFC = mean(ptmp.FC);

stdPD = std(ptmp.PD);
stdFT = std(ptmp.FT);
stdCT = std(ptmp.CT);
stdTT = std(ptmp.TT);
stdFC = std(ptmp.FC);

%%
clear ptmp SSPD

%% Contact Analysis - Frequency

[Frequency,Total,Media,Impeller,Shell,Subplot, Energy]=
readContacts(Mill,tStart,SStStop);

savefig(Frequency,strcat(sprintf('%.1f',round(tip,1)),'_',Mill,'_','Frequen
cy','.fig'));
savefig(Total,strcat(sprintf('%.1f',round(tip,1)),'_',Mill,'_','Total','.fi
g'));
savefig(Media,strcat(sprintf('%.1f',round(tip,1)),'_',Mill,'_','Media','.fi
g'));
savefig(Impeller,strcat(sprintf('%.1f',round(tip,1)),'_',Mill,'_','Impeller
','.fig'));
savefig(Shell,strcat(sprintf('%.1f',round(tip,1)),'_',Mill,'_','Shell','.fi
g'));
savefig(Subplot,strcat(sprintf('%.1f',round(tip,1)),'_',Mill,'_','Subplot',
'.fig'));
```

```
clear Frequency Total %Media Impeller Shell Subplot Contacts

%% Contact Analysis - Spatial

% 'z', 'r', 'theta'
bins = [30, 20, 2];
localness = [NaN, 3, NaN];
dimBounds = {{}, {}, []};

etmp = applyIndex_gen(Energy, ~isoutlier(Energy.Collision_energy));
[bin, ~, ~, ~, ~] = binStruct_cylindrical(etmp, bins, localness,
dimBounds);

EDR = plot2SidedDiv(bin,0,'TotalDissipationRateVector',Mill);
NDR = plot2Sided(bin,Q,'NormalDissipationRate',Mill);
TDR = plot2Sided(bin,Q,'ShearDissipationRate',Mill);
ED = plot2SidedDiv(bin,0,'TotalDissipation',Mill);
FR = plot2SidedDiv(bin,0,'occ',Mill);

%% Energy Figures
savefig(EDR,strcat(sprintf('%.1f',round(tip,1)),'_',Mill,'_','EDR','.fig'))
;
savefig(ED,strcat(sprintf('%.1f',round(tip,1)),'_',Mill,'_','ED','.fig'));
savefig(FR,strcat(sprintf('%.1f',round(tip,1)),'_',Mill,'_','FR','.fig'));

clear etmp bins localness dimBounds EDR ED FR bin
%% Velocity Analysis - Spatial

Velocity = readVelocity(Mill, tStop);
vtmp = applyIndex_gen(Velocity, ~isoutlier(Velocity.V));

% 'z', 'r', 'theta'
bins = [round(0.315/diameter), round(radius/diameter)*2, 2];
localness = [NaN, 3, NaN];
dimBounds = {{}, {}, []};

%
[vbin, ~, ~, ~, ~] = binStruct_cylindrical(vtmp, bins, localness,
dimBounds);

Vt2S = plot2SidedDiv(vbin,1,'Vt',Mill);
V2S = plot2SidedDiv(vbin,0,'V',Mill);

%%
[vbin1, vbin2,vbin3] = binRadialProfile(vtmp, bins);

Vt = plotRadialProfile(vbin1, vbin2, vbin3,'Vt');
Vr = plotRadialProfile(vbin1, vbin2, vbin3,'Vr');
Vz = plotRadialProfile(vbin1, vbin2, vbin3,'Vz');
V = plotRadialProfile(vbin1, vbin2, vbin3,'V');

%% Velocity Figures
savefig(V2S,strcat(sprintf('%.1f',round(tip,1)),'_',Mill,'_','V2S','.fig'))
;
savefig(Vt2S,strcat(sprintf('%.1f',round(tip,1)),'_',Mill,'_','Vt2S','.fig'
));
savefig(Vt,strcat(sprintf('%.1f',round(tip,1)),'_',Mill,'_','Vt','.fig'));
```

```
savefig(V,strcat(sprintf('%.1f',round(tip,1)),'_',Mill,'_','V','.fig'));
savefig(Vr,strcat(sprintf('%.1f',round(tip,1)),'_',Mill,'_','Vr','.fig'));
savefig(Vz,strcat(sprintf('%.1f',round(tip,1)),'_',Mill,'_','Vz','.fig'));
savefig(VzS,strcat(sprintf('%.1f',round(tip,1)),'_',Mill,'_','VzS','.fig'))
;
savefig(VrS,strcat(sprintf('%.1f',round(tip,1)),'_',Mill,'_','VrS','.fig'))
;

clear vtmp bins localness dimBounds V2S Vt2S Vt Vr Vz VzS Vts xyzbins vbin
vbin1 vbin2 vbin3 V VrS

%% Fluid Velocity Analysis - Spatial

fluidvelocity = readFluidVelocity(Mill,tStart,SStStop);

% 'z', 'r', 'theta'
bins = [60, 100, 2];
localness = [NaN, 3, NaN];
dimBounds = {{}, {}, []};

ftmp = applyIndex_gen(fluidvelocity, ~isoutlier(fluidvelocity.V));
[fbin, ~, ~, ~, ~] = binStruct_cylindrical(ftmp, bins, localness,
dimBounds);

Vf2S = plot2SidedDiv(fbin,1,'V',Mill);
Af = plot2Sided(fbin,1,'A');
Pf = plot2SidedDiv(fbin,0,'Pressure',Mill);
BF = plot2SidedDiv(fbin,0,'Volume_fraction_body',Mill);
RD = plot2SidedDiv(fbin,0,'RelativeDensity',Mill);

savefig(BF,strcat(sprintf('%.1f',round(tip,1)),'_',Mill,'_','BodyFraction',
'.fig'));
savefig(RD,strcat(sprintf('%.1f',round(tip,1)),'_',Mill,'_','RelativeDensit
y','.fig'));

%%
[fbin1, fbin2, fbin3] = binRadialProfile(ftmp, bins);

Vf = plotRadialProfile(fbin1, fbin2, fbin3,'V');
A = plotRadialProfile(fbin1, fbin2, fbin3,'A');

%% Fluid Figures
savefig(Vf2S,strcat(sprintf('%.1f',round(tip,1)),'_',Mill,'_','Vf2S','.fig'
));
savefig(Pf,strcat(sprintf('%.1f',round(tip,1)),'_',Mill,'_','Pf','.fig'));
savefig(BF,strcat(sprintf('%.1f',round(tip,1)),'_',Mill,'_','BodyFraction',
'.fig'));
savefig(RD,strcat(sprintf('%.1f',round(tip,1)),'_',Mill,'_','RelativeDensit
y','.fig'));
savefig(Vf,strcat(sprintf('%.1f',round(tip,1)),'_',Mill,'_','Vf','.fig'));

clear ftmp bins localness dimBounds fbin fbin1 fbin2 fbin3 xyzbins Vf2S Pf
BF RD Vf PS BFS

%% Dimensional Number Analysis - Spatial

dnbins = [120, 60, 2];
localness = [NaN, 3, NaN];
```

```
dimBounds = {[0,0.315], [0,1], []};

ftmp = applyIndex_gen(fluidvelocity, ~isoutlier(fluidvelocity.V));
vtmp = applyIndex_gen(Velocity, ~isoutlier(Velocity.V));

[Dbin, ~, ~, ~, ~] = binStruct_cylindrical(ftmp, dnbins, localness,
dimBounds);
[Nbin, ~, ~, ~, ~] = binStruct_cylindrical(vtmp, dnbins, localness,
dimBounds);

%%
vrel1 = abs(sqrt(Dbin{1}.V.*Dbin{1}.V + Nbin{1}.V.*Nbin{1}.V -
2*(Dbin{1}.Vx.*Nbin{1}.Vx + Dbin{1}.Vy.*Nbin{1}.Vy +
Dbin{1}.Vz.*Nbin{1}.Vz)));
vrel2 = abs(sqrt(Dbin{2}.V.*Dbin{2}.V + Nbin{2}.V.*Nbin{2}.V -
2*(Dbin{2}.Vx.*Nbin{2}.Vx + Dbin{2}.Vy.*Nbin{2}.Vy +
Dbin{2}.Vz.*Nbin{2}.Vz)));

density1 = density0 * power(1+ Dbin{1}.Pressure .*
(n/(density0*c0^2)),1/n);
density2 = density0 * power(1+ Dbin{2}.Pressure .*
(n/(density0*c0^2)),1/n);

Nbin{1}.Re = density1.*vrel1 * diameter/viscosity .* (1-
Dbin{1}.Volume_fraction_body);
Nbin{1}.Fr = vrel1.*power(gravity*diameter.*(( bdensity./density1) -
1),0.5);

Nbin{2}.Re = density2.*vrel2 * diameter/viscosity .* (1-
Dbin{2}.Volume_fraction_body);
Nbin{2}.Fr = vrel2.*power(gravity*diameter.*(( bdensity./density2) -
1),0.5);

Nbin{1}.Vrel = vrel1;
Nbin{2}.Vrel = vrel2;

Nbin{1}.density = density1;
Nbin{2}.density = density2;

%%
Fr = plot2Sided(Nbin,0,'Fr',Mill);
Re = plot2Sided(Nbin,0,'Re',Mill);

%% Dimensionless Number Figures

savefig(Fr,strcat(sprintf('%.1f',round(tip,1)),'_',Mill,'_','Froud','.fig')
);
savefig(Re,strcat(sprintf('%.1f',round(tip,1)),'_',Mill,'_','Re','.fig'));

%% Dimensional Number Analysis - Statistics

[Dime,Test]=readDimensionless(radius,tStart-1,tStart+(tStop)-1);
Dimes = collateCellArrayOfStructs_timefix(Dime);
fullDime = Dime(~cellfun('isempty', Dime'));

for i= 1:1:length(fullDime)
    MedRe(i) = median(fullDime{1, i}.Re);
    MedFr(i) = median(fullDime{1, i}.Fr);
```

```
end

%%
clear vtmp ftmp dnbins localness dimBounds Dbin Nbin vrel1 vrel2 density1
density2 ReP FrP Fr Re gridMask Dime Test Dimes

%% Still Analysis

[StillVelocity, rev]=readStillVelocity(Mill,rpm,tStart);

[Impz1, Impz2]=plotFlatSlices(StillVelocity,'Vz', tStart, rev, Mill);
[Impr1, Impr2]=plotFlatSlices(StillVelocity,'Vr', tStart, rev, Mill);
[Impt1, Impt2]=plotFlatSlices(StillVelocity,'Vt', tStart, rev, Mill);

%%
StillFluid=readStillFluidVelocity(Mill,tStart,rev);

[FImpz1, FImpz2]=plotFlatSlices(StillVelocity,'Vz', tStart, rev, Mill);
[FImpr1, FImpr2]=plotFlatSlices(StillVelocity,'Vr', tStart, rev, Mill);
[FImpt1, FImpt2]=plotFlatSlices(StillVelocity,'Vt', tStart, rev, Mill);

%% Still Figures

savefig(Impz1,strcat(sprintf('%.1f',round(rpm,1)),'_',Mill,'_','Impz1','.fi
g'));
savefig(Impz2,strcat(sprintf('%.1f',round(rpm,1)),'_',Mill,'_','Impz2','.fi
g'));
savefig(Impr1,strcat(sprintf('%.1f',round(rpm,1)),'_',Mill,'_','Impr1','.fi
g'));
savefig(Impr2,strcat(sprintf('%.1f',round(rpm,1)),'_',Mill,'_','Impr2','.fi
g'));
savefig(FImpz1,strcat(sprintf('%.1f',round(tip,1)),'_',Mill,'_','FImpz1','.
fig'));
savefig(FImpz2,strcat(sprintf('%.1f',round(tip,1)),'_',Mill,'_','FImpz2','.
fig'));
savefig(FImpr1,strcat(sprintf('%.1f',round(tip,1)),'_',Mill,'_','FImpr1','.
fig'));
savefig(FImpr2,strcat(sprintf('%.1f',round(tip,1)),'_',Mill,'_','FImpr2','.
fig'));

clear Impz1 Impz2 Impr1 Impr2 FImpz1 FImpz2 FImpr1 FImpr2

%% Save Workspace
save(strcat(sprintf('%.1f',round(tip,1)),'_Mill',Mill));
```

## D.3 Steady State Analysis

```
% Author: Divine Ssebunnya
% Steady State Data Analysis Protocol

%% Data Import
%  NB: the code is built for DEM body data. Remember to check the boxes in
paraview for what data is being exported.

function [SSE,SSPD, State ]=readSteadyState(rho,rpm, SStStop)
tStart = 0;
Steady = table;

f = waitbar(0, 'Loading DEM Steeady State Data',
'CreateCancelBtn','setappdata(gcbf,''canceling'',1)');

for d=tStart:1:SStStop

    Steady = readtable(strcat('steady','_',sprintf('%d',d),'.csv'));

    if ismember('surface_velocity_0',Steady.Properties.VariableNames)
        Steady.surface_velocity_0=[];
        Steady.surface_velocity_1=[];
        Steady.surface_velocity_2=[];
    end

    Steady= unique(Steady);% Sorts points into unique bodies

    toDelete = Steady.body_number < 0;% Deletes shell geometry
    Steady(toDelete,:) = [];

    State.KE{1+d-tStart,1} = sum(Steady.kinetic_energy(Steady.body_number
>= 1));
    State.PE{1+d-tStart,1} = sum(Steady.potential_energy(Steady.body_number
>= 1));
    State.t{1+d-tStart,1} = d/100; % cs to s

    State.FT{1+d-tStart,1}=
sqrt(Steady.body_fluid_torque_0(1)*Steady.body_fluid_torque_0(1) +
Steady.body_fluid_torque_1(1)*Steady.body_fluid_torque_1(1) +
Steady.body_fluid_torque_2(1)*Steady.body_fluid_torque_2(1));
    State.CT{1+d-tStart,1}=
sqrt(Steady.contact_torque_0(1)*Steady.contact_torque_0(1) +
Steady.contact_torque_1(1)*Steady.contact_torque_1(1) +
Steady.contact_torque_2(1)*Steady.contact_torque_2(1));

    State.TT{1+d-tStart,1}=
sqrt((Steady.body_fluid_torque_0(1)+Steady.contact_torque_0(1))^2 +
(Steady.body_fluid_torque_1(1)+Steady.contact_torque_1(1))^2 +
(Steady.body_fluid_torque_2(1)+Steady.contact_torque_2(1))^2);

    State.PD{1+d-tStart,1} = State.TT{1+d-tStart,1}*rpm*2*pi;

    waitbar((d)/(SStStop-tStart), f, sprintf('Reading DEM timestep %d of
%d', d+1, SStStop))
end

delete(f)
```

```
%% Data Import SPH
%  Add Meta Data

tStart = 0;

f = waitbar(0, 'Loading SPH Steady State Data', 
'CreateCancelBtn','setappdata(gcbf,''canceling'',1)');

for d=tStart:1:SStStop

    Steady = readtable(strcat('fluid','_',sprintf('%d',d),'.csv'));

    if isempty(Steady)
        continue
    end

    Steady.velocity = ((Steady.Velocity_0 .* Steady.Velocity_0) + 
(Steady.Velocity_1 .* Steady.Velocity_1) + (Steady.Velocity_2 .* 
Steady.Velocity_2)).^0.5;
    Steady.kinetic_energy = 0.5*rho*Steady.Volume .* Steady.velocity .* 
Steady.velocity;
    Steady.potential_energy = 9.81*rho*Steady.Volume .*Steady.Points_2;

    States.KE{1+d-tStart,1} = sum(Steady.kinetic_energy);
    States.PE{1+d-tStart,1} = sum(Steady.potential_energy);
    States.t{1+d-tStart,1} = d/100; % cs to s

    waitbar((d)/(SStStop-tStart), f, sprintf('Reading SPH timestep %d of 
%d', d+1, SStStop))
end

delete(f)

%% Steady State Energy Plot

figure
hold on

plot(cell2mat(State.t),cell2mat(State.KE));
plot(cell2mat(State.t),cell2mat(State.PE));
plot(cell2mat(States.t),cell2mat(States.KE));
plot(cell2mat(States.t),cell2mat(States.PE));

set(gca, 'FontName', 'Calibri');
legend('Media Kinetic Energy', 'Media Potential Energy', 'Fluid Kinetic 
Energy', 'Fluid Potential Energy')
xlabel('Time(s)');
ylabel('Energy (J)');

SSE=gcf;

hold off

%% Steady State Power Draw Plot

figure
```

```
hold on

plot(cell2mat(State.t),cell2mat(State.PD));
plot(cell2mat(State.t),smooth(cell2mat(State.PD),0.05)); % Moving average
with 5 percent span

set(gca, 'FontName', 'Calibri');
legend('Power Draw');
xlabel('Time(s)');
ylabel('Power (W)');

SSPD =gcf;

hold off
end
```

## D.4 Contact Data Extraction

```
% Author: Divine Ssebunnya
% Contact Data Analysis Protocol

%% Data Import
function [Frequency,Total,Media,Impeller,Shell,Subplot,
Energy]=readContacts(Mill,tStart,tStop)
%Frequency,Total,Media,Impeller,Shell,Subplot, Energy

f = waitbar(0, 'Loading Contact Data',
'CreateCancelBtn','setappdata(gcbf,''canceling'',1)');

Contact = table;

for d=tStart:1:tStop

        T = readtable(strcat('contact',sprintf('%d',d),'.txt'));
        if isempty(T)
            continue
        end
        T.NormalDissipationRate = T.Normal_dissipation./(T.t_end-
T.t_start); % Matlab doesn't like long arrays from division & ./ is still a
thing
        T.ShearDissipationRate = T.Shear_dissipation./(T.t_end-T.t_start);
        T.TotalDissipationRateVector =
hypot(T.NormalDissipationRate,T.ShearDissipationRate);
        T.TotalDissipation =
hypot(T.Normal_dissipation,T.Shear_dissipation);
        Contact = vertcat(Contact, T);  %#ok<*AGROW>

    waitbar((d-tStart)/(tStop-tStart), f, sprintf('Reading timestep %d till
%d', d+1, tStop))
end

delete(f)

%% Removing INF

Raw = Contact;
toDelete = Contact.NormalDissipationRate == Inf;
Contact(toDelete,:) = [];
```

```
size(Contact)

% Finding INF

INF = Raw;
toDelete = INF.NormalDissipationRate ~= Inf;
INF(toDelete,:) = [];

Body0 = INF;
toDelete = Body0.body_2 ~= 0; % INF contacts with the impeller
Body0(toDelete,:) = [];

other = INF;
toDelete = other.body_2 == 0; % INF contacts between bodies
other(toDelete,:) = [];

clear Raw

%% Contact Data Prep

if Mill=='A'
    vfluid = 1944*10^-6;
elseif Mill =='B'
    vfluid = 1212*10^-6;
elseif Mill == 'C'
    vfluid = 696*10^-6;
end

Contact.Collision_energy=Contact.Collision_energy/vfluid;
Contact.NormalDissipationRate=Contact.NormalDissipationRate/vfluid;
Contact.ShearDissipationRate=Contact.ShearDissipationRate/vfluid;
Contact.TotalDissipation=Contact.TotalDissipation/vfluid;
Contact.TotalDissipationRateVector=Contact.TotalDissipationRateVector/vflui
d;

Contacts = table2struct(Contact,'ToScalar',true);
ctmp = applyIndex_gen(Contacts,
~isoutlier(Contacts.TotalDissipationRateVector));
Contacts = struct2table(ctmp);

%% Impeller Collisions

Impeller = Contacts;
toDelete = Impeller.body_2 ~= 0;
Impeller(toDelete,:) = [];

%% Mill Shell collisions

Shell = Contacts;
toDelete = Shell.body_2 ~= -1;
Shell(toDelete,:) = [];

%% Media Media collisions

Media = Contacts;
toDelete = Media.body_2 == -1;
Media(toDelete,:) = [];
```

```
toDelete = Media.body_2 == 0;
Media(toDelete,:) = [];

%% Frequency Plots - LOG Binning

Frequency =figure;
axes('XScale', 'log', 'YScale', 'linear')

hold on
% Collision frequency plot
[~, edges]= histcounts(log10(Contacts.Collision_energy));
[count, TD] = hist(Contacts.Collision_energy, 10.^(Medges));
loglog(TD,count/5);

% Media Collision frequency plot
[~, Medges]= histcounts(log10(Media.Collision_energy));
[Mcount, MTD] = hist(Media.Collision_energy, 10.^Medges);
loglog(MTD,Mcount/5);

% Shell Collision frequency plot
[~, Sedges]= histcounts(log10(Shell.Collision_energy));
[Scount, STD] = hist(Shell.Collision_energy, 10.^Sedges);
loglog(STD,Scount/5);

% Impeller Collision frequency plot
[~, Iedges]= histcounts(log10(Impeller.Collision_energy));
[Icount, ITD] = hist(Impeller.Collision_energy, 10.^Iedges);
loglog(ITD,Icount/5);

legend('Total', 'Media-Media','Media-Shell','Media-Impeller' )
xlabel('Collision Energy (J/m^3 fluid)');
ylabel('Frequency (per revolution)');

hold off

%% Total Collisions Plots

figure
axes('XScale', 'log', 'YScale', 'log')

hold on

% Total Energy dissipation plot
[~,TDRsum, TD_bins] = binscontact(Contacts.Collision_energy,
Contacts.TotalDissipationRateVector);
loglog(TD_bins(1:length(TD_bins)-1),TDRsum);

% Shear Energy dissipation plot
[~,SDRsum, SD_bins] = binscontact(Contacts.Collision_energy,
Contacts.ShearDissipationRate);
loglog(SD_bins(1:length(SD_bins)-1),SDRsum);

% Normal Energy dissipation plot
[~,NDRsum, ND_bins] = binscontact(Contacts.Collision_energy,
Contacts.NormalDissipationRate);
loglog(ND_bins(1:length(ND_bins)-1),NDRsum);

xline(TD_bins(TDRsum==max(TDRsum)));
```

```
yline(max(TDRsum));

legend('Total', 'Shear', 'Normal')
xlabel('Collision Energy (J/m^3 fluid)');
ylabel('Energy Dissipation Rate (W/m^3 fluid)');

total = gca;
Total = gcf;

hold off

%% Impeller Collision Plots

figure
axes('XScale', 'log', 'YScale', 'log')

hold on

% Total Energy dissipation plot
[~,ITDRsum, ITD_bins] = binscontact(Impeller.Collision_energy,
Impeller.TotalDissipationRateVector);
loglog(ITD_bins(1:length(ITD_bins)-1),ITDRsum);

% Shear Energy dissipation plot
[~,ISDRsum, ISD_bins] = binscontact(Impeller.Collision_energy,
Impeller.ShearDissipationRate);
loglog(ISD_bins(1:length(ISD_bins)-1),ISDRsum);

% Normal Energy dissipation plot
[~,INDRsum, IND_bins] = binscontact(Impeller.Collision_energy,
Impeller.NormalDissipationRate);
loglog(IND_bins(1:length(IND_bins)-1),INDRsum);

xline(ITD_bins(ITDRsum==max(ITDRsum)));
yline(max(ITDRsum));

legend('Total', 'Shear', 'Normal')
xlabel('Collision Energy (J/m^3 fluid)');
ylabel('Energy Dissipation Rate (W/m^3 fluid)');

impeller = gca;
Impeller = gcf;
hold off

%% Mill Shell collision plots

figure
axes('XScale', 'log', 'YScale', 'log')
hold on

% Total Energy dissipation plot
[~,STDRsum, STD_bins] = binscontact(Shell.Collision_energy,
Shell.TotalDissipationRateVector);
loglog(STD_bins(1:length(STD_bins)-1),STDRsum);

% Shear Energy dissipation plot
[~,SSDRsum, SSD_bins] = binscontact(Shell.Collision_energy,
Shell.ShearDissipationRate);
```

```
loglog(SSD_bins(1:length(SSD_bins)-1),SSDRsum);

% Normal Energy dissipation plot
[~,SNDRsum, SND_bins] = binscontact(Shell.Collision_energy,
Shell.NormalDissipationRate);
loglog(SND_bins(1:length(SND_bins)-1),SNDRsum);

xline(STD_bins(STDRsum==max(STDRsum)));
yline(max(STDRsum));

legend('Total', 'Shear', 'Normal')
xlabel('Collision Energy (J/m^3 fluid)');
ylabel('Energy Dissipation Rate (W/m^3 fluid)');

shell = gca;
Shell = gcf;

hold off
%% Media Media collision plots

figure
axes('XScale', 'log', 'YScale', 'log')
hold on

% Total Energy dissipation plot
[~,MTDRsum, MTD_bins] = binscontact(Media.Collision_energy,
Media.TotalDissipationRateVector);
loglog(MTD_bins(1:length(MTD_bins)-1),MTDRsum);

% Shear Energy dissipation plot
[~,MSDRsum, MSD_bins] = binscontact(Media.Collision_energy,
Media.ShearDissipationRate);
loglog(MSD_bins(1:length(MSD_bins)-1),MSDRsum);

% Normal Energy dissipation plot
[~,MNDRsum, MND_bins] = binscontact(Media.Collision_energy,
Media.NormalDissipationRate);
loglog(MND_bins(1:length(MND_bins)-1),MNDRsum);

xline(MTD_bins(MTDRsum==max(MTDRsum)));
yline(max(MTDRsum));

legend('Total', 'Shear', 'Normal')
xlabel('Collision Energy (J/m^3 fluid)');
ylabel('Energy Dissipation Rate (W/m^3 fluid)');

media = gca;
Media = gcf;

hold off
%% Subplot Energy dissipation

figure
axes('XScale', 'log', 'YScale', 'log')
hold on

a1 = subplot(2,2,1);
a2 = subplot(2,2,2);
```

```
a3 = subplot(2,2,3);
a4 = subplot(2,2,4);

copyobj(get(total,'Children'),a1);
copyobj(get(media,'Children'),a2);
copyobj(get(impeller,'Children'),a3);
copyobj(get(shell,'Children'),a4);

Subplot = gcf;

hold off

%% Energy for XYZ plots

[Contact.th, Contact.radius] = cart2pol(Contact.x, Contact.y);
Contact.Properties.VariableNames{'t_start'}='t';
Contacts = removevars(Contact,{'body_1', 'body_2'});

Energy = table2struct(Contacts,'ToScalar', true);

if Mill=='C'
    radius= 0.0775;
elseif Mill =='B'
    radius= 0.1015;
elseif Mill == 'A'
    radius = 0.128;
end
Energy.r = Energy.radius/radius;
end
```

## D.5 DEM Velocity Data Extraction

```
% Author: Divine Ssebunnya
% Velocity Data Analysis Protocol

%% Data Import
%  NB: the code is built for only body data. Remember to check the boxes in
%  paraview for what data is being exported.#NoMetaData

function [Velocity ]=readVelocity(Mill, tStop)

tStart = 0;
Velo = table;
f = waitbar(0, 'Loading Velocity Data',
'CreateCancelBtn','setappdata(gcbf,''canceling'',1)');

for d=tStart:1:tStop

    Velo = readtable(strcat('city','_',sprintf('%d',d),'.csv'));

    Velo= unique(Velo);% Sorts points into unique bodies

    toDelete = Velo.body_number < 1;% Deletes shell and impeller geometry
    Velo(toDelete,:) = [];

    Cities = table2struct(Velo,'ToScalar', true);
    Cities.t = d;
```

```
    Velocities{1+d-tStart}=Cities;

   waitbar((d)/(tStop-tStart), f, sprintf('Reading Velocity Data timestep
%d of %d', d+1, tStop))
end

delete(f)

%% Data collation and variable renaming

if Mill=='C'
    radius= 0.0775;
elseif Mill =='B'
    radius= 0.1015;
elseif Mill == 'A'
    radius = 0.128;
end

Velocity = collateCellArrayOfStructs_timefix(Velocities); % Complete range
of data

Velocity.x=Velocity.centreOfMass_0;
Velocity.y=Velocity.centreOfMass_1;
Velocity.z=Velocity.centreOfMass_2;

Velocity.r=Velocity.radius/radius;
Velocity.th=Velocity.theta;

Velocity.Vx=Velocity.average_velocity_0;
Velocity.Vy=Velocity.average_velocity_1;
Velocity.Vz=Velocity.average_velocity_2;

Velocity.Vr=Velocity.radial_velocity;
Velocity.Vt=Velocity.tangential_velocity;

Velocity.V=sqrt(Velocity.Vx.*Velocity.Vx + Velocity.Vy.*Velocity.Vy +
Velocity.Vz.*Velocity.Vz);

if isfield(Velocity,'body_fluid_torque_0')
    Velocity = rmfield(Velocity,
{'body_fluid_torque_0','body_fluid_torque_1','body_fluid_torque_2'});
end
if isfield(Velocity,'contact_torque_0')
    Velocity = rmfield(Velocity,
{'contact_torque_0','contact_torque_1','contact_torque_2'});
end
if isfield(Velocity,'body_fluid_force_0')
    Velocity = rmfield(Velocity,
{'body_fluid_force_0','body_fluid_force_1','body_fluid_force_2'});
end
if isfield(Velocity,'contact_force_0')
    Velocity = rmfield(Velocity,
{'contact_force_0','contact_force_1','contact_force_2'});
end
if isfield(Velocity,'surface_velocity_0')
    Velocity = rmfield(Velocity,
{'surface_velocity_0','surface_velocity_1','surface_velocity_2'});
end
if isfield(Velocity,'kinetic_energy')
```

```
    Velocity = rmfield(Velocity, {'kinetic_energy'});
end
if isfield(Velocity,'potential_energy')
    Velocity = rmfield(Velocity, {'potential_energy'});
end
if isfield(Velocity,'power_draw')
    Velocity = rmfield(Velocity, {'power_draw'});
end

Velocity = rmfield(Velocity, {'average_velocity_0',
'average_velocity_1','average_velocity_2','radial_velocity',
'tangential_velocity', 'centreOfMass_0','centreOfMass_1','centreOfMass_2',
'theta'});
end
```

## D.6 SPH Velocity Data Extraction

```
% Author: Divine Ssebunnya
% Fluid Velocity Data Analysis Protocol

%% Data Import
%  NB: Fluid must import with metadata

function [Velocity]=readFluidVelocity(Mill,tStart,tStop)

Velo = table;

f = waitbar(0, 'Loading Velocity Data',
'CreateCancelBtn','setappdata(gcbf,''canceling'',1)');

for d=tStart:1:tStop

    Velo = readtable(strcat('fluid','_',sprintf('%d',d),'.csv'));

    Cities = table2struct(Velo,'ToScalar', true);
    Cities.t = d;
    Velocities{1+d-tStart}=Cities;

    waitbar((d-tStart)/(tStop-tStart), f, sprintf('Reading Velocity Data
timestep %d of %d', d+1, tStop))
end

delete(f)

%% Data collation and variable renaming

if Mill=='C'
    radius= 0.0775;
elseif Mill =='B'
    radius= 0.1015;
elseif Mill == 'A'
    radius = 0.128;
end

Velocity = collateCellArrayOfStructs_timefix(Velocities); % With range of
data
```

```
Velocity.x=Velocity.Points_0;
Velocity.y=Velocity.Points_1;
Velocity.z=Velocity.Points_2;

Velocity.Vx=Velocity.Velocity_0;
Velocity.Vy=Velocity.Velocity_1;
Velocity.Vz=Velocity.Velocity_2;

Velocity.V=sqrt(Velocity.Vx.*Velocity.Vx + Velocity.Vy.*Velocity.Vy +
Velocity.Vz.*Velocity.Vz);

Velocity.Ax=Velocity.Acceleration_0;
Velocity.Ay=Velocity.Acceleration_1;
Velocity.Az=Velocity.Acceleration_2;

Velocity.A=sqrt(Velocity.Ax.*Velocity.Ax + Velocity.Ay.*Velocity.Ay +
Velocity.Az.*Velocity.Az);

[Velocity.th, Velocity.radius] =cart2pol(Velocity.x,Velocity.y);
Velocity.r=Velocity.radius/radius;

Velocity.Ar = Velocity.Ax .* cos(Velocity.th) + Velocity.Ay .*
sin(Velocity.th);
Velocity.Vr = Velocity.Vx .* cos(Velocity.th) + Velocity.Vy .*
sin(Velocity.th);

Velocity = rmfield(Velocity, {'Velocity_0', 'Velocity_1','Velocity_2',
'Points_0','Points_1','Points_2','Acceleration_0','Acceleration_1','Acceler
ation_2'});

if isfield(Velocity,'Strainrate_0')
    Velocity = rmfield(Velocity,
{'Strainrate_0','Strainrate_1','Strainrate_2','Strainrate_3','Strainrate_4'
,'Strainrate_5','Strainrate_6','Strainrate_7','Strainrate_8'});
end
end
```

## D.7 Dimensionless Number Data Extraction

```
% Author: Divine Ssebunnya
% Dimensionless Number Data Analysis Protocol

function [Dime,Test]=readDimensionless(radius,tStart,tStop)
%%
bdensity = 2700;%kg/m3
diameter = 0.005;%m
density0 = 1379;%kg/m3
viscosity = 0.022;%Pa.s
gravity = 9.81;%m/s2
c0 = 20;%m/s;
n=7;

Media = table;
Fluid = table;

f = waitbar(0, 'Loading Velocity Stills',
'CreateCancelBtn','setappdata(gcbf,''canceling'',1)');

for v=tStart:1:tStop

    Media = readtable(strcat('city','_',sprintf('%d',round(v-
tStart)),'.csv'));

    Media= unique(Media);% Sorts points into unique bodies
    toDelete = Media.body_number < 1;% Deletes shell and impeller geometry
    Media(toDelete,:) = [];

    Fluid = readtable(strcat('fluid','_',sprintf('%d',round(v)),'.csv'));

    Medium = table2struct(Media,'ToScalar', true);
    Fluent = table2struct(Fluid,'ToScalar', true);

    %
    Medium.t = v;
    Fluent.t = v;

    Medium.x=Medium.centreOfMass_0;
    Medium.y=Medium.centreOfMass_1;
    Medium.z=Medium.centreOfMass_2;

    Medium.r=Medium.radius/radius;
    Medium.th=Medium.theta;

    Medium.Vx=Medium.average_velocity_0;
    Medium.Vy=Medium.average_velocity_1;
    Medium.Vz=Medium.average_velocity_2;

    Medium.Vr=Medium.radial_velocity;
    Medium.Vt=Medium.tangential_velocity;

    Medium.V=sqrt(Medium.Vx.*Medium.Vx + Medium.Vy.*Medium.Vy +
Medium.Vz.*Medium.Vz);
```

```
    Medium = rmfield(Medium, {'average_velocity_0',
'average_velocity_1','average_velocity_2','radial_velocity',
'tangential_velocity', 'centreOfMass_0','centreOfMass_1','centreOfMass_2',
'theta'});

    if isfield(Medium,'body_fluid_force_0')
        Medium = rmfield(Medium,
{'body_fluid_force_0','body_fluid_force_1','body_fluid_force_2'});
    end
    if isfield(Medium,'contact_force_0')
        Medium = rmfield(Medium,
{'contact_force_0','contact_force_1','contact_force_2'});
    end

    %
    Fluent.x=Fluent.Points_0;
    Fluent.y=Fluent.Points_1;
    Fluent.z=Fluent.Points_2;

    Fluent.Vx=Fluent.Velocity_0;
    Fluent.Vy=Fluent.Velocity_1;
    Fluent.Vz=Fluent.Velocity_2;

    Fluent.V=sqrt(Fluent.Vx.*Fluent.Vx + Fluent.Vy.*Fluent.Vy +
Fluent.Vz.*Fluent.Vz);
    [Fluent.th, Fluent.radius] =cart2pol(Fluent.x,Fluent.y);
    Fluent.r=Fluent.radius/radius;

    Fluent = rmfield(Fluent, {'Velocity_0', 'Velocity_1','Velocity_2',
'Points_0','Points_1','Points_2','Acceleration_0','Acceleration_1','Acceler
ation_2'});

    if isfield(Fluent,'Strainrate_0')
        Fluent = rmfield(Fluent,
{'Strainrate_0','Strainrate_1','Strainrate_2','Strainrate_3','Strainrate_4'
,'Strainrate_5','Strainrate_6','Strainrate_7','Strainrate_8'});
    end

    %
    dnbins = [round(0.315/0.005), round(radius/0.005)*2,
round(radius/0.005)*2];
    localness = [NaN, NaN, NaN];
    dimBounds = {[0,0.315], [], []};

    ftmp = applyIndex_gen(Fluent, ~isoutlier(Fluent.V));
    vtmp = applyIndex_gen(Medium, ~isoutlier(Medium.V));

    [Dbin, ~, ~, ~, ~] = binStruct_cylindrical_cartesian(ftmp, dnbins,
localness, dimBounds);
    [Nbin, ~, ~, ~, ~] = binStruct_cylindrical_cartesian(vtmp, dnbins,
localness, dimBounds);

    for i=1:1:dnbins(3)
        vrel = abs(sqrt(Dbin{i}.V.*Dbin{i}.V + Nbin{i}.V.*Nbin{i}.V -
2*(Dbin{i}.Vx.*Nbin{i}.Vx + Dbin{i}.Vy.*Nbin{i}.Vy +
Dbin{i}.Vz.*Nbin{i}.Vz)));

        density = density0 * power(1+ Dbin{i}.Pressure .*
(n/(density0*c0^2)),1/n);
```

```
        Nbin{i}.Re = density.*vrel * diameter/viscosity .* (1-
Dbin{1}.Volume_fraction_body);
        Nbin{i}.Fr = vrel.*power(gravity*diameter.*(( bdensity./density) -
1),0.5);

        Nbin{i}.Vrel = vrel;

        Nbin{i}.density = density;
    end

    N= collateCellArrayOfStructs_timefix(Nbin);

    Re = N.Re(:);
    Re = rmmissing(Re);

    Fr = N.Fr(:);
    Fr = rmmissing(Fr);

    %
    Test{1+v-tStart}=Nbin;

    Dime{1+v-tStart}.t = v;

    Dime{1+v-tStart}.Re = Re;
    Dime{1+v-tStart}.Fr = Fr;

    Dime{1+v-tStart}.ReMean = mean(Re);
    Dime{1+v-tStart}.FrMean = mean(Fr);

    waitbar((v-tStart)/(tStop-tStart), f, sprintf('Reading Fluid and Media
Velocity Data timestep %d of %d', v+1, tStop));
end

delete(f)
end
```

## D.8 R-Z Two-sided Surface Plots

```
% Authors: Divine Ssebunnya & Max Richter
% Two-Sided Colour Plot with Quiver Option

function [twoS]= plot2SidedDiv(bin, Q,field,Mill)

vb = bin{1};

gridMask = abs(bsxfun(@rdivide, vb.occ, mean(vb.occ)));
gridMask(gridMask<0.25e-3)=NaN;
gridMask(gridMask>(1))=1;

figure;
hold on;

w = pcolor(vb.radius, vb.z, vb.(field).*gridMask);
w.EdgeColor = 'none';

Qscale = 3;

if Q==1 && contains(field,'V')
    quiver(vb.radius, vb.z, gridMask.*vb.Vr, gridMask.*vb.Vz, Qscale,
'Color', 'w' ,'LineWidth', 2)
elseif Q==1 && contains(field,'cF')
    quiver(vb.radius, vb.z, gridMask.*vb.cFr, gridMask.*vb.cFz, Qscale,
'Color', 'w' ,'LineWidth', 2)
elseif Q==1 && contains(field,'fF')
    quiver(vb.r, vb.z, gridMask.*vb.fFr, gridMask.*vb.fFz, Qscale, 'Color',
'w' ,'LineWidth', 2)
elseif Q==1 && contains(field,'A')
    quiver(vb.r, vb.z, gridMask.*vb.Ar, gridMask.*vb.Az, Qscale, 'Color',
'w' ,'LineWidth', 2);
end

vb = bin{2};

gridMask = bsxfun(@rdivide, vb.occ, mean(vb.occ));
gridMask(gridMask<0.25e-3)=NaN;
gridMask(gridMask>1)=1;

w = pcolor(vb.radius, vb.z, vb.(field).*gridMask);
w.EdgeColor = 'none';
H = hgtransform('Matrix', makehgtform('yrotate', pi));
w.Parent = H;

if Q==1 && contains(field,'V')
    qh = quiver(vb.radius, vb.z, gridMask.*vb.Vr, gridMask.*vb.Vz, Qscale,
'Color', 'w' ,'LineWidth', 2);
    qh.Parent = H;
elseif Q==1 && contains(field,'cF')
    qh = quiver(vb.r, vb.z, gridMask.*vb.cFr, gridMask.*vb.cFz, Qscale,
'Color', 'w' ,'LineWidth', 2);
    qh.Parent = H;
elseif Q==1 && contains(field,'fF')
    qh = quiver(vb.r, vb.z, gridMask.*vb.fFr, gridMask.*vb.fFz, Qscale,
'Color', 'w' ,'LineWidth', 2);
    qh.Parent = H;
```

```
elseif Q==1 && contains(field,'A')
    qh = quiver(vb.r, vb.z, gridMask.*vb.Ar, gridMask.*vb.Az, Qscale,
'Color', 'w' ,'LineWidth', 2);
    qh.Parent = H;
end

colormap('jet');
d=colorbar;
shading interp;
ffSw.figDim = [0.5, 1];
formatFigure(gcf, ffSw);

ylabel('z');
xlabel('r');
ylabel(d,field);
grid off;
set(gca, 'FontName', 'Calibri Light');
plotNormImpeller(Mill);

twoS = gcf;
hold off
end
```

## D.9 R-θ Slices at Impeller Pins

### D.9.1 Data Extraction

```
% Author: Divine Ssebunnya
% Superimposing Still Datasets

%% Data Import
function [Velocity, rev, start]=readStillVelocity(Mill,rpm,tStart)
%%
Velo = table;
rev= 100*60/rpm;
%Mill at 45 degree from horizontal
r = mod(tStart,rev);
t= 90/360*rev;
if r<=t
    start= t-r;
else
    start= rev-r+t;
end
%%
f = waitbar(0, 'Loading Velocity Stills',
'CreateCancelBtn','setappdata(gcbf,''canceling'',1)');

for i=1:1:4

    d=round(start):round(rev-1):(round(4*rev));

    Velo = readtable(strcat('city','_',sprintf('%d',round(d(i))),'.csv'));

    Velo= unique(Velo);% Sorts points into unique bodies

    toDelete = Velo.body_number < 1;% Deletes shell and impeller geometry
    Velo(toDelete,:) = [];
```

```
    Cities = table2struct(Velo,'ToScalar', true);
    Cities.t = d(i);
    Velocities{i}=Cities;
    waitbar((i)/(5), f, sprintf('Reading Velocity Data timestep %d of %d',
i, 5))
end

delete(f)
```

### D.9.2 Plotting

```
% Author: Divine Ssebunnya
% Plots XY Binned Axial Slices

function [Imp1, Imp2]=plotFlatSlices(StillVelocity,field, tStart, rev,
Mill)
%%
%Mill= 'C';
%field = 'Vz';

if Mill=='C'
    radius= 0.0775;
    rshaft=(0.00625);
elseif Mill =='B'
    radius= 0.1015;
    rshaft=(0.00625);
elseif Mill == 'A'
    radius = 0.128;
    rshaft=(0.00625);
end

%% Bottom Impeller
City = struct2table(rmfield(StillVelocity,{'t'}));
vImp2 = table2struct(City(City.z > 0.0229-2*0.00375 & City.z <
0.0304+2*0.00375,:),'ToScalar', true);
vImp2.t = StillVelocity.t;

Struct= vImp2;

bins = [70, 70, 1];
localness = [2, 2, NaN];
dimBounds = {{}, {}, {}};

Struct.Z=Struct.z;
[binned, ~, ~, zbins, ~] = ...
    binStruct_cylindrical_cartesian(Struct, bins, localness, dimBounds);

binned{1}.Z(~isnan(binned{1}.Z))=(zbins.ranges(1)+zbins.ranges(2))/2;
%%
figure
hold on

pcolor(binned{1,1}.x,binned{1,1}.y,binned{1,1}.(field));

dtmp= binned;
D = cell2mat(cellfun(@(d)d.(field), dtmp, 'UniformOutput', false));
colormap(darkb2r(min(D(:)), max(D(:))));
d=colorbar;
```

```
shading interp;

theta = (tStart/rev)*360;
R = [cosd(theta) -sind(theta); sind(theta) cosd(theta)];
Imp=[-0.00375, -0.91*radius; -0.00375, 0.91*radius; 0.00375, 0.91*radius;
0.00375, -0.91*radius; -0.00375, -0.91*radius]*R';

plot(Imp(:,2),Imp(:,1),'--k','LineWidth',2);

Imp2 =gcf;
hold off

%% Top Impeller
City = struct2table(rmfield(StillVelocity,{'t'}));
vImp1 = table2struct(City(City.z > 0.07-2*0.00375 & City.z <
0.0775+2*0.00375,:),'ToScalar', true);
vImp1.t = StillVelocity.t;

Struct= vImp1;

bins = [70, 70, 1];
localness = [2, 2, NaN];
dimBounds = {{}, {}, {}};

Struct.Z=Struct.z;
[binned, ~, ~, zbins, ~] = ...
    binStruct_cylindrical_cartesian(Struct, bins, localness, dimBounds);

binned{1}.Z(~isnan(binned{1}.Z))=(zbins.ranges(1)+zbins.ranges(2))/2;

figure
hold on
pcolor(binned{1,1}.x,binned{1,1}.y,binned{1,1}.(field));

dtmp= binned;
D = cell2mat(cellfun(@(d)d.(field), dtmp, 'UniformOutput', false));
colormap(darkb2r(min(D(:)), max(D(:))));

d=colorbar;
shading interp;

Imp1=rot90(Imp)';
plot(Imp1(:,2),Imp1(:,1),'--k','LineWidth',2);

Imp1 = gcf;
hold off

end
```

## D.10 Segmented Radial Profiles

### D.10.1 Binning

```
% Author: Divine Ssebunnya
% Two Dimensional Radial Profile

function [vbin1,vbin2,vbin3] = binRadialProfile(Velocity, vbins)

Sect = [0.0229,0.0775];
City = struct2table(rmfield(Velocity,{'t','n'}));
vOne = table2struct(City(City.z < Sect(1),:),'ToScalar', true);% cutting
the table into sections of the impeller
vTwo = table2struct(City(City.z > Sect(1) & City.z < Sect(2),:),'ToScalar',
true);
vThree = table2struct(City(City.z > Sect(2),:),'ToScalar', true);

vOne.t = Velocity.t;
vTwo.t = Velocity.t;
vThree.t = Velocity.t;

%% 'z', 'r', 'theta'
localness = [NaN, NaN, NaN];
dimBounds = {{}, {}, []};

vbin = [1, vbins(2), 1];
vbin1 = binStruct_cylindrical(vOne, vbin, localness, dimBounds);
vbin2 = binStruct_cylindrical(vTwo, vbin, localness, dimBounds);
vbin3 = binStruct_cylindrical(vThree, vbin, localness, dimBounds);

end
```

### D.10.2 Plotting

```
% Author: Divine Ssebunnya
% Two Dimensional Radial Profile

function [rp] = plotRadialProfile(vbin1, vbin2,vbin3, field)
figure
hold on

plot(vbin1{1,1}.r(1,:),vbin1{1,1}.(field)(1,:));
plot(vbin2{1,1}.r(1,:),vbin2{1,1}.(field)(1,:));
plot(vbin3{1,1}.r(1,:),vbin3{1,1}.(field)(1,:));

ylabel(field);
xlabel('normalised radius');
legend('Base to Pin 1', 'Pin 1 to Pin 2', 'Above Pin 2')
xline(0.91);

rp = gcf;
hold off

end
```

# Appendix E: Supplementary Results

## E.1 Run-time data for DEM-SPH and DEM only simulations

Table E.1 provides a collation of run time data for simulations run in Mill A, B and C that have consistent media and fluid quantities with the same simulation parameters, and only differ in media shape and/or tip speed. This consists of all the scale-up assessment simulations. All the dry DEM simulations are also included, along with two performance assessment simulations. The average iteration time at steady state is provided. This is average duration of time it took to perform an iteration that moves the simulation by one SPH timestep. The average SPH timestep at steady state and the DEM timestep is also provided. For the dry simulations, the iteration time is moving the simulation by $4\times10^{-5}$s. From this data, the run time of simulation at steady state can be estimated as the product of the iteration time and the number of iterations needed.

*Table E.1: Run-time data compilation for wet and dry simulations*

| Mill Size | Media Shape | Tip Speed (m/s) | Average Iteration Time (ms) | Average SPH Timestep (s) | DEM Timestep (s) |
|---|---|---|---|---|---|
| A | Spherical | 1.5 | 218 | 3.66E-05 | 4.87E-06 |
| | | 1.8 | 209 | 3.73E-05 | 4.87E-06 |
| | | 2.2 | 213 | 3.67E-05 | 4.87E-06 |
| | | | 109 | (Dry) 4.00E-05 | 4.87E-06 |
| | Group 1 | 1.8 | 10519 | 3.07E-05 | 9.70E-07 |
| | | | 5444 | (Dry) 4.00E-05 | 9.70E-07 |
| | Group 2 | | 16375 | 3.12E-05 | 9.70E-07 |
| | | | 8987 | (Dry) 4.00E-05 | 9.70E-07 |
| | Group 3 | | 17528 | 3.06E-05 | 9.70E-07 |
| | | | 11636 | (Dry) 4.00E-05 | 9.70E-07 |
| B | Spherical | 1.5 | 306 | 3.48E-05 | 4.87E-06 |
| | | 1.8 | 294 | 3.50E-05 | 4.87E-06 |
| | | 2.2 | 310 | 3.52E-05 | 4.87E-06 |
| | | | 155 | (Dry) 4.00E-05 | 4.87E-06 |
| | Group 1 | 1.8 | 24147 | 3.44E-05 | 9.70E-07 |
| | Group 2 | | 37733 | 3.68E-05 | 9.70E-07 |
| | Group 3 | | 40391 | 3.61E-05 | 9.70E-07 |
| | | | 20485 | (Dry) 4.00E-05 | 9.70E-07 |
| C | Spherical | 1.5 | 427 | 3.12E-05 | 4.87E-06 |
| | | 1.8 | 431 | 3.08E-05 | 4.87E-06 |
| | | 2.2 | 438 | 3.05E-05 | 4.87E-06 |
| | | | 176 | (Dry) 4.00E-05 | 4.87E-06 |
| | | *3.7 | 361 | 3.15E-05 | 4.87E-06 |
| | | *8.5 | 269 | 2.97E-05 | 4.87E-06 |
| | Group 1 | 1.8 | 43494 | 3.38E-05 | 9.70E-07 |
| | Group 2 | | 56140 | 3.58E-05 | 9.70E-07 |
| | Group 3 | | 57727 | 3.58E-05 | 9.70E-07 |
| | | | 24466 | (Dry) 4.00E-05 | 9.70E-07 |

* These are performance assessment simulations, the 3.7 and 8.5 m/s runs recorded here were simulated with all other parameters identical to the other spherical Mill C simulations.

## E.2 Supplementary energy figures for the Chapter 7 simulations

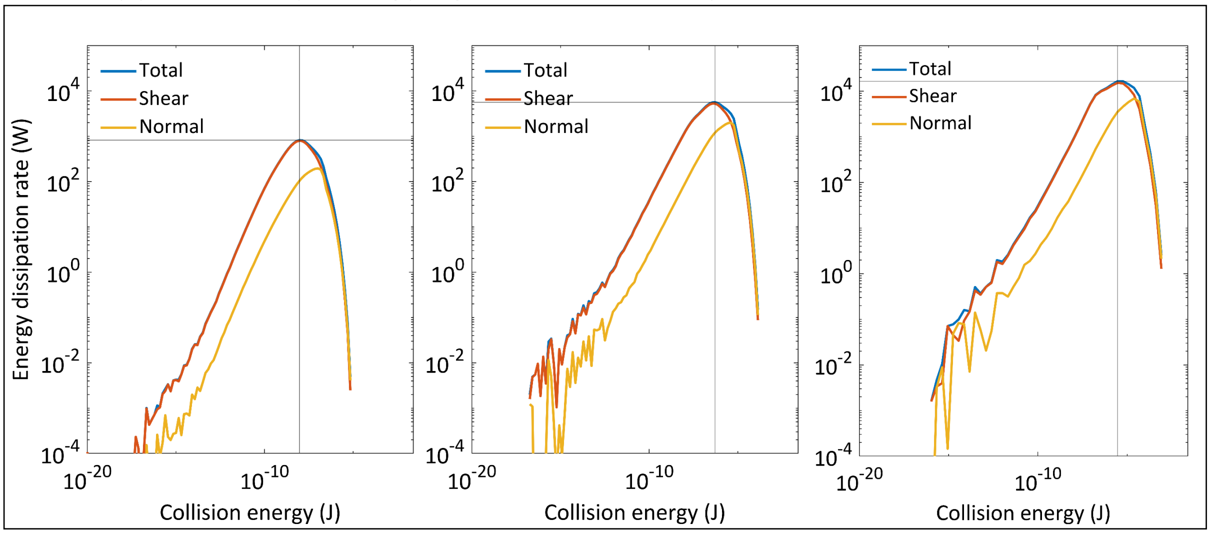

*Figure E.1: Total dissipation rate spectra over collision energy for low, medium and high media size experiments, respectively*

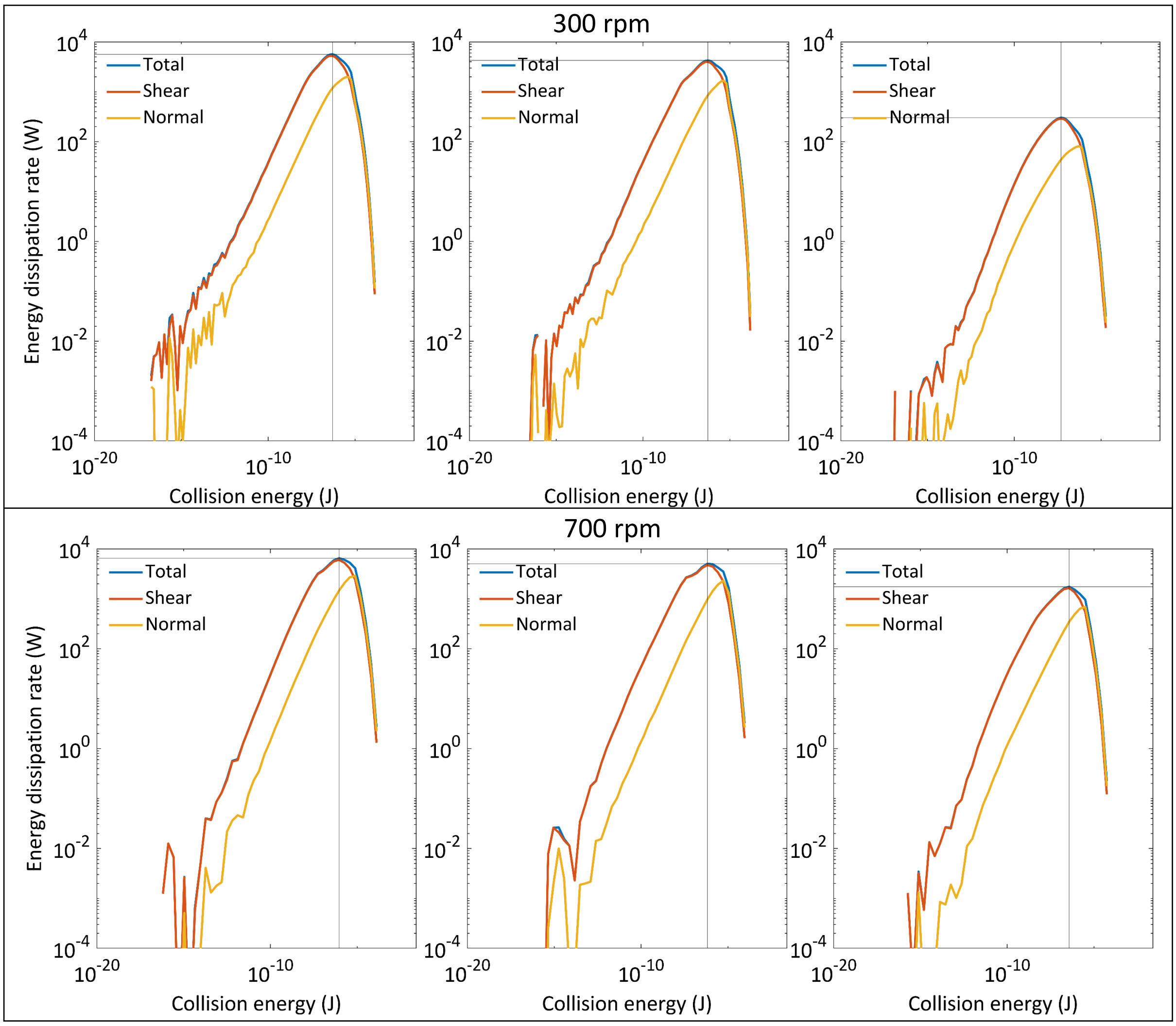

*Figure E.2: Total dissipation rate spectra over collision energy for low, medium and high media density experiments, respectively, at 300 and 700 rpm*

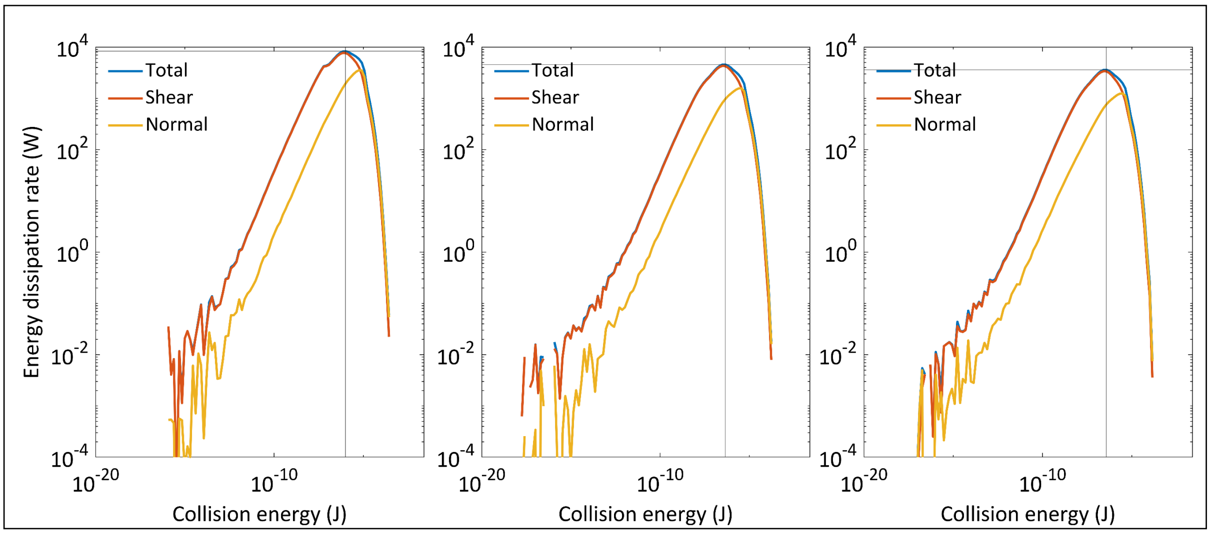

*Figure E.3: Total dissipation rate spectra over collision energy for low, medium and high slurry density experiments, respectively*

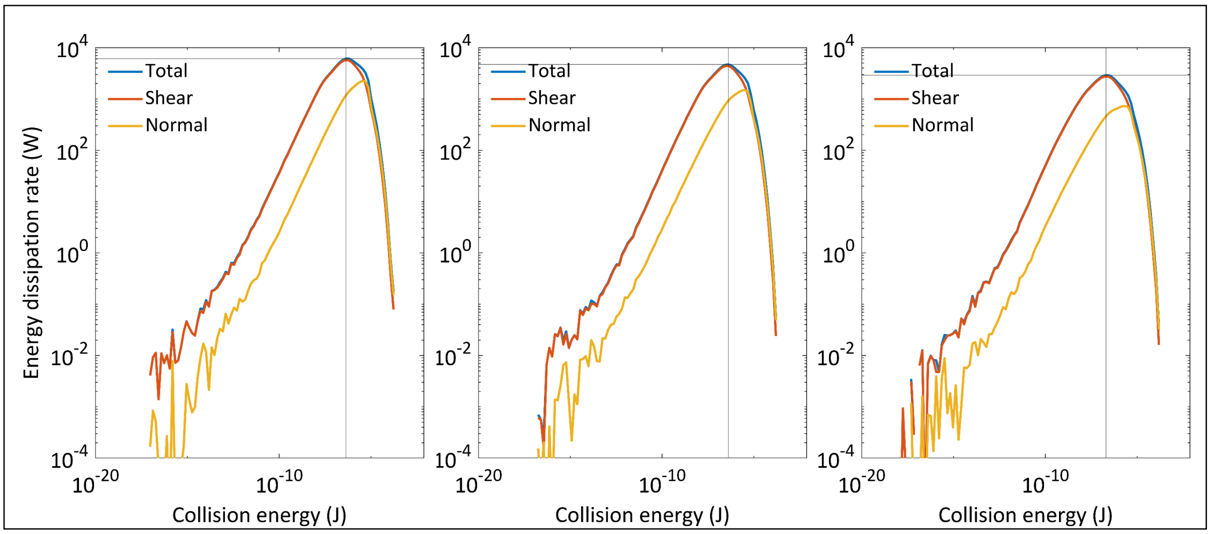

*Figure E.4: Total dissipation rate spectra over collision energy for low, medium and high slurry viscosity experiments, respectively*

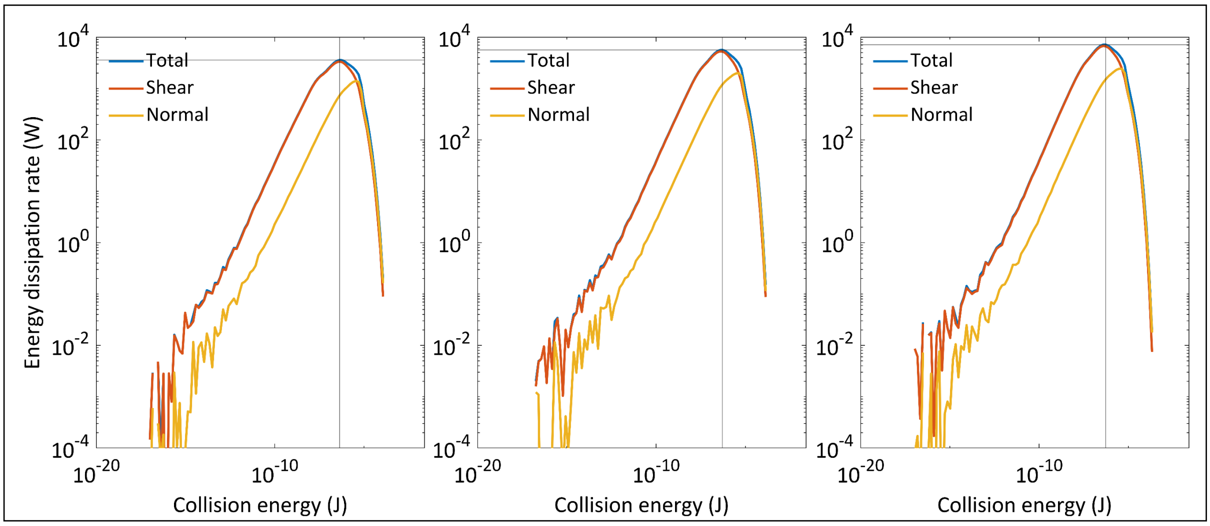

*Figure E.5: Total dissipation rate spectra over collision energy for low, medium and high media to slurry volume ratio experiments, respectively*

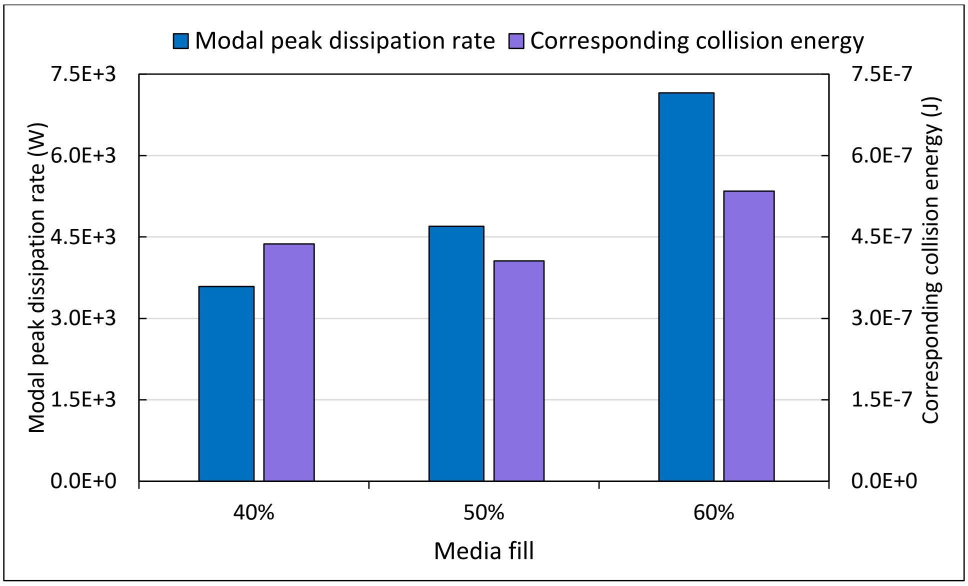

*Figure E.6: Raw modal peak dissipation rate and collision energy for the media fill simulations*

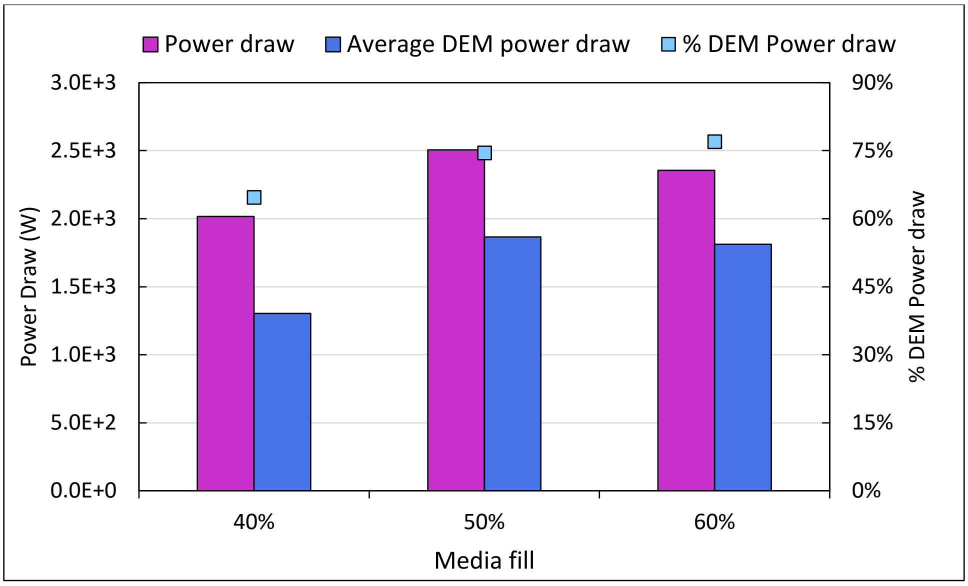

*Figure E.7: Raw total power draw and its DEM component for the media fill simulations*

## E.3 Reynolds and Froude number distributions

The Reynolds and Froude number distributions within each mill space are distributed similarly as shown in Figure E.8. The distributions are extremely positively skewed; therefore, the median is the most accurate measure of central tendency to use to represent the distribution.

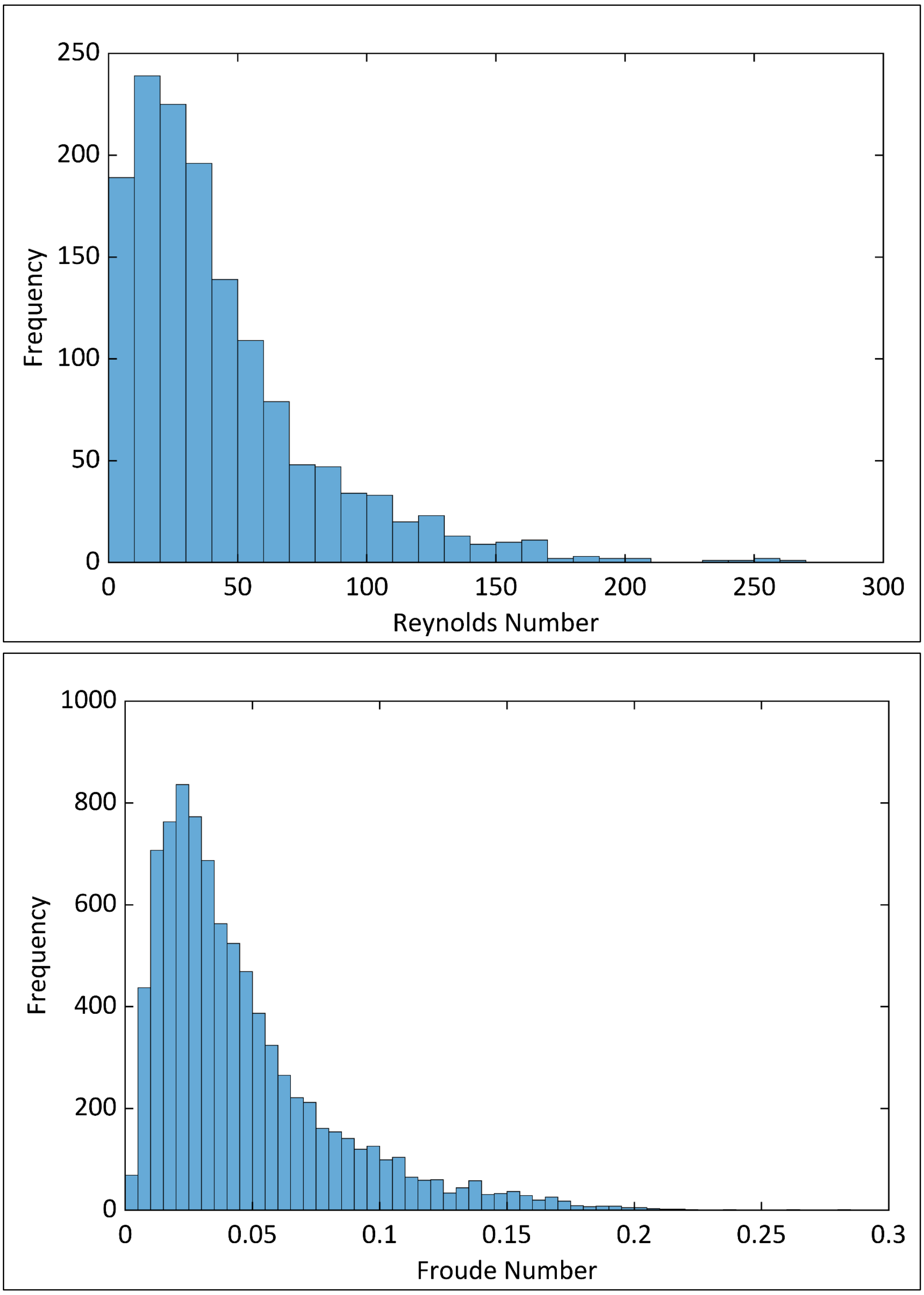

*Figure E.8: Raw Reynolds and Froude number distributions for Mill C at 1.8 m/s at 163 cs*

## E.4 Temporal distributions of the parameters that make up Reynolds number

The parameters that vary in the constitution of the Reynolds number are the relative velocity, solids fraction and fluid density. The fluid viscosity is constant due to the Newtonian flow regime and the DEM bodies are monodisperse.

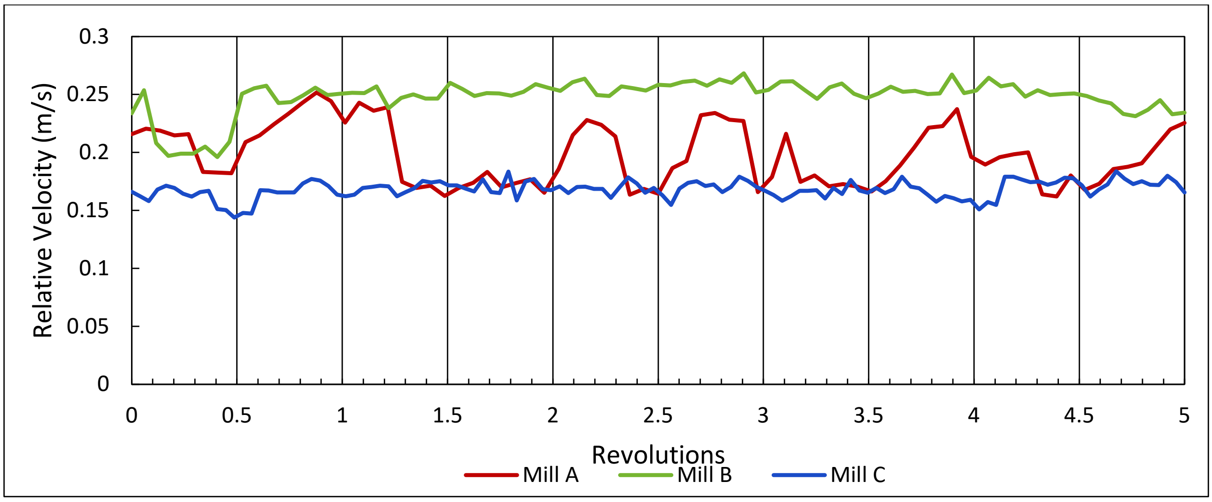

*Figure E.9: Median relative velocity profile for the 1.5 m/s tip speed*

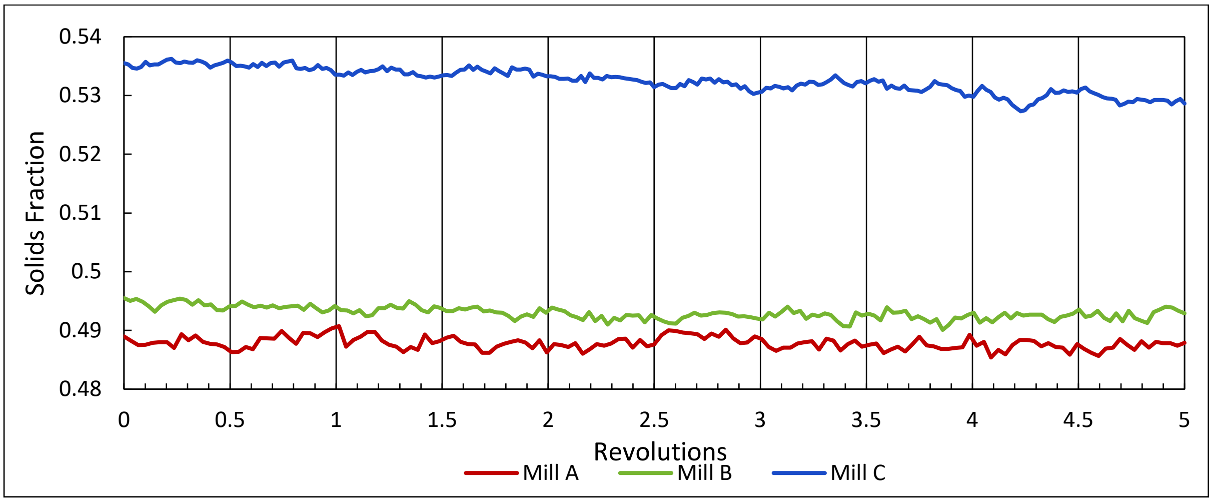

*Figure E.10: Median solids fraction profile for the 1.5 m/s tip speed*

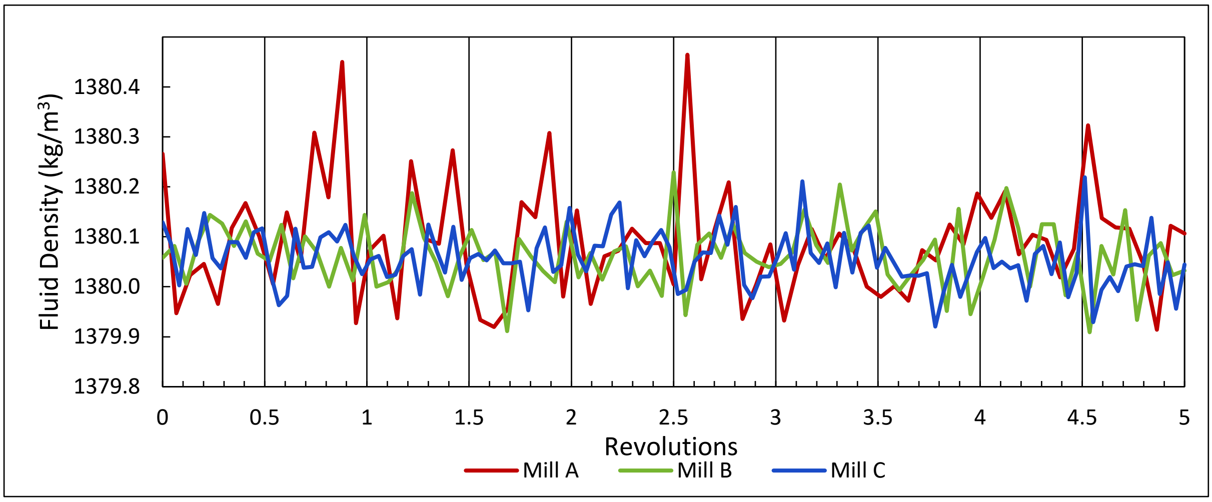

*Figure E.11: Median fluid density profile for the 1.5 m/s tip speed*

## E.5 Tables of raw values corresponding to figures in Chapter 8

The following tables consist of the values illustrated in these figures, Figure 8.17, Figure 8.24, Figure 8.25, Figure 8.26, respectively.

*Table E.2: Median Reynolds and Froude number data for all mill sizes at each of the tip speeds*

| | | Median Re | Median Fr | STDev.S Re | STDev.S Fr |
|---|---|---|---|---|---|
| 1.5 m/s | Mill A | 27 | 0.043 | 5.7998 | 0.0056 |
| | Mill B | 34 | 0.053 | 7.1438 | 0.0033 |
| | Mill C | 23 | 0.036 | 6.3189 | 0.0016 |
| 1.8 m/s | Mill A | 50 | 0.077 | 6.8116 | 0.0029 |
| | Mill B | 45 | 0.071 | 7.5485 | 0.0024 |
| | Mill C | 28 | 0.042 | 7.6356 | 0.0031 |
| 2.2 m/s | Mill A | 36 | 0.055 | 4.5131 | 0.0036 |
| | Mill B | 48 | 0.074 | 8.0165 | 0.0026 |
| | Mill C | 30 | 0.047 | 6.2490 | 0.0040 |

*Table E.3: Modal peak dissipation rate and corresponding collision energy data for all mill sizes at each of the tip speeds*

| | | Modal peak dissipation rate (W/m$^3$ fluid) | Corresponding collision energy (J/m$^3$ fluid) | STDev.S MP | STDev.S CE |
|---|---|---|---|---|---|
| 1.5 m/s | Mill A | 1.05E+06 | 1.24E-04 | 1.70E+05 | 2.44E-05 |
| | Mill B | 1.02E+06 | 7.74E-05 | 1.69E+05 | 1.16E-05 |
| | Mill C | 7.34E+05 | 2.43E-05 | 6.07E+04 | 2.59E-06 |
| 1.8 m/s | Mill A | 1.51E+06 | 2.88E-04 | 2.48E+05 | 4.48E-05 |
| | Mill B | 1.50E+06 | 1.19E-04 | 2.49E+05 | 3.08E-05 |
| | Mill C | 1.09E+06 | 4.13E-05 | 1.77E+05 | 1.00E-05 |
| 2.2 m/s | Mill A | 4.03E+06 | 4.38E-04 | 5.02E+05 | 6.91E-05 |
| | Mill B | 2.00E+06 | 2.07E-04 | 3.25E+05 | 2.48E-05 |
| | Mill C | 1.52E+06 | 7.17E-05 | 2.46E+05 | 1.52E-05 |

*Table E.4: Summary of power draw for all mill sizes at each tip speed*

| | | Total power draw (kW/m$^3$ fluid) | DEM power draw (kW/m$^3$ fluid) | SPH power draw (kW/m$^3$ fluid) |
|---|---|---|---|---|
| 1.5 m/s | Mill A | 375 | 275 | 101 |
| | Mill B | 343 | 251 | 91 |
| | Mill C | 221 | 172 | 49 |
| 1.8 m/s | Mill A | 558 | 410 | 148 |
| | Mill B | 524 | 405 | 120 |
| | Mill C | 309 | 229 | 80 |
| 2.2 m/s | Mill A | 792 | 531 | 262 |
| | Mill B | 753 | 548 | 206 |
| | Mill C | 454 | 362 | 92 |

*Table E.5: Summary of power draw for all mill sizes, in wet or dry operation, at 2.2 m/s*

| | | Total power draw (kW/m$^3$ fluid) | DEM power draw (kW/m$^3$ fluid) | SPH power draw (kW/m$^3$ fluid) |
|---|---|---|---|---|
| Mill A | Dry | 592 | | |
| | Wet | 789 | 524 | 265 |
| Mill B | Dry | 552 | | |
| | Wet | 735 | 536 | 199 |
| Mill C | Dry | 299 | | |
| | Wet | 452 | 352 | 100 |

## E.6 Supplementary tables and Dry DEM figures of Chapter 9

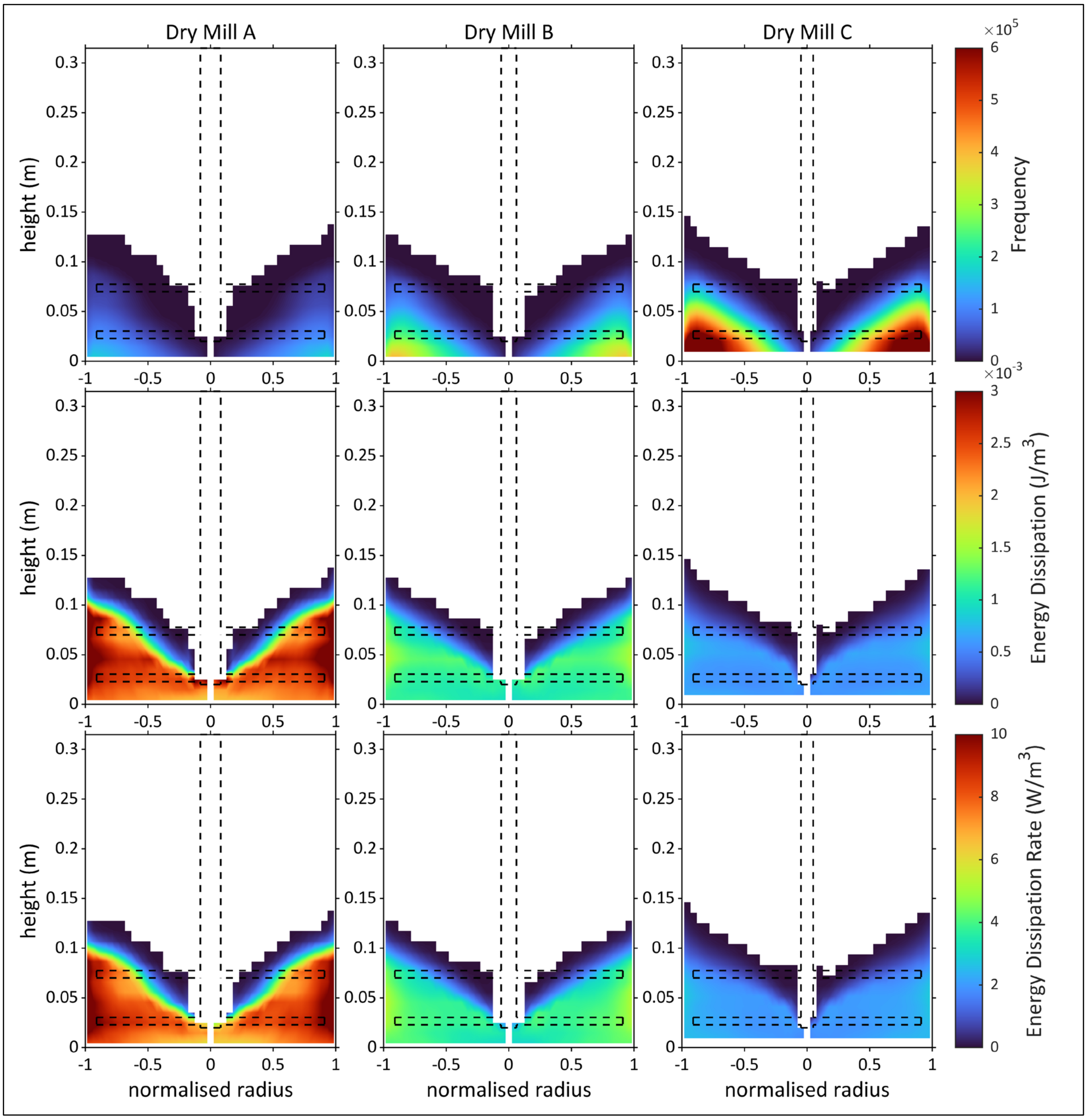

*Figure E.12: Frequency, energy dissipation and energy dissipation rate colourmaps for dry DEM simulations of Mill A, B and C of group 3 super quadrics*

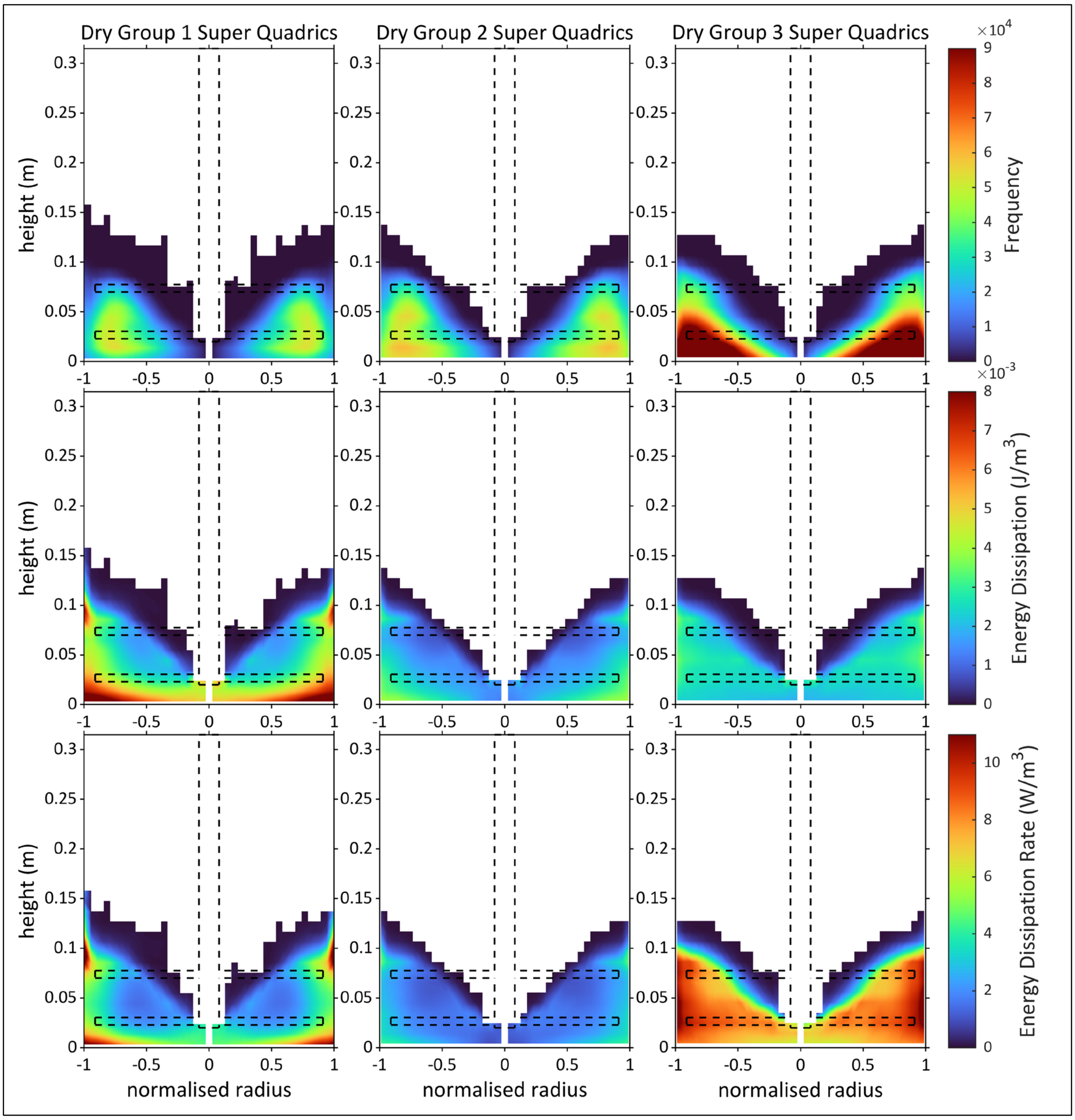

*Figure E.13: Frequency, energy dissipation and energy dissipation rate colourmaps for dry DEM simulations of Mill A of group 1,2 and 3 super quadrics*

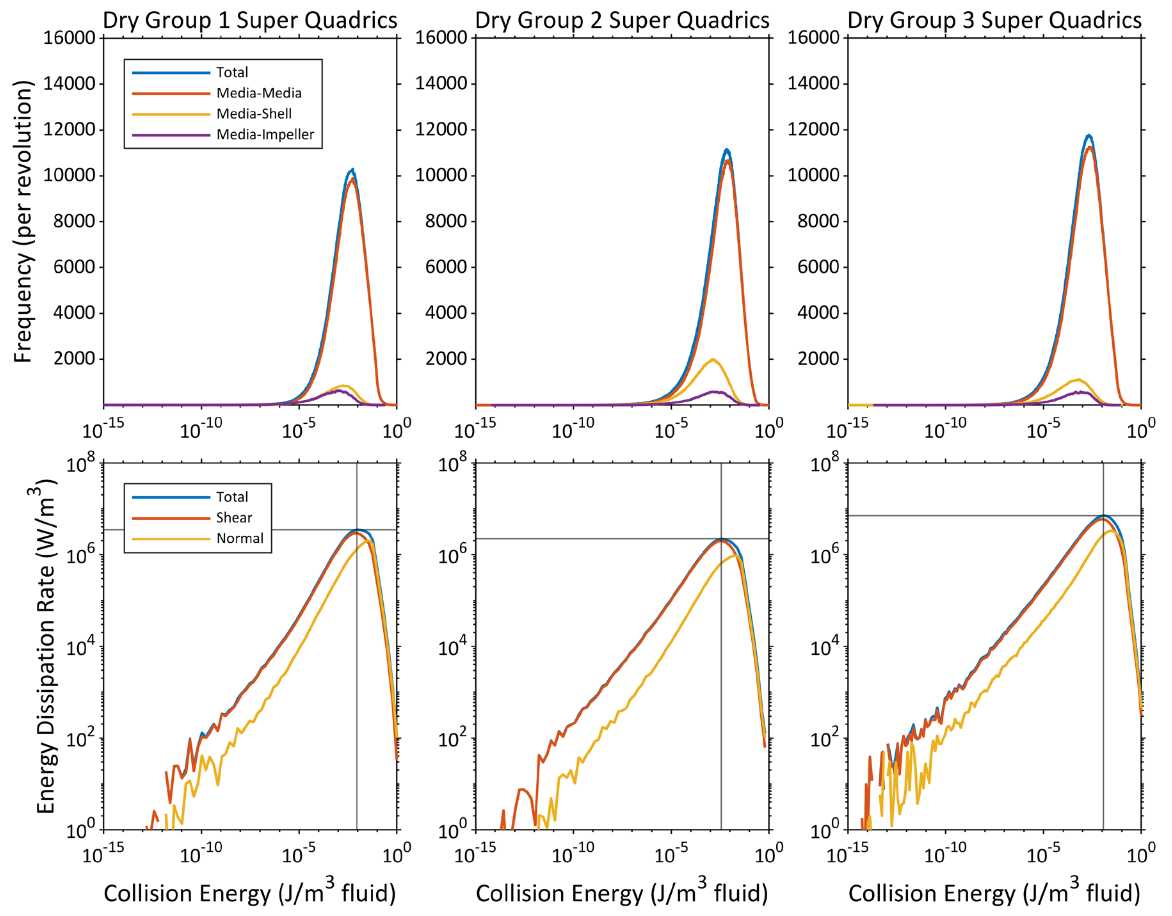

*Figure E.14: Collision frequency and energy dissipation rate spectra for the dry DEM simulations of Mill A for group 1, 2 and 3 super quadrics*

*Table E.6: Mean velocity data for all the media shape simulations*

| | | Mean Velocity(m/s) DEM-SPH | Mean Velocity(m/s) DEM only |
|---|---|---|---|
| Group 1 | Mill A | 0.668 | 0.713 |
| | Mill B | 0.643 | |
| | Mill C | 0.600 | |
| Group 2 | Mill A | 0.616 | 0.606 |
| | Mill B | 0.587 | |
| | Mill C | 0.534 | |
| Group 3 | Mill A | 0.573 | 0.545 |
| | Mill B | 0.544 | 0.500 |
| | Mill C | 0.508 | 0.467 |

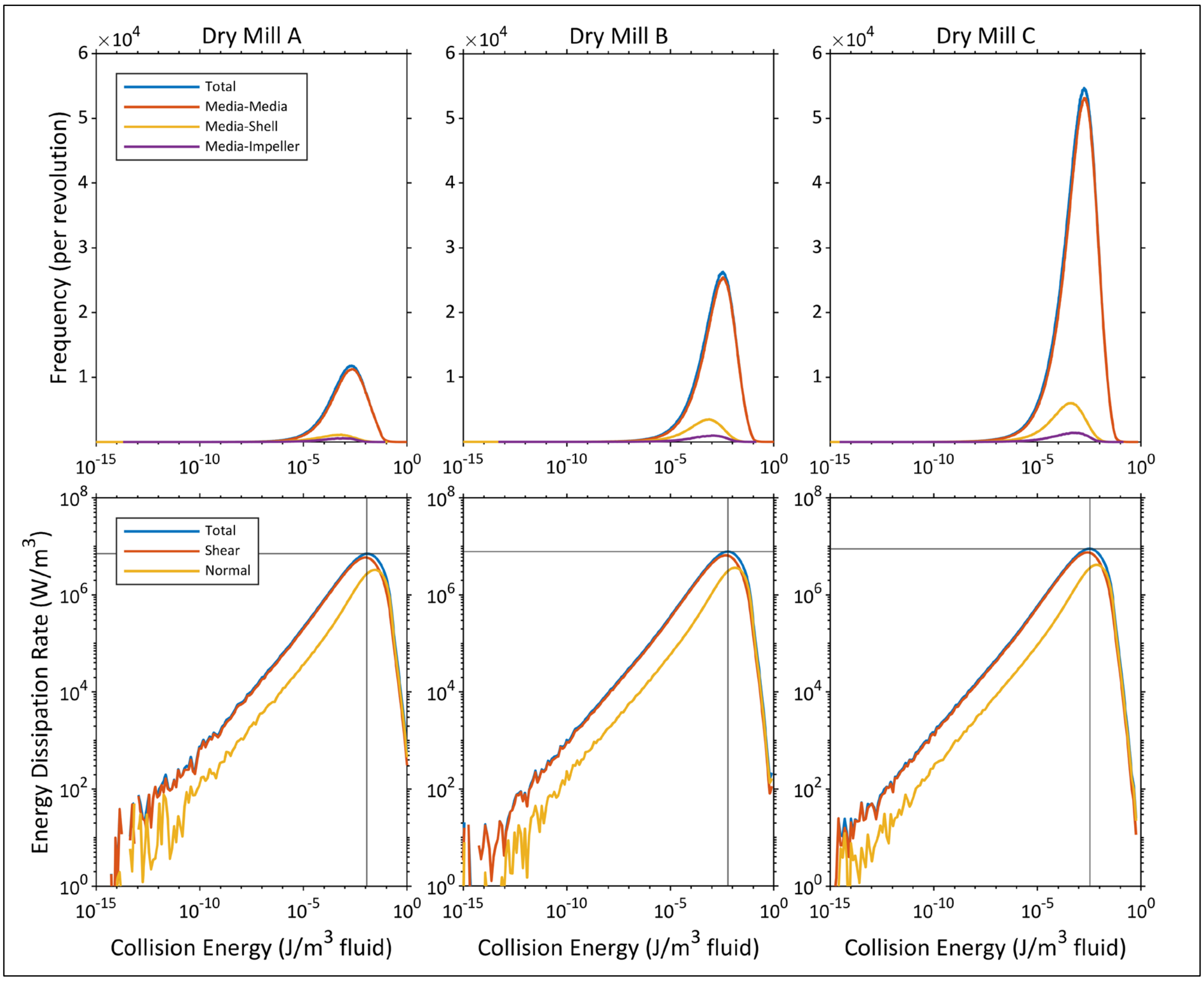

*Figure E.15: Collision frequency and energy dissipation rate spectra for the dry DEM simulations of Mill A, B and C*

*Table E.7: Median Reynolds and Froude number data for the media shape simulations*

| | | Median Re | Median Fr | STD Re | STD Fr |
|---|---|---|---|---|---|
| Group 1 | Mill A | 52 | 0.082 | 4.58 | 0.0071 |
| | Mill B | 44 | 0.070 | 4.78 | 0.0075 |
| | Mill C | 37 | 0.059 | 3.97 | 0.0062 |
| Group 2 | Mill A | 41 | 0.072 | 3.64 | 0.0066 |
| | Mill B | 35 | 0.062 | 1.37 | 0.0021 |
| | Mill C | 27 | 0.048 | 2.05 | 0.0036 |
| Group 3 | Mill A | 46 | 0.086 | 2.14 | 0.0036 |
| | Mill B | 38 | 0.070 | 3.00 | 0.0057 |
| | Mill C | 32 | 0.058 | 1.97 | 0.0037 |

*Table E.8: Modal peak and collision energy data for media shape simulations*

| | | Modal Peak Dissipation Rate (W/m³) | Corresponding Collision Energy (J/m³) | STD Modal Peak Dissipation Rate | STD Corresponding Collision Energy |
|---|---|---|---|---|---|
| Group 1 | Mill A | 3.00E+07 | 1.02E+00 | 2.29E+06 | 1.54E-01 |
| | Mill B | 2.32E+07 | 5.13E-01 | 1.43E+06 | 1.28E-01 |
| | Mill C | 1.55E+07 | 3.61E-01 | 4.55E+05 | 4.16E-02 |
| Group 2 | Mill A | 1.15E+07 | 6.11E-01 | 2.18E+05 | 2.25E-01 |
| | Mill B | 9.26E+06 | 2.48E-01 | 3.99E+05 | 5.13E-02 |
| | Mill C | 8.45E+06 | 1.89E-01 | 1.35E+06 | 3.60E-02 |
| Group 3 | Mill A | 2.22E+07 | 1.96E-02 | 3.15E+05 | 5.66E-03 |
| | Mill B | 1.55E+07 | 1.22E-02 | 7.91E+05 | 4.50E-03 |
| | Mill C | 1.63E+07 | 5.67E-03 | 1.11E+06 | 2.33E-03 |
| Dry Mill A (W) and (J) | Group 1 | 2.88E+04 | 9.17E-04 | 6.69E+02 | 6.25E-05 |
| | Group 2 | 1.06E+04 | 4.26E-04 | 5.63E+02 | 2.02E-04 |
| | Group 3 | 2.21E+04 | 4.64E-05 | 7.19E+02 | 1.38E-05 |
| Dry Group 3 (W) and (J) | Mill B | 2.71E+04 | 3.86E-05 | 1.21E+03 | 1.07E-05 |
| | Mill C | 4.86E+04 | 2.91E-05 | 8.44E+02 | 2.75E-06 |

*Table E.9: Power draw data for the wet media shape simulations*

| | | Total power draw (kW/m³) | DEM (kW/m³) | SPH (kW/m³) | % DEM |
|---|---|---|---|---|---|
| Group 1 | Mill A | 1114 | 918 | 195 | 82% |
| | Mill B | 818 | 692 | 127 | 85% |
| | Mill C | 556 | 496 | 60 | 89% |
| Group 2 | Mill A | 1135 | 930 | 205 | 82% |
| | Mill B | 784 | 664 | 120 | 85% |
| | Mill C | 632 | 542 | 90 | 86% |
| Group 3 | Mill A | 1249 | 1030 | 219 | 82% |
| | Mill B | 818 | 658 | 160 | 80% |
| | Mill C | 641 | 548 | 94 | 85% |

*Table E.10: Power draw data for the dry media shape simulations*

| | | Total power draw (W) |
|---|---|---|
| Group 1 | Mill A | 498 |
| Group 2 | Mill A | 541 |
| Group 3 | Mill A | 673 |
| | Mill B | 883 |
| | Mill C | 1272 |

*Eno y'enkomerero.*

*Mwebale nnyo okutuwa obudde.*